Polyvalent Glycan – Nanomaterials as Structural and Mechanistic Probes for Viral Receptor Proteins DC-SIGN and DC-SIGNR

Emma Charlotte Poole

Submitted in accordance with the requirements for the degree of
Doctor of Philosophy

The University of Leeds
School Of Chemistry

July 2019

The candidate confirms that the work submitted is her own, except where work which has formed part of jointly-authored publications has been included. The contribution of the candidate and the other authors to this work has been explicitly indicated below. The candidate confirms that appropriate credit has been given within the thesis where reference has been made to the work of others.

Synthesis included in Chapter 2 and the contents of Chapter 3 is based on work from the following publication:

Y. Guo, I. Nehlmeier, E. Poole, C. Sakonsinsiri, N. Hondow, A. Brown, Q. Li, J. Whitworth, Z. Li, A. Yu, R. Brydson, W. B. Turnbull, S. Pöhlmann and D. Zhou, *J. Am. Chem. Soc.*, 2017, **139**, 11833-11844.

"Emma Poole synthesised the cap-exchange ligands and produced the QDs as well as performed the apparent K_d determination studies. Inga Nehlmeier and Stefan Pöhlmann completed the Viral Inhibition studies outlined in this paper. Yuan Guo and Dejian Zhou wrote the manuscript."

In Memory of Yvonne Poole and Louise Prince
Two people lost way too soon…

I. Acknowledgements

I would like to thank Professor Dejian Zhou for his help and support throughout my PhD as well as providing an interdisciplinary project to fulfil my interests and also Dr Yuan Guo for assisting and introducing the biological aspects of my project. I would also like to thank EPSRC for providing me the funding for my doctoral training as well as the University of Leeds.

I would like to thank our collaborators: Professor Bruce Turnbull, Dr Chadamas Sakonsinsiri (for providing the synthetic protocols of mannose sugars within this project), Inga Nehlmeier, Professor Stefan Pöhlmann (our collaborators in Germany for the work they have done on the viral inhibition assays) and Dr Nicole Hondow and the team at Leeds Electron Microscopy and Spectroscopy centre (LEMAS) (for providing the TEM images throughout this project). I would also like to thank the technicians within the School of Chemistry for their help and support and training of various equipment Martin, Simon and Tanya.

A special mention goes to the people of the Zhou research group that have I have got to know throughout my PhD. Without them I would not learnt how to be as effective in the laboratory and had the confidence to talk about my research. Thanks to Welli for assisting with my cap-exchange methods and Yuanyuan for helping with synthesis of the sugar materials. Thanks to the current members of the group for being there when I have had my down times through writing, , or by hitting up the pub for an impromptu lunch or a change of office topic when I was feeling a little worse for wear, Liz, Darshita and Akshath. Also the small distractions of Jamie teaching Zeyang a new daily thing he didn’t know. Thanks to Rahman for the delicious traditional Baklava that helped me treat myself as I wrote. Finally I want to thank the guy that has supported me through so much, as we were basically the group together for both our PhDs, I don’t think I would have got through it with you, Anjo.

I would also like to thank all the wonderful friends that I have made during my time at Leeds, from the rest of the inorganic offices, my second office for general distraction and also delicious baked goods, as well as providing a life outside the laboratory. The true lunch crew, Frances, Kevin, Chris, Kay, Becky and Tom for the pleasure of just eating lunch

away from work and fighting the undergraduates for the best tables in the CCL. Running off for a short break with Ed, Sam and Zeyang to make sure that I catch them all in Pokemon go. I also want to thank the people of Leeds University Dancesport Society for giving balance to the hectic life of a PhD student by providing a way of escaping and different aspects of drama to laugh and cry about. The amount of friends that I will hold for life from the society from different backgrounds is something I will always look back on. A special thanks to two people who a normal conversation goes, "do you want to go to the pub tonight… yeah go on then", Katie and Chrissi, always the way to relax after a long day.

The few remaining people to thank for me are my highly supportive family, my dad, and Grandparents. I have always had a passion for making a difference with the research work that I have done as it holds a special place in my heart after the loss of my mum as a child. They have supported me through it and have always been close enough away to meet up when I've had a bad week or just simply want to go home for the weekend. Or even simply just wanted my washing ironing for once, thanks for that grandma you helped a girl out. They may not understand anything of what I do but they couldn't be more supportive.

II. Abstract

Multivalent protein-carbohydrate interactions are crucial in many aspects of biology as they initiate the first contact between pathogens and host cells which ultimately leads to infection. Developing an understanding of the structures and binding modes used for these interactions will help develop specific, potent multivalent glycan inhibitors that can block such interactions, thereby preventing infection. This work focuses on two closely related tetrameric C-type lectins, DC-SIGN and DC-SIGNR, collectively abbreviated as DC-SIGN/R. These proteins are known to bind multivalently to multiple glycans, specifically mannose, found within the surface glycoproteins of many viruses, such as human immunodeficiency virus (HIV), Ebola Virus and West Nile Virus, and facilitate their infections. Despite significant research over the past 20 years, knowledge on the binding characteristics and structural mechanisms of these proteins remains limited because their tetrameric structures remain unknown. This project aims to develop novel glyconanoparticle probes to establish a valid structural model of the binding domains with these proteins and to reveal the mechanisms behind the multivalent glycan – DC-SIGN/R interactions. This objective has been achieved through the development of two sensitive fluorescent based assays, Förster resonance energy transfer (FRET) and fluorescence quenching, using polyvalent glycan coated quantum dots (QDs) and gold nanoparticles (AuNPs) by exploiting their unique strong fluorescence and fluorescence quenching properties respectively. In particular, the biocompatible, low cytotoxic AuNP-saccharide conjugates make them potentially suitable for in vivo studies in the future.

This thesis has specifically designed a series of multifunctional glycan ligands for nanoparticle surface coating. Each ligand consists of three unique functional domains, a dihydrolipoic acid (DHLA) for strong nanoparticle capping, an oligo(ethylene glycol, EG_n) linker for promoting hydrophilicity and reducing non-specific adsorptions, and a terminal mannose sugar moiety for specific DC-SIGN/R binding. Both the monosaccharide and disaccharide forms of a mannose sugar were investigated. Our group has previously found that the mono-mannose capped QDs have much weaker affinity for DC-SIGNR than that of DC-SIGN, suggesting that the binding sites in DC-SIGN/R orient differently, although their exact binding modes remain unclear as DC-SIGNR binding is too weak to be distinguished from monovalent CRD. In this thesis, by displaying the dimannose ligands on the QD surface to increase monovalent binding affinity and developing a novel multimodal readout strategy consisting of FRET and TEM imaging, the exact binding modes of DC-SIGN/R have been revealed. The four carbohydrate recognition domains in

DC-SIGN face in the same direction and bind tetravalently to a single glycan-QD; while those in DC-SIGNR are split into a pair of back-to-back dimers and bind bis-divalently with two different saccharides-QDs. Furthermore, QD-saccharides capped with two different ligand series have been prepared and their binding affinities, K_ds, with DC-SIGN/R have been investigated. Initial studies using QD-EG_n- Saccharide (where n = 3 or 11, Saccharide = α-Man and Man-α-1,2-Man) to study their DC-SIGN/R interactions revealed that dilution of the surface saccharide ligand using an inert zwitterionic ligand resulted in a decrease in binding. So a second dendritic glycan ligand series, DHLA-(EG_n-Glycan)$_m$, (where n = 1 or 2; m =1, 2, or 3 and Glycan = α-Man and Man-α-1,2-Man) was synthesised to further increase the nanoparticle surface glycan density to investigate how this affects DC-SIGN/R binding.

Significant results were observed using these ligand series and the different scaffold materials. In general, reducing the ethylene glycol linker length and using DiMan ligand capped nanoparticles led to enhanced binding affinity with DC-SIGN. For example, DC-SIGN binds more strongly to QD-EG_3-DiMan than QD-EG_{11}-DiMan (K_d: 0.61 ± 0.07 v.s. 2.1 ± 0.5 nM) and its monosaccharide equivalent, QD-EG_3-Man (K_d = 35 ± 7 nM). Interestingly, further increasing the glycan density on the nanoparticle surface using dendritic sugar ligands weakened their binding with DC-SIGN but enhanced the binding with DC-SIGNR. The K_d values for DC-SIGN binding to QD-EG_2-DiMan and QD-(EG-DiMan)$_3$ were 1.7 ± 0.1 and 1.59 ± 0.2 nM, while those for DC-SIGNR were 1.59 ± 0.2 and 0.49 ± 0.6 nM respectively. The same binding affinity trend of was also observed for AuNPs capped with such glycan ligands, which gave one of the smallest reported K_d values for DC-SIGN/R interactions. Finally the potency of these materials in inhibiting DC-SIGN mediated Ebola virus glycoprotein driven viral infection of target cells were investigated, giving impressively low IC_{50} values, e.g. 0.7 ± 0.2 nM for QD-EG_3-DiMan and 0.2 ± 0.04 nM for AuNP-EG_2-DiMan. These IC_{50} values make these materials to be the most potent glyco-nanoparticle inhibitors.

III. Table Of Contents

Chapter 4 105

IV. List of Schemes

V. List of Tables

VI. List of Figures

VII. List of Abbreviations

ATP	Adenosine Triphosphate
AuNP	Gold Nanoparticle
BSA	Bovine Albumin Serum
^{13}C-NMR	Carbon-13 Nuclear Magnetic Resonance
CDL	Chelating Dendritic Ligand
$CHCl_3$	Chloroform
CRD	Carbohydrate Recognition Domain
DCC	*N,N'*-Dicyclohexylcarbodiimde
DCM	Dichloromethane
DC-SIGN	Dendritic-cell-specific Intercellular Adhesion Molecule
DC-SIGNR	DC-SIGN Related Receptor
D_h	Hydrodynamic Size
DHLA	Dihydrolipoic Acid
DiMan	Disaccharide (Mannose-α1,2-mannose)
DLS	Dynamic Light Scattering
DMAP	4-Dimethylaminopyridine
DMEM	Dulbecco's Modified Eagle Medium
DMF	Dimethylformamide
DMSO	Dimethyl Sulfoxide
DTT	Dithiothreitol
EBOV-GP	Ebola Virus Glycoprotein
EDTA	Ethylenediaminetetraacetic acid
EG	Ethylene Glycol
EtOAc	Ethyl Acetate
EtOH	Ethanol
FBS	Fetal Bovine Serum
FRET	Förster/ Fluorescence Resonance Energy Transfer
FWHM	Full width at Half Maximum
IC_{50}	Half Maximal Inhibitory Concentration
IR	Infrared Spectroscopy
LA	Lipoic Acid
^{13}H-NMR	Proton Nuclear Magnetic Resonance
HEPES	4-(2-hydroxyethyl)-1-piperazineethanesulfonic acid

HIV	Human Immunodeficiency Virus
Man	Mannose
MeOH	Methanol
$MgSO_4$	Magnesium Sulphate
MLV	Murine Leukemia Virus
MS	Mass Spectrometry
MWCO	Molecular Weight Cut Off
Na_2CO_3	Sodium Carbonate
$NaHCO_3$	Sodium Hydrogen Carbonate
Na_2SO_4	Sodium Sulphate
NC	Nanocrystal
NP	Nanoparticle
pcDNA	Empty Plasmid
PEG	Poly (ethylene glycol)
QD	Quantum Dot
QY	Quantum Yield
PPh_3	Triphenylphosphine
Rf	Retention Factor
RT	Room Temperature
SET	Surface Energy Transfer
STEM	Scanning Transition Electron Microscopy
TBTA	Tris((1-benzyl-4-triazolyl)methyl)amine
TCEP	*Tris* (2-carboxyethyl) phosphine
TEM	Transition Electron Microscopy
THF	Tetrahydrofuran
TLC	Thin Layer Chromatography
TMAH	Tetramethylammonium hydroxide
TOPO	Trioctylphophine oxide
UV/Vis	Ultra-Violet/ Visible Light Spectrometry
VSV-G	Vesicular Stomatitis Virus Glycoprotein
WT	Wild-type
XPS	X-Ray Photoelectron Spectroscopy
ZW	Zwitterion

Chapter 1

Introduction

The field of nanotechnology is a mixture of science and engineering which is dedicated to working with materials which range in a size of 1 – 100 nm. [1] Nanotechnology simply refers to the technology which is used at a nanoscale and has wide applications in the real world. Nanoparticles are unique materials and they possess many features which differ significantly from those of larger scales.[2] Some of these properties include quantum size effects and large surface to volume ratios.

1.1 Quantum Dots

Over the past two decades, fluorescence semiconductor nanocrystals, also known as quantum dots, QDs, have been a significant research focus due to their multiple advantageous properties, which include size-tuneable emission spectra, broad absorption spectra, high quantum yield, easily achievable large Stokes shift and a great resistance to photo-bleaching.[3] Furthermore QDs, depending on size, can be twenty times brighter and one hundred times more stable against photobleaching in comparison to organic dyes, as reported by Chan *et al.*.[4] QDs have been further developed and used for mapping and imaging biological tissues, cells and live animals. They have been widely used for biosensing and bio-diagnositics applications including immunoassays, specific sensing/detection of both small and macromolecule targets and multiplex optical barcoding.[5] Synthesis of QDs can be achieved in many different ways using a wide range of materials. QDs consist of highly crystalline inorganic colloidal semiconductor particles. Semiconductors made from groups 2 and 6 or 3 and 5 elements are often used to synthesise QDs. [6] As the particles sizes are reduced to physical dimensions smaller than the exciton Bohr radius R,[7] the mean distance that separates an electron-hole pair, strong confinement of exciton is observed, turning the nanoparticle into a QD. R can be calculated by using (**Eq. 1**) below:

$$R = R_H \times \varepsilon \times \frac{m_0}{\mu} \qquad \textbf{(Eq. 1)}$$

Where R_H is the Bohr radius of a hydrogen atom, ε is the dielectric constant, m_0 is the resting weight of an electron and μ is the reduced mass of the exciton.

The properties of QDs are dominated by quantum confinement in three dimensions, as their sizes become smaller than the exciton Bohr radii, typically 1 – 50 nm for different semiconductor materials.[4] This quantum confinement effect is observed when the size of the particle decreases into the nanoscale causing the widening of the band gap as a result of the energy spectrum becoming discrete for that material meaning it becomes numerical and categorical. [8] This effect in relation to band gap is shown in **Figure 1.1.1**. The optical and spectroscopic properties expressed by QDs are determined by their effective bandgap, where the smaller the size of the particle the bigger the bandgap.[9]

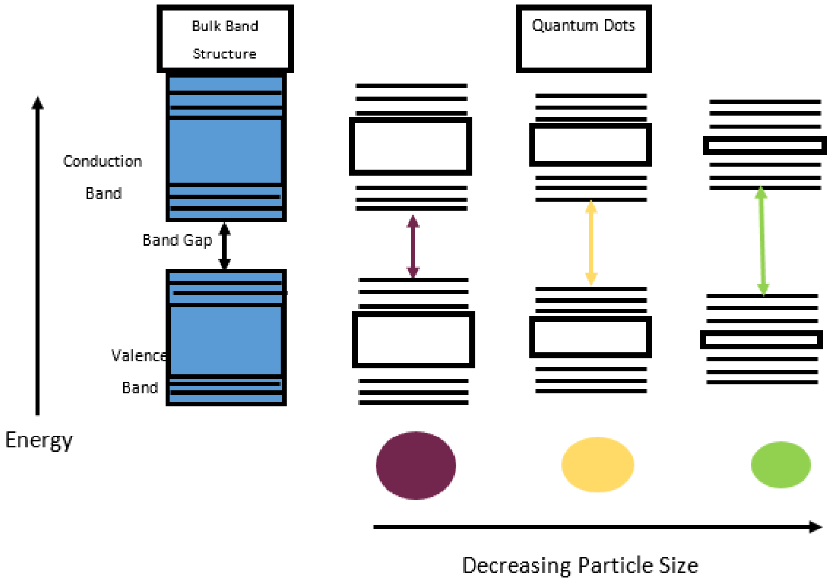

Figure 1.1.1: A Schematic showing the quantum confinement effect observed for QDs and the resulting effects on band gap size and band gap energy as a change in particle size is witnessed.

1.1.1 Quantum Dots as Fluorophores

Due to their size-dependent bandgap structure, QDs are ideal fluorophores, as their emitting energy matches the bandgaps (**Eq. 2**). The emission wavelength can be tuned by manipulation of the particle size through the following relationship.[10]

$$E_m = Bandgap \qquad \textbf{(Eq. 2)}$$

As a result of quantum confinement, QDs possess a broad absorption and narrow symmetric emission as shown in **Figure 1.1.2**. This means that a single wavelength can excite a number of different sized QDs simultaneously to exhibit an extensive range of coloured crystals, as shown below in **Figure 1.1.3**. QDs can be excited to any wavelength as long as it is shorter than the emission peak wavelength.[11] The following equation (**Eq. 3**) describes the rough relationship between the bang gap of QD and their size in relation to quantum confinement:

$$E_{QD} = E_B + \frac{h^2}{[8\mu D^2]} \qquad \textbf{(Eq. 3)}$$

Where E_{QD} is the band gap of the QD, E_B is the band gap of the bulk material, h is Plancks constant, µ is the reduced mass of the exciton and D is the diameter of the QD. The fluorescent properties of QDs can be further manipulated by coating the QD with a material that possesses a larger bandgap to create a core shell structure to enhance the quantum confinement effects. Furthermore, capping the QD with organic ligands such as PEGylated compounds can also be done to trap any surface defects causing fluorescence inconsistencies. QDs show a high quantum yield, ranging from 40% - 100% another useful advantageous property for being a good fluorophore.[6] The fluorescence properties of QDs has opened up many areas of research, for example, QD based solar cells and light emitting diodes (LEDs), [12] and also QDs can be used as labelling reagents for biological applications. [4,11]

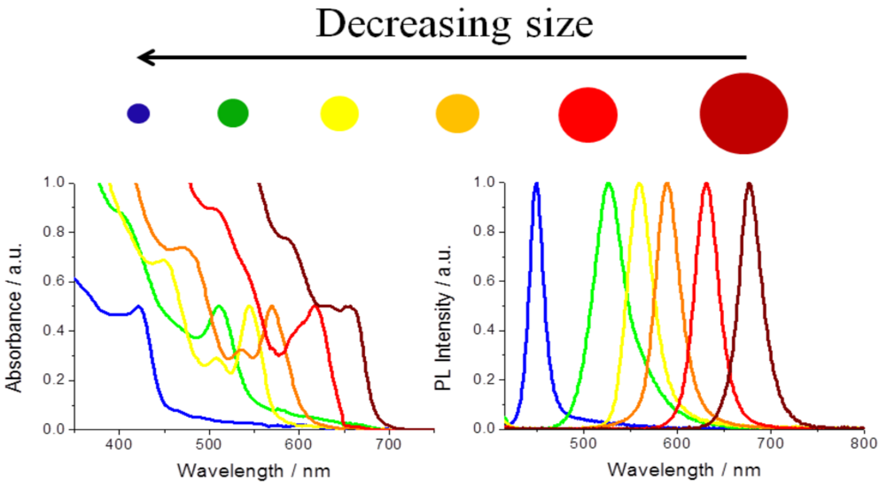

Figure 1.1.2: A schematic showing the absorption spectra and emission spectra for differing QDs as a decrease in particle size occurs. Reprinted from reference[13]

Figure 1.1.3: Ten easily distinguishable emission colours of (CdSe)ZnS quantum dots ranging from blue to red, with emissions located at 443, 473, 481, 500, 518, 543, 565, 587, 610 and 655 nm respectively excited by a single light source. Reprinted from reference.[10]

1.1.1.1 Core Shell QDs

Conventional core only QDs have limited stability and relatively low quantum yield. In order to improve these optical properties of simple QDs the core is coated with a shell of a higher bandgap material to form a core-shell structure, such as CdSe/ZnS.[14] An extensive review on core-shell QDs has been published by Chaudhuri *et al.,* highlighting some of their key properties and the wide range of practical uses.[15] The presence of a flexible band gap between the two materials, as well as the photoluminescence properties are tuned in relation to the size of the QD making these materials of great interest. An advantage to using core-shell materials is that coating the inorganic fluorescent core with a higher bandgap shell can increase its quantum yield via the removal of surface defects.[6] **Figure 1.1.4** below shows the transmission emission microscopy, TEM, images of two types of core only (e.g. CdTe, CdSe) and two types of core-shell (CdTe/CdSe and CdSe/ZnTe) QDs. A clearly larger particle size can be observed for those containing a core shell structure.

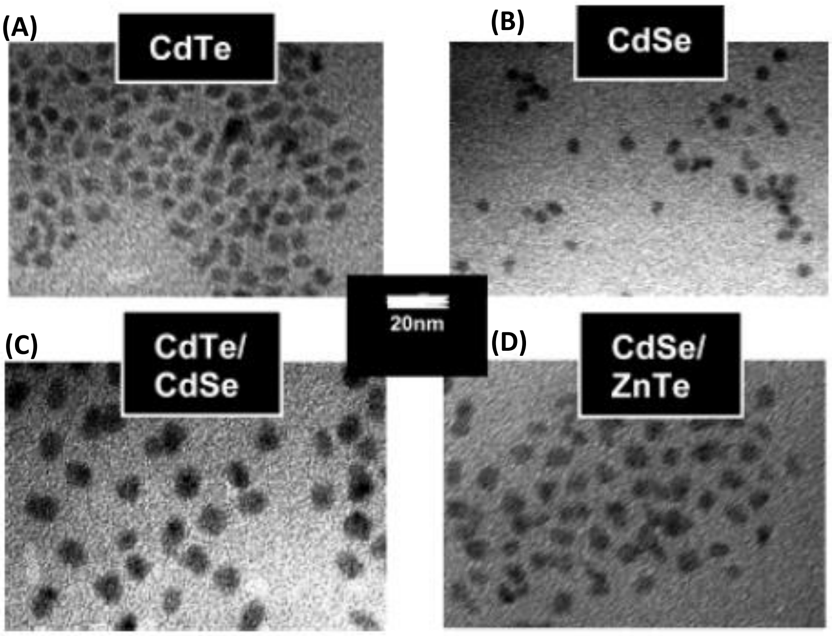

Figure 1.1.4: Bright field TEM image of core and core-shell QDs. (**A**) 32 Å radius CdTe QD, (**B**) 22 Å radius CdSe QD, (**C**) 32 Å radius core with 11 Å shell CdTe/CdSe QD and (**D**) 22 Å radius core with 18 Å shell CdSe/ZnTe QD. Reprinted from reference.[14]

Despite multiple advantages of QD fluorophores, one disadvantage observed is the phenomenon known as "blinking". Both Chan *et al.*[4] and Stanisavljevic *et al.* have reported this.[6] "Blinking" is a process in which a single QD loses its fluorescence and then regains it intermittently. An apparent minor flaw, this fluorescent change is seen to switch between on and off in an unpredictable time scale ranging from sub-milliseconds to an hour. This affects the results in that sample saturation occurs during the off time which ultimately reduces sample brightness. It's more critical for long time tracking as the effect becomes more apparent. Currently the dark state of the materials is untraceable. This problem can be overcome using a range of methods but is most commonly corrected by coating the surfaces with short thiol chains or a thick-multilayer shell [16]

1.1.2 Synthesis of Quantum Dots

QDs synthesis was first published by Murray *et al*. [17] it requires pyrolysis of an organometallic complex through injection into hot coordinating solvent to produce high-quality, nearly monodisperse CdS, CeSe and CdTe NCs. **Figure 1.1.5(A)** shows a TEM image of the NCs produced. The difference between NCs and a QD is that NCs don't exhibit fluorescence. The QDs exhibit sharp adsorption and emission features at room temperature.[17] Hines *et al.* [18] presented a new method for synthesising core-shell QDs. Starting again with an organometallic starting material but uses a two-step-single-flask method, involving firstly producing the core and then adding a zinc and sulphur solution to overcoat the core. **Figure 1.1.5(B)** shows a TEM image of the particles synthesised in this method. The advantage of this method over the previous pyrolysis method is that a smaller amount of NCs can be produced over a faster turnover time, thus more batches of QDs (in small quantities) can be made over the same time period. [18]

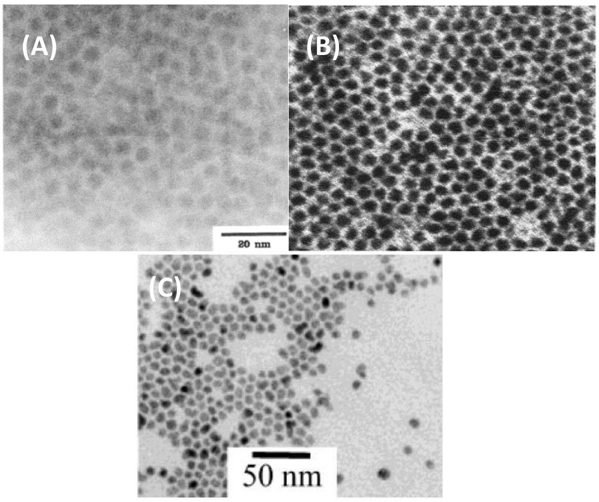

Figure 1.1.5: TEM picture of a range of different (CdSe)ZnS nanocrystals that have been synthesised in a range of different ways, (A) Murray et al. [17] synthesised these using pyrolysis of an organometallic, (B) Hines et al. [18] synthesised these using a two-step single flask method with organometallic starting material and (C) Peng et al. [19] synthesised using a CdO starting material. All reprinted from corresponding references.

A newer method by Peng *et al.* [19] shows the synthesis of QDs without the need for the organometallic starting material. Instead a one-pot synthesis is used, starting with an air-stable cadmium precursor, cadmium oxide, CdO. They reported that this synthetic method worked significantly better than other strategies reported. The advantages are that the results are more reproducible, the method itself is easier and also has great potential to be scaled up for industrial production.[19] QDs prepared in this manner can be seen in the TEM image above, **Figure 1.1.5(C)**. Peng *et al.* identified that loading CdO, trioctylphosphine oxide, TOPO, and either the ligand hexylphosphonic acid or tetradecylphosphonic acid produced a homeogenous solution in which the non-metal precursors could be added to yield high quality CdX QDs (where X=S, Te or Se).[19]

An important aspect to consider in the synthesis of QDs is whether they are being used for biological applications, as for this purpose the QDs must be hydrophilic and water-soluble.[11] This is determined by the type of ligand used during further modifications. Since most high quality QDs are prepared by the organometallic route, they are naturally coated with hydrophobic ligands and therefore water-insoluble. Previously reported methods of making QDs hydrophilic and water-soluble involve the use of PEGylated phospholipid or amphiphilic polymer encapsulation, however the resulting QDs have relatively large hydrodynamic sizes that can limit their applications.[9] One way to produce compact, water-soluble QDs is to simply displace their original hydrophobic ligands with hydrophilic ones such as dithiothreitol,[20] dihyrolipoic acid,[21] oligomeric phosphines,[22] peptides[23] and cross-linked dendrons etc.[24] Also the addition of a silica coating is another way to produce water-soluble QDs and further modifications with different functionalities.[25] The methods of producing hydrophilic QDs are shown in **Figure 1.1.6**.

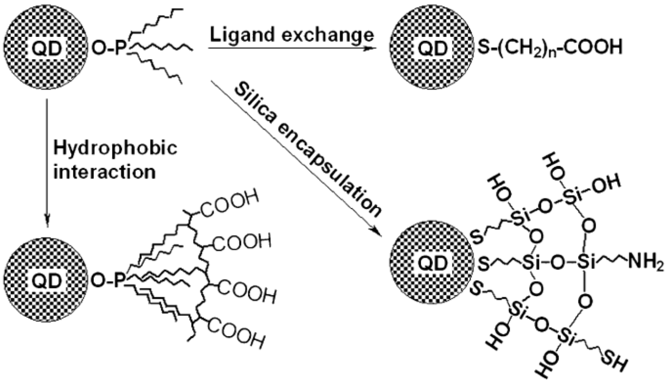

Figure 1.1.6: QD water solubilisation strategies including ligand interaction, hydrophobic interaction and silica encapsulation. Reprinted from reference. [25]

1.1.3 Quantum Dots Bioconjugates

More research is being carried out into the use of QDs as bioconjugates in a plethora of different applications because of their incredible optical properties, which make them outstanding fluorescence probes for long term intracellular imaging and tracking. In comparison to organic fluorescent dyes, QDs do not have the problems of pH dependent fluorescence, a high susceptibility to photobleaching and a narrow excitation with broad emission.[26] Many publications have used a range of different QD-bioconjugates including: QD-peptide conjugates[3], QD-protein conjugates[27], QD-DNA conjugates[28], QD-antibody conjugates[29] and QD-enzyme conjugates.[30] The major challenge with these materials is their safe removal from the body after potential in vivo applications. A targeted delivery is often needed to consider how the QD will pass through the cell membranes and become internalized within the cell. A simple solution by Derfus *et al.*[31] is to conjugate QDs with cell penetrating peptides. The removal of these conjugates must then not casue any adverse effects on cells. One major problem is that most QDs contain toxic cadmium, after being broken down the leakage of the cadmium ions can casue major toxic effects on cells caused by the oxidation of CdSe either by air or UV light.[9] The use of a core shell structure can reduce cadmium oxidation but not completely stop it. Further research by Derfus *et al.* shows that QD toxicity is strongly related to the processing parameters during synthesis, exposure to UV light and the surface coatings.[32]

Two major approaches to produce QD-bioconjugates have included cross-linking chemistry and direct linkage to the QD surface via functional interactions.[33] Although QD-bioconjugate synthetic methods are reported, a major challenge in cellular application of these materials, as reported by Derfus *et al.*, is the lack of a delivery system for intra-cellular detection, which would allow us to inject cells with these markers and get real-time results.[31] Different forms of delivery systems for cell internalisation need to be explored. The delivery is highly dependent on the specific application in which the QD-conjugates will be used. In the case of *in vitro* sensing a delivery system is unnecessary. Since Derfus' publication, further research has been completed in this area by Biju *et al*, which examines different delivery systems.[34] The need for improvement in the development and characterization of different delivery schemes are highlighted.[34] A major investigation that is needed is targeting strategies for these materials for subcellular regions. A great review by Breger *et al.* looks at the research progression of delivery systems of QDs over the past few years.[35] They define three categorical methods to which most of the delivery systems used fit into. These include passive, in which the QD material is utilized within the delivery; facilitated, which relies on the association of the QD with the biological polymer; and active, which is the direct approach with manipulation of the cell.[35] In order to specify delivery the QD-bioconjugates have specific biomacromolecules on the surface that can enhance specific interactions targeting.

1.1.3.1 Quantum Dot - Protein Conjugates

A main focus for the use of QD-protein conjugates is to try to achieve clear intracellular labelling to characterize long-term in vivo/in vitro biological functions without causing adverse effects.[3] The main focus lies on producing a QD-bioconjugate that contains a protein to probe the function of interest, and the QD acts as a fluorescent marker. Applications include, the imaging of cargo transport of cell penetrating proteins (CPP),[27] selective intracellular delivery for labelling different cell organelles [3] and QD immunoassays [36].

The use of QD-bioconjugates for imaging intracellular protein cargo transport has been reported many times, for example Medintz *et al.* has specifically used CPPs in promoting the effective delivery of QD cargos in which they use both a small and a large fluorescent QD-protein bioconjugate as protein cargo. [27] Results have shown the successful passing of the protein across the cell membrane via the CPP mechanisms. This comes as a breakthrough as until this point the literature has relied on intracellular delivery by receptor-mediated or nonspecific endocytosis,[3] where the specific binding with cell surface receptors leads to enhanced cell uptake of QD-bioconjugates.[37] This shows that CPPs can be used as a method for an intracellular delivery for the imaging of cells.[27] **Figure 1.1.7** shows the successful cellular uptake of the different modified large and small protein cargos via CPPs. However the CPP mechanism is non-specific so although shows successful uptake of QD into cells it cannot be used for cell-specific targeting as it doesn't differentiate the different cell types.

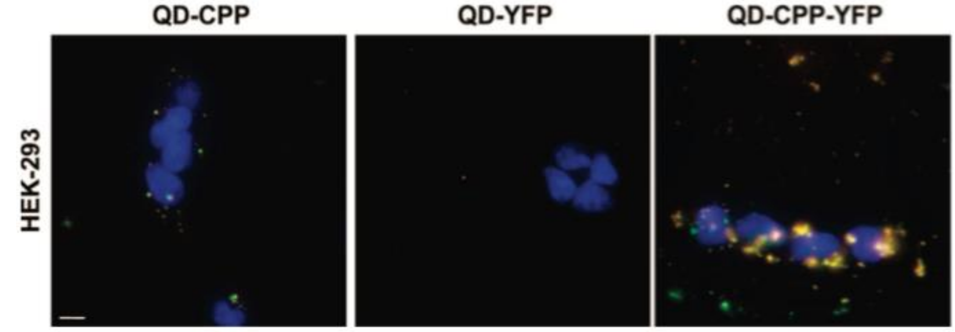

Figure 1.1.7: Cellular uptake of different fluorescent modified QD-bioconjugates. The QD-bioconjugates used were QD-CCP, cell-penetrating peptides, QD-YFP, yellow fluorescent protein, QD-CPP-YPD, a combination of the two previous bioconjugates. The QDs were incubated with HEK-293, human embryonic kidney cells. Scale bar in 10 µm. Reprinted from reference. [27]

Another method of producing fluorescently active QD-peptide conjugates is reported by J. B. Delehanty *et al.* which does not require the use of any CPP. It just uses the molecule itself as the probe for cellular labelling. [3] **Figure 1.1.8** shows cells have been successfully labelled, using only the QD-conjugate as the probing material where a series of cross sectional confocal imaging slices appearing from (a) below to (e) above the cell, though this method can be further enhanced by using multi-peptide labelled QDs.

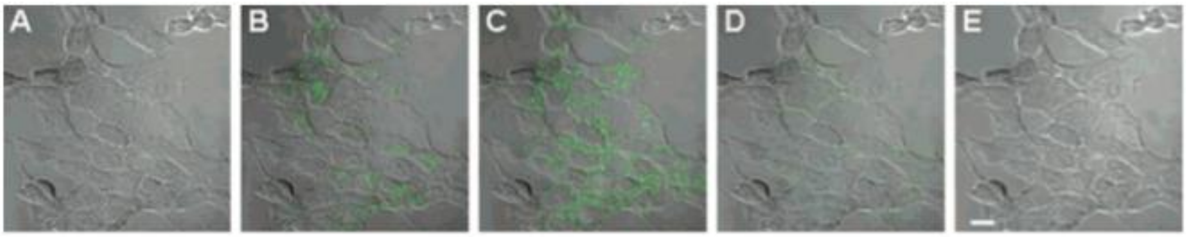

Figure 1.1.8: Laser scanning fluorescence images of cross-sectional slices of the internalised modified QD cell assemblies using HEK 392T/17 cells. Panel (a) shows underneath the cells and the images work through to panel (e) which shows the effects above the cells. Scale bar is 10 µm. Reprinted from reference. [3]

A more recently discovered method of producing QD-protein conjugates is to modify the QD and protein with complementary functional groups that can bind together via a simple click chemistry. This method has been used to produce QD-transferrin conjugates by Schieber *et al.*[38] Transferrin is a glycoprotein that specifically binds to iron that is present within the blood plasma. They use an azide-modified core-shell QD and a cyclooctyne moiety functionalized into the protein. **Figure 1.1.9** shows the successful uptake of the QD-protein conjugate into the cells via the QD fluorescence. This method is versatile and has scope for further development in that you can control the azide surface modification to suit a specific purpose. It can also be applied to other functional groups such as the extremely rapid tetrazine-TCO click reactions.[38]

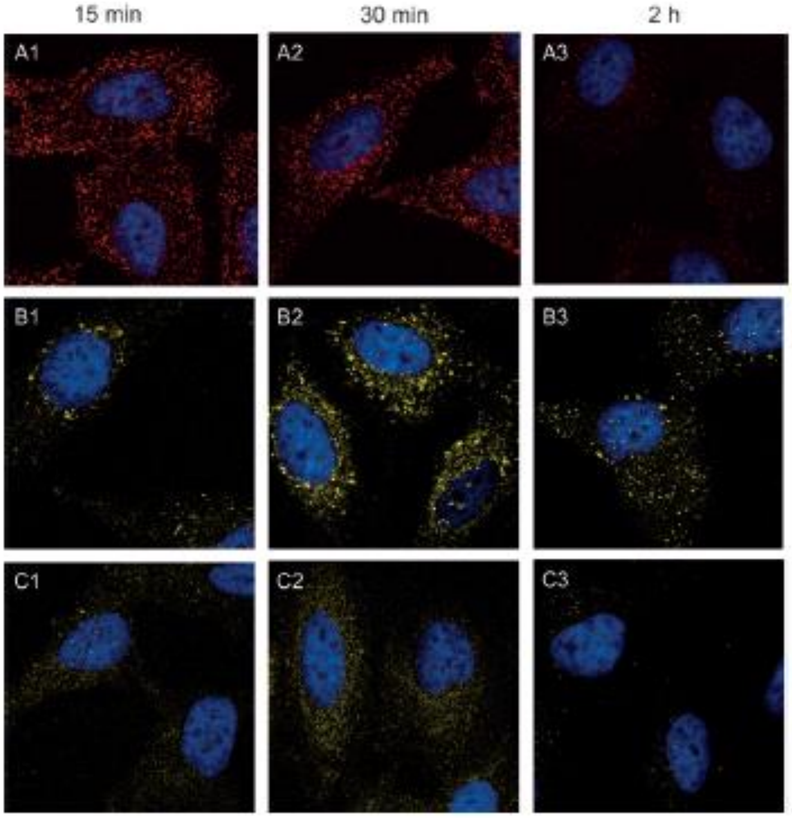

Figure 1.1.9: Fe_2-transferrin uptake into cells using A568-Fe_2Tf (A1-A3), QD100-Fe_2Tf (B1-B3) and QD100 (C1-C3) at a 15, 30min and 2 hr interval at 37°C. Reprinted from reference.[38]

1.1.3.2 Quantum Dot – DNA Conjugates

As DNA can be used as a tool for probing gene functions and holds excellent potential as a treatment for a wide range of diseases the area of QD-DNA conjugates has shown large promise. Many papers have outlined the formation of QD-DNA conjugates formed by both covalent or electrostatic interactions.[39] Zhou *et al*. [28, 40] demonstrates the successful synthesis of a compact QD-DNA conjugate using self-assembly between thiolated DNA and a mercaptopropionic acid (MPA) capped QD, where extremely high fluorescence energy transfer efficiency of >80% was achieved at a DNA:QD molar ratio of 1:1. However, the DNA was found to irreversibly absorb onto the QD surface, making hybridization to complementary strands hard to achieve. To overcome this problem, a tri(ethylene)glycol, TEG, linker was introduced between the QD surface ligand and DNA which improved stability and prevented the non-specific DNA adsorption on the QD surface.[28] Zhou *et al*. further demonstrated that QD-DNA conjugates can be used for label and label-free detection of the complementary DNA target using the schematic procedures shown in **Figure 1.1.10**. It also demonstrates how the optical properties of QDs can be harnessed to detect a labelled DNA target and also in label-free DNA detection using the intercalated ethidium bromide.

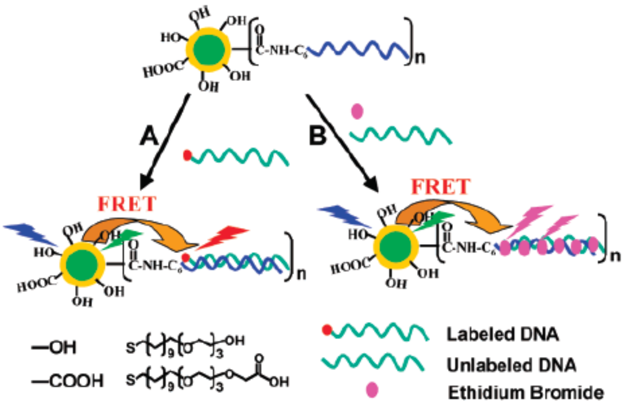

Figure 1.1.10: A schematic representation of the principles for hybridisation and label-free detection of DNA probes coupled to a QD conjugate using a FRET detection system. Reprinted from reference. [28]

Further work in this area has used the above concept to build and create DNA dendrimers to coat the surface of the QDs. Samanta *et al*.[41] utilize this and in the presence of fluorescence dyes have created an energy transfer based system to explore attachment chemistry through using light harvesting properties. Through the attachments of fluorescence dyes upon the DNA strands present on the QD surface, **Figure 1.1.11**. This creates a whole new area of scope for these materials away from the biosensor, bioimaging approaches as it could be used as a nanoatenna. There is potential however to further improve the concept through adding florescence quenching materials for use as a biosensor. As the DNA could have target specific recognition and then direct the energy transfer upon binding to its target.

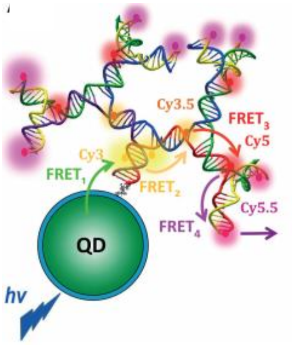

Figure 1.1.11: Schematic of the QD-dendrimer structures and linkage chemistry, the circles illustrate the dyes at their estimated locations while each of the DNA strands are presented with distinct colours. For clarity only one dendrimer is shown appended to the QD, but ideally there should be six of them centrosymmetrically arrayed around it. Reprinted from reference. [41]

1.1.3.3 Quantum Dot – Antibody Conjugates

Antibody conjugated QDs have excelled in the research area of QD-bioconjugates as they are able to give high-resolution specific labelling of biological systems.[42] They are used for the immunofluorescent staining of cells and tissues.[39] The production of these conjugates has provided an excellent milestone for the integration of QDs into clinical and *in vivo* experiments.[29] This is down to the specificity that antibodies have for their target cell receptors. The first example is adhering avidin, a highly positively charged tetrameric protein, to the QD surface and using it as a bridge to conjugate a biotinylated antibody onto the surface via the extremely strong biotin-avidin interaction, highlighted in **Figure 1.1.12**.[43] A similar approach can be achived through using a protein called streptavidin, also a member of the avidin family but with the protein surface glycans removed to make it roughly neutral, and this then greatly reduces the non-specific binding experienced by avidin. Most papers describe these methods as having a higher sensitivity on read-out for immunostaining other classical techniques due to the excellent fluorescent brightness of the QDs.

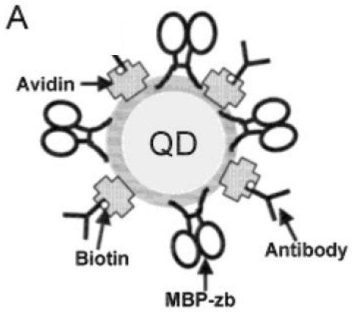

Figure 1.1.12: Schematic of a QD-antibody conjugate in which avidin bridges are harnessed for the interaction between the nanocrystal and the biotin modified antibody. Reprinted from reference. [43]

A recent problem that has been highlighted with these conjugates is that the antibody orientation upon the QD surface is often random which hampers their sensing performance.[44] These materials are often used in immunoassays so a display of the correct antibody orientation is highly important. A heavily reported immunoassay which utilises QD-antibody conjugates is an energy transfer assay which involves terbium complexes, Tb.[45] The immunoassay involves the detection of the prostate specific antigen (tPSA) which is known to have strong links to prostate cancer. Annio et al. shows the problem of antibody orientation can simply be corrected by increasing the conjugation ratio which has led to significant improvements in the immunoassay.[44]

1.2 Fluorescence Resonance Energy Transfer

Fluorescence, or Förster, resonance energy transfer (FRET) is an analytical technique which is used to measure the separation distance between two fluorophores, commonly known as the donor and acceptor.[46] The mechanisms behind FRET come from the intermolecular dipole-dipole interactions between fluorophores. The excitation energy of the donor is transferred non-radiatively to the adjacent acceptor, leading to donor quenching and acceptor emission simultaneously. The FRET efficiency is strongly dependent on the centre-to-centre donor-acceptor separation distance, allowing for accurate measure of nanometer distances. It is named after Theodor Förster, the German scientist who established the theory behind it.[6] He proposed the quantitative theory of molecular resonance energy transfer and derived the kinetics required for the theoretical basis of FRET.[47, 48] The applications of FRET has expanded significantly in the last 30 years, ranging across biology, chemistry, public safety and environmental protection. **Figure 1.2.1** highlights the areas in which this mechanism can be used.

Figure 1.2.1: A summary of all the different applications available for QD-FRET sensors. Reprinted from reference. [6]

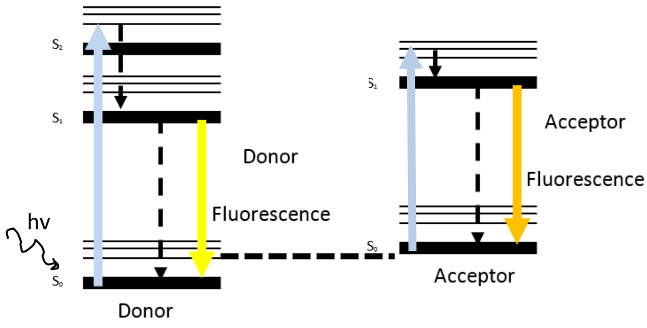

Figure 1.2.2: A schematic which shows fluorescence energy transfer between the donor and acceptor present within FRET experiments.

The FRET process can be described by a simple modified Jablonski diagram, **Figure 1.2.2**, showing the electronic states of molecules.[49] Non-radiative energy transfers in the process of FRET are seen as intersystem crossings or internal conversions in which the energy from the excited state donor is transferred to the excited state of the acceptor.[50] These non-radiative energy transfers are represented by the black arrows within the simplified Jablonski diagram. The donor electrons energy from returning to ground state must match the energy required to excite the acceptor.[51] The efficiency of this energy transfer is calculated using the Förster theory (**Eq. 4**), showing the dependency on the distance between the two fluorophores.

$$E = \frac{k_{ET}}{k_f + k_{ET} + \sum k_i} \qquad \textbf{(Eq. 4)}$$

Where k_{ET} is the rate of energy transfer, k_f is the radiative decay rate of the donor and k_i are the rates of and other relaxation pathways which exclude energy transfers to the acceptor. FRET efficiency is the quantum yield measurement of the energy transfer which is the fraction of energy transfer that occurs per donor excitation. In order to witness the energy transfer there should be a non-zero spectral overlap between the donor emission and the acceptor absorption spectra, an example of this can be seen in **Figure 1.2.3**.[5] Both species, acceptor and donor, must be related by Fermi's Golden Rule, the rate of which atomic or electronic transitions take place between two states, for interacting dipoles in order to undergo FRET.[52] Fermi's Golden Rule applies to a wide range of optical and electronic processes in which both the initial and final states are described as wave functions it is calculated from the probabilities from transition matrix elements as part of quantum mechanics.[53] Taking into consideration the extra dependencies, donor and acceptor distance and orientation and spectral overlap the fret efficiency can be calculated using (**Eq. 5**) below.

$$E = \frac{1}{[1 + \left(\frac{r}{R_0}\right)^6]} \qquad \textbf{(Eq. 5)}$$

Where E is the efficiency of the energy transfer, r is the distance between the acceptor and the donor and R_0 is the Förster radius under which the FRET efficiency is 50%.

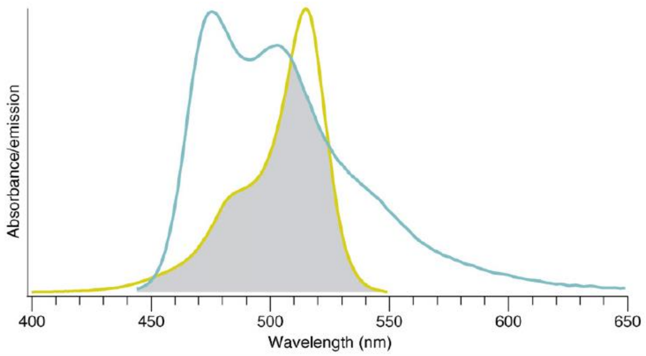

Figure 1.2.3: The spectral overlap as indicated by the grey area is determined by the spectral overlap between the emission spectrum of the donor (blue line) and the absorbance spectrum of the acceptor (yellow line). Reprinted from reference.[54]

QDs have been widely used in FRET based studies because of their highly attractive spectral characteristics such as broad absorption and narrow symmetric emission. As a result, a broad range of excitation wavelengths can be selected to minimize the direct-excitation of the acceptor, thereby reducing the background signal. Most commonly in QD-FRET experiments QDs are the donor and an organic dye as the acceptor. However QDs can act as either the donor or acceptor.[51] The role of donor is preferred due to the broad adsorption spectra of QDs makes direct excitation unavoidable. QDs are reported as great acceptors when combined with luminescence lanthanide labels as donors via time gated detection. [55] **Figure 1.2.4** (**A**) shows how QD-conjugates have been used to determine the separation distance between the acceptor and donor, highlighting the energy transfer between them. The relationship between the acceptor and donor is shown in **Figure 1.2.4** (**B**), which also illustrates molecules sitting in close proximity to each other, within FRET the donor and acceptor are usually fluorescence materials.

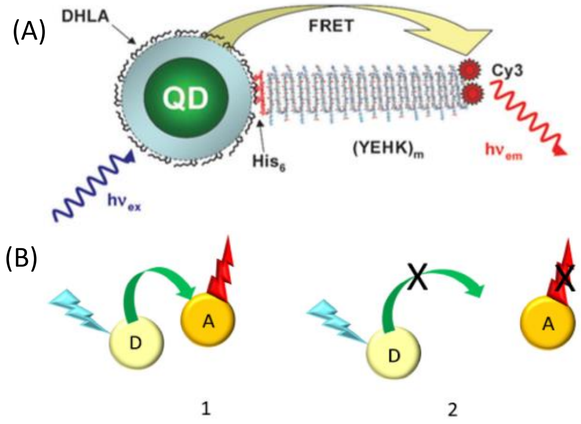

Figure 1.2.4: An example of QD-FRET system: (**A**) A schematic of a type of QD-conjugate that can be applied for use with FRET.[50] (B) Excitation light is absorbed by donor (D) and transferred by non-radiative transfer to acceptor (A), resulting in acceptor emission if donor-acceptor is in close proximity (scenario 1), however if they are separated too far, then no FRET will happen (scenario 2). Reprinted from reference. [6]

1.2.1 FRET in Biodetection

FRET has important applications in areas such as labelling biological molecules, cellular labelling, tissue imaging and developing immunoassays.[50] FRET is a powerful technique as it can provide accurate measure over small separation distances (ca. 1-10 nm). It can then provide an insight into in-depth complicated biological processes, such as protein-protein interactions and ligand-receptor binding as well as in imaging changes in protein and oligonucleotide structure and conformation as a result of a known biological stimulus. [50] P. Babu *et al.*[56] has shown the successful tracking and detection of the interactions of carbohydrate-binding proteins by using modified glucose-QDs, through showing that using a thiol functionality is key in the synthesis of glucose modified QDs by the addition of oligosaccharides to the QDs. The modified QDs were seen to successfully agglutinate together in the presence of the carbohydrate-binding proteins.

Other FRET based techniques which do not just use QDs and organic dyes are available. Examples include bioluminescence resonance energy transfer,[57] chemiluminescence resonance energy transfer,[58] Homo-FRET[59] and fluorescent protein-based FRET.[60] In each of these cases the fluorophore used is different to that of the standard FRET experiment. The difference between homo-FRET and regular FRET, also known as hetero-FRET, is that in homo-FRET the donor and acceptor are the same fluorophore. All other principles remain the same. Fluorescent protein based FRET harnesses fluorescent proteins where a cyan fluorescent protein are often used as the donor and a yellow fluorescent protein used as the acceptor.[60]

1.3 Gold Nanoparticles

In addition to QDs, gold nanoparticles, AuNPs, have been used throughout nanoscience for energy transfer applications. [61] AuNPs are also known as colloidal gold because they are made from tiny colloidal suspension of gold particles. They have been used throughout history from staining glass in windows to treating a wide range of diseases.[62] They also possess some unique optical properties which makes them useful for energy transfer studies.[63] AuNPs are effective fluorescence quenchers due to strong localised surface plasma absorption.[64] The size, shape and surface properties of the AuNPs can be widely changed in a similar way to QDs. **Figure 1.3.1** shows the effect of AuNP size on the colour of the nanoparticles, NPs. AuNPs exhibit unique properties such as surface plasmon resonance[65], surface enhanced Raman spectroscopy[66] and fluorescence quenching effects.[67] A full review of the properties of gold nanoparticles and their applications in Biology and Nanotechnology has been published and reviewed by M. Daniel *et al*.[68]

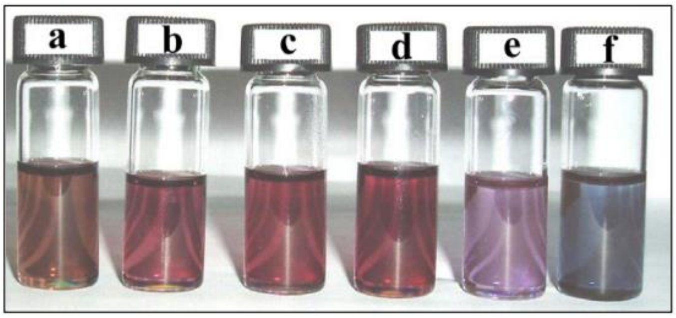

Figure 1.3.1: Optical colour of a range of gold nanoparticles showing the colour change over increased particle size. Reprinted from reference. [69]

A major advantage of AuNPs over QDs is that AuNPs are more biocompatible and do not contain toxic heavy metal ions, hence they are more suitable for *in vivo* applications.[70] Another advantage is that they possess high extinction coefficients and have a broad absorption spectrum in the visible part of the spectrum.[71] Also the separation distance that fluorescence quenching can measure is much larger (15 - 70 nm) than that of FRET (<10 nm). These distances were confirmed by an experiment by Samanta *et al.* in which a DNA origami structure is used to control the distance between the donor and the quencher.[72] This is because the energy transfer now has an inverse d^4 dependency rather than an inverse d^6 dependency, found in FRET, where d is the distance between the interacting dipoles. This comes from the differences in the energy transfer equations for both processes.[73] **(Eq. 6)** shows the interaction for energy transfer rate within FRET and **(Eq. 7)** shows the energy transfer rate for the AuNP fluorescence quenching behaviour also known as surface energy transfer, SET.

$$k_{FRET} = \left(\frac{1}{d^3}\right)\left(\frac{1}{d^3}\right) = \left(\frac{1}{d^6}\right) \qquad \textbf{(Eq. 6)}$$

$$k_{SET} = \left(\frac{1}{d^3}\right)\left(\frac{1}{d}\right) = \left(\frac{1}{d^4}\right) \qquad \textbf{(Eq. 7)}$$

These differences come from the difference in materials in which the energy transfer comes and goes too. Both interactions within FRET are dipoles so have the same contribution where in AuNP quenching is surface energy transfer, SET, which is a dipolar energy transfer to a metallic surface mechanism. This is the difference that comes into play, causing the larger separation distances that can be measured by the AuNP quenching mechanism.[73]

1.3.1 AuNPs as Fluorescence Quenchers

AuNP are known to be strong fluorescence quenchers when paired with fluorescent dyes or QDs showing a high quenching efficiency (up to 99 %).[74] Similar to that seen previously in the FRET experiments using glycan-QDs,[75] AuNPs use a similar method of energy transfer from a donor but instead of transferring the energy to enhance acceptor fluorescence, the donor is quenched without producing acceptor fluorescence. This method is also known as dynamic quenching.[76] The quenching efficiency with AuNPs has many dependencies which include the surface plasmon resonance, particle size and shape and the distance away from the fluorescent donor.[74] Although this is a significant advantage of AuNP quenching method as it can extend to beyond the conventional FRET distance of *ca*. <10 nm.[61] This method can be used as another way to quantify the binding between glycans and multivalent proteins using modified polyvalent ligands functionalised to enhance binding affinity and specificity. In this case the percentage quenching efficiency is calculated using the integrated fluorescence intensity with and without the quenching material.

1.3.2 AuNP Synthesis

AuNPs can be easily synthesised with high precision and purity for a large range of diameters between 2 nm and 100 nm. The first synthesis of AuNPs was introduced by Turkevitch *et al*.[77] in the early 1950's using a citrate reduction method. This is still a common methodology today for making AuNPs. **Figure 1.3.2**(**A**) below shows the original electron micrograph image form showing the production of the gold nanoparticles using the citrate reduction method. This method utilizes the redox properties of gold and uses sodium citrate to reduce a chloroauric acid, $HAuCl_4$, in water. The limitation of the method is that it produces a polydisperse solution of AuNPs which means the NPs are of various shape and size which can affect the accuracy of their average size calculation. Further improvements to this method have been made and new protocols have emerged which results in a specific size or shape of AuNP being synthesised by varying the molar ratio of the sodium citrate: gold. [78] The resulting NPs are capped with weak ligands which can be exchanged for specific materials for particular applications.

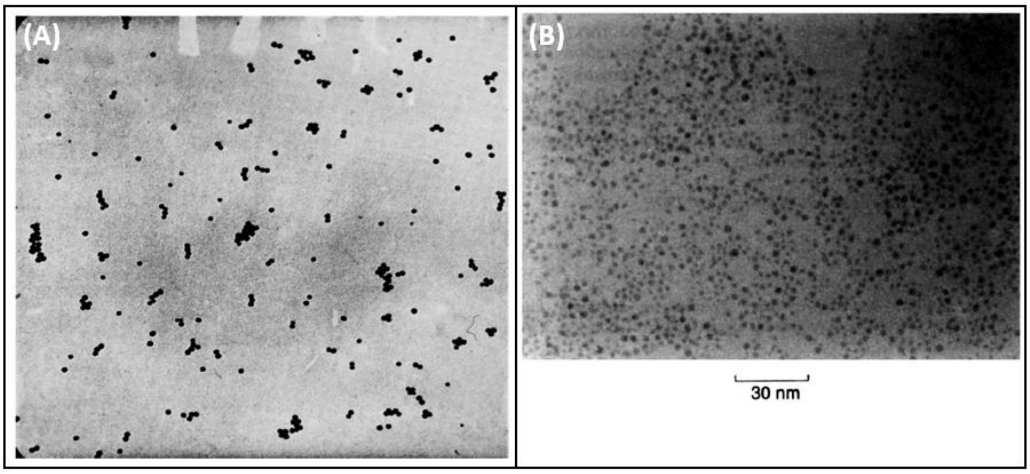

Figure 1.3.2: (**A**) Electron microscope of the gold sol using the citrate reduction method from the original synthesis in the 1950's by Turkevich *et al*.[77] and (**B**) Transition electron microscope image of thiol derivatised AuNPs by the Brust – Schiffin method by Brust *et al*. Reprinted from reference.[79]

Another common method for synthesising AuNPs is the Brust – Schiffin Method which was first reported in the early 1990's by Brust *et al*.[79] This method is based on a two phase liquid-liquid system which involves growing metallic clusters, starting with gold chloride, in which thiol monolayers are attached to the surface of the growing nuclei, forming particles that are then thermally stable and air stable. Within this method $AuCl_4^-$ is transferred to toluene using tetraoctylammonium bromide, a phase transfer reagent, and the gold ions are then reduced by sodium borohydride in the presence of dodecanethiol. This reduction can be seen through a colour change of the solution from orange to brown. The AuNP size can be controlled by the thiol to gold chloride ratio. [68] A recent review published by Herizchi *et al*. highlights a vast array of methods that have been further developed for the synthesis of AuNPs including an electrochemical method[80] and also a biological method[1] and the seeding growth method.[81]

1.3.3 AuNP Bioconjugates

Gold nanoparticles provide a good scaffold in which a wide variety of molecular species can be capped onto the surface. [82] This is highlighted below in **Figure 1.3.3** showing the variety of biological scaffolds that can be capped onto the surface of NPs. A review by Sapsford *et al*.[83] highlights some of the methods used to create these materials in which nanomaterials have been created to further bridge the gap between nanotechnology and biology. Gold is an inert material meaning that it can easily be used for in *vivo* studies and is much less toxic in comparison to QDs. As well as their facile preparation and modification and the liable use for various sensing methods.[84] These properties have led to the formation of many different AuNP conjugates with such materials as peptides, proteins, DNA and antibodies. These materials can be further combined with another material such as a lanthanide[82] for imaging agents or a fluorescent labelled protein[61] for sensing applications.

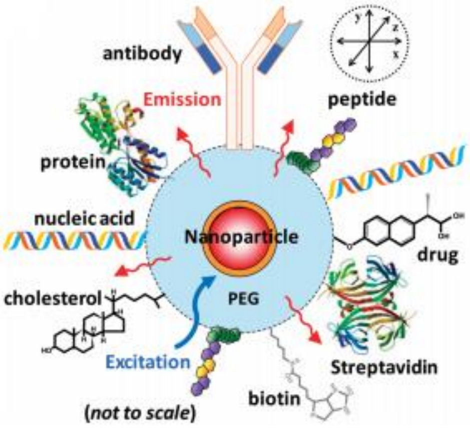

Figure 1.3.3: Nanomaterial- bioconjugate multifunctional NP assembly: A representative NP decorated with multiple disparate functional molecules (e.g., nucleic acids, proteins, drugs, peptides) is depicted. Reprinted from reference.[83]

1.3.3.1 AuNP – Peptide Conjugates

The functionalization of AuNPs with peptides allows them to be used as intercellular drug and gene delivery nanocarriers.[85] The targeting properties of peptides can be used to deliver materials to specific parts of the body for potential use as in *vivo* sensors. A recent review by Zong et al. highlights the range of different uses that peptide-functionalized AuNPs have ranging from detection agents of metal ions, enzymes and antibodies, targeted drug delivery and cellular uptake to a more specific delivery of anti-cancer peptides.[86] **Figure 1.3.4** shows some of the ways in which peptide/protein functionalised NPs are used. The detection of metal ions was first reported by Si *et al*. in which they detected mercury ions, Hg^{2+}, via a shift in the UV-Vis spectra as well as slight colour change in from red to purple.[87] A common enzyme that is detected by these materials is thrombin, a serine protease, which hydrolyses peptide bonds so the functionalised AuNPs aggregate after cleavage of some peptide chains. This work was first published by Zhen *et al.*[88] Cell penetrating peptides can also be conjugated to the surface of AuNPs, as these are short peptide chains that assist in cellular uptake of various cargo materials, ranging from small chemical molecules to nanosized particles. [89] Peptide functionalised AuNP that has shown potential as cell-targeting agents by allowing the specific detection of the cell nucleus and endoplasmic reticulum using bright field microscopy has been developed by Sun *et al*. [90] They use a AuNP functionalised with the arginine rich peptide CALNN and its derivative $CALNNR_8$ and show their capability to cross the membrane by endocytosis.

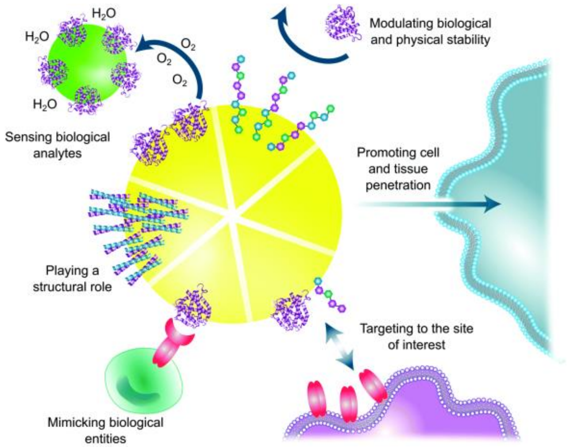

Figure 1.3.4: The features imparted by the peptide/protein functionalisation of NP surface and how they influence NP behaviour. Reprinted from reference. [91]

1.3.3.2 AuNP - Protein Conjugates

Protein-gold bioconjugates are key to studying important roles found within biological systems.[92] AuNP – protein conjugates are formed due to the interaction between the surface and proteins. This can be achieved in 3 different ways through a surface adsorption, cross-linking and electrostatic absorption. For example the presence of cysteine residues within the protein can directly chemi-adsorb to the surface of the AuNPs, alternatively charged proteins can absorb to oppositely charged AuNPS electrostatically.[93] Protein – nanoparticle interactions can also lead to the formation of a protein corona, a biological coating that forms around NPs within biological media first shown by Monopoli *et al*.[94] The corona consists of an inner shell of proteins, hard corona, in which the proteins have a high affinity to the NP and an outer shell of proteins, soft corona, which has a low affinity to the NP.[95] A predominant example of protein corona formation with AuNPs has been the Human Serum Albumin as shown by Canaveras *et al*. these blood proteins high affinities for AuNPs especially within biological media due to their high abundance.[92]

1.3.3.3 AuNP – DNA Conjugates

Over the past three decades DNA has been used to design a wide range of facilitating materials such as DNA nanostructures, DNAzymes and DNA aptamers which combined with AuNPs further enhances their properties.[96] These DNA functionalised AuNPs allow for molecular recognition and directed assembly via DNA's unique and specific molecular recognition. Mirkin *et al*. led the way of AuNP-DNA conjugates studies who created the first bioconjugate assembly using thiolated DNA capped AuNPs.[97] A recent review by Liu *at al*. highlights some further examples of preparation methods for these materials and their application as powerful diagnostic tools.[96]

1.3.3.4 AuNP – Antibody Conjugates

Antibody-AuNPs provide an essential part to new biosensing technologies as they provide the specificity of the antibody-antigen interaction as well as showing the unique properties of nanoparticles. [98] This makes them great tools for immunosensing which relies on the specific recognition between biosensor and the biomolecule. These bioconjugates can easily be formed through the direct adsorption of antibodies onto citrate-capped AuNPs. However this method can lead to orientation issues with how the antibody is presented on the AuNP surface.[84] There are three main ways reported in the literature to present antibodies on the surface of AuNPs. Simple hydrophobic interactions between the hydrophobic structure of the antibody and the metal surface. [99] Ionic interactions can also play a key role in attachment of antibodies to AuNPs as the surface charge of the AuNP is negative so the positively charged amino acids and N-terminal groups can interact. The final method is to provide a linker material that covalently attaches to the AuNP through coordination to the gold surface. **Figure 1.3.5** depicts these different conjugation methods and shows the corresponding orientations. AuNP-antibody conjugates have been used in two different ways as biosensor materials and as part of competitive immunoassays. Rayavarapu *et al*. have used ionic interactions to create AuNP-antibody conjugates for binding to the Human epidermal growth factor receptor 2, HER2, in which the materials have then been used as contrast agents for the imaging of breast cancer.[101] A competitive immunoassay for malaria antigen detection based on a fluorescence-quenching mechanism by Cavadas *et al*. has been developed.[102] An IgG monoclonal antibody recognises the antigen, *Plasmodium falciparum*, was used in malaria diagnostics.

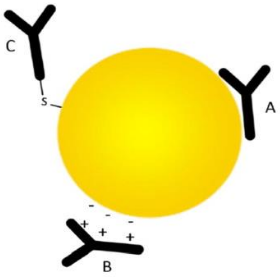

Figure 1.3.5: Hydrophobic and ionic interactions between antibody and gold nanoparticle surface. A) Hydrophobic interactions, B) ionic interactions and C) covalent bond is formed due to dative binding. Reprinted from reference. [100]

1.3.3.5 AuNP – QD Conjugates

As AuNPs show great quenching properties a large amount of research have used them as part of FRET in order to quench donor fluorescence over larger separation distances then average FRET.[103] These QD-AuNPs conjugates energy transfer mechanism is known as a nanometal surface energy transfer, NSET. The energy donor within the mechanism is usually a simple organic dye but has been modified to include QDs. [103] The combination of the QD and AuNP, into a single system can further enhance the excellent optical properties already seen individually and even lead to new properties. [104] Using a QD and AuNP pair, an inhibition assay was created that could be used as a high throughput screening method of inhibitors. Oh *et al*. utilized a streptavidin-biotin interaction and the assay works through monitoring the photoluminescence quenching of QDs conjugated with streptavidin. This quenching is caused by the biotin modified AuNP binding to QD-Steptavidin, which can be competed off by the free avidin.[71] **Figure 1.3.6** shows schematically how the inhibition assay works.

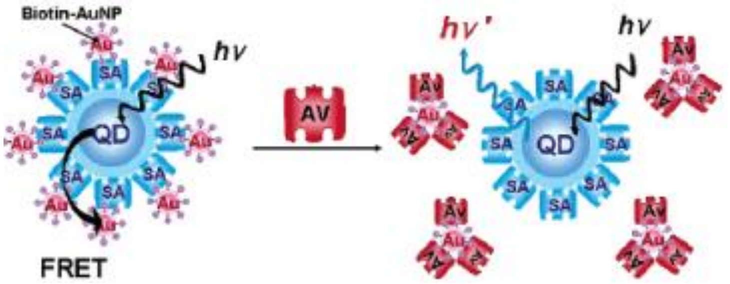

Figure 1.3.6: Schematic illustration of the inhibition assay by Oh *et al*. based on the photoluminescence quenching of Streptavidin-QDs by Biotin-AuNPs. Reprinted from reference. [71]

1.4 Click Chemistry

A common method used to produce NP-bioconjugate based fluorescence probes is the highly efficient click chemistry reaction also known as a 1,3 – dipolar cycloaddition occurring between an azide and a terminal alkyne. [105] This technique can be done in two ways. The first is a copper (I) catalysed reaction which forms a highly stable triazole linked molecule along with a limited amount of by-products. This method was first reported by Sharpless *et al*. in 2001.[106] **Scheme 1.4.1** below shows the scheme in which copper catalysts are harnessed for use during click chemistry. It also highlights how the conjugation occurs and the formation of the cyclic product. The copper (I) is usually generated in *situ* with the use of a stabilizing agent. The reaction is highly powerful and versatile due to its ability to offer excellent functional group selectivity and high yield.[107] This process has been identified for use in producing a large variety of bioconjugates, for example: silica, gold and magnetic nanoparticles, carbon nanotubes, as well as synthetic polymers. However, this process has a major disadvantage in that the copper ion is found to quench QD fluorescence due to reacting with the zinc ions present within the core-shell QD structure.

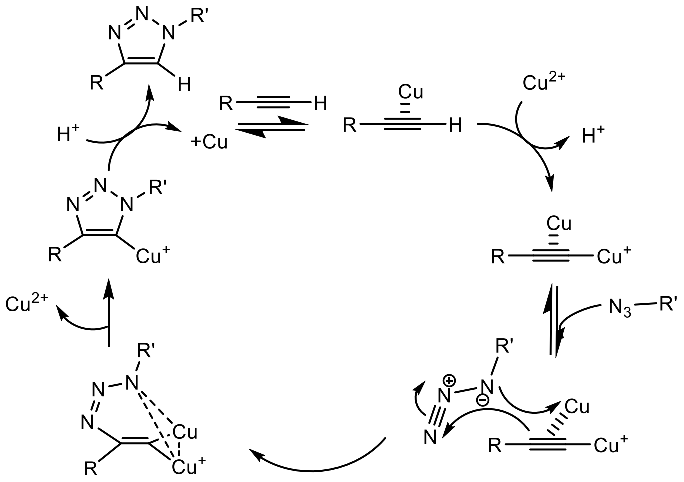

Scheme 1.4.1: A reaction scheme for copper catalysed click chemistry in which metallic copper can be used.

This, on the other hand, has been found to be an advantage in the design of sensitive cation detectors. For example Li *et al.* modified the QD surface with a cadmium ion detector using click chemistry to achieve binding, which is then used to detect the presence of cadmium ions, a chemosensor.[108] Beaune *et al.* manages to successfully give the reason for the quenching and how to overcome it.[109] They suggest that the problem can be overcome by adding a thick negatively charged shell, as quenching occurs due to copper ions reacting to the core shell. Cu-catalysed click chemistry is not suitable for QD-conjugates based fluorescence probes when used directly in the ligand exchange. Bernardin *et al.* actually hypothesises reasons why the quenching is observed; the first hypothesis being electron transfer between the semiconductor material, the QD, and the copper ions, and the second being that a chemical reaction may be occurring between the QD's surface and the copper, suggesting displacement of the zinc by copper, forming CuS, causing damage to the fluorescent donor.[105] This is further confirmed from the simple solubility product point of view as the solubility constant, K_{sp}, for CuS is ~10^{-36} where as it is ~10^{-23} for ZuS therefore it is favorable for Cu^{2+} to replace the Zn^{2+} surface.[110]

The second method is the copper free click chemistry reaction, which is essentially the same as that used previously, but without the need of a copper catalyst. It is usually referred to as strain promoted azide-alkyne cycloaddition, SPACC, which involves a 1, 3-dipolar cyclocaddition. The reaction is driven by the high ring strain in the cyclooctyne ring system which favours the formation of the triazole species as shown in **Scheme 1.4.2** below. The reaction itself is highly flexible and can be done between any strained alkynes and azide that are present on two molecules at room temperature and pressure. This method is being harnessed especially for producing conjugates for use in *in vivo* studies, avoiding the apparent toxicity effects of copper. The disadvantages of this method is that it can sometimes be slow and low yielding with bulkier ligands.

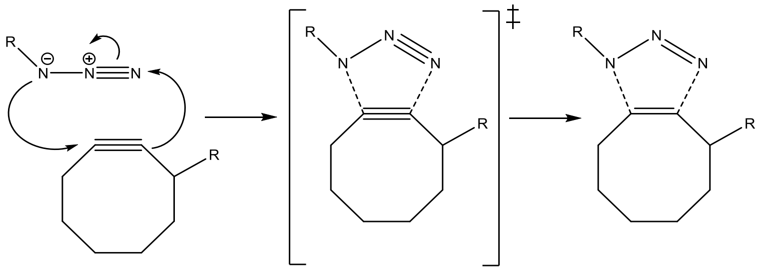

Scheme 1.4.2: A reaction scheme to show the 1, 3-dipolar cyclocaddition reaction mechanism between the strained alkyne and an azide as part of the copper free click chemistry mechanism.

1.5 Nanoparticle Characterisation Techniques

Characterisation of NPs is highly important in the nanotechnology field especially for understanding the toxicity effects of the particles.[111] The main two parameters that must be determined for any NPs used for understanding interactions with living systems are particle size and size distribution. Determination of the particle size is key for any work using biological media especially for in *vitro* and in *vivo* studies so that you know what you are putting into the cell/body. The use of poorly characterised NPs has often led to confusing and mis-interpreted data.[111] Two techniques that have been widely used to determine these two parameters, dynamic light scattering and transition electron microscopy, are outlined below.

1.5.1 Dynamic Light Scattering

Dynamic light scattering, DLS, is a technique that is used to determine the size distribution profile of the particles found within a suspension. This is achieved by using a light source to hit all the particles, the light is then diffracted in different directions and analysed. A simple schematic of the basic DLS instrumentation is shown in **Figure 1.5.1**. NPs that are dispersed in a solution scatter light proportional to the 6th power of their nucleus radii and the scattering can be done through three mechanisms, elastic scattering, Mie Scattering and Rayleigh scattering.[112] The mechanism chosen is dependent on the size threshold of the particles. Using light in this way the structure and state of motion of the particles can be measured. [113] The scattering intensity of particles fluctuates over time due to Brownian motions, the random motion of particles within a suspension, causing constructive and destructive interferences. Results observed from the light scattered experiments are manipulated using the Stokes – Einstein relationship (**Eq. 8**) below to give the hydrodynamic sizes of the particles within the solution:

$$D_h = \frac{K_b T}{3\pi\eta D_t} \qquad \textbf{(Eq. 8)}$$

Where D_h is the hydrodynamic diameter of the particles, D_t is the translational diffusion coefficient, K_b is the Boltzmann's constant, η is the dynamic viscosity and T is the temperature. The hydrodynamic size, D_H, is the diameter of the hard sphere particle that diffuses at the same speed as the particle and is a hypothetical measurement calculated in DLS. The hard sphere does not exist in most colloidal dispersions as this is dynamic and fluctuates with time.[112] Thus DLS calculates an average colloidal size it doesn't signify true particle size. An advantage to this technique is that it can measure a large number of particles in comparison to other methods of calculating particle size such as TEM which requires a small sample.

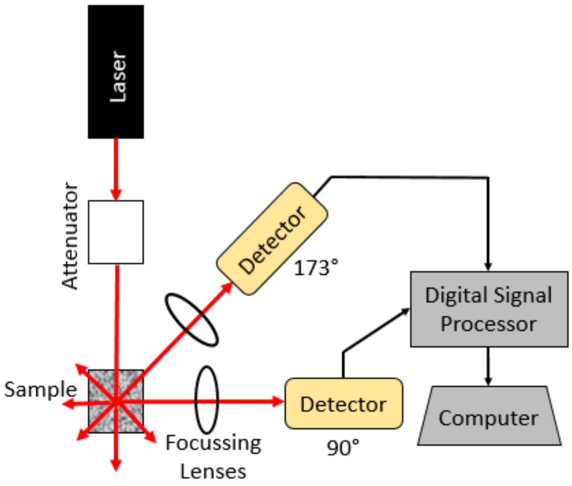

Figure 1.5.1: Schematic of Dynamic Light Scattering, DLS, instrumentation.

1.5.2 Transmission Electron Microscopy

Transmission electron microscopy, TEM, is widely used for the characterisation of nanoparticles with sub-nm resolutions.[114] This technique uses a powerful finely focused electron probe which can help identify specific structural characteristics of nanoparticles down to the atomic resolution.[114] It is used widely as a major analytical technique in all areas of science, physical, chemical and biological. This technique was first founded by Knoll *et al*. in the early 1930's.[115] This means that you can get good atomic resolution for real-space imaging of nanoparticles. The working principle for TEM is based on that of a simple light microscope but instead of using light, a focused high energy electron beam is used to probe the structure, **Figure 1.5.2**. Given that the high energy electron has a much shorter wavelength, λ, than light it can give a much higher resolution. This comes from the De Broglie principle of electrons in that electrons are charged particles that act as waves. The electrons are produced and emitted by the electron gun through thermionic emission from either tungsten cathodes or LaB_6 rods. [116] Most modern microscopes use a field emission gun which includes a tungsten tip with a layer of ZrO_2 on an emitter. The samples are placed in a vacuum and hit with electrons, which interact using elastic and inelastic scattering and then an image recorded using the multiple lenses present within the microscope.

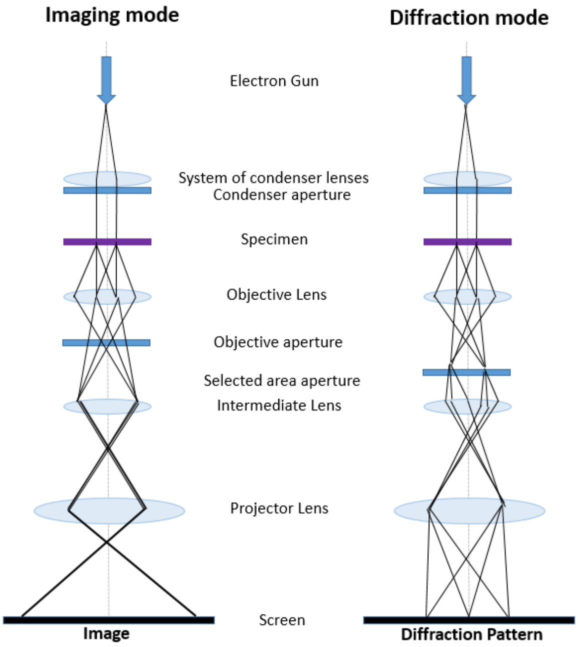

Figure 1.5.2: A schematic showing both the imaging modes and diffraction mode of Transmission electron microscopy, TEM. A simple Fourier transform is used to convert the diffraction pattern into an image.

1.6 Multivalent Protein – Ligand Interactions

In order to prepare the QD-conjugates used in FRET analysis and the AuNP-conjugates for fluorescence quenching analysis, specific ligands must be designed and developed that can easily bind to both the NPs and the biological macromolecule. Synthesis of QDs usually leaves them coated in hydrophobic ligands making them unsuitable for biological purposes this is different for AuNPs as they are usually already hydrophilic. The surface coatings of the NPs are key for developing materials suitable to size, shape and specific functionality. Multivalent interactions are used throughout biology and are important because of two factors; for strength and for providing the basis to biological mechanisms.[117] Suggesting that ligands used for this purpose must contain multiple binding sites attached to the surface of one NP. As many proteins are multivalent, meaning that they have multiple binding sites, it is important that we characterize them using materials that contain multivalent ligands.[117] The ligands must also form stable coatings on the NPs and also be resistant to non-specific interactions. The mechanisms behind how multivalent interactions are formed are currently poorly understood due to the nature of multiple interactions at once.[118]

A wide range of ligands showing multivalency have been synthesized and can be used to explore multivalent interactions.[117, 119, 120] Example ligands that show all the specific properties required for probing multivalent protein interactions consist of: a chelative dihydrolipoic acid group that can bind strongly to both QDs and AuNPs, and one or more carboxylic acid groups which can be further modified with specific functionalities.[121] The structural design of these ligands can further split into an anchor segment, a hydrophilic segment and a functional group, as shown in **Figure 1.6.1**. [122] Each specific section then specifically enhances the properties of the ligand for probing multivalent interactions.

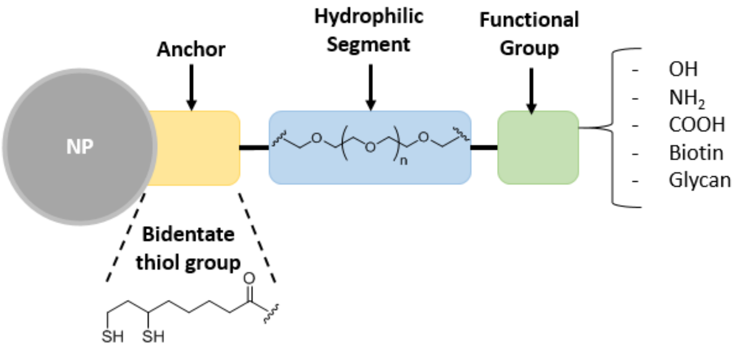

Figure 1.6.1: DHLA-based multifunctional ligands are used as a linking group between the protein and NP using different terminal groups.

The properties provided by each section will in turn make the ligand more specified to its function as a NP bioconjugate. A di-thiol group is preferred, as the anchor because it can chelate strongly to the NP surface to produce compact and stable NPs easily and cheaply. [121] The di-thiolate provides a stronger binding affinity for the NP surface over a monodendate thiolate ligand. The functional group is to promote the linkage to the target molecule. [122] A compound which is widely used is dihydrolipoic acid, DHLA, based ligands as they are shown to have a greater enhancement of colloidal stability over a wide variety of biological conditions which is also further.[123] This enhancement of colloidal stability in biological media is further stabilized through the addition of oligoethylene glycol, EG, linkers, or a zwitterionic section to the ligand. These materials are also biologically inert when not in the presence the functional group.[124] The polymer chain is there to help separate of the functional group from the NP surface, and further works to promote water-solubility and resistance to non-specific adsorption of biomolecules.

A dendron, hyperbranched organic molecules connected to a central point, is a type of ligand that has been commonly used to achieve multivalency and produce NP-bioconjugates.[125] The surface densities of specific functionalities can be enhanced through using such ligands multiple from one anchor point known as a chelating dendritic ligand, CDL. This now included the di-thiol function to chelate to the metal surface of the NPs, **Figure 1.6.2** shows a CDL taken by Zhou *et al*.[121] These materials don't differ too much from each other just in the chelation of the surfaces as the dendron has been further modified to chelate to NPs. These materials are widely used part of a NP-bioconjugate surface functionality research for specific multivalent interactions.

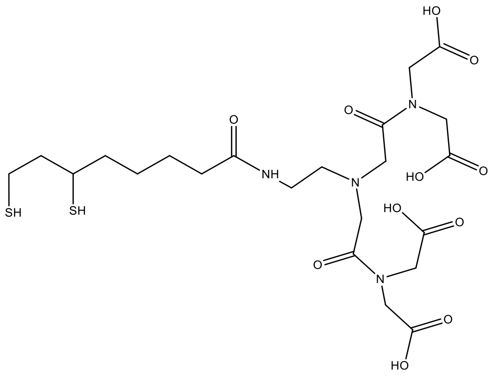

Figure 1.6.2: Molecular structures of a chelating dendritic ligand, CDL.[121]

1.6.1 Glyconanoparticles

Current research is being undertaken to understand the structural mechanisms of multivalent interactions between c-type lectins and glycans, particularly the spatial arrangement of their carbohydrate binding domains with specific proteins. [126] One way to monitor this interaction is by using modified nanoparticles, NPs. Nanoparticles include gold, iron oxide or semiconductor nanoparticles. These NPs are bound to sugar molecules and thus are given the name glyconanoparticles. These materials are known to be a good mimics of carbohydrate presentation upon the surface of different cells making them great tools for glycobiology and biomedicine research.[127] This is due to their large surface area to volume ratio in comparison to other types of related compounds already used within this field as we can place a large amount of functional groups upon the surface for high loading efficiency.[128] Many reviews have been published in this area highlighting the importance of these materials. Hao *et al.* summaries the synthesis of many different types of glyconanoparticles and how they are being used in biosensing[129] as well as a review by de la Fuente *et al*.[127] Cunha *et al*. have published a review highlighting the biomedical applications of quantum dot based glyconanoparticles.[130]

There is a range of papers in the literature showing many NP scaffold examples of glyconanoparticles. Park *et al.* synthesised a glyconanoparticle using silica, containing rhodamine B isothiocyanate, to over-coat cobalt ferrite nanocrystals which integrated two properties within one, fluorescence and magnetism,[128] also known as a dual-modal fluorescent magnetic nanoparticle, FMNP. These materials were then successfully used to block the adhesion of the infectious stomach bacteria *Helicobacter pylori* on mammalian cells by expressing different carbohydrate-binding proteins.[128] Yang et al. prepared a lactose CdSeS/ZnS quantum dot conjugates to further study specific carbohydrate-protein interactions.[131]

1.7 C-type Lectin Based Viral Receptors

All mammalian cells are covered by a dense array of carbohydrates called the glycocalyx.[132] The carbohydrates within this bind to proteins and lipids creating glycoproteins and glycolipids respectively. These biomaterials play key roles with the human biological system in such processes as cell-cell signalling and cell-environment interactions.[133] Singular carbohydrate interactions are weak and biologically non-functional so to overcome this, nature has created a unique multivalent receptor – ligand presentation. Multivalent interactions can increase the binding affinities and further enhance the biological functions. Increasing the valency of carbohydrates can positively enhance the protein-carbohydrate interaction by positive co-cooperativity. Whereas, the weak interactions can be of negative cooperativity leading to decrease in binding efficiency.[117] This is further highlighted by some basic thermodynamics as highlighted in **Figure 1.7.1**.

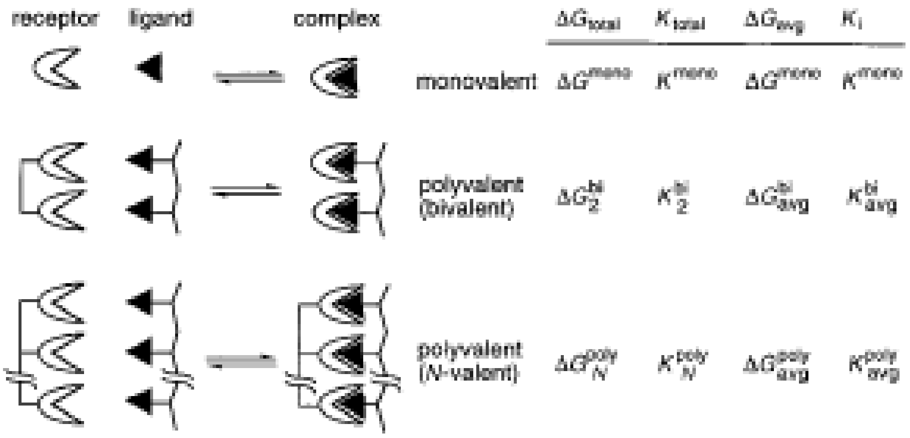

Figure 1.7.1: The proposed names for multivalent interactions and the thermodynamic relationships of the Gibbs free energy of binding (ΔG) and inhibition constants (K_i) of these interactions. Reprinted from reference.[117]

In which the singular bond becomes enhanced through multiple of the same bonds. These multivalent – ligand interactions occurs within c-type lectin proteins. C-type lectins are calcium-dependent carbohydrate binding proteins.[134] They play important roles in many biological processes, some of which include cell – cell adhesion, innate immunity and serum glycoprotein clearance.[135] A major characteristic of a c-type lectin is the presence of one or multiple carbohydrate recognition domains (CRDs) within their structure.[136] C-type lectins binding domains attach together to make a multivalent arrays forming dimers, trimers and tetramers in which the different multivalences are presented in a multiple orientations. [137]

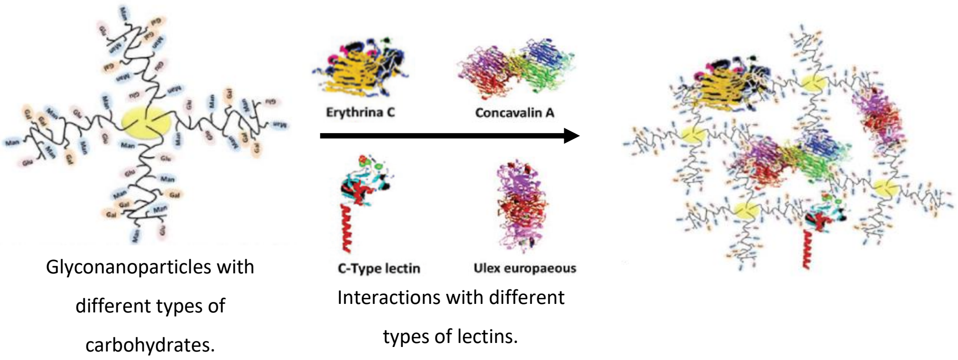

Figure 1.7.2: Schematic representation of nanoparticles showing the interactions of different types of carbohydrates with different types of lectin. Reprinted from reference.[138]

These molecules are primarily used in the body for detecting high mannose oligosaccharides found on anything from viruses' surfaces to toxins. A large amount of research carried out by Feinberg *et al.* has looked at the specific binding of mannose oligosaccharides to c-type lectin carbohydrate recognition domains (CRD).[139, 140] It was found that high mannose oligosaccharides bind to the c-type lectin receptors via principal calcium ion via the vicinal hydroxyl groups on the pyranose ring of mannose.[139] **Figure 1.7.2** below represents nanoparticles containing different types of carbohydrates that can interact with different lectins (erythina C, concavalin A, ulex europaeous). It shows multiple nanoparticles are bound to each of the lectins, meaning each lectin has multiple binding sites.

Two examples of c-type lectins are DC-SIGN and DC-SIGNR they are found within the peripheral immune system of the body.[134, 141] DC-SIGN, dendritic cell-specific intercellular adhesion molecule grabbing nonintegrin and DC-SIGNR, DC-SIGN- related, both contain four CRDs. A common primary structure for them contains a short N-terminal tail, a transmembrane anchor, a tetramerisation domain and also a c-terminal CRD.[139] The schematic shown in **Figure 1.7.3** highlights some of the key characteristic sections of these proteins, in this case the schematic of a DC-SIGN. In addition to this there is also a calcium ion siting within the structure. This is known as the principal Ca^{2+}, which is the distinctive feature of the carbohydrate binding site as it undergoes coordination with the hydroxyl groups of the sugar.[139] The two binding hydroxyls are presented in an equatorial array at the 3' and 4' positions within the mannose ring.

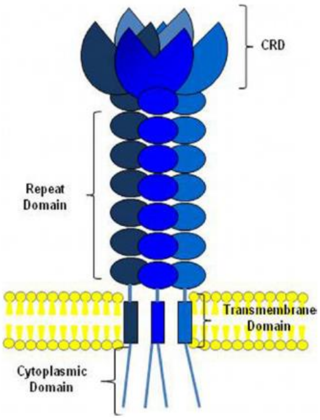

Figure 1.7.3: A schematic of the predicted domains for DC-SIGN and DC-SIGNR showing the common features. Reprinted from reference.[142]

1.7.1 DC-SIGN

DC-SIGN, first sequenced in 1992 after it was found for its properties in binding to the glycoprotein, gp120, found upon the human immunodeficiency virus, HIV.[143] It is a type II membrane protein found in dendritic cells, DCs, and macrophages but are more specifically present in the lamina propina of mucosal tissues found in the rectum, uterus and cervix.[140] The protein contains an extracellular domain consisting of a tetrameric stalk. Further details about the tetrameric stalk, such as its structural properties, are yet to be determined. As well as being found to bind to mannose containing oligosaccharides, DC-SIGN has also shown to bind with fucose-containing sugars. Due to its affinity for high mannose oligosaccharides, DC-SIGN can act as a receptor for different infectious viruses such as HIV, hepatitis C virus and Ebola virus. Due to it being a DC it has thus been associated with acting as an intercellular adhesion molecule.[144] Part of its function is to sense any unknown invading pathogens, which then leads to a signaling pathway of a specific response in which T cells are differentiated in order to provide the immune response against the found foreign entity.

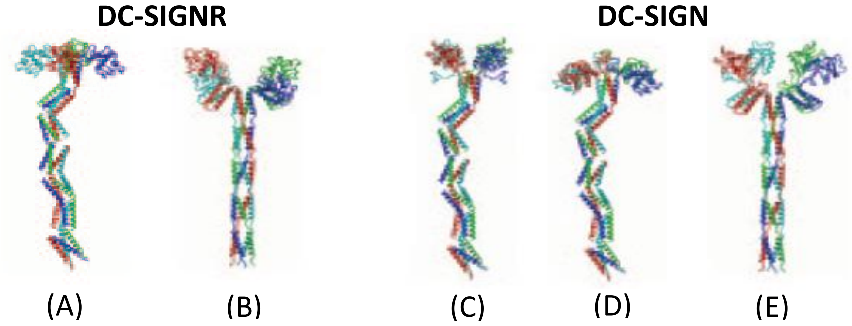

Figure 1.7.4: Best predicted models of the extracellular domain of DC-SIGN and DC-SIGNR, best fitting to the experimental data obtained by Feinberg et al., (A) single tetrameric stalk model for DC-SIGNR, (B) Y-shaped dimer model for DC-SIGNR, (C) and (D) two single tetrameric stalk model for DC-SIGN and (E) Y-shaped dimer model for DC-SIGN. Reprinted from reference.[144]

Figure 1.7.4 (C), (D) and (E) shows the most plausible models that have been presented for the extracellular segment of DC-SIGN by Feinberg *et al.* based on their hydrodynamic experiments. The model suggests a non-spherical shape due to the values of the sedimentation and diffusion coefficient being lower than expected for spherical molecules. They also found a lack of flexibility between the repeated coiled-coil neck, which suggests a structure more like those pictured above.[144] The CRD is located within the neck region that sits above the surface of the cell.

Although these proteins specially bind to high mannose oligosaccharides, research has suggested binding has been found to other sugars. For example, in the case of DC-SIGN, fucose binding has been found. This is highlighted in a paper by van Liempt *et al.* showing the specificity that DC-SIGN has for both sugars.[145] In terms of sugar specific binding, Feinberg *et al.* showed that the CRD selectively recognises the internal portion of the carbohydrate moiety. Specifically the proteins were also found to bind to the outer-branched tri-mannose unit that were unique to the mannose type used for this particular study.[139] The binding mode between the oligomannose, $GlcNAc_2Man_3$, and CRD of DC-SIGN, is shown below in the crystal structure in **Figure 1.7.5**, with the sugar shown in yellow and the protein in blue. It also shows how calcium plays a large role within the specific binding for these prticular proteins. Within this interaction two mannose sugars can be seen to interact with the protein-binding site. Binding with the fucose sugar occurs in a different manner to the binding seen with mannose. It was found to bind at a galanin residue via binding of the essential calcium ion.[146]

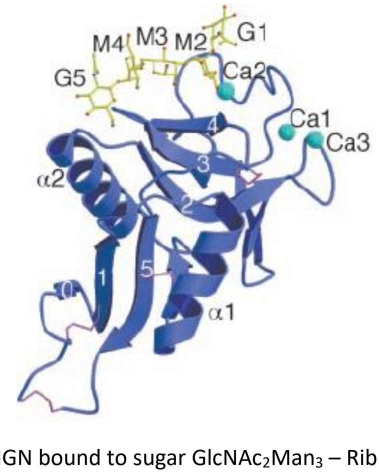

Figure 1.7.5: Structure of CRD of DC-SIGN bound to sugar $GlcNAc_2Man_3$ – Ribbon diagram of the DC-SIGN CRD (blue) with bound oligosaccharide residues shown via a single lettering system G for GlcNAc and M for mannose. Calcium ions are also shown in cyan and the dusulfide bonds are shown in pink. Reprinted from reference.[140]

1.7.2 DC-SIGNR

DC-SIGNR, DC-SIGN related, also known as L-SIGN, is again another type II membrane protein consisting of a c-type lectin viral receptor. They are closely related as 77% of the amino acid sequences in DC-SIGNR and DC-SIGN are identical, suggesting that similarities and differences can be seen between each of the c-type lectins.[140] The major similarities between the two are that they have the same overall tetrameric structure, both bind to high-mannose containing oligosaccharides and are both classed as a C-type receptors. DC-SIGNR has the ability to bind to the same viruses as DC-SIGN due to its affinity for mannose sugars.[147] A significant difference between them is the location in which these types of cells can be found within the body, DC-SIGNR is commonly found in the endothelial cells in the liver as well as the lymph nodes and the placenta.[147] Despite such close resemblance, distinct multivalent ligand binding specificities[147] as well as virus transfection properties have also been reported.

Similarly to DC-SIGN, there is currently no published detailed structure of DC-SIGNR, but predicted models of the extracellular domain have been hypothesised (**Figure 1.7.4** (A) and (B) above). These are taken from the same published paper that developed the models for DC-SIGN based on hydrodynamic size values by Feinberg *et al*.[144] It has been proposed that DC-SIGNR has the same structure as DC-SIGN in terms of fitting to the same model approaches, in that one is with the tetrameric stalk and the other has the y-shaped model. This is because the binding affinity between a singular CRD and glycan molecule was worked out to be the same for each of the proteins. The individual binding between a mannose containing glycan and DC-SIGNR CRD is shown in the crystal structure below, **Figure 1.7.6**. Similarly to DC-SIGN, they propose that in DC-SIGNR the neck region sits on top of the cell surface where the tetrameric binding site lies.

In comparison to DC-SIGN, DC-SIGNR does not bind to fucose containing sugars as reported by Guo *et al.,* who compared the distinct ligand binding properties for both DC-SIGN and DC-SIGNR.[147] Mannose sugars also bind to DC-SIGNR in a similar way to that shown for DC-SIGN in **Figure 1.7.6**.

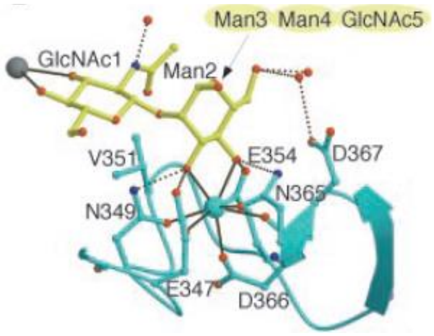

Figure 1.7.6: Interaction of the α1-3-linked branch of the molecule GlNAc$_2$-Man$_2$ with DC-SIGNR. The remaining mannose residues are drawn schematically. Again the calcium ion dependency can be seen due to the black lines showing the Ca^{2+} coordination. Reprinted from reference.*[140]*

1.7.3 Pathogen Internalisation Via C-type Lectins

Pathogen internalisation, the transport of pathogen into the cell, occurs via the c-type lectins that are found within the body and even more specifically the DC-SIGN/R. These particular proteins are pattern recognition receptors that are used to sense the invading pathogens leading to immune responses occurring as a result. This includes protein cell signaling and the differentiation of T-helper cells.[148] There are many viruses and bacteria (e.g. *Mycobacterium tuberculosis*, and HIV-1 and *Helicobacter pylori)* that are internalised into the cell via DC-SIGN/R due to their high surface sugar content. The process is very highly dependent on the lectin extracellular domain of the DCs, which is known to bind to HIV surface glycoprotein 120, gp120, for both DC-SIGN and DC-SIGNR.[141] Research by Chung *et al.* has found that DC-SIGN can recognise and transmit some viruses better than DC-SIGNR and vice versa. Some examples include some HIV strains which are recognised by DC-SIGN while west Nile virus is recognised by DC-SIGNR.[149]

There has been a wide range of research into the internalisation mechanisms and the most common one is HIV internalisation. Auwerx *et al.* showed that this internalisation occurred via the capture of the virus molecules by DC-SIGN expressing cells. They successfully used a carbohydrate-binding agent, CBAs, to block this capture.[150] The same conclusion has been shown by both Balarani [151] and Truville *et al*.[152] There are two proposed mechanisms of how DCs bind and internalise HIV as suggested by Wu *et al*. These are the trans pathway and the cis pathway which are highlighted below in **Figure 1.7.7**.[153] There are two differing trans pathways. The first includes transport across the infectious synapse, a cell-to-cell junction formed when a HIV virus is captured. The second trans pathway is achieved using both mature and immature cells crossing the synapse via exocytosis. The cis pathway is shown to play a key role in the long term infection of HIV transmission, which leads to replication and production of new HIV within the cell membrane.

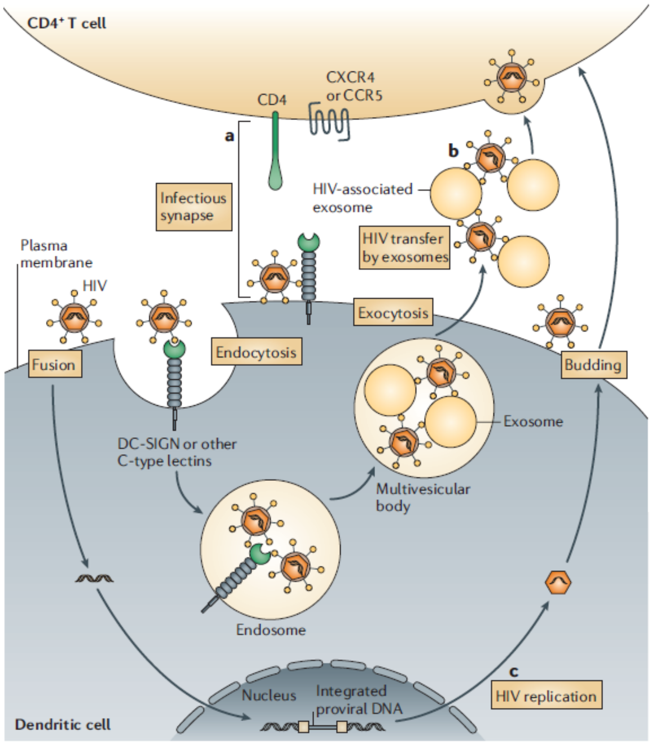

Figure 1.7.7: Schematic showing the mechanism of dendritic cell mediated HIV transmission. Shown here are two different proposed pathways: (a), (b) are two different mechanisms for trans-infection and (c) is the method of cis-infection. Reprinted from reference. *153*

Infection can also be caused by DCs interacting with the glycoprotein 120 subunit situated on the viral surface. This causes a conformational change of the protein structure, which means that it is recognised and further internalised via cell signalling.[141] Although these models have been proposed, there is still key structural and mechanistic information missing in regards to how the proteins differentiate between different targets, as well as exactly how the CRDs sit and flex upon viral binding. This information will be key for future research, especially in developing an effective vaccine that targets DCs to fight the infectious diseases[134], in drug development for treating these infections that are internalised[150] and in designing specific targeted inhibitors against these proteins.

1.8 Conclusion

Nanomaterials such as QDs and AuNPs both show a variety of different properties that showcase how they can be used as potential NP-bioconjugates when functionalized with various biological macromolecules such as DNA, peptides and proteins. These nanomaterials have shown so much promise across a wide range of areas from use as biosensors, nanocarriers, bio-imaging agents and as part of immunoassays. Due to the significant optical properties of both QDs (size-dependent bandgap structure) and AuNPs (strong localised surface plasma absorption) they can be useful as part of a highly sensitive fluorescence based read-out strategies. These materials can now be synthesised through relatively simple one-pot methods. Ligand exchange can then be used to introduce specific functional groups. Glyconanoparticles can easily be synthesised using these materials when a glycan is placed as the surface functionality. An apparent knowledge gap in the literature is found on how the viral receptors, DC-SIGN and DC-SIGNR, binding domains are presented on the surface of cells which control the nature of their multivalent interactions with glycoproteins. Although the literature has provided key information on the binding affinity of the monovalent interactions of the CRD with different glycan materials. Glyconanomaterials show great potential as multivalent probes for these interactions due to the surface being coated with the functional glycan material of the interaction. These functionalised glycan-NPs can also be characterised in a variety of different ways to reveal useful structural information on the glycan-protein interaction.

1.9 Aims of this Project

The major objective of this project is to produce a wide range of NP-sugar conjugates, which will be used to further understand and elucidate the structural and mechanistic properties of the c-type lectins, and more specially DC-SIGN and DC-SIGNR. Currently little is known about their structure and CRD spatial arrangement, which is key to the multivalent binding nature of these proteins. These proteins are also of high interest due to their involvement in the viral infections of diseases such as HIV, West Nile Virus and Ebola. The investigations will be done using QD-saccharides conjugates as FRET probes and using AuNP-saccharides as fluorescence quenchers. The fluorescence based read-out strategies will be developed into a rapid, sensitive method to deduce the binding affinities and thermodynamics of the multivalent NP probe-protein interactions, **Figure 1.9.1**. By systematically tuning the QD/GNP surface saccharides valency, inter glycan distance and flexibility, we expect to see that the binding site and sugar spacing distance match, leading to a greatly enhanced affinity and specificity via the formation of simultaneous multivalent binding.

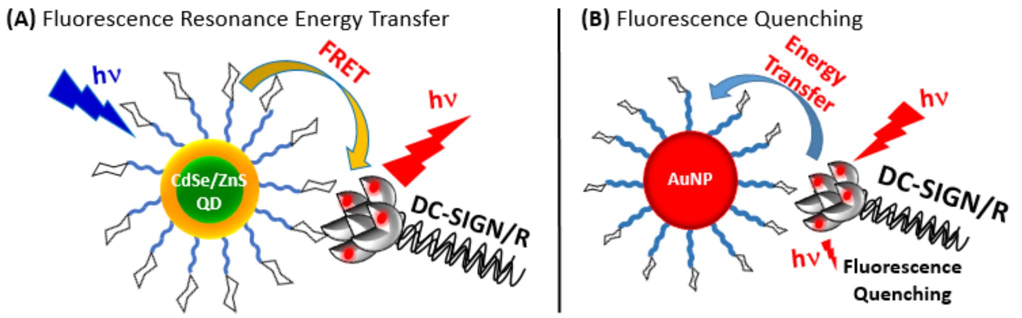

Figure 1.9.1: Schematic of the fluorescence based read- out strategies used within this project. (**A**) Flourescence resonance energy transfer and (**B**) fluorescence quenching.

This work will continue on from the recent successful work by Guo *et al*.[154] Two NP scaffolds will be investigated, QDs and AuNPs, capped with both monosaccharide and disaccharide mannoses to study the apparent binding affinity, K, and the binding dissociation constant, K_d, using the two sensitive fluorescence energy transfer mechanisms. QDs will be used for their advantageous optical properties such as strong size dependence fluorescence, high quantum yields, however they can be cytotoxic due to potential cadmium ion leakage. This is why AuNPs are also investigated as they are great fluorescence quenchers but do not contain toxic heavy metals. They can also offer a larger range of sizes over QDs which can be manipulated to help calculate the distances between the CRD groups found within the proteins. Both materials can efficiently cap-exchange with custom ligands designed for binding with DC-SIGN/R. The sugar ligands series, LA-EG$_n$-Man^s (where n= 3 and 11 and s = 1 and 2) and LA-(EG$_n$-Man^s)$_m$ (where n = 1 or 2, s = 1 and 2 and m = 1, 2 and 3), **Figure 1.9.2**, will be synthesised using two different click chemistry methods. The mannose functional group will be spaced by a defined oligo(ethylene glycol) linker from the NP surface anchoring group, lipoic acid, LA. The specificity of the NP-glycan protein interaction will be quantified by competition experiments using free sugar as well as unlabelled proteins to calculate the respective binding inhibition constant, K_i. This also confirms the binding specificity between the saccharide -protein interactions.

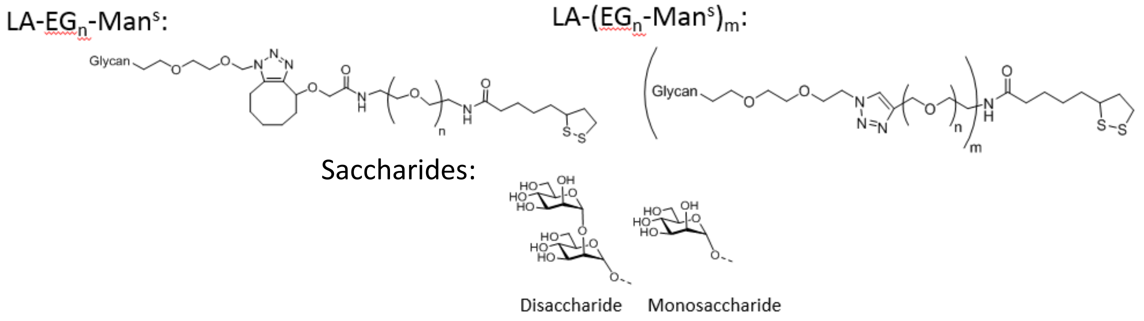

Figure 1.9.2: The proposed ligand structures of the ligand series used throughout this project, LA-EG$_n$-Man^s (where n= 3 and 11 and s = 1 and 2) and LA-(EG$_n$-Man^s)$_m$ (where n = 1 or 2, s = 1 and 2 and m = 1, 2 and 3).

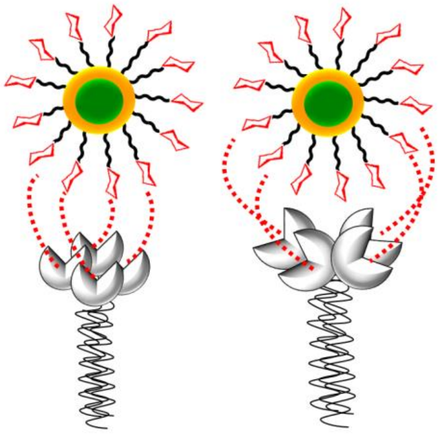

Figure 1.9.3: Specific binding between the proteins DC-SIGN/R and the novel multivalent QD- saccharides based viral inhibitor. Schematic based on predicted structures of these materials.

Different characterisation techniques, such as DLS and TEM, will also be used to elucidate a structural binding model for the dimensions of the CRDs found within both the proteins. **Figure 1.9.3** shows the intended specific binding of the glycan-QDs to the proteins DC-SIGN/R. The mian aim is to try and develop a further understanding of the geometries of the CRD head groups in both proteins, as this is still unknown. There is a clear knowledge gap within the literature for DC-SIGN/R regarding their structural and mechanistic which is critical for designing more specific treatments for the viral infections in which DC-SIGN/R are involved. Once a valid structural model is revealed, investigations into the use of these NP-glycan probes as novel multivalent anti-viral inhibitors can be conducted to inhibit viral infections by blocking the initial viral-cell interactions.

1.10 References

1. R. Herizchi, E. Abbasi, M. Milani and A. Akbarzadeh, *Artif. Cells. Nanomed. B*, 2016, **44**, 596-602.
2. B. Bhushan, *Springer handbook of nanotechnology*, Springer Heidelberg Dordrecht London New York, 2017.
3. J. B. Delehanty, I. L. Medintz, T. Pons, F. M. Brunel, P. E. Dawson and H. Mattoussi, *Bioconjug. Chem.*, 2006, **17**, 920-927.
4. W. C. Chan and S. Nie, *Science*, 1998, **281**, 2016-2018.
5. A. R. Clapp, I. L. Medintz, J. M. Mauro, B. R. Fisher, M. G. Bawendi and H. Mattoussi, *J. Am. Chem. Soc.*, 2004, **126**, 301-310.

6. M. Stanisavljevic, S. Krizkova, M. Vaculovicova, R. Kizek and V. Adam, *Biosens. Bioelectron.*, 2015, **74**, 562-574.

7. W. C. Chan, D. J. Maxwell, X. Gao, R. E. Bailey, M. Han and S. Nie, *Curr. Opin. Biotech.*, 2002, **13**, 40-46.

8. B. Dabbousi, J. Rodriguez-Viejo, F. V. Mikulec, J. Heine, H. Mattoussi, R. Ober, K. Jensen and M. Bawendi, *J. Phys. Chem. B.*, 1997, **101**, 9463-9475.

9. R. C. Somers, M. G. Bawendi and D. G. Nocera, *Chem. Soc. Rev*, 2007, **36**, 579-591.

10. M. Han, X. Gao, J. Z. Su and S. Nie, *Nat. Biotechnol*, 2001, **19**, 631-635.

11. M. Bruchez, M. Moronne, P. Gin, S. Weiss and A. P. Alivisatos, *Science*, 1998, **281**, 2013-2016.

12. W. U. Huynh, J. J. Dittmer and A. P. Alivisatos, *Science*, 2002, **295**, 2425-2427.

13. Y. Yuan and M. Krüger, *Polymers*, 2011, **4**, 1-19.

14. S. Kim, B. Fisher, H.-J. Eisler and M. Bawendi, *J. Am. Chem. Soc.*, 2003, **125**, 11466-11467.

15. R. Ghosh Chaudhuri and S. Paria, *Chem. Rev.*, 2011, **112**, 2373-2433.

16. S. Hohng and T. Ha, *J. Am. Chem. Soc.*, 2004, **126**, 1324-1325.

17. C. Murray, D. J. Norris and M. G. Bawendi, *J. Am. Chem. Soc.*, 1993, **115**, 8706-8715.

18. M. A. Hines and P. Guyot-Sionnest, *J. Phys. Chem.*, 1996, **100**, 468-471.

19. Z. A. Peng and X. Peng, *J. Am. Chem. Soc.*, 2001, **123**, 183-184.

20. S. Pathak, S.-K. Choi, N. Arnheim and M. E. Thompson, *J. Am. Chem. Soc.*, 2001, **123**, 4103-4104.

21. H. Mattoussi, J. M. Mauro, E. R. Goldman, G. P. Anderson, V. C. Sundar, F. V. Mikulec and M. G. Bawendi, *J. Am. Chem. Soc.*, 2000, **122**, 12142-12150.

22. S. Kim and M. G. Bawendi, *J. Am. Chem. Soc.*, 2003, **125**, 14652-14653.

23. F. Pinaud, D. King, H.-P. Moore and S. Weiss, *J. Am. Chem. Soc.*, 2004, **126**, 6115-6123.

24. W. Guo, J. J. Li, Y. A. Wang and X. Peng, *Chem. Mater.*, 2003, **15**, 3125-3133.

25. W. Y. William, E. Chang, R. Drezek and V. L. Colvin, *Biochem. Bioph. Res. Co.*, 2006, **348**, 781-786.

26. I. L. Medintz, A. R. Clapp, H. Mattoussi, E. R. Goldman, B. Fisher and J. M. Mauro, *Nat. Mater.*, 2003, **2**, 630.

27. I. L. Medintz, T. Pons, J. B. Delehanty, K. Susumu, F. M. Brunel, P. E. Dawson and H. Mattoussi, *Bioconjug. Chem.*, 2008, **19**, 1785-1795.

28. D. Zhou, L. Ying, X. Hong, E. A. Hall, C. Abell and D. Klenerman, *Langmuir*, 2008, **24**, 1659-1664.

29. L. Mattera, S. Bhuckory, K. D. Wegner, X. Qiu, F. Agnese, C. Lincheneau, T. Senden, D. Djurado, L. J. Charbonnière and N. Hildebrandt, *Nanoscale*, 2016, **8**, 11275-11283.
30. M. J. Ruedas-Rama and E. A. Hall, *Anal. Chem.*, 2010, **82**, 9043-9049.
31. A. M. Derfus, W. C. Chan and S. N. Bhatia, *Adv. Mater.*, 2004, **16**, 961-966.
32. A. M. Derfus, W. C. Chan and S. N. Bhatia, *Nano. Lett.*, 2004, **4**, 11-18.
33. I. L. Medintz, L. Berti, T. Pons, A. F. Grimes, D. S. English, A. Alessandrini, P. Facci and H. Mattoussi, *Nano. Lett.*, 2007, **7**, 1741-1748.
34. V. Biju, T. Itoh and M. Ishikawa, *Chem. Soc. Rev*, 2010, **39**, 3031-3056.
35. J. Breger, J. B. Delehanty and I. L. Medintz, *WIREs. Nanomed. Nanobiotechnol.*, 2015, **7**, 131-151.
36. I. L. Medintz, H. T. Uyeda, E. R. Goldman and H. Mattoussi, *Nat. Mater.*, 2005, **4**, 435-446.
37. P. Decuzzi and M. Ferrari, *Biomaterials*, 2007, **28**, 2915-2922.
38. C. Schieber, A. Bestetti, J. P. Lim, A. D. Ryan, T. L. Nguyen, R. Eldridge, A. R. White, P. A. Gleeson, P. S. Donnelly and S. J. Williams, *Angew. Chem. Int. Ed.*, 2012, **51**, 10523-10527.
39. R. Bilan, F. Fleury, I. Nabiev and A. Sukhanova, *Bioconjug. Chem.*, 2015, **26**, 609-624.
40. D. Zhou, J. D. Piper, C. Abell, D. Klenerman, D.-J. Kang and L. Ying, *Chem. Commun.*, 2005, 4807-4809.
41. A. Samanta, S. Buckhout-White, E. Oh, K. Susumu and I. L. Medintz, *MSDE*, 2018, **3**, 314-327.
42. S. Pathak, M. C. Davidson and G. A. Silva, *Nano. Lett.*, 2007, **7**, 1839-1845.
43. E. R. Goldman, E. D. Balighian, H. Mattoussi, M. K. Kuno, J. M. Mauro, P. T. Tran and G. P. Anderson, *J. Am. Chem. Soc.*, 2002, **124**, 6378-6382.
44. G. Annio, T. L. Jennings, O. Tagit and N. Hildebrandt, *Bioconjug. Chem.*, 2018, **29**, 2082-2089.
45. H. S. Afsari, M. C. Dos Santos, S. Lindén, T. Chen, X. Qiu, P. M. v. B. en Henegouwen, T. L. Jennings, K. Susumu, I. L. Medintz and N. Hildebrandt, *Sci. Adv.*, 2016, **2**, e1600265.
46. A. R. Clapp, I. L. Medintz, B. R. Fisher, G. P. Anderson and H. Mattoussi, *J. Am. Chem. Soc.*, 2005, **127**, 1242-1250.
47. T. Forster, *Naturwissenschaften*, 1946, **33**, 166-175.
48. T. Förster, *Ann. Phys-Berlin.*, 1948, **437**, 55-75.
49. E. Bowen, *Q. Rev. Chem. Soc.*, 1947, **1**, 1-15.
50. I. L. Medintz and H. Mattoussi, *Phys. Chem. Chem. Phys.*, 2009, **11**, 17-45.

51. J. Saha, A. D. Roy, D. Dey, D. Bhattacharjee and S. A. Hussain, *Mater. Today-Proc.*, 2018, **5**, 2306-2313.

52. A. Shamirian, A. Ghai and P. T. Snee, *Sensors*, 2015, **15**, 13028-13051.

53. S. Saini, H. Singh and B. Bagchi, *Journal of Chemical Sciences*, 2006, **118**, 23-35.

54. D. W. Piston and G.-J. Kremers, *Trends. Biochem. Sci.*, 2007, **32**, 407-414.

55. D. Geissler, S. Linden, K. Liermann, K. D. Wegner, L. J. Charbonniere and N. Hildebrandt, *Inorg. Chem.*, 2013, **53**, 1824-1838.

56. P. Babu, S. Sinha and A. Surolia, *Bioconjug. Chem.*, 2007, **18**, 146-151.

57. M.-k. So, C. Xu, A. M. Loening, S. S. Gambhir and J. Rao, *Nat. Biotechnol*, 2006, **24**, 339-343.

58. X. Huang and J. Ren, *Anal. Chim. Acta.*, 2011, **686**, 115-120.

59. A. N. Bader, E. G. Hofman, J. Voortman, P. M. v. B. en Henegouwen and H. C. Gerritsen, *Biophys. J.*, 2009, **97**, 2613-2622.

60. M. Tramier, M. Zahid, J. C. Mevel, M. J. Masse and M. Coppey-Moisan, *Microsc. Res. Techniq.*, 2006, **69**, 933-939.

61. A. Kapur, F. Aldeek, X. Ji, M. Safi, W. Wang, A. Del Cid, O. Steinbock and H. Mattoussi, *Bioconjug. Chem.*, 2017, **28**, 678-687.

62. D. A. Giljohann, D. S. Seferos, W. L. Daniel, M. D. Massich, P. C. Patel and C. A. Mirkin, *Angew. Chem. Int. Ed.*, 2010, **49**, 3280-3294.

63. K. L. Kelly, E. Coronado, L. L. Zhao and G. C. Schatz, ACS Publications, Editon edn., 2003.

64. J. Shi, C. Chan, Y. Pang, W. Ye, F. Tian, J. Lyu, Y. Zhang and M. Yang, *Biosens. Bioelectron.*, 2015, **67**, 595-600.

65. Y. Cao, B. Griffith, P. Bhomkar, D. S. Wishart and M. T. McDermott, *Analyst*, 2018, **143**, 289-296.

66. J. Song, J. Zhou and H. Duan, *J. Am. Chem. Soc.*, 2012, **134**, 13458-13469.

67. C. Xue, Y. Xue, L. Dai, A. Urbas and Q. Li, *Adv. Opt. Mater.*, 2013, **1**, 581-587.

68. M.-C. Daniel and D. Astruc, *Chem. Rev.*, 2004, **104**, 293-346.

69. Y. Yang, Y. Yan, W. Wang and J. Li, *Nanotechnology*, 2008, **19**, 175603.

70. D. Arosio, F. Chiodo, J. J. Reina, M. Marelli, S. Penadés, Y. van Kooyk, J. J. Garcia-Vallejo and A. Bernardi, *Bioconjug. Chem.*, 2014, **25**, 2244-2251.

71. E. Oh, M.-Y. Hong, D. Lee, S.-H. Nam, H. C. Yoon and H.-S. Kim, *J. Am. Chem. Soc.*, 2005, **127**, 3270-3271.

72. A. Samanta, Y. Zhou, S. Zou, H. Yan and Y. Liu, *Nano. Lett.*, 2014, **14**, 5052-5057.

73. C. Yun, A. Javier, T. Jennings, M. Fisher, S. Hira, S. Peterson, B. Hopkins, N. Reich and G. Strouse, *J. Am. Chem. Soc.*, 2005, **127**, 3115-3119.

74. M. Swierczewska, S. Lee and X. Chen, *Phys. Chem. Chem. Phys.*, 2011, **13**, 9929-9941.

75. Y. Guo, I. Nehlmeier, E. Poole, C. Sakonsinsiri, N. Hondow, A. Brown, Q. Li, S. Li, J. Whitworth and Z. Li, *J. Am. Chem. Soc.*, 2017, **139**, 11833-11844.

76. P. P. H. Cheng, D. Silvester, G. Wang, G. Kalyuzhny, A. Douglas and R. W. Murray, *J. Phys. Chem. B.*, 2006, **110**, 4637-4644.

77. J. Turkevich, P. C. Stevenson and J. Hillier, *Discuss. Faraday. Soc.*, 1951, **11**, 55-75.

78. G. Frens, *Nat. Phys. Sci.*, 1973, **241**, 20.

79. M. Brust, M. Walker, D. Bethell, D. J. Schiffrin and R. Whyman, *J. Chem. Soc. Chem. Comm.*, 1994, 801-802.

80. M. T. Reetz and W. Helbig, *J. Am. Chem. Soc.*, 1994, **116**, 7401-7402.

81. N. R. Jana, L. Gearheart and C. J. Murphy, *Langmuir*, 2001, **17**, 6782-6786.

82. D. J. Lewis and Z. Pikramenou, *Coordin. Chem. Rev.*, 2014, **273**, 213-225.

83. K. E. Sapsford, K. M. Tyner, B. J. Dair, J. R. Deschamps and I. L. Medintz, *Anal. Chem.*, 2011, **83**, 4453-4488.

84. C. Parolo, A. de la Escosura-Muñiz, E. Polo, V. Grazú, J. M. De La Fuente and A. Merkoçi, *ACS Appl. Mater. Interfaces*, 2013, **5**, 10753-10759.

85. A. Kumar, H. Ma, X. Zhang, K. Huang, S. Jin, J. Liu, T. Wei, W. Cao, G. Zou and X.-J. Liang, *Biomaterials*, 2012, **33**, 1180-1189.

86. J. Zong, S. L. Cobb and N. R. Cameron, *Biomater. Sci.*, 2017, **5**, 872-886.

87. S. Si, A. Kotal and T. K. Mandal, *J. Phys. Chem. C.*, 2007, **111**, 1248-1255.

88. S. J. Zhen, Y. F. Li, C. Z. Huang and Y. F. Long, *Talanta*, 2008, **76**, 230-232.

89. L. A. Dykman and N. G. Khlebtsov, *Chem. Rev.*, 2013, **114**, 1258-1288.

90. L. Sun, D. Liu and Z. Wang, *Langmuir*, 2008, **24**, 10293-10297.

91. C. D. Spicer, C. Jumeaux, B. Gupta and M. M. Stevens, *Chem. Soc. Rev*, 2018, **47**, 3574-3620.

92. F. Cañaveras, R. Madueño, J. M. Sevilla, M. Blázquez and T. Pineda, *J. Phys. Chem. C.*, 2012, **116**, 10430-10437.

93. C. Couto, R. Vitorino and A. L. Daniel-da-Silva, *Crit. Rev. Biotechnol.*, 2017, **37**, 238-250.

94. M. P. Monopoli, C. Åberg, A. Salvati and K. A. Dawson, *Nat. Nanotechnol.*, 2012, **7**, 779.

95. J. Wolfram, Y. Yang, J. Shen, A. Moten, C. Chen, H. Shen, M. Ferrari and Y. Zhao, *Colloid. Surface. B.*, 2014, **124**, 17-24.

96. B. Liu and J. Liu, *Anal. Methods*, 2017, **9**, 2633-2643.

97. C. A. Mirkin, R. L. Letsinger, R. C. Mucic and J. J. Storhoff, *Nature*, 1996, **382**, 607.

98. S. L. Filbrun, A. B. Filbrun, F. L. Lovato, S. H. Oh, E. A. Driskell and J. D. Driskell, *Analyst*, 2017, **142**, 4456-4467.

99. R. Bhattacharya, C. R. Patra, A. Earl, S. Wang, A. Katarya, L. Lu, J. N. Kizhakkedathu, M. J. Yaszemski, P. R. Greipp and D. Mukhopadhyay, *Nanomedicine*, 2007, **3**, 224-238.

100. M. H. Jazayeri, H. Amani, A. A. Pourfatollah, H. Pazoki-Toroudi and B. Sedighimoghaddam, *Sens. Biosensing. Res.*, 2016, **9**, 17-22.

101. R. G. Rayavarapu, W. Petersen, C. Ungureanu, J. N. Post, T. G. van Leeuwen and S. Manohar, *Int. J. Biomed. Imaging.*, 2007, **2007**.

102. M. A. Cavadas, M. P. Monopoli, C. S. e. Cunha, M. Prudêncio, E. Pereira, I. Lynch, K. A. Dawson and R. Franco, *Part. Part. Syst. Char.*, 2016, **33**, 906-915.

102. M. H. Jazayeri, H. Amani, A. A. Pourfatollah, H. Pazoki-Toroudi and B. Sedighimoghaddam, *Sens. Biosensing. Res.*, 2016, **9**, 17-22.

103. M. Li, S. K. Cushing, Q. Wang, X. Shi, L. A. Hornak, Z. Hong and N. Wu, *The Journal of Physical Chemistry Letters*, 2011, **2**, 2125-2129.

104. B. Szychowski, M. Pelton and M.-C. Daniel, *Nanophotonics*, 2019.

105. A. Bernardin, A. Cazet, L. Guyon, P. Delannoy, F. Vinet, D. Bonnaffé and I. Texier, *Bioconjug. Chem.*, 2010, **21**, 583-588.

106. H. C. Kolb, M. Finn and K. B. Sharpless, *Angew. Chem. Int. Ed.*, 2001, **40**, 2004-2021.

107. H. Zhang, G. Feng, Y. Guo and D. Zhou, *Nanoscale*, 2013, **5**, 10307-10315.

108. Y. Li, J. Zhou, C. Liu and H. Li, *J. Mater. Chem.*, 2012, **22**, 2507-2511.

109. G. Beaune, S. Tamang, A. Bernardin, P. Bayle-Guillemaud, D. Fenel, G. Schoehn, F. Vinet, P. Reiss and I. Texier, *Chem. Phys. Chem.*, 2011, **12**, 2247-2254.

110. L. G. Sillen, A. E. Martell and J. Bjerrum, *Stability constants of metal-ion complexes*, Chemical Society, 1964.

111. I. Montes-Burgos, D. Walczyk, P. Hole, J. Smith, I. Lynch and K. Dawson, *J. Nanopart. Res.*, 2010, **12**, 47-53.

112. S. Bhattacharjee, *J. Control. Release.*, 2016, **235**, 337-351.

113. W. Goldburg, *Am. J. Phys.*, 1999, **67**, 1152-1160.

114. Z. Wang, *J. Phys. Chem. B.*, 2000, **104**, 1153-1175.

115. M. Knoll and E. Ruska, *Z. Phys.*, 1932, **78**, 318-339.

116. L. Reimer, *Transmission electron microscopy: physics of image formation and microanalysis*, Springer, 2013.

117. M. Mammen, S.-K. Choi and G. M. Whitesides, *Angew. Chem. Int. Ed.*, 1998, **37**, 2754-2794.

118. M. Marradi, F. Chiodo, I. Garcia and S. Penadés, *Chem. Soc. Rev*, 2013, **42**, 4728-4745.

119. M. T. Haynes and L. Huang, *Mol. Ther.*, 2016, **24**, 849-851.

120. R. J. Pieters, *Org. Biomol. Chem.*, 2009, **7**, 2013-2025.

121. D. Zhou, Y. Li, E. A. Hall, C. Abell and D. Klenerman, *Nanoscale*, 2011, **3**, 201-211.

122. K. Susumu, B. C. Mei and H. Mattoussi, *Nat. Protoc.*, 2009, **4**, 424-436.

123. F. Aldeek, D. Hawkins, V. Palomo, M. Safi, G. Palui, P. E. Dawson, I. Alabugin and H. Mattoussi, *J. Am. Chem. Soc.*, 2015, **137**, 2704-2714.

124. D. Ling, M. J. Hackett and T. Hyeon, *Nano. Today.*, 2014, **9**, 457-477.

125. Y. A. Wang, J. J. Li, H. Chen and X. Peng, *J. Am. Chem. Soc.*, 2002, **124**, 2293-2298.

126. B. Imperiali, ACS Publications, Editon edn., 2012.

127. M. Jesús and S. Penadés, *Biochim. Biophys. Acta.*, 2006, **1760**, 636-651.

128. S. Park, G.-H. Kim, S.-H. Park, J. Pai, D. Rathwell, J.-Y. Park, Y.-S. Kang and I. Shin, *J. Am. Chem. Soc.*, 2015.

129. N. Hao, K. Neranon, O. Ramström and M. Yan, *Biosens. Bioelectron.*, 2016, **76**, 113-130.

130. C. Cunha, A. Oliveira, T. Firmino, D. Tenório, G. Pereira, L. Carvalho Jr, B. Santos, M. Correia and A. Fontes, *Biochim. Biophys. Acta.*, 2018, **1862**, 427-439.

131. Y. Yang, M. Yu, T.-T. Yan, Z.-H. Zhao, Y.-L. Sha and Z.-J. Li, *Bioorganic Med, Chem.*, 2010, **18**, 5234-5240.

132. S. Weinbaum, J. M. Tarbell and E. R. Damiano, *Annu. Rev. Biomed. Eng.*, 2007, **9**, 121-167.

133. A. Varki, *Glycobiology*, 1993, **3**, 97-130.

134. T. B. Geijtenbeek and S. I. Gringhuis, *Nat. Rev. Immunol.*, 2009, **9**, 465-479.

135. J. R. Walker, B. Nagar, N. M. Young, T. Hirama and J. M. Rini, *Biochemistry-US*, 2004, **43**, 3783-3792.

136. G. A. Snyder, M. Colonna and P. D. Sun, *J. Mol. Biol.*, 2005, **347**, 979-989.

137. K. Drickamer, *Curr. Opin. Struct. Biol.*, 1999, **9**, 585-590.

138. G. Yilmaz and C. R. Becer, *Polym. Chem.*, 2015.

139. H. Feinberg, R. Castelli, K. Drickamer, P. H. Seeberger and W. I. Weis, *J. Biol. Chem.*, 2007, **282**, 4202-4209.

140. H. Feinberg, D. A. Mitchell, K. Drickamer and W. I. Weis, *Science*, 2001, **294**, 2163-2166.

141. A. L. Smith, L. Ganesh, K. Leung, J. Jongstra-Bilen, J. Jongstra and G. J. Nabel, *J. Exp. Med.*, 2007, **204**, 421-430.

142. R. C. da Silva, L. Segat and S. Crovella, *Hum. Immunol.*, 2011, **72**, 305-311.

143. B. M. Curtis, S. Scharnowske and A. J. Watson, *P. Natl. Acad. Sci. USA*, 1992, **89**, 8356-8360.

144. H. Feinberg, Y. Guo, D. A. Mitchell, K. Drickamer and W. I. Weis, *J. Biol. Chem.*, 2005, **280**, 1327-1335.

145. E. van Liempt, C. Bank, P. Mehta, Z. S. Kawar, R. Geyer, R. A. Alvarez, R. D. Cummings, Y. v. Kooyk and I. van Die, *FEBS Lett.*, 2006, **580**, 6123-6131.

146. R. T. Lee, T.-L. Hsu, S. K. Huang, S.-L. Hsieh, C.-H. Wong and Y. C. Lee, *Glycobiology*, 2011, **21**, 512-520.

147. Y. Guo, H. Feinberg, E. Conroy, D. A. Mitchell, R. Alvarez, O. Blixt, M. E. Taylor, W. I. Weis and K. Drickamer, *Nat. Struct. Mol. Biol.*, 2004, **11**, 591-598.

148. S. I. Gringhuis, J. den Dunnen, M. Litjens, M. van der Vlist and T. B. Geijtenbeek, *Nat. Immunol*, 2009, **10**, 1081-1088.

149. N. P. Chung, S. K. Breun, A. Bashirova, J. G. Baumann, T. D. Martin, J. M. Karamchandani, J. W. Rausch, S. F. Le Grice, L. Wu and M. Carrington, *J. Biol. Chem.*, 2010, **285**, 2100-2112.

150. J. Auwerx, K. O. François, E. Vanstreels, K. Van Laethem, D. Daelemans, D. Schols and J. Balzarini, *Antivir. Res*, 2009, **83**, 61-70.

151. J. Balzarini, *Nat. Rev. Microbiol.*, 2007, **5**, 583-597.

152. S. G. Turville, K. Vermeire, J. Balzarini and D. Schols, *J. Virol.*, 2005, **79**, 13519-13527.

153. L. Wu and V. N. KewalRamani, *Nat. Rev. Immunol.*, 2006, **6**, 859-868.

154. Y. Guo, C. Sakonsinsiri, I. Nehlmeier, M. A. Fascione, H. Zhang, W. Wang, S. Pöhlmann, W. B. Turnbull and D. Zhou, *Angew. Chem. Int. Ed.*, 2016, **55**, 4738-4742.

Chapter 2

Probing Multivalent DC-SIGN/R-Saccharide Binding Affinities using QD-EGn-Saccharide Conjugates

2.1 Introduction

Sugar binding proteins play a key role in many viral infections, such as Human Immunodeficiency virus (HIV), Ebola virus disease (Ebola) and West Nile Virus.[1] The multivalent protein-carbohydrate interactions which initiate the first pathogen-host contact are responsible for infection. [2] Monovalent binding is weak and hence biologically inactive, the formation of multivalent interactions can dramatically enhance the binding affinity, making them biologically functional.[3] Multivalent glycoconjugates that can potently block, or inhibit these interactions can thus be harnessed as entry inhibitors to prevent such infections. The challenge to overcome is that to make the binding specific these multivalent partners should have their binding orientation and spacing between the partners match but this is difficult without knowing the lectin structure. Due to the multivalent nature of the binding, crystal structures are hard to determine. Multivalent protein-carbohydrate interactions are also important in other significant biological events such as cell-cell communication and host immune response regulation so it is key that we develop further knowledge of these interactions.[3]

These interactions are most commonly found in C-type lectins, also known as calcium dependent carbohydrate binding proteins, which bind to sugars presented on the glycoproteins found upon the surface of a variety of viruses.[3] Two C-type lectins of special interest here are the tetrameric DC-SIGN[4] and DC-SIGNR[5] (abbreviated collectively as DC-SIGN/R) which play a key role in facilitating viral and bacterial infections by specific binding to array of glycans found on the glycoproteins of virus surfaces. Despite extensive research, their overall tetrameric structure and hence CRD spatial arrangement are currently unknown. **Figure 2.1.1** below shows the similarities and differences in the previously proposed structures of both proteins.

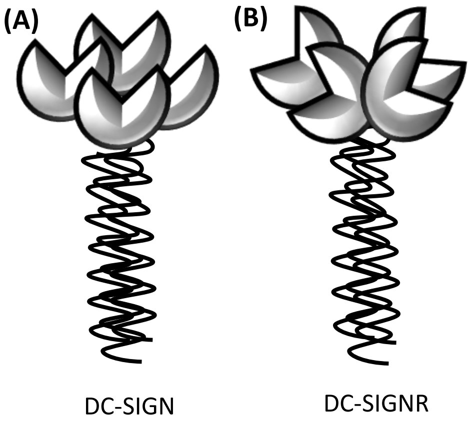

Figure 2.1.1: Schematic structure models of the C-type lectins (**A**) DC-SIGN and (**B**) DC-SIGNR proposed based on our own results. It shows the key difference in the layout of the four CRD groups between the two proteins, which may account for the difference in binding specificity.

Many synthetic glyconanoparticles have been developed to block and inhibit the multivalent lectin-glycan interactions responsible for virus infections.[6, 7] The inhibition efficiency depends critically on matching the relative spatial distances and orientations of the two binding partners. Many reviews have been published decribing the types of glyconanoparticles and how they are used in biomedicine by modulating specific carbohydrate – protein interactions. [8-10] As many multimeric lectins are highly flexible and complex membrane proteins, this creates a major challenge to determine their structural information. Although multivalent glycans built upon nanoparticle scaffolds have been developed to study multivalent glycan-lectin interactions by isothermal titration calorimetry, ITC,[11] and surface plasmon resonance, SPR.[12] Fluorescent semiconductor nanocrystals, quantum dots (QDs), can be harnessed to dissect these multivalent interactions because of their unique properties which include size-tuneable emission spectra, broad absorption spectra, high quantum yield and resistance to photobleaching.[13] These properties make QDs a powerful tool to develop fluorescent resonance energy transfer (FRET) based assays to probe multivalent interactions. FRET can provide an accurate measure of small separation distances (ca. 1-10 nm) which is useful to provide an insight into complicated biological interactions, such as protein-protein and ligand-receptor interactions. This technique can also be used to quantify the binding affinity between glycans and the multimeric proteins.

In order to use the QD-FRET mechanisms to probe multivalent protein-glycan interactions probes containing both monosaccharide and disaccharide mannose sugars were designed. The major challenge to develop effective QD-FRET probes was the inability to produce stable compact, polyvalent saccharide QDs, which are essential for strong multivalent binding and a sensitive FRET readout strategy. The published literature cap-exchange methods lacked efficiency and so they required a large excess of the ligands (e.g. typical ligand: QD molar ratio >10^4), making it impractical for precious sugar ligands. [14] This problem has been overcome by the development of a highly efficient capping method recently published by Guo *et al*,[15] in our group, making it possible to determine the binding affinities, K_d, *via* a sensitive FRET readout strategy for the first time. **Figure 2.1.2** below shows a schematic of experimental strategy used to probe these interactions.

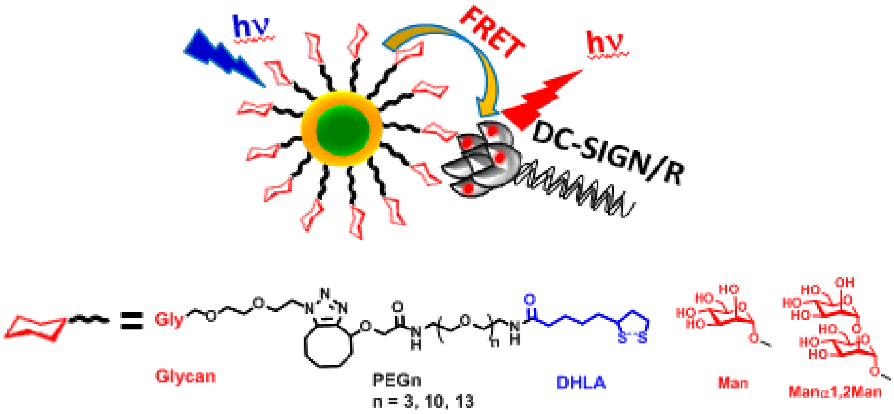

Figure 2.1.2: A schematic diagram to show probing of multivalent saccharide-protein binding via FRET using a QD capped with different DHLA-based saccharide ligands and acceptor dye-labelled lectins DC-SIGN/R.

2.2 Polyvalent Saccharide Quantum Dot Design

In order to probe how multivalent binding sites are presented within DC-SIGN/R we need to design and construct a QD-conjugate that can specifically bind to the protein. First, there must be a sugar ligand that can bind to both the QD and the proteins. Second, the resulting QD-conjugate must be stable and water soluble for biological use. In this case, a multifunctional ligand containing three unique functional domains is designed and shown schematically in **Figure 2.2.1**. A dihydrolipoic acid, (DHLA), group for robust QD capping via a chelative binding mechanism; a flexible oligo(ethylene glycol), (EG), linker for introducing water solubility, stability and resistance to non-specific adsorption as well as tuning the inter-glycan spacing on the QD surface; and a terminal functional sugar for specific protein binding. The production of the polyvalent saccharide-QD includes three key steps, synthesis of functional LA-EG_n ligand and its glycosylation via strain promoted alkyne azide click chemistry, ligand reduction to its DHLA-equivalent and finally cap-exchange with commercial hydrophobic QDs.

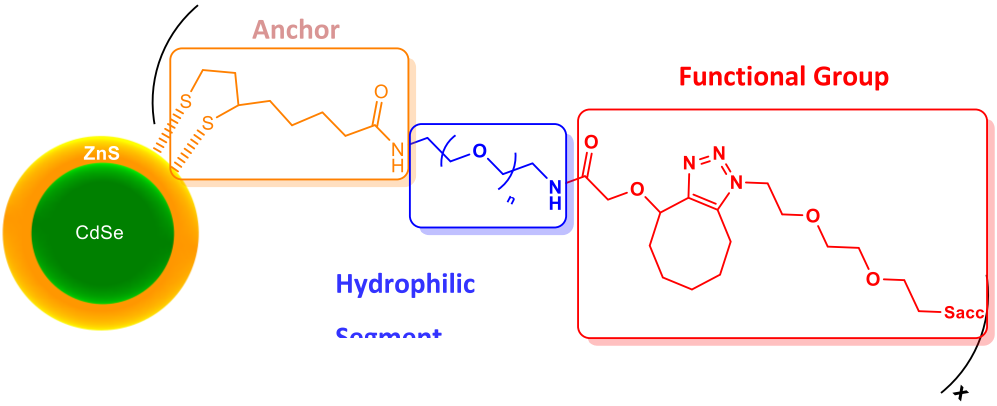

Figure 2.2.1: A schematic of a CdSe/ZnS core/shell QD capped with a DHLA-based multifunctional ligand containing three different functional domains: an anchor, hydrophilic segment and functional sugar terminal group.

2.2.1 Ligand Synthesis

The synthesis of lipoic acid (LA)-EG$_n$-cyclooctyne, (where n=3 and 11) as shown in **Scheme 2.2.1** is based on the published protocol by Susumu *et al.*[16] It has been replicated easily and used in other publications from the Zhou group, e.g. by Zhang *et al.*[17] and Guo *et al.*[15]. The synthesis of these ligands are given in **Chapter 5**.

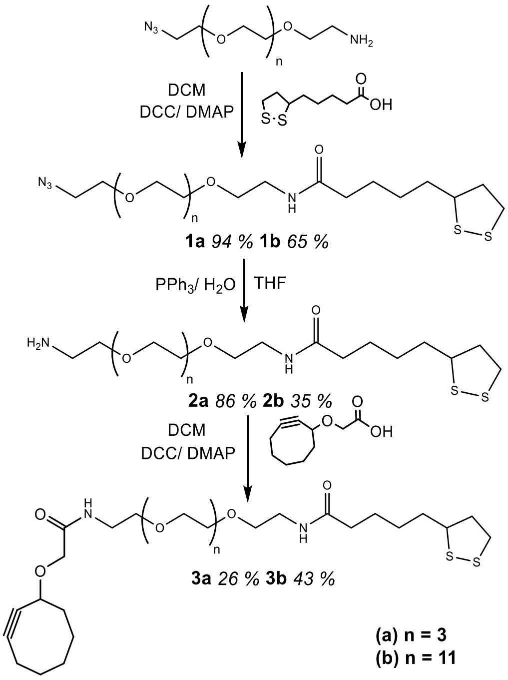

Scheme 2.2.1: A reaction scheme showing the formation of special designed ligand, LA-EG$_n$-Cyclooctyne (where n=3 or 11). (**A**) DCC, DMAP, LA and dry DCM, (**B**) PPh$_3$, H_2O and dry THF and (**C**) DCC, DMAP, Cyclooct-1-yn-3-glycolic acid and dry DCM.

2.2.2 Ligand Reduction and Exchange

To chelate to the QD surface, LA must be reduced to its DHLA equivalent, as the literature suggests that efficient QD cap-exchange can only be achieved using DHLA-based ligand, and not the disulphide LA form.[16] Moreover, the binding between the QD surface Zn^{2+} ions and deprotonated thiolate is much stronger than that with non-deprotonated thiol. Tris (2-carboxyethyl) phosphine (TCEP) is used as the reducing agent. **Scheme 2.2.2** below shows the outline of the reduction using TCEP. The resulting NMR spectra for both the starting material and the product is shown in **Chapter 5.6**.

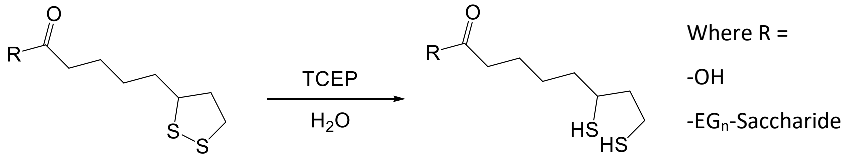

Scheme 2.2.2: The reduction of the LA-based ligand to its DHLA-equivalent using Tris (2-carboxyethyl) phosphine (TCEP) in H_2O.

After reduction, the LA-EG_n-cyclooctyne, (where n=3 and 11) were purified by silica gel column chromatography, deprotonated with NaOH and then added to commercial hydrophobic CdSe/ZnS core/shell QD (λ_{em} 560 nm) at a ligand:QD molar ratio of 800:1 in a homogenous solution (EtOH/$CHCl_3$). Full experimental details can be found in **Chapter 5**. **Figure 2.2.2** shows the schematic process of the ligand exchange. The commercial QDs are coated with trioctylphosphine oxide (TOPO) ligands, which are displaced by the hydrophilic sugar ligands. Addition of water is used to test if the cap-exchange reaction has occurred as the resulting QD-saccharide conjugates are hydrophilic and so should form a stable solution in water with no aggregation.

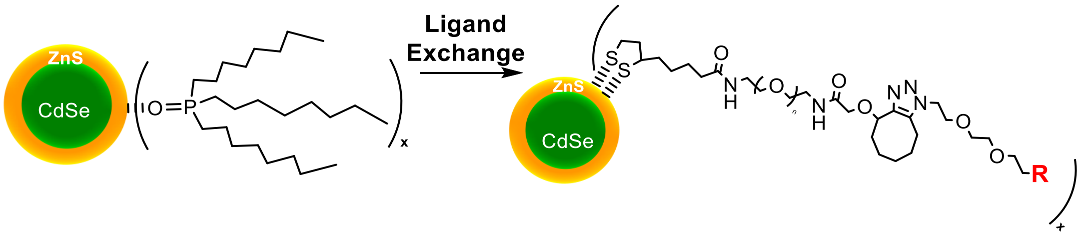

Figure 2.2.2: The schematic of ligand exchange reaction to prepare QD-saccharide conjugates from the commercial TOPO ligand coated CdSe/ZnS QD, where R= mannose or dimannose.

After ligand exchange, the resulting water soluble QDs are purified by washing with water to remove any unbound ligands in a centrifugal filter as outlined in the experimental procedure. The stock QD concentration is calculated by the Beer-Lambert Law using the absorbance of the

QD at its first excitation peak of 546 nm (for QD with λ_{em} = 560 nm) and an extinction coefficient, ε, of 1.3 x 10^5 M^{-1} cm^{-1} as provided by supplier. **Figure 2.2.3** shows the absorption spectra of (**A**) QD-Mannose and (**B**) QD-DiMannose conjugates respectively.

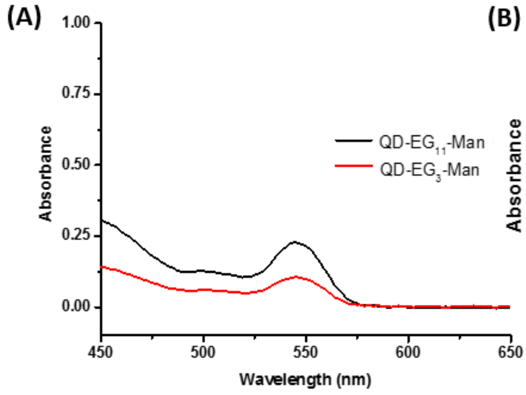

Figure 2.2.3: UV-Vis spectra of the (**A**) QD-Mannose and (**B**) QD-DiMannose conjugates used to determine the concentration of the particles after ligand exchange.

2.1.1 QD-(EG_n-Man)$_m$ Characterization

2.1.1.1 Dynamic Light Scattering

The hydrodynamic sizes, D_hs, of freshly prepared QD-saccharide conjugates are determined by dynamic light scattering, DLS. The resulting hydrodynamic diameter, D_h, (volume populations) in H_2O for the QD-EG_3-DiMan and QD-EG_{11}-DiMan are shown in **Figure 2.2.4**. A single D_h size distribution of *ca.* 6 and 13 nm for QD-EG_3-DiMan and QD-EG_{11}-DiMan are obtained. Such D_h sizes are consistent with the expected values of the QD core plus the suagr ligand length, suggesting that the ligand exchange has occurred and the QDs are not aggregated. A summary of the D_h sizes and fitting parameters are seen in **Table 2.2.1**.

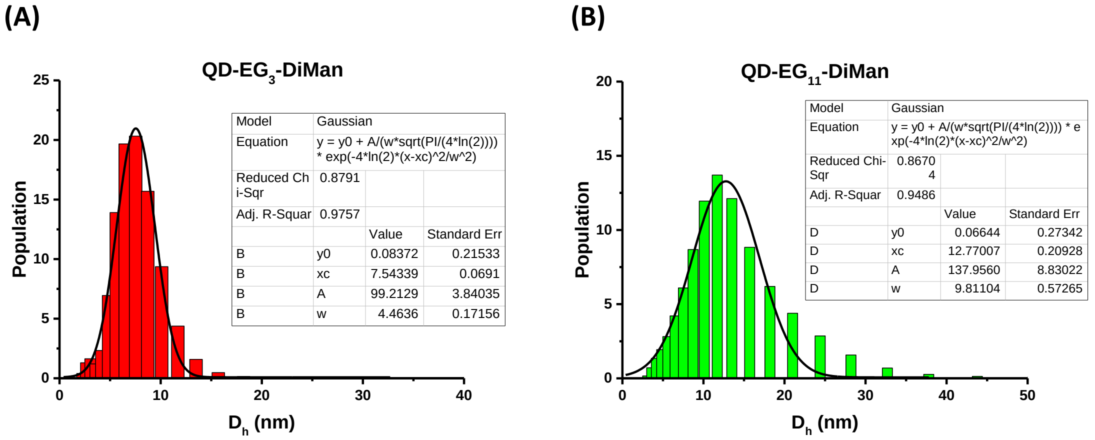

Model	Gaussian		
Equation	y = y0 + A/(w*sqrt(PI/(4*ln(2)))) * exp(-4*ln(2)*(x-xc)^2/w^2)		
Reduced Chi-Sqr	0.8791		
Adj. R-Squar	0.9757		
		Value	Standard Err
B	y0	0.08372	0.21533
B	xc	7.54339	0.0691
B	A	99.2129	3.84035
B	w	4.4636	0.17156

Model	Gaussian		
Equation	y = y0 + A/(w*sqrt(PI/(4*ln(2)))) * exp(-4*ln(2)*(x-xc)^2/w^2)		
Reduced Chi-Sqr	0.86704		
Adj. R-Squar	0.9486		
		Value	Standard Err
D	y0	0.06644	0.27342
D	xc	12.77007	0.20928
D	A	137.9560	8.83022
D	w	9.81104	0.57265

Figure 2.2.4: The hydrodynamic size histograms for (A) QD-EG_3-DiMan and (B) QD-EG_{11}-DiMan in H_2O.

Table 2.2.1: Summary of the hydrodynamic sizes of the QD-saccharides after ligand exchange.

Capping Ligand	Hydrodynamic Size (nm)	Full Width at half maximum (nm)
LA-EG$_3$-DiMan	7.5 ± 0.1	4.5 ± 0.2
LA-EG$_{11}$-DiMan	12.8 ± 0.2	9.8 ± 0.6

2.1.1.2 Quantum Yields

Quantum yield, QY, is a measurement of the number of defined events occurring per photon absorbed by the system used. In our case the QY is described as the fluorescence QY (Φ_F) which measures the ratio of the number of photos emitted, to those absorbed. The QYs of the QDs are determined against Rhodamine 6G in ethanol (QY = 95%, λ_{ex}= 480 nm), as the reference standard.[16] The integrated fluorescence spectra of multiple concentrations against the absorbance for both the QD and reference materials are measured first and the QY is calculated by (**Eq.9**) based on the method first published by Williams *et al.*.[17]

$$QDQY = \frac{Gradient_{QD} \times 0.95}{Gradient_{Rhod6G}} \times 100 \qquad \textbf{(Eq. 9)}$$

Where QDQY is the QD quantum yield, $\text{Gradient}_{\text{QD}}$ and $\text{Gradient}_{\text{Rhod6G}}$ are the linear fitting gradients of the integrated. The methodology used here is slightly different from that of Williams method although it is still a comparative model in which they directly compare the areas of the fluorescence emission spectra. This method calculates the gradients by performing absorption measurements on a range of different concentrations and noting the absorbance at 480 nm. This is then used as the excitation wavelength to collect a fluorescence spectrum at the same concentrations. The area of fluorescence curve is plotted against the maximum absorbance at 480 nm for each of the QDs as well as the reference, rhodamine 6G. A linear plot is then fitted through and the gradient is calculated from that. The absorption spectra of the QDs and the reference are shown in **Figure 2.2.5** and **Figure 2.2.6** respectively. The fluorescence emission spectra of the QDs are given in the **Appendix**. The resulting integrated fluorescence intensity versus absorption plots are shown in **Figure 2.2.7**.

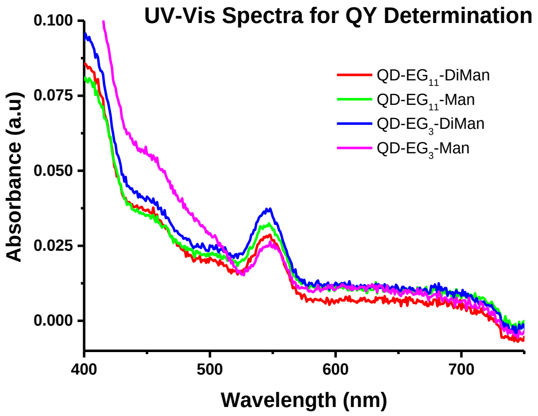

Figure 2.2.5: UV-Vis (background corrected) spectra of the QDs after ligand exchange with the functional ligands.

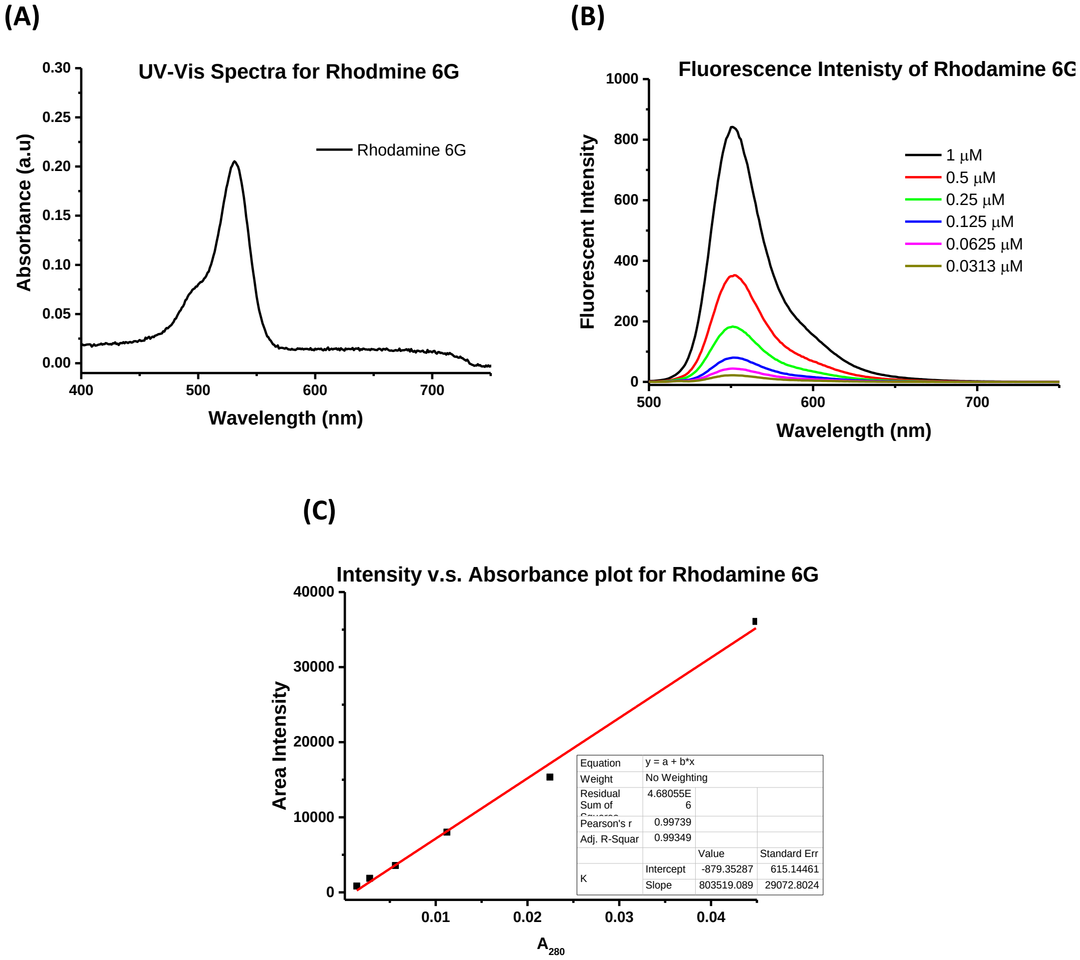

Equation	y = a + b*x		
Weight	No Weighting		
Residual Sum of Squares	4.68055E6		
Pearson's r	0.99739		
Adj. R-Squar	0.99349		
		Value	Standard Err
K	Intercept	-879.35287	615.14461
	Slope	803519.089	29072.8024

Figure 2.2.6: **(A)** UV-Vis spectra of a Rhodamine 6G sample in ethanol, **(B)** Fluorescence spectra of Rhodamine 6G at different concentrations (0.0313 - 1 µM) excited at λ_{Ex} = 480 nm, and **(C)** a plot of integrated fluorescence intensity versus t absorbance (λ = 480) for Rhodamine 6G.

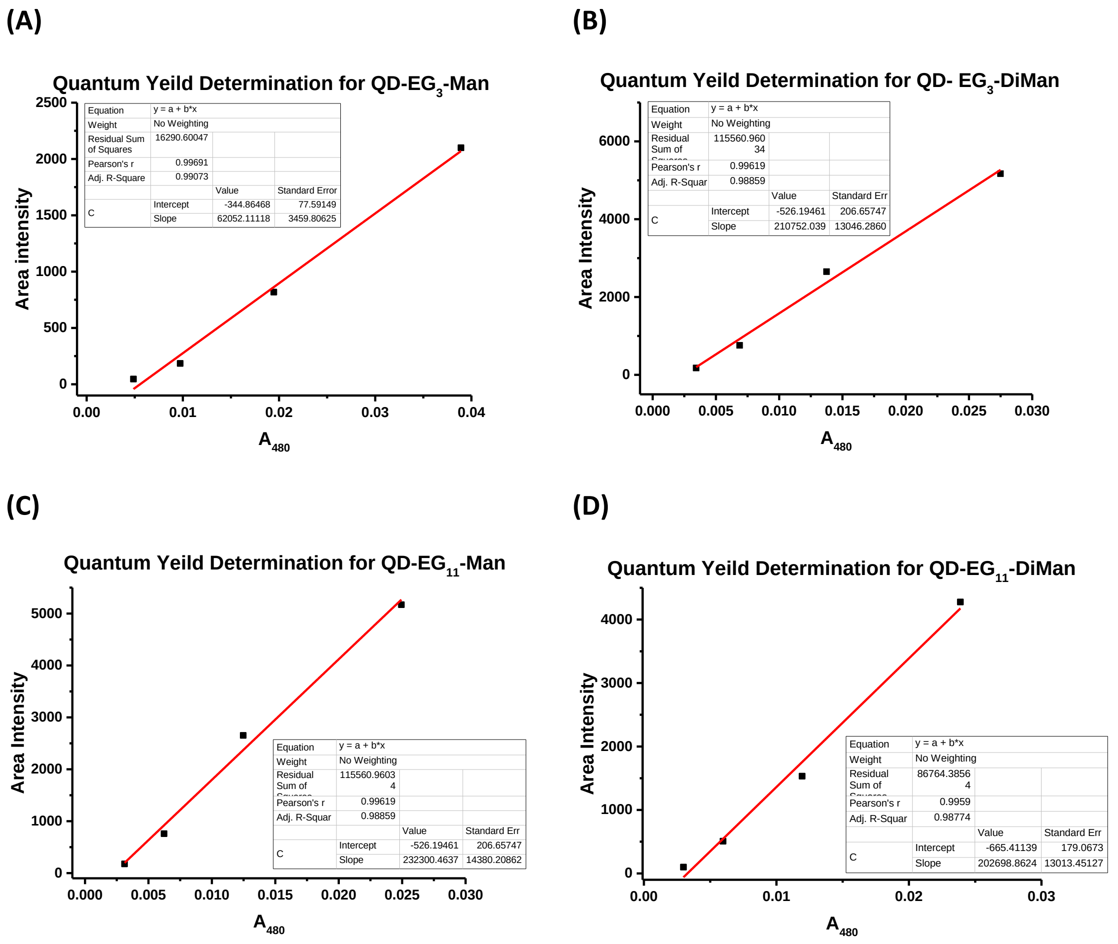

Figure 2.2.7: Integrated fluorescence intensity v.s. absorption plots for different QDs fitted by linear relationship.

Table 2.2.2 summarises the results. A significantly lower QY for QD EG$_3$-Man is seen in comparison to the literature (e.g. Guo *et al.*[15] shows a 33% and 24% QY for QD-EG$_{11}$-Man and QD-EG$_3$-Man respectively). The difference may be caused by different batches of the QD which may have different original QYs.

Table 2.2.2: A summary of the QYs for the QDs after ligand exchange with different DHLA-based sugar ligands.

Surface Ligand	**Quantum Yield (%)**
DHLA-EG$_3$-Man	7
DHLA-EG$_3$-DiMan	25
DHLA- EG$_{11}$-Man	28
DHLA- EG$_{11}$-DiMan	24

2.3 Protein Labelling

After the successful production of both DC-SIGN and DC-SIGNR via the protocol outlined in **Chapter 5.5.9** labelling was done at a site-specific introduced cysteine residue using a maleimide modified ATTO594 dye. The labelling process consists of a simple nucleophilic Michael addition reaction in which the lone pair on the cysteine residue of the protein attacks the double bond of the maleimide. **Scheme 2.3.1** below outlines the process of the nucleophilic addition between the dye and the protein via the free cysteine.

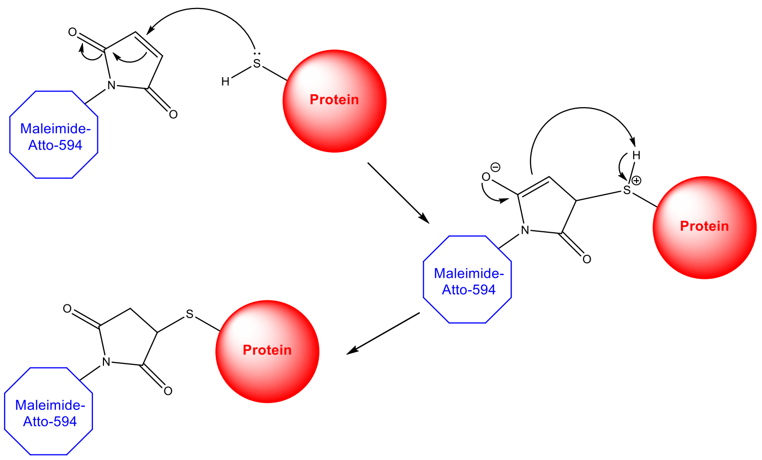

Scheme 2.3.1: A schematic to show the Michael addition reaction mechanism used for labelling a protein with the organic dye maleimide-atto-594.

The concentration, c, of the labelled protein was then calculated using beer-lambert law. The dye absorption maxima is at A_{609} and the protein absorption is at A_{280}, this can be seen clearly on the absorption spectra for a labelled protein sample **Figure 2.3.1**. The contribution of the dye absorbance at 280 nm is taken into consideration in calculating the concentration of the protein. The extinction coefficients for the proteins at 280 nm are 70400 L mol^{-1} cm^{-1} for DC-SIGN and 60890 L mol^{-1} cm^{-1} for DC-SIGNR.

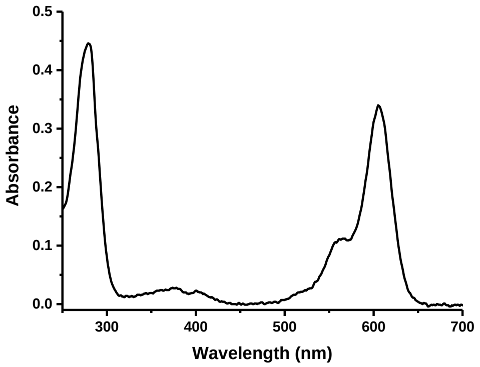

Figure 2.3.1: A typical UV/Vis spectrum for labelled protein DC-SIGNR (36 µM) showing major absorbance's from the dye and protein at 280 and 609 nm respectively.

2.4 Differentiating QD-DiMan-DC-SIGN/R Binding Modes

2.4.1 FRET Studies between QD-DiMan and DC-SIGN/R

FRET can be used to calculate the changes in separation distance between two fluorophores. It is also a useful method to measure specific donor-acceptor binding interactions. Since FRET occurs over a short separation distance (ca. < 10 nm), any unbound species will be too far away to contribute to the energy transfer process. Binding of the labelled DC-SIGN/R (acting as the acceptor) to the QD-saccharide (acting as the donor) should result in a quenching of the QD fluorescence and an increase in the dye fluorescence simultaneously. In the case of our experiment, a His_6-Cys peptide is added to the solutions as previous group members have found that it can significantly enhance the QD fluorescence.[17] The peptides can bind to the free Zn^{2+} ions on the QD surface and also help reduce the non-specific adsorption of the QDs onto the sample tubes. **Figure 2.4.1** shows the resulting background corrected fluorescence spectra with a fixed amount of QD (40 nM) with varying amounts of DC-SIGN/R. The apparent binding affinity can then be calculated by plotting the fluorescence intensity ratio between the protein emission maxima (λ = 626 nm) and the QD emission maxima (λ = 554 nm). We expect to see that over increasing the protein concentration that the QD emission maxima decreases and the protein emission increases. The work done on the QD-EG_{11}-DiMan was performed by Dr Yuan Guo, who also performed another experiment with the QD-EG_3-DiMan using a difference batch of QDs, this can be found within the **Appendix**. The study has only been done with the QD-DiMans as previously the binding constant has already been determined for the QD-Mans with DC-SIGN. For DC-SIGNR, its binding affinity with QD-Man was too weak to measure at 40 nM QD.[15]

Table 2.4.1: Fitting parameters summary for QD- DC-SIGNR binding curves fitted using the Hill Equation (**Eq. 15**) (**Figure 2.4.1**).

QD + Protein	**R_{max}**	**K**	**n**	**R^2**
QD-EG_3-DiMan + DC-SIGNR	2.5 ± 0	5.3 ± 0.8	1.9 ± 0.9	0.8957
QD-EG_{11}-DiMan + DC-SIGNR	2.6 ± 0.9	17.2 ± 6.1	1.5 ± 0.1	0.9984

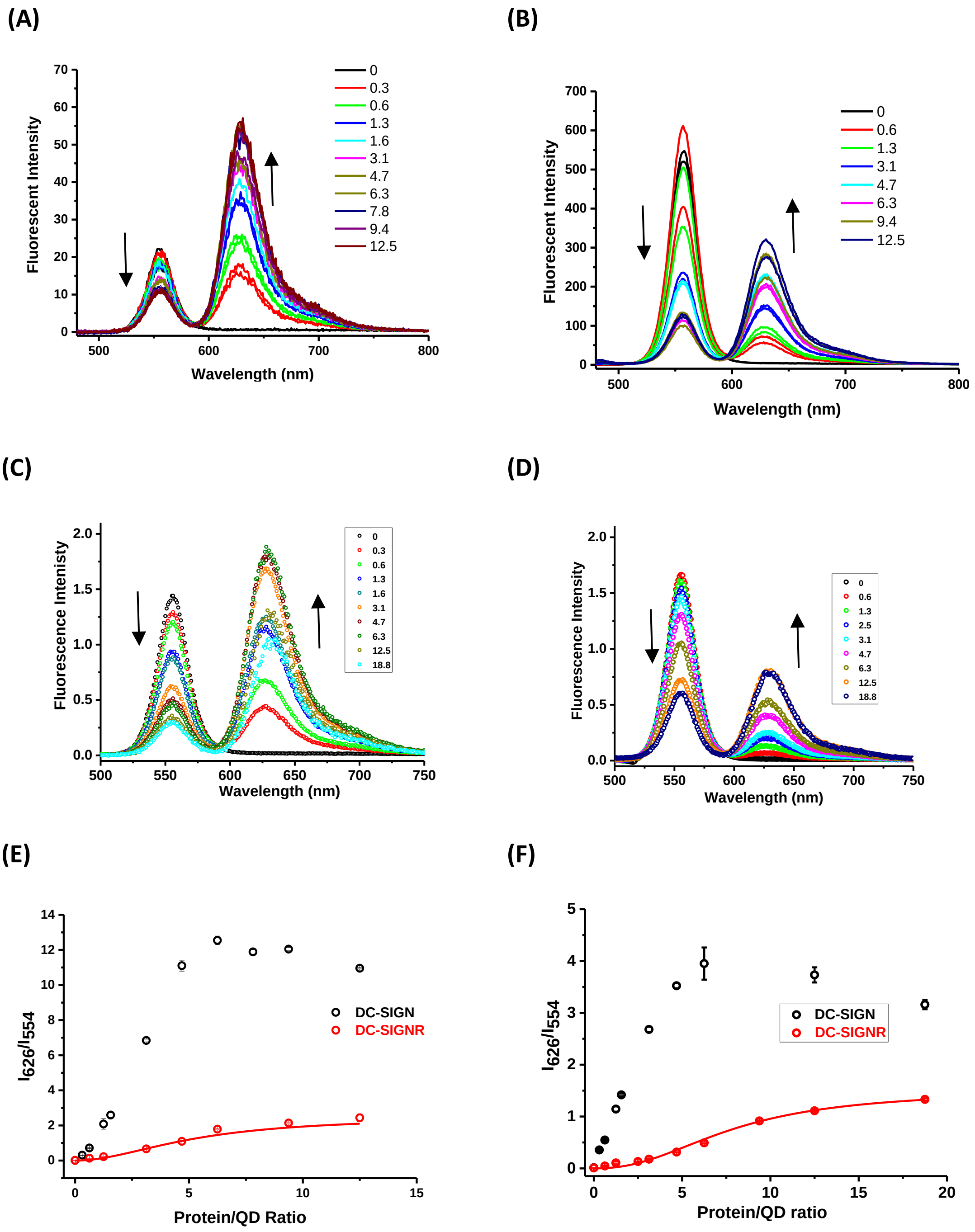

Figure 2.4.1: Dye direct excitation background corrected fluorescence spectra of QD-DiMan (12 – 752 nM) after binding to labelled proteins, DC-SIGN/R, (40 nM) at varying protein: QD ratios where (**A**) QD-EG$_3$-DiMan + DC-SIGN, (**B**) QD-EG$_3$-DiMan + DC-SIGNR (**C**) QD-EG$_{11}$-DiMan + DC-SIGN, (**D**) QD-EG$_{11}$-DiMan + DC-SIGNR and the resulting FRET ratio versus protein: QD ratio for (**E**) QD-EG$_3$-DiMan and (**F**) QD-EG$_{11}$-DiMan. **Table 2.4.1** above shows the fitting parameters for DC-SIGNR binding.

Significant quenching of the QD fluorescence is observed after incubating the QD-DiMan samples with DC-SIGN, similar to that found previously within the group with QD-Man conjugates.[15] On the other hand, using the QD-DiMan to replace QD-Man greatly enhances the FRET signals for binding to DC-SIGNR. The result contrasts significantly with that of the QD-Man which showed weak and indistinguishable signals from the background. The FRET signal for DC-SIGN binding is still higher than that of DC-SIGNR, suggesting that the two lectins may adopt different binding modes. This result is significant as it matches well to our proposed binding mechanisms for DC-SIGN and DC-SIGNR in that DC-SIGN binds to a singular QD and that DC-SIGNR binds to multiple QDs. The binding curves for DC-SIGN show a linear increase to the maximum, then followed by a decrease. This result is also different from that observed previously with QD-Man[15] which display typical binding curves toward maximum without decrease this is due to light effects coming from fluorimeter and quenching effects from the large concentrations of proteins. In contrast, binding to DC-SIGNR gives an "S" shaped response curve. Moreover, fitting the binding curves with Hill's equation give an Hill coefficients of 1.9 ± 0.9 and 2.4 ± 0.4 which are both > 1, indicating positive cooperativity in the QD-DiMan-DC-SIGNR binding, possibility due to QD-DC-SIGNR cross-linking.

2.4.2 Dilution of Surface Sugars

As part of these experiments we want to control the QD surface sugar density to reduce FRET quenching observed at high protein/QD ratios for DC-SIGN. In order to achieve this, a certain amount of an inert spacer ligand, DHLA-zwitterion, (DHLA-ZW, **Figure 2.4.2**), is mixed with the DHLA-sugar ligands to perform cap-exchange. Given both ligands chelate to the QD via the same DHLA-units, we expect they display very similar binding affinities with the QD and hence the ligand ratio used in cap-exchange may be transferred to the QD surface ligand coating. The LA-ZW ligand was reduced to DHLA-ZW using dithiothreitol, and deprotonated by tetramethylammonium hydroxide. Dilution of the QD surface sugar ligands with the DHLA-ZW would increase the inter-sugar distance, allowing us to probe how this affects their binding affinity with DC-SIGN/R. Two different QD surface sugar densities are used QDs, 73% and 25%, and the data are compared to those of the 100% sugar density above, **Figure 2.4.1**. Experimental details can be found within **Chapter 5**.

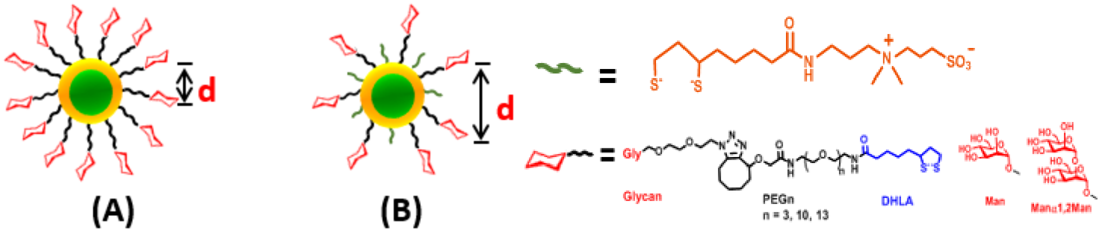

Figure 2.4.2: A schematic show of changing inter-sugar distance, d, before (**A**) and after (**B**) diluting the QD surface sugar ligands with the inert LA-ZW ligand.

2.4.2.1 FRET Analysis upon Surface Dilution

The resulting fluorescence spectra are given in **Figure 2.4.3** and the corresponding FRET efficiency-protein/QD ratio relationship curves are shown in **Figure 2.4.4**. The first major difference observed is a significantly reduced FRET ratio for QDs with diluted surface sugar density. Since the FRET ratio is linearly proportional to the amount of labelled protein bound to the QD at the same distance, this result suggests a reduced DC-SIGN binding capacity for the surface sugar diluted QDs. This result is consistent to that of the earlier results obtained with QD-Man.

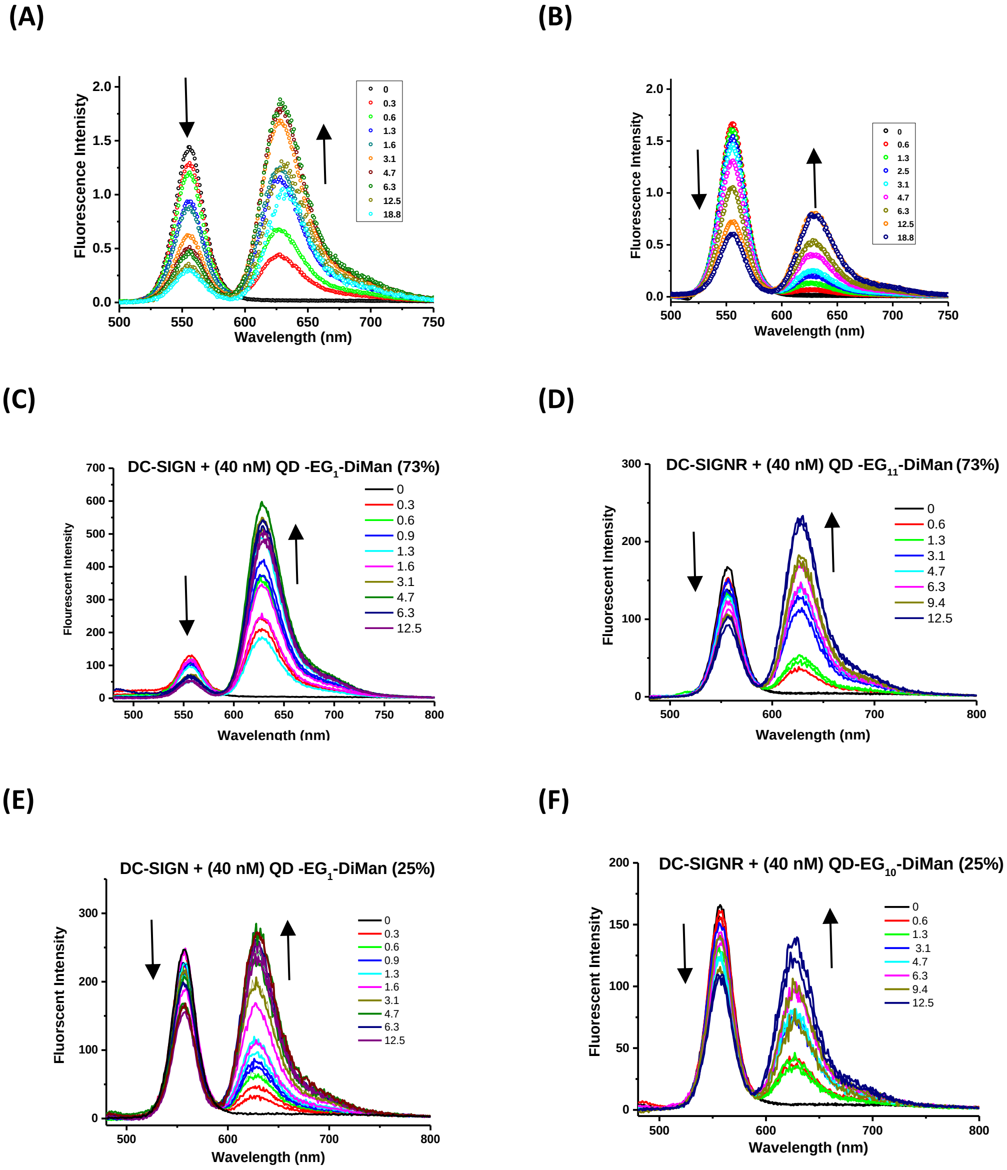

Figure 2.4.3: Dye direct excitation background corrected fluorescence spectra of QD-DiMan at a reduced surface dilution after binding to labelled proteins, DC-SIGN/R, at varying protein: QD ratios where (**A**) QD-EG$_{11}$-DiMan (40 nM, 100 %) + DC-SIGN (12 – 752 nM), (**B**) QD-EG$_{11}$-DiMan (40 nM, 100 %) + DC-SIGNR (24 – 752 nM) (**C**) QD-EG$_{11}$-DiMan (40 nM, 73 %) + DC-SIGN (12 – 500 nM), (**D**) QD-EG$_{11}$-DiMan (40 nM, 73 %) + DC-SIGNR (24 – 500 nM), (**E**) QD-EG$_{11}$-DiMan (40 nM, 25 %) + DC-SIGN (12 – 500 nM) and (**F**) QD-EG$_{11}$-DiMan (40 nM, 25 %) + DC-SIGNR (24 – 500 nM).

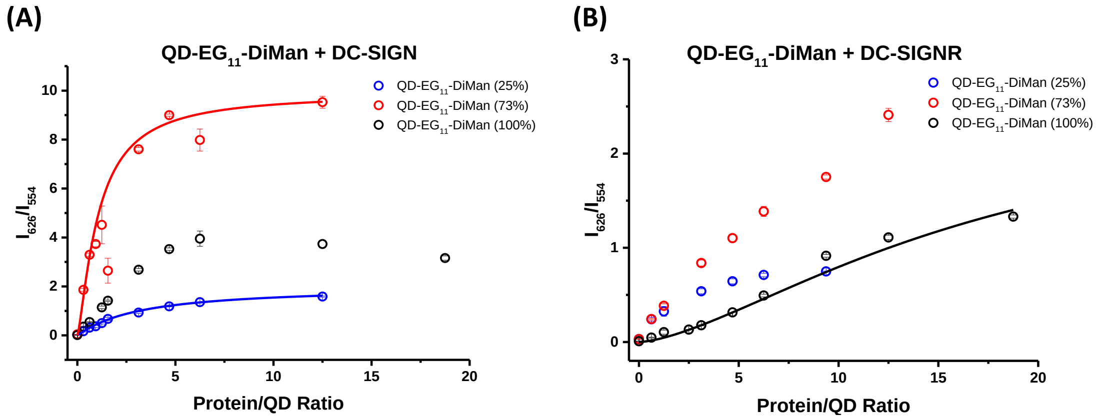

Figure 2.4.4: The FRET ratio versus protein: QD ratio for QD-EG$_{11}$-DiMan with (**A**) DC-SIGN and (**B**) DC-SIGNR with 100 %, 73 % and 25 % sugar surface density. The binding curves are fitted to the Hill's Equation.

Table 2.4.2: Fitting parameters summary for QD- DC-SIGNR binding curves fitted using the Hill Equation (**Figure 2.4.4**).

QD + Protein	R_{max}	K	N	R^2
QD-EG$_3$-DiMan (100%) + DC-SIGN	-	-	-	-
QD-EG$_{11}$-DiMan (73%) + DC-SIGN	9.9 ± 0.0	1.1 ± 0.1	1.3 ± 0.2	0.9841
QD-EG$_{11}$-DiMan (25%) + DC-SIGN	2.0 ± 0.6	3.1 ± 2.2	1.1 ± 0.3	0.9902

Dilution of the surface sugar has resulted in a change of binding curve with DC-SIGN with the decrease phase after saturation being removed. This could be due to the proteins bound to the QD surface being overcrowded with 100% density, causing the labelled dyes to be brought into close proximity to each other, resulting in quenching because of the flexible nature of the neck region of the protein.[18] The quenching likely comes from crowding-induced reorganisation of the QD-DC-SIGN. This is supported further as when the surface sugar density is decreased, lower FRET ratios are observed, suggesting a reduced binding capacity for the diluted surface but with no observed quenching effects from dyes in proximity. To investigate this fully, a new ligand series with increasing sugar density will be created to reveal the whole picture on how QD surface sugar density affect the FRET readout signal upon DC-SIGN binding.

2.5 FRET Analysis for QD-DC-SIGN/R binding K_d Determination

In order to determine the binding dissociation constant, K_d, a fixed QD: protein ratio of 1:1 was used for DC-SIGN and 1:4 for DC-SIGNR meaning that throughout the experiment the concentrations are simultaneously increased in sample preparations. These ratios were chosen as they represent the proteins concentrations as which showed the maximum efficiency of FRET in earlier studies (Chapter 2. A larger ratio of DC-SIGNR was used to compensate the low FRET ratio observed when the QD: protein ratio is 1. Fluorescence spectra can be seen for both QD-EG_3-DiMan (**Figure 2.5.1** and **Figure 2.5.2**) with DC-SIGN/R and the spectra for QD-EG_{11}-DiMan with DC-SIGN/R can be found within the **Appendix**. Dye direct excitation background corrected fluorescence spectra reveal clear emission peaks for the QD (λ_{em}= 554 nm) and in some cases the labelled protein (λ_{em}= 626 nm). Due to the large difference of QD/protein concentrations used, different setting parameters have been used to avoid signal saturation of the fluorimeter. This only affects the absolute individual fluorescence intensity, the FRET intensity ratio, in which the K_d can be determined from, will not be affected, which is a significant advantage of ratiometric analysis.

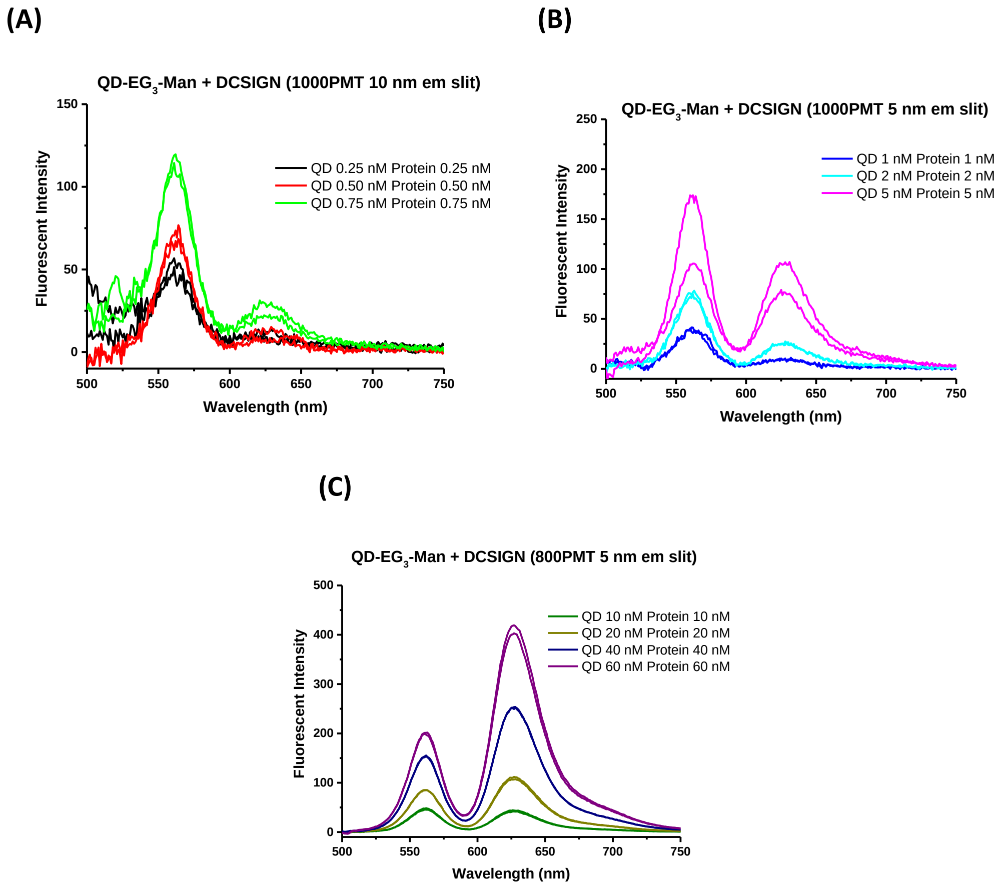

Figure 2.5.1: Fluorescence spectra obtained for determination of the accurate K_D for QD-EG_3-Man + DC-SIGN using a standard protein molar ratio: QD ratio of 1:1. (**A**) Low concentrations of QDs and DC-SIGN (0.25 – 0.75 nM) (; (**B**) intermediate concentrations of QDs and DC-SIGN (1 – 5 nM) and (**C**) high concentrations of QDs and DC-SIGN (10 – 60 nM).

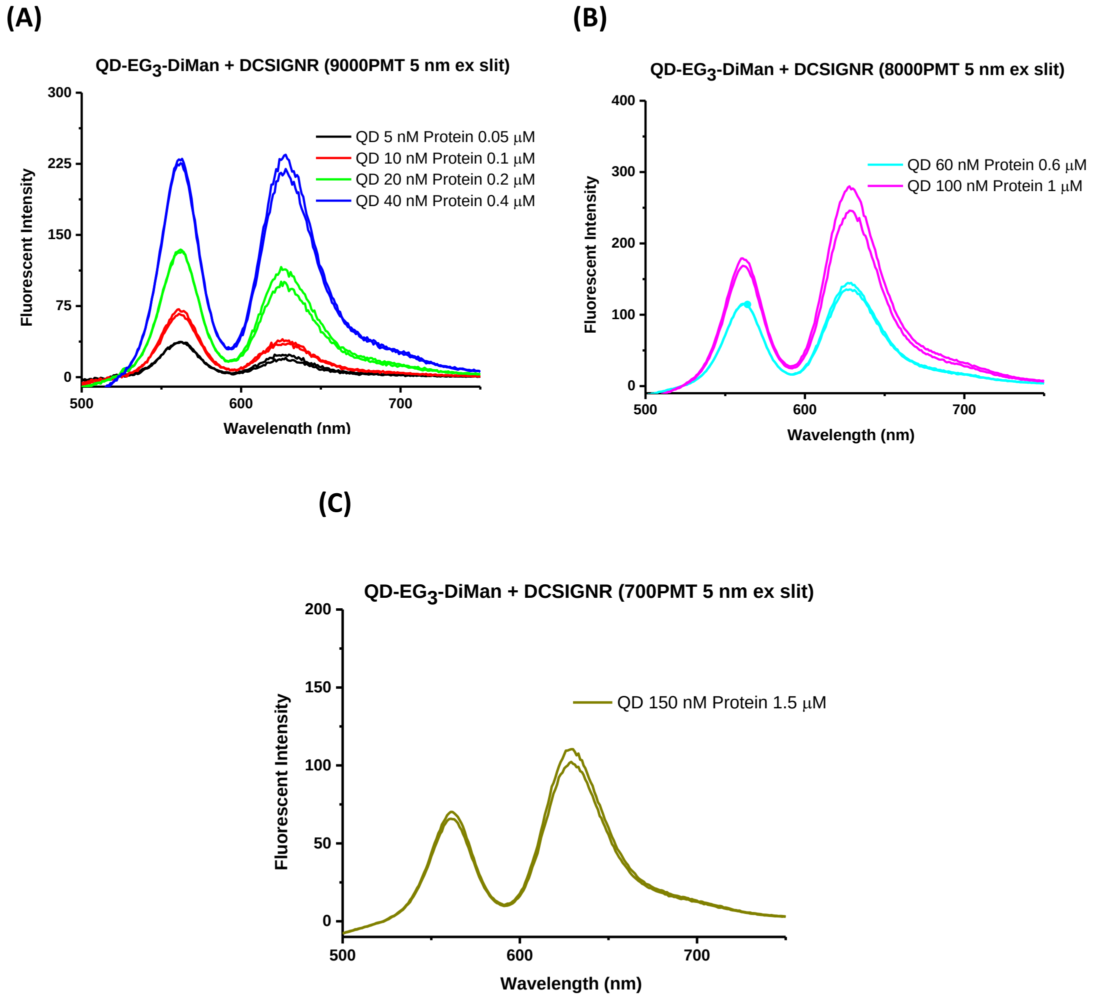

Figure 2.5.2: Fluorescence spectra obtained for determination of the accurate K_D for QD-EG$_3$-DiMan + DC-SIGNR (where n= 3 or 11) using a standard protein molar ratio: QD ratio of 10:1. (**A**) Low concentrations of QDs (5 – 40 nM) and DC-SIGNR (0.05 – 0.4 µM); (**B**) intermediate concentrations of QDs (60 – 100 nM) and DC-SIGNR (0.6 – 1 µM) and (**C**) high concentrations of QDs (150 nM) and DC-SIGNR (1.5 µM).

2.5.1 Ratiometric Quantification of QD-DC-SIGN/R Binding Affinity

The apparent K_d is the equilibrium dissociation constant that measures the concentration that gives 50% binding. The smaller the K_d, the stronger the binding affinity and vice versa. The apparent FRET ratio, I_{626}/I_{554}, is linearly correlated to the number of proteins (acceptors) bound to the QDs (donors) hence it is reliable signal for quantifying the proportion of QD-protein complexes in the QD-DC-SIGN/R mixtures. This relationship can be given through combining (**Eq. 10** and **Eq.11**) both used to calculate the FRET efficiency, *E*, for a single QD donor which interacts through FRET with a number, *N*, of identical acceptors.[15]

$$E = \frac{N \times {R_0}^6}{[N \times {R_0}^6 + r^6]} = \frac{1}{[1 + \frac{\left(\frac{r}{R_0}\right)^6}{N}]} \qquad \textbf{(Eq. 10)}$$

Where R_0 is the Förster radius of the QD-single dye FRET pair and *r* is the donor –acceptor distance. Efficiency can also be measured through the enhanced acceptor emission using (**Eq. 11**).

$$E = \frac{I_{Dye}}{[I_{Dye}+\gamma\times I_{QD}]} = \frac{1}{[1+\gamma \times \frac{I_{QD}}{I_{Dye}}]} \quad \textbf{(Eq. 11)}$$

Where γ is a correcting factor for the different QY from the dye and QD. Assuming the shape of both fluorescence spectra are independent of the intensity, then the integrated I_{QD}/I_{Dye} ratio should be linearly proportional to the peak intensity ratio *e.g.* $I_{QD}/I_{Dye} = \alpha\ I_{554}/I_{626}$. A combination of both (**Eq. 10**) and (**Eq. 11**) gives the following:

$$\frac{1}{[1+\gamma \times \frac{I_{QD}}{I_{Dye}}]} = \frac{1}{[1+\gamma \times \alpha \times \frac{I_{554}}{I_{626}}]} = \frac{1}{[1+\frac{\left(\frac{r}{R_0}\right)^6}{N}]} \quad \textbf{(Eq. 12)}$$

Resulting in the following relationship (**Eq. 13**):

$$\gamma \times \alpha \times \frac{I_{554}}{I_{626}} = \frac{\left(\frac{r}{R_0}\right)^6}{N} \quad \textbf{(Eq. 13)}$$

This can then be rearranged to give the following relationship (**Eq.14**) the linear relationship of the FRET ratio with the number of acceptors if all QD-protein interactions are the same distance:

$$\frac{I_{626}}{I_{554}} = N[\gamma \times \alpha \times \left(\frac{r}{R_0}\right)^6] \quad \textbf{(Eq. 14)}$$

Where γ, α and R_0 are all constant values. **Figure 2.5.3**, shows the typical titration curves where all the FRET ratios increase with concentration and finally reach saturation where the stronger the binding the sharper the FRET ratio increase. The resulting K_{ds} are obtained from fitting the titration curves with a non-linear fitting plot based on the Hill equation, (**Eq. 15**) below.

$$\theta = \frac{[L]^n}{k_d + [L]^n} \quad \textbf{(Eq. 15)}$$

Where θ is the fraction of the receptor (protein) concentration that is bound by the ligand which is our case is the FRET ratio between the two emission maxima (I_{626}/I_{554}), [L] is the concentration of unbound ligand, K_d is the dissociation constant and n is the hill coefficient. The FRET ratio was then plotted against protein concentrations and fitted using the following form of the Hill equation (**Eq. 16**) (OriginPro, Origin Lab).

$$y = \frac{R_{max}\times x^n}{(K^n+x^n)} \quad \textbf{(Eq. 16)}$$

Where R_{max} is the maximum I_{626}/I_{554} ratio, K is the apparent K_d, n is the Hill coefficient and x is the protein concentration. The resulting fitting parameters are summarised in **Table 2.5.1**.

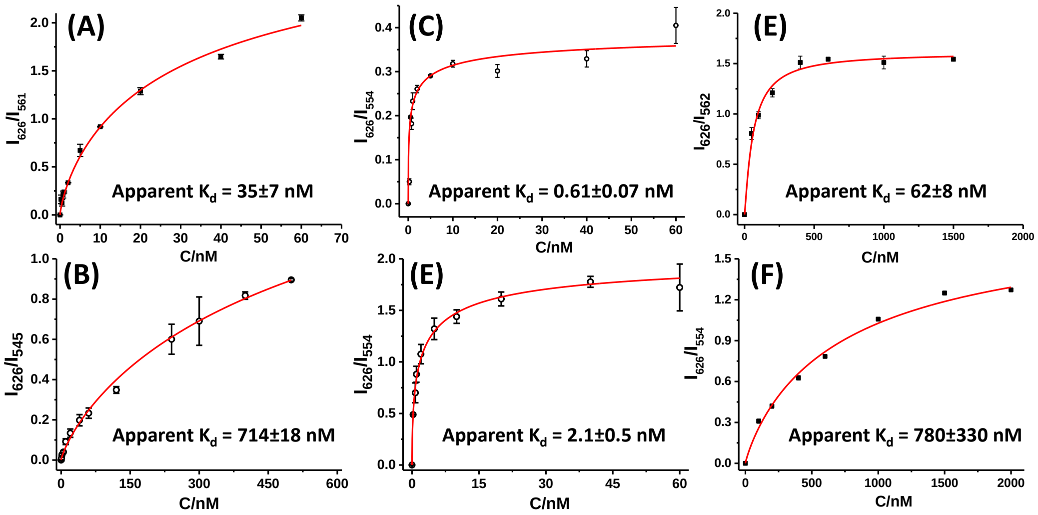

Figure 2.5.3: FRET intensity ratio (I_{626}/I_{554}) curves shown as a function of the QD: protein molar ratio, 1:1 for DC-SIGN and 1:10 for DC-SIGNR. (**A**) QD-EG_3-Man + DC-SIGN (**B**) QD-EG_{11}-Man + DC-SIGN (**C**) QD-EG_3-DiMan + DC-SIGN (**D**) QD-EG_{11}-DiMan + DC-SIGN (**E**) QD-EG_3-DiMan + DC-SIGNR and (**F**) QD-EG_3-DiMan + DC-SIGNR. Fitted using the Hill's equation.

Table 2.5.1: Summary of the fitting parameters for calculating the apparent K_d using the Hill Equation to fit the QD-EG_n-Man^m- DC-SIGN/R binding curves (**Figure 2.5.3**).

QD + Protein	R_{max}	Apparent K_d (nM)	n	R^2
QD- EG_3-Man + DC-SIGN	3.3 ± 0.3	35 ± 7	0.76 ± 0.02	0.9999
QD- EG_{11}-Man + DC-SIGN	2.1 ± 0.1	714 ± 18	0.81 ± 0.03	0.9991
QD- EG_3-DiMan + DC-SIGN	0.41 ± 0.01	0.61 ± 0.07	0.45 ± 0.03	0.9982
QD- EG_{11}-DiMan + DC-SIGN	2.09 ± 0.09	2.1 ± 0.5	0.56 ± 0.03	0.9998
QD- EG_3-DiMan + DC-SIGNR	1.61 ± 0.06	62 ± 8	1.2 ± 0.3	0.9987
QD- EG_{11}-DiMan + DC-SIGNR	1.86 ± 0.31	780 ± 330	0.88 ± 0.16	0.9983

Table 2.5.2: Key parameters calculated for the QD-EG_n-Man^m (where n= 3 or 11 and m=1 or 2) and their binding affinities with DC-SIGNR.

QD-Surface Ligands	Glycan Valency (N)	Apparent K_d DC-SIGN (nM)	Apparent K_d DC-SIGNR (nM)	Enhancement Factor β*	β/N
DHLA-EG_3-Man	330 ± 70	35 ± 7	-	100, 000	~ 300
DHLA-EG_{11}-Man	222 ± 62	715 ± 18	-	4, 900	~ 22
DHLA-EG_{11}-DiMan	369 ± 38	0.61 ± 0.07	62 ± 8	1, 480, 000	~ 4, 000
DHLA-EG_3-DiMan	281 ± 25	2.1 ± 0.5	780 ± 330	430, 000	~ 1, 530

*DC-SIGN/R affinity enhancement factor is calculated by: $\beta = \frac{K_{d(CRD-Glycan)}}{Apparent\ K_{d(DC-SIGN-QD)}}$ where $K_{d\ CRD\text{-}Man}$ = 3.5 mM and $K_{d\ CRD\text{-}DiMan}$ = 0.9 mM. [21]

The binding affinities and other important parameters (e.g. glycan valency, overall binding affinity enhancement factor, β, over monovalent CRD-Glycan binding) are shown above in **Table 2.5.2**. The results give three notable findings. First, using a QD displayed with a polyvalent array of DiMan functional group greatly enhances the binding affinity with DC-SIGN, where a K_d as low as 610 pM is achieved with QD-EG_3-DiMan, which translates into a huge affinity enhancement factor, β, of about 1.5 million over the corresponding monovalent binding, K_d = 0.9 mM.[21] Second, the level of enhancement afforded by mannose is significantly lower than that of the DiMan, around 100 fold lower, even though the polyvalent binding significantly enhanced the binding affinity for both of them. The difference could be due to the extended binding site of the DC-SIGN CRD which is known to contain primary and secondary mannose binding sites. [22] The QD-Man may only bind to the primary site however, being a disaccharide, QD-Diman may bind to both the primary and secondary sites, leading to a greater degree of affinity enhancement. This also highlights the importance of the protein binding surface for designing different multivalent inhibitors. Finally, the ethylene glycol, EG, linker length also plays an important role on the multivalent affinity, increasing the EG linear repeat length from 3 to 11 results in a lower affinity. This is likely to be due to the flexibility of the EG polymer chain. The higher the flexibility the more disordered the terminal sugars will be, giving rise to a higher entropy penalty upon protein binding. As mentioned previously, a suitable length of oligo(ethylene glycol) groups is essential for QD stability and water solubility in buffers, which is also needed to minimise non-specific interactions.

2.6 Competition Studies

2.6.1 Protein Competition Studies

To confirm that the FRET signals observed between the QD and labelled proteins are a true reflection of the native QD-protein interactions, a competitive binding using native proteins are also carried out by adding an increasing concentration of wild-type DC-SIGN or wild-type DC-SIGNR to each QD-DC-SIGN (labelled) sample. We expect that competition of wild-type protein (unlabelled) should displace the labelled protein binding to the QD, resulting in a decrease in FRET effect. **Figure 2.6.1** and **Figure 2.6.2** show the fluorescence spectra of the QD and DC-SIGN (labelled) mixture after adding increasing concentrations of WT DC-SIGN and WT DC-SIGNR, respectively. We expect effective competition to happen with WT DC-SIGN and not with WT DC-SIGNR because DC-SIGN binds to the QD-DiMan >100 fold stronger than DC-SIGNR does (**Table 2.5.1**). The predicted results are confirmed by the fluorescence spectra, where addition of WT DC-SIGN results in a decrease of the FRET effect, while almost no change is observed with WT

DC-SIGNR, suggesting no competition happened. These results are also shown within the FRET ratio curves for this experiment seen below in **Figure 2.6.6**. **Figure 2.6.3** shows the schematic of the results, showing the competition between (**A**) labelled DC-SIGN and WT DC-SIGN and (**B**) labelled DC-SIGN and WT DC-SIGNR.

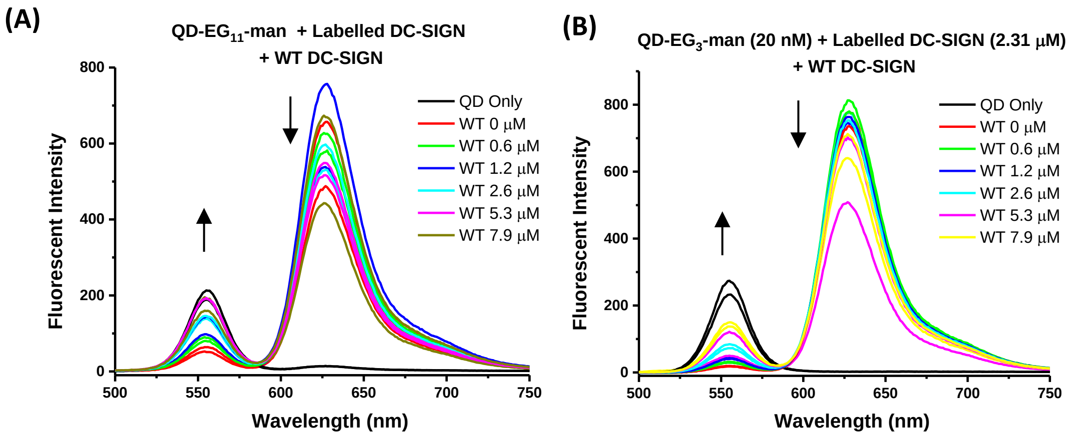

Figure 2.6.1: Fluorescence spectra showing data for (A) labelled DC-SIGN competing with wild-type DC-SIGN using QD-EG$_{11}$-man and (B) labelled DC-SIGN competing with WT DC-SIGN using QD-EG$_3$-man.

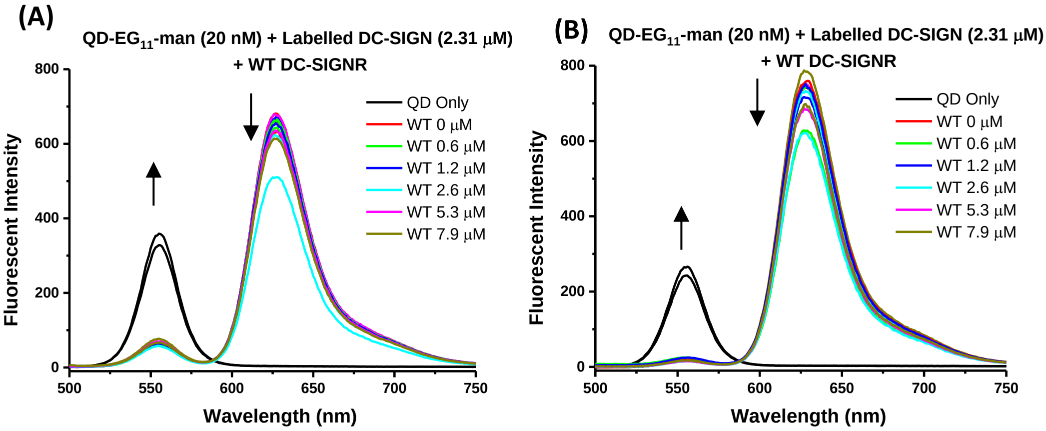

Figure 2.6.2: Fluorescence spectra showing data for (A) labelled DC-SIGN competing with wild-type DC-SIGNR using QD-EG$_{11}$-man and (B) labelled DC-SIGN competing with WT DC-SIGNR using QD-EG$_3$-man.

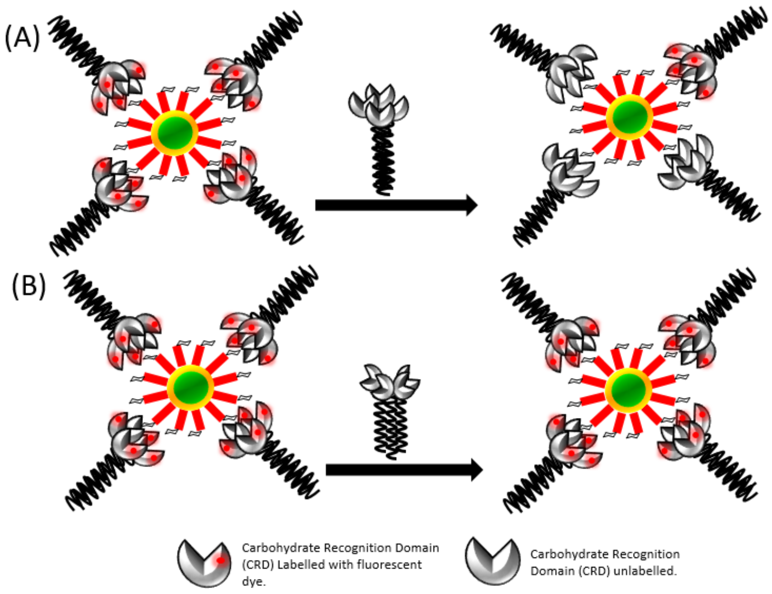

Figure 2.6.3: Schematic showing the expected labelled/unlabelled protein competition upon QD surface using QD-EG$_{11}$-man with (A) DC-SIGN and (B) DC-SIGNR.

2.1.1.3 Truncated DC-SIGN

To investigate the basis of the different CRD orientation between DC-SIGN and DC-SIGNR, competition between a labelled DC-SIGN and unlabelled truncated DC-SIGN is carried out. Despite sharing 77 % amino acid sequence identity between DC-SIGN and DC-SIGNR, a careful analysis of the DC-SIGN sequence reveals an extra-segment at the CRD/neck interface which is absent in DC-SIGNR. We suspect that the extra segment may restrict the flexibility of the CRDs in DC-SIGN, contributing to the binding affinity. By removing this segment, this truncated DC-SIGN may act more likely to wild-type DC-SIGNR because they are now structurally similar. This hypothesis is shown schematically in **Figure 2.6.4**. The resulting fluorescence spectra are shown in **Figure 2.6.5** below.

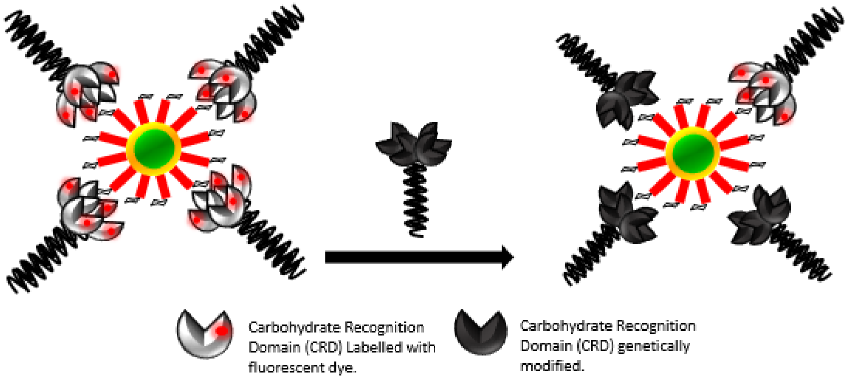

Figure 2.6.4: A schematic showing the expected results of the protein competition between the labelled DC-SIGN and the truncated DC-SIGNR.

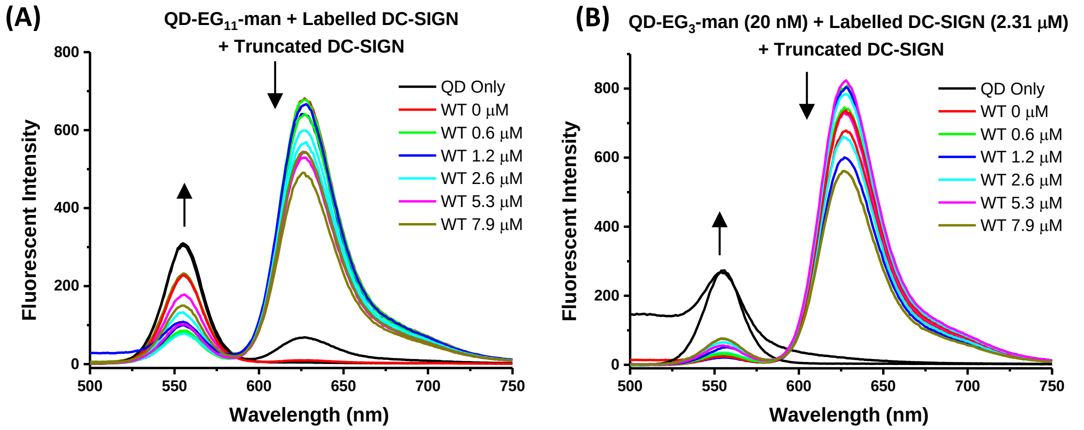

Figure 2.6.5: Fluorescence spectra showing data for (A) labelled DC-SIGN competing with truncated DC-SIGNR using QD-EG$_{11}$-man and (B) labelled DC-SIGN competing with truncated DC-SIGNR using QD-EG$_3$-man.

2.1.1.4 Ratiometric Analysis and Determination of Inhibition Constant

A decrease in the FRET intensity ratio (I_{626}/I_{554}) is expected as the number of labelled receptors (acceptor fluorophores) bound to the QD is reduced. **Figure 2.6.6** show the resulting FRET ratio as a function of unlabelled/labelled protein ratio for QD-EG$_3$-DiMan and QD-EG$_{11}$-DiMan respectively fitted by (**Eq. 15**) below.

$$y = \frac{K_i}{K_i + x} \qquad (\textbf{Eq. 17})$$

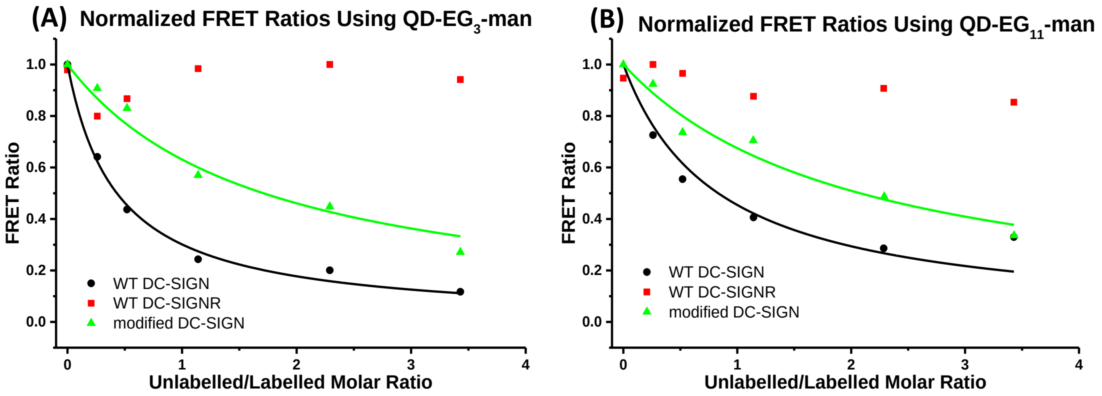

Figure 2.6.6: Graph to show the comparison of normalized FRET ratios when investigating unlabelled protein competition using (A) QD-EG$_3$-Man and (B) QD-EG$_{11}$-Man when increasing the concentration of the competing protein.

Table 2.6.1: A table to show the summary of the K_i values for the unlabelled protein competition studies against labelled DC-SIGN.

QD-Sample	**DC-SIGN**		**DC-SIGNR**		**Truncated DC-SIGN**	
	Ki	**R^2**	**Ki**	**R^2**	**Ki**	**R^2**
QD-EG_3-Man	0.43	0.994	-		1.71	0.973
QD-EG_{11}-Man	0.83	0.936	-		2.07	0.966

The apparent FRET ratio decreases when both the WT and truncated DC-SIGN are introduced to compete for labelled DC-SIGN binding with both QDs, suggesting the labelled proteins have the same binding modality as wild-type protein with the QDs. On the other hand, this effect is not seen for WT DC-SIGNR suggesting that WT DC-SIGNR is too weak to displace bound DC-SIGN. This is not unexpected as its binding affinities are >100 fold weaker. Interestingly, the truncation of DC-SIGN also produces some degrees of competition, but its efficiency appears to be in between DC-SIGN and DC-SIGNR, suggesting a reduced binding affinity with the QDs. This result may suggest that its structure may lie in between DC-SIGN and DC-SIGNR. **Table 2.6.1** shows a summary of the K_i values calculated from the curve fitting. Evaluation of the results was done in comparison to a simple competitive model, (**Eq. 16**).

$$F = \frac{IR_{50}}{[IR_{50} + \frac{C_{WT}}{C_{LP}}]} \qquad \textbf{(Eq. 18)}$$

Where F is the normalized FRET ratio in the presence of WT protein, C_{WT} and C_{LP} are the WT and labelled protein concentrations and IR_{50}, K_i in this case, is the molar ratio of WT protein: labelled protein required to reduce F by 50 %. If the $IR_{50} = 1$ this indicates that both WT and labelled protein bind with equal affinity then if $IR_{50} < 1$ this indicates that the labelled protein binds more weakly then the WT. Fitting the data gives us an IR_{50} value of 0.43 and 0.83 for QD-EG_n-Man (where n= 3 and 11) with DC-SIGN respectively. This shows that the site-specific mutation and dye labelling has slightly weakened its affinity for QDs. The results are similar to those find for the disaccharide ligands where the IR_{50} values are 0.37 and 0.88 for QD-EG_n-DiMan (where n= 3 and 11) with DC-SIGN respectively.[23]

2.7 Mannose Competition Studies

To confirm that the FRET signal is due to specific QD surface sugar-protein binding, a further binding competition study with free mannose is also carried out using fixed concentrations of the QD and labelled protein (QD: protein ratio of 1:1 for DC-SIGN and a 1:10 for DC-SIGNR) with increasing concentrations of mannose. **Table 2.7.1** shows the sample make up. If mannose competes with QD-saccharide binding to the labelled protein, then the FRET ratio will decrease.

Table 2.7.1: A table to show the concentrations of the samples prepared for mannose competition studies. QD (2 μM) to protein ratios of 1:1 and 1:10 was used for DC-SIGN (3 μM) and DC-SIGNR (15 μM) respectively. Each sample also contains 5 μg/mL of His$_6$-Cys peptide (final concentration) in a final volume of 400 μL in HEPES buffer.

Sample	QD Volume (μL)	DC-SIGN (3 μM) Volume (μL)	DC-SIGNR (15 μM) Volume (μL)	Mannose Conc (μM)
1	8	0	0	0
2	8	21.33	21.33	0
3	8	21.33	21.33	0.25
4	8	21.33	21.33	0.5
5	8	21.33	21.33	1
6	8	21.33	21.33	10
7	8	21.33	21.33	100
8	8	21.33	21.33	1 000
9	8	21.33	21.33	10 000
10	8	21.33	21.33	100 000
11	8	21.33	21.33	1 000 000

Figure 2.7.1 shows the fluorescence spectra of the samples competing against DC-SIGN (**A, B**) and for DC-SIGNR (**C, D**). An increase of QD donor intensity (λ= 562 nm) and a decrease of the acceptor fluorescence is observed with the increasing mannose concentration, confirming that free mannose effectively competes with DC-SIGN/R binding to the QD-saccharide, suggesting that the FRET signal observed above is indeed due to specific protein-sugar interaction. No competition could be recorded at higher mannose (<1 M) concentrations as problems occur to viscosity of the solution.

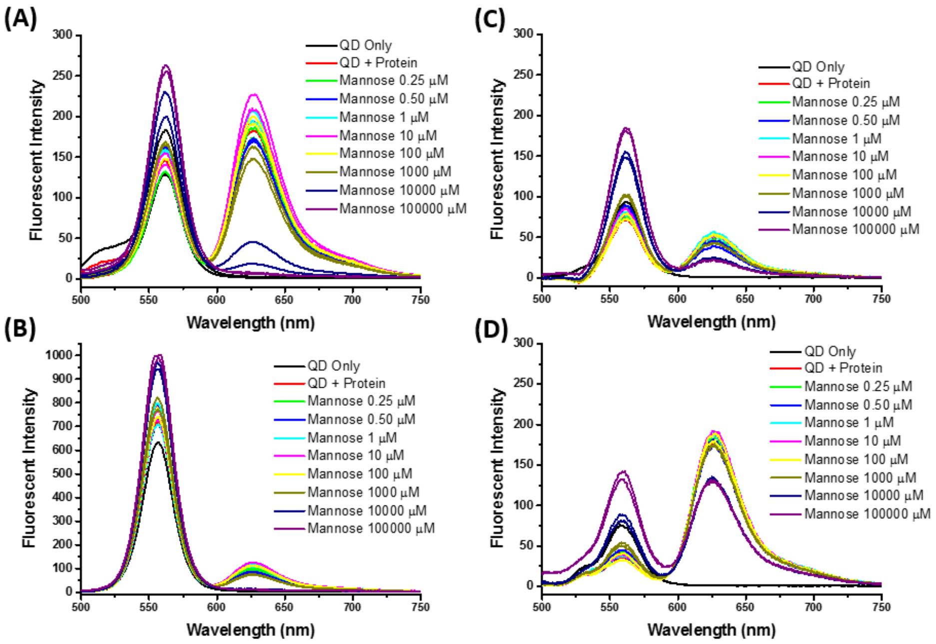

Figure 2.7.1: Background corrected fluorescence Spectra of (**A**) QD-EG$_3$-Man + DC-SIGN, (**B**) QD-EG$_{11}$-Man + DC-SIGN, (**C**) QD-EG$_3$-DiMan + DC-SIGNR, (**D**) QD-EG$_{11}$-DiMan + DC-SIGNR over the addition of an increasing concentration of Mannose. A standard concentration of QDs was used and also a fixed QD: Protein molar ratio of 1:1 for DC-SIGN and 1:10 for DC-SIGNR.

2.7.1 Ratiometric Determination of Mannose Competition

Figure 2.7.2 shows the resulting FRET ratio as a function of mannose concentration for both QD-EG$_n$-Man (where n= 3 and 11) with DC-SIGN and QD-EG$_n$-DiMan (where n= 3 and 11) with DC-SIGNR. The data are fitted by (**Eq. 15**) to derive the inhibition constant, K$_i$, an indication of the potency of a potential inhibitor. It is also known as the concentration which produces 50% of the maximum inhibition.

$$y = \frac{K_i}{K_i + x} \qquad \textbf{(Eq. 17)}$$

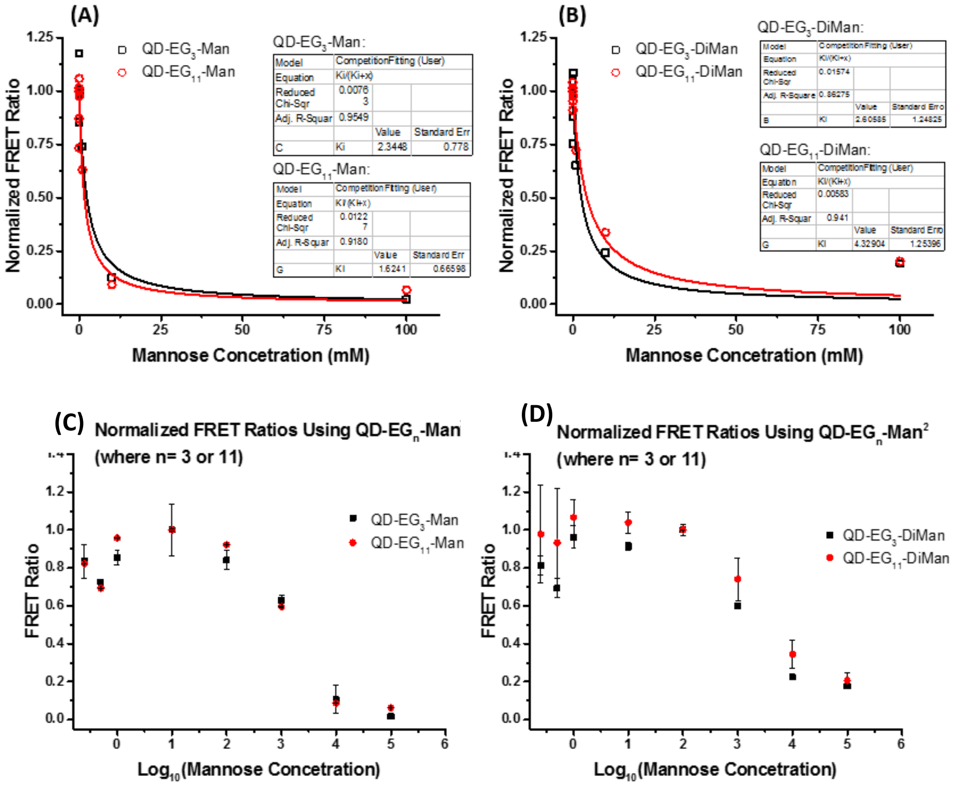

QD-EG$_3$-Man:

Model	CompetitionFitting (User)		
Equation	Ki/(Ki+x)		
Reduced Chi-Sqr	0.00763		
Adj. R-Squar	0.9549		
		Value	Standard Err
C	Ki	2.3448	0.778

QD-EG$_{11}$-Man:

Model	CompetitionFitting (User)		
Equation	Ki/(Ki+x)		
Reduced Chi-Sqr	0.01227		
Adj. R-Squar	0.9180		
		Value	Standard Err
G	Ki	1.6241	0.66598

QD-EG$_3$-DiMan:

Model	CompetitionFitting (User)		
Equation	Ki/(Ki+x)		
Reduced Chi-Sqr	0.01574		
Adj. R-Square	0.86275		
		Value	Standard Erro
B	Ki	2.60585	1.24825

QD-EG$_{11}$-DiMan:

Model	CompetitionFitting (User)		
Equation	Ki/(Ki+x)		
Reduced Chi-Sqr	0.00583		
Adj. R-Squar	0.941		
		Value	Standard Erro
G	Ki	4.32904	1.25396

Figure 2.7.2: FRET intensity ratio (I_{626}/I_{562}) curves shown as a function of mannose concentration. Mannose competition curves are shown for (**A**) QD-EG$_n$-Man (where n= 3 or 11) + DC-SIGN and (**B**) QD-EG$_n$-Man (where n= 3 or 11) + DC-SIGNR and (**C** and **D**) are the log$_{10}$ of mannose concentrations plots. Curve plotted in accordance to (**Eq. 15**) above.

Table 2.7.2: Summary of the inhibition constant, K_i, obtained from **Figure 2.7.2**.

QD	**Ki$_{(DC-SIGN)}$ (mM)**	**Binding affinity enhancement factor***	**Ki$_{(DC-SIGNR)}$ (mM)**	**Binding affinity enhancement factor***
QD-EG$_3$-Man	2.35 ± 0.8	58750	-	-
QD-EG$_{11}$-Man	1.62 ± 0.7	40500	-	-
QD-EG$_3$-DiMan	-	-	2.61 ± 1.2	65250
QD-EG$_{11}$-DiMan	-	-	4.32 ± 1.3	108000

* DC-SIGN/R binding affinity enhancement factor is calculated by, K_i/C_{QD}.

As expected the apparent FRET ratio decreases when the mannose was introduced suggesting that the FRET signal observed are due to the specific DC-SIGN/R-sugar interactions. When the free mannose concentration equals that of the Ki the amount of DC-SIGN bound to the QD and free mannose are the same, where a much greater Ki then C_{QD} confirms that DC-SIGN binds much more strongly to the QDs than free mannose, the enhancement factors further confirm this. The binding K_d are confirmed here as the lower the K_d the higher the K_i meaning a stronger binding requires more free mannose to compete for the binding. Kinetic studies of the mannose competition experiments using conventional fluorescence spectroscopy without stopped-flow attachment are also attempted, however, the competition reaction appears to occur too quickly to be able to measure accurately. The binding enhancement factor has been calculated to show the degree of competition, the higher the enhancement the easier the competition (**Table 2.7.2**).

2.8 Transmission Electron Microscopy

Transmission electron microscopy, TEM, is used to confirm the structural model of DC-SIGN/R based on their distinct QD-mannose binding properties initially proposed by Guo *et al.*[13] The hypothesis suggested that the CRD binding sites in DC-SIGN all face in the same direction, which is upwards. In comparison, the CRD binding sites in DC-SIGNR are facing outwards in opposite directions. These predicted geometries can be seen in **Figure 2.8.1** below.

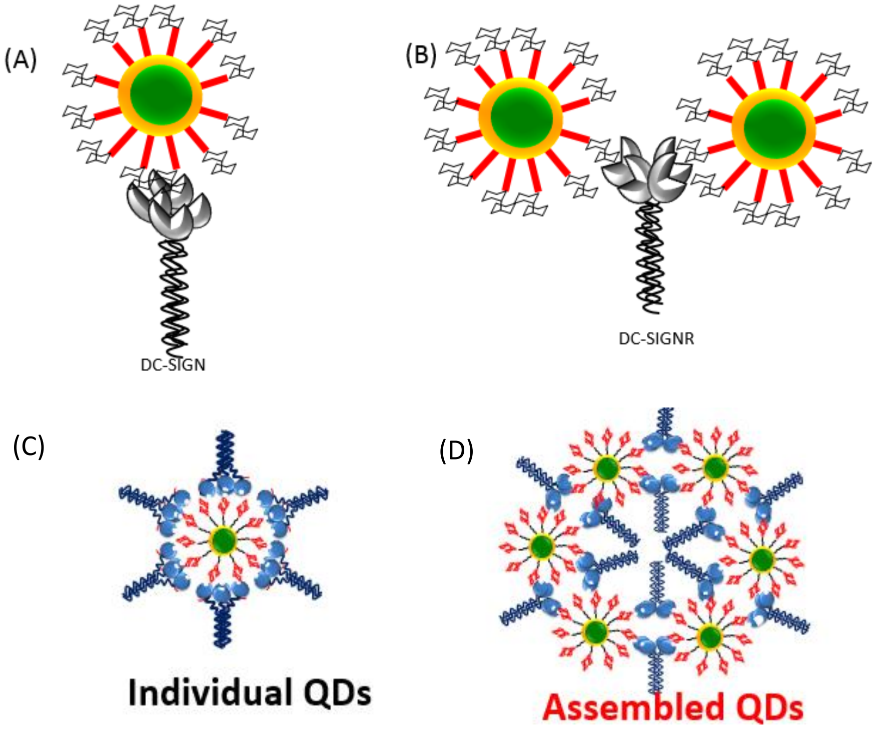

Figure 2.8.1: Schematic showing the predicted tetrameric structure for the proteins DC-SIGN/R where (A and C) shows the predicted multilinking structure of DC-SIGN and (B and D) show the predicted crosslinking structure of DC-SIGNR in the assembled arrangement.

The TEM images below, **Figure 2.8.2**, show the predicted sugar-CRD interactions proposed from the fluorescence data. Binding of the tetrameric DC-SIGN with the QD produces **Figure 2.8.2(B)**, isolated QDs without any observable aggregation/clustering, this is similar to that seen for the pure QD-sugar conjugate alone, **Figure 2.8.2(A)**. This observation is fully consistent with the expectation that all four CRDs in DC-SIGN are bound to sugars present on the same QD surface. On the other hand, the QDs in the presence of DC-SIGNR appear in clusters in the TEM image **Figure 2.8.2(C)**, suggesting that DC-SIGNR has cross-linked with the QDs. We believe this is down to two of the four CRDs binding to sugars on one QD while the other two bind to another QD. Besides, each QD can bind to two or more proteins. As a result of both QD and protein cross-linking effect, the net result is the formation of clustered QDs. This is the first time that both the fluorescence properties and the high TEM contrast of QDs have been combined to create a novel multimodal readout strategy for multimeric sugar – protein interactions. Dynamic light scattering measurements, done by Dr Yuan Guo, also confirm the distinct D_h sizes between the singular QD-EG_{11}-DiMan-DC-SIGN binding, $D_h = 41 \pm 0.5$ nm, and the clustering QD EG_{11}-DiMan - DC-SIGNR particles, $D_h = 138 \pm 2$ and 217 ± 12 nm (**Figure 2.8.3**).

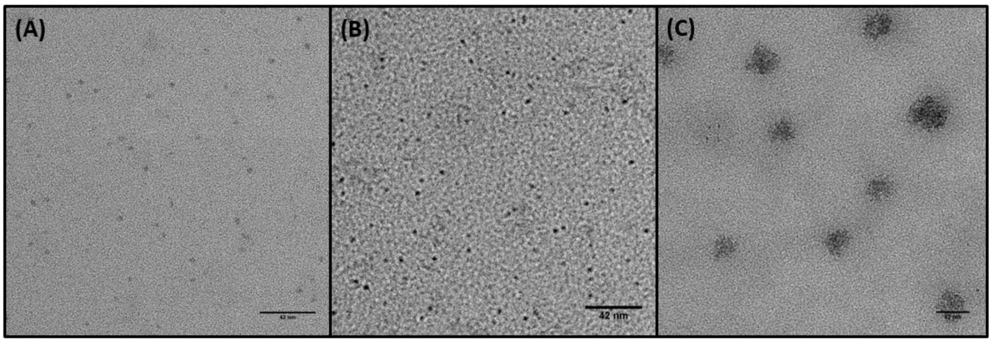

Figure 2.8.2: TEM images of (**A**) QD-EG_{11}-DiMan (**B**) QD-EG_{11}-DiMan+DC-SIGN and (**C**) QD-EG_{11}-DiMan+DC-SIGNR. Scale bar 42 nm.

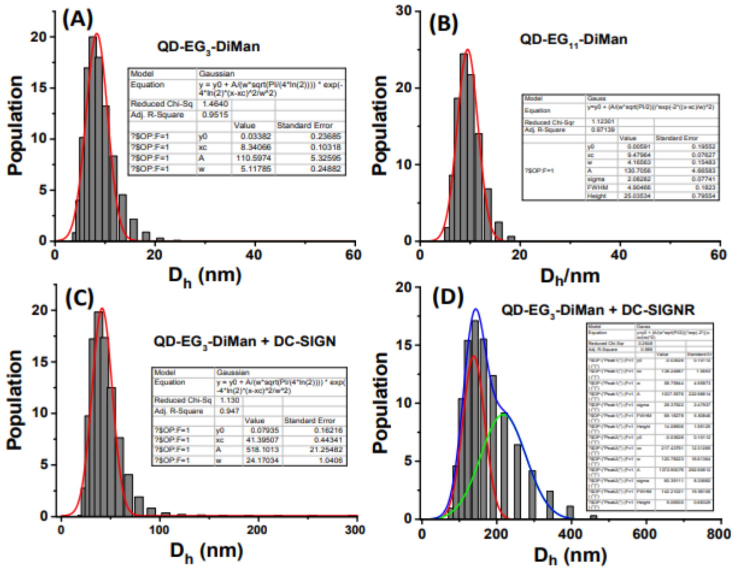

Model	Gaussian		
Equation	y = y0 + A/(w*sqrt(PI/(4*ln(2)))) * exp(-4*ln(2)*(x-xc)^2/w^2)		
Reduced Chi-Sq	1.4640		
Adj. R-Square	0.9515		
		Value	Standard Error
?$OP:F=1	y0	0.03382	0.23685
?$OP:F=1	xc	8.34066	0.10318
?$OP:F=1	A	110.5974	5.32595
?$OP:F=1	w	5.11785	0.24882

Model	Gauss		
Equation	y=y0 + (A/(w*sqrt(PI/2)))*exp(-2*((x-xc)/w)^2)		
Reduced Chi-Sqr	1.12301		
Adj. R-Square	0.97139		
		Value	Standard Error
?$OP:F=1	y0	0.00591	0.19552
	xc	9.47964	0.07627
	w	4.16563	0.15483
	A	130.7056	4.66583
	sigma	2.08282	0.07741
	FWHM	4.90466	0.1823
	Height	25.03534	0.79554

Model	Gaussian		
Equation	y = y0 + A/(w*sqrt(PI/(4*ln(2)))) * exp(-4*ln(2)*(x-xc)^2/w^2)		
Reduced Chi-Sq	1.130		
Adj. R-Square	0.947		
		Value	Standard Error
?$OP:F=1	y0	0.07935	0.16216
?$OP:F=1	xc	41.39507	0.44341
?$OP:F=1	A	518.1013	21.25482
?$OP:F=1	w	24.17034	1.0406

Figure 2.8.3: Hydrodynamic size (D_h) histograms of (**A**) QD-EG_3-DiMan and (**B**) QD-EG_{11}-DiMan in H_2O and then the D_h histograms of QD-EG_3-DiMan after binding with (**C**) DC-SIGN and (**D**) DC-SIGNR in binding buffer. All measurements performed by dynamic light scattering. [23]

2.9 Inhibiting Ebola Virus Host Cell Entry

Note: *The work is performed by our collaborator Professor Stefan Pöhlmann and his colleagues at the German Primate Center, Göttingen, Germany. The author of this thesis Emma C Poole has only interpreted the data and written her own account of the findings of the collaborators.*

The binding affinity between DC-SIGN and QD-EG_n-DiMan is very strong, suggesting that the QDs may act as potential inhibitors for effectively blocking DC-SIGN mediated virus infections, e.g. HIV and Ebola. To investigate this potential, a murine leukemia virus, MLV, is used as a vector modified to express the Ebola virus glycoprotein, EBOV-GP, on the surface along with a modified genetic code which contains the luciferase gene. A model of the MLV used is shown below in **Figure 2.9.1**. Luciferase is an oxidative enzyme that produces bioluminescence in the presence of ATP, oxygen and a substrate.[24] The virus particles can bind to the DC-SIGN/R expressed on the cell surface by the EBOV-GP and enter the target Human embryonic kidney cells, 293T. The luciferase gene can then be transfected into the cell and thus express luciferase. Luciferase activity is then monitored from the lysate of the 293T cells. If the 293T cells are pre-treated with QDs then its surface DC-SIGN/R will be occupied by the QDs, preventing them binding to the virus particles and greatly reduce the uptake of viruses and the luciferase expression. A simplified version of the inhibitory action of the QDs within this assay is shown in **Figure 2.9.1**. To test that the inhibition is specific, a control viral glycoprotein is also used, the vesicular stomatitis virus glycoprotein, VSV-G which does not use DC-SIGN/R for cell entry. In addition, cells transfected using an empty plasmid, pcDNA, which does not express luciferase activity is also used as the background control as described in an earlier publication by Guo *et al.*[15]

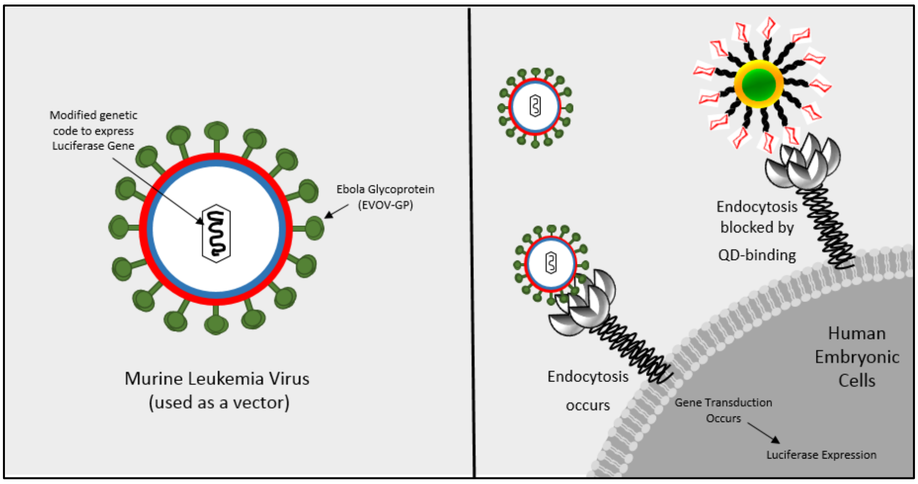

Figure 2.9.1: A schematic showing (**A**) the murine leukemia virus (MLV) used as a vector for viral inhibition assays bearing the Ebola glycoprotein (EBOV-GP) and (**B**) the inhibition of DC-SIGN using QD-EG_n-Man^m (where n=3 or 11 and m= 1 or 2) and how the luciferase action occurs via cell endocytosis of the modified MLV to express bioluminescence.

The cells are pre-treated with the QDs twice, washed and then treated with the MLV and the control VSV-G virus particles and incubated for 72 hours. The resulting luciferase activities from the cell lysates are shown below for QD-EG$_3$-DiMan, **Figure 2.9.2** (**A and B**) and QD-EG$_{11}$-DiMan, **Figure 2.9.2** (**C and D**). These initial results show that the presence of the QDs greatly reduces the luciferase activity, confirming the high inhibitory potency of these materials. This inhibition is presumably due to the strong binding between the QD and DC-SIGN/R which can effectively block the EBOV-MLV entry.

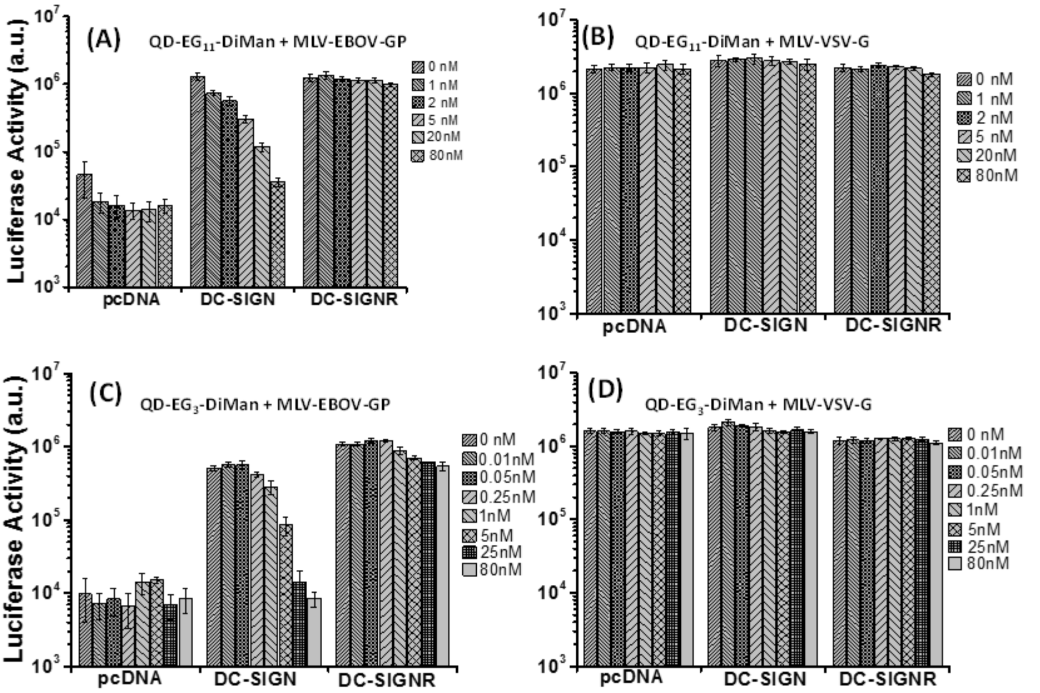

Figure 2.9.2: Human embryonic kidney cells (293 T) were transfected with the identified plasmids and pre incubated with (**A and B**) QD-EG$_{11}$-DiMan and (**C and D**) QD-EG$_3$-DiMan and inoculated with Murine Leukemia Virus (MLV) particles modified to contain the Ebola Virus Glycoprotein (EBOV-GP) or a control, vesicular stomatitis virus glycoprotein (VSV-G). The inhibitor concentrations were calculated after addition of particles. Luciferase activities in cell lysates were measured at 72 hrs post-transduction.

Finally from these results gene transduction of the control cells (pcDNA) and the transduction driven by control of a vector bearing the VSV-G, which cannot bind to DC-SIGN/R for host cell entry aren't affected by QD-EG$_n$-DiMan treatment. As the pcDNA does not express the gene for the luciferase production and so only shows low luciferase activity. These results confirm that the viral internalisation is blocked in the presence of the QDs. The normalised inhibition data are fitted using the standard inhibition model to calculate the IC$_{50}$ values for each QD-conjugate and shown in **Figure 2.9.3**. The IC$_{50}$ value is the QD concentration which gives 50% of original luciferase activity. The lower the value the more potent the inhibitor. The IC$_{50}$ values for QD-EG$_3$-DiMan and QD-EG$_{11}$-DiMan inhibiting DC-SIGN expression cells are calculated as 0.70 ± 0.20

and 1.42 ± 0.09 nM, respectively. Such IC_{50} values are comparable against some of the most potent glycoconjugate inhibitors reported in literature, e.g. 0.667 nM for multivalent glycofullerene molecules, Munoz *et al.*,[25] and 0.9 nM for glcodendrinanoparticles, Ribeiro-Viana *et al*,[6] against virus infection of target cells.

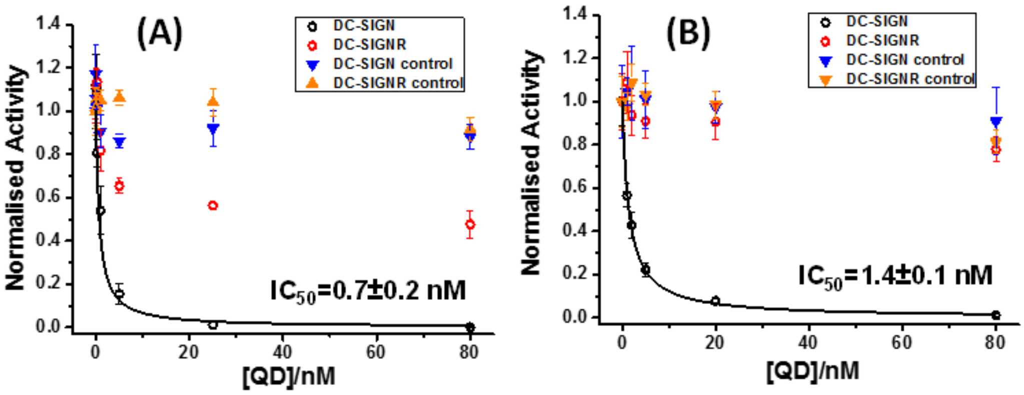

Figure 2.9.3: Normalised luciferase activities of the DC-SIGN or DC-SIGNR expressing 293T cells measured as a function of the pre-treatment (**A**) QD-EG_{11}-DiMan and (**B**) QD-EG_3-DiMan concentrations. The data shown in open circles correlate to the virus particles containing the EBOV-GP and the triangles to the control glycoprotein (VSV-G). Data was fitted using a comparable competitive binding model.[15]

An interesting observation is that the IC_{50} values are very similar to that of the binding constant, K_d, calculated previously using FRET. **Table 2.9.1** below shows the values for each and the values are within the error of each other. These results suggest that the FRET based binding affinity method could be potentially used as a way to predict the viral inhibition potency (IC_{50}) of the QDs and other glyconanoparticles.

Table 2.9.1: A summary of both the apparent K_d values and the IC_{50} values for comparison of the inhibition potency of QD-EG_n-DiMan (where n = 3 and 11) with DC-SIGN.

QD Surface Ligands	**Apparent K_d DC-SIGN (nM)**	**IC_{50} DC-SIGN (nM)**
QD- EG_3-DiMan + DC-SIGN	0.61 ± 0.07	0.70 ± 0.20
QD- EG_{11}-DiMan + DC-SIGN	2.10 ± 0.50	1.42 ± 0.09

2.10 Conclusion

In conclusion, QDs displaying polyvalent DHLA-EG_n-Saccharide (where n= 3 or 11 and Saccharide = α-Man and Man-α-1,2-Man) ligands are powerful probes for dissecting the multivalent protein – glycan interactions using FRET techniques and TEM imaging. More significantly, we have revealed that the different CRD orientation of DC-SIGN and DC-SIGNR determines the way they bind to the QDs. DC-SIGN binds tetravalently to a single QD and DC-SIGNR binds divalently to two different QDs. A new FRET based binding affinity, K_d, method has been developed and revealed that DC-SIGN binds much stronger to the QDs than DC-SIGNR does, and is consistent with their binding multiplicity difference. In addition, three other significant results are obtained, first, displaying a manno-disaccharide polyvalently on QD greatly enhances the binding affinity with DC-SIGN, giving an apparent K_d of 610 pM which is ~1.5 million-fold stronger than the monovalent interaction, $K_{d(monovalent)}$ = 0.9 mM. Second, a polyvalent display of DiMan on the QD gives a greater level of affinity enhancement than that of Man in binding to DC-SIGN and DC-SIGNR, possibly due to that both the primary and secondary binding sites of the CRD are involved in the former but only the primary binding site is involved in the latter. Finally, the length of flexible EG linker also plays a key role in determining the strength of the binding affinity. Increasing linker length from 3 to 11 EG repeating unit's results in weaker affinity, due to the flexible nature of the linker which leads to higher levels of entropic penalty for binding to occur.

More importantly, the QD-saccharides are found to exhibit very high potencies against Ebola glycoprotein driven viral infection of DC-SIGN expressing cells with an IC_{50} value as low as 0.7 nM, placing them among the most potent glycoconjugate inhibitors. Interestingly, the IC_{50} values are comparable to their DC-SIGN binding affinity measured by our new FRET based method, suggesting that the sensitive ratiometric FRET based K_d measurement method developed in this study could be potentially used to predict the viral inhibition potency of glycan-nanoparticles. Further work investigating different EG chain lengths and different surface sugar densities is to be performed as diluting the density reduced the FRET readout. Also work on a more biocompatible nanomaterial will be considered as QDs are cytotoxic to cells due to the presence of cadmium within the core. To still exploit fluorescence energy transfer mechanisms gold nanoparticles, AuNPs, are suitable to use.

2.11 Experimental Procedures

2.11.1 Ligand Synthesis and Preparation of QDs

All the relevant synthesis methods for the ligands and QDs used within this chapter can be found within **Chapter 5**. All the ligands have been fully characterised using NMR, LC-MS and TLC.

2.11.2 Protein Production and Purification

All the details to produce and purify the proteins (DC-SIGN/R) used within this chapter can be found within **Chapter 5**.

2.11.3 Viral Inhibition Studies [23]

The experiments were performed using human embryonic kidney 293T cells. Target 293 T cells seeded in 96- well plates were transfected with plasmids encoding DC-SIGN, DC-SIGNR or control transfected with empty plasmid (pcDNA). The cells were washed at 16 h post transfection and further cultivated at 37 °C, 5 % CO_2 in Dulbecco's modified eagle medium (DMEM) containing 10 % fetal bovine serum (FBS). At 48 h post transfection, the cells were exposed to twice the final concentration of QD-EG_n-Man^m inhibitor in DMEM supplemented with 10 % FBS for 30 minutes in a total colume of 50 μL. Thereafter, the cells with inoculated with 50 μL of preparations of MLV vector particles encoding the luciferase gene and bearing either EBOV-GP or the VSV-G as control. Binding of QD-EG_n-Man^m to DC-SIGN/R on the surface of 293T cells can black the interaction of these lectins with the EBOV-GP on the particle surface, reducing the cellular uptake of vector particles and thus reducing transduction efficiency. At 6 h post inoculation, 100 μL of fresh DMEM culture medium was added, and the cells were incubated for another 72 h. Thereafter, luciferase activities in cell lysates were determined using a commercially available kit (PJK), following the instructions as described by Guo *et al*.[13]

2.12 References

1. L. Wu and V. N. KewalRamani, *Nat. Rev. Immunol.*, 2006, **6**, 859-868.
2. A. Bernardi, J. Jiménez-Barbero, A. Casnati, C. De Castro, T. Darbre, F. Fieschi, J. Finne, H. Funken, K.-E. Jaeger and M. Lahmann, *Chem. Soc. Rev*, 2013, **42**, 4709-4727.
3. S. Bhatia, L. C. Camacho and R. Haag, *J. Am. Chem. Soc.*, 2016, **138**, 8654-8666.
4. T. B. Geijtenbeek, D. S. Kwon, R. Torensma, S. J. van Vliet, G. C. van Duijnhoven, J. Middel, I. L. Cornelissen, H. S. Nottet, V. N. KewalRamani and D. R. Littman, *Cell*, 2000, **100**, 587-597.
5. S. Pöhlmann, E. J. Soilleux, F. Baribaud, G. J. Leslie, L. S. Morris, J. Trowsdale, B. Lee, N. Coleman and R. W. Doms, *P. Natl. Acad. Sci. USA*, 2001, **98**, 2670-2675.

6. R. Ribeiro-Viana, M. Sánchez-Navarro, J. Luczkowiak, J. R. Koeppe, R. Delgado, J. Rojo and B. G. Davis, *Nat. Commun.*, 2012, **3**, 1303.
7. A. Muñoz, D. Sigwalt, B. M. Illescas, J. Luczkowiak, L. Rodríguez-Pérez, I. Nierengarten, M. Holler, J.-S. Remy, K. Buffet and S. P. Vincent, *Nat. Chem.*, 2016, **8**, 50-57.
8. M. Jesús and S. Penadés, *Biochim. Biophys. Acta.*, 2006, **1760**, 636-651.
9. A. K. Adak, H.-J. Lin and C.-C. Lin, *Org. Biomol. Chem.*, 2014, **12**, 5563-5573.
10. N. Hao, K. Neranon, O. Ramström and M. Yan, *Biosens. Bioelectron.*, 2016, **76**, 113-130.
11. C. Diehl, O. Engström, T. Delaine, M. Håkansson, S. Genheden, K. Modig, H. Leffler, U. Ryde, U. J. Nilsson and M. Akke, *J. Am. Chem. Soc.*, 2010, **132**, 14577-14589.
12. M. J. Linman, J. D. Taylor, H. Yu, X. Chen and Q. Cheng, *Anal. Chem.*, 2008, **80**, 4007-4013.
13. J. B. Delehanty, I. L. Medintz, T. Pons, F. M. Brunel, P. E. Dawson and H. Mattoussi, *Bioconjug. Chem.*, 2006, **17**, 920-927.
14. K. Susumu, H. T. Uyeda, I. L. Medintz, T. Pons, J. B. Delehanty and H. Mattoussi, *J. Am. Chem. Soc.*, 2007, **129**, 13987-13996.
15. Y. Guo, C. Sakonsinsiri, I. Nehlmeier, M. A. Fascione, H. Zhang, W. Wang, S. Pöhlmann, W. B. Turnbull and D. Zhou, *Angew. Chem. Int. Ed.*, 2016, **55**, 4738-4742.
16. K. Susumu, B. C. Mei and H. Mattoussi, *Nat. Protoc.*, 2009, **4**, 424-436.
17. H. Zhang, G. Feng, Y. Guo and D. Zhou, *Nanoscale*, 2013, **5**, 10307-10315.
18. T. Karstens and K. Kobs, *J. Phys. Chem.*, 1980, **84**, 1871-1872.
19. A. T. R. Williams, S. A. Winfield and J. N. Miller, *Analyst*, 1983, **108**, 1067-1071.
20. S. Menon, K. Rosenberg, S. A. Graham, E. M. Ward, M. E. Taylor, K. Drickamer and D. E. Leckband, *P. Natl. Acad. Sci. USA*, 2009, **106**, 11524-11529.
21. A. Holla and A. Skerra, *Protein Eng. Des. Sel.*, 2011, **24**, 659-669.
22. H. Feinberg, D. A. Mitchell, K. Drickamer and W. I. Weis, *Science*, 2001, **294**, 2163-2166.
23. Y. Guo, I. Nehlmeier, E. Poole, C. Sakonsinsiri, N. Hondow, A. Brown, Q. Li, S. Li, J. Whitworth and Z. Li, *J. Am. Chem. Soc.*, 2017, **139**, 11833-11844.
24. S. J. Gould and S. Subramani, *Anal. Biochem.*, 1988, **175**, 5-13.
25. A. Muñoz, D. Sigwalt, B. M. Illescas, J. Luczkowiak, L. Rodríguez-Pérez, I. Nierengarten, M. Holler, J.-S. Remy, K. Buffet and S. P. Vincent, *Nat. Chem.*, 2016, **8**, 50-57.

Chapter 3

Effect of Quantum Dot Surface Glycan Density upon DC-SIGN/R Binding

3.1 Introduction

Glycodendrimers or glycopolymers over the last few years have been synthesised to study the interactions between carbohydrates and proteins.[1] These ligands are designed to increase the glycan concentration; as a dendron is a hyperbranched organic molecule connected to a central point.[2] These usually have peptide linkages attaching multiple glycan moieties to a central chelation point, a simple glycodendrimer is shown below in **Figure 3.1.1**. These materials show unique recognition properties as they can be synthesised to have controlled lengths, specific compositions and architectures.[3] Such molecules over recent times have provided solid foundations for constructing densely packed glycan arrays.[4] Glycans play a crucial role in many biological interactions.[5] Many papers have been published showing positive effects on improving binding affinity constants when the glycan density is increased through using a branched system.[3, 5] However, their potentials have not been harnessed by displaying them on a nanoparticle scaffold they have instead been used on their own. Other potential scaffolds have been used such as fullerenes[6], simple organic based amine frameworks[7] and sugar molecules.[8]

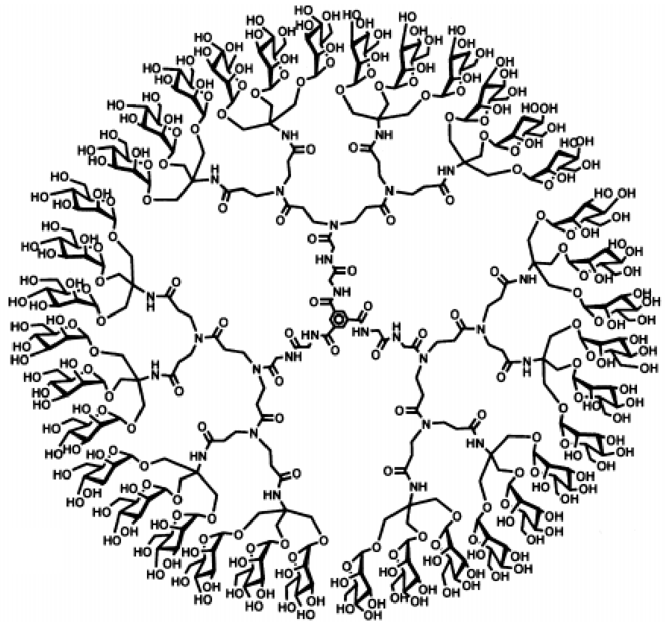

Figure 3.1.1: A third generation glycodendrimer bearing 36 α-ᴅ- mannopyranosyl residues by Turnbull *et al.* Taken from reference. [7]

QDs, AuNPs and magnetic nanoparticles make good scaffolds for glycodendrimer ligands as they possess a unique set of properties. Such as size-tuneable emission spectra, high quantum yield, broad absorption spectra and great resistance to photo-bleaching[9] that can be used to dissect further the binding modes between glycans and c-type lectins. These materials have been designed to have a greater contact surface area for measuring the key multivalency effects of lectin type proteins.[1] The fluorescence properties of QDs will be combined using a fluorescently labelled protein in a FRET based assay to probe the multivalent interactions. A recent study by Lin *et al*. [10] shows the importance of glycan density for multivalent binding affinity between glycan and lectin. However a key point in relation to this type of ligand is that just because singular carbohydrate protein interactions are weak, changing to a high density of ligands may not correlate with an increase in binding affinity.[11] Increasing glycan densities has already shown a positive impact on the interactions between the glycan (mannose) and the lectins (DC-SIGN/R). These are highlighted in a review by Johannssen *et al*.[12]

Our previous work has shown diluting the QD surface sugar density that resulted in lower FRET ratio indicative of weaker binding.[13] In order to compensate for the loss of signal the next step is to use a new series of glycodendrimer like ligands to increase surface glycan density on QDs by using branched multivalent glycans attached to one LA surface anchoring group. The sugar ligand series designed would still contain the same functional segments as in **Chapter 2**, an anchor, hydrophilic segment and functional group. Copper click chemistry will be used to create the smaller triazole, less sterically hindered than the cyclooctyne; previously used for creating the more densely packed surfaces. An example of the branched ligand to increase sugar density has been done by Ribeiro-Viana *et al.*[14] The QDs schematic design is outlined in **Figure 3.1.2** highlighting the different anchor to glycan ratios as well as the designs for the ligand series.

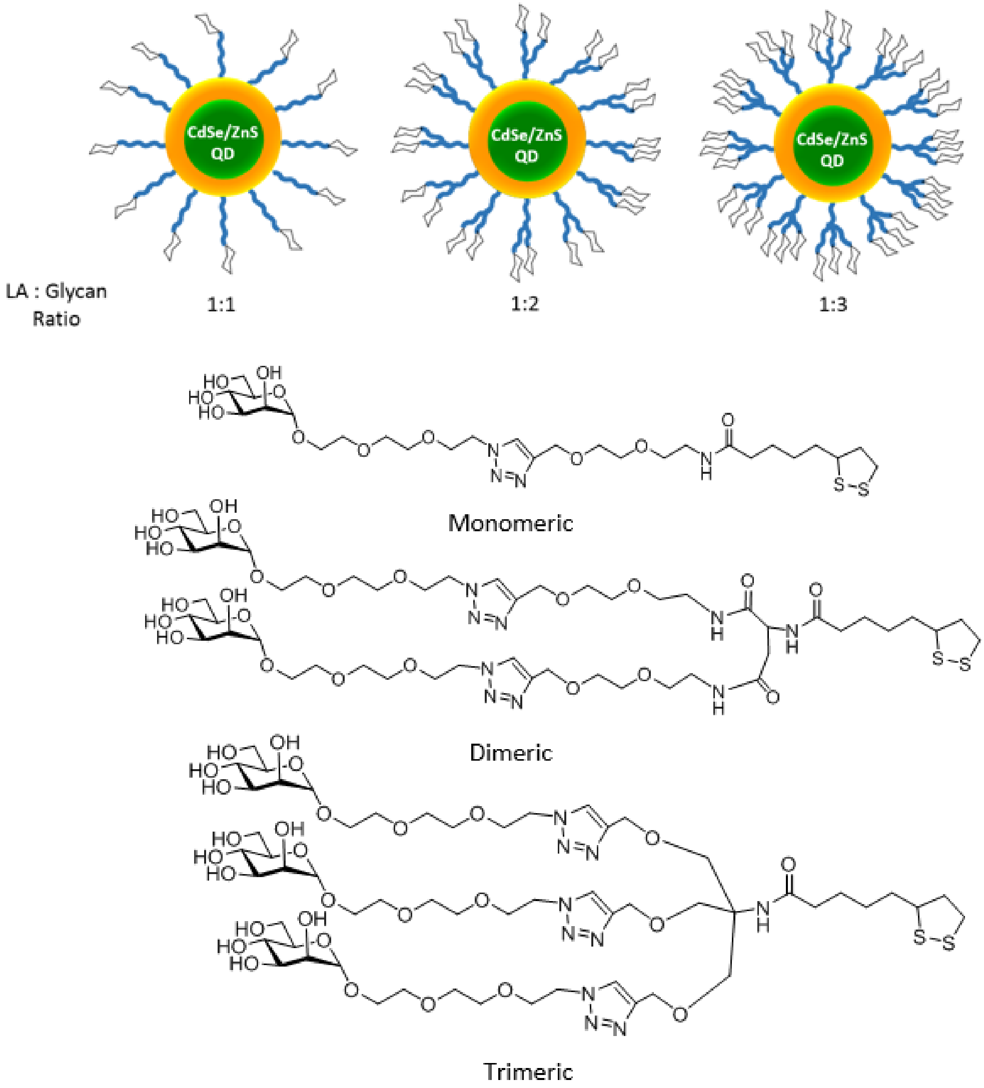

Figure 3.1.2: A schematic of the QDs used to investigate the effects of increasing glycan density on DC-SIGN/R binding by increasing the number of glycans conjugated to each LA anchor group using a lipoic acid, LA, to glycan ratio present in the specially designed ligand serious ranging from 1:1 to 1:3. The ligand series for the monosaccharide mannose is also shown to show how the number of glycans is increased.

3.2 Polyvalent Quantum Dot-Mannose Design

3.2.1 Ligand Exchange with QDs

The ligands were deprotonated for ligand exchange in the same way as before, using NaOH and added to commercially available hydrophobic gradient alloyed CdSe/ZnS core-shell QDs (λ_{em} 560 nm) using a ligand: QD molar ratio of 2000:1 in a homogenous solution of ($CHC_3/MeOH/H_2O$). Full experimental details are available in **Chapter 5. Figure 3.2.1** below shows the chelation of the di-thiol functional group of the ligands to the QD surface. The commercial QDs have an octadecylamine (ODA) coated surface, making them only dispersible in non-polar organic solvent and not suitable for biomedical applications. The ligands are replaced to make the QDs water dispersible through ligand exchange.

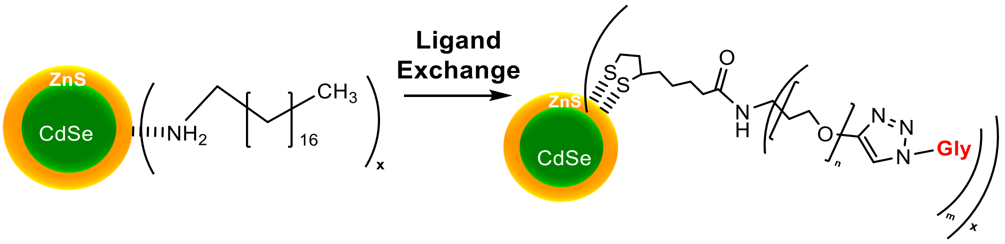

Figure 3.2.1: The ligand exchange reaction undertaken with octadecylamine (ODA) stabilized QDs by glycan ligands [LA-(EG_n-Glycan)$_m$ (where n = 1 or 2, m= 1, 2 and 3 and Glycan = α-Man and Man-α-1,2-Man)].

The concentration of the hydrophilic QDs dissolved in water can be calculated using UV-Vis absorption and the Beer-Lambert Law. The absorbance, A, was obtained using the QD absorption peak maxima at 536 nm for the QD (λ_{em} 560 nm) and an extinction coefficient, ε, of 1.2 x 10^5 M^{-1} cm^{-1} to calculate the concentration.

3.3 QD-(EG_n-Man)$_m$ Characterization

3.3.1 Hydrodynamic Size Determination of QDs

The hydrodynamic sizes, D_h, of freshly prepared QD-glcyan conjugates were determined by DLS. The resulting volume population versus hydrodynamic size graphs for each of the QDs before and after ligand exchange in H_2O are given in **Figure 3.3.1**. A full summary of the of the D_h values for each of the QD conjugates and the relevant fitting parameters can be seen in **Table 3.3.1**. a small change in size is expected for the QDs after they have undergone ligand exchange. One key difference to be noted is that using these commercial QDs in comparison to those used in Chapter 2 their initial size is larger so even though LA-EG_2-Mannose is smaller in length then LA-EG_3-Mannose the overall size is still larger due to the QDs core-shell size.

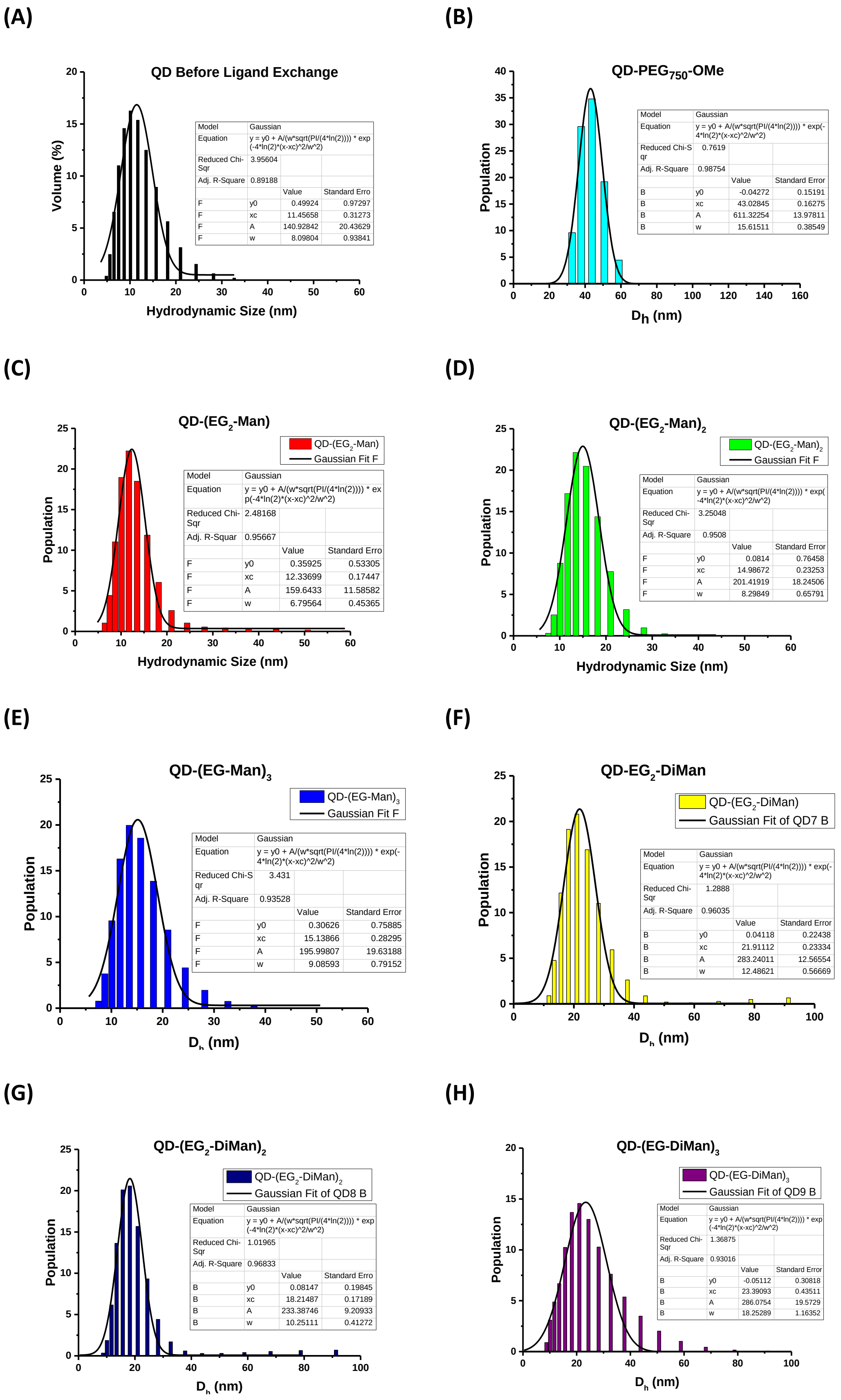

Model	Gaussian		
Equation	y = y0 + A/(w*sqrt(PI/(4*ln(2)))) * exp(-4*ln(2)*(x-xc)^2/w^2)		
Reduced Chi-Sqr	3.95604		
Adj. R-Square	0.89188		
		Value	Standard Erro
F	y0	0.49924	0.97297
F	xc	11.45658	0.31273
F	A	140.92842	20.43629
F	w	8.09804	0.93841

Model	Gaussian		
Equation	y = y0 + A/(w*sqrt(PI/(4*ln(2)))) * exp(-4*ln(2)*(x-xc)^2/w^2)		
Reduced Chi-Sqr	0.7619		
Adj. R-Square	0.98754		
		Value	Standard Error
B	y0	-0.04272	0.15191
B	xc	43.02845	0.16275
B	A	611.32254	13.97811
B	w	15.61511	0.38549

Model	Gaussian		
Equation	y = y0 + A/(w*sqrt(PI/(4*ln(2)))) * exp(-4*ln(2)*(x-xc)^2/w^2)		
Reduced Chi-Sqr	2.48168		
Adj. R-Squar	0.95667		
		Value	Standard Erro
F	y0	0.35925	0.53305
F	xc	12.33699	0.17447
F	A	159.6433	11.58582
F	w	6.79564	0.45365

Model	Gaussian		
Equation	y = y0 + A/(w*sqrt(PI/(4*ln(2)))) * exp(-4*ln(2)*(x-xc)^2/w^2)		
Reduced Chi-Sqr	3.25048		
Adj. R-Square	0.9508		
		Value	Standard Error
F	y0	0.0814	0.76458
F	xc	14.98672	0.23253
F	A	201.41919	18.24506
F	w	8.29849	0.65791

Model	Gaussian		
Equation	y = y0 + A/(w*sqrt(PI/(4*ln(2)))) * exp(-4*ln(2)*(x-xc)^2/w^2)		
Reduced Chi-Sqr	3.431		
Adj. R-Square	0.93528		
		Value	Standard Error
F	y0	0.30626	0.75885
F	xc	15.13866	0.28295
F	A	195.99807	19.63188
F	w	9.08593	0.79152

Model	Gaussian		
Equation	y = y0 + A/(w*sqrt(PI/(4*ln(2)))) * exp(-4*ln(2)*(x-xc)^2/w^2)		
Reduced Chi-Sqr	1.2888		
Adj. R-Square	0.96035		
		Value	Standard Error
B	y0	0.04118	0.22438
B	xc	21.91112	0.23334
B	A	283.24011	12.56554
B	w	12.48621	0.56669

Model	Gaussian		
Equation	y = y0 + A/(w*sqrt(PI/(4*ln(2)))) * exp(-4*ln(2)*(x-xc)^2/w^2)		
Reduced Chi-Sqr	1.01965		
Adj. R-Square	0.96833		
		Value	Standard Erro
B	y0	0.08147	0.19845
B	xc	18.21487	0.17189
B	A	233.38746	9.20933
B	w	10.25111	0.41272

Model	Gaussian		
Equation	y = y0 + A/(w*sqrt(PI/(4*ln(2)))) * exp(-4*ln(2)*(x-xc)^2/w^2)		
Reduced Chi-Sqr	1.36875		
Adj. R-Square	0.93016		
		Value	Standard Error
B	y0	-0.05112	0.30818
B	xc	23.39093	0.43511
B	A	286.0754	19.5729
B	w	18.25289	1.16352

Figure 3.3.1: Histogram of the hydrodynamic diameters of **(A)** QDs before ligand exchange, **(B)** QD-PEG_{750}-OMe, **(C)** QD-EG_2-Man, **(D)** QD-$(EG_2\text{-Man})_2$, **(E)** QD-$(EG\text{-Man})_3$, **(F)** QD-EG_2.DiMan, **(G)** QD-$(EG_2\text{-DiMan})_2$ and finally **(H)** QD-$(EG\text{-DiMan})_3$.

Table 3.3.1: A table to show a summary of the hydrodynamic sizes of the QDs before and after ligand exchange as determined by Dynamic Light Scattering, DLS.

Surface Ligand	Hydrodynamic Diameter (nm)	FWHM (nm)
ODA	11.5 ± 0.3	8.1 ± 0.9
DHLA-EG$_2$-Man	12.3 ± 0.2	6.8 ± 0.5
DHLA-(EG$_2$-Man)$_2$	15.0 ± 0.2	8.3 ± 0.7
DHLA-(EG-Man)$_3$	15.1 ± 0.3	9.1 ± 0.8
DHLA-EG$_2$-DiMan	21.9 ± 0.2	12.5 ± 0.6
DHLA-(EG$_2$-DiMan)$_2$	18.2 ± 0.2	10.3 ± 0.4
DHLA-(EG-DiMan)$_3$	23.4 ± 0.4	18.3 ± 1.2
DHLA-PEG$_{750}$-OMe	43.0 ± 0.2	15.6 ± 0.4

The change in size of the quantum dots suggests that ligand exchange has been carried out successfully along with the stability in water. A key observation is the difference in the size of the particles between the monosaccharide series and the disaccharide series, this may come from the fact that the disaccharide ligands are much bulkier, creating a larger hydrodynamic size in solution. The large size of the control QD suggests minor of aggregation or clustering of particles is occurring which may be due to the difference in ligand exchange methods. Although a larger hydrodynamic size is expected for the control QD due to the much longer polyethylene glycol units of the ligands and hence extra contributions from the Flory radius which calculates the size of the polymeric chain when its stretched out at its longest, (**Eq.19**).[15]

$$F = \alpha n \frac{3}{5} \qquad \textbf{(Eq. 19)}$$

Where F is the Flory radius, α is the length of one monomer in Angstroms (α = 3.5 Å for PEG) and n is the number of repeating units (~ 17 here). So it would have an extra contribution of 35.7 Å for PEG$_{750}$.

3.3.2 Quantum Yields

QY, defined earlier, were calculated for the QD-(EG$_n$-Man$_s$)$_m$ against the same reference standard, Rhodamine 6G (QY = 95%, λ_{ex}= 480 nm). As before the integrated fluorescence spectra over multiple concentrations against absorbance for the QDs and the reference are measured. Initial UV/Vis measurements are done at a higher concentration to give more reliable results due to the linear relationship between absorbance and concentration. The absorption spectra of the QDs and reference are shown in **Figure 3.3.2** and **Figure 3.3.3** respectively. Fluorescence emission spectra can be found within the **Appendix**. The QY is then calculated using (**Eq. 9**), defined previously, **Chapter 2**, for each QD in this chapter. The resulting integrated fluorescence intensity versus absorption plots are shown in **Figure 3.3.4**.

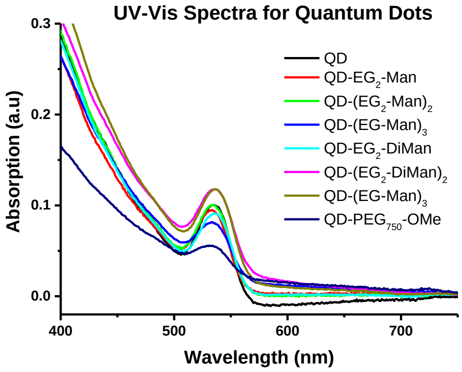

Figure 3.3.2: UV-Vis (background corrected) spectra of the QDs before ligand (**black**) exchange and after ligand exchange with the functional ligands.

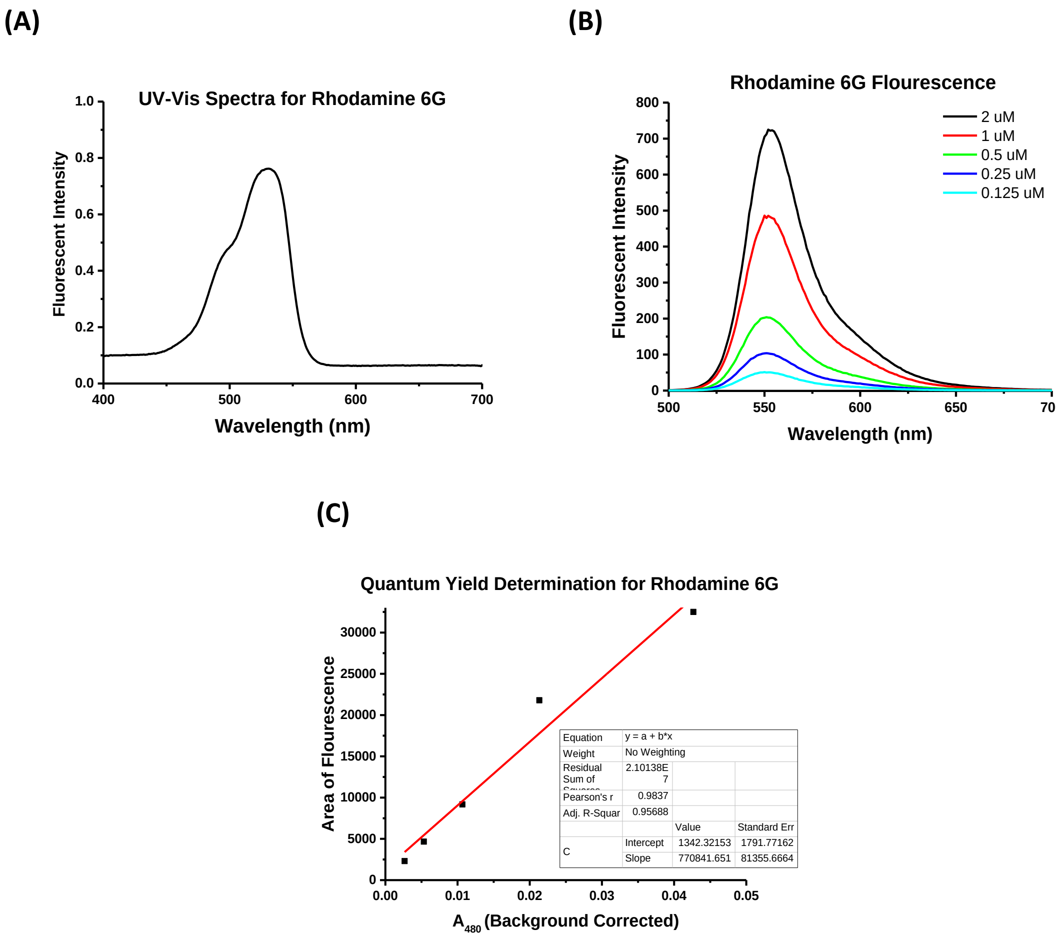

Figure 3.3.3: **(A)** UV-Vis spectra for Rhodamine 6G sample, **(B)** Fluorescence spectra for a range of concentrations between 0.125 - 2 μM at λ_{Ex} = 480 nm and **(C)** a graph to show the plot of fluorescence area intensity against the background corrected Absorbance (λ = 480). The absorbance is calculated using the Beer-Lambert Law using an extinction coefficient, ε, of 17, 129 cm^{-1} M^{-1}.

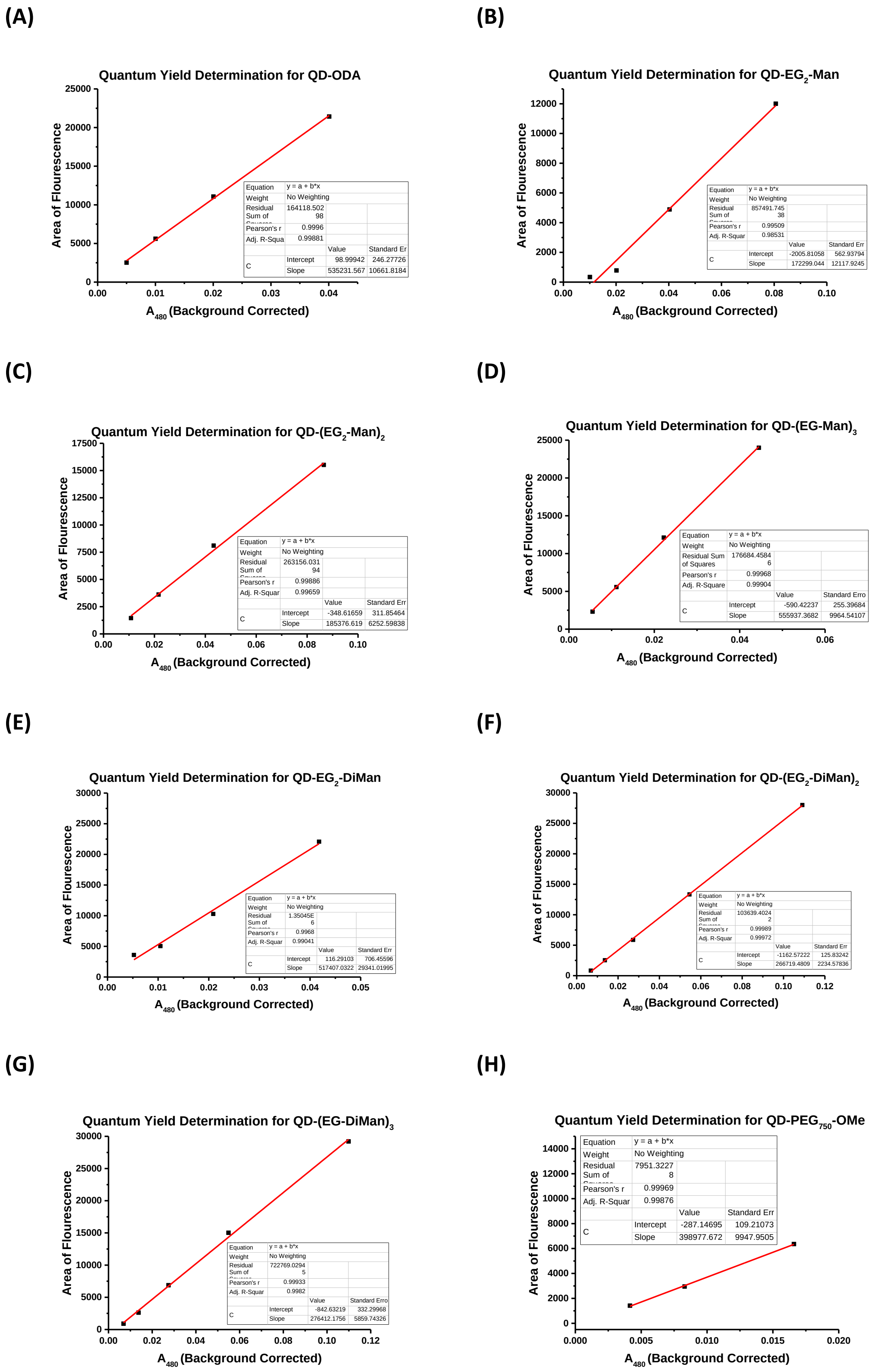

(A)

Equation	y = a + b*x		
Weight	No Weighting		
Residual Sum of	164118.50298		
Pearson's r	0.9996		
Adj. R-Squa	0.99881		
		Value	Standard Er
C	Intercept	98.99942	246.27726
	Slope	535231.567	10661.8184

(B)

Equation	y = a + b*x		
Weight	No Weighting		
Residual Sum of	857491.74538		
Pearson's r	0.99509		
Adj. R-Squar	0.98531		
		Value	Standard Err
C	Intercept	-2005.81058	562.93794
	Slope	172299.044	12117.9245

(C)

Equation	y = a + b*x		
Weight	No Weighting		
Residual Sum of	263156.03194		
Pearson's r	0.99886		
Adj. R-Squar	0.99659		
		Value	Standard Err
C	Intercept	-348.61659	311.85464
	Slope	185376.619	6252.59838

(D)

Equation	y = a + b*x		
Weight	No Weighting		
Residual Sum of Squares	176684.45846		
Pearson's r	0.99968		
Adj. R-Square	0.99904		
		Value	Standard Erro
C	Intercept	-590.42237	255.39684
	Slope	555937.3682	9964.54107

(E)

Equation	y = a + b*x		
Weight	No Weighting		
Residual Sum of	1.35045E6		
Pearson's r	0.9968		
Adj. R-Squar	0.99041		
		Value	Standard Err
C	Intercept	116.29103	706.45596
	Slope	517407.0322	29341.01995

(F)

Equation	y = a + b*x		
Weight	No Weighting		
Residual Sum of	103639.40242		
Pearson's r	0.99989		
Adj. R-Squar	0.99972		
		Value	Standard Err
C	Intercept	-1162.57222	125.83242
	Slope	266719.4809	2234.57836

(G)

Equation	y = a + b*x		
Weight	No Weighting		
Residual Sum of	722769.02945		
Pearson's r	0.99933		
Adj. R-Squar	0.9982		
		Value	Standard Erro
C	Intercept	-842.63219	332.29968
	Slope	276412.1756	5859.74326

(H)

Equation	y = a + b*x		
Weight	No Weighting		
Residual Sum of	7951.32278		
Pearson's r	0.99969		
Adj. R-Squar	0.99876		
		Value	Standard Err
C	Intercept	-287.14695	109.21073
	Slope	398977.672	9947.9505

Figure 3.3.4: Fluorescence area verses absorption linear plots to determine the quantum yield for the QDs.

Table 3.3.2 shows a summary of the results. The new alloyed commercial QDs used in this work were already brighter in comparison to ones used previously before ligand exchange (**Chapter 2**), it is therefore expected that the quantum yield would be higher for these ligands exchanged QDs. This is shown in all the cases as the QY is either maintained or slightly weakened by the ligand exchange reaction. Usually the longer the reaction time the weaker the QY becomes. As the maximum QY recorded for the QD-saccharides in Chapter 2 was 28% in comparison to the maximum of 68% in this case. This new batch of commercial QDs was actually purchased for their higher QY values for more efficient results for the FRET measurements.

Table 3.3.2: A table summarising the Quantum Yields for the Quantum Dots before and after ligand exchange.

Surface Ligand	Quantum Yield (%)
ODA	66.0 ± 2.0
DHLA-EG$_2$-Man	21.2 ± 7.0
DHLA-(EG$_2$-Man)$_2$	22.9 ± 3.4
DHLA-(EG-Man)$_3$	68.5 ± 1.8
DHLA-EG$_2$-DiMan	63.7 ± 5.7
DHLA-(EG$_2$-DiMan)$_2$	32.8 ± 0.8
DHLA-(EG-DiMan)$_3$	34.0 ± 2.1
DHLA-PEG$_{750}$-OMe	49.1 ± 2.5

3.3.3 Transmission Electron Microscopy and Scanning Transmission Electron Microscopy

Scanning transmission electron microscopy, STEM, was used to confirm the core size of the QDs to be 3.5 nm with further confirmation of the stability of singular particles. **Figure 3.3.5** shows the STEM images of the QDs that have been cap-exchanged with the LA-EG$_2$-Man. Energy-dispersive x-ray spectroscopy, EDX was used to determine particle composition and the resulting spectra show the presence of the Cadmium, Selenium, Zinc and Sulphur, confirming that they are indeed the QDs and then the Copper and Silica of the sample grid. Carbon and Oxygen are also present from the surface ligands as well as the grid. Further TEM images of the QDs after cap-exchange with LA-EG$_3$-DiMan show that they exist as individual particles despite a much bigger hydrodynamic size. The QD core shell size remains about the same, 3.5 nm. **Figure 3.3.6** below shows the image of the cluster of QDs.

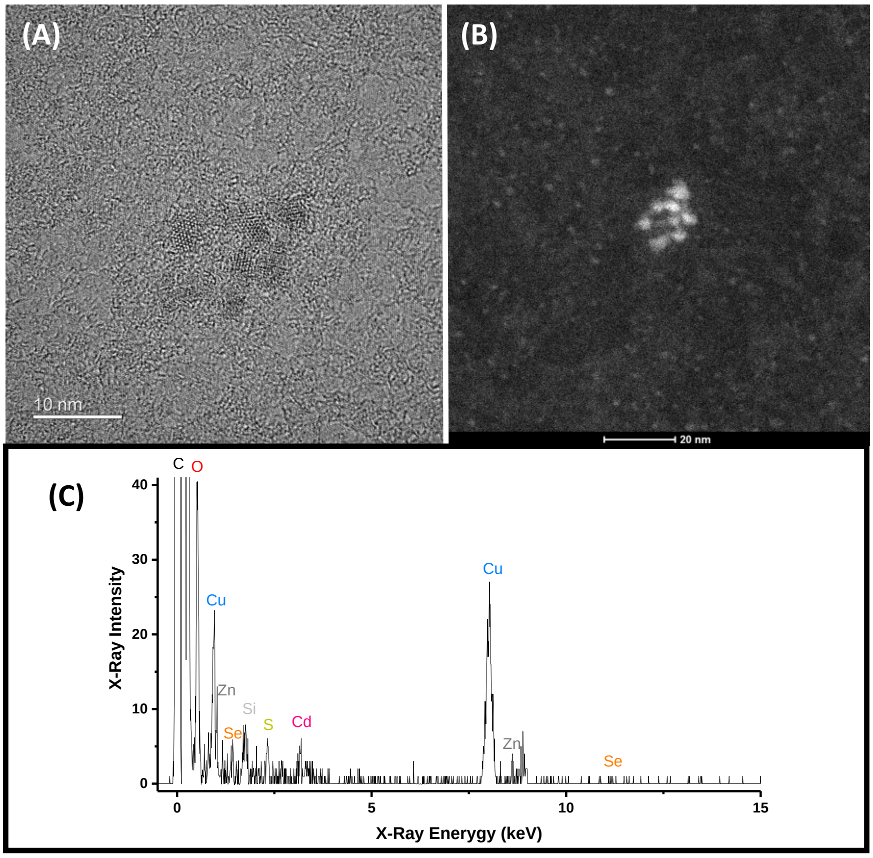

Figure 3.3.5: (A) Transmission Electron Microscopy image showing a cluster of QD-EG$_2$-Man with (B) showing a Scanning Transmission Electron Microscopy (STEM) image of the same area. (C) An Energy Disperse X-Ray (EDX) spectra taken of the cluster of QD-EG$_2$-Man confirming the elemental composition to be as for the type of QD's used.

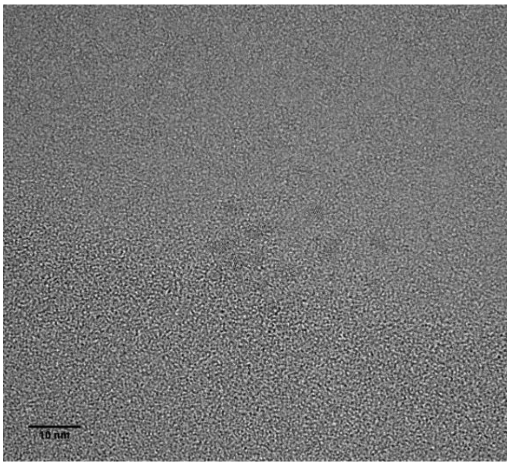

Figure 3.3.6: Transmission Electron Microscopy image showing a cluster of QD-EG$_2$-DiMan. Scale bar 10 nm.

3.4 FRET Analysis for QD-Glycan-DC-SIGN Binding

To determine the apparent binding affinity, K_d, for the multivalent interactions between the QD-glycans and DC-SIGN, fluorescence spectra have been recorded across a range of concentrations using a fixed ratio of 1: 1 for QD: DC-SIGN. The QD and DC-SIGN concentrations were increased simultaneously, as described in **Chapter 2**, in order to maintain the fixed ratio. The samples were made up as before in binding buffer containing 1 mg/ mL bovine serum albumin, BSA, to reduce QD and Protein surface absorption as well as the addition of the short cysteine- histidine$_6$. Dye direct excitation background corrected fluorescence spectra reveal clear emission peaks for the QD (λ_{em} = 551 nm) and the labelled protein (λ_{em} = 626 nm) as seen in previous work. Fluorescence spectra have been shown for both QD-EG$_2$-Man (**Figure 3.4.1**) and QD-EG$_2$-DiMan (**Figure 3.4.2**) with the rest of the QDs data in the **Appendix**.

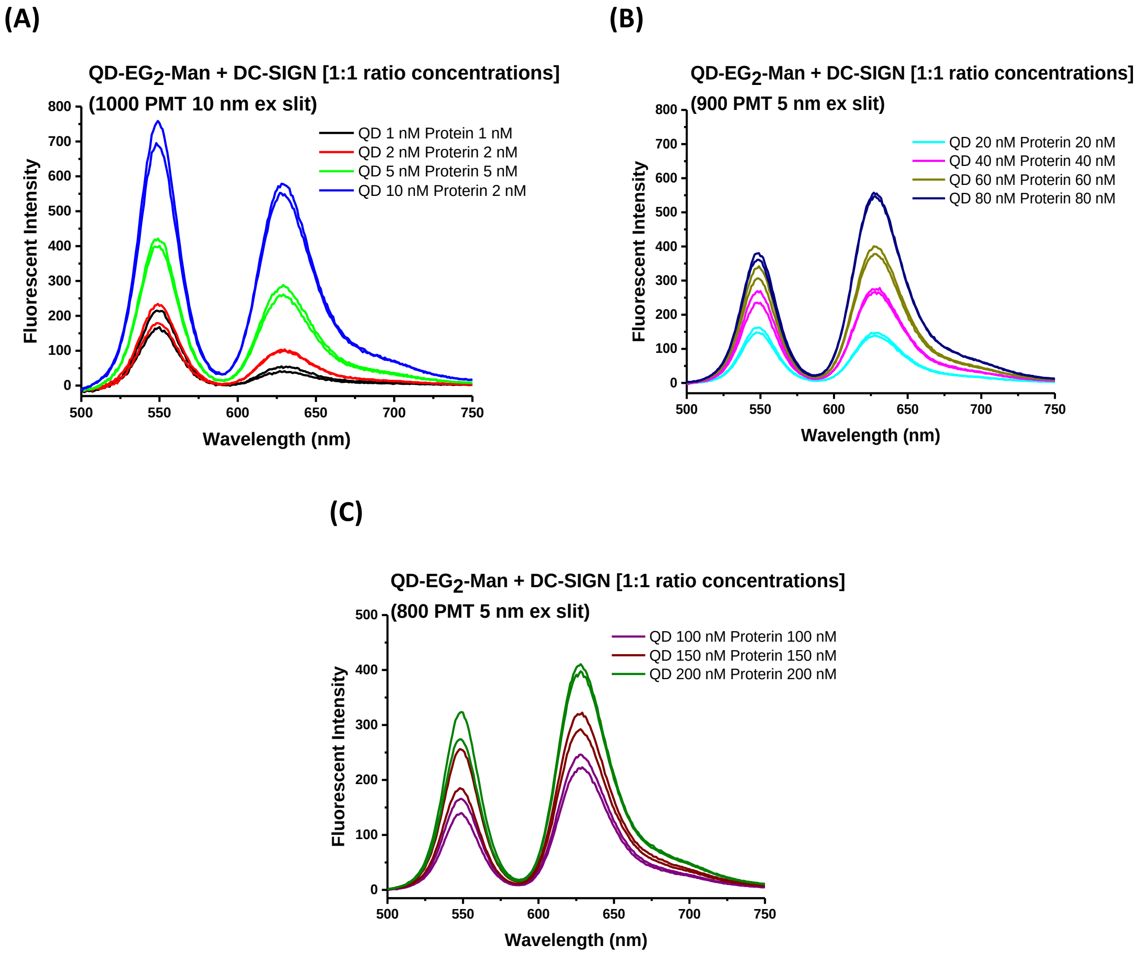

Figure 3.4.1: Background corrected fluorescence spectra QD-EG$_2$-Man + DC-SIGN at different protein concentrations using a QD molar ratio of 1:1. (**A**) Low concentrations of QDs (1 – 10 nM) and DC-SIGN (1 – 10 nM) (**B**) Intermediate concentrations of QDs (20 – 80 nM) and DC-SIGN (20 – 80 nM) and (**C**) High concentrations of QDs (100 – 200 nM) and DC-SIGN (100 – 200 nM).

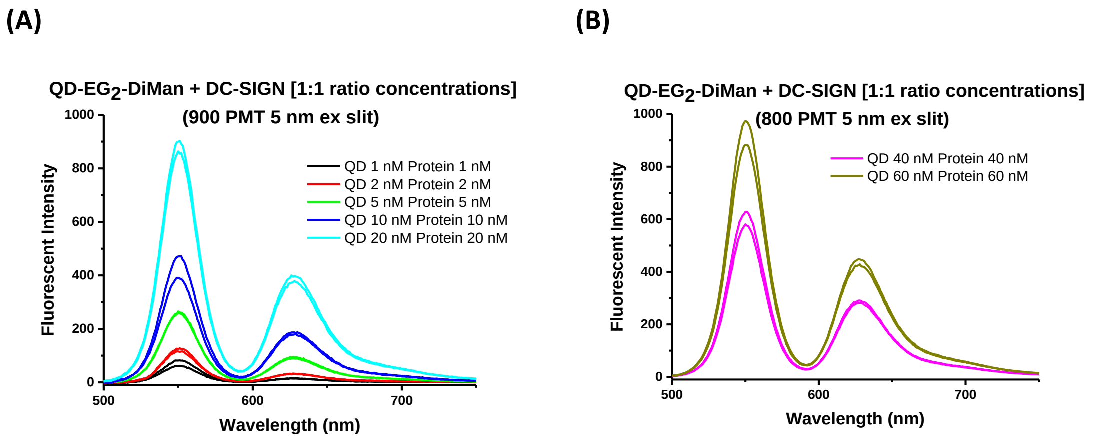

Figure 3.4.2: Background corrected fluorescence spectra obtained for determination of the apparent K_D for QD-EG_2-Man + DC-SIGN using a protein QD molar ratio of 1:1. (**A**) Low concentrations of QDs (1 – 20 nM) and DC-SIGN (1 – 20 nM) and (**C**) High concentrations of QDs (40 – 60 nM) and DC-SIGN (40 – 60 nM).

A control QD sample was then made to show that any energy transfer that was exhibited was coming from the binding interaction between the sugar and the protein. This was done by performing the ligand exchange with an inert ligand that is not known to bind to DC-SIGN. The ligand used was a PEGylated ligand, LA-PEG_{750}-OMe, as these should not bind to the protein. In this case if the proteins are not bound to the QD they will be not in close enough proximity to the QD for energy transfer to occur resulting in the spectra only showing one emission maxima from the QD (λ_{em} = 551 nm). The resulting spectra for QD-PEG_{750}-OMe with the labelled DC-SIGN is shown, **Figure 3.4.3**. The samples were prepared in exactly the same way as that for the sugar QDs. The resulting direct excitation background corrected fluorescence spectra only shows one emission maxima so this suggests highly that the labelled protein dye emission comes from the energy transfer as a results of the sugar protein interaction.

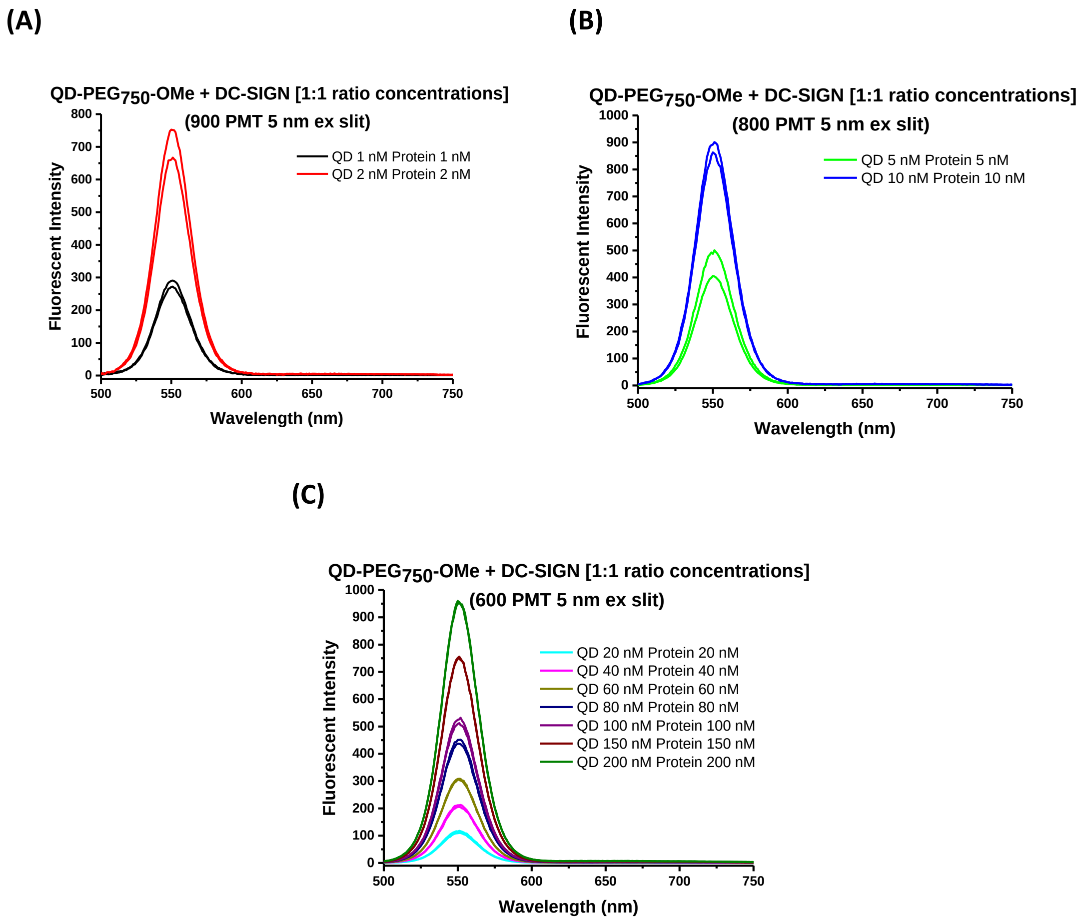

Figure 3.4.3: Background corrected fluorescence spectra for QD-PEG$_{750}$-OMe + DC-SIGN mixture (**A**) Low concentrations of QDs (1 – 2 nM) and DC-SIGN (1 – 2 nM), intermediate concentrations of QDs (5 – 10 nM) and DC-SIGN (5 – 10 nM) (**C**) High concentrations of QDs (20 – 200 nM) and DC-SIGN (20 – 200 nM). No apparent dye FRET signal is observed.

3.4.1 Ratiometric Quantification of QD-DC-SIGN Binding Affinity

The apparent K_d values have then been calculated from the apparent FRET ratio of the two intensity maxima's, I_{626}/I_{551}. The resulting titration curves for each of the QDs bound to DC-SIGN can be seen in **Figure 3.4.4**. The curves are fitted by a non-linear Hill equation function as done for the QD-Protein accurate K_d determination in the last chapter. The calculated binding affinity constants are summarised in **Table 3.4.1** along with the different fitting parameters for both the glycan-QDs and the control.

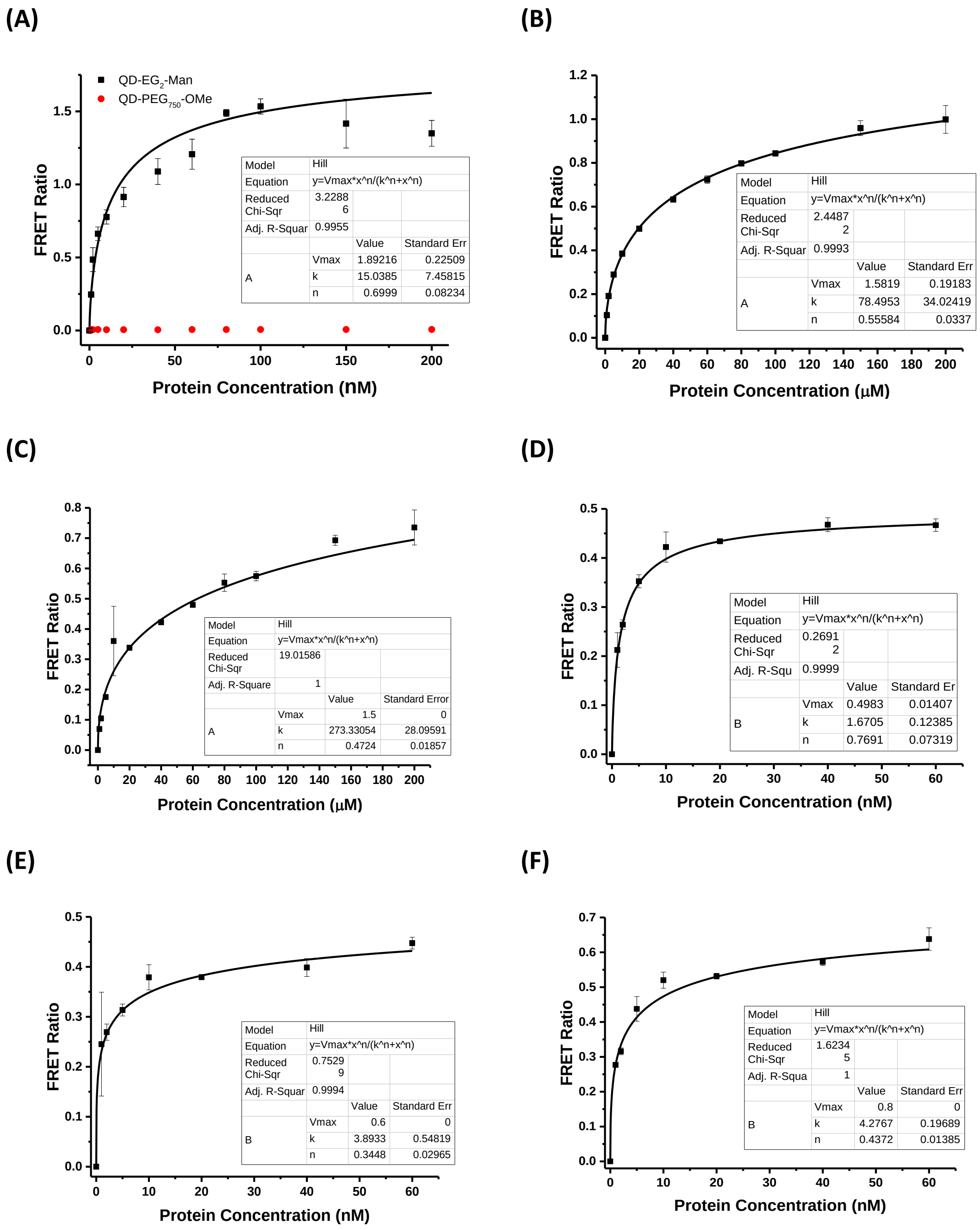

Figure 3.4.4: FRET intensity ratio (I_{626}/I_{551}) curves as a function of the DC-SIGN concentrations. (**A**) and (**D**) QD-EG$_2$-Man^s + DC-SIGN, (**B**) and (**E**) QD-(EG$_2$-Man^s)$_2$ + DC-SIGN and (**C**) and (**F**) QD-(EG-Man^s)$_3$ + DC-SIGN (where s = 1 and 2). Fitted using the Hill Equation.

Table 3.4.1: Summary of the fitting parameters for calculating the apparent K_d using the Hill Equation to fit QD-(EG$_n$-Man)$_m$-DC-SIGN binding curves (where n= 1 or 2 and m= 1, 2 and 3) (**Figure 3.4.4**).

QD + Protein	R_{max}	Apparent K_d (nM)	n	R^2
QD-EG$_2$-Man + DC-SIGN	1.9 ± 0.2	15 ± 7	0.70 ± 0.08	0.9956
QD-(EG$_2$-Man)$_2$ + DC-SIGN	1.6 ± 0.2	78 ± 34	0.56 ± 0.03	0.9993
QD-(EG-Man)$_3$ + DC-SIGN	1.5 ± 0.0	273 ± 28	0.47 ± 0.02	1
QD-EG$_2$-DiMan + DC-SIGN	0.5 ± 0.0	1.7 ± 0.1	0.77 ± 0.07	0.9999
QD-(EG$_2$-DiMan)$_2$ + DC-SIGN	0.6 ± 0.0	3.9 ± 0.5	0.34 ± 0.03	0.9994
QD-(EG-DiMan)$_3$ + DC-SIGN	0.8 ± 0.0	4.3 ± 0.2	0.44 ± 0.01	1

The results give two notable findings. First using dendritic style ligands to increase glycan to LA ratio decreases the binding affinity with DC-SIGN. This may suggest that the use of dendritic ligands may not increase the overall glycan density due to steric hindrance caused by the packing of glycan moieties around the diameter of the QD. Secondly, we see further confirmation of the stronger binding affinity that DC-SIGN has for the dimannose.

3.5 FRET Analysis for QD-Glycan-DC-SIGNR Binding

As carried out previously, fluorescence spectra were recorded across a range of concentrations using a fixed ratio of 1: 10 for QD: DC-SIGNR, as used previously in **Chapter 2**. The samples were prepared in the same way as above for the QD-DC-SIGN investigations. **Figure 3.5.1** and **Figure 3.5.2** shows the fluorescence spectra for QD-EG$_2$-Man and QD-EG$_2$-DiMan receptively. The rest of the data can be found in the **Appendix.** As high ratios of mannose are required for binding with DC-SIGNR a reduced amount of points are shown here due to the low concentration level as ideally no binding should be seen.

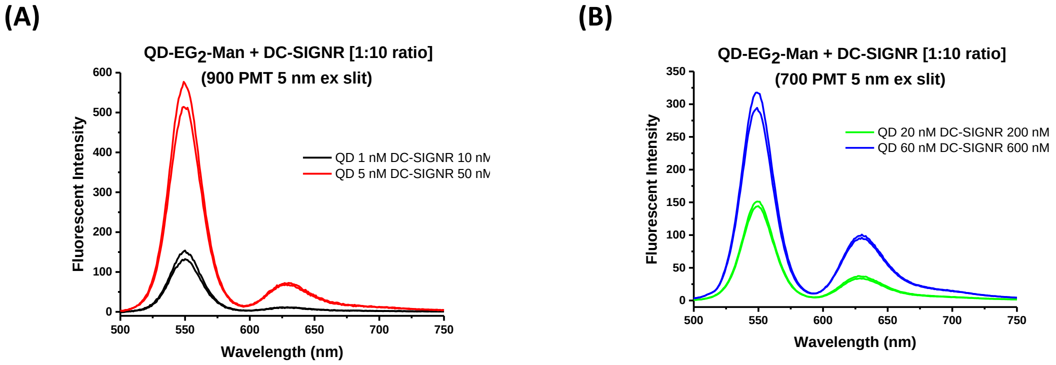

Figure 3.5.1: Background corrected fluorescence spectra for QD-EG$_2$-Man + DC-SIGNR mixture at a fixed protein: QD ratio of 10:1. (**A**) Low concentrations of QDs (1 – 5 nM) and DC-SIGNR (10 – 50 nM) and (**B**) High of QDs (20 – 60 nM) and DC-SIGNR (200 – 600 nM).

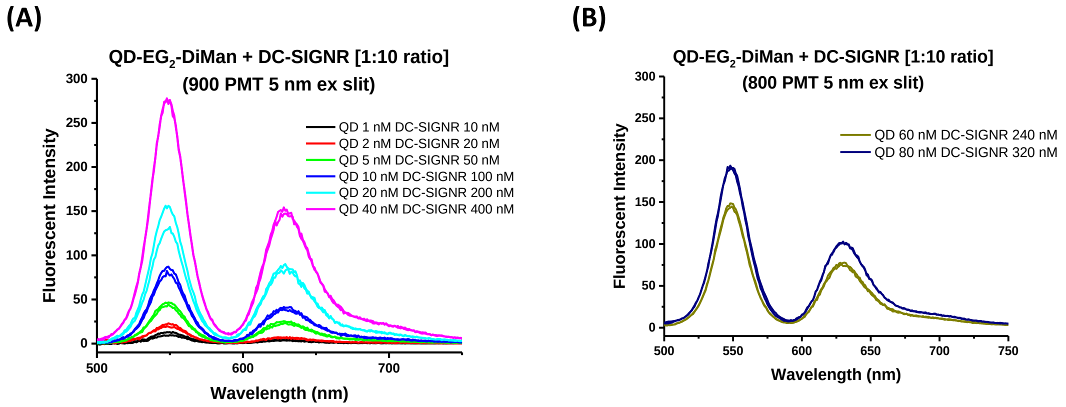

Figure 3.5.2: Background corrected fluorescence spectra for QD-EG2-DiMan + DC-SIGNR mixture at a fixed protein: QD ratio of 10:1. (A) Low concentrations of QDs (1 – 40 nM) and DC-SIGNR (10 – 400 nM) and (B) High concentrations of QDs (60 – 80 nM) and DC-SIGNR (600 – 800 nM).

The same control sample run as before with labelled DC-SIGN was run with labelled DC-SIGNR again using the same parameters as the QD-glycan experiments. As before we only see one emission peak suggesting the same that the dye emission is a results of the specific sugar-DC-SIGNR interaction. The resulting dye direct excitation background corrected fluorescence spectra for QD-PEG$_{750}$-OMe with DC-SIGNR is shown in **Figure 3.5.3**.

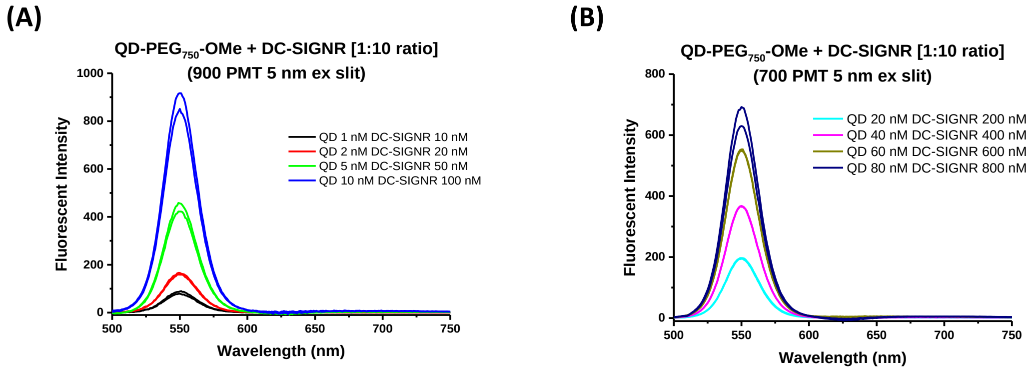

Figure 3.5.3: Background corrected fluorescence spectra for QD-PEG$_{750}$-OMe + DC-SIGNR mixture at a fixed protein: QD ratio of 10:1. (**A**) Low concentrations of QDs (1 – 10 nM) and DC-SIGNR (10 – 100 nM) and (**B**) High concentrations of QDs (20 – 80 nM) and DC-SIGNR (200 – 800 nM)

3.5.1 Ratiometric Quantification of QD-DC-SIGNR Binding Affinity

The resulting titration curves for each of the QDs bound to DC-SIGNR can be seen in **Figure 3.5.4**. The binding affinity constants are summarised in **Table 3.5.1** along with the fitting parameters. This was done using the same methods as that seen previously in this chapter as well as in the last chapter.

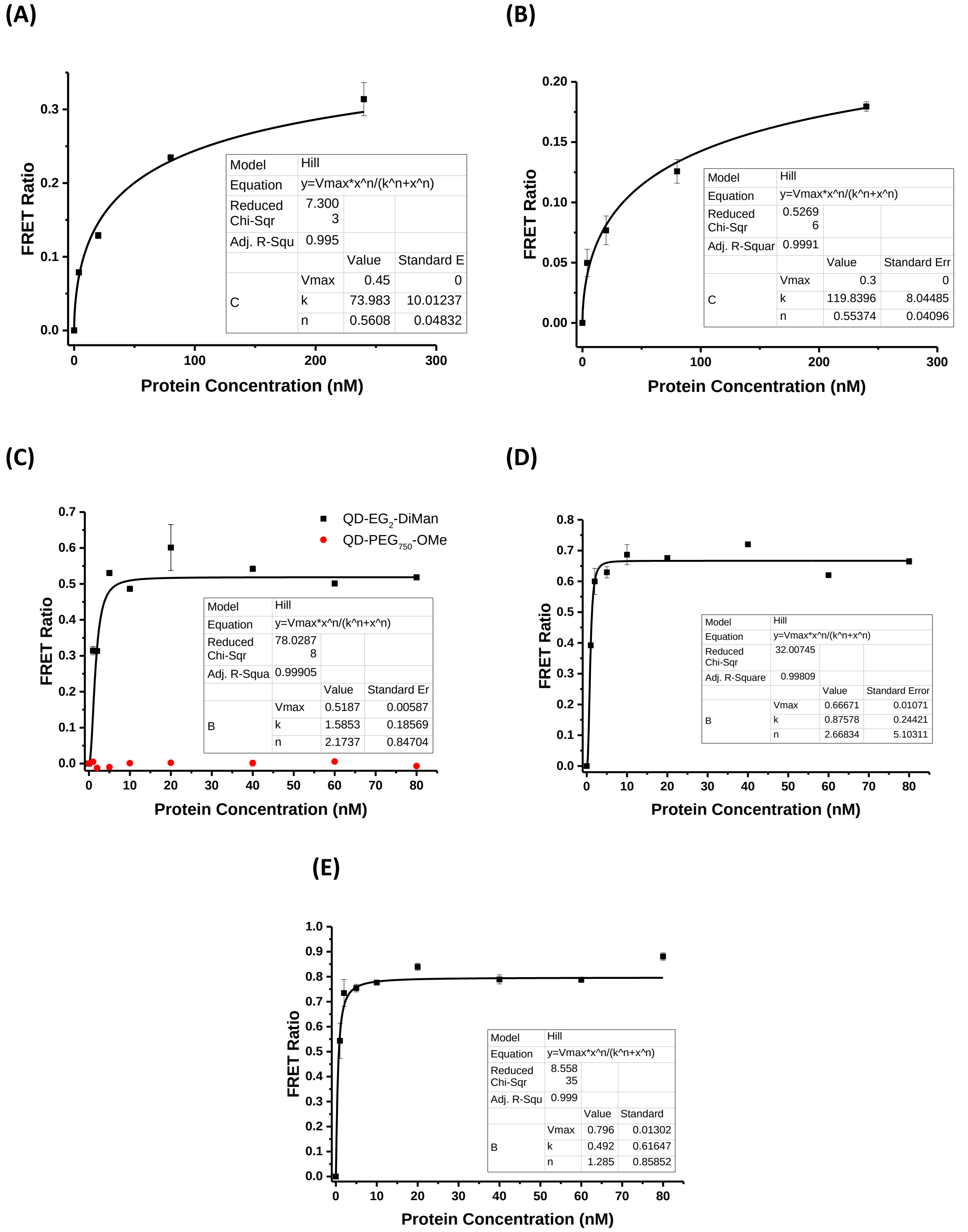

Figure 3.5.4: FRET intensity ratio (I_{626}/I_{554}) a function of the QD: Protein molar ratio 1:4 for DC-SIGNR. (**A**) and (**C**) QD-EG$_2$-Man^s + DC-SIGNR, (**B**) and (**D**) QD-(EG$_2$-Man^s)$_2$ + DC-SIGNR and (**F**) QD-(EG-Man^s)$_3$ + DC-SIGNR (where s = 1 and 2). Fitted using the Hill Equation.

The results show an opposite trend to that found for the QD-DC-SIGN for the disaccharide series in that when you use the trimeric glycan ligand you get an increase in binding affinity over the monomeric ligand. This could be due to the orientations of the CRDs found within DC-SIGNR fitting around the dendritic style of glycan layout of the ligands. There is also a significant enhancement (around 40 times) of the binding affinity with this ligand series compared to that of the synthesised using strain promoted click chemistry as the K_d decreases from 62 ± 8 to 1.59 ± 0.6 nM for QD-EG_3-DiMan and QD-EG_2-DiMan, respectively. Unfortunately issues were also found with the less hydrophilic nature of the cap- exchanged QD-$(EG\text{-}Man)_3$ which often resulted in aggregation in water so some experiments could not be performed. The cap-exchange was attempted with various QD: ligand ratios and also performed removing the TCEP after reduction without significant improvement. The resulting QDs were also found to be aggregated after increasing the time used for the ligand exchange reaction. The results show the importance of the EG linker length on the water solubility of the cap-exchanged QDs. In contrast, QD-$(EG\text{-}DiMan)_3$ was easily formed as the more hydrophilic nature of the disaccharide can compensate the loss of the EG linker group. Further optimisation of cap-exchange conditions are necessary to make it robust for QD-$(EG\text{-}Man)_3$.

Table 3.5.1: Summary of the fitting parameters for calculating the apparent K_d using the Hill Equation to fit QD-$(EG_n\text{-}Man^s)_m$-DC-SIGNR binding curves (where n= 1 or 2 and m= 1, 2 and 3) (**Figure 3.5.4**).

QD + Protein	R_{max}	Apparent K_d (nM)	n	R^2
QD-EG_2-Man + DC-SIGNR	0.45 ± 0	74 ± 10	0.6 ± 0.04	0.9954
QD-$(EG_2\text{-}Man)_2$ + DC-SIGNR	0.3 ± 0	120 ± 8	0.6 ± 0.04	0.9991
QD-$(EG\text{-}Man)_3$ + DC-SIGNR	-	-	-	-
QD-EG_2-DiMan + DC-SIGNR	0.52 ± 0.01	1.59 ± 0.19	2.2 ± 0.8	0.9991
QD-$(EG_2\text{-}DiMan)_2$ + DC-SIGNR	0.67 ± 0.01	0.88 ± 0.24	2.7 ± 5.1	0.9981
QD-$(EG\text{-}DiMan)_3$ + DC-SIGNR	0.80 ± 0.01	0.49 ± 0.62	1.3 ± 0.8	0.9990

3.6 Mannose Competition Studies

To further confirm the proteins affinity for the QD-Glycans and the FRET signal was due to specific protein-glycan interactions, a competition study with free mannose was carried out. This is similar to the experimental procedure in **Chapter 2.6.2**, using fixed concentrations of QD and labelled protein (QD: protein ratio 1:1 for DC-SIGN and 1:10 for DC-SIGNR). As before if we see the mannose competing with the QD-glycan binding to the labelled protein then the FRET ratio will decrease. **Figure 3.6.1** shows the fluorescence spectra of the QD-Man competing against

DC-SIGN and **Figure 3.6.2** for QD-DiMan competing against DC-SIGNR. An increase of the QD fluorescence (λ = 551 nm) and a decrease of intensity of FRET signal (λ = 626 nm) is seen upon increasing mannose concentration, confirming effective competition of mannose with QD-DC-SIGN/R binding. This confirms that the FRET signal observed is due to the specific protein-sugar interaction. The results also suggest that the QD-DC-SIGN/R binding is much stronger than that of the mannose-DC-SIGN/R as major changes in FRET ratio are observed at high concentrations of mannose (> 1 mM). This is further confirmed by the high values of the K_i, **Figure 3.6.3**. This data were fitted using **Eq. 15**. These reactions were due to be carried out with the QD-(EG-Man)$_3$ + DC-SIGN but unfortunately these materials were aggregated when dissolved in water after ligand exchange and a new batch of the same QDs was no longer available commercially. As seen above in **Chapter 3.4.4**.

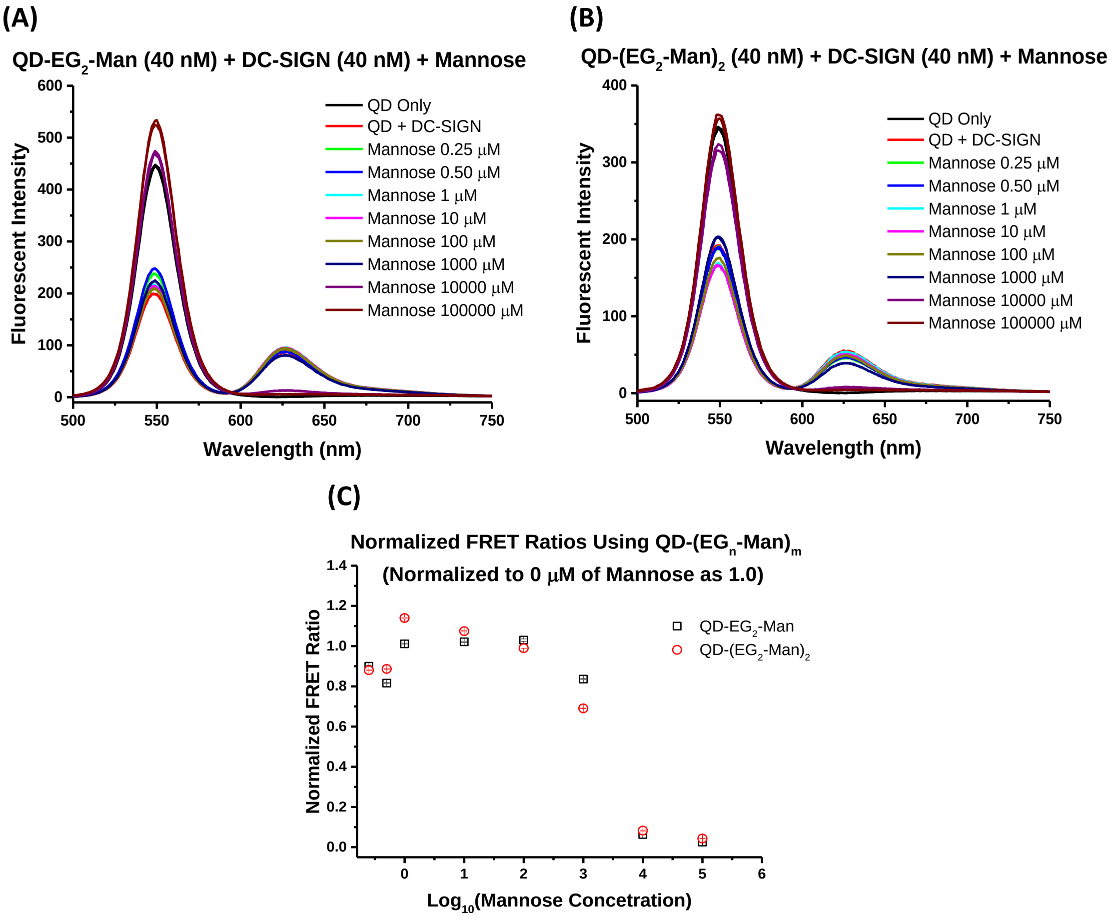

Figure 3.6.1: Background corrected fluorescence spectra of QD-EG$_2$-Man (40 nM), (**A**), and QD-(EG$_2$-Man)$_2$ (40 nM), (**B**), + DC-SIGN (40 nM) respectively over the addition of increasing the concentration of Mannose (0.25 – 10000 μM). (**C**) Normalized FRET ratio curve as a function of the logarithm to the base 10 of mannose concentration for each of the QDs with DC-SIGN.

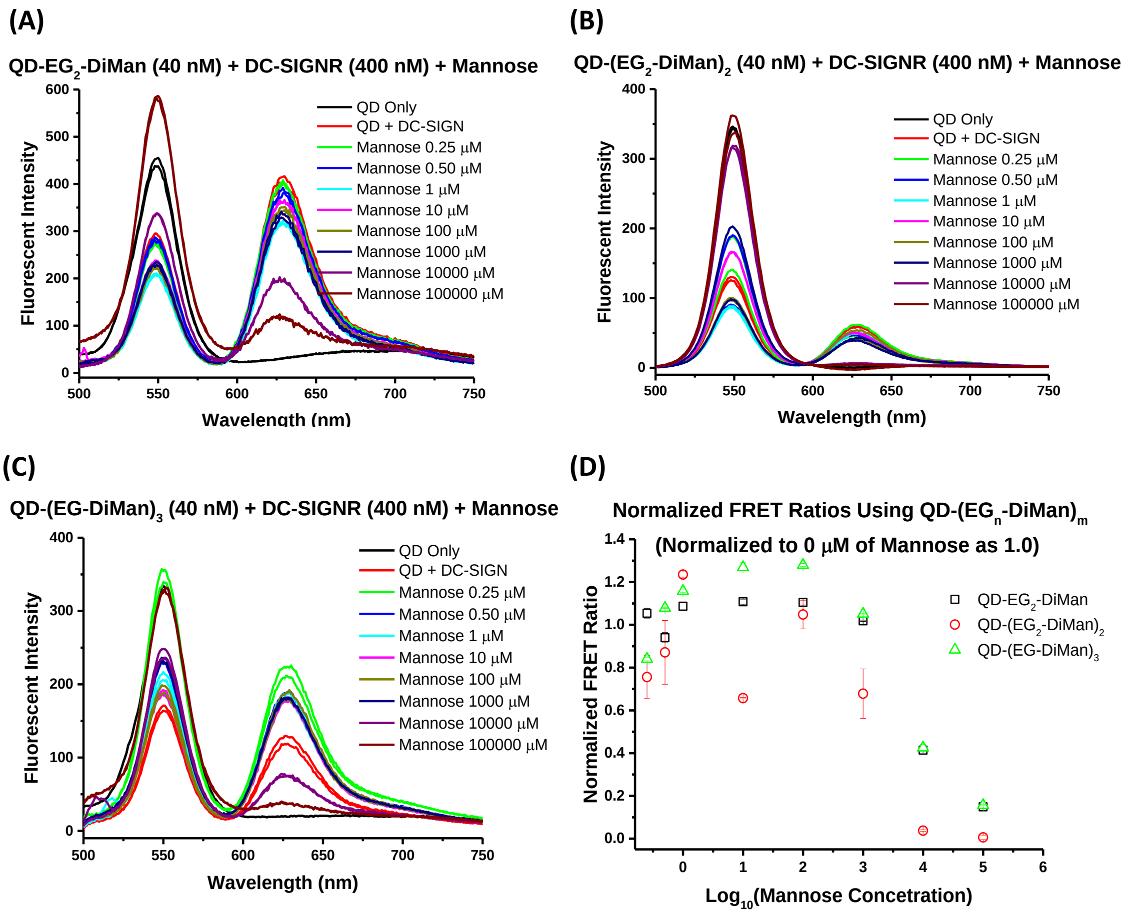

Figure 3.6.2: (A-C) Background corrected fluorescence spectra of QD-EG$_2$-DiMan (40 nM), QD-(EG$_2$-DiMan)$_2$ (40 nM) and QD-(EG-DiMan)$_3$ + DC-SIGNR (400 nM) respectively with the increasing concentration of free Mannose (0.25 – 10000 µM). (**D**) Normalized FRET ratio as a function of the logarithm to the base 10 of mannose concentration for each of the QDs.

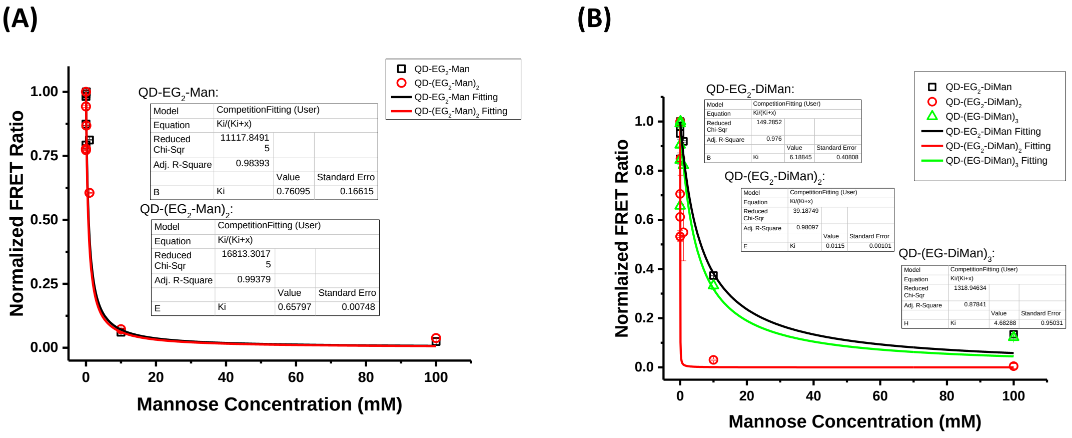

QD-EG$_2$-Man:

Model	CompetitionFitting (User)		
Equation	Ki/(Ki+x)		
Reduced Chi-Sqr	11117.8491 5		
Adj. R-Square	0.98393		
		Value	Standard Erro
B	Ki	0.76095	0.16615

QD-(EG$_2$-Man)$_2$:

Model	CompetitionFitting (User)		
Equation	Ki/(Ki+x)		
Reduced Chi-Sqr	16813.3017 5		
Adj. R-Square	0.99379		
		Value	Standard Erro
E	Ki	0.65797	0.00748

QD-EG$_2$-DiMan:

Model	CompetitionFitting (User)		
Equation	Ki/(Ki+x)		
Reduced Chi-Sqr	149.2852		
Adj. R-Square	0.976		
		Value	Standard Error
B	Ki	6.18845	0.40808

QD-(EG$_2$-DiMan)$_2$:

Model	CompetitionFitting (User)		
Equation	Ki/(Ki+x)		
Reduced Chi-Sqr	39.18749		
Adj. R-Square	0.98097		
		Value	Standard Error
E	Ki	0.0115	0.00101

QD-(EG-DiMan)$_3$:

Model	CompetitionFitting (User)		
Equation	Ki/(Ki+x)		
Reduced Chi-Sqr	1318.94634		
Adj. R-Square	0.87841		
		Value	Standard Error
H	Ki	4.68288	0.95031

Figure 3.6.3: Normalized FRET intensity ratio (I_{626}/I_{562}) as a function of added mannose concentration. (**A**) QD-(EG$_2$-Man)$_m$ (where m= 1 or 2) + DC-SIGN and (**B**) QD-(EG$_n$-DIMan)$_m$ (where n= 1 or 2 and m = 1, 2 and 3) + DC-SIGNR.

Table 3.6.1: Summary of the inhibition constant, K_i, obtained from **Figure 3.6.3**.

QD	$Ki_{(DC\text{-}SIGN)}$ (mM)	Binding affinity enhancement factor*	$Ki_{(DC\text{-}SIGNR)}$ (mM)	Binding affinity enhancement factor*
QD-EG$_2$-Man	0.76 ± 0.17	19000	-	-
QD-(EG$_2$-Man)$_2$	0.66 ± 0.01	16500	-	-
QD-EG$_2$-DiMan	-	-	6.2 ± 0.41	155000
QD-(EG$_2$-DiMan)$_2$	-	-	0.01 ± 0.001	250
QD-(EG-DiMan)$_3$	-	-	4.7 ± 0.95	117500

* DC-SIGN/R binding affinity enhancement factor is calculated by, K_i/C_{QD}.

The results follow the prediction in that when the mannose sugar is introduced the FRET ratio decreases. This shows that DC-SIGN/R has a higher affinity for mannose than the QD-glycans. Significantly the monosaccharide-QDs have a Ki <1 mM which shows that the QDs bind more strongly to DC-SIGN over mannose. This shows that these materials may be useful as inhibitors. This is in agreement with the binding constants for these materials as the K_i is an inverse measurement of the K_d, so the higher the value the less competition. However, the result for QD-(EG$_2$-DiMan)$_2$ appears to be anomalous and not fit the pattern predicted, by increasing number of glycans the binding affinity increases for DC-SIGNR based on the results of the K_d also the fit looks out of place on this data so it will need to be repeated. These results will need to be repeated to see if they are a true representation of what is occurring. The binding enhancement factor has been calculated to show the degree of competition, the higher the enhancement the easier the mannose can compete for the binding site (**Table 3.6.1**).

3.7 Conclusion

In conclusion, we have successfully developed a new ligand series which changes the LA: glycan ratio for both the monosaccharide and disaccharide mannose. We have then capped these ligands to QDs and used FRET technology to determine the binding dissociation constant of the QD-DC-SIGN/R interactions for each QD. Further confirmation for mannose affinity for DC-SIGN over DC-SIGNR has been shown using this ligand series. The trend of a decreasing binding affinity with DC-SIGN from the monomeric to the trimeric glycan ligand series was not expected as the aim was to increase surface glycan density. One possible reason is that we may not be seeing an increase in glycan density on the QD surface. However, for the QD-DiMan- DC-SIGNR interaction we do see that increasing the glycan number on each LA ligand the affinity becomes stronger (>3 x). Moreover, this strategy has significantly improved the binding affinities of glycan-DC-

SIGNR interactions over our previous glycan-QDs (**Chapter 3**) from 62 ± 8 to 1.7 ± 0.1 nM. Further work to be done should investigate the cause of the improved binding affinity, if it is due to the shortening of EG linker or the change of type of click chemistry which gives the smaller less sterically hindered triazole linker. As such positive effects have been seen for the binding affinities with DC-SIGN/R, these ligands could be used with gold nanoparticles, AuNPs. This is because the QDs are highly cytotoxic, and so the use of much less cytotoxic AuNPs could make the resulting glycan nanoparticles more biocompatible, allowing them to be used in potential in *vivo* applications.

3.8 Experimental Procedures

All the relevant experimental procedures for this chapter can be found with **Chapter 5**.

3.9 References

1. S. Penadés, B. G. Davis and P. H. Seeberger, 2017.

2. Y. A. Wang, J. J. Li, H. Chen and X. Peng, *J. Am. Chem. Soc.*, 2002, **124**, 2293-2298.

3. C. R. Becer, *Macromol. Rapid. Comm.*, 2012, **33**, 742-752.

4. R. S. Bagul, M. Hosseini, T. C. Shiao, N. K. Saadeh and R. Roy, *Polym. Chem.*, 2017, **8**, 5354-5366.

5. A. Varki, *Glycobiology*, 2017, **27**, 3-49.

6. A. Muñoz, D. Sigwalt, B. M. Illescas, J. Luczkowiak, L. Rodríguez-Pérez, I. Nierengarten, M. Holler, J.-S. Remy, K. Buffet and S. P. Vincent, *Nat. Chem.*, 2016, **8**, 50-57.

7. W. B. Turnbull and J. F. Stoddart, *Rev. Mol. Biotechnol.*, 2002, **90**, 231-255.

8. T. K. Lindhorst and M. Dubber, *Carbohyd. Res.*, 2015, **403**, 90-97.

9. J. B. Delehanty, I. L. Medintz, T. Pons, F. M. Brunel, P. E. Dawson and H. Mattoussi, *Bioconjug. Chem.*, 2006, **17**, 920-927.

10. J. Lin, K. Wang, X. Xia and L. Shen, *Langmuir*, 2018, **34**, 8415-8421.

11. M. Marradi, F. Chiodo, I. Garcia and S. Penadés, *Chem. Soc. Rev*, 2013, **42**, 4728-4745.

12. T. Johannssen and B. Lepenies, *Trends. Biotechnol.*, 2017, **35**, 334-346.

13. Y. Guo, I. Nehlmeier, E. Poole, C. Sakonsinsiri, N. Hondow, A. Brown, Q. Li, S. Li, J. Whitworth and Z. Li, *J. Am. Chem. Soc.*, 2017, **139**, 11833-11844.

14. R. Ribeiro-Viana, M. Sánchez-Navarro, J. Luczkowiak, J. R. Koeppe, R. Delgado, J. Rojo and B. G. Davis, *Nat. Commun.*, 2012, **3**, 1303.

15. J. V. Jokerst, T. Lobovkina, R. N. Zare and S. S. Gambhir, *Nanomedicine*, 2011, **6**, 715-728

Chapter 4

Effect of Gold Nanoparticle Surface Glycan Density on DC-SIGN/R Binding.

4.1 Introduction

Gold nanoparticles (AuNPs) have many advantageous features for use as inhibitory materials. They are non-toxic, good fluorescence quenchers and can offer a large surface area to volume ratio to display a large array of glycans upon their surface.[1] AuNPs quenching potential allows them to be used in an energy transfer based system over a much larger separation distance compared to that of donor to acceptor with QDs.[2] **Figure 4.1.1** shows the schematic process of fluorescence quenching by exciting the fluorescence donor, the ATTO 594 label on the protein, where the energy is transferred to a glycan-AuNP in close proximity bound through multivalent glycan-protein interactions.

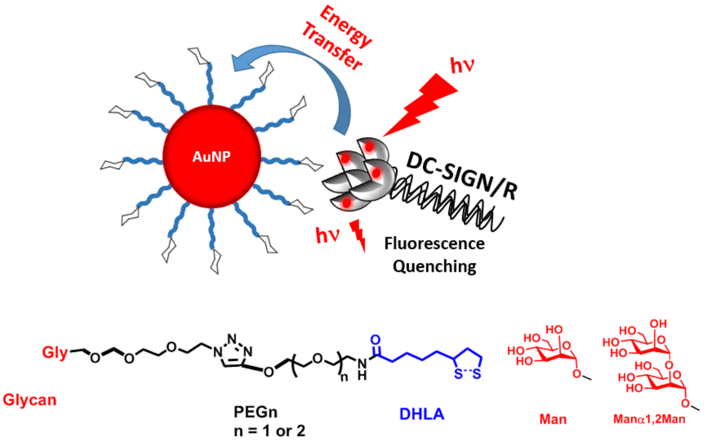

Figure 4.1.1: A schematic showing the probing of multivalent glycan-protein binding via a fluorescence quenching mechanism ligand using AuNPs capped with glycans.

The aim of the project is to look to further build a knowledge of the multivalent viral receptor proteins DC-SIGN[3] and DC-SIGNR[4] as currently there is no crystal structure available for these tetrameric proteins. These proteins are found to be key in many important biological roles and processes including innate immunity and serum glycoprotein clearance[5] as well as viral infections (e.g. Human Immunodeficiency Virus, HIV, Ebola Virus and West Nile Virus).[4, 6 7] These two proteins share the same primary structure, and 77% amino acid identity and until recently they were proposed to have the same binding modes.[8] However, recent work has found that the way they interact with glycan-QDs are very different, **Chapter 2**.[9] DC-SIGN possess a tetrameric binding with a single QD, giving isolated QDs, whereas DC-SIGNR binds bis - divalently to two different QDs, leading to protein QD and inter-crosslinking. This binding mode is confirmed by scanning electron transmission microscopy, STEM, imaging of the resulting QD-DC-SIGN/R assemblies (**Figure 4.1.2**).

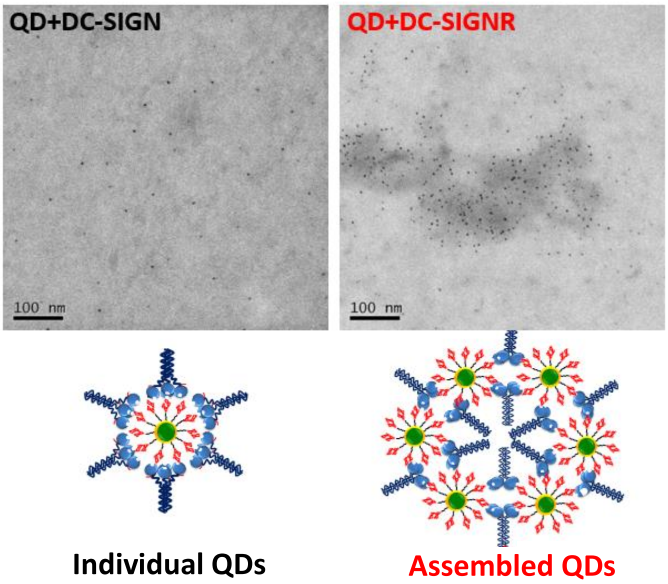

Figure 4.1.2: STEM images of the QD-glycan bioconjugates after binding with DC-SIGN/R showing significantly different binding modes. Taken from reference.[9]

The focus of this part of the project is to develop a new biophysical method for the quantification of multivalent lectin-glycan binding by exploiting the unique fluorescence quenching property of AuNPs. This is another fluorescence readout strategy that can be developed as a fast, sensitive way to gather binding information using a small amount of material while using a less cytotoxic material. A series of AuNPs particles will be produced with increasing surface glycan densities using a monosaccharide and disaccharide mannose glycans. This will be achieved by producing DHLA-based ligands each appending multiple (e.g. 1, 2, or 3) glycan units as described in **Chapter 3** to produce similar AuNP conjugates as shown schematically in **Figure 4.1.3**. The apparent binding equilibrium dissociation constant, K_d, will then be calculated for the resulting quenching efficiency-concentration relationship. These glycan-AuNPs will then be further exploited as novel inhibition agents against viral infections by binding to the cell surface DC-SIGN/R to block virus binding.[9] The correlation between the IC_{50} values and binding K_ds will be investigated in a similar way as the earlier QD work. By using AuNPs as scaffolds instead of QDs, the toxic cadmium metal will be eliminated. The resulting AuNP-glycans may allow potential applications *in vivo*.[10] Similar work done has been previously in this field by Martinez-Avila *et al*.[11]

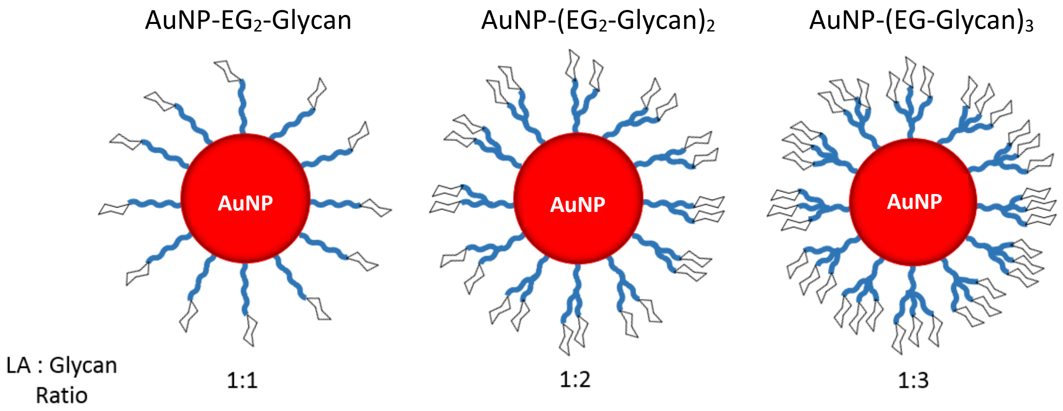

Figure 4.1.3: A schematic of the AuNPs that will be used to investigate the effects of increasing glycan surface density using a lipoic acid, LA, modified with different glycan ratio ranging from 1:1 to 1:3.

The sugar ligands, DHLA-(EG$_n$-glycan)$_m$ (where n = 1 or 2, m = 1, 2 or 3, and glycan = α-Man or Man-α-1,2-Man), as used in **Chapter 3,** are synthesised by copper-catalysed click chemistry. Ligand design is shown above in **Figure 4.1.1** and mannose based glycans will be used as they possess a high affinity for DC-SIGN/R. The linker length will not change across the series as the focus is on changing the glycan density rather than the linker length. Moreover, a short EG chain length (EG$_3$) has shown to have high binding affinities in previous studies.[9] The specificity and affinity of mannose-protein interactions will be investigated and then compared using a range of control ligands, with no functional mannose present, to check for non-specific interactions. In addition, calcium dependency studies will be performed.

One of the reasons to increase glycan density came from the fact that we found the QD-glycan binding with DC-SIGN/R was significantly weakened upon diluting the QD-surface sugar density using an inert DHLA-zwitterion spacer ligand[9] as described in **Chapter 2**. We hypothesised that a further increase in nanoparticle surface glycan density would further enhance its binding affinity to DC-SIGN/R. The glycoprotein 120, gp120, on the surface of HIV is densely covered in clusters of *N*-linked mannose glycans, the virus has evolved to use these clusters as a way of infecting humans via binding to the c-type lectins DC-SIGN/R.[11] Recent advances have shown that mimicking these mannose clusters is valid a way of developing potent carbohydrate-based antiviral materials.[12] So far many approaches to create multivalent mannose clusters as inhibitory materials for HIV using a range of different scaffolds have been successful. Moreover, we also hope to use the glycan-nanoparticles to mimic the HIV surface gp120. In fact, it is gp120-DC-SIGN/R interaction that mediates HIV virus infection of host cells.[13-15] The sizes of the glycan-NPs used here are also comparable to that of the gp120 (**Figure 4.1.4**). Martinez-Avila et al.[12] has shown that AuNPs covered with multiple copies of high-mannose clusters effectively mimic the behaviour of the gp120 and the internalisation pathway. Thus they show great promise for development of HIV microbicides and vaccines. Increasing the glycan density has shown positive effects with improving the binding using AuNPs as a scaffold. The hypothesis is that we may find similar effect on the inhibition of the Ebola virus as that of HIV.

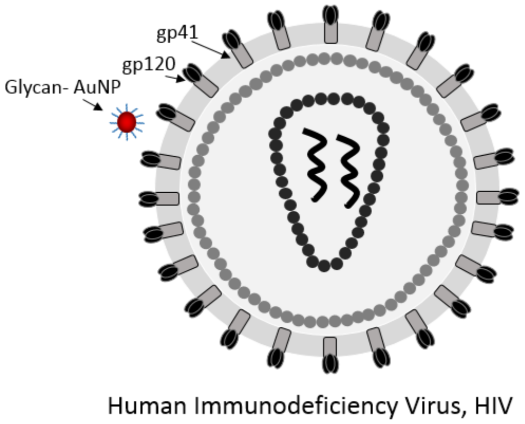

Figure 4.1.4: A schematic of a HIV virus including NP bioconjugates to show the size matches and in comparison, to the full virus size.

4.2 Polyvalent AuNP-Mannose Design

4.2.1 Ligand Exchange with AuNPs

The ligands were added straight into the commercially available AuNPs along with the TCEP reduction agent using a ligand: AuNP molar ratio of 2000:1 in H_2O. This is possible as there is no need for deprotection as there is with the QDs. Full experimental details are available in **Chapter 5**. **Figure 4.2.1** below shows the chelation of the di-thiol functional group of the ligand to the AuNPs surface. The commercially available AuNPs have a citrate ligand coated surface. The AuNPs are soluble in water before and after ligand exchange reaction. If any aggregation has occurred, indicating an unsuccessful ligand exchange, the solution colour will change from red to purple.

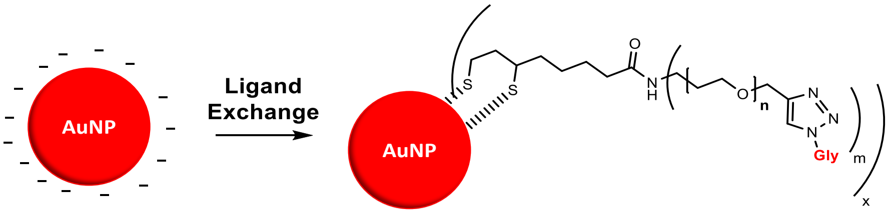

Figure 4.2.1: The ligand exchange reaction undertaken with citrate stabilised AuNPs coated and stabilised with by glycan ligands [LA-$(EG_n\text{-Man})_m$ (where n = 1 or 2 and m= 1, 2 and 3)].

The concentration of the AuNPs was calculated using UV-Vis absorption and the Beer-Lambert Law. The absorbance, A, was obtained from the AuNP absorption peak maxima at 515 nm and an extinction coefficient, ε, of 1.1×10^7 M^{-1} cm^{-1} was used to calculate the concentration.[16] **Figure 4.2.2** below shows the UV-Vis spectra for each of the successfully capped AuNPs with all the ligand series (LA-(EG$_n$-Man)$_m$, LA-(EG$_n$-DiMan)$_m$, and LA-(PEG$_{750}$-OMe)$_m$, where n=1 or 2 and m= 1, 2 and 3). For later results we used some AuNPs synthesised by Dr. Akshath Uchangi Satyaprasad, a postdoc within the group, based on a procedure by Piella *et al.*[17] these were citrate stabilised particles with a similar core size to that of the commercial AuNPs.

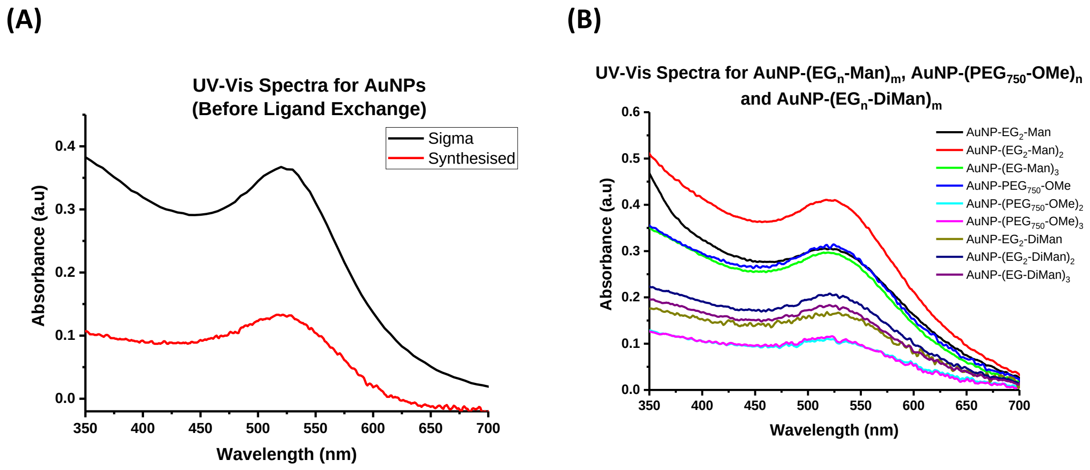

Figure 4.2.2: UV-vis spectra of **(A)** the commercial AuNPs and the synthesised AuNPs before ligand exchange that are used throughout this chapter **(B)** the different AuNP-(EG$_n$-Man)$_m$ and AuNP-(EG$_n$-DiMan)$_m$ conjugates(where n= 1 or 2 and m= 1, 2 and 3) as well as AuNP-(PEG$_{750}$-OMe)$_n$ (where n= 1, 2 and 3) conjugates.

4.2.2 AuNP-(EG$_n$-Man)$_m$ Characterisation

4.2.2.1 Hydrodynamic Size Determination of AuNP

The stability and the hydrodynamic sizes of freshly prepared AuNP-glycan conjugates were determined by DLS. The resulting volume population versus hydrodynamic size graphs for each of the AuNPs before and after ligand exchange in water are given in **Figure 4.2.3**. Data was also collected after the particles were left for a week in order to test stability. In order to determine the stability of particles in biological relevant media the same tests were performed in buffer solution (20 mM HEPES pH 7.8, 100 nM NaCl and 10 mM CaCl$_2$).

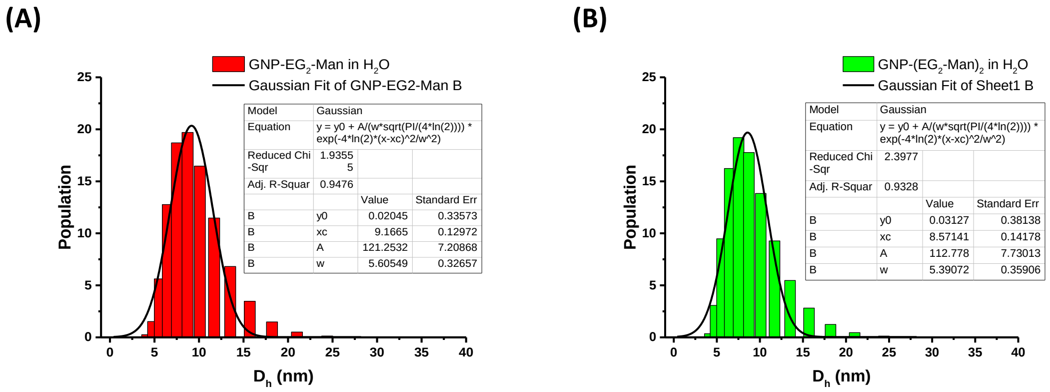

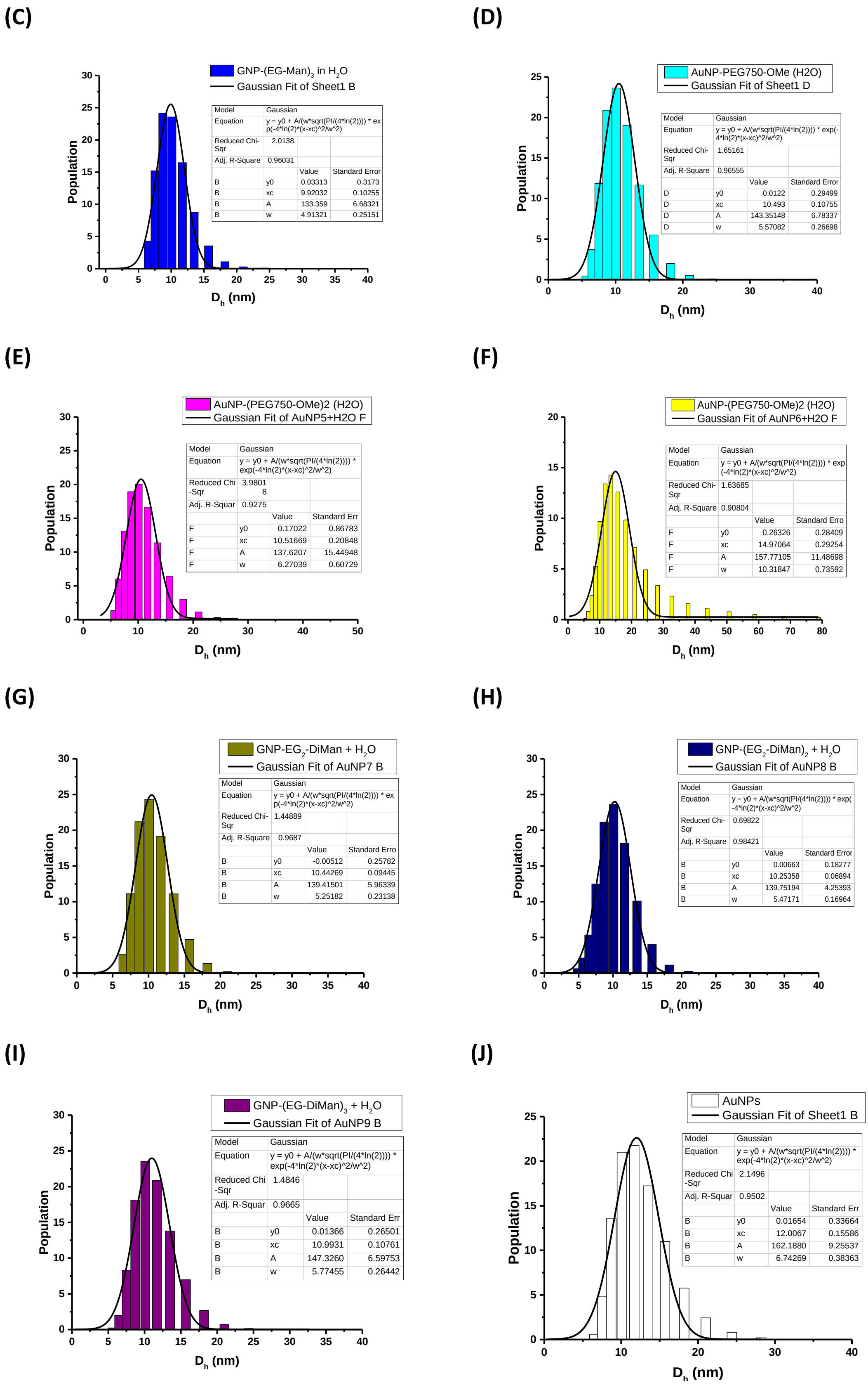

Model	Gaussian		
Equation	y = y0 + A/(w*sqrt(PI/(4*ln(2)))) * exp(-4*ln(2)*(x-xc)^2/w^2)		
Reduced Chi-Sqr	2.0138		
Adj. R-Square	0.96031		
		Value	Standard Error
B	y0	0.03313	0.3173
B	xc	9.92032	0.10255
B	A	133.359	6.68321
B	w	4.91321	0.25151

Model	Gaussian		
Equation	y = y0 + A/(w*sqrt(PI/(4*ln(2)))) * exp(-4*ln(2)*(x-xc)^2/w^2)		
Reduced Chi-Sqr	1.65161		
Adj. R-Square	0.96555		
		Value	Standard Error
D	y0	0.0122	0.29499
D	xc	10.493	0.10755
D	A	143.35148	6.78337
D	w	5.57082	0.26698

Model	Gaussian		
Equation	y = y0 + A/(w*sqrt(PI/(4*ln(2)))) * exp(-4*ln(2)*(x-xc)^2/w^2)		
Reduced Chi-Sqr	3.98018		
Adj. R-Squar	0.9275		
		Value	Standard Err
F	y0	0.17022	0.86783
F	xc	10.51669	0.20848
F	A	137.6207	15.44948
F	w	6.27039	0.60729

Model	Gaussian		
Equation	y = y0 + A/(w*sqrt(PI/(4*ln(2)))) * exp(-4*ln(2)*(x-xc)^2/w^2)		
Reduced Chi-Sqr	1.63685		
Adj. R-Square	0.90804		
		Value	Standard Erro
F	y0	0.26326	0.28409
F	xc	14.97064	0.29254
F	A	157.77105	11.48698
F	w	10.31847	0.73592

Model	Gaussian		
Equation	y = y0 + A/(w*sqrt(PI/(4*ln(2)))) * exp(-4*ln(2)*(x-xc)^2/w^2)		
Reduced Chi-Sqr	1.44889		
Adj. R-Square	0.9687		
		Value	Standard Erro
B	y0	-0.00512	0.25782
B	xc	10.44269	0.09445
B	A	139.41501	5.96339
B	w	5.25182	0.23138

Model	Gaussian		
Equation	y = y0 + A/(w*sqrt(PI/(4*ln(2)))) * exp(-4*ln(2)*(x-xc)^2/w^2)		
Reduced Chi-Sqr	0.69822		
Adj. R-Square	0.98421		
		Value	Standard Error
B	y0	0.00663	0.18277
B	xc	10.25358	0.06894
B	A	139.75194	4.25393
B	w	5.47171	0.16964

Model	Gaussian		
Equation	y = y0 + A/(w*sqrt(PI/(4*ln(2)))) * exp(-4*ln(2)*(x-xc)^2/w^2)		
Reduced Chi-Sqr	1.4846		
Adj. R-Squar	0.9665		
		Value	Standard Err
B	y0	0.01366	0.26501
B	xc	10.9931	0.10761
B	A	147.3260	6.59753
B	w	5.77455	0.26442

Model	Gaussian		
Equation	y = y0 + A/(w*sqrt(PI/(4*ln(2)))) * exp(-4*ln(2)*(x-xc)^2/w^2)		
Reduced Chi-Sqr	2.1496		
Adj. R-Squar	0.9502		
		Value	Standard Err
B	y0	0.01654	0.33664
B	xc	12.0067	0.15586
B	A	162.1880	9.25537
B	w	6.74269	0.38363

Figure 4.2.3: Histograms of the hydrodynamic sizes for the AuNPs (50 nM) in water solution **(A)** AuNP-EG$_2$-Man, **(B)** AuNP-(EG$_2$-Man)$_2$, **(C)** AuNP-(EG-Man)$_3$, **(D)** AuNP-PEG$_{750}$-OMe, **(E)** for AuNP-(PEG$_{750}$-OMe)$_2$, **(F)** AuNP-(PEG$_{750}$-OMe)$_3$, **(G)** AuNP-EG$_2$-DiMan, **(H)** AuNP-(EG$_2$-DiMan)$_2$, **(I)** AuNP-(EG-DiMan)$_3$ and (J) AuNPs before ligand exchange. All samples run using 50 nM AuNPs.

Table 4.2.1: A table to show the summary of the hydrodynamic sizes of the AuNPs (50 nM) after ligand exchange as determined by DLS both initially after and then after a week.

Ligand + Media	Hydrodynamic Size Initial (d.nm)	FWHM (d.nm)	Hydrodynamic Size *after 1 week* (d.nm)	FWHM *after 1 week* (d.nm)
Citrate	12.0 ± 0.2	6.7 ± 0.4	13.1 ± 0.1	6.3 ± 0.3
LA-EG$_2$-Man + H_20	9.2 ± 0.1	5.6 ± 0.3	9.2 ± 0.1	5.6 ± 0.3
LA-(EG$_2$-Man)$_2$ + H_20	8.6 ± 0.1	5.4 ± 0.4	8.8 ± 0.1	5.3 ± 0.3
LA-(EG-Man)$_3$ + H_20	9.9 ± 0.1	4.9 ± 0.3	10.1 ± 0.1	4.1 ± 0.1
LA-PEG$_{750}$-OMe + H_2O	10.5 ± 0.1	5.6 ± 0.3	10.5 ± 0.1	5.8 ± 0.3
LA-(PEG$_{750}$-OMe)$_2$ + H_2O	10.5 ± 0.2	6.3 ± 0.6	10.8 ± 0.2	6.1 ± 0.6
LA-(PEG$_{750}$-OMe)$_3$ + H_2O	15.0 ± 0.3	10.3 ± 0.7	16.3 ± 0.3	14.1 ± 0.8
LA-EG$_2$-DiMan + H_2O	10.4 ± 0.1	5.3 ± 0.2	11.6 ± 0.1	5.9 ± 0.3
LA-(EG$_2$-DiMan)$_2$ + H_2O	10.3 ± 0.1	5.5 ± 0.2	10.4 ± 0.1	5.4 ± 0.2
LA-(EG-DiMan)$_3$ + H_2O	11.0 ± 0.1	5.8 ± 0.3	10.8 ± 0.1	5.7 ± 0.3
LA-EG$_2$-Man + Buffer	10.3 ± 0.1	5.3 ± 0.3	9.4 ± 0.1	5.5 ± 0.3
LA-(EG$_2$-Man)$_2$ + Buffer	9.4 ± 0.1	5.4 ± 0.3	9.6 ± 0.1	4.7 ± 0.2
LA-(EG-Man)$_3$ + Buffer	11.6 ± 0.2	6.1 ± 0.5	10.1 ± 0.1	5.3 ± 0.2
LA-PEG$_{750}$-OMe + Buffer	11.3 ± 0.1	5.1 ± 0.2	11.4 ± 0.1	± 0.3
LA-(PEG$_{750}$-OMe)$_2$ + Buffer	10.8 ± 0.1	5.3 ± 0.2	11.1 ± 0.1	5.3 ± 0.4
LA-(PEG$_{750}$-OMe)$_3$ + Buffer	14.9 ± 0.3	10.5 ± 0.7	12.7 ± 0.2	9.1 ± 0.6
LA-EG$_2$-DiMan + Buffer	12.5 ± 0.3	8.1 ± 0.7	11.3 ± 0.2	7.1 ± 0.5
LA-(EG$_2$-DiMan)$_2$ + Buffer	11.4 ± 0.2	7.1 ± 0.4	11.4 ± 0.1	6.2 ± 0.3
LA-(EG-DiMan)$_3$ + Buffer	11.3 ± 0.2	6.8 ± 0.4	11.5 ± 0.2	6.5 ± 0.4

A small change in particle size was observed after ligand exchange with the range of different ligands indicating that ligand exchange has happened, although this does not fully confirm ligand exchange has occured. This can be shown by the particle's stability in buffer solution. As their stability is not affected by changing water to buffer solution as little changes in hydrodynamic size is observed. This confirms that ligand exchange has occurred as the citrate stabilised AuNPs readily aggregate in buffer. Furthermore, the particles show no sign of aggregation after storage for one week and retain their initial sizes. A full summary of the results are given in **Table 4.2.1** and the full D_h histograms can be found in **Appendix**.

4.2.2.2 Transmission Electron Microscopy and Scanning Transmission Electron Microscopy

TEM was used to confirm the core size of the AuNPs, 2 nm, with further confirmation of the stability of the singular particles. **Figure 4.2.4** (**A-C**) shows the TEM images of the AuNPs that have been coated with the LA-EG$_2$-Man. Scanning transition electron microscopy, STEM, was used upon the cluster of particles shown in **Figure 4.2.4** (**D**) and EDX **Figure 4.2.4** (**H**) was used to determine particle composition the results can be seen in below. It shows the presence of Gold, confirming AuNPs, and then Copper and Silica found in the TEM grid. Carbon and Oxygen are from the surface ligands and the TEM grid.

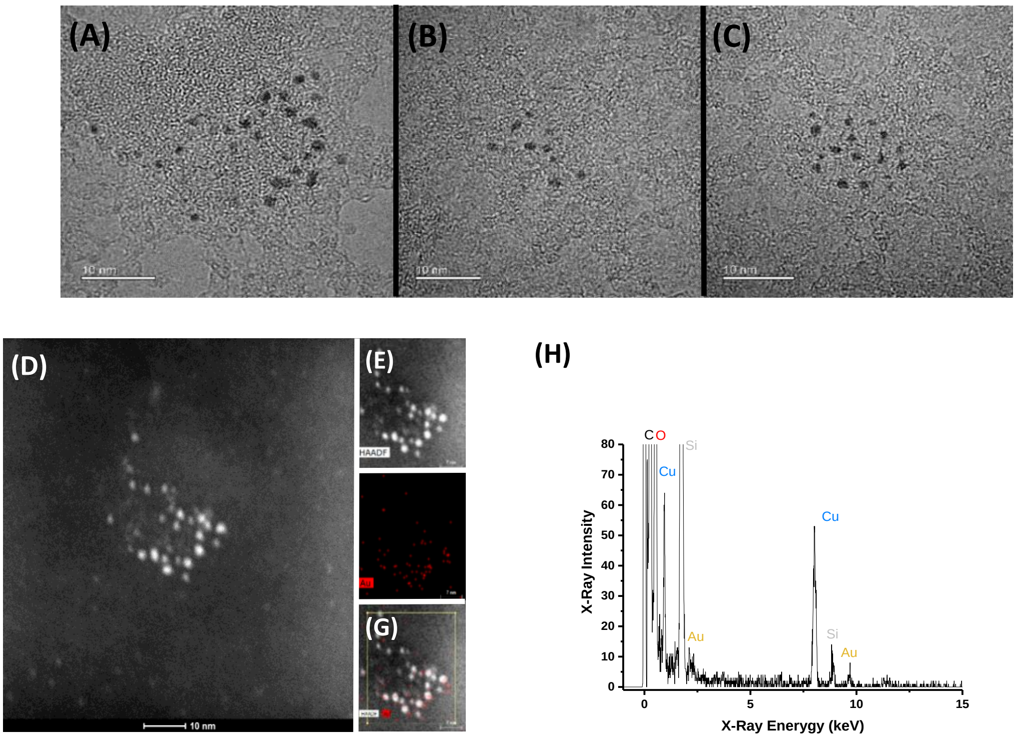

Figure 4.2.4: (**A-C**) TEM images of AuNP-EG$_2$-Man. Scale bar 10 nm. (**D-G**) STEM images of the same AuNP-EG$_2$-Man as in (**A**) characterised using EDX to show that they are the AuNPs with (**H**) showing EDX spectrum of the scanned region confirmed presence of gold as indicated by the red.

4.2.3 Ligand Exchange Calibration

In order to determine whether or not the ligand exchange had occurred and also determine ligand loading upon AuNP surface, a calibration curve was done using the ligand using LC-MS. Different amounts of ligands were made into standard solutions under the same conditions and volumes as the washings taken after the ligand exchange of the AuNPs to generate a calibration curve. The washing samples were run alongside the standard samples. A decrease in the amount of ligand lower than initially used was considered to be capped on the AuNP. The resulting calibration curves for the disaccharide ligand series are shown in the **Appendix Chapter 2**.

Through using the linear equation, (**Eq. 20**), (where y = chromatogram area, m = slope of linear calibration, x = ligand amount (nmol) and c = y intercept) unknown amounts of unbound ligand were calculated for each of the ligand exchanges. **Table 4.2.2** shows the values calculated for the calibration equation. This amount is then taken from the overall ligand amount added and the ligand that has been exchanged is then calculated by collecting the supernatant of the spin column purification through using the area of the chromatogram. These values are shown below in **Table 4.2.3**.

$$y = mx + c \qquad \textbf{(Eq. 20)}$$

Table 4.2.2: A table to show the amounts of the variables present in the linear equation to calculate the amount of ligand not loaded on to AuNP surface.

Ligand	Value of Slope	Value of Intercept (nmol)
LA-EG$_2$-Man	2.88×10^5	1.53×10^7
LA-(EG$_2$-Man)$_2$	1.35×10^6	-4.73×10^7
LA-(EG-Man)$_3$	4.35×10^5	3.16×10^7
LA-EG$_2$-DiMan	3.17×10^4	5.52×10^5
LA-(EG$_2$-DiMan)$_2$	5.05×10^5	1.19×10^7
LA-(EG-DiMan)$_3$	1.61×10^6	-4.25×10^7

The results show that there is a distinct reduction in the number of ligands conjugated to each AuNP by changing the monomer to trimer glycan ligand, suggesting that instead of having the same number of ligands on each AuNP less ligands can bind to the AuNP surface as the ligands become bulkier. This reduction is presumably due to increased steric hindrance of the ligands as the terminal glycan number increases. There is however an anomalous result within the series possibly due to the column impurities of the LC-MS so to fully understand what is happening this needs to be repeated in the future. The results suggest that although we have created a ligand series for increasing glycan surface density, the number of sugars bound to the AuNP surface may have actually decreased due to increased steric hindrance. **Figure 4.2.5** shows the calibration curve and the sample of unknown concentration after ligand exchange for the TA-(EG$_2$-DiMan)$_2$.

Table 4.2.3: The amounts of ligand bound to the AuNPs and glycan valency per AuNP for the different AuNP-Glycan series.

Unknown Sample Ligand	Ligand Amount Bound (nmol)	Glycan Valency per AuNP
LA-EG$_2$-Man	200^{*2}	1099
LA-(EG$_2$-Man)$_2$	174^{*2}	1912
LA-(EG-Man)$_3$	58^{*2}	957
LA-EG$_2$-DiMan	287^{*1}	1577
LA-(EG$_2$-DiMan)$_2$	106^{*2}	1164
LA-(EG-DiMan)$_3$	24^{*2}	395

^{*1} Starting ligand amount 400 nmol with AuNP 0.182 nmol.

^{*2} Starting ligand amount 200 nmol with AuNP 0.182 nmol.

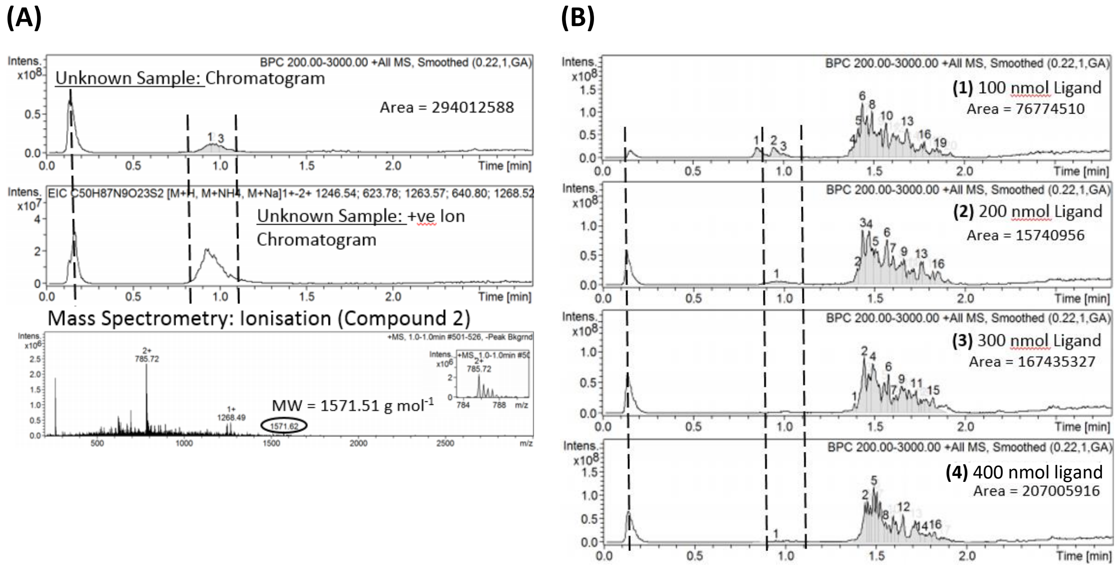

Figure 4.2.5: (**A**) LC-MS chromatograms showing the Sample of TA-(EG$_2$-DiMan)$_2$ of unknown concentration taken after ligand exchange and (**B**) LC-MS chromatograms for the calibration curve with known concentrations of TA-(EG$_2$-DiMan)$_2$.

The chromatograms show some inconsistencies which may attribute to the large varying slope and intercept values seen above. In some of the calibrations an injection peak is seen to contain product and so is accounted for in the total area of the ligand samples but this injection peak could also contain the impurities from the column. The area calculated for this peak maybe not a true representation of just the ligand leading to inaccuracies in calibration. Claibration curves using LC-MS in the case of this experiment don't appear accurate enough to calculate an accurate representation of ligand loading on the surface of the AuNPs, a different method should be utilized in the future such as a phenol- sulfuric acid method.[9]

4.3 Fluorescence Quenching for AuNP-DC-SIGN Conjugates

To determine the apparent binding affinity, K_d, for the multivalent interactions between the AuNP-glycans and DC-SIGN, fluorescence spectra have been recorded across a range of concentrations at a fixed molar ratio of 1: 1.25 for AuNP: DC-SIGN. The samples were made in a binding buffer containing 1 mg/ mL BSA to reduce non-specific absorption of AuNP and protein on surfaces. This is a known to be the major source of error when working with low concentrations (ca. <10 nM) of materials.[18] The tables below show sample preparation for the glycan AuNP-DC-SIGN with monosaccharide (**Table 4.3.1**) and disaccharide mannose (**Table 4.3.2**).

Table 4.3.1: The concentrations and amounts of the differing components used for the determination of the apparent K_d with AuNP(Man)-DC-SIGN bioconjugates.

Tube	**AuNP Stock (200 nM)**		**Protein Stock (100 nM)**		**HEPES Buffer (1 mg/ mL BSA)**
	Conc (nM)	**vol (µM)**	**Conc (nM)**	**vol (µL)**	
1	0	0	0	0.00	400.00
5	2.4	4.8	3	12.00	383.20
6	4.8	9.6	6	24.00	366.40
7	9.6	19.2	12	48.00	332.80
8	19.2	38.4	24	96.00	265.60
9	28.8	57.6	36	144.00	198.40
10	40	80	50	200.00	120.00
Tube	**AuNP Stock (350 nM)**		**Protein Stock (218.75 nM)**		**HEPES Buffer (1 mg/ mL BSA)**
	Conc (nM)	**vol (µL)**	**Conc (nM)**	**vol (µL)**	
11	70	80	87.5	160.00	160.00
12	105	120	131.25	240.00	40.00

Table 4.3.2: The concentrations and amounts of the differing components used for the determination of the apparent K_d with AuNP(DiMan)-DC-SIGN bioconjugates.

Tube	**AuNP Stock (10 nM)**		**Protein Stock (12.5 nM)**		**HEPES Buffer (1 mg/ mL BSA)**
	Conc (nM)	**vol (µL)**	**Conc (nM)**	**vol (µL)**	
0	0	0	0	0.00	400.00
1	0.2	8	0.25	8.00	384.00
2	0.4	16	0.5	16.00	368.00
3	0.8	32	1	32.00	336.00
4	1.8	72	2.25	72.00	256.00
Tube	**AuNP Stock (200 nM)**		**Protein Stock (100 nM)**		**HEPES Buffer (1 mg/ mL BSA)**
	Conc (nM)	**vol (µL)**	**Conc (nM)**	**vol (µL)**	
5	2.4	4.8	3	12.00	383.20
6	4.8	9.6	6	24.00	366.40
7	9.6	19.2	12	48.00	332.80
8	19.2	38.4	24	96.00	265.60
9	28.8	57.6	36	144.00	198.40
10	40	80	50	200.00	120.00

Fluorescence spectra reveal a clear emission peak for the labelled DC-SIGN only (λ_{em}=626 nm). The fluorescence spectra for the AuNP-(EG_2-Man) + DC-SIGN samples are shown in **Figure 4.3.1**, the rest of the fluorescence spectra for other AuNP-glycan + DC-SIGN samples are given in **Appendix, Chapter A2**. Due to the increasing concentrations of DC-SIGN a range of different machine parameters have been used to avoid signal saturation on the instrument. This only affects the absolute individual fluorescence intensity, as long as the protein - only sample is run using the same parameters then the resulting quenching efficiency should not be affected.

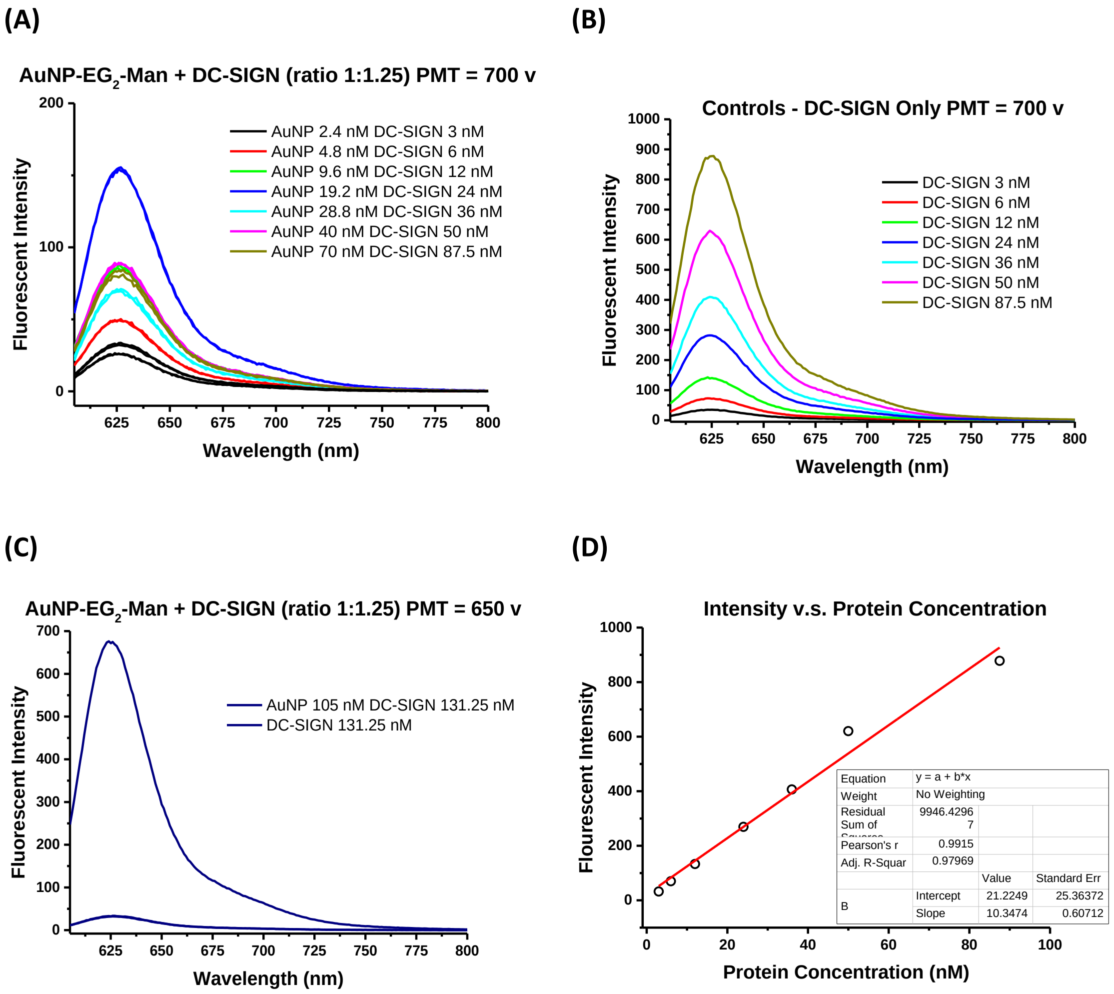

Equation	y = a + b*x		
Weight	No Weighting		
Residual Sum of	9946.42967		
Pearson's r	0.9915		
Adj. R-Squar	0.97969		
		Value	Standard Err
B	Intercept	21.2249	25.36372
	Slope	10.3474	0.60712

Figure 4.3.1: Fluorescence spectra for **(A)** AuNP-EG$_2$-Man (2.4 – 70 nM) + labelled DC-SIGN (3 – 87.5 nM), (**B**) Control samples where only labelled DC-SIGN (3 – 87.5 nM) was used at the same concentrations and the same machine settings, **(C)** AuNP-EG$_2$-Man (105 nM) + labelled DC-SIGN (131.25 nM) as well as the control sample labelled DC-SIGN (131.25 nM) and **(D)** intensity verses concentration plot of protein data.

4.3.1 Quenching Efficiency

Quenching efficiency is a comparison between the fluorescence of a fluorophore with and without the presence of a fluorescence quenching material, through using the integrated fluorescence from 605 – 800 nm specifically chosen for the atto-594 dye used for the labelling the proteins as shown in **Chapter 2**. (**Eq. 21**) below is then used to calculate the resulting quenching efficiency of each of the samples.

$$QE\ (\%) = \left(\frac{P-NP}{P}\right) \times 100 \qquad \textbf{(Eq. 21)}$$

Where P= Spectral integral (between 605 – 800 nm) of DC-SIGN only and NP =Spectral integral (between 605-800 nm) of GNP + DC-SIGN. The apparent K_d, was obtained by the Hill Equation, (**Eq. 16**) below.

$$y = \frac{R_{max} \times x^n}{(K^n + x^n)} \qquad \textbf{(Eq. 16)}$$

Where R_{max} is the maximum fluorescence quenching percentage (=100%), K is the apparent K_d, n is the Hill coefficient and x is the protein concentration. The resulting binding curves are shown below in **Figure 4.3.2** and **Figure 4.3.3** for each series of ligands. The apparent K_d for each of the glycan-AuNPs with DC-SIGN, with the fitting parameters can be seen in **Table 4.3.3** and the apparent K_d for the control PEG-AuNPs in **Table 4.3.5**.

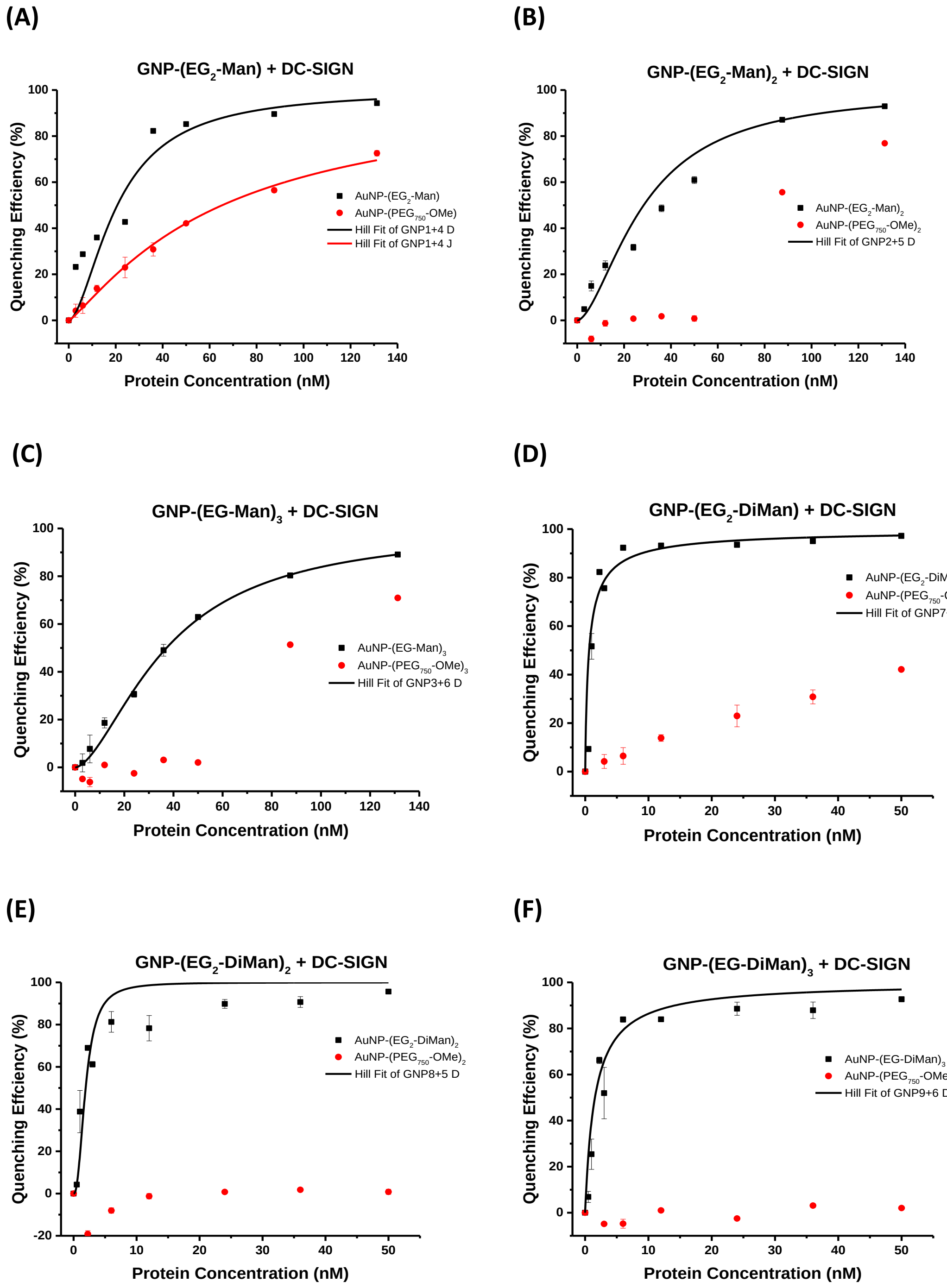

Figure 4.3.2: Percentage fluorescence quenching curves shown as a function of the protein concentration (DC-SIGN). (**A**) AuNP-(EG_2-Man) and its control AuNP-PEG_{750}-OMe, (**B**) AuNP-(EG_2-Man)$_2$ and its control AuNP-(PEG_{750}-OMe)$_2$, (**C**) AuNP-(EG-Man)$_3$ and its control AuNP-(PEG_{750}-OMe)$_3$. (**D**) AuNP-(EG_2-DiMan) and its control AuNP-PEG_{750}-OMe, (**E**) AuNP-(EG_2-DiMan)$_2$ and its control AuNP-(PEG_{750}-OMe)$_2$ and finally (**F**) AuNP-(EG-DiMan)$_3$ and its control AuNP-(PEG_{750}-OMe)$_3$. Fitted using the Hill's equation.

Table 4.3.3: Summary of the fitting parameters for calculating the apparent K_d using the Hill Equation to fit the AuNP-(EG$_n$-Man)$_m$ and AuNP-(EG$_n$-DiMan)$_m$ DC-SIGN binding curves **Figure 4.3.2**.

AuNP	R_{max}	Apparent K_d (nM)	n	R^2
AuNP-EG$_2$-Man	100	21 ± 3	1.7 ± 0.35	0.99376
AuNP-(EG$_2$-Man)$_2$	100	28 ± 1	1.7 ± 0.05	1
AuNP-(EG-Man)$_3$	100	37 ± 1	1.7 ± 0.02	1
AuNP-PEG$_{750}$-OMe	100	65 ± 1	1.2 ± 0.05	0.99984
AuNP-EG$_2$-DiMan	100	0.61 ± 0.3	0.8 ± 0.10	0.99972
AuNP-(EG$_2$-DiMan)$_2$	100	1.91 ± 0.2	2.3 ± 0.14	1
AuNP-(EG-DiMan)$_3$	100	1.54 ± 0.3	1.0 ± 0.17	0.99322

Table 4.3.4 below shows a comparison of the binding affinities and the overall enhancement factor, β, which is comparing the calculated apparent K_d for the tetravalent CRD-saccharide binding against the monovalent CRD-glycan binding. These results show two notable findings. As seen before with the QD-saccharides, changing the sugar from a monosaccharide to a disaccharide mannose has caused a larger increase in the binding affinity with DC-SIGN, although the binding of DC-SIGN with the AuNP-Man also shows a significant improvement over the monovalent CRD across all of the glycan surface densities. As with the QDs this could come from the dimannose can bind to secondary site binding as well as primary sites.[19]

Table 4.3.4: Key parameters calculated for the AuNP-(EG$_n$-Man^s)$_m$ (where n= 1 or 2 and m= 1, 2 and 3, and s= 1 or 2) and their binding affinities with DC-SIGN.

AuNP	Glycan Valency (N)	Apparent K_d DC-SIGN (nM)	Enhancement Factor β*	β/N
AuNP-EG$_2$-Man	1099	21 ± 3	167, 000	152
AuNP-(EG$_2$-Man)$_2$	1912	28 ± 1	125, 000	65
AuNP-(EG-Man)$_3$	957	37 ± 1	95, 000	99
AuNP-EG$_2$-DiMan	1577	0.61 ± 0.3	1, 475, 000	935
AuNP-(EG$_2$-DiMan)$_2$	1164	1.91 ± 0.2	470, 000	404
AuNP-(EG-DiMan)$_3$	395	1.54 ± 0.3	580, 000	1468

*DC-SIGN/R affinity enhancement factor is calculated by: $\beta = \frac{K_{d(CRD-Glycan)}}{Apparent\ K_{d(DC-SIGN-QD)}}$ where K_d CRD-Man = 3.5 mM and K_d CRD-DiMan = 0.9 mM. [20]

Figure 4.3.3 shows the quenching efficiency for the DHLA-PEG ligand capped control AuNPs, which should not bind to DC-SIGN due to absence of glycan groups. The initial hypothesis is that there should be no fluorescence quenching observed. However, this hypothesis is only true for the lower concentrations of DC-SIGN with dimeric and trimeric PEG ligand, upon increasing the concentration a significant amount of fluorescence quenching is observed (**Figure 4.3.3**). This suggests the AuNPs and DC-SIGN are within close proximity to each other despite no binding between the ligand and the protein as quenching can occur though static, via binding, and dynamic interactions, via collision within solution. **Table 4.3.6** shows the summary of the fitting parameters for the control ligand binding curves. The binding curve could not be fitted to AuNP-(PEG_{750}-OMe)$_3$ as it did not converge correctly in the fitting programme.

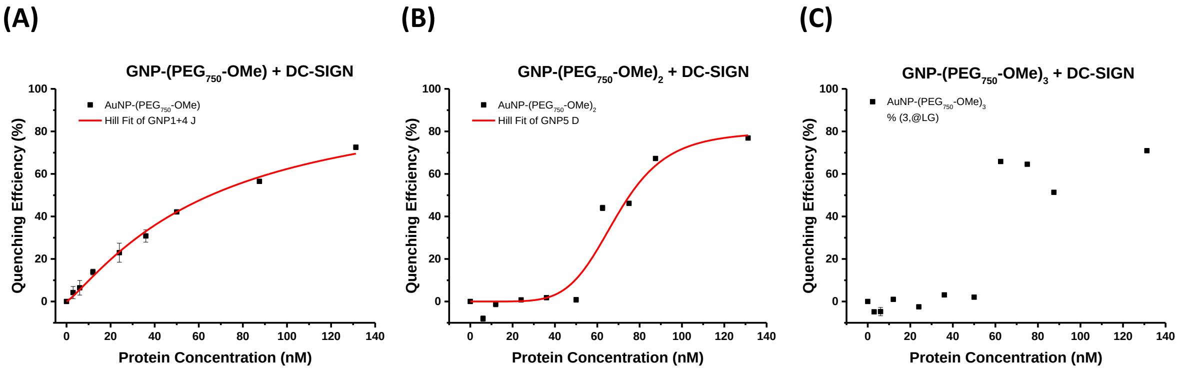

Figure 4.3.3: Percentage fluorescence quenching curves shown as a function of the protein concentration (DC-SIGN). (**A**) Control AuNP-(PEG_{750}-OMe), (**B**) Control AuNP-(PEG_{750}-OMe)$_2$ and (**C**) Control AuNP-(PEG_{750}-OMe)$_3$. Fitted using the Hill's equation.

Table 4.3.5: Summary of the fitting parameters for calculating the apparent K_d using the Hill Equation to fit the AuNP-(PEG_{750}-OMe)$_m$ DC-SIGN binding curves (**Figure 4.3.3**).

AuNP	R_{max}	Apparent K_d (nM)	n	R^2
AuNP-PEG_{750}-OMe	100	65 ± 1	1.2 ± 0.05	0.99984
AuNP-(PEG_{750}-OMe)$_2$	80	69 ± 2	5.8 ± 0.34	0.97822
AuNP-(PEG_{750}-OMe)$_3$	-	-	-	-

4.4 Fluorescence Quenching for AuNP-DC-SIGNR Conjugates

To determine the glycan-AuNP binding with DC-SIGNR, by fluorescence quenching, the fluorescence spectra over different protein concentrations have been recorded the same as that with DC-SIGN. In comparison to DC-SIGN we now use a protein: AuNP ratio of 5:1 as NP-glycan binding with DC-SIGNR is known to be weaker than that with DC-SIGN.[9] The samples were made up in the same HEPES buffer with BSA addition as those used with DC-SIGN. **Table 4.4.1** and **Table 4.4.2** below show the sample make up for the monosaccharide and disaccharide mannose AuNPs respectively.

Table 4.4.1: The concentrations and amounts of the differing components used for sample preparation of the fluorescence spectra used in the determination of the apparent K_d between AuNP(Man) and DC-SIGNR.

Tube	**AuNP (200 nM)**		**Protein (250 nM)**		**HEPES Buffer** (1 mg/ mL BSA)
	Conc (nM)	**vol (µL)**	**Conc (nM)**	**vol (µL)**	
0	0	0	0	0	400.00
6	4.8	9.6	24	38.40	352.00
8	19.2	38.4	96	153.60	208.00
9	28.8	57.6	144	230.40	112.00
10	40	80	200	320.00	0.00

Table 4.4.2: The concentrations and amounts of the differing components used for sample preparation of the fluorescence spectra used in the determination of the apparent K_d between AuNP(DiMan) and DC-SIGNR.

Tube	**AuNP (10 nM)**		**Protein (25 nM)**		**HEPES Buffer (1 mg/ mL BSA)**
	Conc (nM)	**vol (µL)**	**Conc (nM)**	**vol (µL)**	
0	0	0	0	0.00	400.00
2	0.4	16	2	32.00	352.00
3	0.8	32	4	64.00	304.00
4	1.8	72	9	144.00	184.00
Tube	**AuNP (200 nM)**		**Protein (250 nM)**		**HEPES Buffer (1 mg/ mL BSA)**
	Conc (nM)	**vol (µL)**	**Conc (nM)**	**vol (µL)**	
5	2.4	4.8	12	19.20	376.00
6	4.8	9.6	24	38.40	352.00
7	9.6	19.2	48	76.80	304.00
8	19.2	38.4	96	153.60	208.00
9	28.8	57.6	144	230.40	112.00
10	40	80	200	320.00	0.00

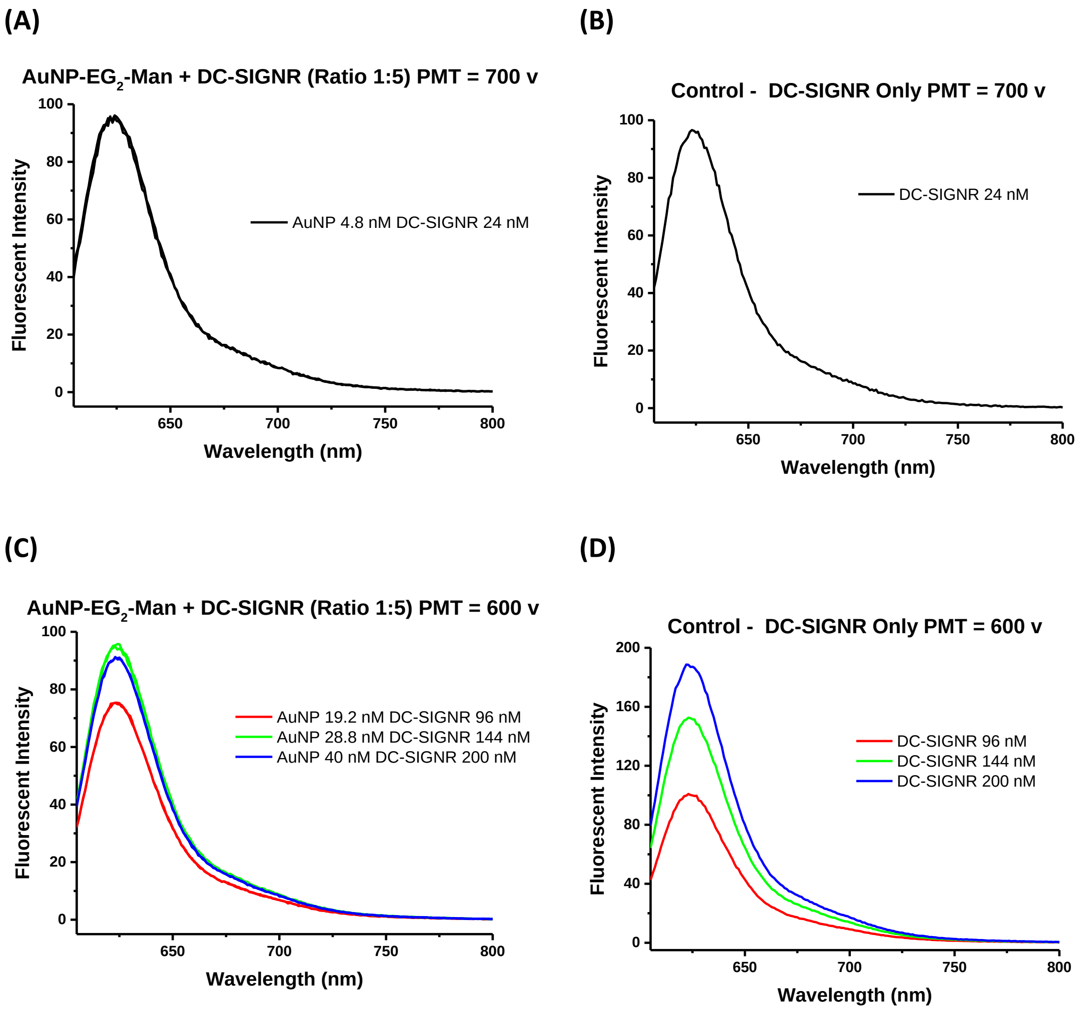

Figure 4.4.1: Fluorescence Measurements between 605 – 800 nm for **(A)** AuNP-EG$_2$-Man (4.8 nM) + labelled DC-SIGNR (24 nM), **(C)** AuNP-EG$_2$-Man (19.2 – 40 nM) + labelled DC-SIGNR (96 – 200 nM) and **(B)** and **(D)** Control samples where only labelled DC-SIGN was used at the same concentrations and the same machine settings.

4.4.1 Quenching Efficiency

The quenching efficiency was calculated using the same method as DC-SIGN. They were then plotted against protein concentration and fitted using the Hill equation to determine the binding affinities. The resulting binding curves are shown below in **Figure 4.4.2** and **Figure 4.4.3** for each series of ligands. The apparent K_d for each of the glycan-AuNPs with DC-SIGNR, with the fitting parameters can be seen in **Table 4.4.3** and **Table 4.4.4**.

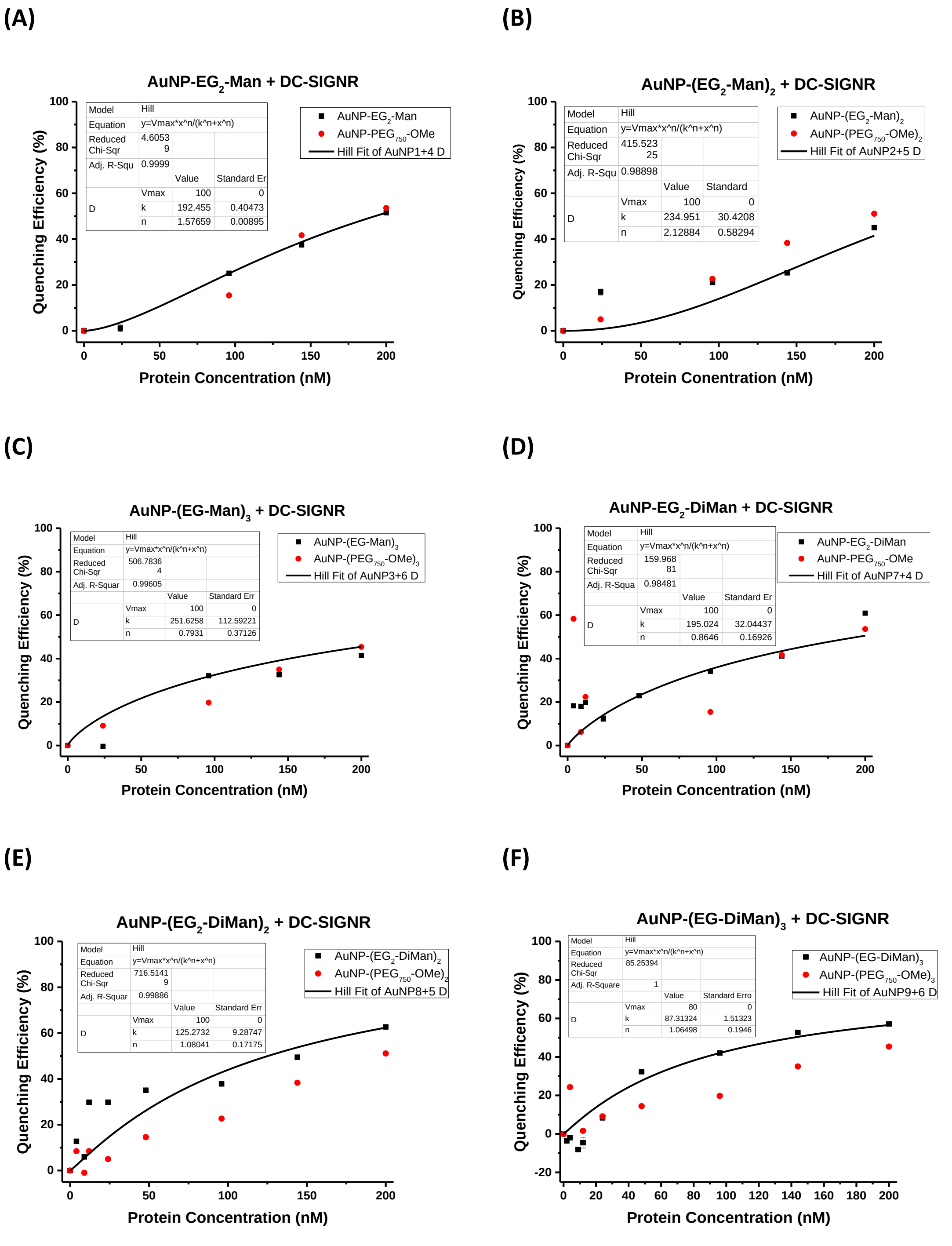

Figure 4.4.2: Percentage fluorescence quenching curves shown as a function of the protein concentration (DC-SIGNR). (**A**) AuNP-(EG$_2$-DiMan) and its control AuNP-PEG$_{750}$-OMe, (**B**) AuNP-(EG$_2$-DiMan)$_2$ and its control AuNP-(PEG$_{750}$-OMe)$_2$ and finally (**C**) AuNP-(EG-DiMan)$_3$ and its control AuNP-(PEG$_{750}$-OMe)$_3$. Fitted using the Hill's equation.

Table 4.4.3: Summary of the fitting parameters for calculating the apparent K_d using the Hill Equation to fit the AuNP-(EG_n-DiMan)$_m$ DC-SIGNR binding curve.

AuNP	R_{max}	Apparent K_d (nM)	n	R^2
AuNP-EG_2-Man	100	192 ± 0.4	1.6 ± 0.01	0.9999
AuNP-(EG_2-Man)$_2$	100	235 ± 30	2.1 ± 0.58	0.9890
AuNP-(EG-Man)$_3$	100	251 ± 113	0.8 ± 0.37	0.9961
AuNP-EG_2-DiMan	100	195 ± 32	0.9 ± 0.17	0.9848
AuNP-(EG_2-DiMan)$_2$	100	125 ± 9	1.1 ± 0.17	0.9989
AuNP-(EG-DiMan)$_3$	80	87 ± 2	1.1 ± 0.19	1

Further work still needs to be done to try to determine why we are getting non-specific binding within the monnosacchairde -DC-SIGNR interactions. The age of the protein is not the cause of these quenching effects as some of these experiments were done with fresh protein. It may due to the weaker nature of the sugar-CRD interaction we may need to lower the maximum quenching threshold in curve fitting or increase the number of data points to include higher protein concentrations to witness the true saturation of the titration binding curves. Another observation is that the binding affinities for the monomeric to the PEG controls the monosaccharide and disaccharide ligands appear to be similar and comparable suggesting that most quenching maybe caused by the non-specific interactions. These results were different from the QD series in that the values are significantly higher and the monomeric dimannose ligand doesn’t have a similar binding constant.

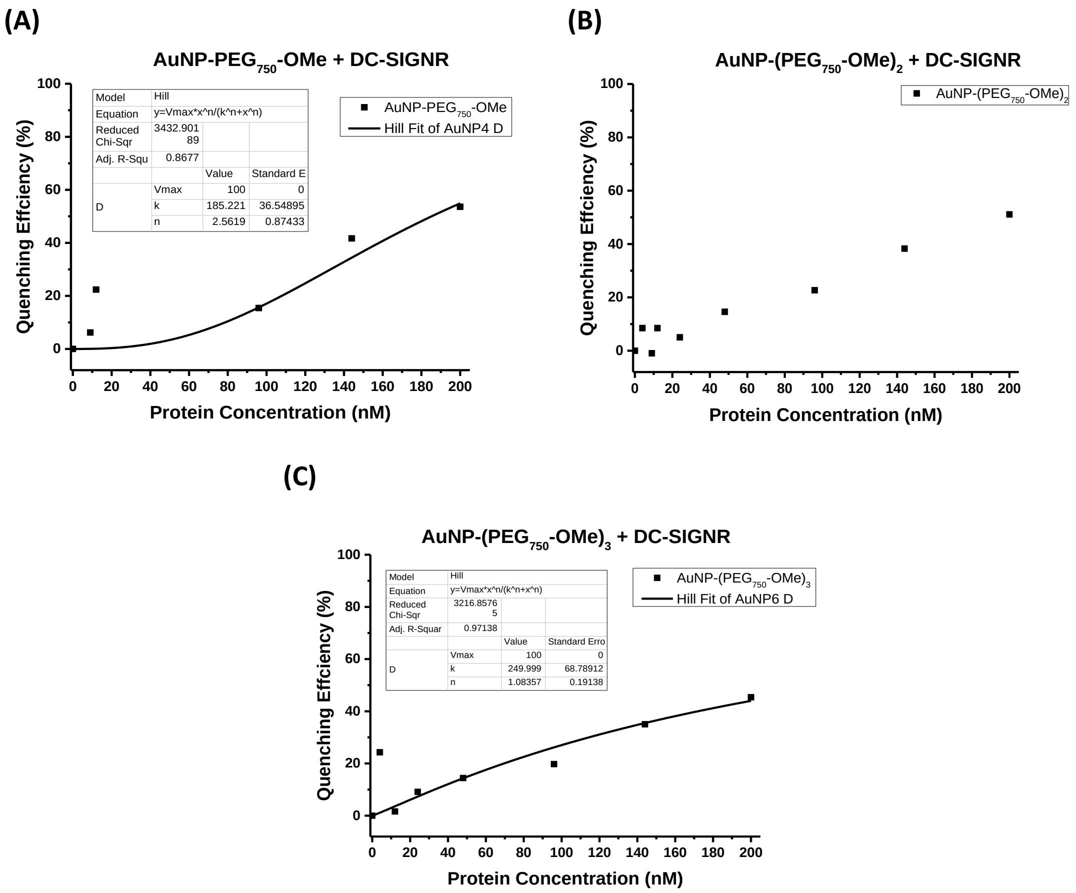

Figure 4.4.3: Percentage fluorescence quenching curves shown as a function of the protein concentration (DC-SIGNR). (**A**) Control AuNP-(PEG$_{750}$-OMe), (**B**) Control AuNP-(PEG$_{750}$-OMe)$_2$ and (**C**) Control AuNP-(PEG$_{750}$-OMe)$_3$. Fitted using the Hill's equation.

Table 4.4.4: Summary of the fitting parameters for calculating the apparent K$_d$ using the Hill Equation to fit the AuNP-(PEG$_{750}$-OMe)$_m$ DC-SIGN binding curves (**Figure 4.4.3**).

AuNP	R$_{max}$	Apparent K$_d$ (nM)	n	R^2
AuNP-PEG$_{750}$-OMe	100	185 ± 37	2.6 ± 0.87	0.8677
AuNP-(PEG$_{750}$-OMe)$_2$	-	-	-	-
AuNP-(PEG$_{750}$-OMe)$_3$	100	250 ± 69	1.1 ± 0.19	0.9714

In comparison to the controls with DC-SIGN there appears to be an increase in the non-specific interactions with DC-SIGNR. A steady increase of fluorescence quenching is observed with the increasing protein concentration even with the branched PEGlyated ligands which is different from that of DC-SIGN where quenching only occurred at high concentrations. Further investigations will be needed to investigate why more non-specific absorptions occur between the AuNP and DC-SIGNR.

4.5 Hydrodynamic Size Investigations of Glycan AuNPs-Protein

To further confirm the differences in binding modes in DC-SIGN/R[9], the hydrodynamic sizes of the new series of AuNPs with the increase in surface glycan density were investigated. This was done with a fixed 25 nM AuNP and mixed with different amounts of both DC-SIGN and DC-SIGNR (wild-type) in accordance to a specific AuNP: Protein ratio. All of the AuNPs, both monosaccharides and disaccharides, were tested against the wild-type proteins. If they do follow the same binding pattern as before then we should see an increase in particle size in the presence of DC-SIGNR due to the crosslinking effect. D_h sizes should be similar to those seen for the QD-EG_n-Man^m, ~41 nm with DC-SIGN and two distinct bands at ~130 and ~210 nm for DC-SIGNR, as the particles are of similar size. On the other hand, we did not expect to see any particle size changes with the monosaccharide AuNPs in the presence of DC-SIGNR as no significant binding was found in previous work.[9]

4.5.1 DC-SIGN/R Only

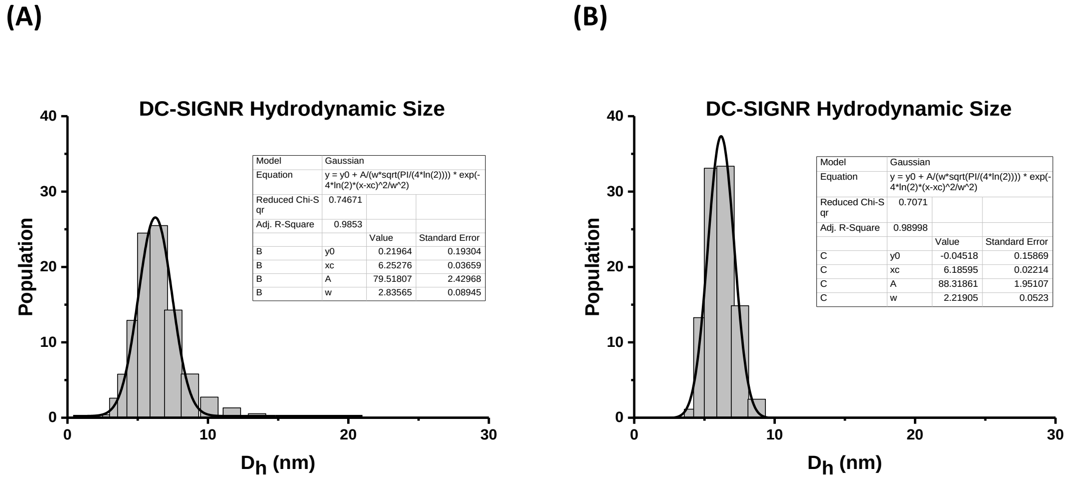

Model	Gaussian		
Equation	y = y0 + A/(w*sqrt(PI/(4*ln(2)))) * exp(-4*ln(2)*(x-xc)^2/w^2)		
Reduced Chi-Sqr	0.74671		
Adj. R-Square	0.9853		
		Value	Standard Error
B	y0	0.21964	0.19304
B	xc	6.25276	0.03659
B	A	79.51807	2.42968
B	w	2.83565	0.08945

Model	Gaussian		
Equation	y = y0 + A/(w*sqrt(PI/(4*ln(2)))) * exp(-4*ln(2)*(x-xc)^2/w^2)		
Reduced Chi-Sqr	0.7071		
Adj. R-Square	0.98998		
		Value	Standard Error
C	y0	-0.04518	0.15869
C	xc	6.18595	0.02214
C	A	88.31861	1.95107
C	w	2.21905	0.0523

Figure 4.5.1: Shows the resulting histograms of the range of hydrodynamic size for the proteins **(A)** DC-SIGN and **(B)** DC-SIGNR at a concentration of 20 nM.

The results obtained at an AuNP: Protein molar ratio of 1:15 show some inconclusive results. As most of the results show just the hydrodynamic size of the protein suggesting that the ratio of protein to AuNP is too high. However they do further confirm that the monosaccharide ligand series does not bind with DC-SIGNR as we just see the D_h of the protein and not the conjugates. The formation of the crosslinked aggregates with larger sizes for AuNP-DiMan + DC-SIGNR can begin to be seen. In order to get a better representation the experiment was repeated using a lower AuNP: Protein ratio of 1:7.5 to reduce the excess protein. This time the monosaccharide ligand series with DC-SIGNR was not repeated as we had already shown non-binding. The results here seemed to show some conclusive evidence of binding with DC-SIGN however again the protein peaks only for DC-SIGNR are seen. The AuNP: protein ratio was then lowered again to

1:3.75 and the results become much clearer in the changes of D_h with DC-SIGNR. Thus the ideal ratio for each protein is shown below in **Figure 4.5.2** and **Figure 4.5.3** with the other data being found in the **Appendix Chapter**. Summaries of all the data using all three ratios can be seen in both

Table 4.5.1 and **Table 4.5.2** below. The data were still inconclusive for the AuNP-DC-SIGN conjugates and further measurement by cryo-TEM would help confirm these.

4.5.2 DC-SIGN (AuNP: Protein Ratio, 1: 7.5)

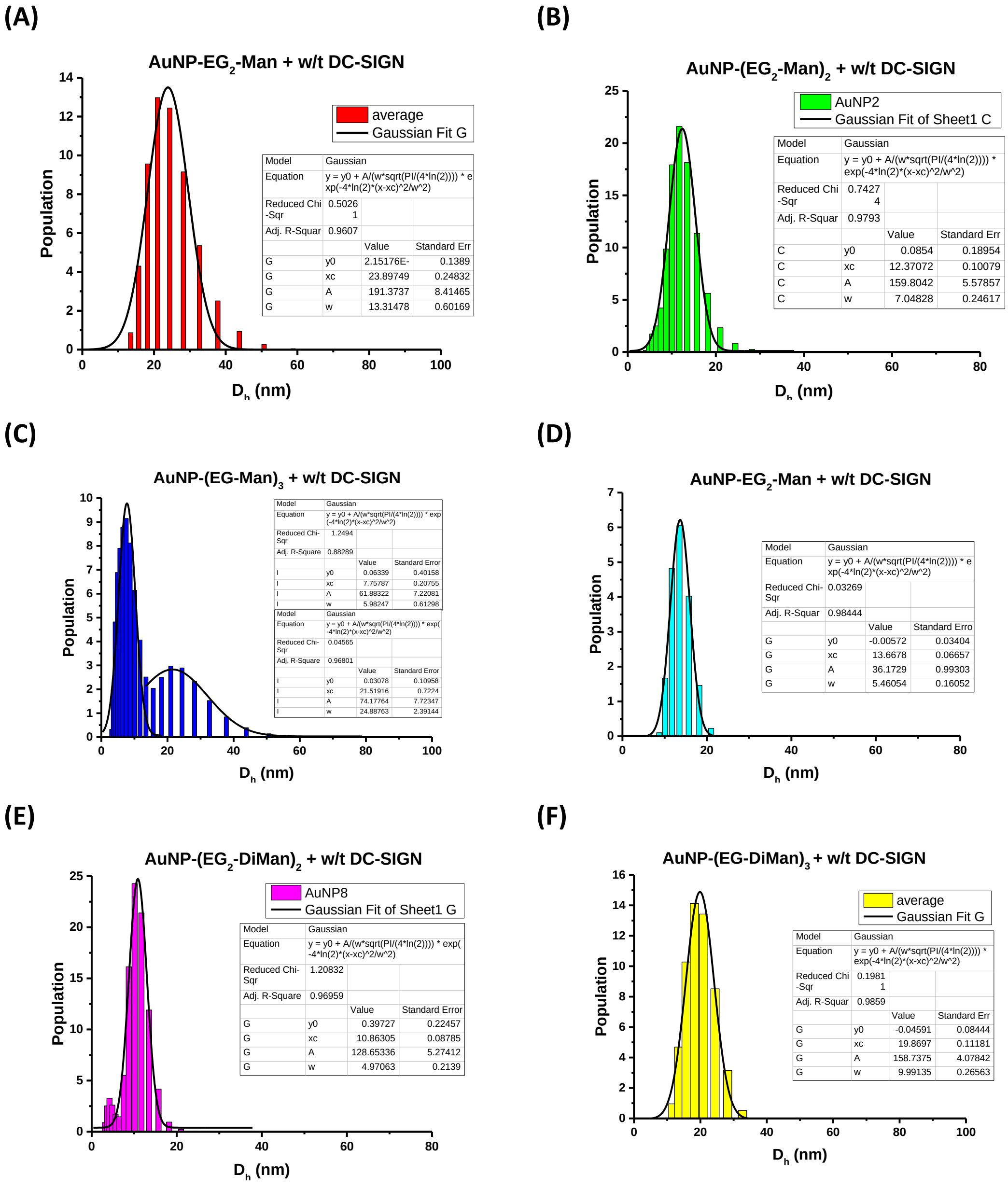

Model	Gaussian		
Equation	y = y0 + A/(w*sqrt(PI/(4*ln(2)))) * exp(-4*ln(2)*(x-xc)^2/w^2)		
Reduced Chi-Sqr	0.50261		
Adj. R-Squar	0.9607		
		Value	Standard Err
G	y0	2.15176E-	0.1389
G	xc	23.89749	0.24832
G	A	191.3737	8.41465
G	w	13.31478	0.60169

Model	Gaussian		
Equation	y = y0 + A/(w*sqrt(PI/(4*ln(2)))) * exp(-4*ln(2)*(x-xc)^2/w^2)		
Reduced Chi-Sqr	0.74274		
Adj. R-Squar	0.9793		
		Value	Standard Err
C	y0	0.0854	0.18954
C	xc	12.37072	0.10079
C	A	159.8042	5.57857
C	w	7.04828	0.24617

Model	Gaussian		
Equation	y = y0 + A/(w*sqrt(PI/(4*ln(2)))) * exp(-4*ln(2)*(x-xc)^2/w^2)		
Reduced Chi-Sqr	1.2494		
Adj. R-Square	0.88289		
		Value	Standard Error
I	y0	0.06339	0.40158
I	xc	7.75787	0.20755
I	A	61.88322	7.22081
I	w	5.98247	0.61298

Model	Gaussian		
Equation	y = y0 + A/(w*sqrt(PI/(4*ln(2)))) * exp(-4*ln(2)*(x-xc)^2/w^2)		
Reduced Chi-Sqr	0.04565		
Adj. R-Square	0.96801		
		Value	Standard Error
I	y0	0.03078	0.10958
I	xc	21.51916	0.7224
I	A	74.17764	7.72347
I	w	24.88763	2.39144

Model	Gaussian		
Equation	y = y0 + A/(w*sqrt(PI/(4*ln(2)))) * exp(-4*ln(2)*(x-xc)^2/w^2)		
Reduced Chi-Sqr	0.03269		
Adj. R-Squar	0.98444		
		Value	Standard Erro
G	y0	-0.00572	0.03404
G	xc	13.6678	0.06657
G	A	36.1729	0.99303
G	w	5.46054	0.16052

Model	Gaussian		
Equation	y = y0 + A/(w*sqrt(PI/(4*ln(2)))) * exp(-4*ln(2)*(x-xc)^2/w^2)		
Reduced Chi-Sqr	1.20832		
Adj. R-Square	0.96959		
		Value	Standard Error
G	y0	0.39727	0.22457
G	xc	10.86305	0.08785
G	A	128.65336	5.27412
G	w	4.97063	0.2139

Model	Gaussian		
Equation	y = y0 + A/(w*sqrt(PI/(4*ln(2)))) * exp(-4*ln(2)*(x-xc)^2/w^2)		
Reduced Chi-Sqr	0.19811		
Adj. R-Squar	0.9859		
		Value	Standard Err
G	y0	-0.04591	0.08444
G	xc	19.8697	0.11181
G	A	158.7375	4.07842
G	w	9.99135	0.26563

Figure 4.5.2: Shows the resulting histograms of the range of hydrodynamic size for glycan AuNP- DC-SIGN interactions, using **(A)** AuNP-EG$_2$-Man, **(B)** AuNP-(EG$_2$-Man)$_2$, **(C)** AuNP-(EG-Man)$_3$, **(D)** AuNP-EG$_2$-DiMan, **(E)** AuNP-(EG$_2$-DiMan)$_2$ and **(F)** AuNP-(EG-DiMan)$_3$.

4.5.3 DC-SIGNR (AuNP: Protein Ratio, 1: 3.75)

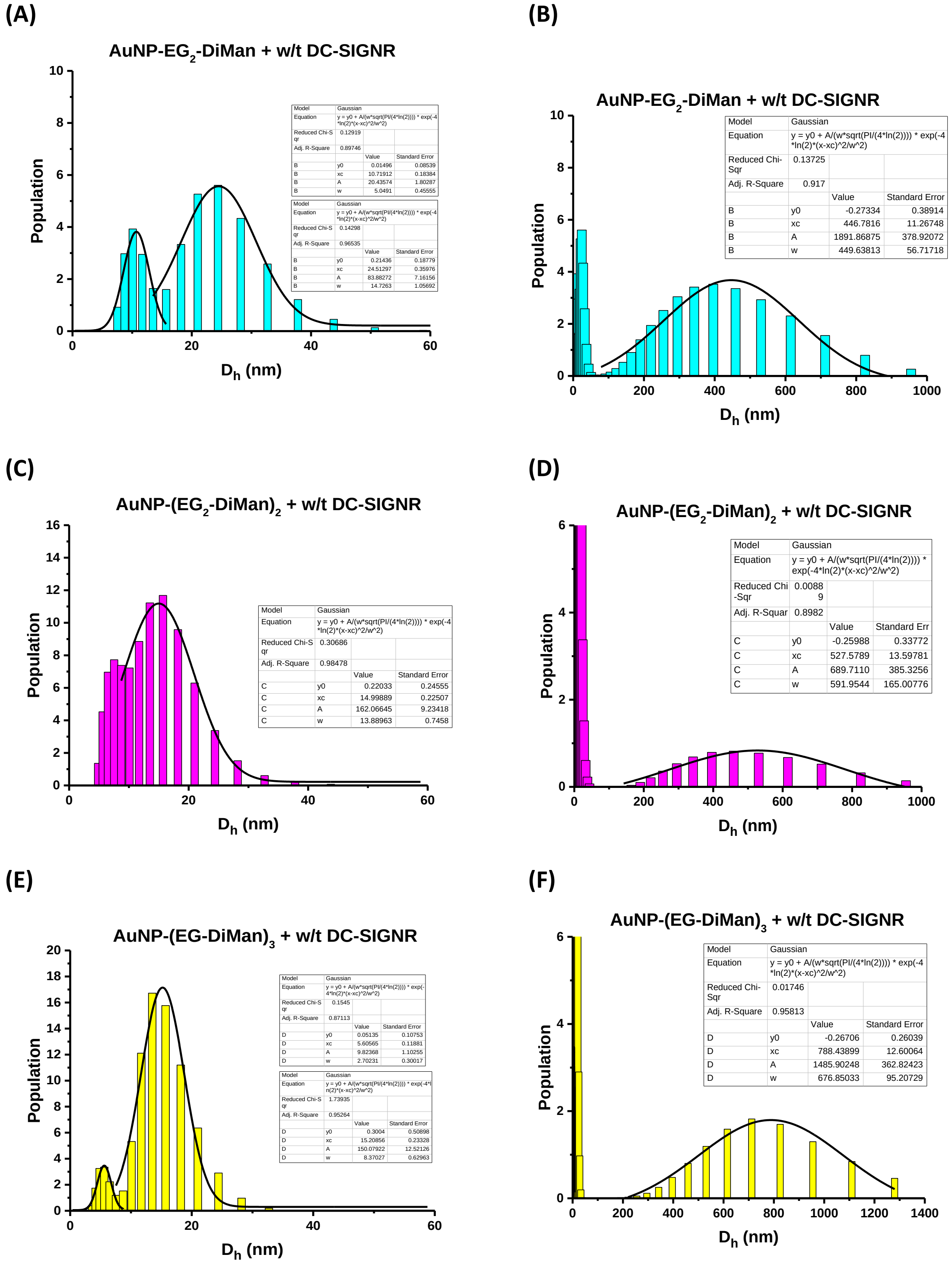

(A)

Model	Gaussian		
Equation	y = y0 + A/(w*sqrt(PI/(4*ln(2)))) * exp(-4*ln(2)*(x-xc)^2/w^2)		
Reduced Chi-Sqr	0.12919		
Adj. R-Square	0.89746		
		Value	Standard Error
B	y0	0.01496	0.08539
B	xc	10.71912	0.18384
B	A	20.43574	1.80287
B	w	5.0491	0.45555

Model	Gaussian		
Equation	y = y0 + A/(w*sqrt(PI/(4*ln(2)))) * exp(-4*ln(2)*(x-xc)^2/w^2)		
Reduced Chi-Sqr	0.14298		
Adj. R-Square	0.96535		
		Value	Standard Error
B	y0	0.21436	0.18779
B	xc	24.51297	0.35976
B	A	83.88272	7.16156
B	w	14.7263	1.05692

(B)

Model	Gaussian		
Equation	y = y0 + A/(w*sqrt(PI/(4*ln(2)))) * exp(-4*ln(2)*(x-xc)^2/w^2)		
Reduced Chi-Sqr	0.13725		
Adj. R-Square	0.917		
		Value	Standard Error
B	y0	-0.27334	0.38914
B	xc	446.7816	11.26748
B	A	1891.86875	378.92072
B	w	449.63813	56.71718

(C)

Model	Gaussian		
Equation	y = y0 + A/(w*sqrt(PI/(4*ln(2)))) * exp(-4*ln(2)*(x-xc)^2/w^2)		
Reduced Chi-Sqr	0.30686		
Adj. R-Square	0.98478		
		Value	Standard Error
C	y0	0.22033	0.24555
C	xc	14.99889	0.22507
C	A	162.06645	9.23418
C	w	13.88963	0.7458

(D)

Model	Gaussian		
Equation	y = y0 + A/(w*sqrt(PI/(4*ln(2)))) * exp(-4*ln(2)*(x-xc)^2/w^2)		
Reduced Chi-Sqr	0.00889		
Adj. R-Squar	0.8982		
		Value	Standard Err
C	y0	-0.25988	0.33772
C	xc	527.5789	13.59781
C	A	689.7110	385.3256
C	w	591.9544	165.00776

(E)

Model	Gaussian		
Equation	y = y0 + A/(w*sqrt(PI/(4*ln(2)))) * exp(-4*ln(2)*(x-xc)^2/w^2)		
Reduced Chi-Sqr	0.1545		
Adj. R-Square	0.87113		
		Value	Standard Error
D	y0	0.05135	0.10753
D	xc	5.60565	0.11881
D	A	9.82368	1.10255
D	w	2.70231	0.30017

Model	Gaussian		
Equation	y = y0 + A/(w*sqrt(PI/(4*ln(2)))) * exp(-4*ln(2)*(x-xc)^2/w^2)		
Reduced Chi-Sqr	1.73935		
Adj. R-Square	0.95264		
		Value	Standard Error
D	y0	0.3004	0.50898
D	xc	15.20856	0.23328
D	A	150.07922	12.52126
D	w	8.37027	0.62963

(F)

Model	Gaussian		
Equation	y = y0 + A/(w*sqrt(PI/(4*ln(2)))) * exp(-4*ln(2)*(x-xc)^2/w^2)		
Reduced Chi-Sqr	0.01746		
Adj. R-Square	0.95813		
		Value	Standard Error
D	y0	-0.26706	0.26039
D	xc	788.43899	12.60064
D	A	1485.90248	362.82423
D	w	676.85033	95.20729

Figure 4.5.3: Shows the resulting histograms of the range of hydrodynamic size for glycan AuNP- DC-SIGNR interactions, using a 1:3.75 AuNP: Protein ratio: **(A and B)** AuNP-EG_2-DiMan, **(C and D)** AuNP-(EG_2-DiMan)$_2$ and **(E and F)** AuNP-(EG-DiMan)$_3$.

Table 4.5.1: Summary of the hydrodynamic sizes for the AuNP conjugates and DC-SIGN.

	D_h (nm) *[% of Area]*

	1:15	1:7.5	1.3.75
AuNP-EG$_2$-Man	A = 7.1 ± 0.1 [*54 %*] B = 20.3 ± 0.3 [*46 %*]	A = 23.9 ± 0.2 [*100 %*]	A = 9.5 ± 0.2 [*33 %*] B = 17.2 ± 0.4 [*67 %*]
AuNP-(EG$_2$-Man)$_2$	A = 7.2 ± 0.1 [*100 %*]	A = 12.4 ± 0.1 [*100 %*]	A = 10.6 ± 0.1 [*100 %*]
AuNP-(EG-Man)$_3$	A = 7.7 ± 0.1 [*100 %*]	A = 7.8 ± 0.2 [*46 %*] B = 21.5 ± 0.7 [*55 %*]	A = 10.9 ± 0.1 [*100 %*]
AuNP-EG$_2$-DiMan	A = 7.8 ± 0.1 [*76 %*] B = 31.0 ± 0.7 [*24 %*]	A = 13.7 ± 0.1 [*100 %*]	A = 10.4 ± 0.1 [*100 %*]
AuNP-(EG$_2$-DiMan)$_2$	A = 6.8 ± 0.1 [*100 %*]	A = 10.9 ± 0.1 [*100 %*]	A = 9.6 ± 0.1 [*100 %*]
AuNP-(EG-DiMan)$_3$	A = 14.3 ± 0.2 [*100 %*]	A = 19.9 ± 0.1 [*100 %*]	A = 10.8 ± 0.1[*100 %*]

Table 4.5.2: Summary of the hydrodynamic sizes for the AuNP conjugates and DC-SIGNR.

	D_h (nm)		
	1:15	1:7.5	1.3.75
AuNP-EG$_2$-Man	A = 8.1 ± 0.1 [*100 %*]	-	-
AuNP-(EG$_2$-Man)$_2$	A = 7.7 ± 0.1 [*100 %*]	-	-
AuNP-(EG-Man)$_3$	A = 7.6 ± 0.1 [*100 %*]	-	-
AuNP-EG$_2$-DiMan	A = 7.2 ± 0.1 [*0.6 %*] B = 29.6 ± 0.7 [*0.7 %*] C = 537 ± 7 [*99 %*]	A = 8.0 ± 0.1 [*1.2 %*] B = 39.1 ± 2.6 [*0.1 %*] C = 488 ± 8 [*99 %*]	A = 10.7 ± 0.2 [*1 %*] B = 24.5 ± 0.4 [*4 %*] C = 446 ± 11 [*95 %*]
AuNP-(EG$_2$-DiMan)$_2$	A = 8.9 ± 0.3 [*1 %*] B = - C = 651 ± 5 [*99 %*]	A = 7.6 ± 0.1 [*100 %*]	A = 10.7 ± 0.2 [*13 %*] B = 24.5 ± 0.4 [*17 %*] C = 527 ± 14 [*70 %*]
AuNP-(EG-DiMan)$_3$	A = 8.2 ± 0.1 [*100 %*]	A = 9.5 ± 0.1 [*100 %*]	A = 5.6 ± 0.1 [*0.6 %*] B = 15.2 ± 0.2 [*9 %*] C = 788 ± 13 [*90 %*]

4.6 Further Investigations into Binding of Control Nanoparticles with DC-SIGN

Upon investigating the inert control AuNPs (AuNP-(PEG$_{750}$-OMe)$_m$ where m= 1, 2 and 3) interaction with DC-SIGN an unexpected observation was made (**Figure 4.3.3**). Above a threshold protein concentration, 50 nM, fluorescence quenching of the labelled DC-SIGN was observed, (**Figure 4.3.3**). This phenomenon however was not observed when investigating these AuNPs with DC-SIGNR as only a maximum of 40 % quenching was ever observed. DC-SIGN/R however were not expected to bind to such PEGylated surface ligands on the AuNPs as many publications have shown the proteins specificity for glycans.[21, 22] Fluorescence quenching usually comes from an energy transfer from a fluorescence donor to a fluorescence quencher when they are in close proximity to each other, which is observed through the glycan-protein interaction. So this shows that the protein and AuNPs must be in close proximity with each other without being chemically bound at these high protein concentrations. A hypothesis for this is the formation of a protein corona around the AuNP as shown in work first published by Monopoli *et al.*.[23] It has since become well established that protein coronas form around AuNPs.[24, 25] A protein corona is a biological coating around NPs formed within biological media due to the high surface free energy of the NPs.[26] The corona is split into two shells surrounding the NP with the inner shell, hard corona, where the proteins have high affinity therefore are strongly bound and the outer shell, soft corona, where the proteins have a low affinity and are weakly bound. This can be seen in the schematic below, **Figure 4.6.1**.

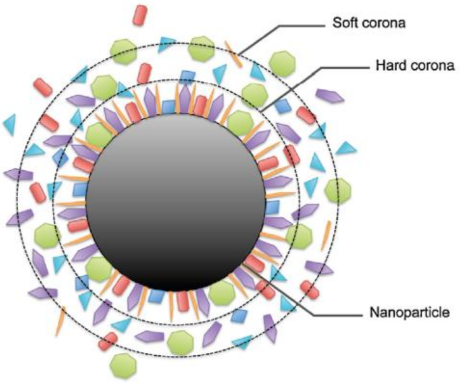

Figure 4.6.1: A schematic of a protein corona proposed by Wolfram *et al.*.[25] Taken from reference.

To investigate this phenomenon further, studies were done to test particle size in solution using DLS and UV/Vis methods. The same experimental procedure as that used in determining the binding dissociation constant (**Chapter 4.3**) were performed to see if this quenching was observed at high protein concentrations for other proteins or if it was just a coincidence with this particular ligand series.

4.6.1 Particle Size Investigations

DLS investigations were performed to show the size of the particles within the buffer solution to see whether a protein corona is formed at high concentrations. Protein concentrations were selected from the quenching efficiency curves for AuNP-$(PEG_{750}\text{-}OMe)_m$ (where m=2 and 3) and

DC-SIGN (**Figure 4.3.3**) just before and then after the quenching was observed. The same AuNP: Protein ratio, 1:1.25, was used for sample preparation for DLS. The resulting histograms for the D_h's for each of the samples are shown below in **Figure 4.6.2** for both AuNPs with the wild-type protein. This can then be compared to the protein only size, 7.3 ± 0.07 nm, as well as the AuNPs only size, 10.8 ± 0.1 and 14.9 ± 0.3 nm for AuNP-(PEG$_{750}$-OMe)$_m$ (where m=2 and 3) respectively.

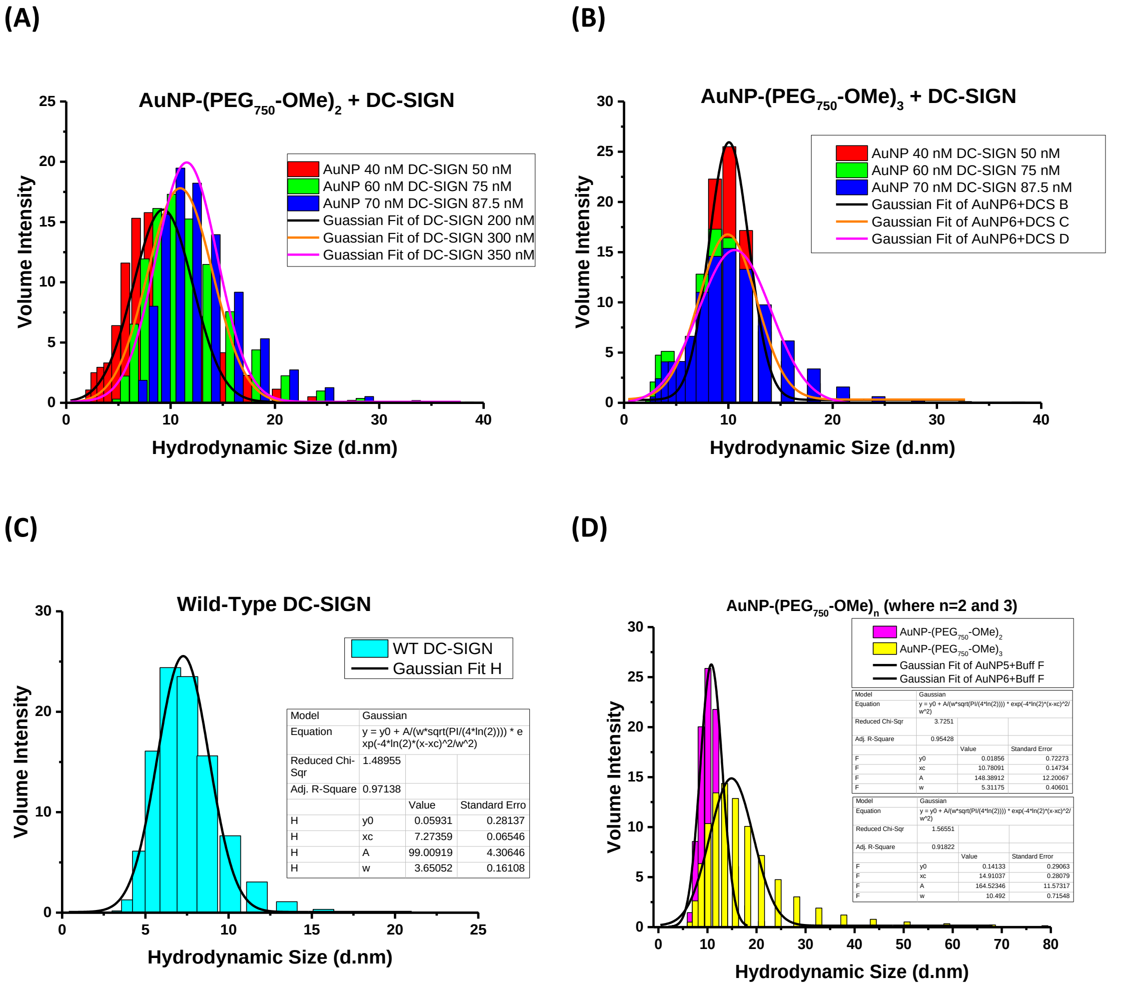

Model	Gaussian		
Equation	y = y0 + A/(w*sqrt(PI/(4*ln(2)))) * exp(-4*ln(2)*(x-xc)^2/w^2)		
Reduced Chi-Sqr	1.48955		
Adj. R-Square	0.97138		
		Value	Standard Erro
H	y0	0.05931	0.28137
H	xc	7.27359	0.06546
H	A	99.00919	4.30646
H	w	3.65052	0.16108

Model	Gaussian		
Equation	y = y0 + A/(w*sqrt(PI/(4*ln(2)))) * exp(-4*ln(2)*(x-xc)^2/w^2)		
Reduced Chi-Sqr	3.7251		
Adj. R-Square	0.95428		
		Value	Standard Error
F	y0	0.01856	0.72273
F	xc	10.78091	0.14734
F	A	148.38912	12.20067
F	w	5.31175	0.40601

Model	Gaussian		
Equation	y = y0 + A/(w*sqrt(PI/(4*ln(2)))) * exp(-4*ln(2)*(x-xc)^2/w^2)		
Reduced Chi-Sqr	1.56551		
Adj. R-Square	0.91822		
		Value	Standard Error
F	y0	0.14133	0.29063
F	xc	14.91037	0.28079
F	A	164.52346	11.57317
F	w	10.492	0.71548

Figure 4.6.2: Hydrodynamic size for **(A)** AuNP-(PEG$_{750}$-OMe)$_2$ + DC-SIGN at increasing concentrations, **(B)** AuNP-(PEG$_{750}$-OMe)$_3$ + DC-SIGN at increasing concentrations but with a constant AuNP: DC-SIGN ratio of 1:1.25, **(C)** wild-type DC-SIGN only and **(D)** AuNPs only.

Table 4.6.1: Summary of the hydrodynamic sizes for PEGlyated control AuNPs mixed with wild-type DC-SIGN at varying concentrations determined by DLS.

AuNP and Protein	Hydrodynamic Size (nm)	FWHM (nm)	R^2

AuNP-(PEG$_{750}$-OMe)$_2$ (40 nM) + DC-SIGN (50 nM)	9.3 ± 0.1	6.7 ± 0.4	0.9506
AuNP-(PEG$_{750}$-OMe)$_2$ (60 nM) + DC-SIGN (75 nM)	10.9 ± 0.2	7.3 ± 0.5	0.9384
AuNP-(PEG$_{750}$-OMe)$_2$ (70 nM) + DC-SIGN (87.5 nM)	11.6 ± 0.9	6.9 ± 0.4	0.9330
AuNP-(PEG$_{750}$-OMe)$_3$ (40 nM) + DC-SIGN (50 nM)	10.1 ± 0.1	4.5 ± 0.2	0.9752
AuNP-(PEG$_{750}$-OMe)$_3$ (60 nM) + DC-SIGN (75 nM)	9.9 ± 0.2	6.5 ± 0.5	0.9247
AuNP-(PEG$_{750}$-OMe)$_3$ (70 nM) + DC-SIGN (87.5 nM)	10.6 ± 0.2	8.2 ± 0.4	0.9651

Table 4.6.1 shows that there is a slight increase in size with increasing the protein concentration for AuNP-(PEG$_{750}$-OMe)$_2$ only but there little difference is seen for AuNP-(PEG$_{750}$-OMe)$_3$ (**Figure 4.2.3**) and so does not give a conclusive result. There is also a small decrease in size from the initial AuNPs, as this is a new batch of the AuNPs this could account for this difference. These results suggest that there is no protein corona formed as the D_h of the AuNPs did not change.

4.6.2 UV/Vis Investigations

UV/Vis investigations were performed to test the stability of the particles and to check whether aggregation was the cause of fluorescence quenching observed with the AuNP controls at higher concentrations (>50 nM). **Figure 4.6.3** below shows the background corrected UV/Vis samples over a range of high protein concentrations for AuNP-(PEG$_{750}$-OMe)$_n$ (where n= 2 and 3). As labelled protein has been used we also observe a small shoulder at around 600 nm. It has been shown that upon formation of a protein corona the absorption maxima of the AuNPs are red shifted.[24, 27] In the case of our AuNPs a small blue shift is witnessed upon increasing the protein concentration. A clear blue shift in the absorption maxima can be seen between the AuNPs before and after ligand exchange, suggesting that UV/Vis could be a method for determining successful ligand exchange. The results suggest no formation of a protein corona at high protein concentrations, but that something is occurring due to the blue shift present as well as the decrease in absorption maxima upon increasing concentration. An interesting observation, occurring for both AuNPs, is that at higher concentrations of AuNPs the linear relationship of absorption and concentration becomes non-linear (**Figure 4.6.3 (C)**). Future investigations are needed to investigate the reason for this.

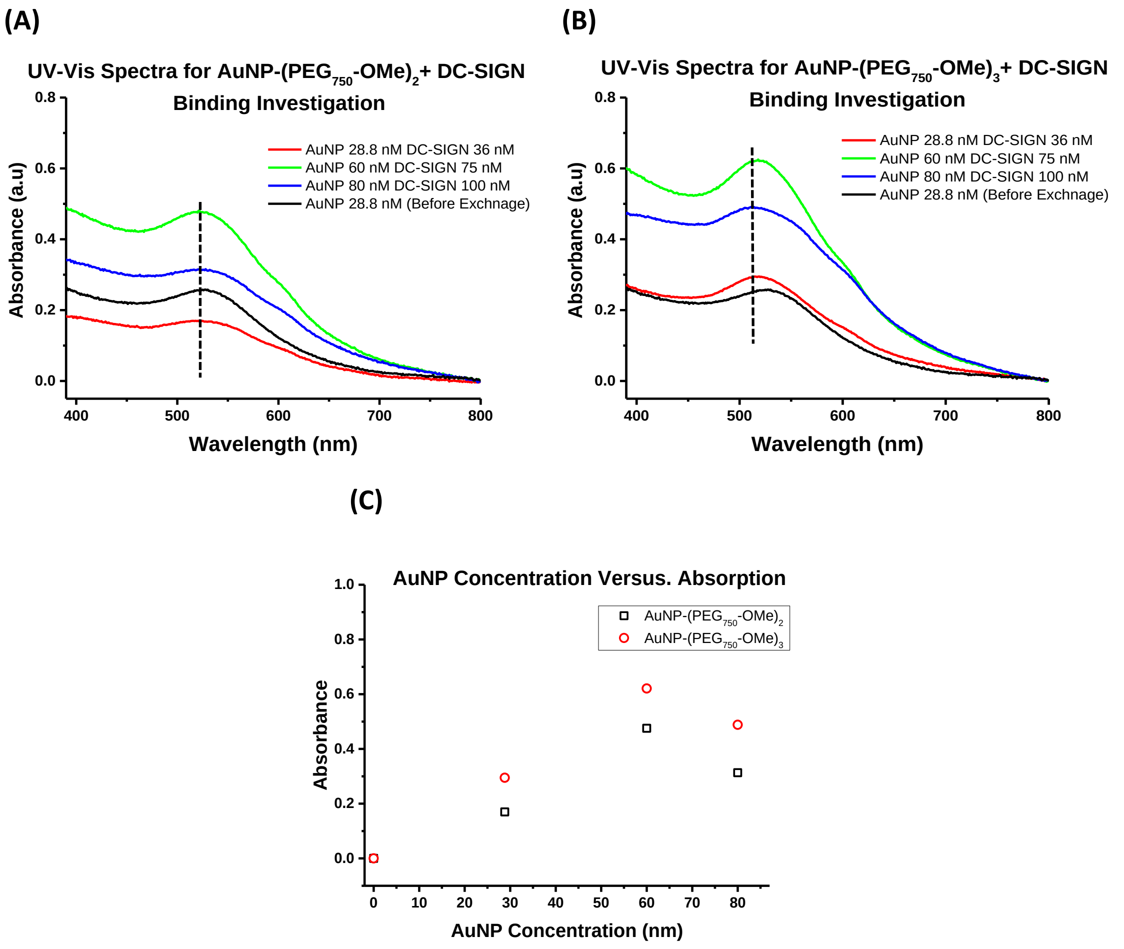

Figure 4.6.3: UV-Vis spectra (400 – 800 nm) of **(A)** AuNP-(PEG$_{750}$-OMe)$_2$ + DC-SIGN at varying concentrations, **(B)** AuNP-(PEG$_{750}$-OMe)$_3$ + DC-SIGN at varying concentrations both with a constant AuNP: DC-SIGN ratio of 1:1.25. Plus a sample run of the AuNPs before ligand exchange. **(C)** The respective AuNP concentrations verses absorption (A = 515 nm) for both **(A)** and **(B)** respectively.

4.6.3 Investigations of Different BSA Concentrations

It was found that the major protein within a protein corona is serum albumin by Garcia-Alvarez *et al.*[25] Investigations were performed to try to inhibit non-specific AuNP-DC-SIGN binding by adding bovine serum albumin, BSA, to form a protein corona over DC-SIGN to block non-specific binding with the controls. As it was found that during the initial glycan-AuNP DC-SIGN/R binding experiments there was a lower amount of BSA present at the higher protein concentrations where more quenching was observed. A schematic of the formation of the BSA protein corona to block non-specific binding is shown in **Figure 4.6.4** below.

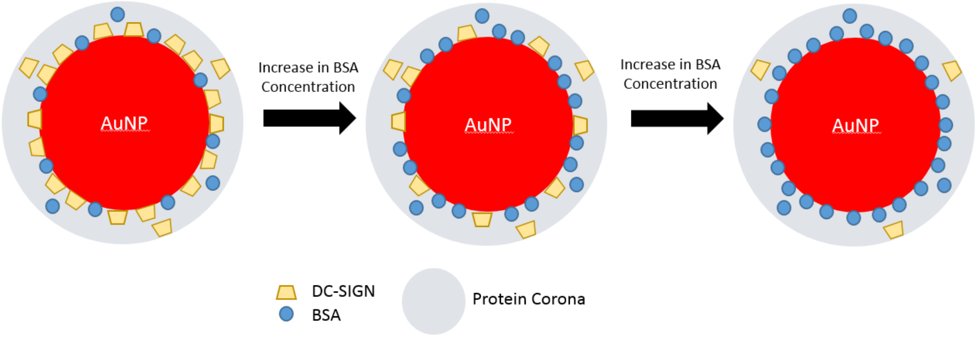

Figure 4.6.4: A schematic showing the expected hypothetical changes to try and reduce non-specific quenching observed between AuNP-(PEG$_{750}$-OMe)$_n$ (where n= 2 and 3) + DC-SIGN by increasing BSA concentration to form a BSA only corona. Sizes are not to scale.

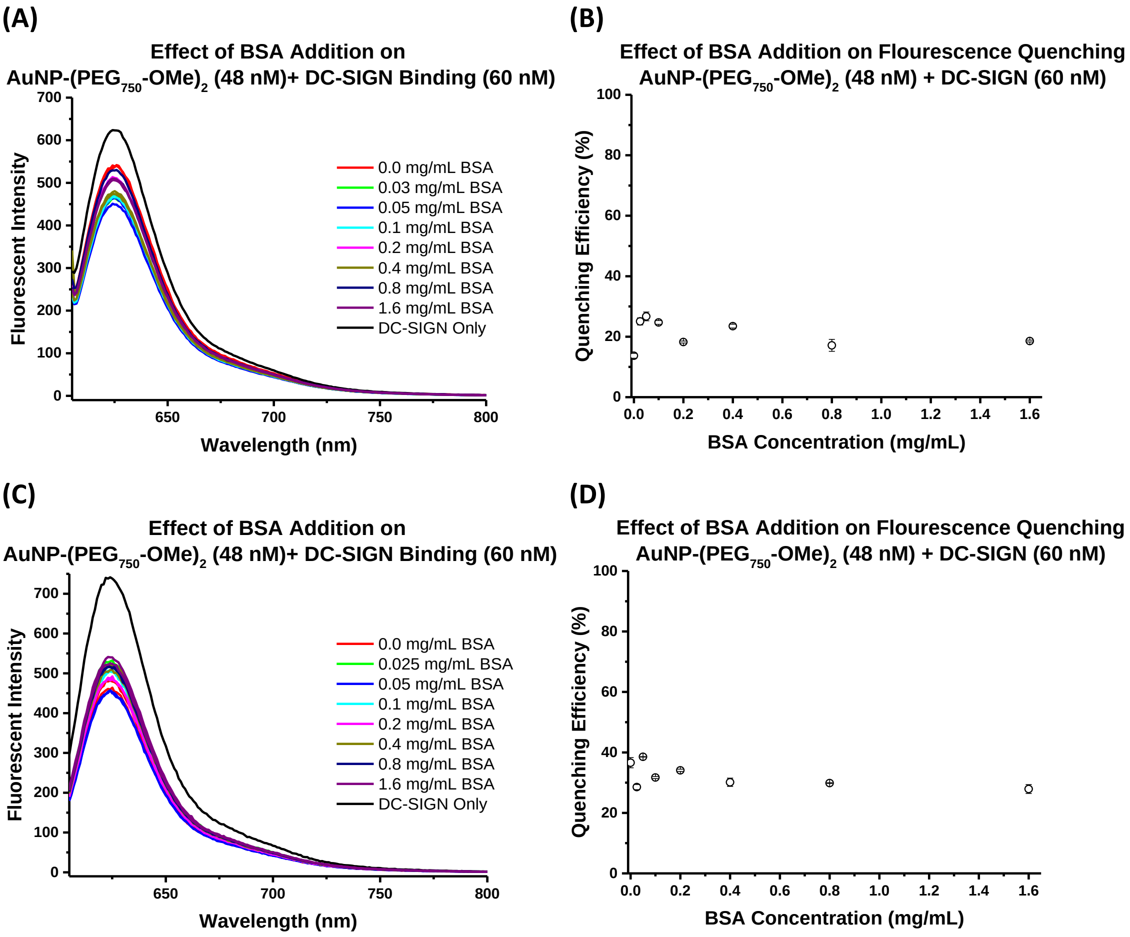

Figure 4.6.5: Fluorescence spectra of **(A)** AuNP-(PEG$_{750}$-OMe)$_2$ (48 nM) + labelled DC-SIGN (60 nM) and **(B)** AuNP-(PEG$_{750}$-OMe)$_3$ (48 nM) + labelled DC-SIGN (60 nM) at varying BSA concentrations (0 – 1.6 mg/mL). **(C)** and **(D)** Percentage fluorescence quenching as a function of the BSA concentration.

The experimental set-up was chosen at AuNP (48 nm) and DC-SIGN (60 nM) concentrations as that showed significant fluorescence quenching during initial experiments. Then a range of BSA concentrations were selected from 0 mg/mL to 1.8 mg/mL. The resulting fluorescence spectra and quenching efficiency curves for AuNP-(PEG_{750}-OMe)$_n$-DC-SIGN (where n=2 and 3) interactions are shown in **Figure 4.6.5**. The results show almost no effect on the quenching at different BSA concentration. This suggests either no protein corona formation or that DC-SIGN interacts more strongly with AuNPs than BSA.

4.7 Calcium Dependency Studies

DC-SIGN/R binding with glycans is calcium dependent. Previous studies done have shown glycans coordinate to a Ca^{2+} bound to the CRD of the protein.[28] **Figure 4.7.1** shows a molecular model of the primary binding site found within DC-SIGN, it also shows that ligand binding is dependent on not only Ca^{2+} presence but also the presence of four amino acid residues, two glutamic acids and two asparagines.

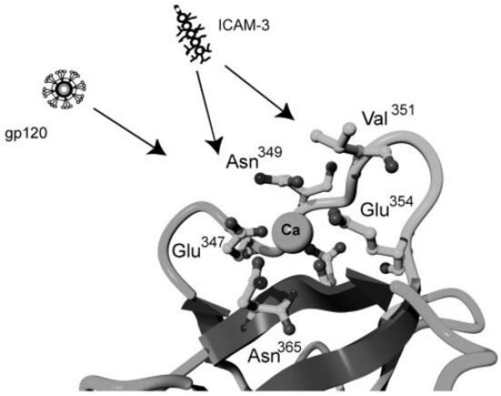

Figure 4.7.1: The primary ligand-binding site within DC-SIGN located at the top of the C-type lectin domain, CRD, and it includes a Ca^{2+}. Along with four amino acid residues, Glu^{347}, Asn^{349}, Glu^{354} and Asn^{365} these materials all contribute to the binding of the ligand within the CRD of DC-SIGN.[28] Taken from reference.

A calcium dependence study can be done to prove that the functionalised AuNPs are binding to DC-SIGN via the surface glycans present. To achieve this a strong Ca^{2+} chelation agent ethylenediamine-tetraacetic acid, EDTA, was added to calcium containing buffer (20 mM HEPES, pH 7.8, 150 mM NaCl, 10 mM $CaCl_2$) to capture the Ca^{2+} ions in solution.[29] Varying concentrations of EDTA are added to samples containing the same AuNP and DC-SIGN concentrations 5 nM and 25 nM respectively. As the buffer already contains 10 mM of $CaCl_2$, EDTA concentration start from 5 mM to begin to show differences within fluorescence quenching. BSA is added to buffer to stop non-specific surface adsorption as done previously. We expect to see reduced fluorescence quenching with the increase the EDTA concentration (**Figure 4.7.2**).

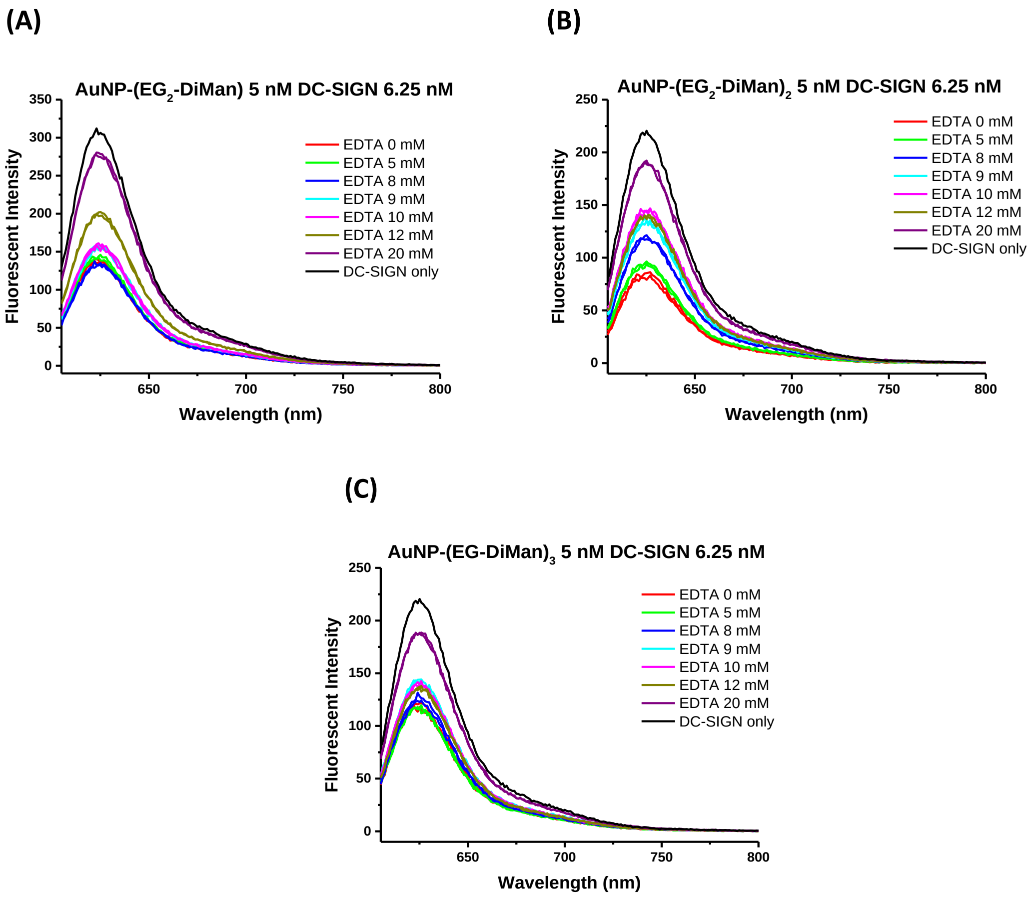

Figure 4.7.2: Fluorescence spectra for **(A)** AuNP-(EG$_2$-DiMan) (5 nM) + labelled DC-SIGN (6.25 nM) with different EDTA concentrations (0 – 20 mM), **(B)** AuNP-(EG$_2$-DiMan)$_2$ (5 nM) + labelled DC-SIGN (6.25 nM) with different EDTA concentrations (0 – 20 mM), **(C)** AuNP-(EG-DiMan)$_3$ (5 nM) + labelled DC-SIGN (6.25 nM) with different EDTA concentrations (0 – 20 mM).

4.7.1 Quenching Efficiency

The percentage quenching efficiency was then calculated using, **(Eq. 16)**, and plotted against EDTA concentration shown in **Figure 4.7.3** below. The spectra show that upon increasing the EDTA concentration there is a decrease of quenching as expected. Since EDTA chelates strongly to the Ca^{2+} ions it can extract the Ca^{2+} ions from CRD structure to eliminate glycan binding. This is further confirmed as there is no fluorescence quenching observed at high EDTA concentrations.

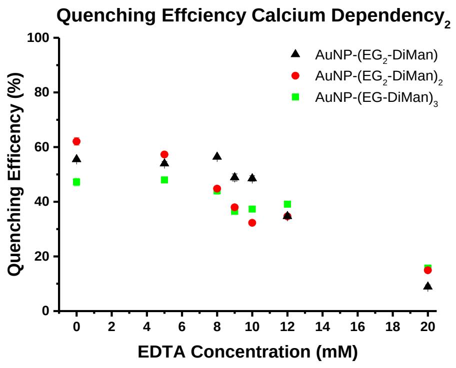

Figure 4.7.3: Percentage fluorescence quenching as a function of the EDTA concentration for AuNP-(EG$_n$-DiMan)$_m$ (5 nM) with DC-SIGN (6.25 nM).

4.7.2 EDTA effects on Protein Only

To investigate if EDTA has any effect on the quenching of the dye fluorescence, an experiment of labelled DC-SIGN with different amounts of EDTA added was performed. **Figure 4.7.4** shows that the addition of EDTA causes around a 50 % decrease in the fluorescent intensity of the labelled protein. It reaches the same intensity at 20 mM EDTA as when the AuNPs are present. This suggests that there are some interactions occurring between the protein and the EDTA. The hypothesis is that the EDTA is interacting with the Ca^{2+} ions within the protein structure and the extraction of these ions is affecting the protein folding. Future investigations into this are being completed by another member of the group.

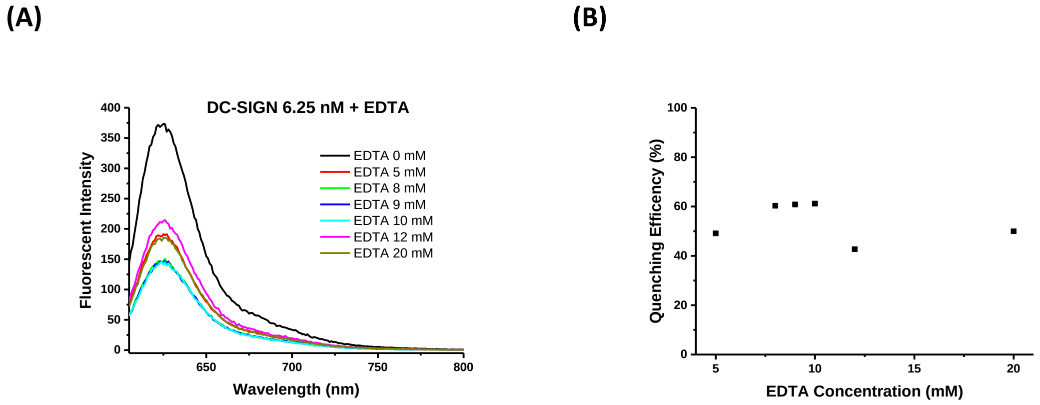

Figure 4.7.4: **(A)** Fluorescence spectra of labelled DC-SIGN (6.25 nM) with different EDTA concentrations (0 – 20 mM) added and **(B)** a plot of the quenching efficiency versus concentration of EDTA.

4.8 Protein- AuNP Ratio Selection

To investigate how the DC-SIGN/R: AuNP ratio effects the quenching efficiency which may provide information on maximum binding capacity of each AuNP-glycan for DC-SIGNR an experiment was done against a range of protein concentrations. As the AuNPs only have a set number of glycan present which will have a maximum binding threshold. This was done using a constant AuNP-EG_2-DiMan concentration of 19.2 nM. The dimannose ligand was chosen for its strong binding with both DC-SIGN and DC-SIGNR. These samples were also made up under the same conditions as those above in BSA containing HEPES buffer solution (**Chapter 3.3**), the only difference was the amount of the protein added. The resulting fluorescence spectra are shown below for both DC-SIGN (**Figure 4.8.1**) and DC-SIGNR (**Figure 4.8.2**).

4.8.1 AuNP-DC-SIGN Ratio Selection

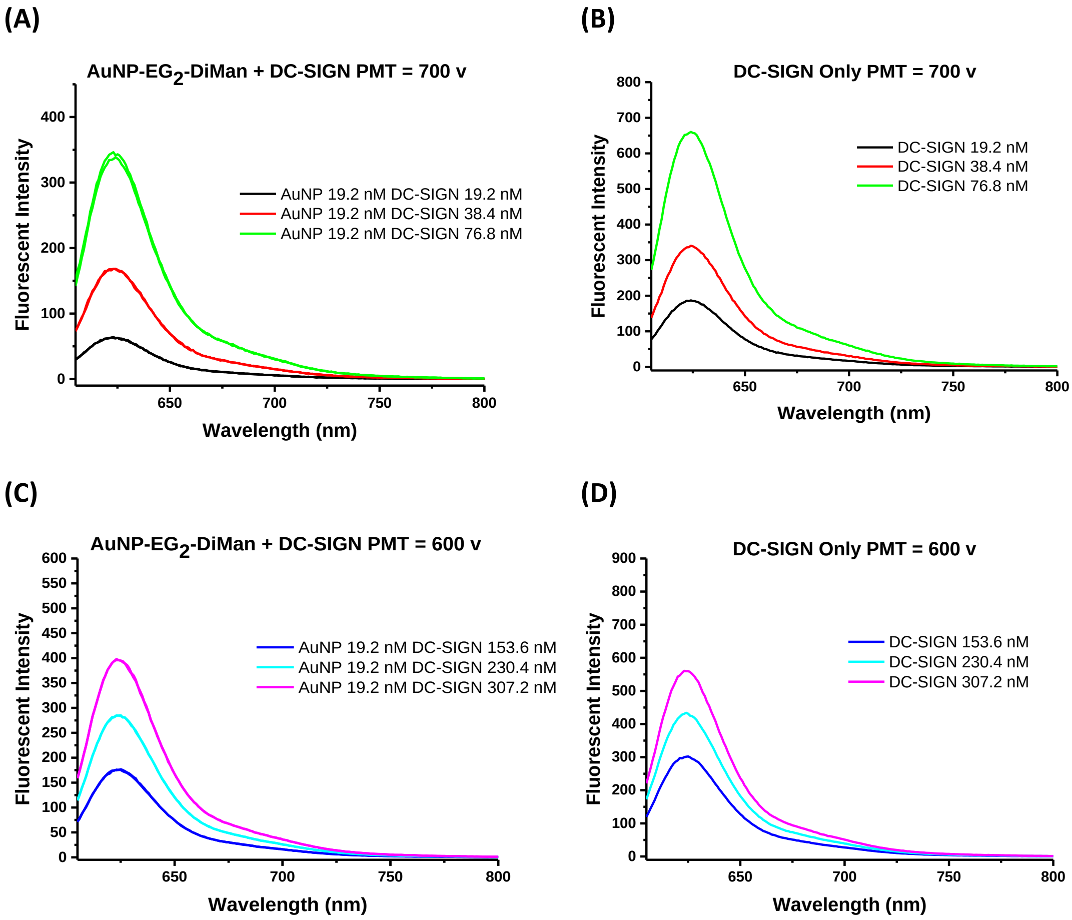

Figure 4.8.1: Fluorescence of AuNP-EG_2-DiMan (19.2 nM) + DC-SIGN at lower ratios **(A)** DC-SIGN concentrations (19.2 – 76.8 nM) and higher ratios **(C)** DC-SIGN concentrations (153.6 – 307.2 nM) and **(B)** and **(D)** labelled DC-SIGN only controls at the same concentrations and machine settings.

4.8.2 AuNP-DC-SIGNR Ratio Selection

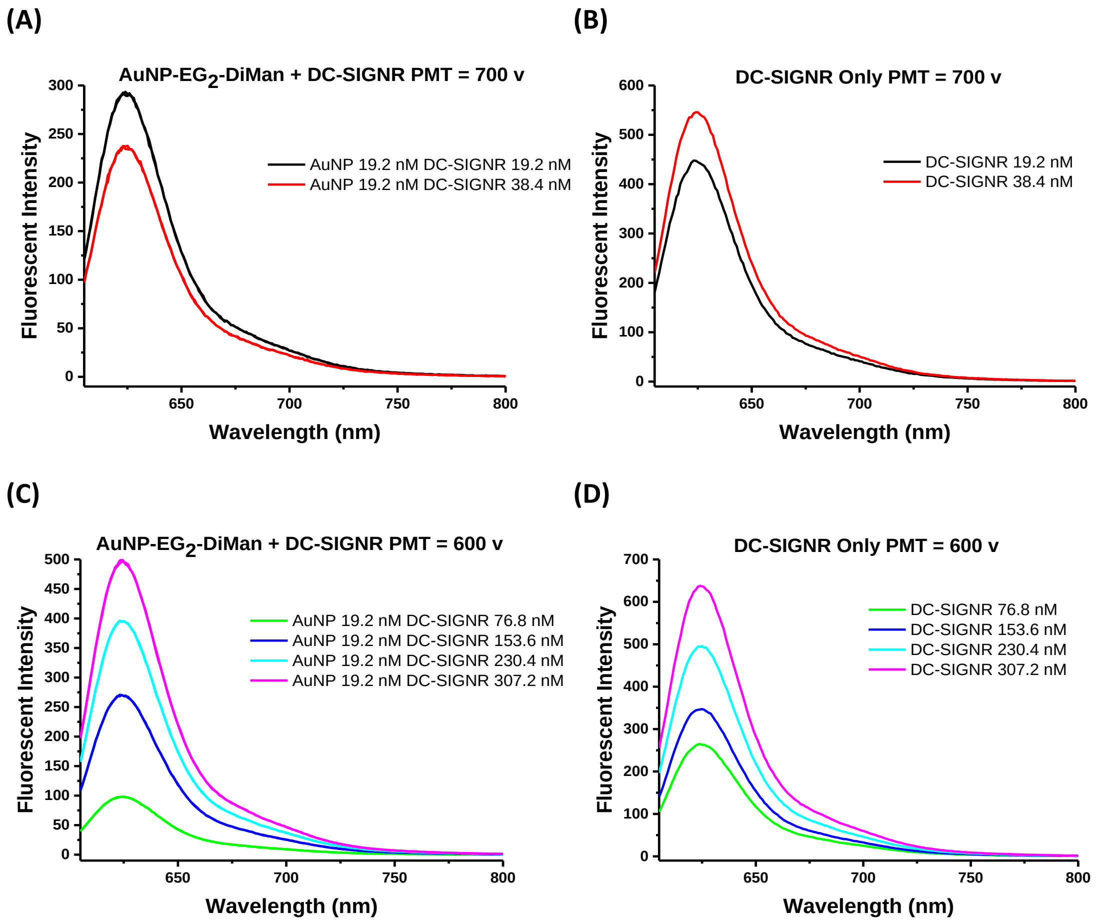

Figure 4.8.2: Fluorescence spectra of AuNP-EG$_2$-DiMan (19.2 nM) + DC-SIGNR at lower ratios **(A)** DC-SIGNR concentrations 19.2 – 38.4 nM) and higher ratios **(C)** DC-SIGNR concentrations (76.8 – 307.2 nM) and **(B)** and **(D)** labelled DC-SIGNR only controls at the same concentrations and machine settings.

4.8.3 Quenching Efficiency

The quenching efficiency for the increasing Protein: AuNP ratios were calculated and plotted against the protein: AuNP ratios shown in **Figure 4.8.3** below. The results show that the use of a lower protein: AuNP ratio, 1:1, is necessary for DC-SIGN oppositely a higher ratio, 1:4, is required for DC-SIGNR. This is expected as previous work has shown the need for a larger ratio requirement of DC-SIGNR. This is due to the crosslinking binding model shown for DC-SIGNR where multiple protein binding to the AuNP are required to produce binding cooperativity. Oppositely it suggests that the binding between DC-SIGN is non-cooperative due to the 1:1 ratio.

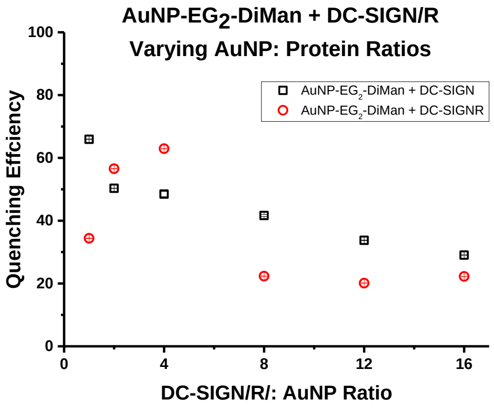

Figure 4.8.3: Percentage fluorescence quenching as a function of the AuNP: Protein ratio for AuNP-EG$_2$-DiMan (19.2 nM) interaction with DC-SIGN and DC-SIGNR.

4.9 Inhibiting Ebola Virus Host Cell Entry

Note: *The work was performed by our collaborator Professor Stefan Pöhlmann and his colleagues at the German Primate Center, Göttingen, Germany. The author of this thesis Emma C Poole has interpreted the data and written her own account of the findings of the collaborators.*

Our previous results show glycan -QDs have shown great potential for inhibiting DC-SIGN mediated viral infections. The IC$_{50}$ values of our QD-Mannose bioconjugates were similar to that of our calculated binding dissociation constants by using FRET. As AuNPs are much less toxic than the cadmium based QDs, they are better suited as potential inhibitors for *in vivo* studies. The same viral inhibition assay was used as the QDs in **Chapter 2**. This would also confirm whether the fluorescence quenching assays were as sensitive as the FRET assays in predicting the IC$_{50}$ values of these materials. The new ligand structures also show significant enhanced DC-SIGNR binding affinity for the trimeric glycan ligand which hopefully would enhance the inhibition of EBOV-GP.

Out of the nine potential AuNPs the assays were performed on six of these. The monomeric ligand coated AuNPs were chosen as they were found to increase the binding affinity with both DC-SIGN over the LA-EG$_3$-(Man)^s alternatives. The trimeric glycan ligand was then chosen to confirm the effects of our binding studies in the decrease shown for DC-SIGN and then the increase shown for DC-SIGNR for binding affinity. The controls in each case were also investigated to show the effects of the non-specific binding on the mediated uptake of the EBOV-GP and see if the non-specific effects do block the CRD binding sites. The luciferase activities of the lysed 293 T cells is shown below in **Figure 4.9.1** after incubation with the active MLV. The results for the luciferase activities of the control VSV-G can be found with the **Appendix**. Also initial studies using higher concentrations of the AuNP-DiMan materials can be found within the **Appendix**.

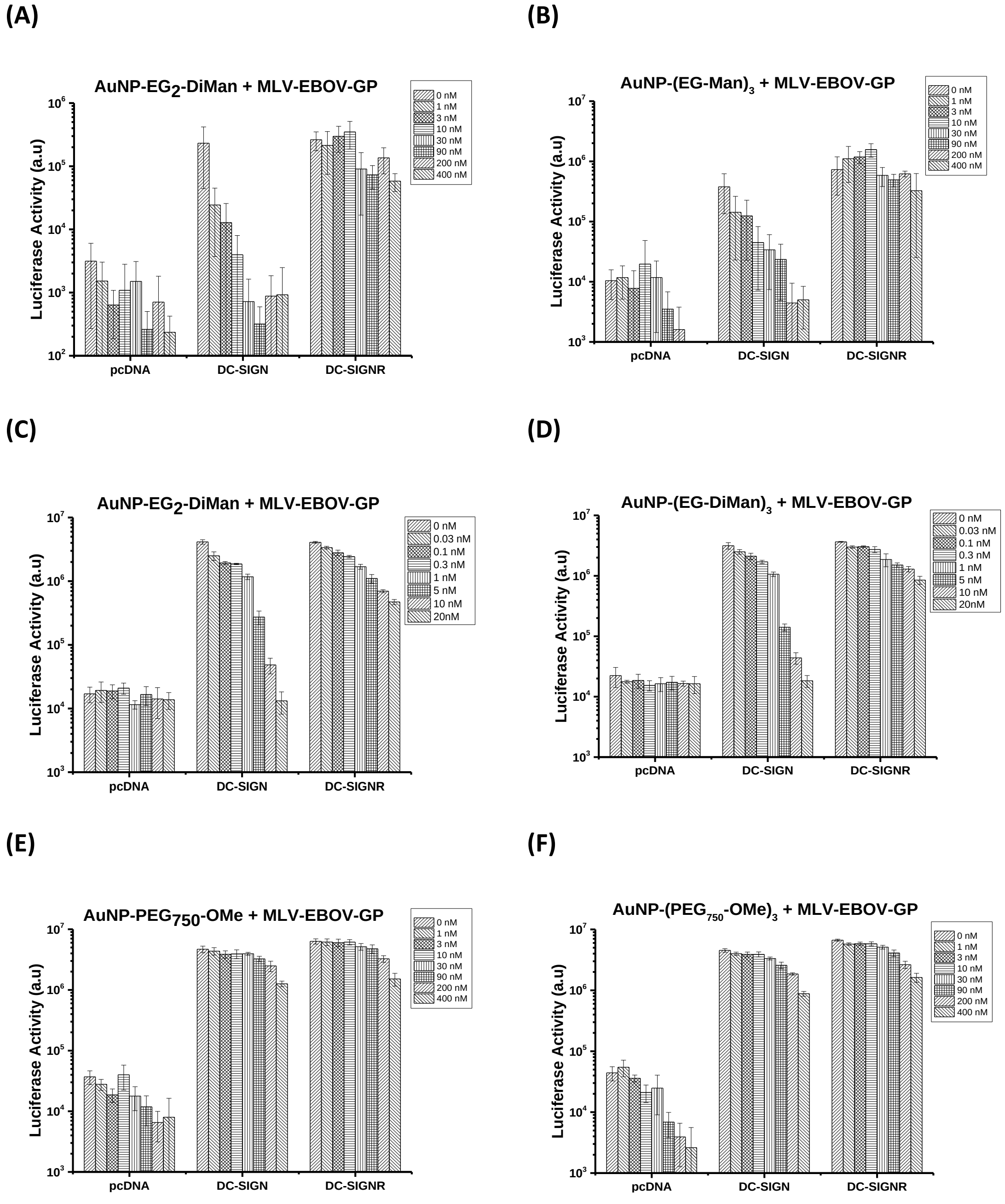

Figure 4.9.1: Human embryonic kidney cells (293 T) were transfected with the identified plasmids and pre incubated with AuNP-EG$_2$-Man (**A**), AuNP-(EG-Man)$_3$ (**B**), AuNP-EG$_2$-DiMan (**C**), AuNP-(EG-DiMan)$_3$ (**D**), AuNP-PEG$_{750}$-OMe (**E**), AuNP-(PEG$_{750}$-OMe)$_3$ (**F**) and inoculated with Murine Leukemia Virus (MLV) particles modified to contain the Ebola Virus Glycoprotein (EBOV-GP). The inhibitor concentrations were calculated after addition of particles. Luciferase activities in cell lysates were measured at 72 hrs post-transduction.

The normalised inhibition data were fitted using the same standard inhibition model as that used in **Chapter 2.8.1** to calculate the IC$_{50}$ values. The data are shown in **Figure 4.9.2** for (**A**) AuNP-EG$_2$-Man, (**B**) AuNP-EG$_2$-DiMan, (**C**) AuNP-(EG-Man)$_3$ and (**D**) AuNP-(EG-DiMan)$_3$. The data for the control AuNPs are shown in **Figure 4.9.3**. The IC_{50} values were calculated as 0.12 ± 0.01, 1.20 ± 0.41, 0.18 ± 0.04 and 0.18 ± 0.05 nM for AuNP-EG_2-Man, AuNP-$(EG\text{-}Man)_3$, AuNP-EG_2-DiMan, and AuNP-$(EG\text{-}DiMan)_3$ against DC-SIGN mediated virus transduction respectively. In comparison to the previous inhibition data collected with glycan-QDs the AuNP materials appear to be more potent viral inhibitors. As the QD alternative, QD-EG_3-DiMan exhibits an IC_{50} value of 0.70 ± 0.20 nM which is about 10 fold less potent. This work shows IC_{50} values that verge on picomolar levels for the first time, Table 4.9.2 shows a comparison of IC_{50} for similar materials.

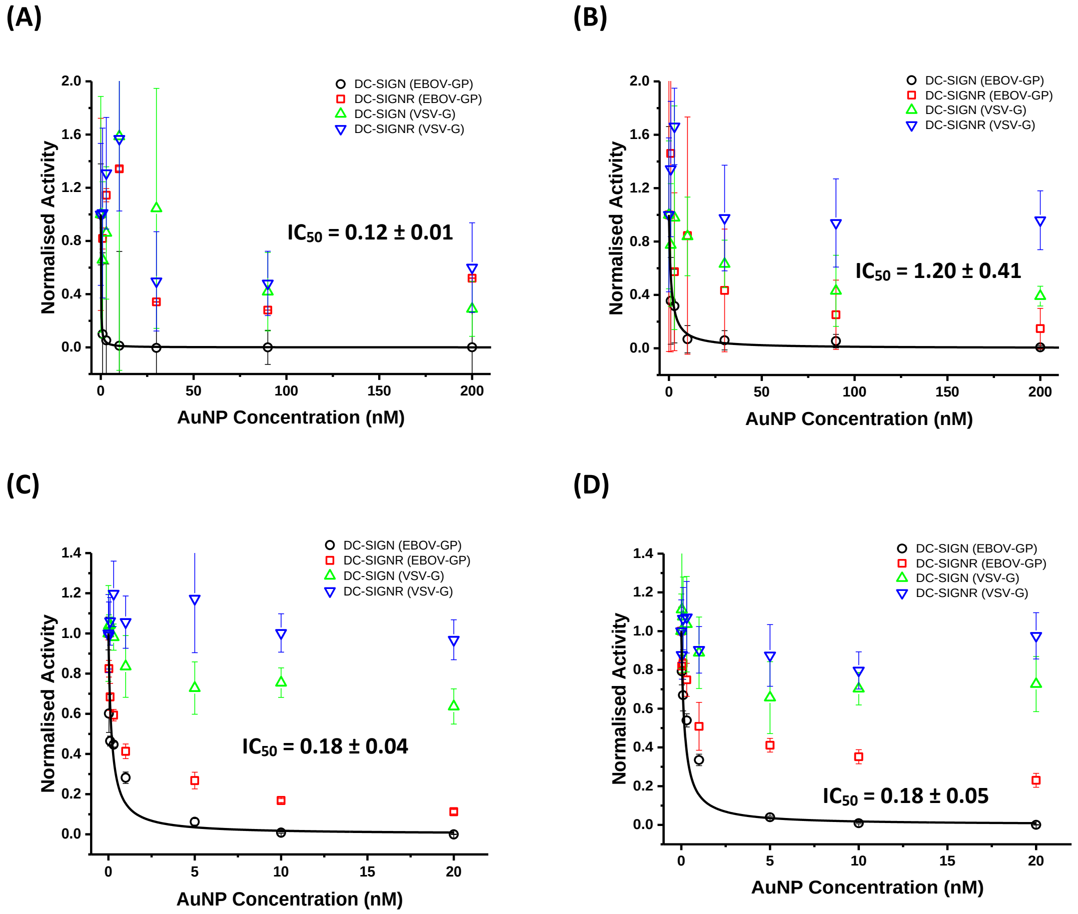

Figure 4.9.2: Normalised luciferase activities of the DC-SIGN or DC-SIGNR expressing 293T cells measured as a function of the pre-treatment (**A**) AuNP-EG_2-Man, (**B**) AuNP-$(EG\text{-}Man)_3$, (**C**) AuNP-EG_2-DiMan and (**D**) AuNP-$(EG\text{-}DiMan)_3$ concentrations. The data shown in circles and squares correlate to the virus particles containing the EBOV-GP and the triangles to the control glycoprotein (VSV-G). Data was fitted using a comparable competitive binding model.

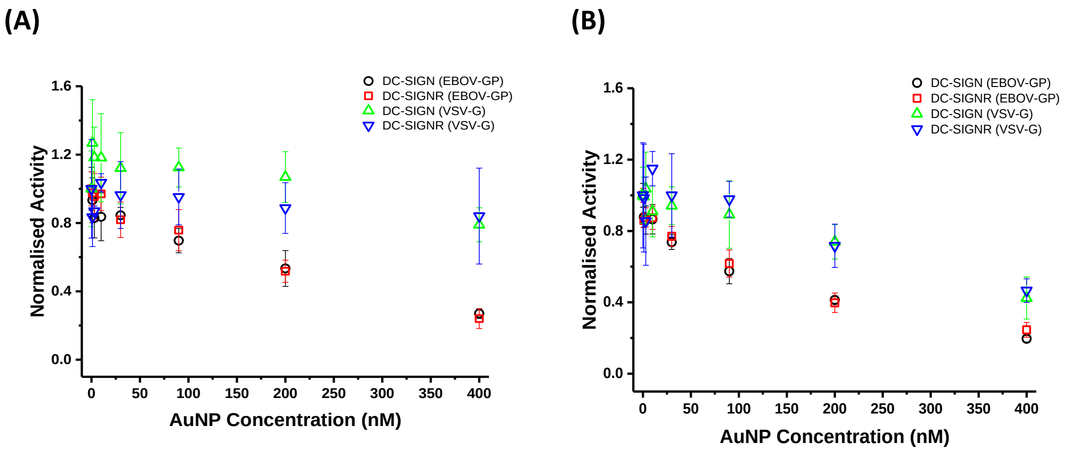

Figure 4.9.3: Normalised luciferase activities of the DC-SIGN or DC-SIGNR expressing 293T cells measured as a function of the pre-treatment (**A**) AuNP-PEG$_{750}$-OMe and (**B**) AuNP-(PEG$_{750}$-OMe)$_3$ concentrations. The data shown in circles and squares correlate to the virus particles containing the EBOV-GP and the triangles to the control glycoprotein (VSV-G). Data was fitted using a comparable competitive binding model.

The results show the same trend between the DC-SIGN binding affinities and virus inhibition potency. The AuNP capped with trimeric glycan ligands have a weaker affinity with DC-SIGN and but proves to be just as good inhibitors to the EBOV-GP binding in the case of the disaccharide. However the K_d measured by fluorescence quenching does not match their IC_{50} values so it cannot be used as a way of predicting the IC_{50} values as seen previously with the QDs. Another observation is that some degree of cytotoxicity is observed at AuNP higher concentrations (eg. ≥ 200 nM) where the normalised activity is reduced to 40 % of the original values for both the active glycoprotein as well as the control. There are many reports of the toxicity of AuNPs at high concentrations as highlighted in the review by Khlebtsov and Dykman.[30] This could also be due to non-specific binding of protein as seen earlier with the PEGlyated AuNPs with DC-SIGN. The data for DC-SIGNR does not fit the standard inhibition model suggesting that it is for more complex then seen for DC-SIGN. Despite this, the AuNP-DiMans do exhibit significant inhibition of DC-SIGN/R expressing cells. It never reaches close to 100 % inhibition even at high concentrations.

Table 4.9.1: A summary of the apparent K_d values agaisnt the IC_{50} values to compare the inhibition potency of the AuNP-(EG_n-$DiMan^s$)$_m$ (where n = 1 or 2, m = 1 and 3 and s = 1 and 2) with DC-SIGN.

AuNPs + Protein	Apparent K_d DC-SIGN (nM)	IC_{50} DC-SIGN (nM)
AuNP-EG_2-Man + DC-SIGN	21 ± 3	0.12 ± 0.01
AuNP-(EG-Man)$_3$ + DC-SIGN	37 ± 1	1.20 ± 0.41
AuNP-EG_2-DiMan + DC-SIGN	0.61 ± 0.3	0.18 ± 0.04
AuNP-(EG-DiMan)$_3$ + DC-SIGN	1.54 ± 0.3	0.18 ± 0.05

Table 4.9.2: A summary of the IC_{50} values of mannose-DC-SIGN binding to compare to the literature.

Glycan Scaffold	IC_{50} DC-SIGN (nM)
First Glycodendrimer Ligand[31]	300
Globular Multivalent Glycofullenes[32]	0.67
Virus-like glycodendri-nanoparticles[33]	0.91
Pseudosaccharide Functionalized Dendrimers[34]	31.5
QD-DiMan (Chapter 3)	0.70
AuNP-DiMan (This Work)	0.06

4.10 AuNP Competition Studies on QD-DC-SIGN Binding

To confirm the similar trends of binding affinities measured with the AuNPs and the QDs, a competition study was done by using QD-glycan (10 nM) and labelled DC-SIGN (10 nM) with varying amounts of AuNP-glycans. The hypothesis is that when the AuNP-glycans are bound to the protein the QDs fluorescence will not be transferred to the dye and thus a decrease in FRET ratio would be expected. Due to the AuNPs being strong fluorescence quenchers there is the possibility for fluorescence to be quenched by the QDs without any ligand binding occurring. Two experiments were done to recognise this competition using the AuNP capped with PEGlyated ligand (negative control) and the dimannose ligands (positive control). Results for the dimannose capped AuNPs is shown below in **Figure 4.10.1** and the results for the negative control AuNPs is shown in **Figure 4.10.2**.

4.10.1 Mannose AuNP Competition

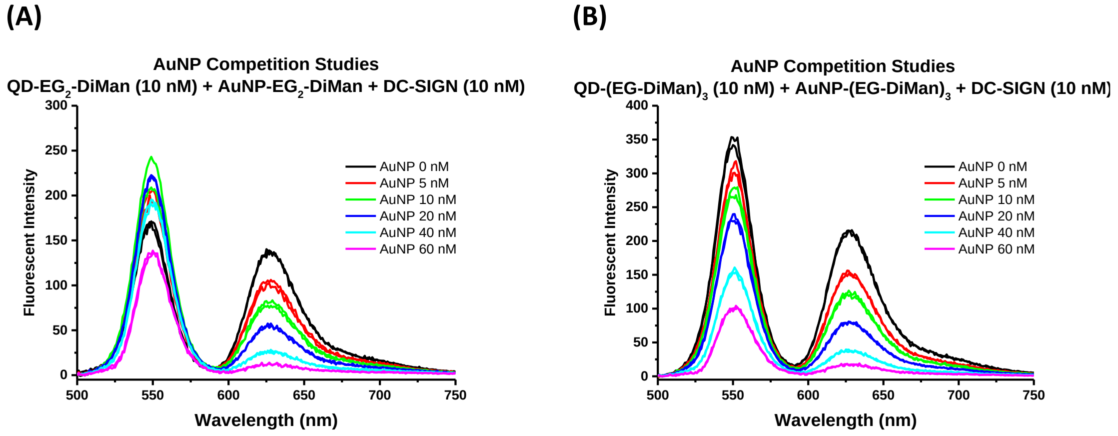

Figure 4.10.1: Background corrected fluorescence spectra obtained for determination of the binding competition for (**A**) QD-EG$_2$-DiMan (10 nM) + AuNP- EG$_2$-DiMan (0 – 60 nM) and (**B**) QD-(EG-DiMan)$_3$ (10 nM) + AuNP- (EG-DiMan)$_3$ (0 – 60 nM) with DC-SIGN (10 nM).

4.10.2 AuNP Control Competition

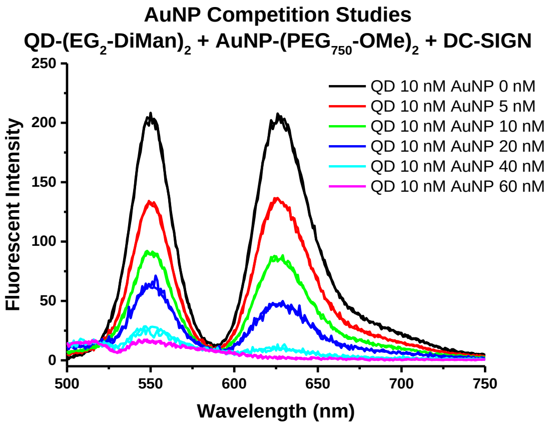

Figure 4.10.2: Background corrected fluorescence spectra obtained for determination of the binding competition for QD-(EG$_2$-DiMan)$_2$ (10 nM) + AuNP-(PEG$_{750}$-OMe)$_2$ (0 – 60 nM) with DC-SIGN (10 nM).

4.10.3 Ratiometric Determination of AuNP Concentration

The results show that the AuNP-glycan can compete with the QD-glycan binding to labelled DC-SIGN leading to significantly reduced dye FRET signal with the increasing AuNP concertation for the case of the monomeric ligand. This is expected as the binding affinity is greater for the AuNP then the QD as the K_d is 0.61 nM and 1.7 nM respectively. The FRET ratio (apparent) versus AuNP: QD ratio plot is used to quantify their relative DC-SIGN binding affinities. **Figure 4.10.3 (C)** shows the plot of the QD maximum fluorescence intensity against the AuNP: QD ratio. It is clear that some interaction between the AuNPs and QD is happening as we observe non-specific quenching in each competition study. The initial hypothesis of competition occurring is shown through the initial increase in donor fluorescence for the monomeric ligand competition. The competition binding curves are shown in **Figure 4.10.3** and the resulting K_i's have been calculated and confirm that the AuNPs have a higher binding affinity for DC-SIGN as the values of K_d suggest.

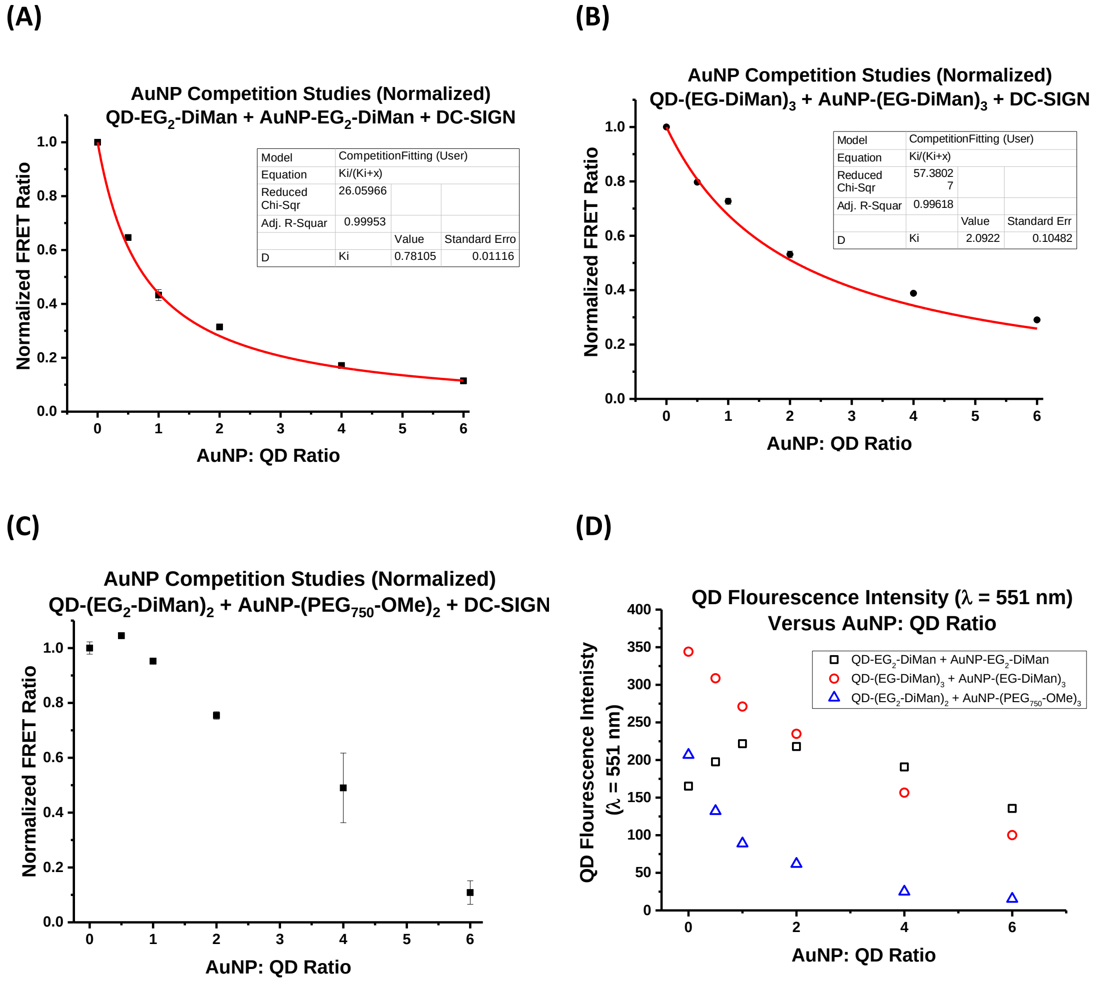

Figure 4.10.3: Normalised FRET Ratio curves shown as a function of the AuNP Ratio added. AuNP competition curved are shown for (**A**) QD-EG$_2$-DiMan + AuNP-EG$_2$-DiMan + DC-SIGN, (**B**) QD-(EG-DiMan)$_3$ + AuNP-(EG-DiMan)$_3$ + DC-SIGN, (**C**) QD-(EG$_2$-DiMan)$_2$ + AuNP-(PEG$_{750}$-OMe)$_2$ + DC-SIGN and (**D**) QD fluorescence intensity (λ = 551 nm) versus AuNP: QD ratio.

4.11 Conclusion

In conclusion, we have developed a second fluorescent assay to improve the understanding of multivalent protein – carbohydrate interactions using the c-type lectins DC-SIGN/R as model examples. We have designed and synthesised a new ligand series (DHLA-(EG$_n$-Man^s)$_m$ where n = 1 or 2, s = 1 and 2 and m = 1, 2 and 3) to increase the nanoparticle surface glycan density by increasing the functional glycan groups attached to each DHLA anchoring group. Unfortunately, due to steric hindrance the surface glycan density doesn't actually increase. The apparent binding affinities, K_d*s*, for these ligands capping AuNPs have been measured via a fluorescence quenching method and revealed some significant results. First, their DC-SIGN binding affinity becomes weaker increasing the number of glycans attached to each DHLA based ligands is further increased for both monosaccharide and disaccharide, AuNP-Mannose, contrary to our original expectation. Second, similar to the QD-DC-SIGN interaction reported previously, a significant increase in glycan-AuNP-DC-SIGN multivalent binding affinity (up to ~1.5 million fold) over the monovalent DC-SIGN-CRD-DiMannose binding is observed and moreover, capping the AuNP with DiMannose gives higher affinity enhancement over that of mannose in accordance to the extended binding site structure of DC-SIGN/R CRDs. The viral inhibitions studies show that these materials have a potency around of 10 fold higher than that of the equivalent QDs, making them the most potent multivalent glycan-nanoparticle ever reported against pseudo-Ebola virus infection. The same trend has been observed for the IC_{50} values as for their binding affinities. The inhibition of these materials with DC-SIGNR expressing cells is more complex than that of DC-SIGN, and the data could not be fitted by the simple inhibition model.

The fluorescence quenching has been verified to be specific for glycan-protein interactions by comparing to control AuNPs capped with a series of inert ligands (DHLA-$(PEG_{750}$-$OMe)_m$ where m = 1, 2 and 3) for DC-SIGN however this is not the case for DC-SIGNR where the controls show similar quenching. Interestingly, the control AuNPs display no minimal fluorescence quenching of DC-SIGN fluorescence at low concentrations (<50 nM) for m= 2 and 3, but show a sudden increase of quenching at higher protein concentrations. Numerous methods have been used to determine why this happens including DLS and UV/Vis but no solid conclusion can be drawn. A probable explanation is due to protein corona formation, but further work is still needed. Cryo-TEM imaging combined with protein staining could be a good tool to investigate the position of proteins around the AuNPs controls capped with PEGlyated ligands.

4.12 Experimental Procedures

4.12.1 Ligand and Nanoparticle Preparation

All the relevant ligand synthesis and nanoparticle preparations can be found within **Chapter 5**. All the ligands have been fully characterised using NMR, LC-MS and TLC.

4.12.2 Protein Production and Purification

All the details to produce and purify the proteins (DC-SIGN/R) used within this chapter can be found within **Chapter 5**.

4.12.3 Viral Inhibition Studies[22]

The viral inhibition studies were performed in a similar manner to the QD-glycan conjugates in **Chapter 3** following the instructions as described by Guo *et al*.[22] using human embryonic kidney 293T cells.

4.13 References

1. K. L. Kelly, E. Coronado, L. L. Zhao and G. C. Schatz, ACS Publications, Editon edn., 2003.
2. C. Yun, A. Javier, T. Jennings, M. Fisher, S. Hira, S. Peterson, B. Hopkins, N. Reich and G. Strouse, *J. Am. Chem. Soc.*, 2005, **127**, 3115-3119.
3. T. B. Geijtenbeek, D. S. Kwon, R. Torensma, S. J. van Vliet, G. C. van Duijnhoven, J. Middel, I. L. Cornelissen, H. S. Nottet, V. N. KewalRamani and D. R. Littman, *Cell*, 2000, **100**, 587-597.
4. S. Pöhlmann, E. J. Soilleux, F. Baribaud, G. J. Leslie, L. S. Morris, J. Trowsdale, B. Lee, N. Coleman and R. W. Doms, *P. Natl. Acad. Sci. USA*, 2001, **98**, 2670-2675.
5. J. R. Walker, B. Nagar, N. M. Young, T. Hirama and J. M. Rini, *Biochemistry-US*, 2004, **43**, 3783-3792.
6. C. W. Davis, H.-Y. Nguyen, S. L. Hanna, M. D. Sánchez, R. W. Doms and T. C. Pierson, *J. Virol.*, 2006, **80**, 1290-1301.
7. C. P. Alvarez, F. Lasala, J. Carrillo, O. Muñiz, A. L. Corbí and R. Delgado, *J. Virol.*, 2002, **76**, 6841-6844.
8. H. Feinberg, R. Castelli, K. Drickamer, P. H. Seeberger and W. I. Weis, *J. Biol. Chem.*, 2007, **282**, 4202-4209.
9. Y. Guo, I. Nehlmeier, E. Poole, C. Sakonsinsiri, N. Hondow, A. Brown, Q. Li, S. Li, J. Whitworth and Z. Li, *J. Am. Chem. Soc.*, 2017, **139**, 11833-11844.
10. X.-D. Zhang, H.-Y. Wu, D. Wu, Y.-Y. Wang, J.-H. Chang, Z.-B. Zhai, A.-M. Meng, P.-X. Liu, L.-A. Zhang and F.-Y. Fan, *Int. J. Nanomed.*, 2010, **5**, 771.
11. O. Martínez-Ávila, K. Hijazi, M. Marradi, C. Clavel, C. Campion, C. Kelly and S. Penadés, *Chem. Eur. J.*, 2009, **15**, 9874-9888.
12. B. Arnáiz, O. Martínez-Ávila, J. M. Falcon-Perez and S. Penadés, *Bioconjug. Chem.*, 2012, **23**, 814-825.
13. N. P. Chung, S. K. Breun, A. Bashirova, J. G. Baumann, T. D. Martin, J. M. Karamchandani, J. W. Rausch, S. F. Le Grice, L. Wu and M. Carrington, *J. Biol. Chem.*, 2010, **285**, 2100-2112.
14. R. C. da Silva, L. Segat and S. Crovella, *Hum. Immunol.*, 2011, **72**, 305-311.
15. N. Izquierdo-Useros, M. Lorizate, P. J. McLaren, A. Telenti, H.-G. Kräusslich and J. Martinez-Picado, *PLOS Pathog.*, 2014, **10**, e1004146.
16. S. Aldrich, *Gold nanoparticles: properties and applications*.
17. J. Piella, N. G. Bastús and V. Puntes, *Chem. Mater.*, 2016, **28**, 1066-1075.
18. Y. Xiao and S. N. Isaacs, *J. Immunol. Methods.*, 2012, **384**, 148-151.
19. H. Feinberg, D. A. Mitchell, K. Drickamer and W. I. Weis, *Science*, 2001, **294**, 2163-2166.

20. A. Holla and A. Skerra, *Protein Eng. Des. Sel.*, 2011, **24**, 659-669.

21. E. van Liempt, C. Bank, P. Mehta, Z. S. Kawar, R. Geyer, R. A. Alvarez, R. D. Cummings, Y. v. Kooyk and I. van Die, *FEBS Lett.*, 2006, **580**, 6123-6131.

22. Y. Guo, C. Sakonsinsiri, I. Nehlmeier, M. A. Fascione, H. Zhang, W. Wang, S. Pöhlmann, W. B. Turnbull and D. Zhou, *Angew. Chem. Int. Ed.*, 2016, **55**, 4738-4742.

23. M. P. Monopoli, C. Åberg, A. Salvati and K. A. Dawson, *Nat. Nanotechnol.*, 2012, **7**, 779.

24. J. Piella, N. G. Bastús and V. Puntes, *Bioconjug. Chem.*, 2016, **28**, 88-97.

25. R. García-Álvarez, M. Hadjidemetriou, A. Sánchez-Iglesias, L. M. Liz-Marzán and K. Kostarelos, *Nanoscale*, 2018.

26. J. Wolfram, Y. Yang, J. Shen, A. Moten, C. Chen, H. Shen, M. Ferrari and Y. Zhao, *Colloid. Surface. B.*, 2014, **124**, 17-24.

27. E. Casals, T. Pfaller, A. Duschl, G. J. Oostingh and V. Puntes, *ACS Nano*, 2010, **4**, 3623-3632.

28. T. B. Geijtenbeek, A. Engering and Y. van Kooyk, *J. Leukocyte. Biol.*, 2002, **71**, 921-931.

29. J. R. Hart, *Ullmann's Encyclopedia of Industrial Chemistry*, 2000.

30. N. Khlebtsov and L. Dykman, *Chem. Soc. Rev*, 2011, **40**, 1647-1671.

31. F. Lasala, E. Arce, J. R. Otero, J. Rojo and R. Delgado, *Antimicrob. Agents. Ch.*, 2003, **47**, 3970-3972.

32. A. Muñoz, D. Sigwalt, B. M. Illescas, J. Luczkowiak, L. Rodríguez-Pérez, I. Nierengarten, M. Holler, J.-S. Remy, K. Buffet and S. P. Vincent, *Nat. Chem.*, 2016, **8**, 50-57.

33. R. Ribeiro-Viana, M. Sánchez-Navarro, J. Luczkowiak, J. R. Koeppe, R. Delgado, J. Rojo and B. G. Davis, *Nat. Commun.*, 2012, **3**, 1303.

34. J. Luczkowiak, S. Sattin, I. Sutkeviciute, J. J. Reina, M. Sánchez-Navarro, M. Thépaut, L. Martínez-Prats, A. Daghetti, F. Fieschi and R. Delgado, *Bioconjug. Chem.*, 2011, **22**, 1354-1365.

Chapter 5

Experimental: Ligand Synthesis and Characterisation

This chapter describes the synthesis of a range of lipoic acid-PEG based ligands containing different alkyne functionalities and also how these materials are exposed to different types of click chemistry, SPACC and Cu-catalysed, to attach the mannose functional group. Each of the ligands contain a lipoic acid, LA, group that provides a strong chelative interaction with the nanomaterials, QDs and AuNPs, used throughout the project. Each ligand has been prepared and purified by following existing literature methods. Each material has been fully characterised using a range of spectroscopic methods such as thin layer chromatography (TLC), infrared spectroscopy (IR), nuclear magnetic resonance spectroscopy (NMR) and mass spectrometry (MS). The protein production used for cultivating both the labelled and wild-type DC-SIGN/R is also shown within this chapter.

5.1 Overview: Ligand Synthesis

5.1.1 Synthesis of LA-EG$_n$-Cyclooctyne

The synthesis of LA-EG$_n$-cyclooctyne, (where n=3 and 11), from N_3-EG$_n$-NH_2, is based on the published protocol by Susumu *et al.*[1] It has been replicated easily and used in other publications by Zhang *et al.*[2] and Guo *et al.*[3] It includes the production of the intermediates LA-EG$_n$-N_3 and LA-EG$_n$-NH_2 (where n=3 or 11), as part of a three step synthesis. The synthesis includes two DCC/DMAP assisted coupling reactions and the reduction of an azide. **Scheme 5.1.1** below shows the synthetic routes to LA-PEG$_n$-cyclooctyne.

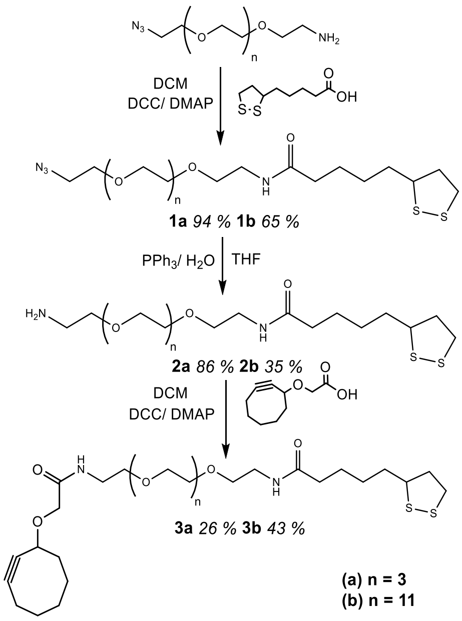

Scheme 5.1.1: A reaction scheme showing the formation of special designed ligand, LA-EG$_n$-Cyclooctyne (where n=3 or 11). (**A**) DCC, DMAP, LA and dry DCM, (**B**) PPh_3, H_2O and dry THF and (**C**) DCC, DMAP, Cyclooct-1-yn-3-glycolic acid and dry DCM.

5.1.2 Synthesis of LA-Zwitterion

The synthesis of LA-Zwitterion is based on the published protocol by Zhan *et al.*[4]. It includes the production of the intermediate LA-N,N-dimethyl-1,3-propanediamine as part of a two-step synthesis. This involves a substitution reaction of the hydroxyl group of the carboxylic acid and a rearrangement substation reaction to form the final product. **Scheme 5.1.2** below shows the synthesis route to LA-Zwitterion.

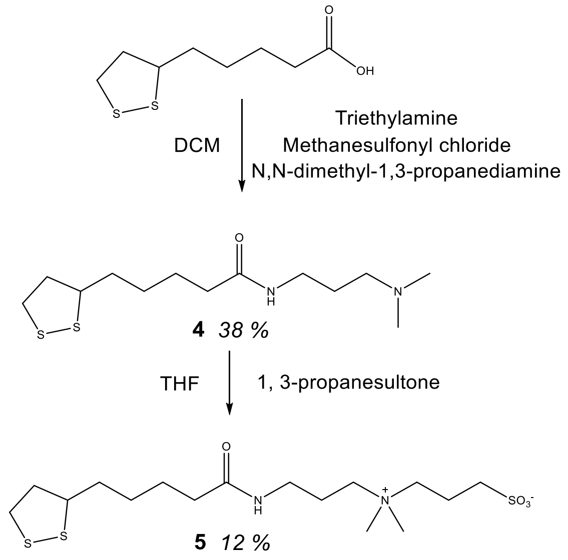

Scheme 5.1.2: A reaction scheme showing the formation of the LA-Zwitterion. (**A**) dry DCM, Triethylamine, Methanesulfonyl chloride and N, N-dimethyl- 1, 3-propanediamine and (**B**) dry THF and 1, 3-propanesultone.

5.1.3 Synthesis of LA-(EG$_n$-C≡CH)$_m$ Ligands

The scheme below shows the overall synthetic route to the alkyne molecules to be used in copper-catalysed click chemistry to vary the number of glycans on each ligand and to tune the AuNP surface glycan densities. The synthesis of 2-(2-(prop-2-yn-1-yloxy) ethoxy) ethan-1-amine from 2-(2-aminoethoxy) ethanol (**Reaction A**) is based on the published protocols of Neklesa *et al.*[5] and Tanaka *et al.*[6] The second step reaction is a simple DCC/DMAP coupling reaction to form LA-EG$_2$-C≡CH. The synthesis of LA-(EG$_2$-C≡CH)$_2$ from Boc-Aspartic Acid (**Reaction C**) is based on a published protocol of Zhan *et al.*[4] Finally the last reaction in this series (**Reaction D**) is based on a published protocol by Sanhueza *et al.*[7] and Chabre *et al.*[8] followed by the same deprotection and coupling reaction methods found in **Reaction C** to create the trimeric dendrimer. **Scheme 5.1.3** below shows the overview of the synthetic steps of each of the above reactions.

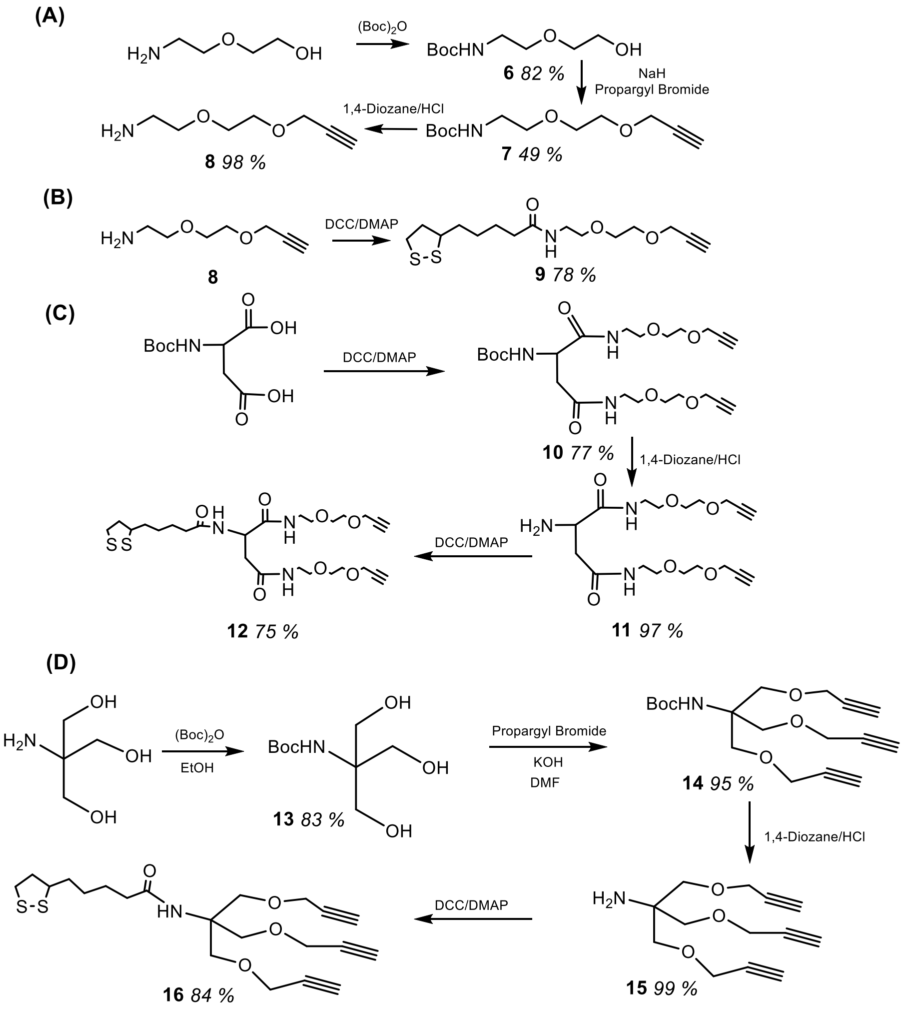

Scheme 5.1.3: An overview of the synthesis of LA-(EG$_n$-Man)$_m$ ligands previously stated in a previous chapter: (**A**) synthesis of H$_2$N-EG$_2$-C≡CH); (**B**) synthesis of LA-EG$_2$-C≡CH; (**C**) synthesis of LA-(EG$_2$-C≡CH)$_2$ and (**D**) synthesis of LA-(EG-C≡CH)$_3$.

5.1.4 Synthesis of LA-PEG750-OMe

The synthesis of N_3-PEG$_{750}$-OMe, **18**, from HO-PEG$_{750}$-OMe is based on the protocols published by Susumu *et al.*[1] It includes the production of the intermediate methanesulfonyl-PEG$_{750}$-OMe as part of a 2-step synthesis. The synthesis includes a nucleophilic reaction forming a tosylate and then an azide substitution. In order to form the ligand LA-PEG$_{750}$-OMe, N_3-PEG$_{750}$-OMe, **18**, is reduced to the intermediate NH_2-PEG$_{750}$-OMe, **18A**, and then coupled to LA using a DCC/DMAP coupling reaction. A previous PhD student within the Zhou group achieved this and so that material was used. Details of the full synthesis can be seen in **Scheme 5.1.4** below which also shows the reaction scheme to form LA-PEG$_{750}$-OMe, **18B**.

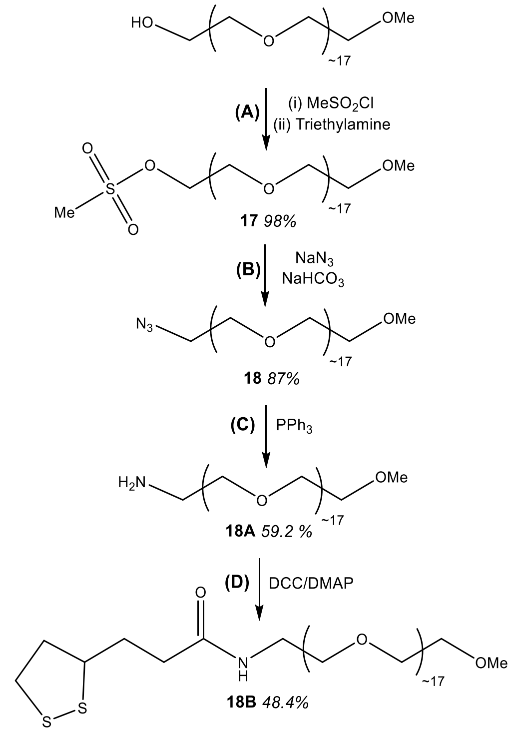

Scheme 5.1.4: A reaction scheme to show the formation of N_3-PEG$_{750}$-OMe. (**A**) HO-PEG$_{750}$-OMe, Methanesulfonyl chloride, trimethylamine and THF, (**B**) Sodium azide, H_2O and THF, (**C**) THF, PPh_3 and H_2O and (**D**) LA, DCC, DMAP and DCM.

5.2 Overview: Click Chemistry

5.2.1 Strain Promoted Alykne/Azide

The formation of LA-EGn-Man^m, (where n=3, 11 and m=1, 2), was successfully achieved using strain promoted azide-alkyne cycloaddition (SPAAC) click chemistry as reported by Bernardi *et al.*[9] (**Scheme 5.2.1**). The reaction is driven by the high ring strain within the cyclooctyne ring system and the favourable formation of the triazole species. High favourability of the product allows the reaction to be easily achieved at RT after leaving for around 3 days. This reaction was done for both the monosaccharide and disaccharide mannose sugars by mixing a 1:1 molar ratio of the azide modified sugar molecule and the LA-EG$_n$-cyclooctyne.

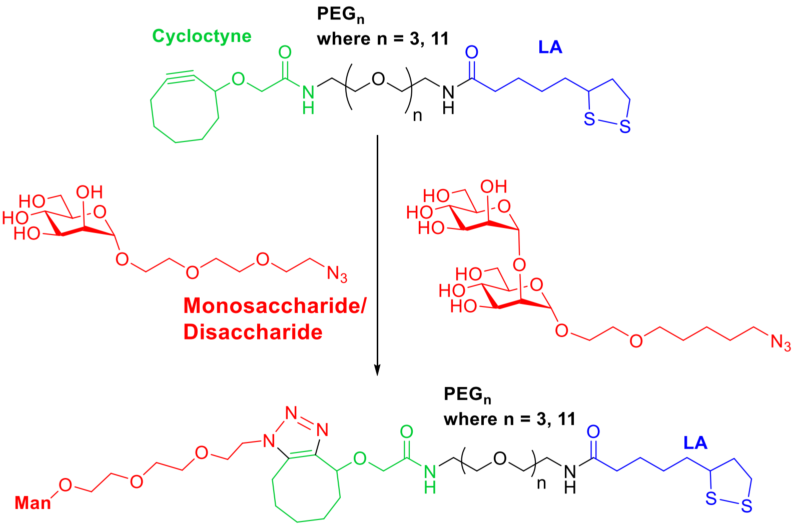

Scheme 5.2.1: A scheme showing the strain promoted click chemistry reaction between the cylooctyne moiety present on the functional ligand and the azide modified glycan moieties.

5.2.2 Copper Catalysed Click Chemistry

The formation of LA-(EG$_n$-Man)$_m$ (where n = 1 or 2; and m = 1, 2 and 3) was achieved using copper catalysed click chemistry between an alkyne-modified LA and azide-modified sugar as reported by Ribeiro-Viana *et al.*[10] (**Scheme 5.2.2**). The reaction is highly favourable and occurs in relatively high yields at room temperature. The reaction was done using a molar ratio of 1:1 for the alkyne and the mannose sugar. A molar ratio of 1: 0.3 was used between mannose and the copper catalyst which must be in an oxidation state of 1+ for the click chemistry to occur. TBTA was added in to stabilise the formed Cu$^+$ produced by in situ reduction of Cu^{2+} by sodium ascorbate.

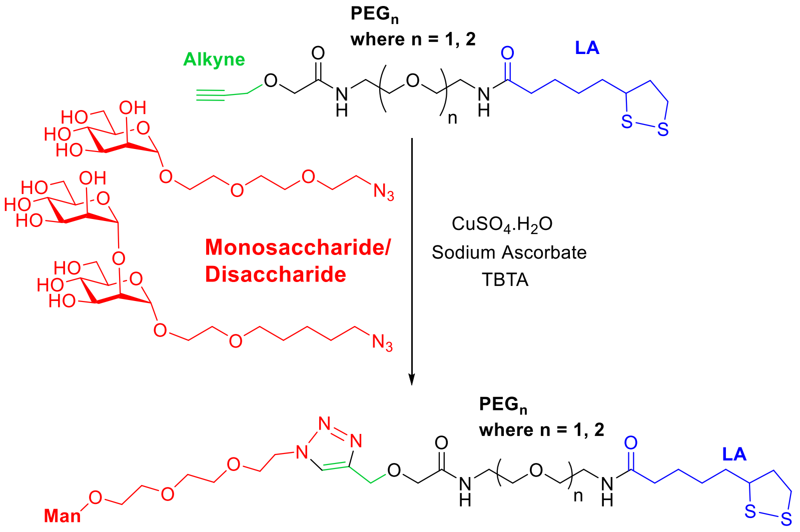

Scheme 5.2.2: A scheme showing the copper catalysed click chemistry reaction between the alkyne functionalised ligand and the azide modified glycan. In this case both the disaccharide and the monosaccharide forms of mannose are used.

5.3 Materials and Methods

5.3.1 Equipment

IR	All IR measurements were carried out on an Alpha FTIR Spectrometer by Bruker.
LC-MS	The mass spectrometry data were initially collected on a Bruker HCT ultra mass spectrometer and then on a UltiMate 3000 HPLC attached to an amazon speed MS (due to the purchase of a new instrument)..
High Resolution MS	All measurements were carried out on a High resolution Bruker Maxis Impact ® mass spectrometer.
NMR	NMR Spectra were recorded on a Bruker Ascend Advance NMR spectrometer (400 MHz for ^{1}H, 100 MHz for ^{13}C) or a Bruker Ascend Advance NMR spectrometer (500 MHz for ^{1}H, 125 MHz for ^{13}C). Samples were taken in the deuterated solvents, $CDCl_3$ and D_2O.
Nanodrop	All absorption spectra were performed by using a Thermo Scientific NanoDrop 2000 UV-Vis Spectrophotometer with an optical path length of 1 mm.
HPLC	HPLC Purification was carried out on a 1260 Infinity II LC System with a 6120 Quadrupole LC-MS attachment.

5.3.2 Materials and Reagents

All the chemicals and reagents that were used for the preparation of the ligands, unless otherwise stated in experimental procedure, were purchased from Sigma-Aldrich, Fisher or Alfa Aesar. CdSe/ZnS Quantum dots (λ_{em} 560 nm) coated in TOPO were purchased from PlasanaChem GmbH (Berlin, Germany). Two different batches of QD were used from the same supplier with different emission wavelengths 554 and 562 nm. These products are no longer commercially available from this company. The alloyed CdS/ZnS QDs were purchased from Mesolight (Suzhou, China) (Product Code - *CdSe-545-25*). Gold Nanoparticles were purchased from Sigma Aldrich (Product Code - *741949)*, apart from those used for the inhibition studies which were prepared by Dr. Akshath Uchangi Satyaprasad, a postdoc within the group, based on a procedure by Piella *et al*.[11] The reagents used for the preparation of the labelled proteins were again all purchased from Sigma-Aldrich or Fisher except the dye which was purchased from Atto-Tec GmbH, Germany. The mannose monosaccharide and disaccharide were synthesised by Chadmas Sakonsinsiri, a PhD student in Bruce Turnbull's group at Leeds, and Dr Yuanyuan Liu, an academic visitor of the Zhou group. The cyclooctyne acid moiety used in the synthesis of the LA-EG_n-Cyclooctyne was synthesised by Dr Guoqiang Feng, a previous visitor of the Zhou group. The final steps in the production of TA-PEG_{750}-OMe were carried out by Lorico Lapitan, a previous PhD student of the group. Dry solvents were obtained from an Innovative Technologies Solvent Drying System and deionised water was obtained from an ELGA Purelab classic UVF system (>18.2 mΩ cm). Column chromatography was carried out using silica gel 60 A to purify the ligands and checked with TLC on silica gel-60 F254 on aluminium plates

5.4 Experimental Procedures: Ligand Synthesis

5.4.1 Synthesis of LA-EG_n-Cyclooctyne Ligands

5.4.1.1 LA-EG_n-N_3 (where n=3 and 11)

LA-EG_3-N_3 (1a):

A solution of N_3-EG_3-NH_2 (1.0 g, 4.58 mmol), DCC (1.040 g, 5.04 mmol) and DMAP (0.0895 g, 0.733 mmol) was prepared in dry DCM (20 mL). The mixture was then cooled to 0˚C under stirring with an ice bath under an N_2 atmosphere. LA (0.95 g, 4.58 mmol) was dissolved in 4 mL of DCM and slowly added through a syringe over 20 minutes again under an N_2 atmosphere. After addition, the reaction was stirred at 0˚C for 1 hour and then was left to gradually return to RT and left for a further 24 hours. The reaction mixture was filtered and the insoluble solid was washed with $CHCl_3$. The combined filtrate and washings were then evaporated to dyness to yield the crude product. The product was purified by silica gel column chromatography using MeOH:

DCM 1:16 (v:v) as eluting solvent. TLC was used to confirm the presence of LA-EG$_3$-N$_3$, **1a**, and the desired fractions were combined and evaporated to dryness, yielding, **1a**, as a yellow oil (1.7489 g, 4.302 mmol, 94% yield).

TLC: (MeOH/CH$_2$Cl$_2$ 1:16) R_f 0.60. **^{1}H-NMR (400 MHz, CDCl$_3$):** δ (ppm) 6.002(s, br, 1H), 3.67 (m, 14H), 3.47 (t, 2H), 3.41 (t, 2H), 3.19 (t, 2H), 3.14 (m, 2H), 2.37 (m, 1H), 2.21 (t, 2H), 1.93 (m, 1H), 1.71 (m, 4H), 1.48 (s, 1H). **{^{1}H}-^{13}C-NMR (100 MHz, CDCl$_3$):** δ (ppm) 172.7 (C, C$_9$), 70.8 – 69.9 (5C, C$_2$-C$_7$), 56.4 (C, C$_{14}$), 50.7 (C, C$_8$), 40.3 (C, C$_{15}$), 39.2 (C, C$_1$), 38.5 (C, C$_{16}$), 36.4 (C, C$_{13}$), 34.7 (C, C$_{10}$), 28.9 (C, C$_{12}$), 25.4 (C, C$_{11}$). **IR**: ν_{max}/cm^{-1} 3322.13 (N-H stretch), 2925.81 and 2854.16 (doublet, C-H), 2099.05 (N=N=N), 1647.28 (C=O), 1536.02 (N-H bending), 1105.23 (C-O). **MS**: calcd *m/z* for C$_{16}$H$_{31}$N$_4$O$_4$S$_2$ (M+ H)$^+$ 407, found 407.8.

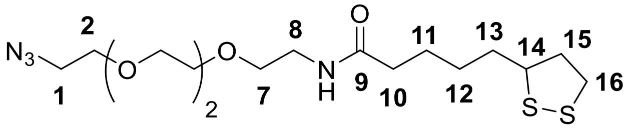

Compound 1a

LA-EG$_{11}$-N$_3$ (1b):

A solution of N$_3$-EG$_{11}$-NH$_2$ (0.481 g, 0.843 mmol), DCC (0.222 g, 1.01 mmol) and DMAP (0.022 g, 0.169 mmol) was prepared in dry DCM (10 mL). The mixture was then cooled to 0˚C under stirring with an ice bath under an N$_2$ atmosphere. LA (0.173 g, 0.843 mmol) was dissolved in 5 mL of DCM and slowly added through a syringe over 20 minutes again under an N$_2$ atmosphere. After addition, the reaction was stirred at 0˚C for 1 hour and then was left to gradually return to RT and left for a further 24 hours. The reaction mixture was filtered and the insoluble solid was washed with CHCl$_3$. The combined filtrate and washings were then evaporated to dyness to yield the crude product. The product was purified by silica gel column chromatography using MeOH: DCM 1:10 (v:v) as eluting solvent. TLC was used to confirm the presence of LA-EG$_{11}$-N$_3$, **1b**, and the desired fractions were combined and evaporated to dryness, yielding, **1b**, as a yellowish oil (0.417 g, 0.549 mmol, 65 % yield).

TLC: (MeOH/CHCl$_3$ 1:10) Rf 0.42. **^{1}H-NMR (400 MHz, CDCl$_3$):** δ (ppm) 6.16 (s, br, 1H), 3.76-3.53 (m, 22H), 3.49 (t, J= 5 Hz, 2H), 3.38 (t, J = 5 Hz, 2H), 3.32 (t, J = 5.2 Hz, 2H), 3.15 (m, 2H), 2.39 (m, 1H), 2.12 (t, J = 7.7 Hz, 2H), 1.84 (m, 1H), 1.60 (m, 4H), 1.51 (s, 1H), 1.40 (m, 2H). **{^{1}H}-^{13}C-NMR (125 MHz, CDCl$_3$):** δ (ppm) 172.8 (C, C$_{25}$), 70.7 – 70.0 (20C, C$_3$-C$_{23}$), 56.5 (C, C$_{30}$), 50.7 (C, C$_{24}$), 40.2 (C, C$_{31}$), 39.2 (C, C$_1$), 38.5 (C, C$_{32}$), 36.3 (C, C$_{29}$), 34.7 (C, C$_{26}$), 28.9 (C, C$_{28}$), 25.4 (C, C$_{27}$). **IR:** ν_{max}/cm^{-1} 3321.94 (N-H stretch), 2915.70 and 2859.78 (doublet, C-H), 2099.40 (N=N=N), 1649.64 (C=O), 1539.87 (N-H bending), 1078.13 (C-O). **MS:** calcd m/z for C$_{32}$H$_{62}$N$_4$O$_{12}$S$_2$Na (M + Na)+ 781, found 781.00.

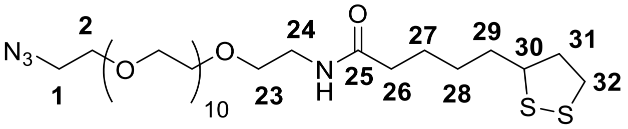

Compound 1b

5.4.1.2 LA-EG$_n$-NH$_2$ (where n= 3 and 11)

LA-EG$_3$-NH$_2$ (2a):

A solution of LA-EG$_3$-N$_3$, **1a**, (1.7489 g, 4.302 mmol) and triphenylphosphine (2.257 g, 8.604 mmol) was prepared in dry THF (30 mL) and then stirred for 1 hour at RT under N$_2$. Next degassed H$_2$O (1.55 mL, 86.04 mmol) was added to the reaction mixture and left to stir for a further 20 hours. The solvent was then removed and crude product was purified using silica gel chromatography. Firstly the by-products were eluted using MeOH: CHCl$_3$ 1:9 (v/v) and then the desired product eluted using MeOH: CHCl$_3$ 3:7 (v/v). TLC then confirmed the presence of LA-EG$_3$-NH$_2$, **2a**, and the desired fractions were combined and evaporated to dryness yielding, **2a**, as a yellowish oil (1.4117 g, 3.710 mmol, 86 % yield).

TLC: (MeOH/CHCl$_3$ 3:7) *Rf* 0.1. **^{1}H-NMR (400 MHz, CDCl$_3$):** δ (ppm) 6.61 (s, br, 1H), 3.36-3.59 (m, 14H), 3.11 (m, 1H), 3.08 (m, 1H), 2.79 (m, 2H), 2.73 (br, 2H), 2.45 (m, 1H), 2.23 (m, 2H), 1.89 (m, 2H), 1.40-1.66 (m, 8H). **{^{1}H}-^{13}C-NMR (100 MHz, CDCl$_3$):** δ (ppm) 172.9 (C, C$_9$), 70.6 – 70.1 (5C, C$_2$-C$_7$), 56.5 (C, C$_{14}$), 50.8 (C, C$_8$), 40.3 (C, C$_{15}$), 39.2 (C, C$_1$), 38.5 (C, C$_{16}$), 36.3 (C, C$_{13}$), 34.7 (C, C$_{10}$), 29.0 (C, C$_{12}$), 25.4 (C, C$_{11}$). **IR**: ν_{max}/cm^{-1} 3344.51 (secondary N-H stretch), 3300.00 (primary N-H stretch), 2926.03 and 2862.35 (doublet C-H), 1672.85 (C=O), 1599.66 (amide N-H bending), 1006.00 (C-O). **MS**: calcd *m/z* for $C_{16}H_{33}N_2O_4S_2$ (M+ H)$^+$ 381.2, found 381.4.

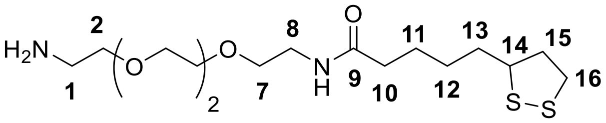

Compound 2a

LA-EG$_{11}$NH$_2$ (2b):

A solution of LA-EG$_{11}$-N$_3$, **1b**, (0.417 g, 0.549 mmol) and triphenylphosphine (0.321 g, 1.098 mmol) was prepared in dry THF (10 mL) and then stirred for 1 hour at RT under N$_2$. Next degassed H$_2$O (0.11 mL) was added to the reaction mixture and left to stir for a further 48 hours. The solvent was then removed and crude product was purified using silica gel chromatography using MeOH: CHCl$_3$ 1:4 (v/v). TLC then confirmed the presence of LA-EG$_{11}$-NH$_2$, **2b**, and the desired fractions were combined and evaporated to dryness yielding, **2b**, as a yellowish oil (0.1448 g, 0.1975 mmol, 35 % yield).

TLC: (MeOH/$CHCl_3$ 1:4) R_f 0.31. **^{1}H-**NMR (400 MHz, $CDCl_3$): δ (ppm) 6.37 (s, br, 1H), 3.69 – 3.53 (m, 44H), 3.48 (m, 2H), 3.17 (m, 2H), 2.90 (m, 2H), 2.81 (s, br, 2H), 2.48 (m, 1H), 2.21 (m, 2H), 1.93 (m, 1H), 1.70 (m, 4H), 1.41 (m, 2H). **{^{1}H}-^{13}C-NMR (125 MHz, $CDCl_3$):** δ (ppm) 172.9 (C, C_{25}), 70.6 – 70.2 (20C, C_3-C_{23}), 56.5 (C, C_{30}), 41.7 (C, C_{24}), 40.2 (C, C_{31}), 39.2 (C, C_1), 38.5 (C, C_{32}), 36.3 (C, C_{29}), 34.7 (C, C_{26}), 28.9 (C, C_{28}), 25.4 (C, C_{27}). **MS**: calcd *m/z* for $C_{32}H_{65}N_2O_{12}S_2$ $(M + H)^+$ 733, found 734.00.

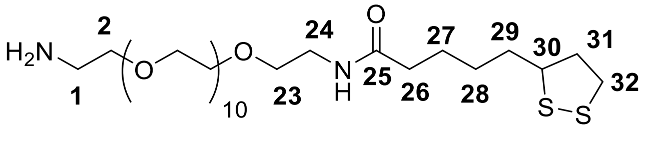

Compound 2b

5.4.1.3 LA-EG$_n$-Cyclooctyne (where n= 3 and 11)

LA-EG$_3$-Cyclooctyne (3a):

A solution of LA-EG$_3$-NH$_2$, **2a**, (1.4117 g, 3.709 mmol), DCC (0.842 g, 4.08 mmol) and DMAP (0.0725 g, 0.594 mmol) was prepared in dry DCM (20 mL). The mixture was then cooled to 0˚C with an ice bath while under N_2. Cyclooctyne acid (0.676 g, 3.709 mmol) was dissolved in 4 mL of DCM and slowly added through a syringe over 20 minutes again under a nitrogen atmosphere. After addition, the reaction was stirred at 0˚C for 1 hour and then was allowed to gradually return to RT and left for stirring for a further 24 hours. The reaction mixture was filtered and the insoluble solid washed with chloroform. The filtrate and washings were combined and evaporated, yielding the crude product. The solution was then purified using silica gel column chromatography MeOH:$CHCl_3$, 1:16 (v/v). TLC then confirmed the presence of LA-EG$_3$-cyclooctyne, **3a**, and the fractions were combined evaporated yielding, **3a**, a yellowish oil (0.5375 g, 0.9866 mmol, 26 % yield).

TLC: (MeOH/CH_2Cl_2 1:16) R_f 0.29. **^{1}H-NMR (400 MHz, $CDCl_3$):** δ (ppm) 6.80 (s, br, 1H), 6.12 (s, br, 1H), 4.18 (s,1H), 3.64-4.01 (m,2H), 3.36-3.59 (m, 14H), 3.11 (m, 1H), 3.10 (m, 1H), 2.41 (m,1H), 2.09-2.40 (m, 4H), 1.19-2.07 (m, 20H). **{^{1}H}-^{13}C-NMR (100 MHz, $CDCl_3$):** δ (ppm) 169.7 (C, C_{19}), 128.5 (C, C_{10}), 73.2 (C, C_8), 70.6 – 69.9 (5C, C_{13}-C_{17}), 68.4 (C, C_2), 56.5 (C, C_{24}), 49.2 (C, C_9), 42.2 (C, C_{18}), 40.3 (C, C_{25}), 39.2 (C, C_{11}), 38.5 (C, C_{26}), 36.4 (C, C_{23}), 34.7 (C, C_{20}), 34.3 (C, C_3), 34.3 (C, C_6), 29.7 (2C, C_4,C_7), 28.9 (C, C_{22}), 25.4 (C, C_{21}), 20.7 (C, C_5). **IR**: ν_{max}/cm^{-1} 3325.56 (N-H stretch), 2925.14 and 2851.31 (doublet, C-H), 2206.01 (weak, C≡C), 1654.91 (C=O), 1533.75 (N-H bending), 1098.83 (C-O). **MS**: calcd *m/z* for $C_{26}H_{46}N_2O_6S_2$ (M+H_2) 546.8, found 546.0.

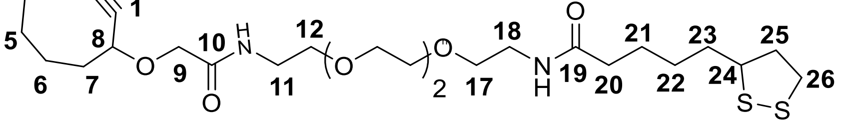

Compound 3a

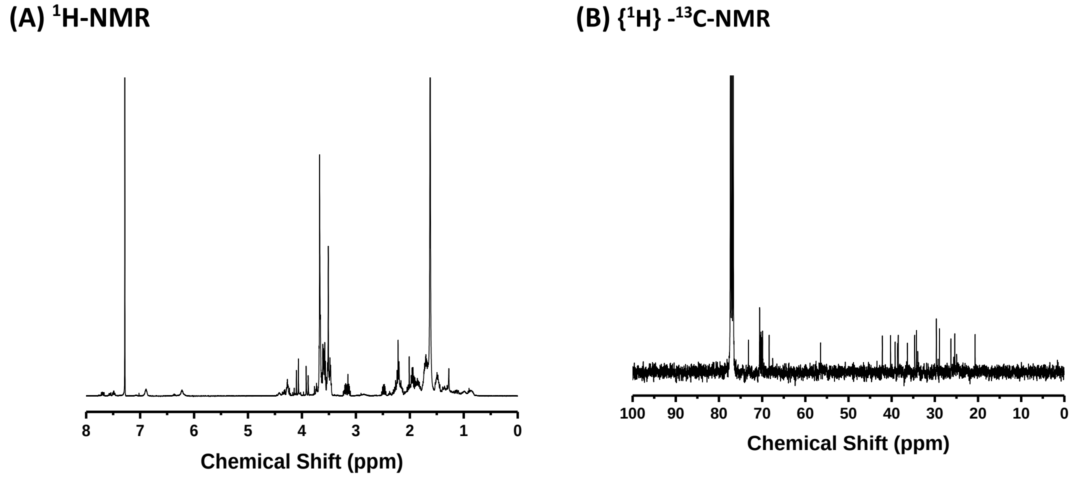

(C) LC-MS

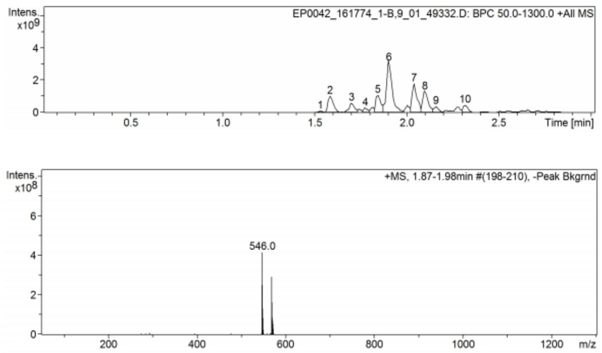

Figure 5.4.1: Spectral Characterisation for final product of synthesis LA-EG$_3$-Cyclooctyne (**3a**) showing **(A)** ^{1}H-NMR spectrum **(B)** ^{13}C-NMR spectrum and **(C)** LC-MS, showing chromatogram and molecular ion peak of compound 6.

LA-EG$_{11}$-Cyclooctyne (3b):

A solution of LA-EG$_{11}$-NH$_2$, **2b**, (0.1448 g, 0.1975 mmol), DCC (0.0489 g, 0.237 mmol) and the cylooctyne acid compound, (0.0360 g, 0.1975 mmol) was prepared in DCM (10 mL). The mixture was then cooled to 0˚C with an ice bath while under N$_2$. A solution of DMAP (0.0050 g, 0.0395 mmol) was prepared in DCM (10 mL) and was added through a syringe over 20 minutes again a nitrogen environment. After addition, the reaction was stirred at 0˚C for 1 hour and then was allowed to gradually return to RT and left for stirring for a further 8 hours. The filtrate and washings were combined and evaporated, yielding the crude product. The solution was then purified using silica gel column chromatography MeOH:CHCl$_3$, 7%:93 %. TLC then confirmed the presence of LA-EG$_{11}$-cyclooctyne, **3b**, and the fractions were combined evaporated yielding, **3b**, a yellowish oil (0.0755 g, 0.0842 mmol, 43 % yield).

TLC: (MeOH/CHCl$_3$ 7 %: 93 %) *Rf* 0.13. **^{1}H-NMR (400 MHz, CDCl$_3$):** δ (ppm) 6.80 (s, br, 1H), 6.19 (s, br, 1H), 4.21 – 4.13 (m, 1H), 3.99 (d, J = 15.1 Hz, 1H), 3.80 (d, J = 15.1 Hz, 1H), 3.61 – 3.51 (m, 4H), 3.50 (m, 2H), 3.40 (m, 2H), 3.08 (m, 2H), 2.39 (m, 1H), 2.12 (m, 2H), 1.84 (m, 1H), 1.62 (m, 4H), 1.39 (m, 2H), 2.3 - 1.3 (m, 10H, ring). **{^{1}H}-^{13}C-NMR (125 MHz, CDCl$_3$):** δ (ppm) 172.1 (C, C$_{35}$), 149.6 (C, C$_{10}$), 94.6 (C, C$_2$), 73.1 (C, C$_8$), 70.6 – 69.7 (20C, C$_{13}$-C$_{33}$), 56.4 (C, C$_{40}$), 49.2 (C, C$_9$), 42.2 (C, C$_{34}$), 40.2 (C, C$_{41}$), 39.1 (C, C$_{11}$), 38.5 (C, C$_{42}$), 36.3 (C, C$_{39}$), 34.7 (C, C$_{36}$), 34.3 (C, C$_3$), 34.0 (C, C$_6$), 29.7 (C, C$_7$), 29.6 (C, C$_4$), 28.9 (C, C$_{38}$), 25.4 (C, C$_{37}$), 20.7 (C, C$_5$). **IR**: ν_{max}/cm^{-1} 3323.50 (N-H stretch), 2924.19 and 2854.80 (doublet, C-H), 2206.25 (weak, C≡C), 1644.98 (C=O), 1533.60 (N-H bending), 1098.83 (C-O). **MS**: calcd *m/z* for $C_{42}H_{76}N_2O_{14}S_2Na$ (M + Na)$^+$ 919, found 919.70.

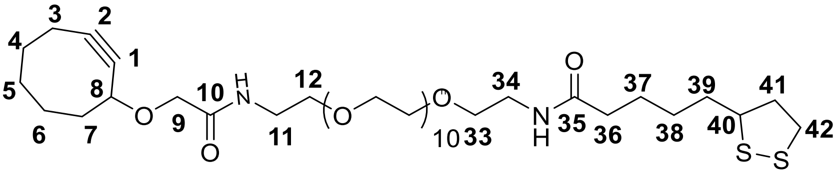

Compound 3b

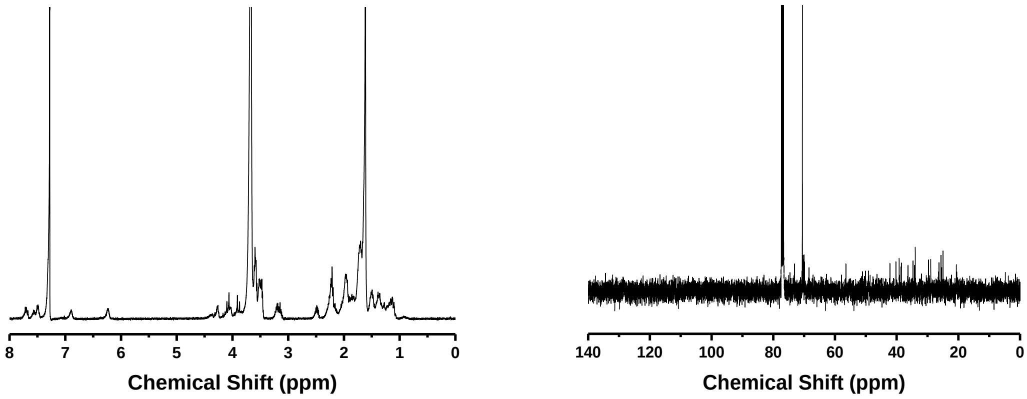
(A) ^{1}H-NMR

(B) {^{1}H}-^{13}C-NMR

(C) LC-MS

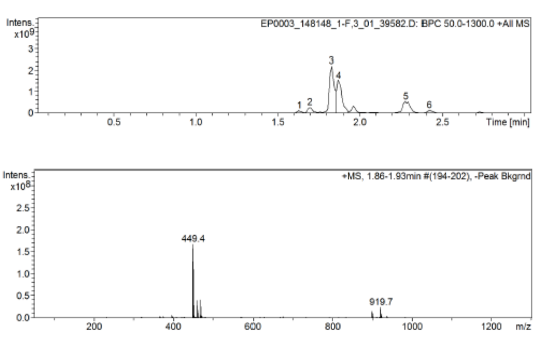

Figure 5.4.2: Spectral Characterisation for final product of synthesis LA-EG$_{11}$-Cyclooctyne (**3b**) showing **(A)** ^{1}H-NMR spectrum **(B)** ^{13}C-NMR spectrum and **(C)** LC-MS, showing chromatogram and molecular ion peak of compound 3.

5.4.2 Synthesis of LA-Zwitterion

5.4.2.1 LA-N,N-dimethyl-1,3-propanediamine (4)

LA (3.0 g, 14.5 mmol) and triethylamine (1.47 g, 14.5 mmol) were dissolved in DCM (30 mL) in a three necked flask and cooled to 0 ˚C in an ice bath under N_2 and stirred for 30 minutes. Methanesulfonyl chloride (1.67 g, 14.5 mmol) was added dropwise through a syringe and then the solution was left to slowly warm back to RT and left to stir for a further 5 hours. After this, N,N-dimethyl-1,3-propanediamine (1.24 g, 11.6 mmol) and trimethylamine (0.61 g,5.8 mmol) were dissolved in DCM (20 mL) and slowly added. The reaction was stirred overnight under N_2 at RT. The resulting solution was then transferred into a separating funnel and washed with water (30 mL x 2) followed by saturated Na_2CO_3 solution (100 mL). The organic layer was then dried using Na_2SO_4 and filtered. The solvent was evaporated, yielding LA-N,N-dimethyl-1,3-propanediamine, **4**, as a yellow oil (1.6131 g, 5.55 mmol, 38 % yield).

^{1}H-NMR (400 MHz, CDCl$_3$): δ (ppm) 6.95 (s, br, 1H), 3.51-3.59 (m, 1H), 3.27-3.32 (m, 2H), 3.10-3.23 (m, 2H), 2.42-2.49 (m, 1H), 2.36 (t, 2H), 2.24 (m, 6H), 2.15 (t, 2H), 1.89-1.97 (m, 1H), 1.65-1.77 (m, 1H), 1.51-1.63 (m, 5H), 1.44-1.51 (m, 2H). **{^{1}H}-^{13}C-NMR (100 MHz, CDCl$_3$):** δ (ppm) 172.6 (C, C$_8$), 58.4 (C, C$_9$), 56.5 (C, C$_3$), 45.2 (2C, C$_{12}$-C$_{13}$), 40.3 (C, C$_2$), 39.2 (C, C$_{11}$), 38.5 (C, C$_1$), 36.6 (C, C$_4$), 34.7 (C, C$_7$), 29.0 (C, C$_5$), 26.0 (C, C$_{10}$), 25.4 (C, C$_6$). **IR**: ν_{max}/cm^{-1} 3276.03 (secondary N-H stretch), 2931.17 and 2856.87 (doublet C-H), 1641.61 (C=O), 1545.26 (N-H bending), 1186.56 (C-N), 1088.61 (C-O). **MS**: calcd *m/z* for $C_{13}H_{27}N_2OS_2$ $(M+H)^+$ 291.48, found 291.2.

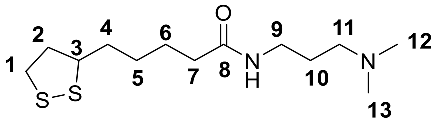

Compound 4

5.4.2.2 LA-Zwitterion (5)

LA-N,N-dimethyl-1,3-propanediamine, **4**, (1.6131 g 5.55 mmol) was dissolved in dry THF (20 mL) and purged with N_2 for 30 minutes. A solution of 1,3-propanesultone (1.0168 g, 8.33 mmol) in dry THF (4 mL) was then added via a syringe. The resulting mixture was left to stir at RT for 3 days. Turbidity was noticed instantly as 1, 3-propanesultone was added, indicating the formation of the desired product which had low stability in THF. After 3 days, the solvent was evaporated and the crude product was washed with chloroform (20 mL x 3). The product was further purified by HPLC to yield the pure LA zwitterion, **5**, as a yellow oil (0.2753 g, 0.668 mmol, 12 % yield).

^{1}H-NMR (400 MHz, D$_2$O): δ (ppm) 3.62-3.69 (m, 1H), 3.39-3.46 (m, 2H), 3.28-3.34 (m, 2H), 3.20-3.27 (m, 2H), 3.10-3.18 (m, 2H), 3.10 (s, 6H), 2.90 (t, 2H), 2.40-2.48 (m, 1H), 2.21 (t, 2H), 2.15 (m,2H) 1.92-2.00 (m, 2H), 1.70 (m, 1H), 1.51-1.59 (m, 4H), 1.33-1.40 (m, 2H). **{^{1}H}-^{13}C-NMR (125 MHz, D_2O):** δ (ppm) 177.2 (C, C_8), 62.2 (2C, $C_{11,\,14}$), 56.6 (C, C_3), 50.7 (2C, $C_{12\text{-}13}$), 47.3 (C, C_9), 47.2 (C, C_{16}), 40.3 (C, C_2), 38.3 (C, C_7), 38.1 (C, C_7), 35.4 (C, C_4), 33.7 (C, C_{15}), 27.9 (C, C_5), 25.0 (C, C_6), 22.3 (C, C_{10}). **MS**: calcd *m/z* for $C_{16}H_{33}N_2O_4S_3$ (M+H$^+$) 413.62, found 413.3.

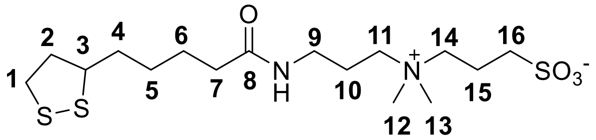

Compound 5

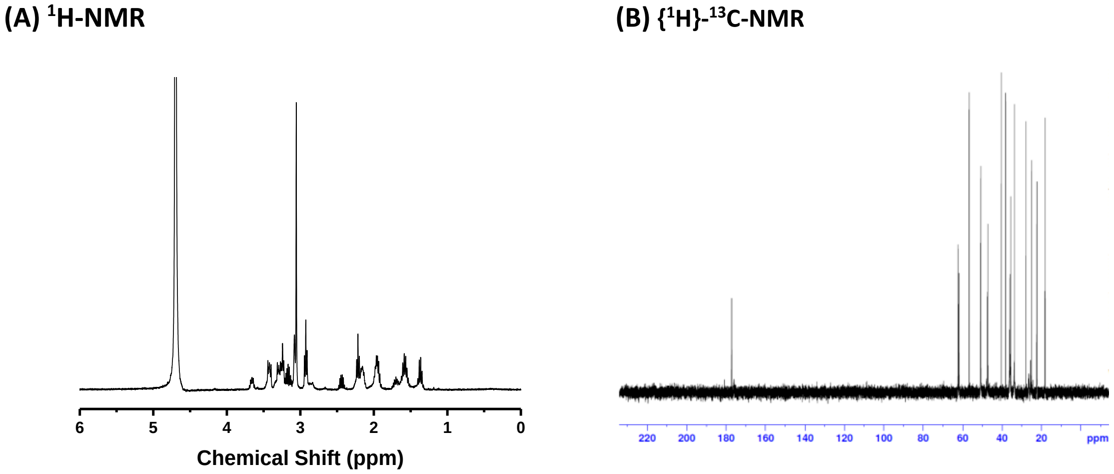
(A) ^{1}H-NMR

(B) {^{1}H}-^{13}C-NMR

(C) LC-MS

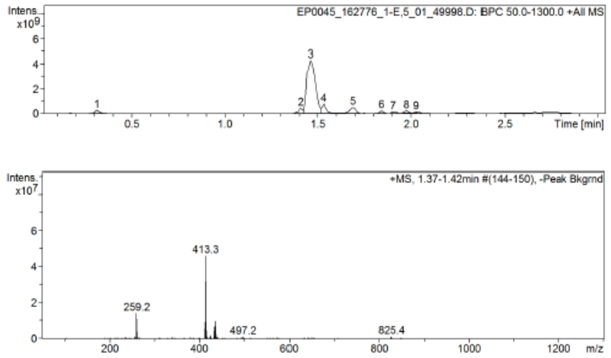

Figure 5.4.3: Spectral Characterisation for final product of synthesis LA-ZW (**5**) showing **(A)** ^{1}H-NMR spectrum **(B)** ^{13}C-NMR spectrum and **(C)** LC-MS, showing chromatogram and molecular ion peak of compound 3.

5.4.3 Synthesis of LA-(EG_n-Man)$_m$ Ligands

5.4.3.1 Synthesis of NH_2-EG_2-Propyne

5.4.3.1.1 *Tert*-butyl 2-(2-hydroxytheoxy) ethylcarbamate (6)

A EtOH (25 mL) solution of 2-(2-aminoethoxy) ethanol, (1.0 g, 9.51 mmol) was cooled to 0˚C into which $(Boc)_2O$ (2.4 mL, 10.46 mmol) was slowly added. The solution was allowed to warm back to RT and was stirred for 5 hrs. The solvent was evaporated and the residue was purified by silica gel chromatography (97:3, $CHCl_3$: MeOH) to yield *tert*-butyl 2-(2-hydroxytheoxy) ethylcarbamate, **6** as a colourless oil, (1.8910 g, 7.76 mmol, 81.6 % yield).

TLC: ($CHCl_3$: MeOH 97:3) R_f 0.20. **^{1}H-NMR (500 MHz, $CDCl_3$):** δ (ppm) 4.91 (br, s, 1H), 3.74 – 3.73 (m, 2H), 3.58 – 3.54 (m, 4H), 3.35 – 3.31 (m, 2H), 2.15 (t, 1H), 1.45 (s, 9H). **{^{1}H}-^{13}C-NMR (125 MHz, $CDCl_3$):** δ (ppm) 156.1 (C, C_5), 79.4 (C, C_4), 72.2 (C, C_8), 70.3 (C, C_6), 61.8 (C, C_9), 40.4 (C, C_7), 28.4 (3C, C_{1-3}). **MS**: calcd *m/z* for $C_9H_{19}NO_4Na$ $(M+Na)^+$ 228.24, found 228.34.

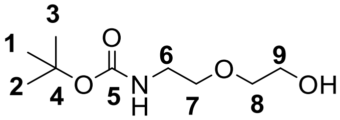

Compound 6

5.4.3.1.2 *Tert*-butyl 2-(2-(prop-2-ynyloxy) ethyoxy) ethylcarbamate (7)

A solution of *tert*-butyl 2-(2-hydroxytheoxy) ethylcarbamate, **6**, (1.8910 g, 7.76 mmol) was prepared in dry THF (20 mL) and cooled to 0˚C. Added to this was 60% NaH (0.37 g, 15.52 mmol) after being washed twice with dry hexane. The solution was then left to stir at 0˚C for 10 minutes. Propargyl bromide (0.727 mL, 8.15 mmol) was added and the solution was allowed to warm to RT and stirred for a further hour. The reaction mixture was then poured into ice-cooled 1 M HCl (30 mL) and the aqueous layer was washed with ethyl acetate (20 mL x 2). The combined organic layer was washed with saturated Na_2CO_3 (20 mL), Brine (20mL), dried over $MgSO_4$, filtered and dried *in vacuo*. The residue was then purified using silica gel chromatography (97:3, $CHCl_3$:MeOH) to yield *tert*-butyl 2-(2-(prop-2-ynyloxy) ethyoxy) ethylcarbamate, **7**, as a yellowish oil, (0.9199 g, 3.78 mmol, 48.8 % yield).

TLC: ($CHCl_3$: MeOH 97:3) R_f 0.78. **^{1}H-NMR (400 MHz, $CDCl_3$)**: δ (ppm) 5.00 (br, s, 1H), 4.21 (d, 2H), 3.70 – 3.68 (m, 2H), 3.65 – 3.63 (m, 2H), 3.55 (t, 2H), 3.34 – 3.30 (m, 2H), 2.44 (t, 1H), 1.44 (s, 9H). **{^{1}H}-^{13}C-NMR (125 MHz, $CDCl_3$):** δ (ppm) 156.1 (C, C_5), 110.7 (C, C_{11}), 79.5 (C, C_4), 74.6 (C, C_{12}), 70.3 (C, C_9), 70.1 (C, C_8), 69.1 (C, C_{10}), 58.5 (C, C_7), 40.4 (C, C_6), 28.4 (3C, C_{1-3}). **MS**: calcd *m/z* for $C_{12}H_{21}NO_4Na$ $(M + Na)^+$ 266.29, found 266.33.

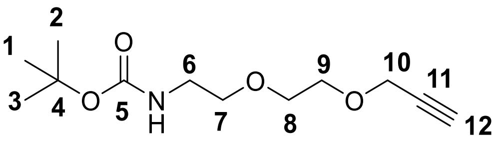

Compound 7

5.4.3.1.3 2-(2-(prop-2-yn-1-yloxy) ethoxy) ethan-1-amine (8)

A solution of *tert*-butyl 2-(2-(prop-2-ynyloxy) ethyoxy) ethylcarbamate, **7**, (0.9199 g, 3.78 mmol) was prepared in 1,4-dioxane (5 mL) and cooled to 0˚C and left to stir for 5 minutes. To this a solution of 4 M HCl in 1,4-Dioxane (15 mL) was added slowly. The resulting solution was left to warm to RT and then stirred overnight. The following day the solution was dried *in vacuo* to yield a yellow oil. H_2O (20 mL) was added to dissolve the residue and the solution was basified to pH 10 using saturated Na_2CO_3 and $NaHCO_3$. The aqueous layer was extracted with $CHCl_3$ (20 mL x 3) and the combined organic layers were dried over $MgSO_4$ and dried under *vacuo* to yield 2-(2-(prop-2-yn-1-yloxy) ethoxy) ethan-1-amine, **8**, (0.5414 g, 3.78 mmol, 100 % yield). TLC was used to confirm that the amine groups were fully deprotected (97:3, $CHCl_3$: MeOH).

TLC: ($CHCl_3$: MeOH 97:3) R_f 0.02. **^{1}H-NMR (400 MHz, $CDCl_3$):** δ (ppm) 8.25 (br, s, 2H), s4.21 (d, J = 2.4 Hz, 2H), 3.72 – 3.70 (m, 2H), 3.66 – 3.65 (m, 2H), 3.52 (t, J = 5.2 Hz, 2H), 2.88 (t, J = 5.2 Hz, 2H), 2.43 (t, J = 2.3 Hz, 1H). **{^{1}H}-^{13}C-NMR (125 MHz, $CDCl_3$):** δ (ppm) 115.3 (C, C_6), 79.3 (C, C_7), 70.1 (C, C_3), 69.1 (C, C_4), 58.5 (C, C_2), 39.8 (C, C_1). **IR**: ν_{max}/cm^{-1} 3380.38 (C-H alkyne), 3217.21 (N-H stretch), 2872.27 (C-H alkane), 2112.12 ($C\equiv C$), 1605.38 (N-H bending), 1351.36 (C-N), 1084.68 (C-O), 1034.79 (C-N). **MS**: calcd *m/z* for $C_7H_{14}NO_2$ $(M + H)^+$ 144.19, found 144.47.

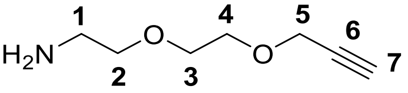

Compound 8

(A) ^{1}H-NMR **(B) {^{1}H}-^{13}C-NMR**

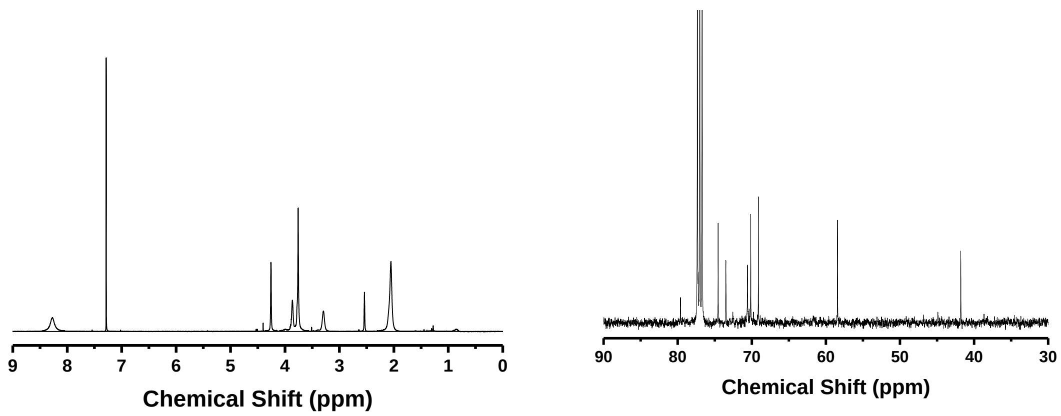

(C) LC-MS

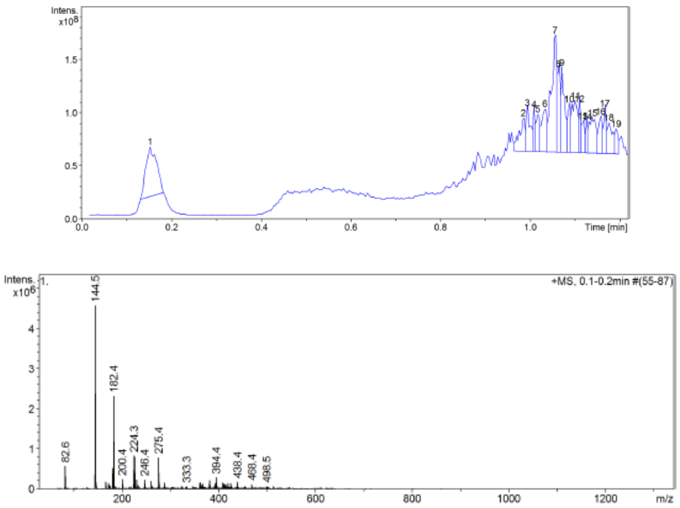

Figure 5.4.4: Spectral Characterisation for final product of synthesis 2-(2-(prop-2-yn-1-yloxy) ethoxy) ethan-1-amine (**8**) showing **(A)** ^{1}H-NMR spectrum **(B)** ^{13}C-NMR spectrum and **(C)** LC-MS, showing chromatogram and molecular ion peak of compound 1.

5.4.3.2 Synthesis of LA-EG$_2$-C≡CH (9)

A solution of 2-(2-(prop-2-yn-1-yloxy) ethoxy) ethan-1-amine, **8**, (6.44 mmol, 0.9226 g), LA, (6.44 mmol, 1.3288 g), and DCC (7.73 mmol, 1.5949 g) was prepared in DCM (20 mL) while stirring under N$_2$. The reaction mixture was then cooled to 0˚C before a solution of DMAP (1.29 mmol, 0.1576 g) in DCM (5 mL) was slowly added over a period of 10 – 15 minutes. The resulting mixture was then stirred at 0˚C for 1 hour before allowing it to warm to RT and stirred for a further 48 hours. The crude product was filtered and washed with DCM and dried under vacuum. The crude product was then purified using silica gel column chromatography (40:1, DCM: MeOH) to yield a yellow oil, TA-EG$_2$-C≡CH, **9**, (1.6700 g, 5.038 mmol, 78.2 % yield).

TLC: (DCM: MeOH 40:1) *R_f* 0.22. **^{1}H-NMR (400 MHz, $CDCl_3$)**: δ (ppm) 6.02 (br, s, 1H), 4.23 (d, 2H), 3.73 – 3.66 (m, 2H), 3.62 – 3.55 (m, 2H), 3.50 – 3.46 (m, 5H), 3.23 – 3.10 (m, 2H), 2.52 - 2.44 (m, 2H), 2.21 (t, 2H), 1.97 – 1.88 (m, 1H), 1.74 – 1.65 (m, 4H), 1.53 – 1.43 (m, 2H). **{^{1}H}-^{13}C-NMR (125 MHz, $CDCl_3$):** δ (ppm) 172.7 (C, C_8), 116.2 (C, C_{14}), 74.8 (C, C_{15}), 70.1 (C, C_{12}), 69.9 (C, C_{11}), 69.1 (C, C_{13}), 58.5 (C, C_{10}), 56.4 (C, C_3), 40.3 (C, C_2), 39.1 (C, C_9), 38.5 (C, C_1), 36.4 (C, C_7), 34.7 (C, C_4), 28.9 (C, C_5), 25.38 (C, C_6). **IR**: ν_{max}/cm^{-1} 3319.24 (N-H stretch), 2926.11 and 2850.03 (doublet C-H alkane), 2112.90 (C≡C), 1641.04 (C=O) 1536.45 (N-H bend), 1087.15 (C-O). **MS**: calcd *m/z* for $C_{15}H_{25}NO_3S_2$ $(M + H)^+$ 332.49, found 332.36.

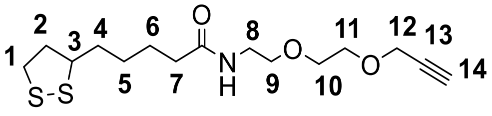

Compound 9

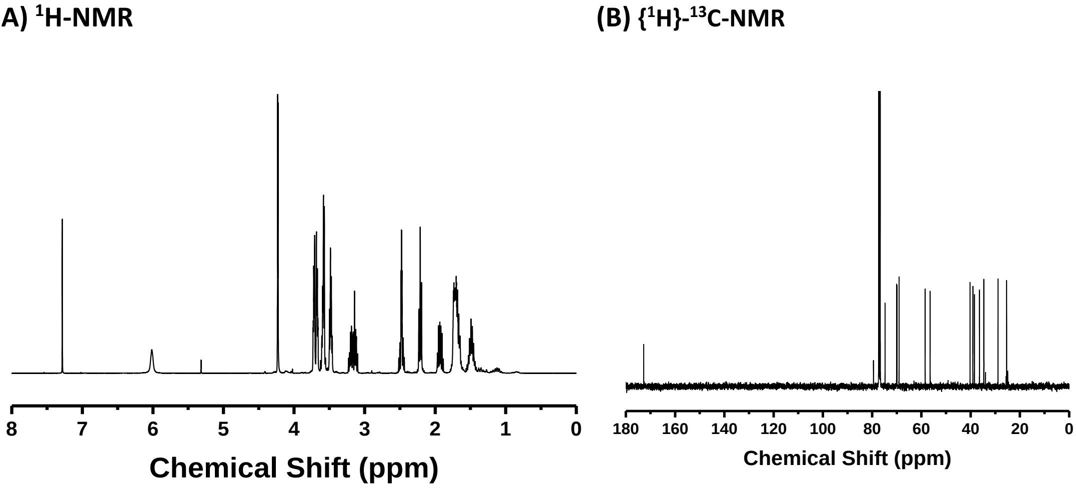
(A) ^{1}H-NMR

(B) {^{1}H}-^{13}C-NMR

(C) LC-MS

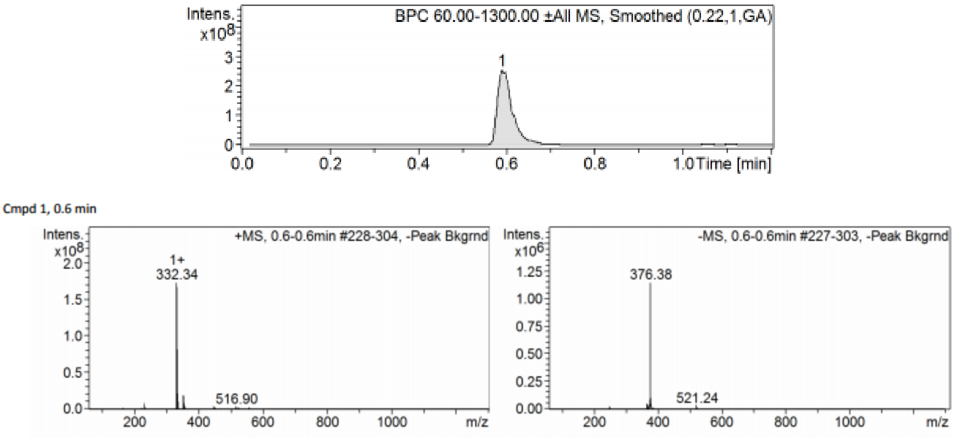

Figure 5.4.5: Spectral Characterisation for final product of synthesis LA-EG_2-CCH (**9**) showing **(A)** ^{1}H-NMR spectrum **(B)** ^{13}C-NMR spectrum and **(C)** LC-MS, showing chromatogram and molecular ion peak (positive and negative ion trace) of compound 1.

5.4.3.3 Synthesis of LA-(EG$_2$-C≡CH)$_2$

5.4.3.3.1 BocNH-(EG$_2$-C≡CH)$_2$ (10)

A solution of Boc-*L*-Aspartic acid, **6**, (1.89 mmol, 0.4408 g), 2-(2-(prop-2-yn-1-yloxy) ethoxy) ethan-1-amine, 8, (3.78 mmol, 0.5414 g), and DCC (2.27 mmol, 0.4684 g) was prepared in DCM/DMF (10 mL/5 mL) while stirring under N_2. The reaction mixture was then cooled to 0˚C before a solution of DMAP (0.38 mmol, 0.0646 g) in DCM (2 mL) was slowly added over a period of 10 – 15 minutes. The resulting mixture was then stirred at 0˚C for 1 hour before allowing it to warm to RT and stirred for a further 48 hours. The crude product was then filtered and washed with DCM and dried under vacuum. The crude product was then purified using silica gel column chromatography (30:1, CH_2Cl_2: MeOH) to yield a colourless oil, BocHN-(EG$_2$-C≡CH)$_2$, **10**, (0.7027 g, 1.45 mmol, 76.9 % yield).

TLC: (CH_2Cl_2: MeOH 15:1) R_f 0.40. **^{1}H-NMR (500 MHz, CDCl$_3$)**: δ 7.11 (bs, 1H), 6.33 (bs, 1H), 6.11 (d, 1H), 4.43 (bs, 1H), 4.2 (d, 4H), 3.68 (m, 4H), 3.63 (m, 4H), 3.53 (m, 4H), 3.42 (m, 4H), 2.87 (d, 1H), 2.53 (dd, 1H), 2.47 (t, 1H), 2.45 (t, 1H), 1.44 (s, 9H). **{^{1}H}-^{13}C-NMR (125 MHz, CDCl$_3$):** 171.2 (C_9), 171.0 (C_8), 155.7 (C_5), 80.1 (C_4), 79.6 (C_{15}), 79.5 (C_{22}), 74.9 (C_{16}), 74.7 (C_{23}), 70.1 (C_{11}), 70.1 (C_{18}), 69.7 (C_{12}), 69.6 (C_{19}), 69.1 (C_{13}), 69.0 (C_{20}), 58.4 (C_{14}), 58.4 (C_{21}), 51.3 (C_6), 39.3 (C_{10}), 39.2 (C_{17}), 37.6 (C_7), 28.3 (C_{1-3}). **MS**: calcd *m/z* for $C_{23}H_{38}N_3O_8$ $(MH)^+$ 484.26, found 484.56.

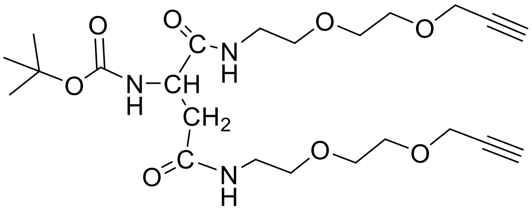

Compound 10

5.4.3.3.2 H$_2$N-(EG$_2$-C≡CH)$_2$ (11)

A solution of BocHN-(EG$_2$-C≡CH)$_2$, **10**, (0.7027 g, 1.45 mmol), was prepared in 1,4 – Dioxane (5 mL) and cooled to 0˚C under N_2. Slowly added to this was 4 M HCl solution prepared in 1,4 – Dioxane (15 mL) and left to stir at 0˚C for 10 minutes, before being allowed to warm to RT and stirred overnight. The solution was dried under vacuum to yield a yellow oil. H_2O (20 mL) was added to the residue and was basified using saturated Na_2CO_3 and $NaHCO_3$. The aqueous layer was then extracted with $CHCl_3$ (20 mL x3) and the combined organic layers were dried over $MgSO_4$ and dried under *vacuo* to yield H$_2$N-(EG$_2$-C≡CH)$_2$, **11**, (0.5561 g, 1.45 mmol, 100 % yield). TLC was used to confirm that the amine groups were fully deprotected (5:1, $CHCl_3$:MeOH).

TLC: ($CHCl_3$: MeOH 5:1) R_f 0.06. **^{1}H-NMR (500 MHz, $CDCl_3$)**: δ 7.73 (t, 1H), 6.75 (bs, 1H), 4.18 (dd, 4H), 3.72 (m, 1H), 3.66 (m, 4H), 3.62 (m, 4H), 3.54 (q, 4H), 3.42 (m, 5H), 2.71 (dd, 1H), 2.61 (bs, 2H), 2.48 (t, 1H), 2.45 (t, 1H). **{^{1}H}-^{13}C-NMR (125 MHz, $CDCl_3$):** 173.7 (C_{11}), 171.1 (C_3), 79.6 (C_{17}), 79.5 (C_9), 74.9 (C_{18}), 74.8 (C_{10}), 70.1 (C_{13}), 70.0 (C_5), 69.7 (C_{14}), 69.7 (C_6), 69.1 (C_{15}), 69.1 (C-7), 58.4 ($C_{16,\,8}$), 52.6 (C_1), 40.7 (C_{12}), 39.1 (C_4), 39.0 (C_2). **MS**: calcd *m/z* for $C_{18}H_{30}N_3O_6$ $(MH)^+$ 384.45, found 384.43.

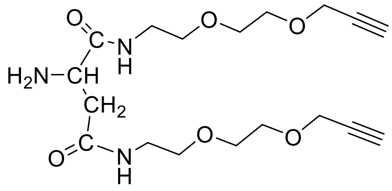

Compound 11

5.4.3.3.3 LA-(EG$_2$-C≡CH)$_2$ (12)

A solution of H_2N-(EG_2-C≡CH)$_2$, **11**, (3.74 mmol, 1.4356 g), LA, (3.74 mmol, 0.7725 g), and DCC (4.49 mmol, 0.9270 g) was prepared in DCM (15 mL) while stirring under N_2. The reaction mixture was then cooled to 0˚C before a solution of DMAP (0.75 mmol, 0.0915 g) in DCM (2 mL) was slowly added over a period of 10 – 15 minutes. The resulting mixture was stirred at 0˚C for 1 hour before being allowed to warm to RT and stirred for a further 48 hours. The crude product was filtered and washed with DCM and organic layers were combined dried under vacuum. The crude product was purified using silica gel column chromatography (15:1, $CHCl_3$: MeOH) to yield a yellow oil, LA-(EG_2-C≡CH)$_2$, **12**, (1.6050 g, 0.32 mmol, 75.1 % yield).

TLC: ($CHCl_3$: MeOH 5:1) R_f 0.34. **^{1}H-NMR (400 MHz, $CDCl_3$)**: δ (ppm) 6.26 (br, s, 1H), 6.02 (br, s, 2H), 4.23 (d, 4H), 4.21 – 4.19 (m, 1H), 3.73 – 3.64 (m, 6H), 3.60 – 3.55 (m, 5H), 3.48 – 3.45 (m, 4H), 3.24 – 3.10 (m, 2H), 2.98 (d, 1H), 2.91 (m, 1H), 2.54 – 2.44 (m, 2H), 2.38 (t, 2H), 2.28 (t, 2H), 1.98 – 1.89 (m, 1H), 1.66 – 1.75 (m, 4H), 1.48 – 1.53 (m, 2H). **{^{1}H}-^{13}C-NMR (125 MHz, $CDCl_3$):** δ (ppm) 171.3 (C, C_8), 170.8 (2C, $C_{10,\,19}$), 74.8 (2C, $C_{17,\,26}$), 70.1 (2C, $C_{13,\,22}$), 69.6 (2C, $C_{14,\,23}$), 58.4 (2C, $C_{15,\,24}$), 56.3 (C, C_3), 49.8 (C, C_9), 40.2 (C, C_2), 39.4 (2C, $C_{11,\,20}$), 38.5 (2C, $C_{1,\,18}$), 37.3 (C, C_7), 36.3 (2C, $C_{12,\,21}$), 34.6 (C, C_4), 28.8 (C, C_5), 25.2 (C, C_6). **IR**: ν_{max}/cm^{-1} 3271.16 (N-H stretch), 2924.04 and 2853.71 (doublet C-H alkane), 2109.76 (C≡C), 1630.70 (C=O), 1547.84 (N-H bend), 1095.88 (C-O). **MS**: calcd *m/z* for $C_{26}H_{42}N_3O_7S_2$ $(M + H)^+$ 572.75, found 572.56.

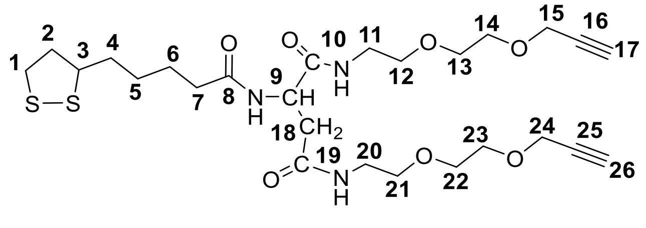

Compound 12

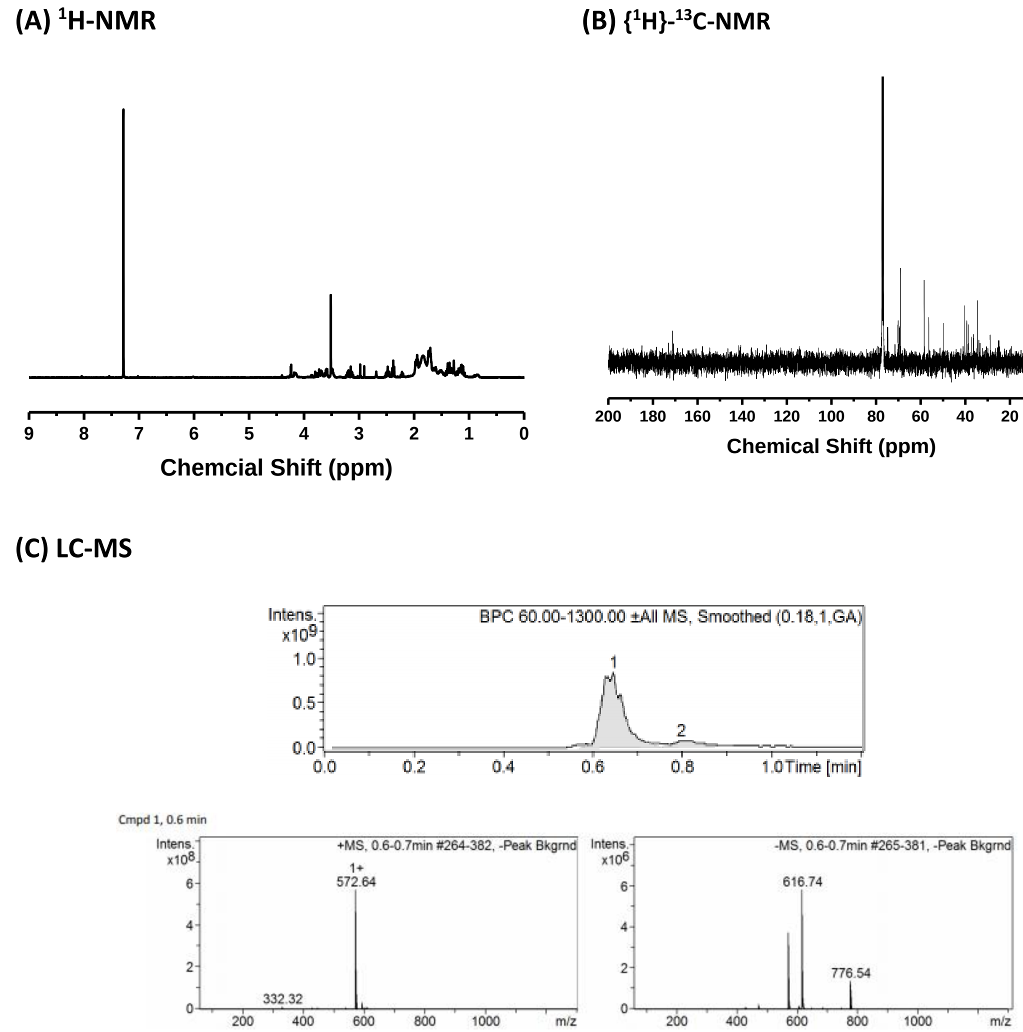

Figure 5.4.6: Spectral Characterisation for final product of synthesis LA-(EG_2-CCH)$_2$ (**12**) showing **(A)** ^{1}H-NMR spectrum **(B)** ^{13}C-NMR spectrum and **(C)** LC-MS, showing chromatogram and molecular ion peak (positive and negative ion trace) of compound 1.

5.4.3.4 Synthesis of LA-(EG-C≡CH)$_3$

5.4.3.4.1 BocNH-(CH_2OH)$_3$ (13)

To a solution of tris(hydroxymethyl)aminomethane, (2.0 g, 16.5 mmol) in EtOH (50 mL) cooled at 0˚C was added slowly $(Boc)_2O$ (4.0 g, 18.2 mmol). The solution was allowed to warm back to RT and was stirred overnight after which the solvent was evaporated to yield the crude product as a white solid. The solid was then purified by recrystallization in EtOAc. The product was then collected via vacuum filtration to yield a white solid, *N-Boc* tris(hydroxymethyl)aminomethane, **13**, (3.02 g, 13.7 mmol, 82.8 % yield).

^{1}H-NMR (400 MHz, D_2O): δ (ppm) 3.65 (s, 6H), 3.46 (s, 1H), 1.37 (s, 9H). **{^{1}H}-^{13}C-NMR (125 MHz, D_2O):** δ (ppm) 155.92 (C, C_5), 62.8 (C, C_4), 60.4 (3C, $C_{7\text{-}9}$), 60.1 (C, C_6), 27.61 (3C, $C_{1\text{-}3}$). **MS**: calcd *m/z* for $C_9H_{19}NO_5Na$ (M + Na)$^+$ 244.24, found 244.12.

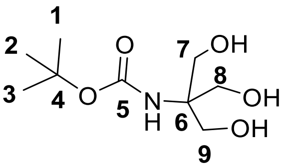

Compound 13

5.4.3.4.2 BocNH-(EG-C≡CH)$_3$ (14)

A solution of *N-Boc* tris(hydroxymethyl)aminomethane, **13**, (1.0 g, 4.52 mmol) in dry DMF (12 mL) was stirred at 0˚C, with propargyl bromide (80 % wt% in toluene) (1.33 mL, 27.2 mmol). Portions of finely ground KOH (1.90 g, 27.2 mmol) were added over a period of 20-30 minutes. The mixture was then heated to 35˚C and stirred for 24 hours under N_2. EtOAc (20 mL) was added to the resulting brown mixture and the resulting solution was transferred to a separating funnel containing EtOAc (80 mL). The solution was then washed with H_2O (60 mL x 3). The organic layer was collected, dried over $MgSO_4$ and rotary evaporated to yield the crude product. This was then purified using silica gel column chromatography (95:5, Hexane: EtOAc) to yield a yellow oil, BocNH-(EG-C≡CH)$_3$, **14**, (0.5502 g, 1.64 mmol, 36.3 % yield).

TLC: (Hexane: EtOAc 7:3) R_f 0.55. **^{1}H-NMR (400 MHz, $CDCl_3$)**: δ (ppm) 4.92 (br, s, 1H), 4.15 (d, 6H), 3.79 (s, 6H), 2.42 (t, 3H), 1.43 (s, 9H). **{^{1}H}-^{13}C-NMR (125 MHz, $CDCl_3$):** δ (ppm) 154.7 (C, C_5), 79.6 (C, C_4), 74.5 (3C, $C_{10, 14, 18}$), 68.9 (3C, $C_{7, 11, 15}$), 58.7 (3C, $C_{8, 12, 16}$), 58.1 (C, C_6), 28.4 (3C, C_{1-3}). **MS**: calcd *m/z* for $C_{18}H_{25}NO_5Na$ $(M + Na)^+$ 358.39, found 358.16.

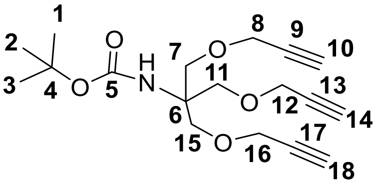

Compound 14

5.4.3.4.3 NH$_2$-(EG-C≡CH)$_3$ (15)

A solution of BocHN-(EG-CCH)$_3$, **14**, (0.5000 g, 1.49 mmol), was prepared in 1,4 – Dioxane (5 mL) and cooled to 0˚C under N_2. Slowly added to this was 4 M HCl solution in 1,4 – Dioxane (15 mL) and the resulting solution was left to stir at 0˚C for 10 minutes, before being allowed to warm to RT and stirred overnight. The solution was dried under vacuum to yield a yellow oil. H_2O (20 mL) was added to dissolve the residue and the resulting solution was basified using saturated Na_2CO_3 and $NaHCO_3$. The aqueous layer was then extracted using $CHCl_3$ (20 mL x 3) and the combined organic layers were dried over $MgSO_4$ and dried under *vacuo* to yield H_2N-(EG-CCH)$_3$, **15**, (0.3508 g, 1.49 mmol, 100 % yield).

^{1}H-NMR (400 MHz, $CDCl_3$): δ (ppm) 4.16 (d, 6H), 3.50 (s, 6H), 2.42 (t, 3H). **{^{1}H}-^{13}C-NMR (125 MHz, $CDCl_3$):** δ (ppm) 74.6 (3C, $C_{5, 9, 13}$), 71.8 (3C, $C_{2, 6, 10}$), 58.7 (3C, $C_{3, 7, 11}$), 55.9 (C, C_1). **MS**: calcd *m/z* for $C_{13}H_{18}NO_3$ (M + H)$^+$ 236.28, found 236.33.

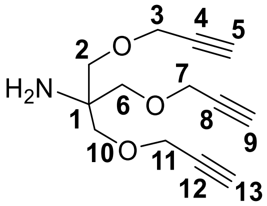

Compound 15

5.4.3.4.4 LA-(EG-C≡CH)$_3$ (16)

A solution of NH_2-(EG-C≡CH)$_3$, **15**, (1.49 mmol, 0.3508 g), thiotic acid, (1.49 mmol, 0.3076 g), and DCC (1.79 mmol, 0.3691 g) was prepared in DCM (20 mL) while stirring under N_2. The reaction mixture was then cooled to 0˚C before a solution of DMAP (0.30 mmol, 0.0364 g) in DCM (5 mL) was slowly added over a period of 10 – 15 minutes. The resulting mixture was then stirred at 0˚C for 1 hour before warming to RT and stirred for a further 48 hours. The crude product was filtered and washed with DCM and the combined organic layers were dried under vacuum. The crude product was purified using silica gel column chromatography (15:1, $CHCl_3$: MeOH) to yield a yellow oil, LA-(EG-C≡CH)$_3$, **16**, (0.5311 g, 1.25 mmol, 84.1 % yield).

TLC: ($CHCl_3$: MeOH 15:1) R_f 0.74. **^{1}H-NMR (400 MHz, $CDCl_3$)**: δ (ppm) 5.70 (br, s, 1H), 4.17 (d, 6H), 3.87 (s, 6H), 3.63 – 3.56 (m, 1H), 3.23 – 3.10 (m, 2H), 2.52 – 2.43 (m, 2H), 2.47 – 2.45 (t, 3H), 2.19 (t, 2H),1.97 – 1.89 (m, 1H), 1.75 – 1.63 (m, 4H), 1.53 – 1.44 (m, 2H). **{^{1}H}-^{13}C-NMR (125 MHz, $CDCl_3$):** δ (ppm) 172.9 (C, C_8), 74.6 (3C, $C_{13, 17, 21}$), 68.6 (3C, $C_{10, 14, 18}$), 59.2 (C, C_9), 58.7 (3C, $C_{11, 15, 19}$), 56.43 (C, C_3), 40.2 (C, C_2), 38.5 (C, C_1), 37.0 (C, C_7), 34.7 (C, C_4), 28.7 (C, C_5), 25.3 (C, C_6). **IR**: ν_{max}/cm^{-1} 3290.32 (N-H stretch) 2926.50 and 2849.72 (doublet C-H alkane), 2115.03 (C≡C), 1657.76 (C=O), 1516.08 (N-H bend) 1086.50 (C-O). **MS**: calcd *m/z* for $C_{21}H_{30}NO_4S_2$ (M + H)$^+$ 424.59, found 424.41.

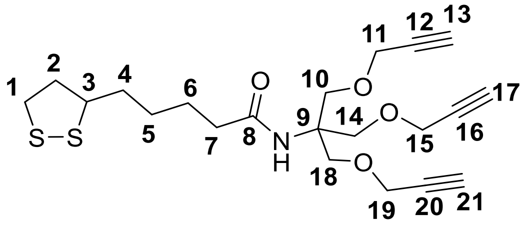

Compound 16

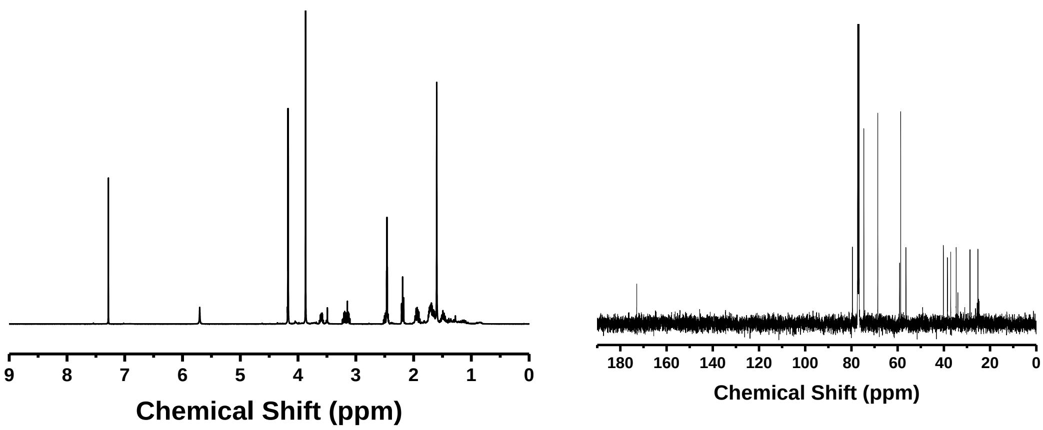

(A) ^{1}H-NMR

(B) {^{1}H}-^{13}C-NMR

(C) LC-MS

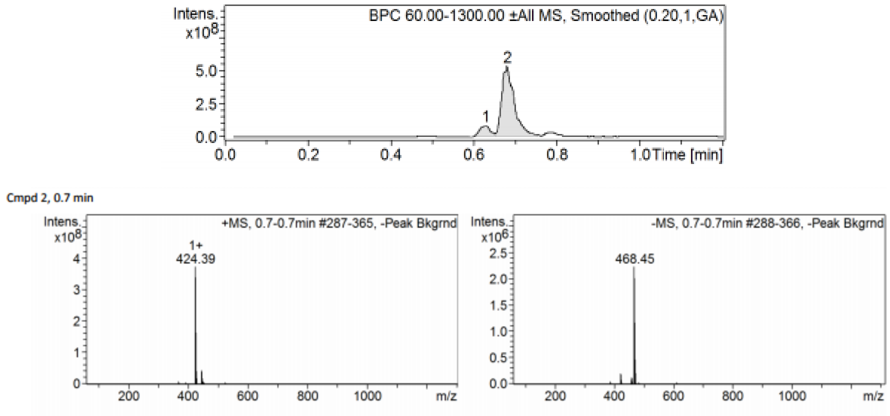

Figure 5.4.7: Spectral Characterisation for final product of synthesis LA-(EG-CCH)$_3$ (**16**) showing **(A)** ^{1}H-NMR spectrum **(B)** ^{13}C-NMR spectrum and **(C)** LC-MS, showing chromatogram and molecular ion peak (positive and negative ion trace) of compound 2.

5.4.4 Synthesis of N$_3$-PEG$_{750}$-OMe

5.4.4.1 Methanesulfonyl-PEG$_{750}$-OMe (17)

A solution of monomethoxypolyetheylene glycol (OH-PEG$_{750}$-OMe) (37.5 g, 50 mmol) and methanesulfonyl chloride (11.45 g, 100 mmol) was prepared in THF (150 mL) and cooled to 0˚C and purged with N$_2$. Triethylamine (15 mL, 111 mmol) was slowly added via an addition funnel over a 30 minute period. The reaction was then allowed to warm to RT and left to stir overnight. The mixture was then diluted using a solution of NaHCO$_3$ (3.125 g, 37 mmol) prepared in H$_2$O (50 mL). The resulting solution was transferred into a separation funnel and extracted with CHCl$_3$ (60 mL x 3). The organic layers were then combined and evaporated to dryness yielding the crude product methanesulfonyl-PEG$_{750}$-OMe, **17**, as a yellow oil (40.86 g, 49.3 mmol, 98 %).

TLC: ($CHCl_3$: MeOH 10:1) R_f 0.65. **^{1}H-NMR (400 MHz, $CDCl_3$)**: δ (ppm) 4.32 – 4.30 (m, 2H), 3.71 – 3.69(m, 2H), 3.59 – 3.47 (m, 68H), 3.49 – 3.47 (m, 2H), 3.31 (s, 3H), 3.01 (s, 3H). **{^{1}H}-^{13}C-NMR (100 MHz, $CDCl_3$):** δ (ppm) 71.6 (C, C_{37}), 70.6 – 70.5 (34C, C_3-C_{36}), 69.3 – 69.0 (2C, C_1, C_2), 59.0 (C, C_{38}). **MS**: *m/z* formula for Me-SO_3-PEG_{750}-OMe $(M + Na)^+$ = 177.17 + 44*n*, found 661.31 (*n=11*), 705.33 (*n=12*), 749.36 (*n=13*) and 793.69 (*n=14*).

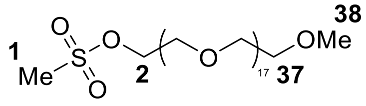

Compound 17

5.4.4.2 N_3-PEG_{750}-OMe (18)

A solution of monomethoxypolyetheylene glycol (OH-PEG_{750}-OMe) (37.5 g, 50 mmol) and methanesulfonyl chloride (11.45 g, 100 mmol) was prepared in THF (150 mL) and cooled to 0˚C and purged with N_2. Triethylamine (15 mL, 111 mmol) was slowly added via an addition funnel over a 30 minute period. The reaction was then allowed to warm to RT and left to stir overnight. The mixture was then diluted using a solution of $NaHCO_3$ (3.125 g, 37 mmol) prepared in H_2O (50 mL). The resulting solution was transferred into a separation funnel and extracted with $CHCl_3$ (60 mL x 3). The organic layers were then combined and evaporated to dryness yielding the crude product methanesulfonyl-PEG_{750}-OMe, **17**, as a yellow oil (40.86 g, 49.3 mmol, 98 %).

TLC: ($CHCl_3$: MeOH 10:1) R_f 0.75. **^{1}H-NMR (400 MHz, $CDCl_3$)**: δ (ppm) 3.68 – 3.63 (m, 70H), 3.55 – 3.53 (m, 2H), 3.37 (s, 3H). **{^{1}H}-^{13}C-NMR (100 MHz, $CDCl_3$):** δ (ppm) 71.9 (C, C_{35}), 70.7 – 70.0 (32C, C_2-C_{34}), 59.0 (C, C_{36}), 50.7 (C, C_1). **MS**: *m/z* formula for N_3-PEG_{750}-OMe $(M + NH_4)^+$ = 119.13 + 44*n*, found 603.38 (*n=11*), 647.41 (*n=12*), 691.43 (*n=13*) and 735.46 (*n=14*).

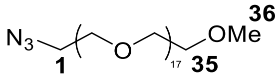

Compound 18

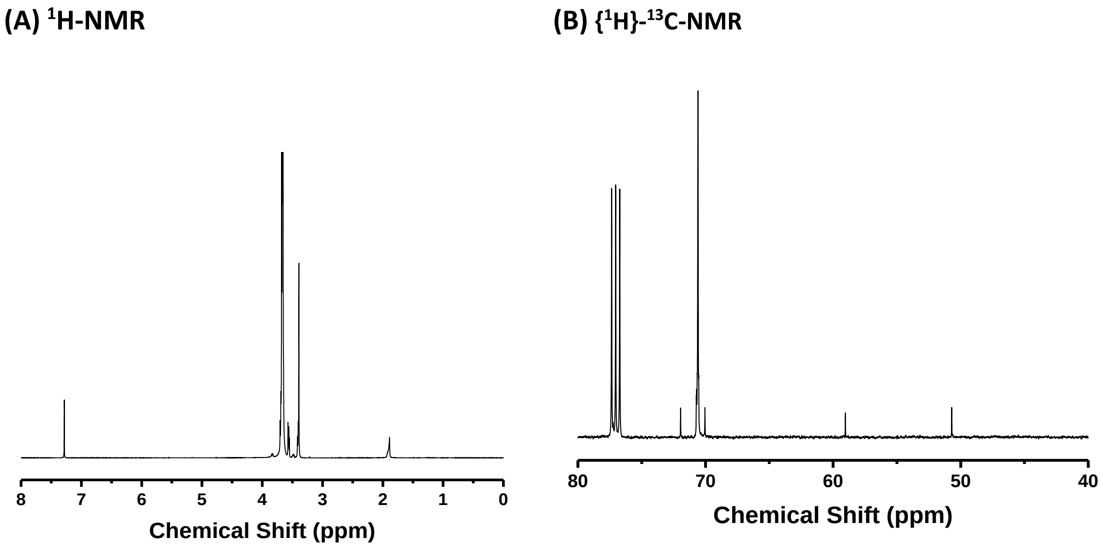

(C) HR-MS

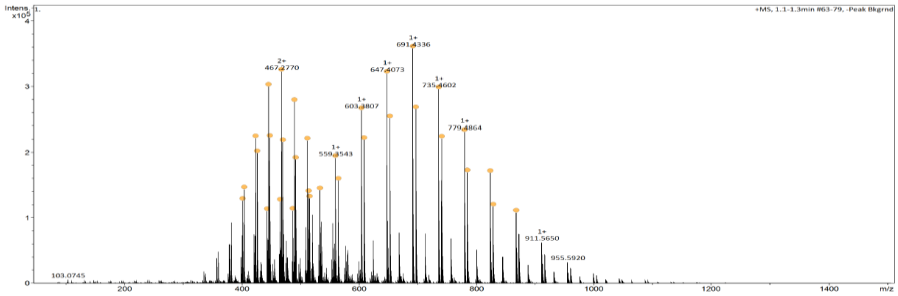

Figure 5.4.8: Spectral Characterisation for final product of synthesis N_3-PEG$_{750}$-OMe (**18**) showing **(A)** ^{1}H-NMR spectrum **(B)** ^{13}C-NMR spectrum and **(C)** HR-MS mass peaks present within the pure sample.

5.5 Click Chemistry Experimental

5.5.1 Strain Promoted Alkyne-Azide Coupling

LA-EG$_n$-Cycloctyne where n= 3 or 11 was prepared in a solution of MeOH. They were then mixed in a 1:1 ratio with 1-Azido-3,6-dioxaoct-8-yl 2-*O*-α-manno-pyranside or 1-Azido-3,6-dioxaoct-8-yl-2-O-α-D-mannopyranosyl-α-D-mannopyranoside according to **Table 5.5.1**. MeOH (~ 100 µL) was added to the click chemistry to make a clear solution. The reaction was then left at RT for three days and monitored using LC-MS and TLC. MeOH: $CHCl_3$ (1 :5 for mannose) and (4 :6 for dimannose) to ensure the click reactions were complete. Then tris(2-carboxyethyl)phosphine hydrochloride, TCEP, (6 µmol) in H_2O was added to the reaction mixture and incubated at RT for 30 min to reduce the ligands into its DHLA equivalents. After evaporation of solvent, the resulting DHLA-EG$_n$-Man^m ligands were purified by silica gel column chromatography using MeOH: $CHCl_3$ (1: 5 for Man) and (4: 6 for DiMan).

Table 5.5.1: The amounts of the LA-EG$_n$-cyclooctyne ligands used in the strain promoted alkyne-azide click chemistry.

Ligand	Concentration (mM)	Amount (Man)$_m$ (µmol)	Volume (µL)	Yield (%)
LA-EG$_3$-Cyclooctyne	100	5	50	57.1
LA-EG$_{11}$-Cyclooctyne	70	5	72	56.7

5.5.2 Monosaccharide Based Ligands

DHLA-EG$_3$-Man:

TLC: ($CHCl_3$: MeOH 5:1) *R$_f$* 0.36. **MS**: *m/z* formula for $C_{38}H_{69}N_5O_{14}S_2$ (M + H)$^+$ = 884.11, found 884.60.

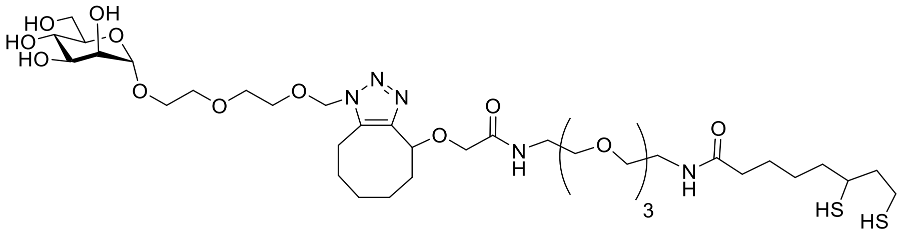

Compound 19

DHLA-EG$_{11}$-Man:

TLC: ($CHCl_3$: MeOH 5:1) *R$_f$* 0.60. **MS**: *m/z* formula for $C_{54}H_{102}N_5O_{22}S_2$ (M + H)$^+$ = 1237.54, found 1238.00.

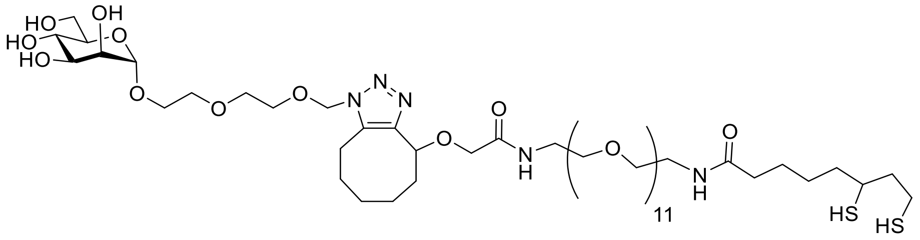

Compound 20

5.5.3 Disaccharide Based Ligands

DHLA-EG$_3$-DiMan:

TLC: (CHCl$_3$: MeOH 6:4) *R$_f$* 0.10. **MS**: *m/z* formula for $C_{44}H_{80}N_5O_{19}S_2$ $(M + H)^+$ = 1046.25, found 1046.20.

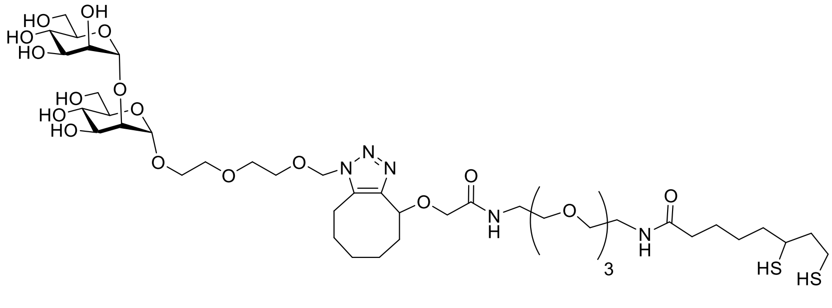

Compound 21

DHLA-EG$_{11}$-DiMan:

TLC: (CHCl$_3$: MeOH 6:4) *R$_f$* 0.60. **MS**: *m/z* formula for $C_{60}H_{111}N_5O_{27}S_2$ $(M + H)^+$= 1398.67, found 1398.70.

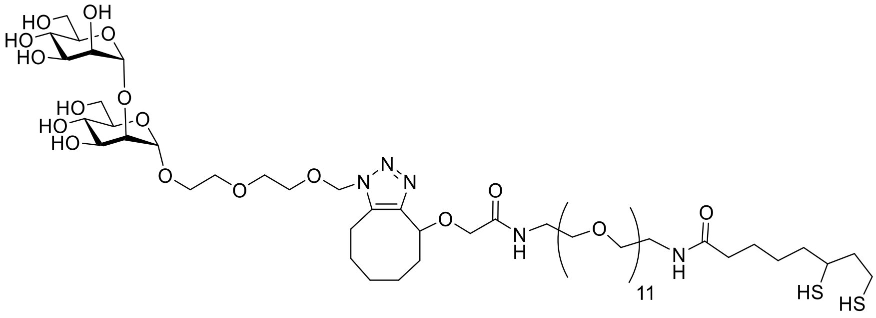

Compound 22

5.6 Copper Catalysed Click Chemistry

5.6.1 Monosaccharide Based Ligands

Stock solutions of LA-(EG$_n$-C≡CH)$_m$ ligands, where n= 1 or 2 and m= 1, 2 and 3, were prepared in H_2O/THF (1:1). They were mixed with 1-Azido-3,6-dioxaoct-8-yl 2-*O*-α-manno-pyranside (30 µmol, 30 µL, 500 mM in H_2O) along with $CuSO_4.5H_2O$ (0.9 µmol, 0.22 mg), Sodium Ascorbate (3.75 µmol, 0.74 mg) and TBTA (1.74 µmol, 0.92 mg) according to the amounts and volumes displayed in **Table 5.6.1** below. The reaction was then left overnight at RT to form the corresponding LA-(EG$_n$-Man)$_m$. The reaction was then dried *in vacuo* and purified using column chromatography using a 5:1 CHCl$_3$: MeOH to give the purified glycan ligands.

Table 5.6.1: The amounts of the LA-(EG_n-C≡CH)$_m$ ligands used in the copper catalysed click chemistry with 1-Azido-3,6-dioxaoct-8-yl 2-*O*-α-manno-pyranside and the product yields.

Ligand	Concentration (mM)	Amount (µmol)	Volume (µL)	Yield (%)
LA-EG_2-C≡CH	500	27.78	55.56	91.2
LA-(EG_2-C≡CH)$_2$	500	13.89	27.78	56.7
LA-(EG-C≡CH)$_3$	250	9.26	37.04	59.7

LA-EG_2-Man:

TLC: ($CHCl_3$: MeOH 5:1) *R_f* 0.32. **^{1}H-NMR (400 MHz, $CDCl_3$)**: δ (ppm) 8.12 (s, 1H), 4.91 (d, 1H), 3.99 (dd, 1H), 3.93 (m, 2H), 3.87 – 3.84 (m, 1H), 3.80 – 3.75 (m, 12H), 3.73 – 3.71 (m, 2H), 3.69 – 3.67 (m, 2H), 3.53 (t, 2H), 3.40 (m, 4H), 3.26 – 3.22 (m, 2H), 2.54 – 2.47 (m, 2H), 2.27 (m, 2H), 1.70 – 1.60 (m, 4H), 1.46 – 1.40 (m, 2H). **MS**: *m/z* formula for $C_{27}H_{49}N_4O_{11}S_2$ $(M + H)^+$ = 669.83, found 669.57.

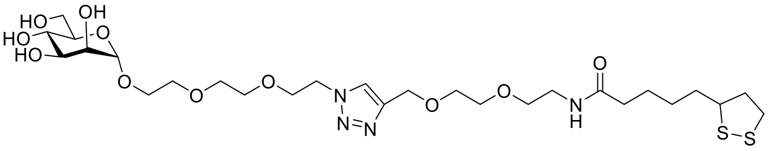

Compound 23

LA-(EG_2-Man)$_2$:

TLC: ($CHCl_3$: MeOH 5:1) *R_f* 0.12. **^{1}H-NMR (400 MHz, $CDCl_3$)**: δ (ppm) 8.12 (s, 2H), 4.89 (d, 4H), 4.01 (d, 4H), 3.96 (dd, 2H), 3.88 – 3.78 (m, 8H), 3.77 – 3.61 (m, 32H), 3.62 (t, 4H), 3.38 (m, 1H), 3.28 – 3.16 (m, 2H), 2.80 – 2.65 (m, 2H), 2.53 – 2.45 (m, 1H), 2.30 (t, 1H), 2.03 – 1.94 (m, 1H), 1.77 – 1.59 (m, 4H), 1.43 – 1.35 (m, 2H). **MS**: *m/z* formula for $C_{50}H_{88}N_9O_{23}S_2$ $(M + H)^+$ = 1247.41, found 1248.28.

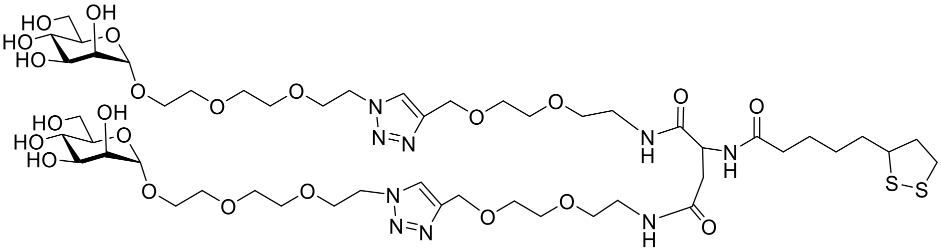

Compound 24

LA-(EG-Man)$_3$:

TLC: ($CHCl_3$: MeOH 5:1) *R$_f$* 0.04. **^{1}H-NMR (400 MHz, $CDCl_3$)**: δ (ppm) 8.05 (s, 3H), 4.89 (d, 3H), 4.65 (d, 6H), 4.00 – 3.96 (m, 9H), 3.91 – 3.88 (m, 3H), 3.83 (t, 6H), 3.78 – 3.65 (m, 36H), 3.38 (s, 1H), 3.25 – 3.13 (m, 2H), 2.48 – 2.40 (m, 2H), 2.21 (t, 2H), 1.98 – 1.90 (m, 1H), 1.61 – 1.52 (m, 4H), 1.39 – 1.33 (m, 2H). **MS**: *m/z* formula for $C_{57}H_{99}N_{10}O_{28}S_2$ $(M + H)^+$ = 1436.58, found 1437.20.

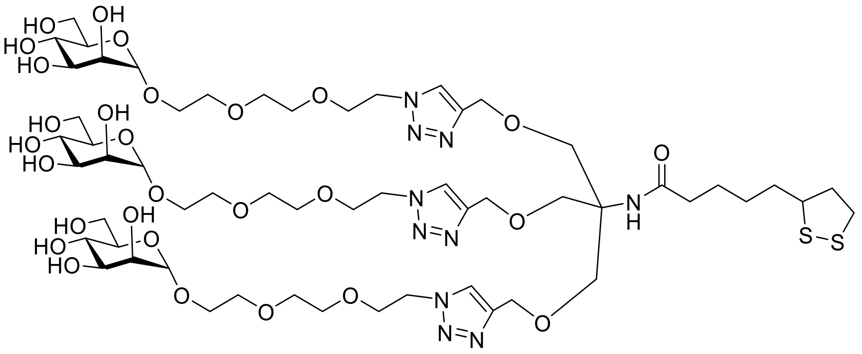

Compound 25

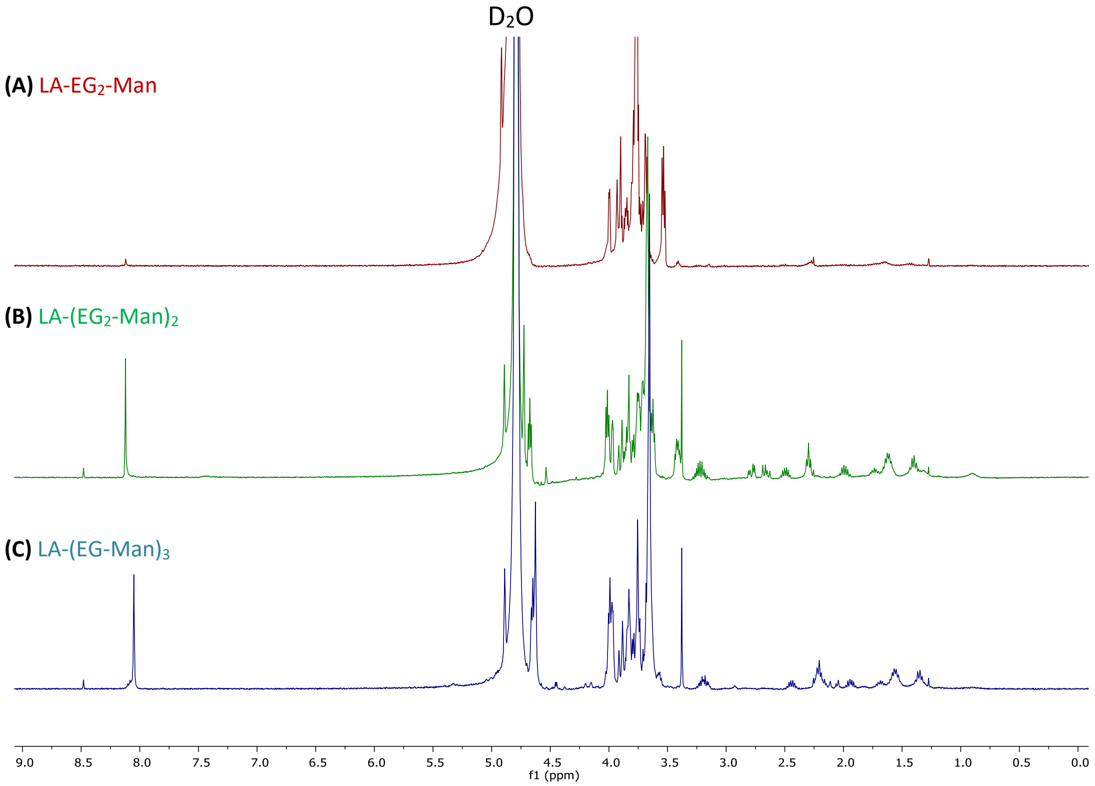

Figure 5.6.1: ^{1}H-NMR Spectrum for the disaccharide ligands overlaid to compare the similarities and differences. **(A)** LA-EG$_2$-Man, **(B)** LA-(EG$_2$-Man)$_2$ and **(C)** LA-(EG-Man)$_3$. All run in D_2O at 400 MHz.

5.6.2 Disaccharide Based Ligands

Stock solutions of LA-(EG$_n$-C≡CH)$_m$ ligands, where n= 1 or 2 and m= 1, 2 and 3, were prepared in H_2O/THF (1:1). They were mixed with 1-Azido-3,6-dioxaoct-8-yl-2-O-α-D-mannopyranosyl-α-D-mannopyranoside (20 μmol, 40 μL, 500 mM in H_2O) along with $CuSO_4.5H_2O$ (0.6 μmol, 0.15 mg), Sodium Ascorbate (2.5 μmol, 0.50 mg) and TBTA (1.16 μmol, 0.62 mg) according to the amounts and volumes displayed in **Table 5.6.2** below. The reaction was then left for 3 days at RT to form the corresponding LA-(EG$_n$-DiMan)$_m$. The reaction was then dried *in vacuo* and purified using column chromatography using a 5:1 $CHCl_3$: MeOH to give the purified glycan ligands.

Table 5.6.2: The amounts of the LA-(EG$_n$-C≡CH)$_m$ ligands used for the copper click chemistry with the 1-Azido-3,6-dioxaoct-8-yl-2-O-α-D-mannopyranosyl-α-D-mannopyranoside and the product yields.

Ligand	Concentration (mM)	Amount (μmol)	Volume (μL)	Yield (%)
LA-EG$_2$-C≡CH	1000	18.52	18.52	51.1
LA-(EG$_2$-C≡CH)$_2$	500	9.26	18.52	37.1
LA-(EG-C≡CH)$_3$	500	6.17	12.35	30.3

LA-EG$_2$-DiMan:

TLC: ($CHCl_3$: MeOH 5:1) R_f 0.24. **^{1}H-NMR (400 MHz, $CDCl_3$)**: δ (ppm) 8.12 (s, 2H), 5.14 (d, 1H), 5.06 (d, 1H), 4.10 (m, 3H), 4.02 (m, 1H), 3.98 - 3.80 (m, 5H), 3.78 – 3.62 (m, 21H), 3.54 (t, 2H), 3.41 (t, 2H) 3.27 – 3.19 (m, 2H), 2.52 – 2.42 (m, 2H), 2.27 (m, 2H), 2.03 – 1.97 (m, 1H), 1.67 – 1.57 (m, 4H), 1.45 – 1.38 (m, 2H). **MS**: *m/z* formula for $C_{33}H_{59}N_4O_{10}S_2$ $(M + H)^+$ = 831.97, found 831.32.

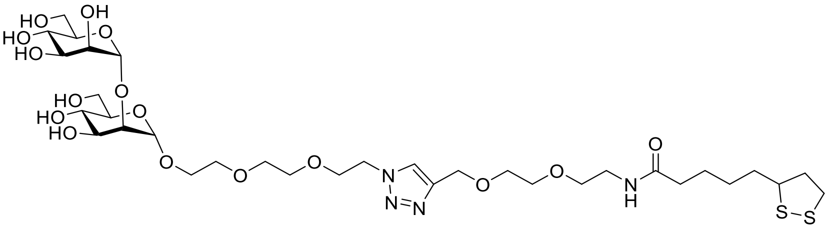

Compound 26

LA-(EG$_2$-DiMan)$_2$:

TLC: ($CHCl_3$: MeOH 5:1) R_f 0.02. **^{1}H-NMR (400 MHz, $CDCl_3$)**: δ (ppm) 8.12 (s, 2H), 5.14 (d, 2H), 5.06 (d, 2H), 4.10 (m, 3H), 4.03 – 3.97 (m, 8H), 3.95 - 3.84 (m, 5H), 3.82 – 3.71 (m, 12H), 3.83 – 3.60 (m, 46H), 3.53 (t, 4H) 3.43 – 3.40 (m, 4H), 3.26 – 3.18 (m, 2H), 2.80 – 2.75 (m, 1H), 2.70 – 2.63 (m, 1H), 2.53 – 2.45 (m, 2H), 2.29 (t, 2H), 2.01 – 1.93 (m, 1H), 1.70 – 1.54 (m, 4H), 1.48 – 1.33 (m, 2H). **MS**: *m/z* formula for $C_{62}H_{108}N_9O_{33}S_2$ (M + H)$^+$ = 1571.70, found 1571.68.

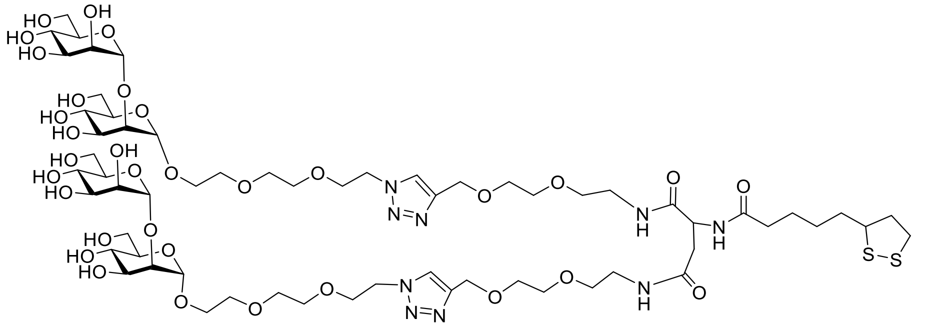

Compound 27

LA-(EG-DiMan)$_3$:

TLC: ($CHCl_3$: MeOH 5:1) R_f 0.02. **^{1}H-NMR (400 MHz, $CDCl_3$)**: δ (ppm) 8.05 (s, 3H), 5.13 (m, 3H), 5.05 (m, 3H), 4.10 (m, 3H), 3.99 (m, 5H), 3.95 - 3.85 (m, 9H), 3.82 – 3.71 (m, 12H), 3.70 – 3.61 (m, 45H), 3.57 – 3.55 (t, 3H) 3.38 (s, 6H), 3.24 – 3.14 (m, 2H), 2.49 – 2.40 (m, 2H), 2.20 (t, 2H), 1.96 - 1.91 (m, 1H), 1.61 – 1.52 (m, 4H), 1.32 – 1.38 (m, 2H). **MS**: *m/z* formula for $C_{75}H_{129}N_{10}O_{43}S_2$ (M + H)$^+$ = 1923.00, found 1923.78.

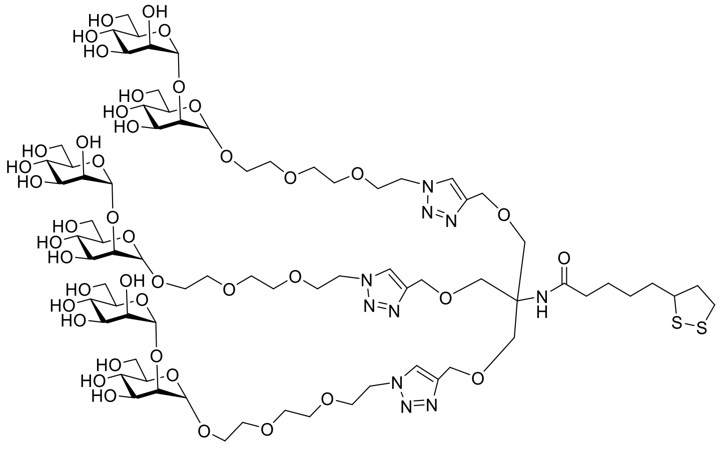

Compound 28

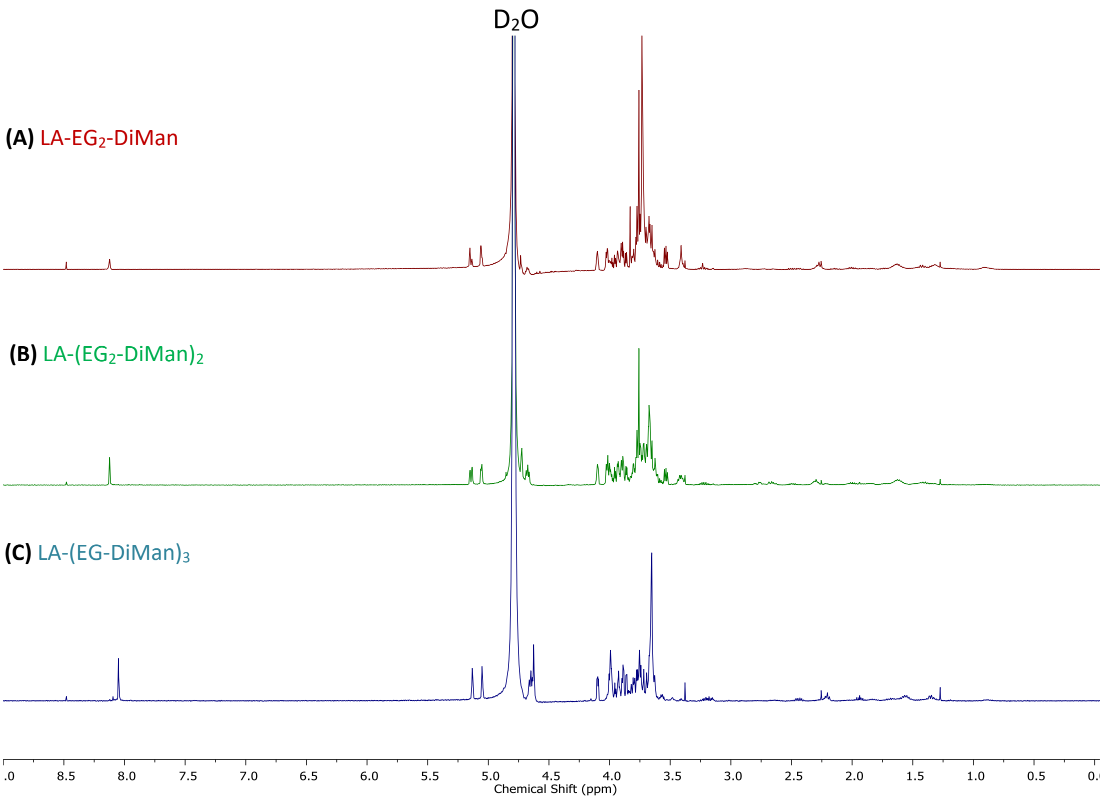

Figure 5.6.2: ^{1}H-NMR spectrum for the disaccharide ligands overlaid to compare the similarities and differences. **(A)** LA-EG$_2$-DiMan, **(B)** LA-(EG$_2$-DiMan)$_2$ and **(C)** LA-(EG-DiMan)$_3$. All run in D_2O at 400 MHz.

5.6.3 PEGylated Based Ligands

Stock solutions of LA-(EG$_n$-C≡CH)$_m$ ligands, where n= 1 or 2 and m= 1, 2 and 3, were prepared in H_2O/THF (1:1). They were mixed with N_3-PEG$_{750}$-OMe (23.5 µmol, 23.5 µL, 1 M in H_2O) along with $CuSO_4.5H_2O$ (0.7 µmol, 0.18 mg), Sodium Ascorbate (3.0 µmol, 0.61 mg) and TBTA (1.41 µmol, 0.75 mg) according to the amounts and volumes displayed in **Table 5.6.3** below. The reaction was then left for 3 days at RT to form the corresponding LA-(PEG)$_m$. The reaction was then dried *in vacuo* and purified using column chromatography using a 10:1 $CHCl_3$: MeOH to give the pure PEG ligands.

Table 5.6.3: The amounts of the LA-(EG$_n$-C≡CH)$_m$ ligands used for the copper click chemistry with the N_3-PEG$_{750}$-and the product yields.

Ligand	Concentration (mM)	Amount (µmol)	Volume (µL)	Yield (%)
LA-(EG$_2$-C≡CH)$_2$	153	10.88	71.11	32.2
LA-(EG-C≡CH)$_3$	250	7.25	29.01	30.0

LA-(PEG$_{750}$-OMe)$_2$:

TLC: ($CHCl_3$: MeOH 10:1) R_f 0.37. **^{1}H-NMR (400 MHz, $CDCl_3$)**: δ (ppm) 7.78 (s, 2H), 5.49 (br, s, 3H), 4.68 (d, 4H), 4.54 (t, 4H), 3.87 (t, 4H), 3.68 – 3.61 (m, 153H), 3.56 – 3.54 (m, 8H), 3.38 (s, 6H), 3.19 – 3.08 (m, 2H), 2.25 – 2.14 (m, 4H), 1.39 – 1.25 (m, 6H). **MS**: *m/z* formula for LA-(PEG$_{750}$-OMe)$_2$ $(M + Na)^+$ = 772.94 + *2n*(44), found 1920.98 (*n=13*), 2008.03 (*n=14*) and 2097.03 (*n=15*).

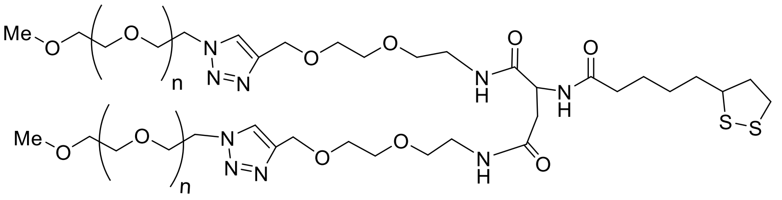

Compound 29

LA-(PEG$_{750}$-OMe)$_3$:

TLC: ($CHCl_3$: MeOH 10:1) R_f 0.12. **^{1}H-NMR (400 MHz, $CDCl_3$)**: δ (ppm) 7.71 (s, 3H), 5.49 (br, s, 1H), 4.58 (s, 6H), 4.54 (t, 6H), 3.88 (t, 6H), 3.68 – 3.61 (m, 229H), 3.56 – 3.54 (m, 12H), 3.38 (s, 9H), 3.19 – 3.08 (m, 2H), 2.25 – 2.14 (m, 4H), 1.39 – 1.25 (m, 6H). **MS**: *m/z* formula for LA-(PEG$_{750}$-OMe)$_2$ $(M + Na)^+$ = 755.96 + *2n*(44), found 2089.15 (*n=10*), 2221.22 (*n=11*) and 2353.30 (*n=12*).

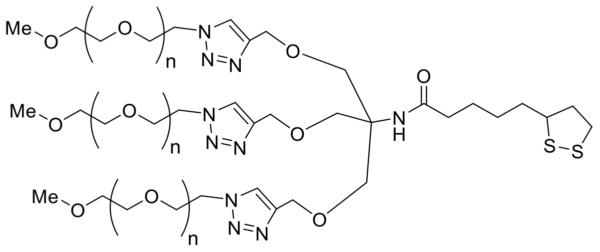

Compound 30

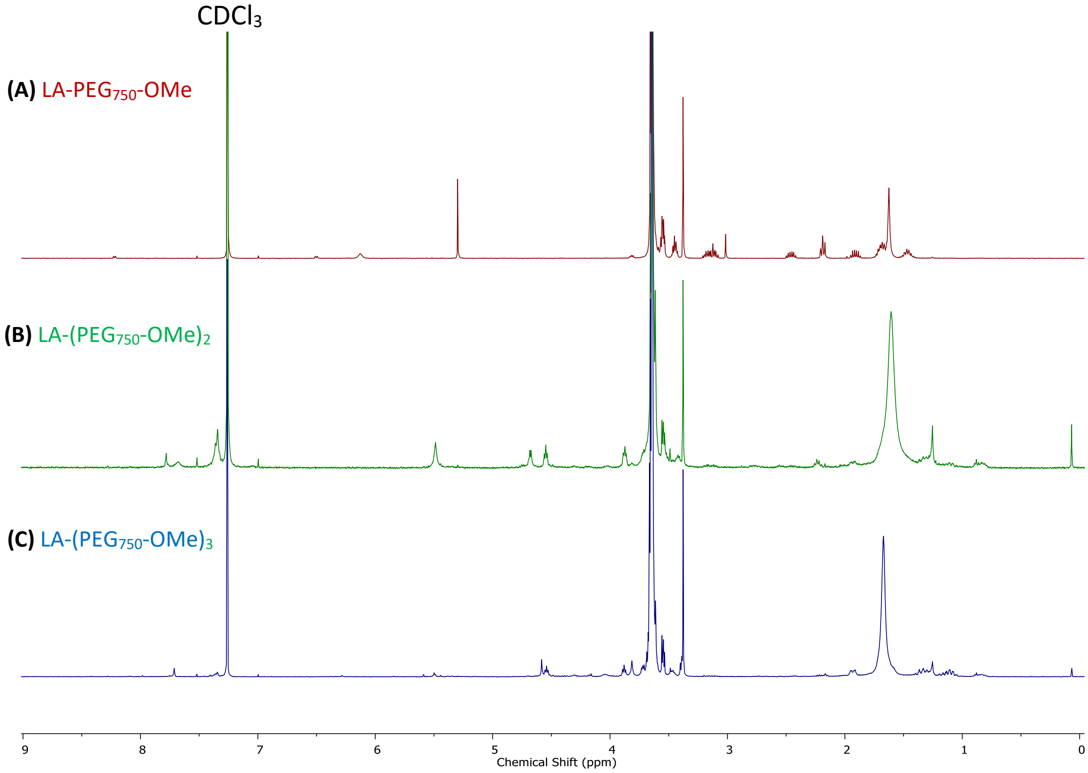

Figure 5.6.3: ^{1}H-NMR spectrum for the control ligands overlaid to compare the similarities and differences. **(A)** LA-PEG$_{750}$-OMe, **(B)** LA-(PEG$_{750}$-OMe)$_2$ and **(C)** LA-(PEG$_{750}$-OMe)$_3$.All ligands were run in CDCl$_3$ at 400 MHz.

5.7 LA-Ligand Reduction

Tris(2-carboxyethyl)phosphine hydrochloride, TCEP, was added to the LA-based ligands at a TCEP: Ligand molar ratio of 1.2: 1 in H_2O and the solution was left at RT for 30 minutes to form the reduced DHLA-form of ligands. The reduction was confirmed by LC-MS from the increase in molecular weight for the additional protons. To characterise this method works NMR assignments of both the reduced and non-reduced form of LA were done. Unfortunately this was not done using the wide range of ligands themselves due to the low amounts of ligands used for reduction. The resulting NMR spectra can be seen below in **Figure 5.7.1** for lipoic acid in both the reduced and non-reduced forms where a shift can be seen in the for both the adjacent carbon and hydrogen atoms from the disulphide group. The hydroxyl hydrogen peak is a found downfield at around 12 ppm so isn’t shown on the spectra. Full assignments are shown in **Table 5.7.1** below.

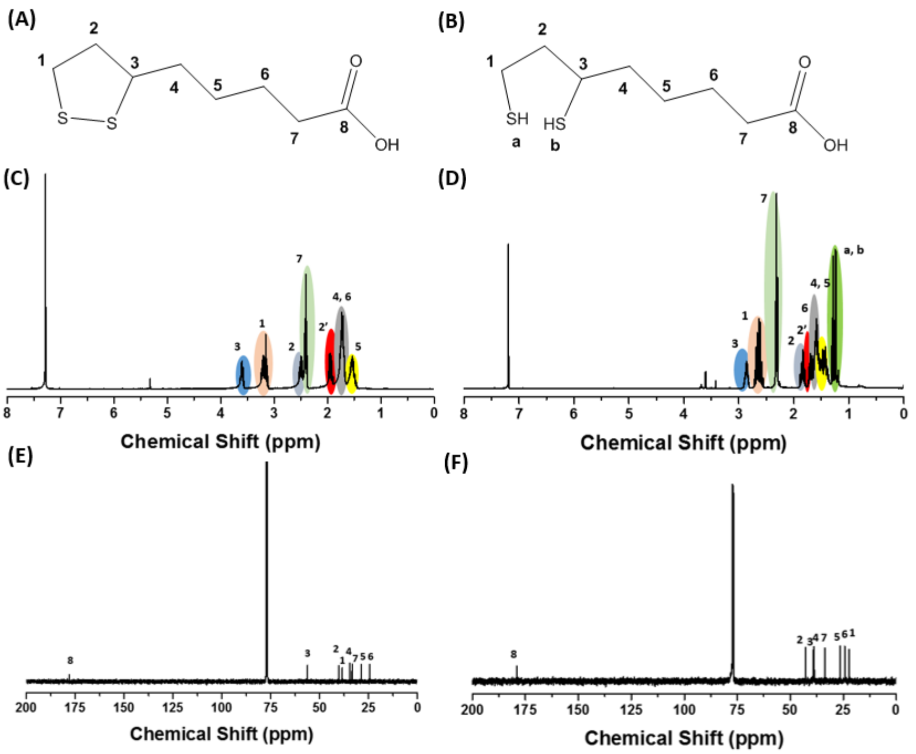

Figure 5.7.1: A figure to show the confirmation of the reduction of Lipoic Acid, LA, (**A**) by Tris (2-carboxyethyl) phosphine, TCEP, to Dihydrolipoic acid, DHLA, (**B**) using ^{1}H-NMR (**C, D**) and ^{13}C-NMR (**E, F**).

Table 5.7.1: The ^{1}H-NMR and ^{13}C-NMR data of Lipoic Acid, LA, and Dihydrolipoic acid, DHLA, prepared by by Tris (2-carboxyethyl) phosphine, TCEP, reduction.

Atom No.	**LA (^{1}H-NMR)**	**LA (^{13}C-NMR)**	**DHLA (^{1}H-NMR)**	**DHLA (^{13}C-NMR)**
1	3.24 – 3.11 (m, 2H)	38.51 (1C)	2.72 – 2.56 (m, 2H)	22.29 (1C)
2, 2'	2.53 – 2.45 (m, 1H) 1.98 – 1.90 (m, 1H)	40.23 (1C)	1.89 – 1.80 (m, 1H) 1.73 – 1.66 (m, 1H)	42.77 (1C)
3	3.63 – 3.56 (m, 1H)	56.29 (1C)	2.90 – 2.82 (m, 1H)	39.29 (1C)
4	1.78 – 1.67 (m, 4H)	34.60 (1C)	1.52 – 1.37 (m, 4H)	38.72 (1C)
5	1.60 – 1.48 (m, 1H)	28.68 (1C)	*Overlap with (4)*	26.47 (1C)
6	*Overlap with (4)*	24.42 (1C)	1.64 – 1.53 (m, 2H)	24.31 (1C)
7	2.40 (t, *J* = 7.4 Hz, 2H,)	33.51 (1C)	2.31 (t, *J* = 7.3 Hz, 2H)	33.74 (1C)
8	-	178.02 (1C)	-	178.96 (1C)
a (SH)	-	-	1.28 (t, *J* = 8.0 Hz, 1H)	-
b (SH)	-	-	1.24 (d, *J* = 7.6 Hz, 1H)	-

5.8 Nanoparticle Synthesis[11]

Method taken from and repeated from J. Piella, N. G. Bastús and V. Puntes methodology from Chemistry Materials. AuNPs were synthesised using a seeded-growth method. This was perfromed and characterised by Dr. Akshath Uchangi Satyaprasad, a postdoc within the group.

A 150 mL of freshly prepared reducing solution of sodium citrate (SC, 2.2 mM) containing 0.1 mL of tannic acid (2.5 mM) and 1 mL of potassium carbonate (K_2CO_3, 150 mM) was heated with a heating mantle in a 250 mL three-necked round-bottom flask under vigorous stirring. When the temperature reached 70 °C, 1 mL of tetrachloroauric acid ($HAuCl_3$, 25 mM) was injected. The colour of the solution changed rapidly to blackgray (less than 10 s) and then to orange-red in the following 1−2 min. The solution was kept at 70 °C for 5 min more to ensure complete reaction of the gold precursor. The resultant particles (∼3.5 nm, 7 × 1013 NPs/mL) were narrowly dispersed, negatively charged and stable for weeks. The addition of 1 mM of K_2CO_3 in the reducing solution resulted in a pH ∼10, which decreased in the reaction mixture to pH ∼8 because of the addition of $HAuCl_4$. This slightly basic value seems to have an advantageous effect resulting in narrower size distributions of the Au NPs

5.9 Nanoparticle Conjugations

5.9.1 Preparation of QD-EG$_n$-Saccharides

CdSe-ZnS core-shell QD (PlasanaChem GmbH QDs) (λ_{em} 560 nm, 1nmol) in toluene (0.2 mL) were precipitated by ethanol (1 mL) and then centrifuged at a speed of 10 kg for 3 mins. The clear supernatant was then removed and chloroform added (50 μL) to dissolve the QD pellet formed. The reduced ligand DHLA-EG$_n$-Saccharide (where n= 3 or 11 and Saccharide = α-Man and Man-α-1,2-Man) was added after deprotonation by NaOH in EtOH (0.10 M) to form a homogenous solution. The reaction was then stirred at RT in darkness for a minimum of 30 mins. Hexane was the added to the reaction until the solution became cloudy. The mixture was then centrifuged at 10 kg for 5 mins obtaining a QD-EG$_n$-Man^m pellet. The clear supernatant was then removed and the pellet was dissolved in H_2O (100 μL). The solution was then transferred to a 30 KD MWCO spin column and washed with H_2O (3 x 100 μL).

Table 5.9.1: Shows the solutions made up for the different QD-Sugar conjugates and the ligand type that was used to synthesise them using a QD: ligand loading ratio of 1: 800 nmol.

QD-Surface Ligands	Ligand Amount (nmol)	QD Amount (nmol)	0.1 M NaOH in EtOH (µL)
DHLA-EG$_3$-Man	2307	2.88	23.1
DHLA-EG$_{11}$-Man	1018	1.27	10.2
DHLA-EG$_{11}$-DiMan	3000	3.75	33.9
DHLA-EG$_3$-DiMan	2000	2.5	22.6

5.9.2 Preparation of QD-EG-Saccharides (Reduced Surface Sugar Density)

CdSe-ZnS core-shell QD (PlasanaChem GmbH QDs) (λ_{em} 560 nm, 1nmol) in toluene (0.2 mL) were precipitated by ethanol (1 mL) and then centrifuged at a speed of 10 kg for 3 mins. The clear supernatant was then removed and chloroform added (50 µL) to dissolve the QD pellet formed. The reduced ligand DHLA-EG$_n$-Saccharide (where n= 3 or 11 and Saccharide = α-Man and Man-α-1,2-Man) was added after deprotonation by NaOH in EtOH (0.10 M) to form a homogenous solution in the ratio shown below with DHLA-ZW which has been reduced using dithiothreitol (DTT). The reaction was then stirred at RT in darkness for a minimum of 30 mins. Hexane was the added to the reaction until the solution became cloudy. The mixture was then centrifuged at 10 kg for 5 mins obtaining a QD-EG$_n$-Man^m pellet. The clear supernatant was then removed and the pellet was dissolved in H_2O (100 µL). The solution was then transferred to a 30 KD MWCO spin column and washed with H_2O (3 x 100 µL).

Table 5.9.2: Shows the solutions made up for the different QD-Sugar conjugates and the ligand type that was used to synthesise them using a QD: ligand loading ratio of 1: 800 nmol.

Percentage Ratio of	Glycan Ligand Amount (nmol)	Control spacer Ligand Amount (nmol)	QD Amount (nmol)	0.1 M NaOH in EtOH (µL)
25 % Sugar	200	600	1	9.04
73 % Sugar	584	216	1	9.04

5.9.3 Preparation of QD-(EG_n-Glycan)$_m$

CdSe-ZnS core-shell QD (Mesolight QDs) (λ_{em} 560 nm, 1 nmol) in toluene (0.2 mL) were precipitated by ethanol (1.5 mL) and then centrifuged at a speed of 10 kg for 5 mins. The clear supernatant was then removed and chloroform added (50 µL) to dissolve the QD pellet formed. In order to make a homogenous solution ($CHCl_3$: MeOH 1:1) 25 µL of MeOH was added and left for 30 minutes before another 25 µL of MeOH was added. The reduced ligands DHLA-(EG_n-Glycan)$_m$ (where n= 1 or 2 and m= 1, 2 and 3 and = Glycan = α-Man and Man-α-1,2-Man) was added after deprotection by NaOH (0.20 M in EtOH) using a ligand to NaOH ratio of 1:6. The reaction was then stirred at RT for a minimum of 3 hours. The mixture is then centrifuged at a speed of 10 kg for 1 min and the aqueous layer was removed. The QDs were then precipitated by Ethanol (1.5 mL) and then centrifuged at a speed of 10 kg for 5 mins. The clear supernatant was then removed and water added (100 µL) to dissolve the QD pellet formed. The solution was then transferred to a 30 KD MWCO spin column and washed with H_2O (2 x 100 µL).

Table 5.9.3: Shows the solutions made up for the different QD-glycan conjugates and the ligand type that was used to synthesise them using a QD: ligand loading ratio of 1:2000 nmol for the monosaccharide and 1: 1000 nmol for the disaccharide.

NP + Ligand	Amount of Ligand (nmol)	Amount (mg) TCEP in 50 µL H_2O
QD + LA-EG_2-Man	2000	6
QD + LA-(EG_2-Man)$_2$	2000	6
QD + LA-(EG-Man)$_3$	2000	6
QD + LA- EG_2-DiMan	1000	3
QD + LA-(EG_2-DiMan)$_2$	1000	3
QD + LA-(EG-DiMan)$_3$	1000	3

5.9.4 Preparation of QD-PEG_{750}-OMe

CdSe-ZnS core-shell QD (Mesolight QDs) (λ_{em} 560 nm, 1 nmol) in toluene (0.2 mL) were precipitated by ethanol (1.5 mL) and then centrifuged at a speed of 10 kg for 5 mins. The clear supernatant was then removed and chloroform added (50 µL) to dissolve the QD pellet formed. In order to make a homogenous solution ($CHCl_3$: MeOH 1:1) 25 µL of MeOH was added and left for 30 minutes before another 25 µL of MeOH was added. The reduced ligands DHLA-PEG_{750}-OMe were added after deprotection by NaOH (0.20 M in EtOH) using a ligand to NaOH ratio of 1:6. The reaction was then stirred at RT for a minimum of 3 hours. Hexane was then added and the aqueous layer was separated off. This was added to a 30 KD MWCO spin column in small amounts diluted with H_2O.

5.9.5 Preparation of AuNP-(EG_n-Glycan)$_m$

Gold Nanoparticles (2 mL, 91 mM) suspended in citrate buffer were first concentrated using a 10 K centrifugal filter to a maximum volume of 200 µL. The AuNP solution was then combined with each of the TA based ligands at a molar ratio of 1:1000 (AuNP: Ligand) in H_2O in the presence of TCEP (1: 1.2 ratio, Ligand: TCEP) and was left to stir overnight. The next day the solution was transferred to a 30, 000 KD MWCO spin column, concentrated down and washed with H_2O (3 x 100 µL) and finally dispersed in H_2O to make the AuNP stock solution.

5.10 Protein Production and Labelling

5.10.1 Protein Purification

Cysteine was introduced into the extracellular segment of DC-SIGN by replacing its residue Q274 or its equivalent residue E287 in DC-SIGNR for the site specific dye labelling (indicated by stars below within the sequence, **Figure 5.10.1**). The mutagenesis was carried out by using a synthetic DNA restriction fragment to replace the wild-type sequences. Standard recombinant DNA techniques were used throughout these experiments. The integrity and successful mutation of the cloned fragments were confirmed by DNA sequencing. The extracellular segments known to form the stable homotetramers and which retained their glycan binding properties were expressed in *E. Coli* and purified by a mannose-Sepharose affinity column as described previously as well as the monomeric DC-SIGN and DC-SIGNR CRDs were constructed.

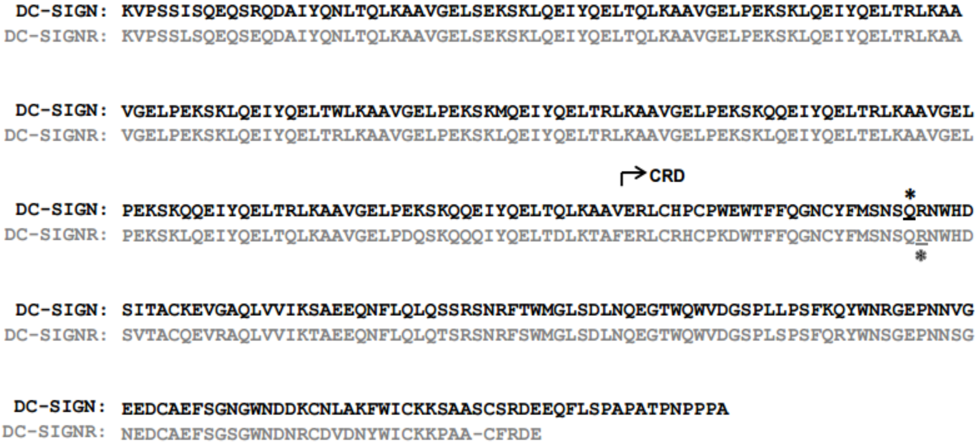

```
 DC-SIGN: KVPSSISQEQSRQDAIYQNLTQLKAAVGELSEKSKLQEIYQELTQLKAAVGELPEKSKLQEIYQELTRLKAA
DC-SIGNR: KVPSSLSQEQSEQDAIYQNLTQLKAAVGELSEKSKLQEIYQELTQLKAAVGELPEKSKLQEIYQELTRLKAA

 DC-SIGN: VGELPEKSKLQEIYQELTWLKAAVGELPEKSKMQEIYQELTRLKAAVGELPEKSKQQEIYQELTRLKAAVGEL
DC-SIGNR: VGELPEKSKLQEIYQELTRLKAAVGELPEKSKLQEIYQELTRLKAAVGELPEKSKLQEIYQELTELKAAVGEL

                                                     ↱CRD
                                                                        *
 DC-SIGN: PEKSKQQEIYQELTRLKAAVGELPEKSKQQEIYQELTQLKAAVERLCHPCPWEWTFFQGNCYFMSNSQRNWHD
DC-SIGNR: PEKSKLQEIYQELTQLKAAVGELPDQSKQQQIYQELTDLKTAFERLCRHCPKDWTFFQGNCYFMSNSQRNWHD
                                                                         *

 DC-SIGN: SITACKEVGAQLVVIKSAEEQNFLQLQSSRSNRFTWMGLSDLNQEGTWQWVDGSPLLPSFKQYWNRGEPNNVG
DC-SIGNR: SVTACQEVRAQLVVIKTAEEQNFLQLQTSRSNRFSWMGLSDLNQEGTWQWVDGSPLSPSFQRYWNSGEPNNSG

 DC-SIGN: EEDCAEFSGNGWNDDKCNLAKFWICKKSAASCSRDEEQFLSPAPATPNPPPA
DC-SIGNR: NEDCAEFSGSGWNDNRCDVDNYWICKKPAA-CFRDE
```

Figure 5.10.1: Protein sequence alignment of DC-SIGN and DC-SIGNR. Indicating the CRD sequences that have been modified to contain cysteine for site-specific labelling is indicated by an (*).

5.10.2 Protein Labelling

The proteins were firstly bound to a mannose-Sepharose affinity column and then thoroughly washed with binding buffer (≈25 mL, 20 mM HEPES pH7.4, 150 mM NaCl, 25 mM $CaCl_2$) to remove the free and weakly bound proteins. The bound proteins were then eluted out using an eluting buffer containing EDTA (20 mM HEPES pH7.4, 150 mM NaCl, 2.5 mM EDTA) due to the calcium dependent DC-SIGN/R-sugar binding. To each fraction $CaCl_2$ was added to reach a final concentration of 25 mM.

A 1:2 ratio of protein (monomer) to dye was used for DC-SIGN and a 1:1.5 ratio was used for DC-SIGNR by adding Atto594-maleimide in DMSO to the protein solutions. The mixture was then rocked in darkness for 1 hr at RT and then further left to incubate at 4°C overnight. The labelled protein was then purified using a mannose-Sepharose affinity column, firstly washed with washing buffer (20 mM HEPES pH7.8, 100 mM NaCl, 10 mM $CaCl_2$) to remove unbound or weakly bound proteins. The bound proteins were then eluted out using eluting buffer (20 mM HEPES pH7.8, 100 mM NaCl, 2.5 mM EDTA). To each eluted fraction $CaCl_2$ was added to reach a final concentration of 10 mM to obtain the labelled protein stock.

5.11 References

1. K. Susumu, B. C. Mei and H. Mattoussi, *Nat. Protoc.*, 2009, **4**, 424-436.

2. H. Zhang, G. Feng, Y. Guo and D. Zhou, *Nanoscale*, 2013, **5**, 10307-10315.

3. Y. Guo, C. Sakonsinsiri, I. Nehlmeier, M. A. Fascione, H. Zhang, W. Wang, S. Pöhlmann, W. B. Turnbull and D. Zhou, *Angew. Chem. Int. Ed.*, 2016, **55**, 4738-4742.

4. N. Zhan, G. Palui, H. Grise, H. Tang, I. Alabugin and H. Mattoussi, *ACS Appl. Mater. Interfaces*, 2013, **5**, 2861-2869.

5. T. K. Neklesa, H. S. Tae, A. R. Schneekloth, M. J. Stulberg, T. W. Corson, T. B. Sundberg, K. Raina, S. A. Holley and C. M. Crews, *Nat. Chem Biol.*, 2011, **7**, 538-543.

6. H. Tanaka, S. Yamaguchi, J.-i. Jo, I. Aoki, Y. Tabata and T. Takahashi, *RSC. Adv.*, 2014, **4**, 7561-7565.

7. C. A. Sanhueza, M. M. Baksh, B. Thuma, M. D. Roy, S. Dutta, C. Préville, B. A. Chrunyk, K. Beaumont, R. Dullea and M. Ammirati, *J. Am. Chem. Soc.*, 2017, **139**, 3528-3536.

8. Y. M. Chabre, C. Contino-Pépin, V. Placide, T. C. Shiao and R. Roy, *J. Org. Chem.*, 2008, **73**, 5602-5605.

9. A. Bernardin, A. Cazet, L. Guyon, P. Delannoy, F. Vinet, D. Bonnaffé and I. Texier, *Bioconjug. Chem.*, 2010, **21**, 583-588.

10. R. Ribeiro-Viana, M. Sánchez-Navarro, J. Luczkowiak, J. R. Koeppe, R. Delgado, J. Rojo and B. G. Davis, *Nat. Commun.*, 2012, **3**, 1303.

11. J. Piella, N. G. Bastús and V. Puntes, *Chem. Mater.*, 2016, **28**, 1066-1075.

Chapter 6

General Conclusions and Future Work Suggestions

6.1 General Conclusions

The overall conclusions are that two sensitive fluorescence based readout strategies have been developed by displaying polyvalent mannose saccharides on two different nanoparticle scaffolds, gold nanoparticle (AuNP) and quantum dot (QD). The resulting glycan-QDs and –AuNPs have then been used to probe the binding affinity and modes of two closely-related, almost identical tetrameric viral receptors DC-SIGN and DC-SIGNR via the ratiometric fluorescence resonance energy transfer, FRET, and fluorescence quenching readout strategies. By combining the fluorescence readouts and exploiting the nanoparticle's unique properties (e.g. high TEM contrast and nanoscale sizes), we have revealed that the carbohydrate-recognition domains (CRDs) of DC-SIGN and DC-SIGNR are oriented differently, resulting in different binding modes. The four CRDs in DC-SIGN face in the same direction and bind tetravalently to a single sugar-nanoparticle; while those in DC-SIGNR are split into a pair of back-to-back dimers and bind bis-divalently with two different sugar-nanoparticles. Initial work using dihydrolipoic acid -oligo(ethylene glycol)-saccharide (DHLA-EG$_n$-Saccharide, n = 3, or 11, Saccharide = α-Man and Man-α-1,2-Man) based multifunctional ligands capped fluorescence QDs has shown three significant results, (**Chapter 2**). Firstly, a polyvalent display of the α-1,2-manno-disaccharide on the QD greatly enhances the multivalent binding affinity with DC-SIGN, by ~1.5 million fold over its corresponding monovalent glycan-CRD binding. Secondly displaying the manno-disaccharide on the QD surface produces significantly higher binding affinity enhancement over that of the manno-monosaccharide. This difference may come from the fact that both the primary and secondary binding sites of the CRD may be involved in binding to the QD for the former while only the primary site is involved in the monosaccharide. Finally, the length of the EG$_n$ linker also plays an important role in determining the binding affinity: increasing the number of EG unit in the linker results in a weaker affinity with DC-SIGN. **Chapter 3** has reported the synthesis a new series of DHLA-based dendritic glycan ligands (DHLA-(EG$_n$-Glycan)$_m$, n = 1 or 2; m =1, 2, or 3 and Glycan = α-Man and Man-α-1,2-Man) with the intention to further increase the nanoparticle sugar surface density. Glycan-QDs have been prepared by cap-exchange using such ligands and their binding affinities with DC-SIGN/R have been determined by FRET and showed two significant results. The first is that a decrease in DC-SIGN binding affinity with the increasing sugar density on the QD. The second is that the binding affinity with DC-SIGNR is increased with the increasing sugar density on the QD surface, and moreover the binding affinity enhancement is significantly greater than that seen before. An impressively low apparent binding K_d of 0.49 ± 0.6 nM between DC-SIGNR and QD-(EG-DiMan)$_3$ (trimeric ligand) is observed.

Chapter 5 has extended the studies of DC-SIGN/R interactions with AuNPs capped with such ligands. The rationales behind here is that AuNPs do not contain toxic heavy metals and hence much less cytotoxic and more biocompatible, making them potentially suitable for in vivo applications. In addition, the strong fluorescence quenching property of AuNP has been exploited to quantify the DC-SIGN/R-glycan-AuNP binding affinity via a fluorescence quenching mechanism. Similar to those observed with the QDs in Chapter 4, the binding affinity between DC-SIGN and glycan-AuNPs decreases with the increasing number of sugars linked to each DHLA-based ligand. In addition, strong binding (K_d ~0.6 nM) between DC-SIGN and monomeric glycan ligand capped AuNP is also observed. However, non-specific adsorption appears to have contributed to the observed fluorescence quenching with the AuNPs as significant quenching is observed for AuNPs capped with the DHLA-PEG based control ligand series which should not show specific binding with DC-SIGN/R. The viral inhibition studies reveal that the glcyan-AuNPs are more potent inhibitors over their respective QD counterparts capped with a similar disaccharide glycan ligand. For example, the IC_{50} values of the DHLA-EG$_n$-DiMan ligand capped AuNP (n = 2) and QD (n=3) are determined as 0.06 ± 0.03 and 0.70 ± 0.20 nM, respectively, the former is about 10 fold more potent than the later.

6.2 Future Work

6.2.1 Chapter 2 – Future Work

Further work that can be achieved from this chapter is to further characterise the binding domains separation distances within DC-SIGNR, the bis-divalent CRDs, by creating a potential dimeric saccharide-QDs that can bind to the two pair of divalent CRDs with a linkage of known length. An example of the linker that can be used for this is DNA as the length of each base pair is well-known (0.34 nm), **Figure 6.2.1**. There are examples of dimeric NPs shown within the literature that show a variety of different methods to connect the two together. Heuer-Jungermann *et al.* use modified DNA strands with an azide on one NP and strained alkyne and use click chemistry to create the dimer.[1] Wang *et al.* use the same complementary DNA approach of creating dimer as suggested.[2] This method can then be used to calculate the distance between the two pairs of CRD dimers, where a spatially matched dimer should result in simultaneous binding to all four DC-SIGNR CRDs, giving greatly enhanced binding affinity that can be measured by FRET. By tuning the linker length and measuring the resulting binding affinity, the optimal DNA linker length for DC-SIGNR binding will be obtained. The inter-QD distance can be further determined by TEM. This information would further help to create specific multivalent glycan inhibitors against DC-SIGNR mediated viral infections.

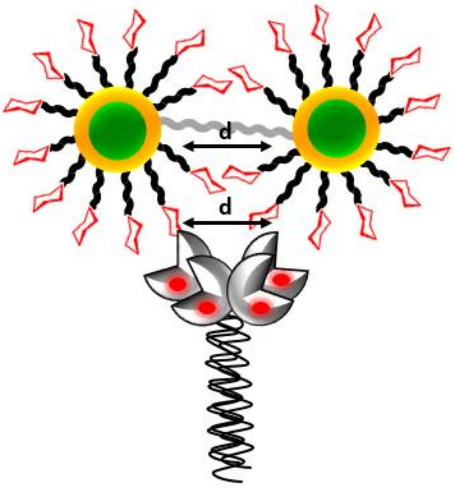

Figure 6.2.1: A schematic showing a QD dimer linked by a strand of DNA to help probe the binding affinity of bis-divalent CRD regions of DC-SIGNR.

6.2.2 Chapter 3– Future Work

In chapter 4 I would suggest further work to investigate how the linker length and structure affect the QD-glycan-DC-SIGN interaction, e.g. whether the increase in binding affinity between DC-SIGN and the QD-glycans is due to the shortening of an EG unit in the linker or reduced steric bulkiness from the cyclooctyne-triazole ring to a triazole ring structure. My current results show that the LA-EG_3-Man capped QD has a DC-SIGN binding K_d of 35 nM, while that capped with LA-EG_2-Man has a K_d of 15 nM, less than half that of the former. So I suppose to create a comparable ligand in which only one of these features is changed. A new ligand such as an LA-EG_3-Man, **Compound 31** in **Figure 6.2.2** below, can be synthesised using the copper click chemistry and used with the QDs via ligand exchange and then compare the results with those of **compounds 19** and **31**.

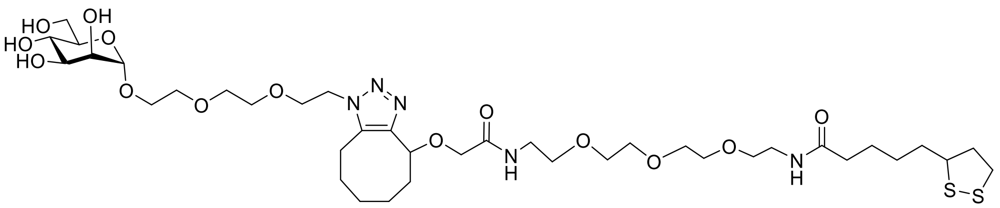

Compound 19 $K_{d(\text{tetra-DC-SIGN})}$ = 35 ± 7

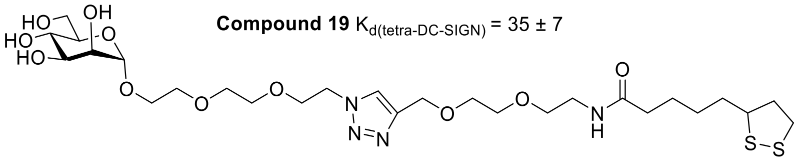

Compound 23 $K_{d(\text{tetra-DC-SIGN})}$ = 15 ± 7

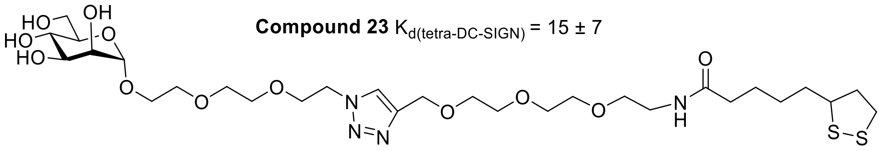

Proposed Compound 31

Figure 6.2.2: A new proposed ligand structure that will determine if the reduction in binding constant is caused by the removal of an EG group or the removal of the bulky cyclooctyne.

Further work in this area could also be done to increase the linker length between the LA chelation and the glycan arrangement as when this modification was done in a paper by Illecas *et al*.[3] they found an improvement of the antiviral activity of the same style trimeric ligand with the EBOV-GP. As within that paper they state that the extra linker length provides a more efficient interaction with the DC-SIGN due to the release of steric congestion upon the surface of the nanoparticle, a fullerene in this case.[3] As the glycans can be spread out further on the AuNP surface to reduce the steric hindrance upon the surfaces.

6.2.3 Chapter 4 – Future Work

In chapter 4, I would suggest that further work be done to investigate the effects of the size of the nanoparticle that the glycan-AuNPs are built upon and how these affect their DC-SIGN/R binding. The results show that the binding constant has decreased, meaning stronger binding, when the particle hydrodynamic size is increased within the AuNP used in this work which have the same core size. This would be done with different sized AuNPs using the same ligand surface and capping method. **Figure 6.2.3** below shows a schematic for the AuNP design. The use of smaller AuNPs would also help remove the non-specific quenching observed for the control ligands which could come from the direct absorption of the excitation light by the AuNPs as smaller AuNPs (<2 nm) do not absorb excitation light.

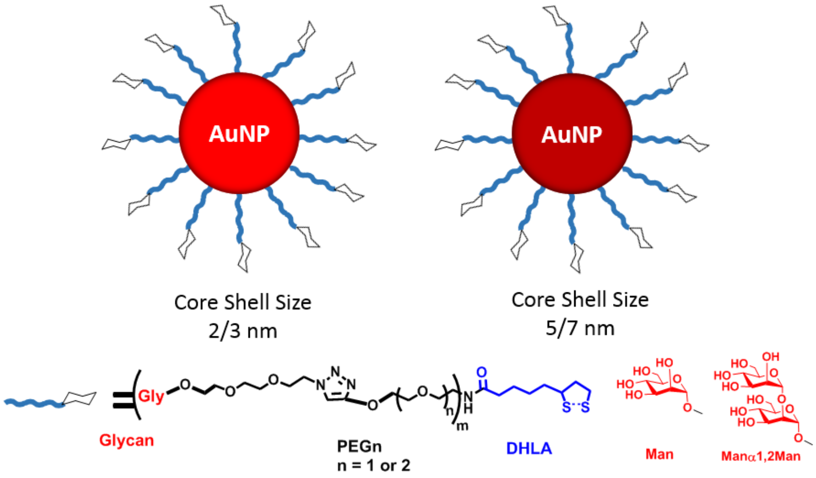

Figure 6.2.3: A schematic showing the AuNP design using two different metallic core sized AuNPs and the ligands used to cap the surfaces.

The ways in which the glycan loading on the AuNP surface is done needs to be recalculated as the data obtained from an LC-MS calibration curve shows inaccuracies. As potential product is being found within injection peaks upon a chromatogram, this injection peak may also contain impurities and so the area may not be a true representation of a particular concentration. Another method that has been successfully used before to determine glycan loading is a phenol-sulfuric acid method.[4] This has given a more accurate calibration curve against which the unknown samples can be measured.

Further work could be done into investigating the reason for the increased binding between the dimeric and trimeric controls and DC-SIGN at higher concentrations but by changing the capping ligand to have a shorter or longer PEG chain lengths and why this isn’t the case for DC-SIGNR. As the investigations I performed suggested that it wasn’t related to the BSA content in the binding media or the size of the particles (they were quite similar to those of the glycan-AuNPs). Through using different lengths of PEGylated ligands we could investigate the reasons for the increased quenching with the control ligands, using much longer PEG chains (e.g. PEG1000, PEG5000, PEG10000) may show an increased quenching shown at potential lower concentrations and a shorter chain length (PEG400) may show a reduced effect.

6.3 References

1. A. Heuer-Jungemann, R. Kirkwood, A. H. El-Sagheer, T. Brown and A. G. Kanaras, *Nanoscale*, 2013, **5**, 7209-7212.
2. G. Wang, Y. Akiyama, S. Shiraishi, N. Kanayama, T. Takarada and M. Maeda, *Bioconjug. Chem.*, 2016.
3. B. M. Illescas, J. Rojo, R. Delgado and N. Martín, *J. Am. Chem. Soc.*, 2017, **139**, 6018-6025.
4. Y. Guo, C. Sakonsinsiri, I. Nehlmeier, M. A. Fascione, H. Zhang, W. Wang, S. Pöhlmann, W. B. Turnbull and D. Zhou, *Angew. Chem. Int. Ed.*, 2016, **55**, 4738-4742.

Appendix

A.1 QD Quantum Yield Fluorescence Spectra

A.1.1 QD- EG$_n$Man^m

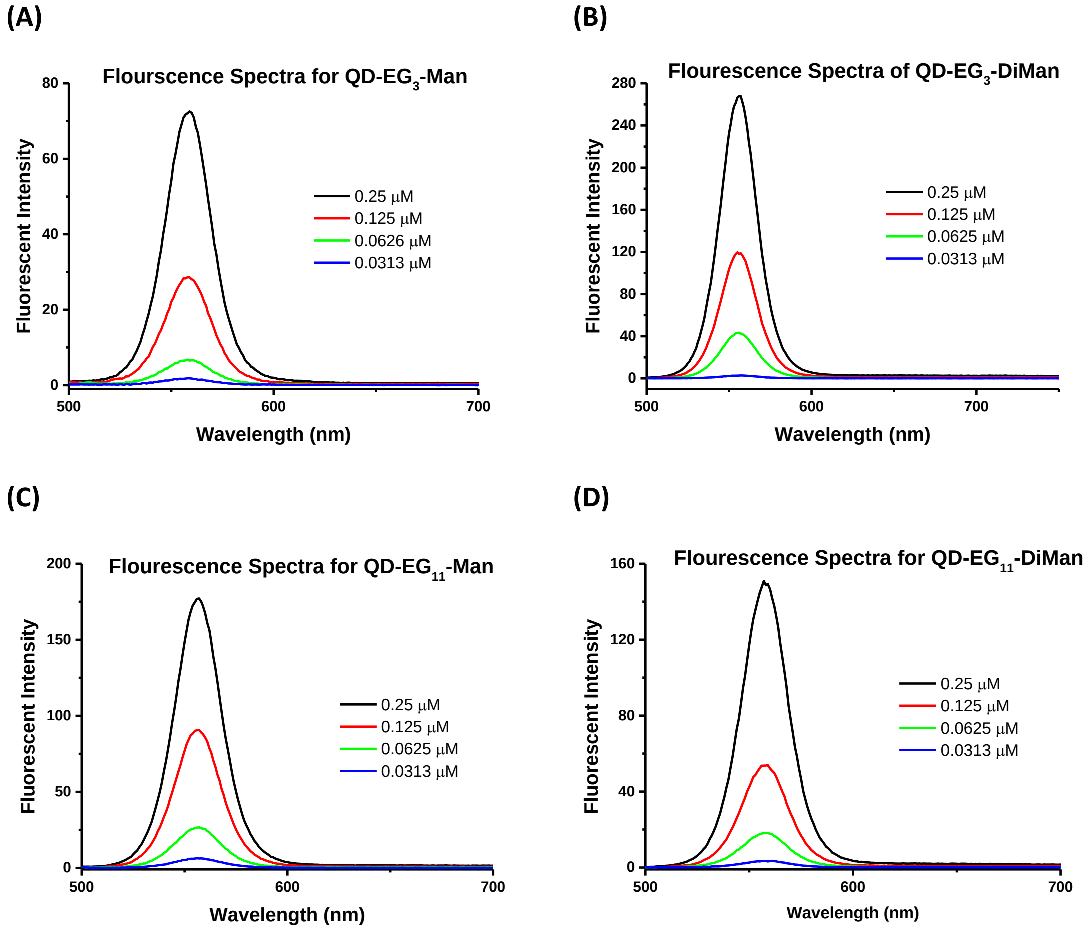

Figure A.1.1: Fluorescence spectra for a range of concentrations between 0.0313 – 0.25 µM at λ_{Ex} = 480 nm for **(A)** QD-EG$_3$-Man, **(B)** QD-EG$_3$-DiMan, **(C)** QD-EG$_{11}$-Man and **(D)** QD-EG$_{11}$-DiMan.

A.1.2 QD-(EG_n-Man^S)$_m$

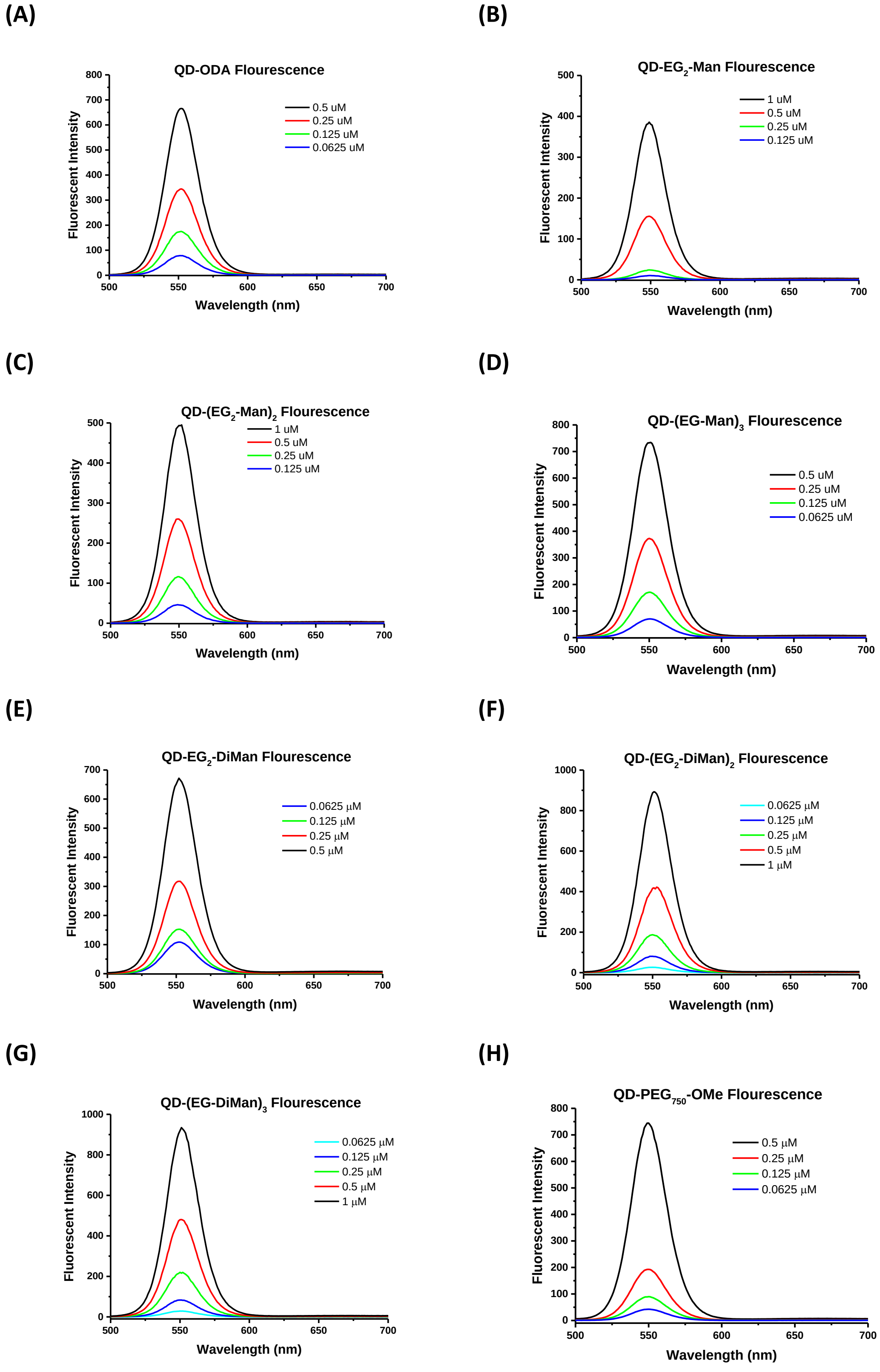

Figure A.1.2: Fluorescence spectra for a range of concentrations between 0.0625 – 1 µM at λ_{Ex} = 480 nm for **(A)** QD-ODA, **(B)** QD-EG_2-Man, **(C)** QD-(EG_2-Man)$_2$, **(D)** QD-(EG-Man)$_3$, **(E)** QD-EG_2-DiMan, **(F)** QD-(EG_2-DiMan)$_2$, **(G)** QD-(EG-DiMan)$_3$ and **(H)** QD-PEG_{750}-OMe.

A.1.3 FRET Studies between QD-DiMan and DC-SIGN/R

This data is has been collected and interpreted by Dr Yuan Guo.

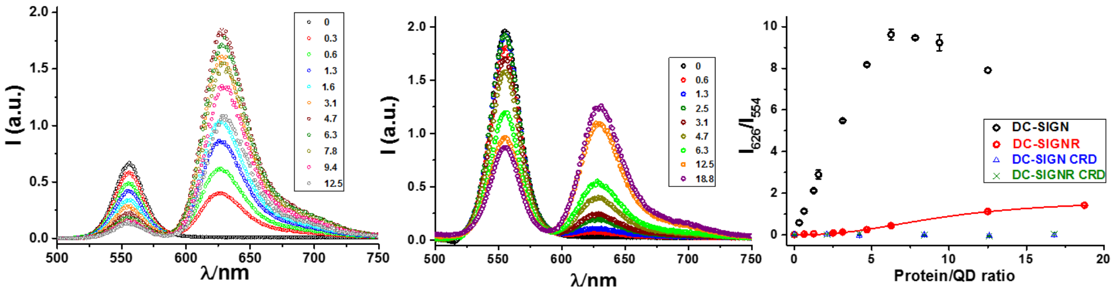

Figure A.1.3: Dye direct excitation background corrected fluorescence spectra of QD-DiMan (40 nM) after binding to labelled proteins, DC-SIGN/R, at varying protein: QD ratios (0 – 752 nM).

A.2 QD-EG$_n$Man^m + DC-SIGN/R Fluorescence Data

A.2.1 DC-SIGN

QD-EG$_{11}$-Man:

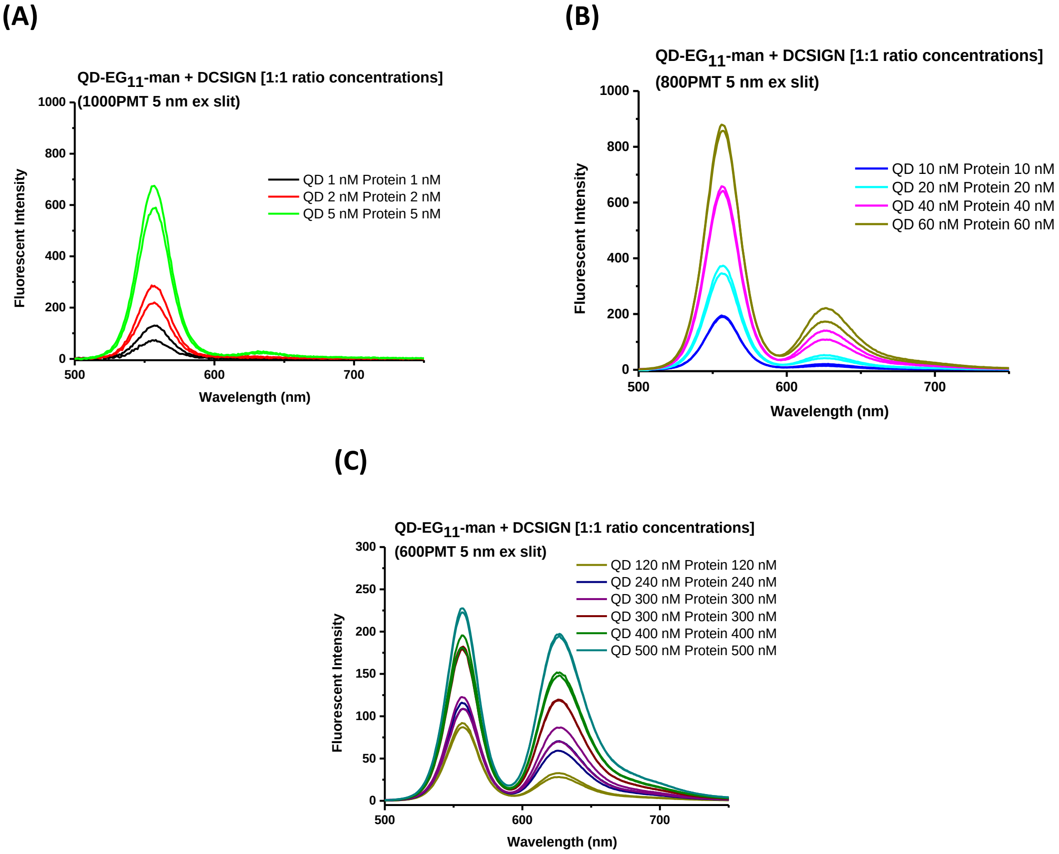

Figure A.2.1: Fluorescence spectra obtained for determination of the accurate K_D for QD-EG$_{11}$-Man + DC-SIGN using a standard protein molar ratio: QD ratio of 1:1. (**A**) Low concentrations of QDs (1 – 5 nM) and DC-SIGN (1 -5 nM), (**B**) Intermediate concentrations of QDs (10 – 60 nM) and DC-SIGN (10 - 60 nM) and (**C**) high concentrations of QDs (120 – 500 nM) and DC-SIGN (120 - 500 nM).

QD-EG$_3$-DiMan:

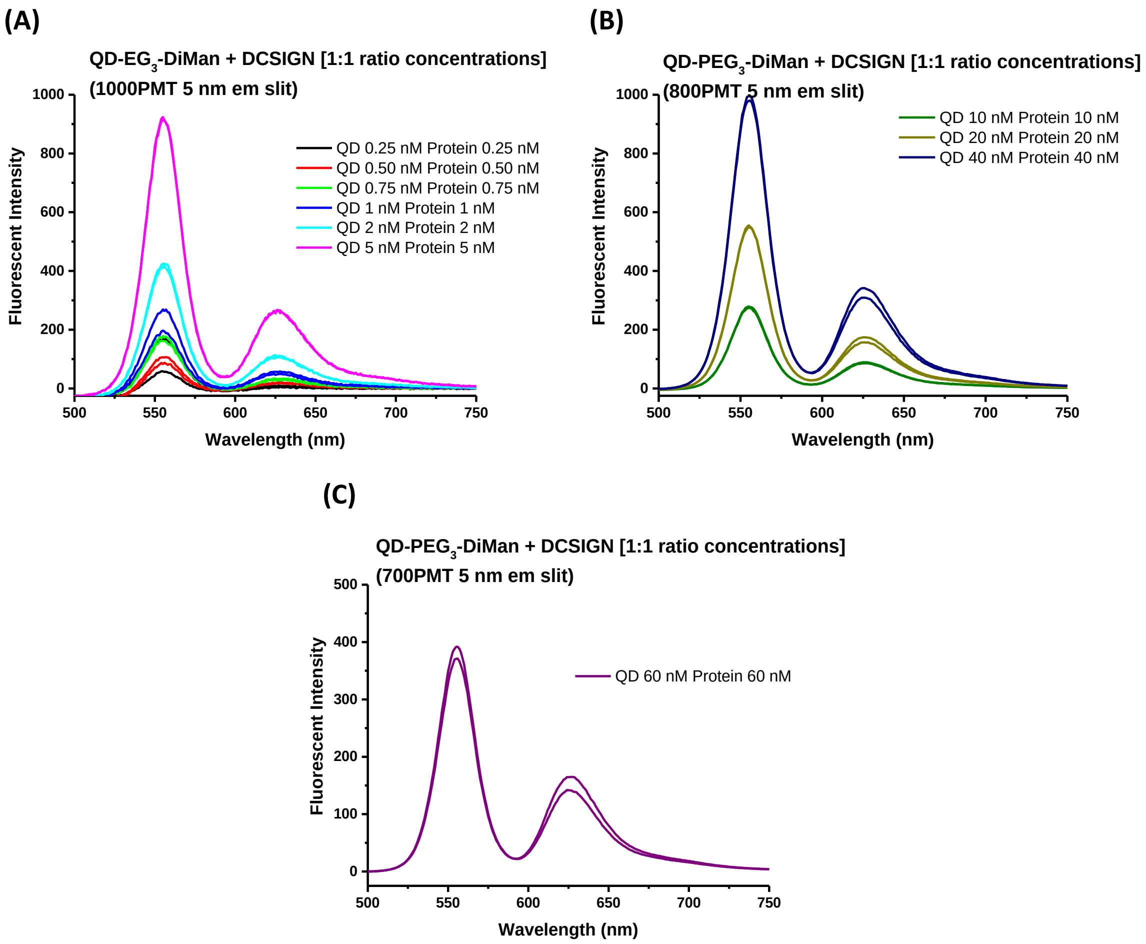

Figure A.2.2: Fluorescence spectra obtained for determination of the accurate K_D for QD-EG$_3$-DiMan + DC-SIGN using a standard protein molar ratio: QD ratio of 1:1. (**A**) Low concentrations of QDs (0.25 – 5 nM) and DC-SIGN (0.25 - 5 nM); (**B**) Intermediate concentrations of QDs (10 – 40 nM) and DC-SIGN (10 - 40 nM) and (**C**) high concentrations of QD (60 nM) and DC-SIGN (60 nM).

QD-EG$_{10}$-DiMan:

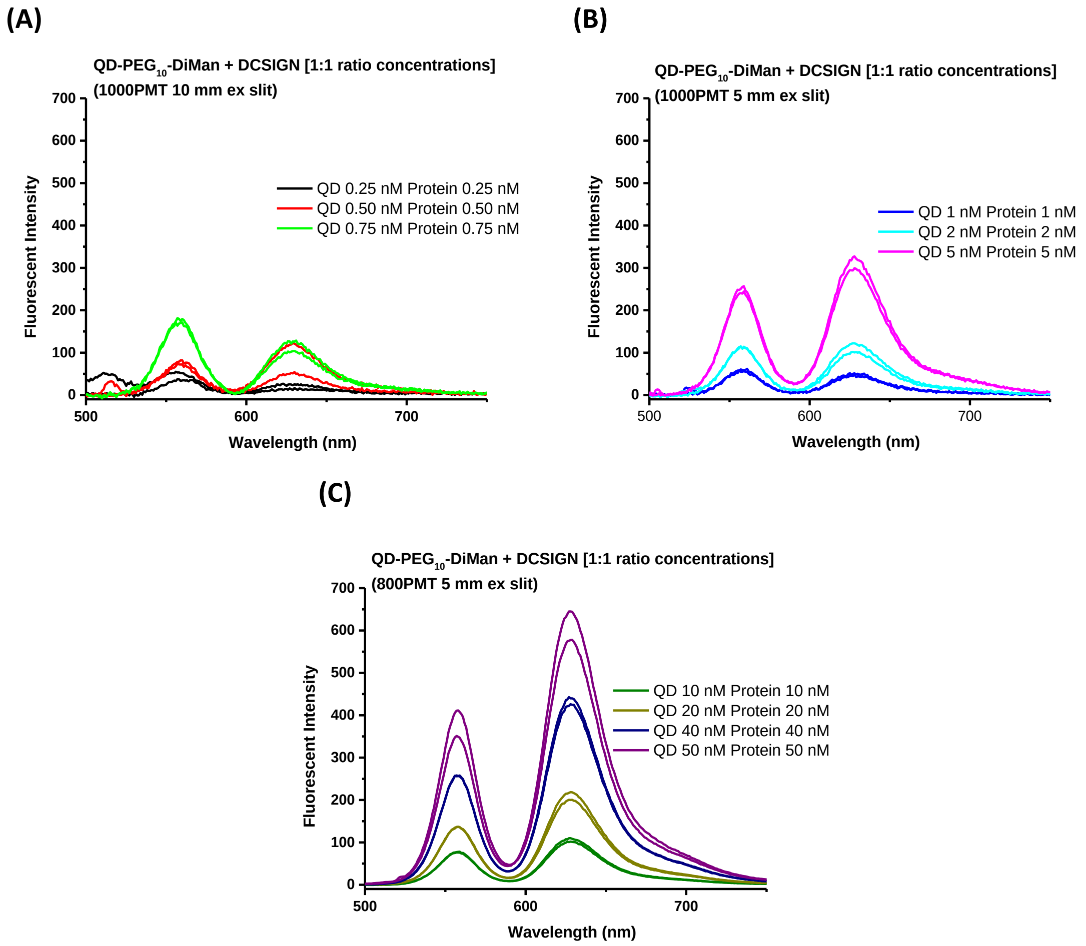

Figure A.2.3: Fluorescence spectra obtained for determination of the accurate K_D for QD-EG$_{11}$-DiMan + DC-SIGN using a standard protein molar ratio: QD ratio of 1:1. (**A**) Low concentrations of QDs (0.25 – 0.75 nM) and DC-SIGN (0.25 – 0.75 nM); (**B**) intermediate concentrations of QDs (1 – 5 nM) and DC-SIGN (1 -5 nM) and (**C**) high concentrations of QDs (10 – 50 nM) and DC-SIGN (10 -50 nM).

A.2.2 DC-SIGNR

QD-EG$_{10}$-DiMan:

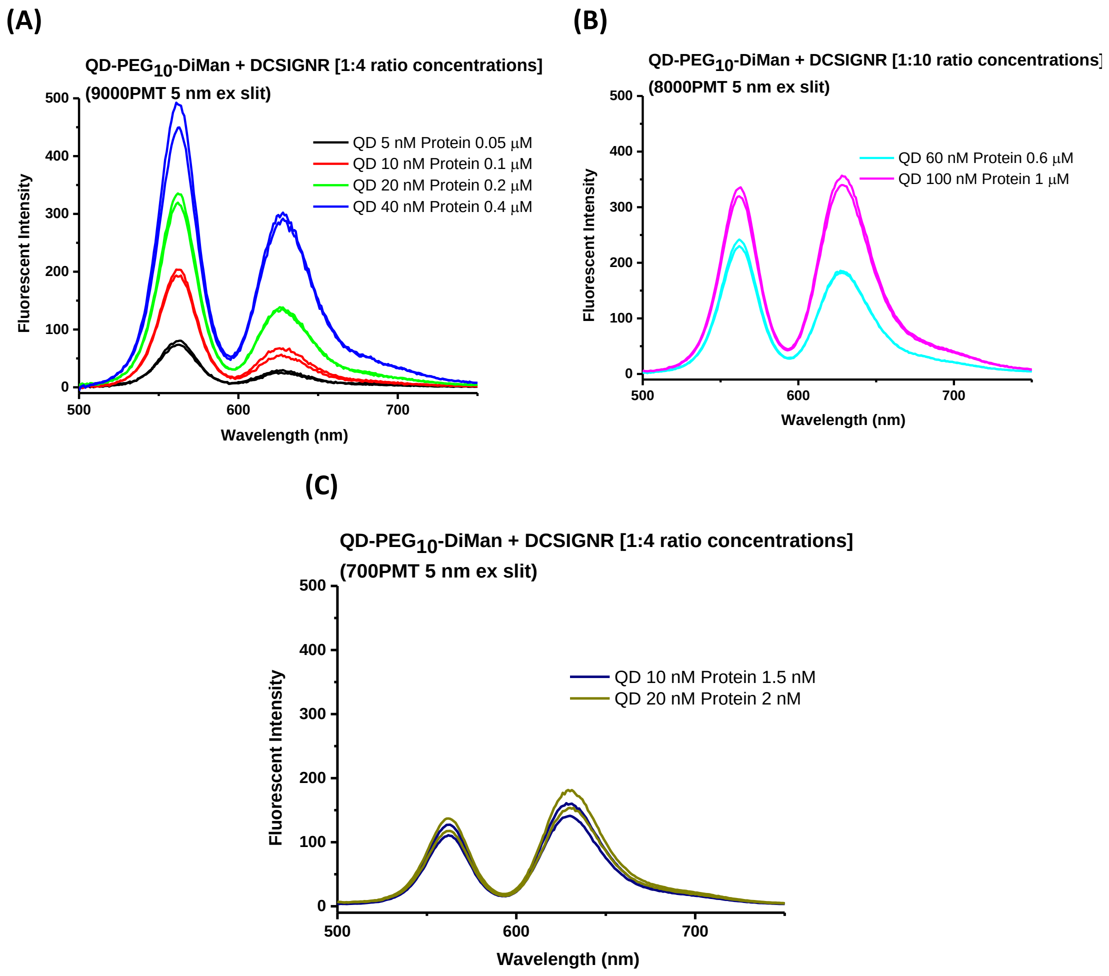

Figure A.2.4: Fluorescence spectra obtained for determination of the accurate K_D for QD-EG$_{11}$-DiMan + DC-SIGNR (where n= 3 or 11) using a standard protein molar ratio: QD ratio of 10:1. (**A**) Low concentrations of QDs (5 – 40 nM) and DC-SIGNR (0.05 – 0.4 μM); (**B**) Intermediate concentrations of QDs (60 – 100 nM) and DC-SIGNR (0.6 – 1 μM) and (**C**) high concentrations of QDs (10 – 20 nM) and DC-SIGNR (1.5 – 2 nM).

A.3 QD-(EG_n-Man^S)$_m$ + DC-SIGN/R Fluorescence Data

A.3.1 DC-SIGN

QD-(EG_2-Man)$_2$:

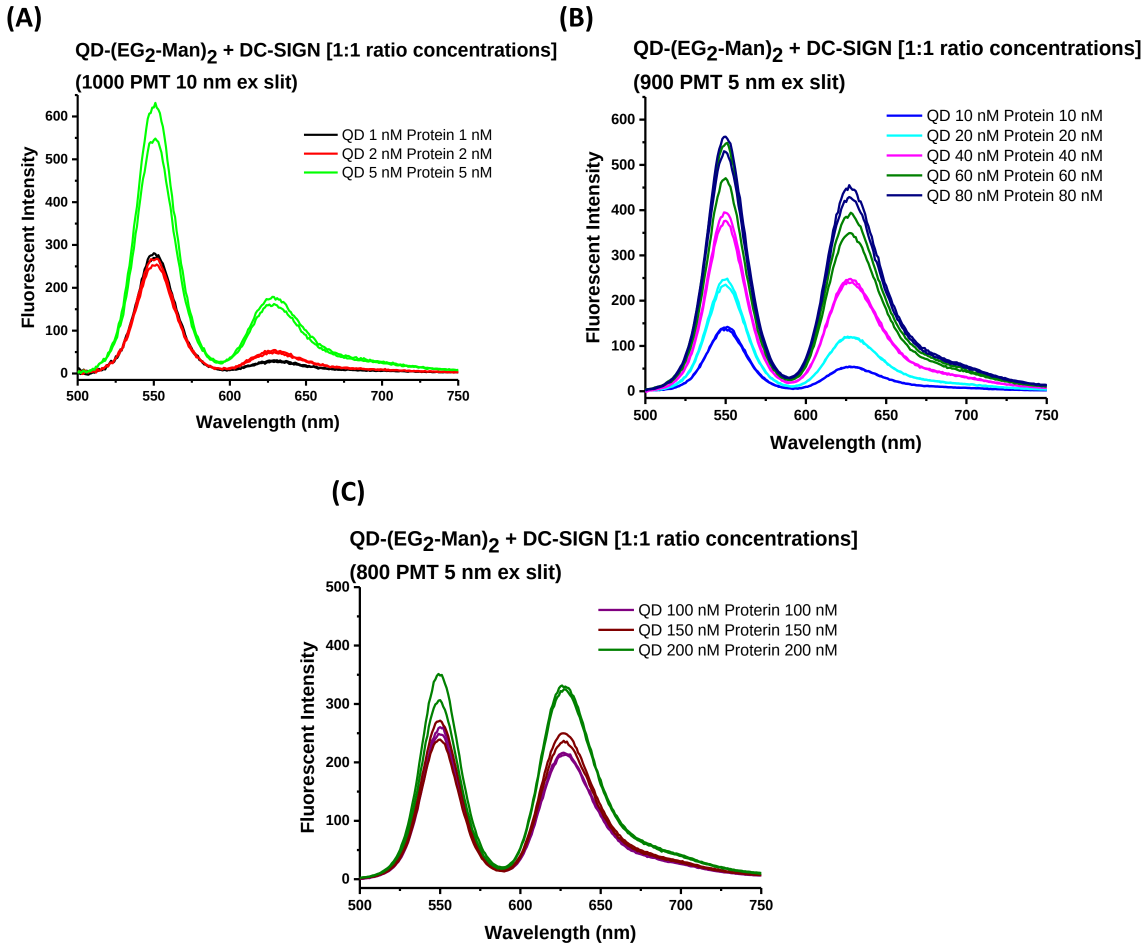

Figure A.3.1: Background corrected fluorescence spectra obtained for determination of the apparent K_D for QD-(EG_2-Man)$_2$ + DC-SIGN using a standard protein molar ratio: QD ratio of 1:1. (**A**) Low concentrations of QDs (1 – 5 nM) and DC-SIGN (1 – 5 nM); (**B**) Intermediate concentrations of QDs (10 – 80 nM) and DC-SIGN (10 – 80 nM) and (**C**) High concentrations of QDs (100 – 200 nM) and DC-SIGN (100 – 200 nM).

QD-(EG-Man)$_3$:

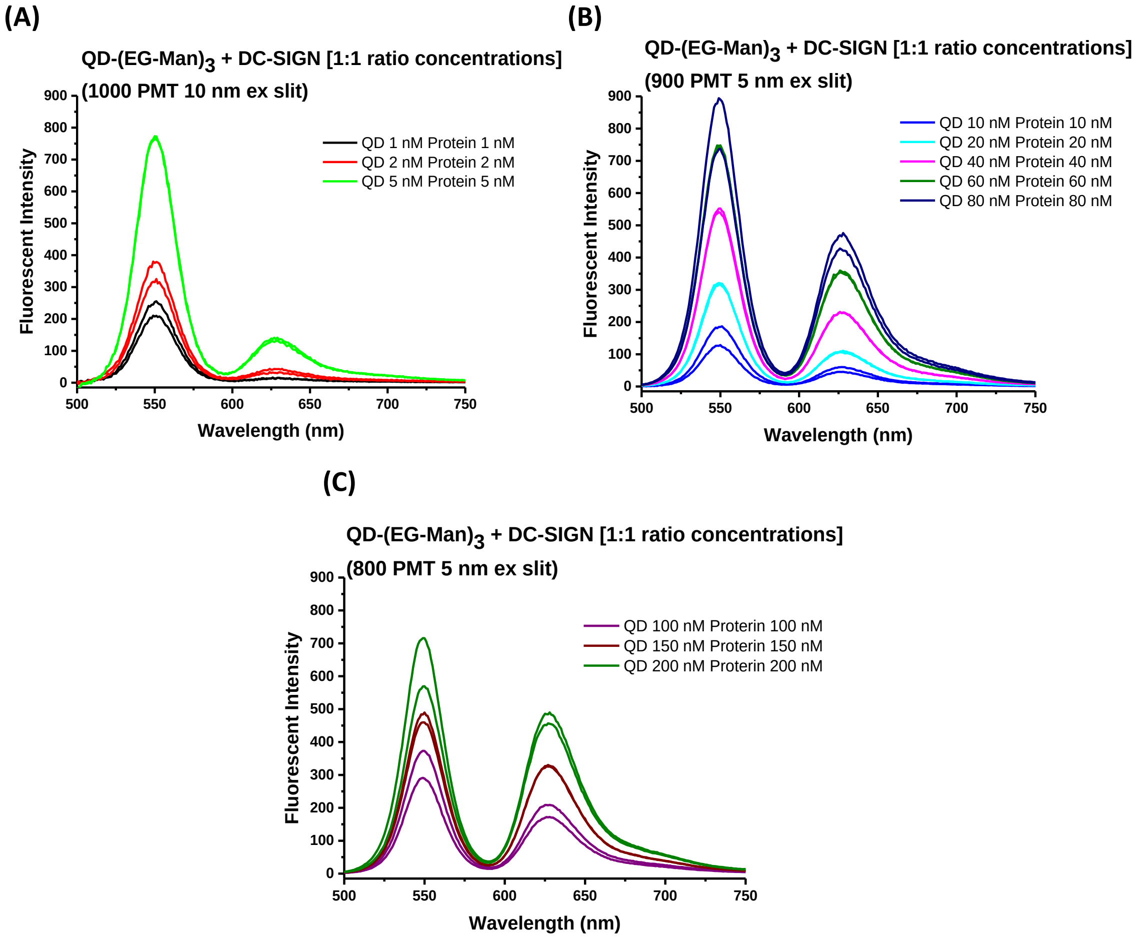

Figure A.3.2: Background corrected fluorescence spectra obtained for determination of the apparent K_D for QD-(EG-Man)$_3$ + DC-SIGN using a standard protein molar ratio: QD ratio of 1:1. (**A**) Low concentrations of QDs (1 – 5 nM) and DC-SIGN (1 – 5 nM); (**B**) Intermediate concentrations of QDs (10 – 80 nM) and DC-SIGN (10 – 80 nM) and (**C**) High concentrations of QDs (100 – 200 nM) and DC-SIGN (100 – 200 nM).

QD-(EG$_2$-DiMan)$_2$:

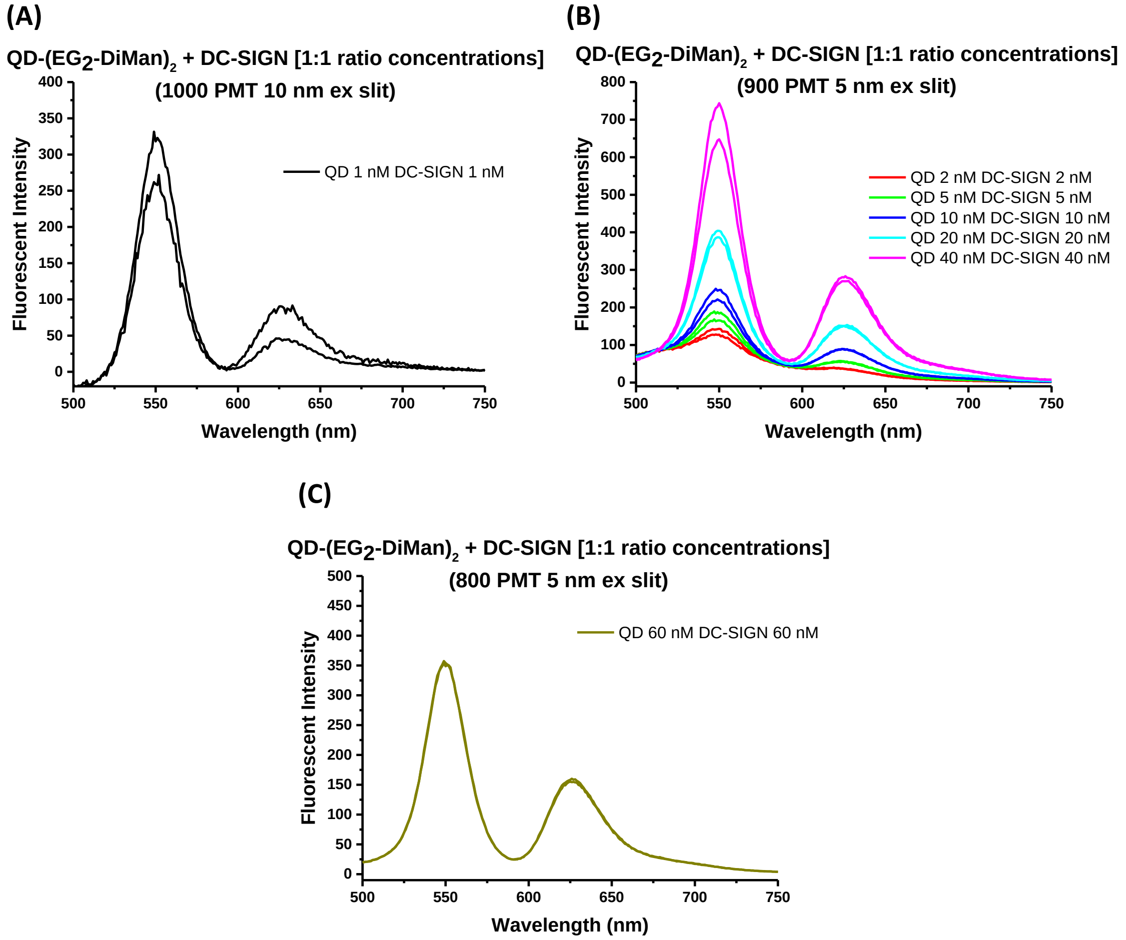

Figure A.3.3: Background corrected fluorescence spectra obtained for determination of the apparent K_D for QD-(EG$_2$-DiMan)$_2$ + DC-SIGN using a standard protein molar ratio: QD ratio of 1:1. (**A**) Low concentrations of QDs (1 nM) and DC-SIGN (1 nM); (**B**) Intermediate concentrations of QDs (2 – 40 nM) and DC-SIGN (2 – 40 nM) and (**C**) High concentrations of QDs (60 nM) and DC-SIGN (60 nM).

QD-(EG-DiMan)$_3$:

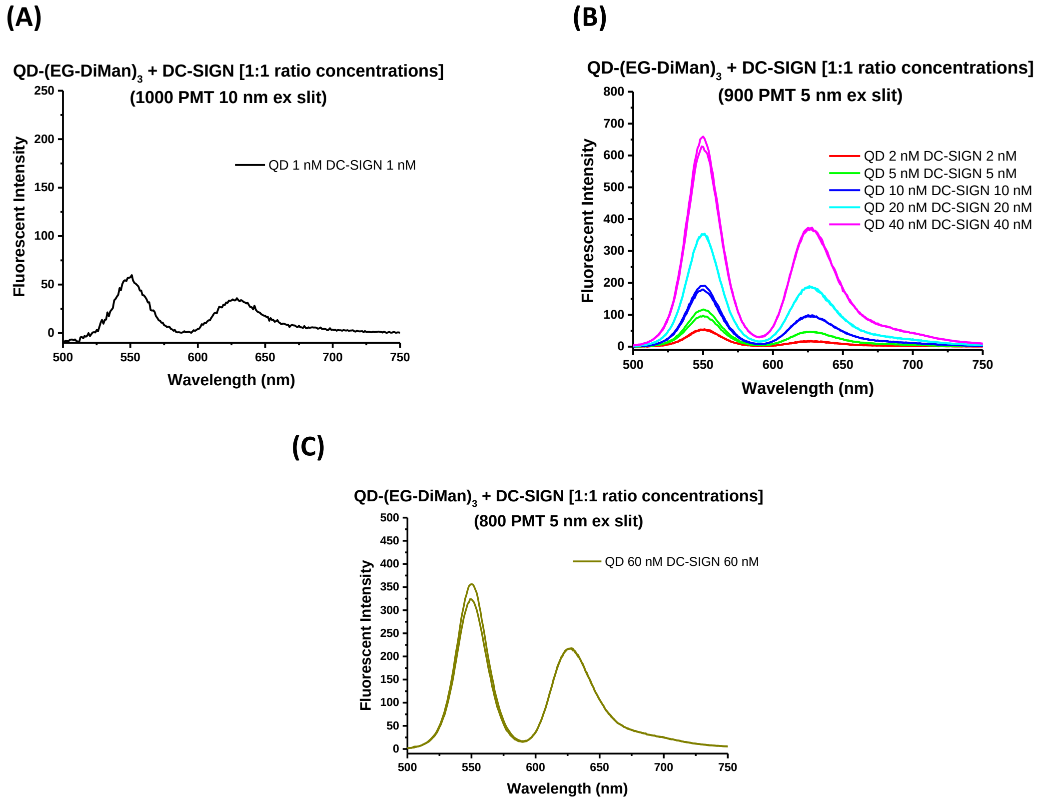

Figure A.3.4: Background corrected fluorescence spectra obtained for determination of the apparent K_D for QD-(EG-DiMan)$_3$ + DC-SIGN using a standard protein molar ratio: QD ratio of 1:1. (**A**) Low concentrations of QDs (1 nM) and DC-SIGN (1 nM); (**B**) Intermediate concentrations of QDs (2 – 40 nM) and DC-SIGN (2 – 40 nM) and (**C**) High concentrations of QDs (60 nM) and DC-SIGN (60 nM).

A.3.2 DC-SIGNR

QD-(EG$_2$-Man)$_2$:

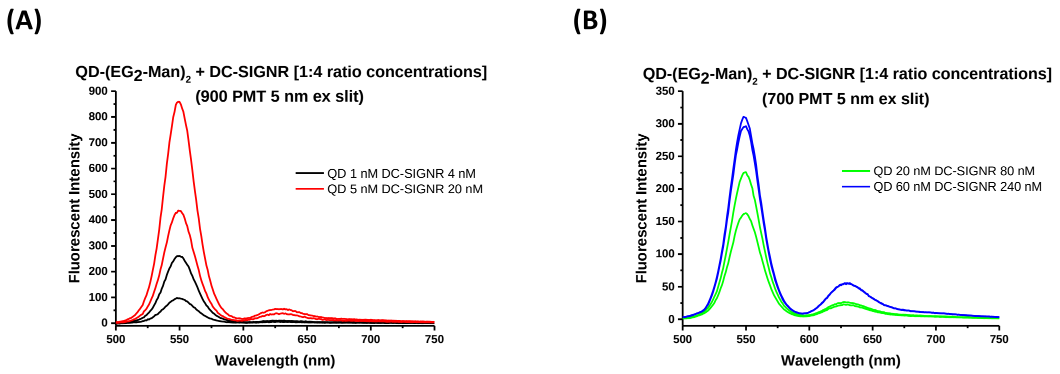

Figure A.3.5: Background corrected fluorescence spectra obtained for determination of the apparent K_D for QD-(EG-DiMan)$_3$ + DC-SIGN using a standard protein molar ratio: QD ratio of 1:1. (**A**) Low concentrations of QDs (1 –5 nM) and DC-SIGNR (4 – 20 nM) and (**B**) Intermediate concentrations of QDs (20 – 60 nM) and DC-SIGNR (80 – 240 nM).

QD-(EG$_2$-DiMan)$_2$:

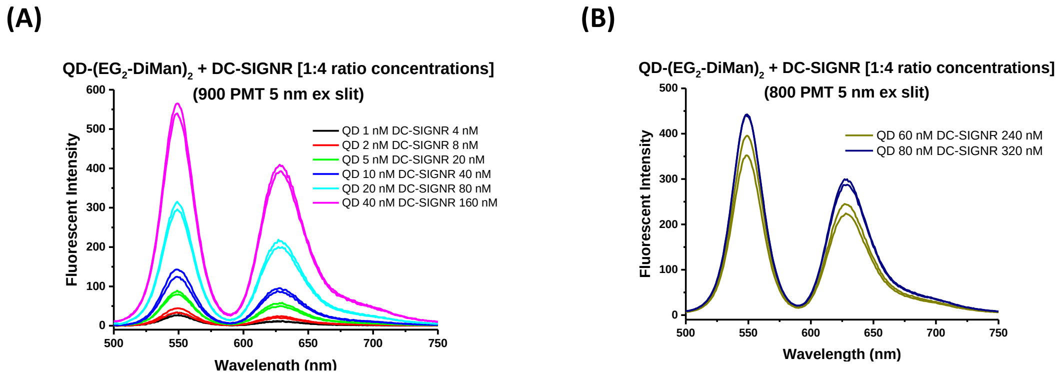

Figure A.3.6: Background corrected fluorescence spectra obtained for determination of the apparent K_D for QD-(EG$_2$-DiMan)$_2$ + DC-SIGNR using a standard protein molar ratio: QD ratio of 1:4. (**A**) Intermediate concentrations of QDs (1 – 40 nM) and DC-SIGNR (4 – 160 nM) and (**B**) High concentrations of QDs (60 – 80 nM) and DC-SIGNR (240 – 320 nM).

QD-(EG-DiMan)$_3$:

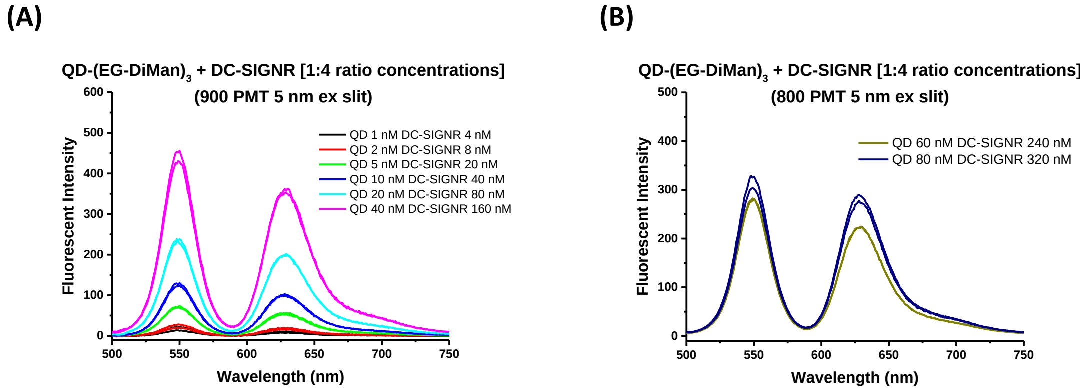

Figure A.3.7: Background corrected fluorescence spectra obtained for determination of the apparent K_D for QD-(EG-DiMan)$_3$ + DC-SIGNR using a standard protein molar ratio: QD ratio of 1:4. (**A**) Intermediate of QDs (1 – 40 nM) and DC-SIGNR (4 – 160 nM) and (**B**) High concentrations of QDs (60 – 80 nM) and DC-SIGNR (240 – 320 nM).

A.4 Nanoparticle Ligand Loading Calibration Curves

A.4.1 Calibration Curves for AuNPs

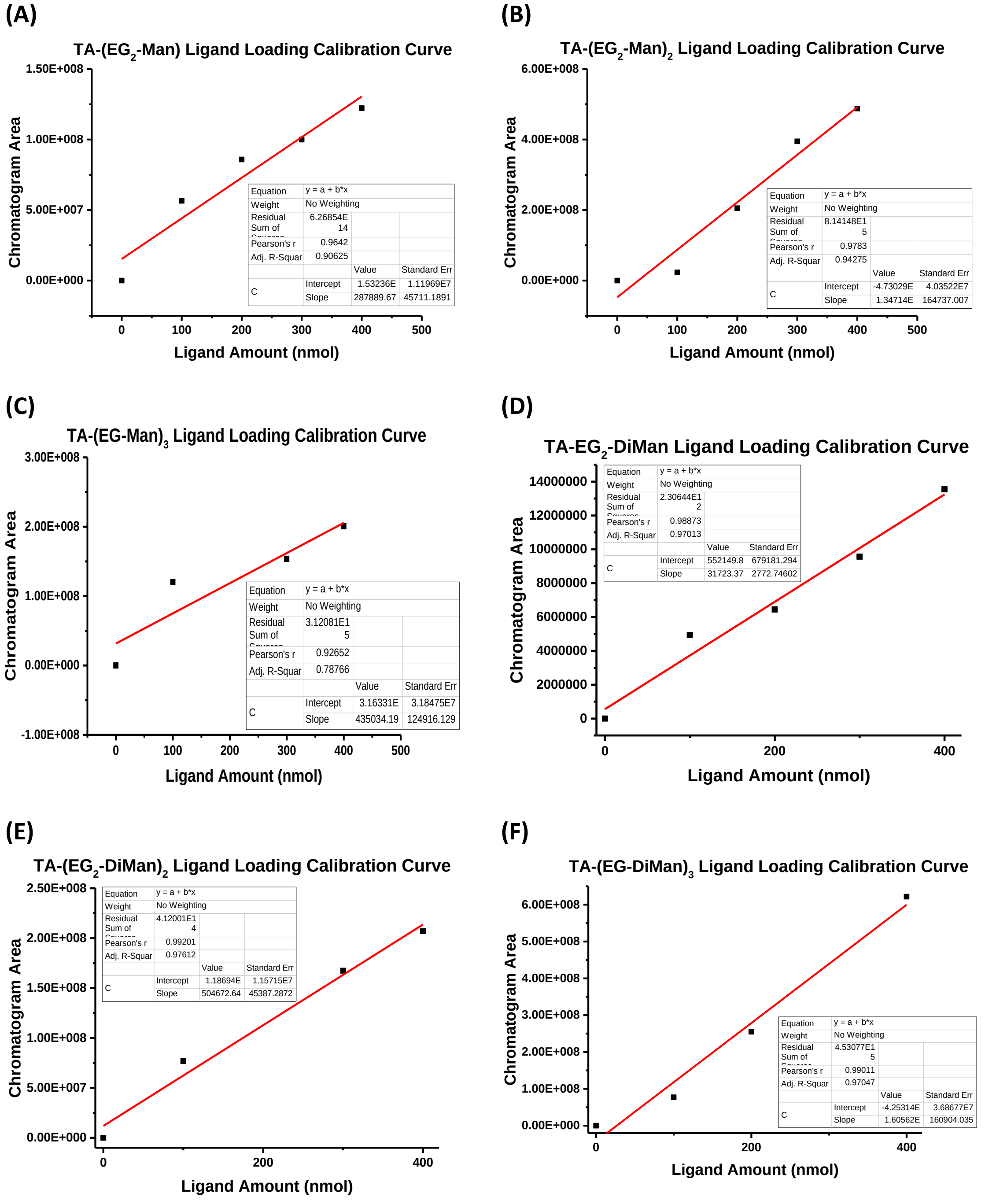

Equation	y = a + b*x		
Weight	No Weighting		
Residual Sum of	6.26854E14		
Pearson's r	0.9642		
Adj. R-Squar	0.90625		
		Value	Standard Err
C	Intercept	1.53236E	1.11969E7
	Slope	287889.67	45711.1891

Equation	y = a + b*x		
Weight	No Weighting		
Residual Sum of	8.14148E15		
Pearson's r	0.9783		
Adj. R-Squar	0.94275		
		Value	Standard Err
C	Intercept	-4.73029E	4.03522E7
	Slope	1.34714E	164737.007

Equation	y = a + b*x		
Weight	No Weighting		
Residual Sum of	3.12081E15		
Pearson's r	0.92652		
Adj. R-Squar	0.78766		
		Value	Standard Err
C	Intercept	3.16331E	3.18475E7
	Slope	435034.19	124916.129

Equation	y = a + b*x		
Weight	No Weighting		
Residual Sum of	2.30644E12		
Pearson's r	0.98873		
Adj. R-Squar	0.97013		
		Value	Standard Err
C	Intercept	552149.8	679181.294
	Slope	31723.37	2772.74602

Equation	y = a + b*x		
Weight	No Weighting		
Residual Sum of	4.12001E14		
Pearson's r	0.99201		
Adj. R-Squar	0.97612		
		Value	Standard Err
C	Intercept	1.18694E	1.15715E7
	Slope	504672.64	45387.2872

Equation	y = a + b*x		
Weight	No Weighting		
Residual Sum of	4.53077E15		
Pearson's r	0.99011		
Adj. R-Squar	0.97047		
		Value	Standard Err
C	Intercept	-4.25314E	3.68677E7
	Slope	1.60562E	160904.035

Figure A.4.1: Ligand loading calibration curves shown against LC-MS chromatogram area of desired product for **(A)** LA-EG$_2$-Dan, **(B)** LA-(EG$_2$-Man)$_2$, **(C)** LA-(EG-Man)$_3$, **(D)** LA-EG$_2$-DiMan, **(E)** LA-(EG$_2$-DiMan)$_2$ and **(F)** LA-(EG-DiMan)$_3$.

A.5 AuNPs Hydrodynamic Size

A.5.1 Initially in Buffer

(A)

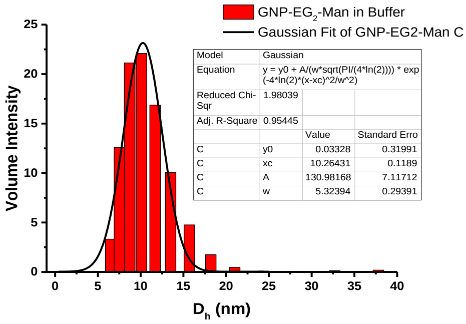

Model	Gaussian		
Equation	y = y0 + A/(w*sqrt(PI/(4*ln(2)))) * exp(-4*ln(2)*(x-xc)^2/w^2)		
Reduced Chi-Sqr	1.98039		
Adj. R-Square	0.95445		
		Value	Standard Erro
C	y0	0.03328	0.31991
C	xc	10.26431	0.1189
C	A	130.98168	7.11712
C	w	5.32394	0.29391

(B)

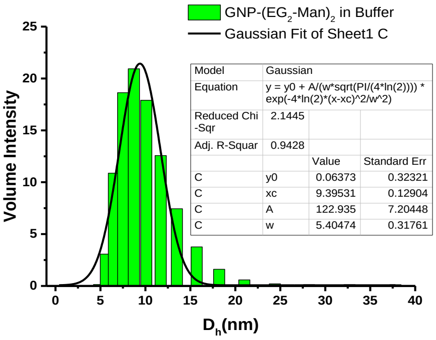

Model	Gaussian		
Equation	y = y0 + A/(w*sqrt(PI/(4*ln(2)))) * exp(-4*ln(2)*(x-xc)^2/w^2)		
Reduced Chi-Sqr	2.1445		
Adj. R-Squar	0.9428		
		Value	Standard Err
C	y0	0.06373	0.32321
C	xc	9.39531	0.12904
C	A	122.935	7.20448
C	w	5.40474	0.31761

(C)

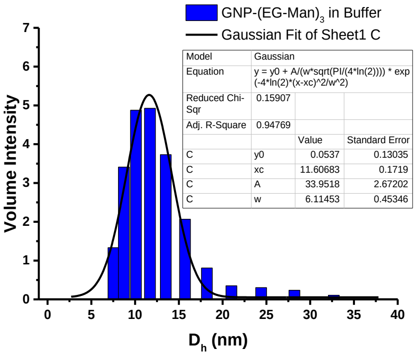

Model	Gaussian		
Equation	y = y0 + A/(w*sqrt(PI/(4*ln(2)))) * exp(-4*ln(2)*(x-xc)^2/w^2)		
Reduced Chi-Sqr	0.15907		
Adj. R-Square	0.94769		
		Value	Standard Error
C	y0	0.0537	0.13035
C	xc	11.60683	0.1719
C	A	33.9518	2.67202
C	w	6.11453	0.45346

(D)

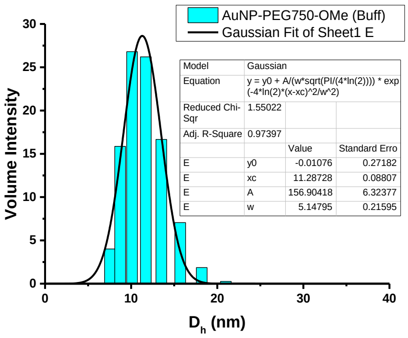

Model	Gaussian		
Equation	y = y0 + A/(w*sqrt(PI/(4*ln(2)))) * exp(-4*ln(2)*(x-xc)^2/w^2)		
Reduced Chi-Sqr	1.55022		
Adj. R-Square	0.97397		
		Value	Standard Erro
E	y0	-0.01076	0.27182
E	xc	11.28728	0.08807
E	A	156.90418	6.32377
E	w	5.14795	0.21595

(E)

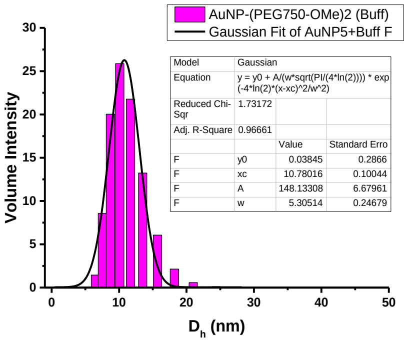

Model	Gaussian		
Equation	y = y0 + A/(w*sqrt(PI/(4*ln(2)))) * exp(-4*ln(2)*(x-xc)^2/w^2)		
Reduced Chi-Sqr	1.73172		
Adj. R-Square	0.96661		
		Value	Standard Erro
F	y0	0.03845	0.2866
F	xc	10.78016	0.10044
F	A	148.13308	6.67961
F	w	5.30514	0.24679

(F)

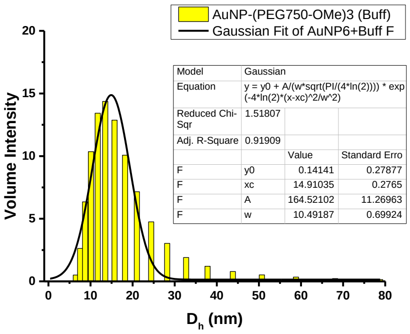

Model	Gaussian		
Equation	y = y0 + A/(w*sqrt(PI/(4*ln(2)))) * exp(-4*ln(2)*(x-xc)^2/w^2)		
Reduced Chi-Sqr	1.51807		
Adj. R-Square	0.91909		
		Value	Standard Erro
F	y0	0.14141	0.27877
F	xc	14.91035	0.2765
F	A	164.52102	11.26963
F	w	10.49187	0.69924

(G)

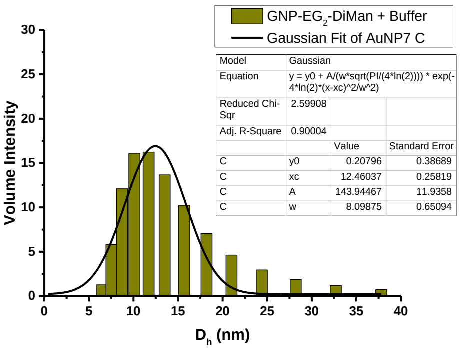

Model	Gaussian		
Equation	y = y0 + A/(w*sqrt(PI/(4*ln(2)))) * exp(-4*ln(2)*(x-xc)^2/w^2)		
Reduced Chi-Sqr	2.59908		
Adj. R-Square	0.90004		
		Value	Standard Error
C	y0	0.20796	0.38689
C	xc	12.46037	0.25819
C	A	143.94467	11.9358
C	w	8.09875	0.65094

(H)

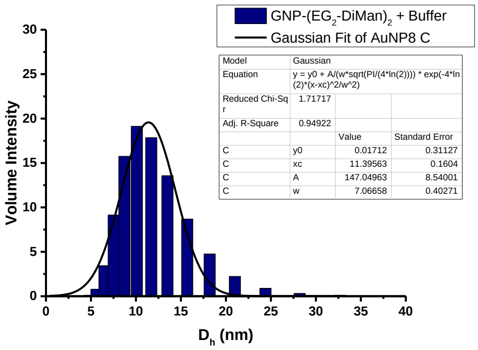

Model	Gaussian		
Equation	y = y0 + A/(w*sqrt(PI/(4*ln(2)))) * exp(-4*ln(2)*(x-xc)^2/w^2)		
Reduced Chi-Sqr	1.71717		
Adj. R-Square	0.94922		
		Value	Standard Error
C	y0	0.01712	0.31127
C	xc	11.39563	0.1604
C	A	147.04963	8.54001
C	w	7.06658	0.40271

(I)

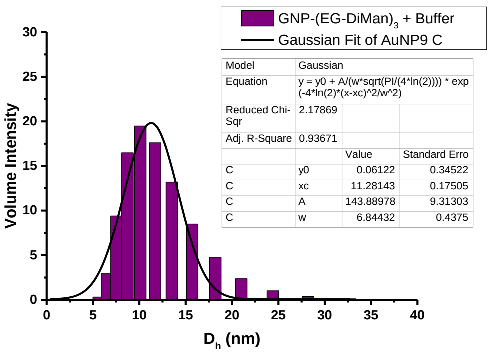

Model	Gaussian		
Equation	y = y0 + A/(w*sqrt(PI/(4*ln(2)))) * exp(-4*ln(2)*(x-xc)^2/w^2)		
Reduced Chi-Sqr	2.17869		
Adj. R-Square	0.93671		
		Value	Standard Erro
C	y0	0.06122	0.34522
C	xc	11.28143	0.17505
C	A	143.88978	9.31303
C	w	6.84432	0.4375

Figure A.5.1: Shows the resulting histograms of the range of hydrodynamic size for the AuNPs in buffer solution (50 nM) **(A)** AuNP-EG$_2$-Man, **(B)** AuNP-(EG$_2$-Man)$_2$, **(C)** AuNP-(EG-Man)$_3$, **(D)** AuNP-PEG$_{750}$-OMe, **(E)** for AuNP-(PEG$_{750}$-OMe)$_2$, **(F)** AuNP-(PEG$_{750}$-OMe)$_3$, **(G)** AuNP-EG$_2$-DiMan, **(H)** AuNP-(EG$_2$-DiMan)$_2$ and finally **(I)** AuNP-(EG-DiMan)$_3$.

A.5.2 Stability over One Week

(A)

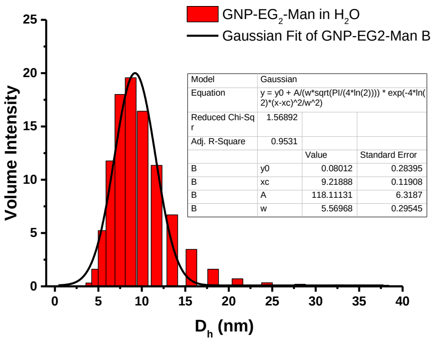

Model	Gaussian		
Equation	y = y0 + A/(w*sqrt(PI/(4*ln(2)))) * exp(-4*ln(2)*(x-xc)^2/w^2)		
Reduced Chi-Sqr	1.56892		
Adj. R-Square	0.9531		
		Value	Standard Error
B	y0	0.08012	0.28395
B	xc	9.21888	0.11908
B	A	118.11131	6.3187
B	w	5.56968	0.29545

(B)

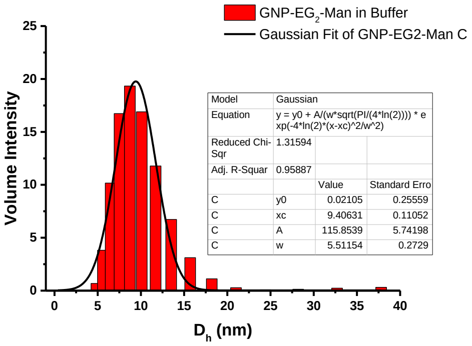

Model	Gaussian		
Equation	y = y0 + A/(w*sqrt(PI/(4*ln(2)))) * exp(-4*ln(2)*(x-xc)^2/w^2)		
Reduced Chi-Sqr	1.31594		
Adj. R-Squar	0.95887		
		Value	Standard Erro
C	y0	0.02105	0.25559
C	xc	9.40631	0.11052
C	A	115.8539	5.74198
C	w	5.51154	0.2729

(C)

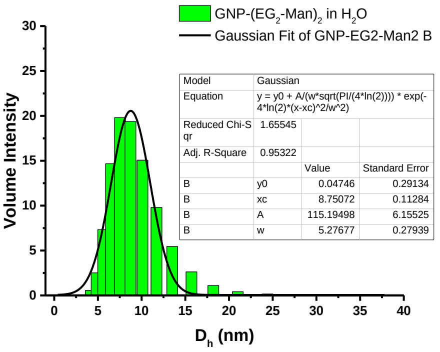

Model	Gaussian		
Equation	y = y0 + A/(w*sqrt(PI/(4*ln(2)))) * exp(-4*ln(2)*(x-xc)^2/w^2)		
Reduced Chi-Sqr	1.65545		
Adj. R-Square	0.95322		
		Value	Standard Error
B	y0	0.04746	0.29134
B	xc	8.75072	0.11284
B	A	115.19498	6.15525
B	w	5.27677	0.27939

(D)

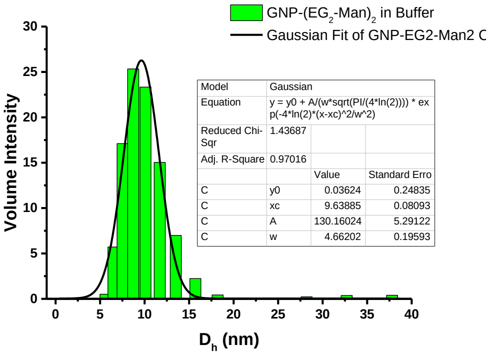

Model	Gaussian		
Equation	y = y0 + A/(w*sqrt(PI/(4*ln(2)))) * exp(-4*ln(2)*(x-xc)^2/w^2)		
Reduced Chi-Sqr	1.43687		
Adj. R-Square	0.97016		
		Value	Standard Erro
C	y0	0.03624	0.24835
C	xc	9.63885	0.08093
C	A	130.16024	5.29122
C	w	4.66202	0.19593

(E)

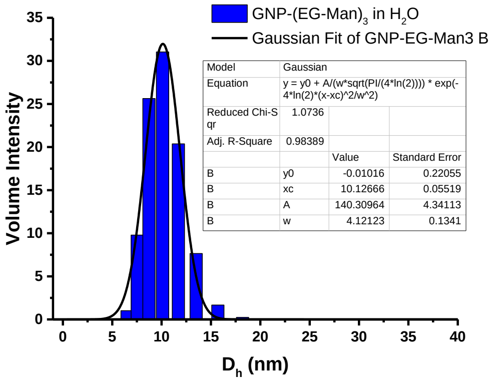

Model	Gaussian		
Equation	y = y0 + A/(w*sqrt(PI/(4*ln(2)))) * exp(-4*ln(2)*(x-xc)^2/w^2)		
Reduced Chi-Sqr	1.0736		
Adj. R-Square	0.98389		
		Value	Standard Error
B	y0	-0.01016	0.22055
B	xc	10.12666	0.05519
B	A	140.30964	4.34113
B	w	4.12123	0.1341

(F)

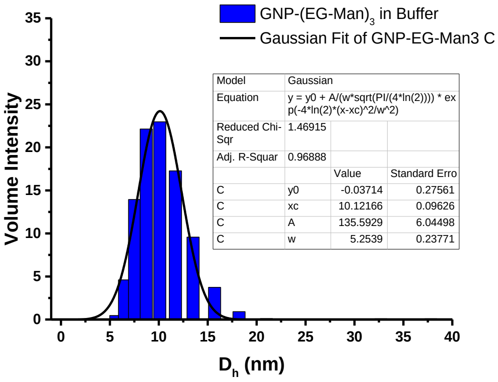

Model	Gaussian		
Equation	y = y0 + A/(w*sqrt(PI/(4*ln(2)))) * exp(-4*ln(2)*(x-xc)^2/w^2)		
Reduced Chi-Sqr	1.46915		
Adj. R-Squar	0.96888		
		Value	Standard Erro
C	y0	-0.03714	0.27561
C	xc	10.12166	0.09626
C	A	135.5929	6.04498
C	w	5.2539	0.23771

(G)

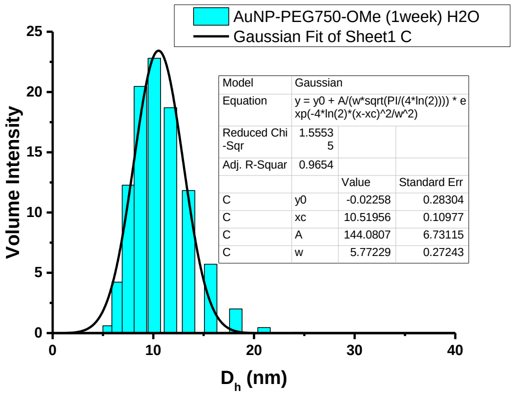

Model	Gaussian		
Equation	y = y0 + A/(w*sqrt(PI/(4*ln(2)))) * exp(-4*ln(2)*(x-xc)^2/w^2)		
Reduced Chi-Sqr	1.55535		
Adj. R-Squar	0.9654		
		Value	Standard Err
C	y0	-0.02258	0.28304
C	xc	10.51956	0.10977
C	A	144.0807	6.73115
C	w	5.77229	0.27243

(H)

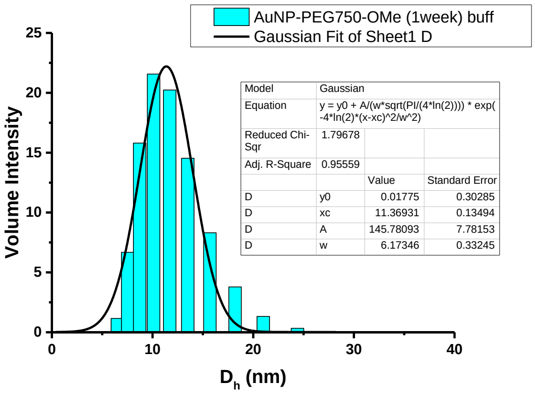

Model	Gaussian		
Equation	y = y0 + A/(w*sqrt(PI/(4*ln(2)))) * exp(-4*ln(2)*(x-xc)^2/w^2)		
Reduced Chi-Sqr	1.79678		
Adj. R-Square	0.95559		
		Value	Standard Error
D	y0	0.01775	0.30285
D	xc	11.36931	0.13494
D	A	145.78093	7.78153
D	w	6.17346	0.33245

(I)

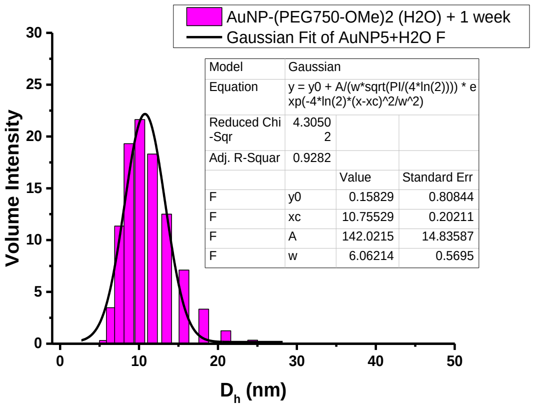

Model	Gaussian		
Equation	y = y0 + A/(w*sqrt(PI/(4*ln(2)))) * exp(-4*ln(2)*(x-xc)^2/w^2)		
Reduced Chi-Sqr	4.30502		
Adj. R-Squar	0.9282		
		Value	Standard Err
F	y0	0.15829	0.80844
F	xc	10.75529	0.20211
F	A	142.0215	14.83587
F	w	6.06214	0.5695

(J)

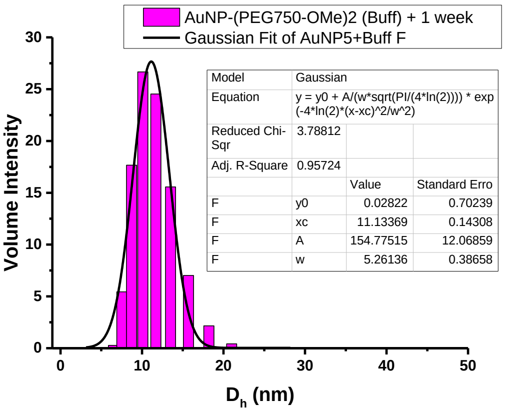

Model	Gaussian		
Equation	y = y0 + A/(w*sqrt(PI/(4*ln(2)))) * exp(-4*ln(2)*(x-xc)^2/w^2)		
Reduced Chi-Sqr	3.78812		
Adj. R-Square	0.95724		
		Value	Standard Erro
F	y0	0.02822	0.70239
F	xc	11.13369	0.14308
F	A	154.77515	12.06859
F	w	5.26136	0.38658

(K)

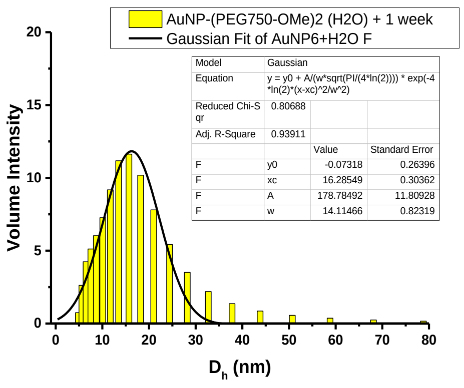

Model	Gaussian		
Equation	y = y0 + A/(w*sqrt(PI/(4*ln(2)))) * exp(-4*ln(2)*(x-xc)^2/w^2)		
Reduced Chi-Sqr	0.80688		
Adj. R-Square	0.93911		
		Value	Standard Error
F	y0	-0.07318	0.26396
F	xc	16.28549	0.30362
F	A	178.78492	11.80928
F	w	14.11466	0.82319

(L)

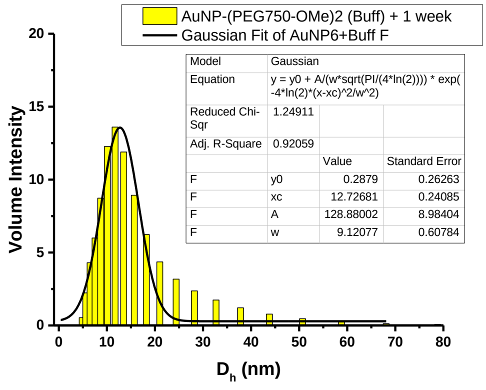

Model	Gaussian		
Equation	y = y0 + A/(w*sqrt(PI/(4*ln(2)))) * exp(-4*ln(2)*(x-xc)^2/w^2)		
Reduced Chi-Sqr	1.24911		
Adj. R-Square	0.92059		
		Value	Standard Error
F	y0	0.2879	0.26263
F	xc	12.72681	0.24085
F	A	128.88002	8.98404
F	w	9.12077	0.60784

(M)

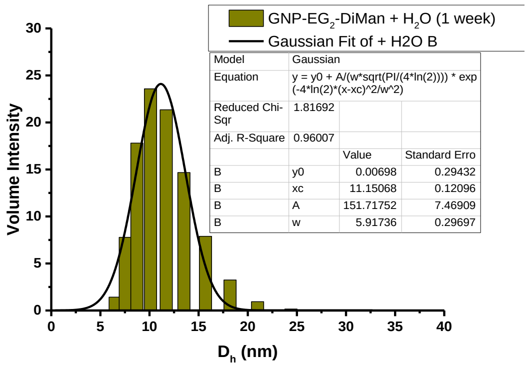

Model	Gaussian		
Equation	y = y0 + A/(w*sqrt(PI/(4*ln(2)))) * exp(-4*ln(2)*(x-xc)^2/w^2)		
Reduced Chi-Sqr	1.81692		
Adj. R-Square	0.96007		
		Value	Standard Erro
B	y0	0.00698	0.29432
B	xc	11.15068	0.12096
B	A	151.71752	7.46909
B	w	5.91736	0.29697

(N)

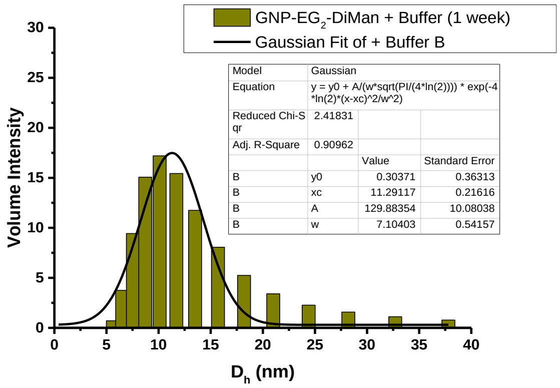

Model	Gaussian		
Equation	y = y0 + A/(w*sqrt(PI/(4*ln(2)))) * exp(-4*ln(2)*(x-xc)^2/w^2)		
Reduced Chi-Sqr	2.41831		
Adj. R-Square	0.90962		
		Value	Standard Error
B	y0	0.30371	0.36313
B	xc	11.29117	0.21616
B	A	129.88354	10.08038
B	w	7.10403	0.54157

(O)

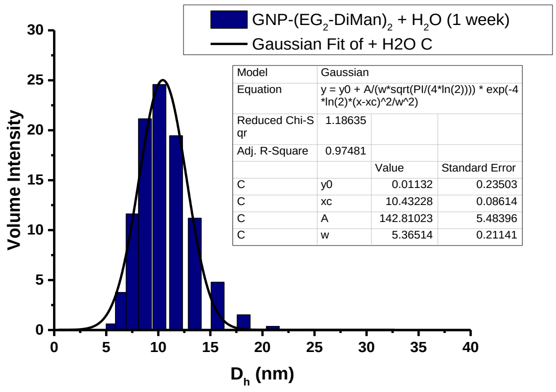

Model	Gaussian		
Equation	y = y0 + A/(w*sqrt(PI/(4*ln(2)))) * exp(-4*ln(2)*(x-xc)^2/w^2)		
Reduced Chi-Sqr	1.18635		
Adj. R-Square	0.97481		
		Value	Standard Error
C	y0	0.01132	0.23503
C	xc	10.43228	0.08614
C	A	142.81023	5.48396
C	w	5.36514	0.21141

(P)

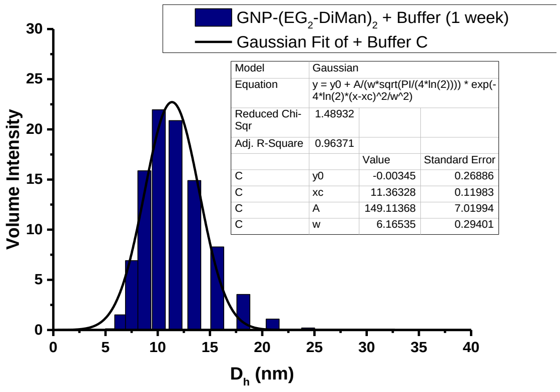

Model	Gaussian		
Equation	y = y0 + A/(w*sqrt(PI/(4*ln(2)))) * exp(-4*ln(2)*(x-xc)^2/w^2)		
Reduced Chi-Sqr	1.48932		
Adj. R-Square	0.96371		
		Value	Standard Error
C	y0	-0.00345	0.26886
C	xc	11.36328	0.11983
C	A	149.11368	7.01994
C	w	6.16535	0.29401

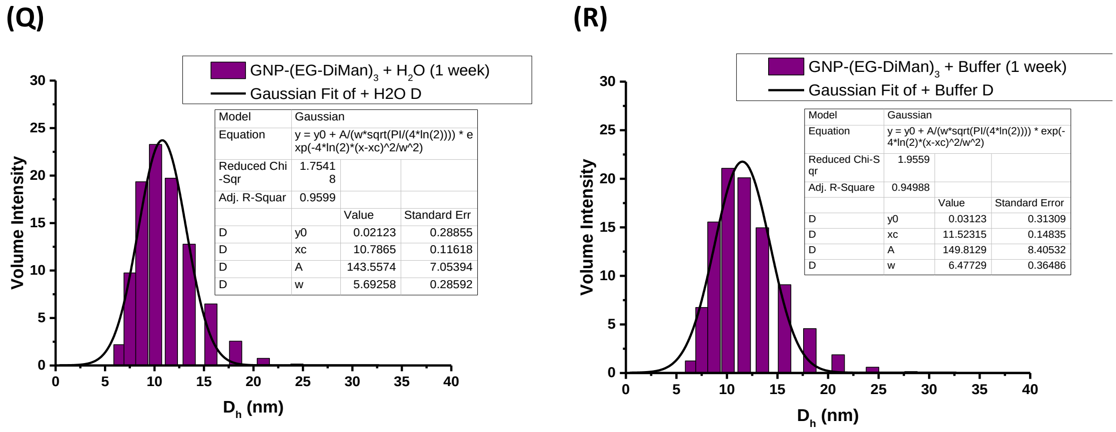

Figure A.5.2: Shows the resulting histograms of the range of hydrodynamic size for the in both water solution and buffer solution after 1 week (50 nM), **(A)** and **(B)** are for AuNP-EG$_2$-Man, **(C)** and **(D)** for AuNP-(EG$_2$-Man)$_2$, **(E)** and **(F)** for AuNP-(EG-Man)$_3$, **(G)** and **(H)** for AuNP-PEG$_{750}$-OMe, **(I)** and **(J)** for AuNP-(PEG$_{750}$-OMe)$_2$, **(K)** and **(L)** for AuNP-(PEG$_{750}$-OMe)$_3$, **(M)** and **(N)** are for AuNP-EG$_2$-DiMan, **(O)** and **(P)** for AuNP-(EG$_2$-DiMan)$_2$ and finally **(Q)** and **(R)** for AuNP-(EG-DiMan)$_3$.

A.6 AuNPs + DC-SIGN/R Fluorescence Data

A.6.1 DC-SIGN

AuNP-(EG_2-Man)$_2$:

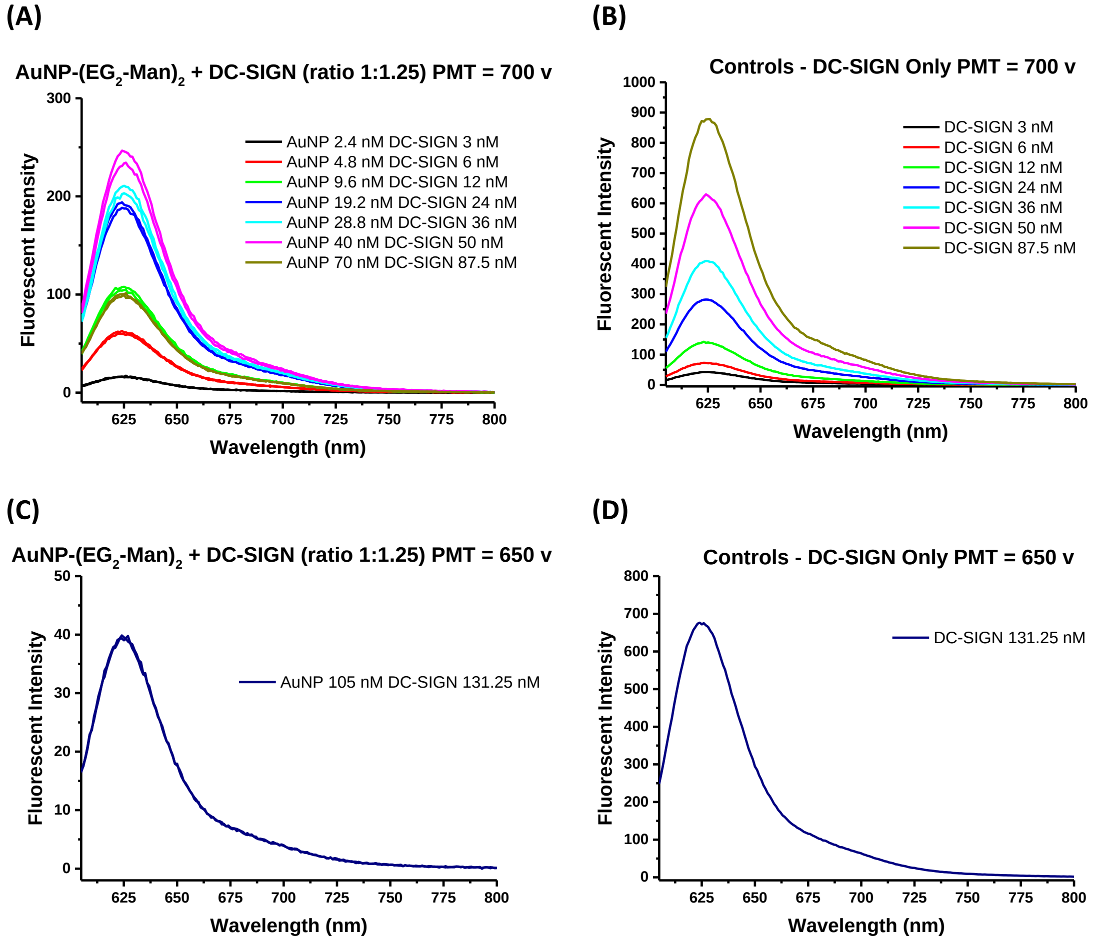

Figure A.6.1: Fluorescence Measurements between 605 – 800 nm for **(A)** AuNP-(EG_2-Man)$_2$ (2.4 – 70 nM) + labelled DC-SIGN (3 – 87.5 nM), **(C)** AuNP-(EG_2-Man)$_2$ (105 nM) + labelled DC-SIGN (131.25 nM) and **(B)** and **(D)** Control samples where only labelled DC-SIGN was used at the same concentrations and the same machine settings.

AuNP-(EG-Man)$_3$:

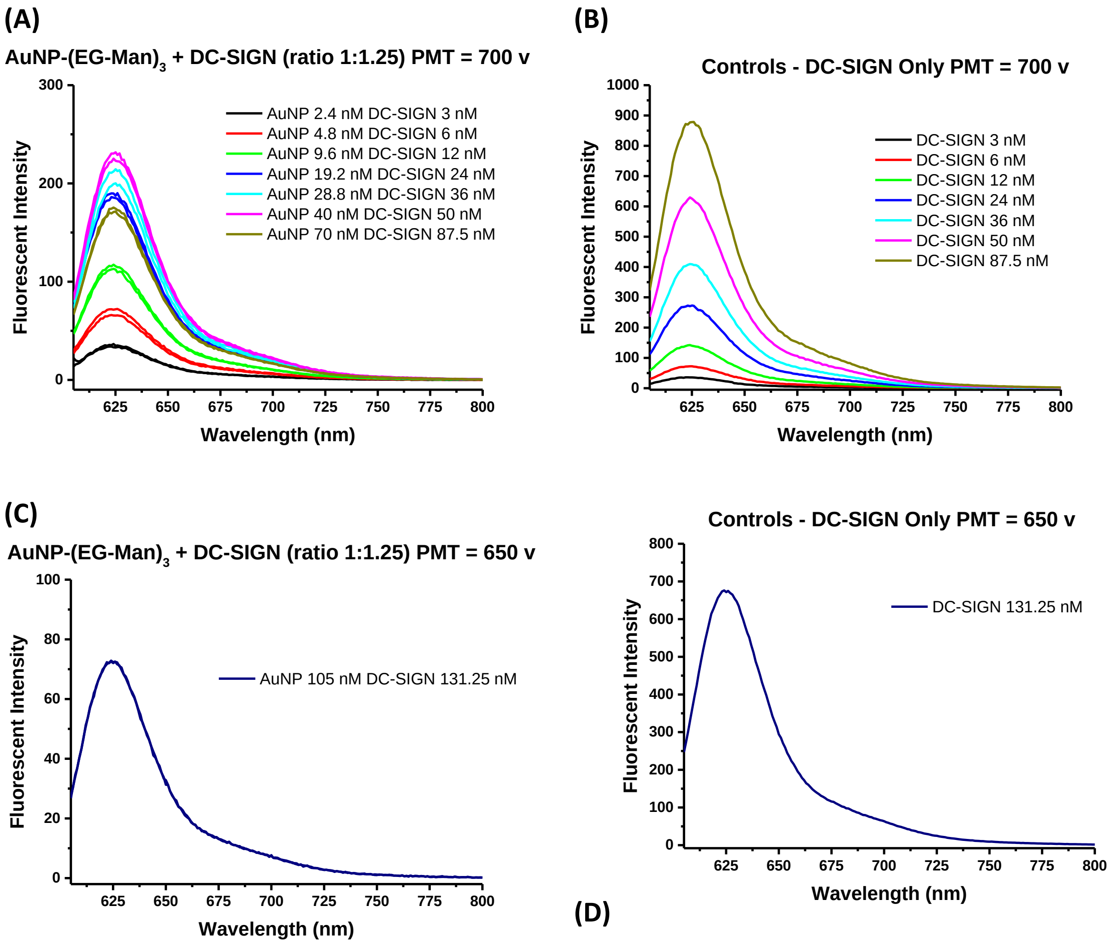

Figure A.6.2: Fluorescence Measurements between 605 – 800 nm for **(A)** AuNP-(EG-Man)$_3$ (2.4 – 70 nM) + labelled DC-SIGN (3 – 87.5 nM), **(C)** AuNP-(EG-Man)$_3$ (105 nM) + labelled DC-SIGN and **(B)** and **(D)** Control samples where only labelled DC-SIGN was used at the same concentrations and the same machine settings.

AuNP-EG$_2$-DiMan:

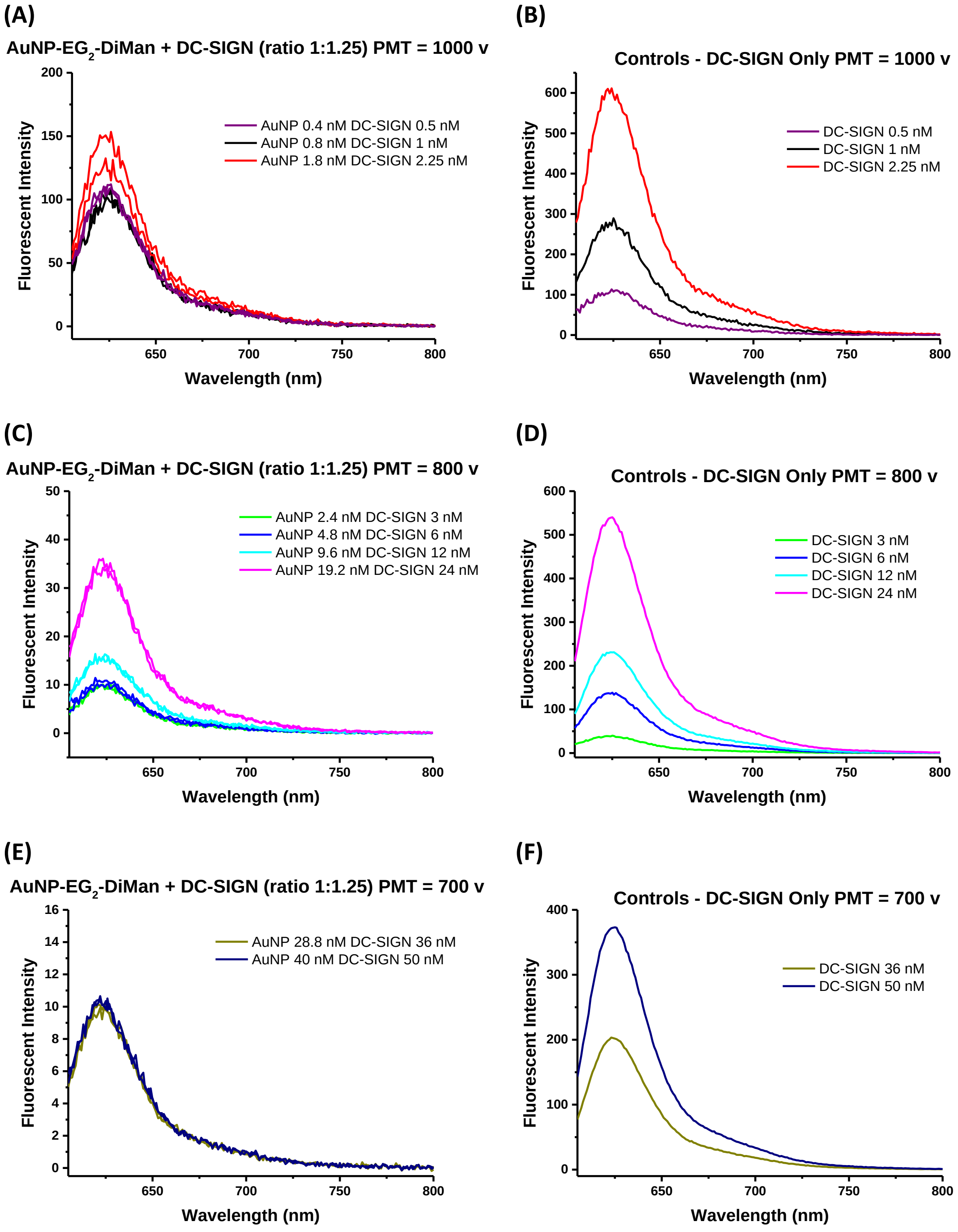

Figure A.6.3: Fluorescence Measurements between 605 – 800 nm for **(A)** AuNP-EG$_2$-DiMan (0.4 – 1.8 nM) + labelled DC-SIGN (0.5 – 2.25 nM), **(C)** AuNP-EG$_2$-DiMan (2.4 – 19.2 nM) + labelled DC-SIGN (3 – 24 nM) **(E)** AuNP-EG$_2$-DiMan (28.8 – 40 nM) + labelled DC-SIGN (36 – 50 nM) and **(B)**, **(D)** and **(F)** Control samples where only labelled DC-SIGN was used at the same concentrations and the same machine settings.

AuNP-(EG$_2$-DiMan)$_2$:

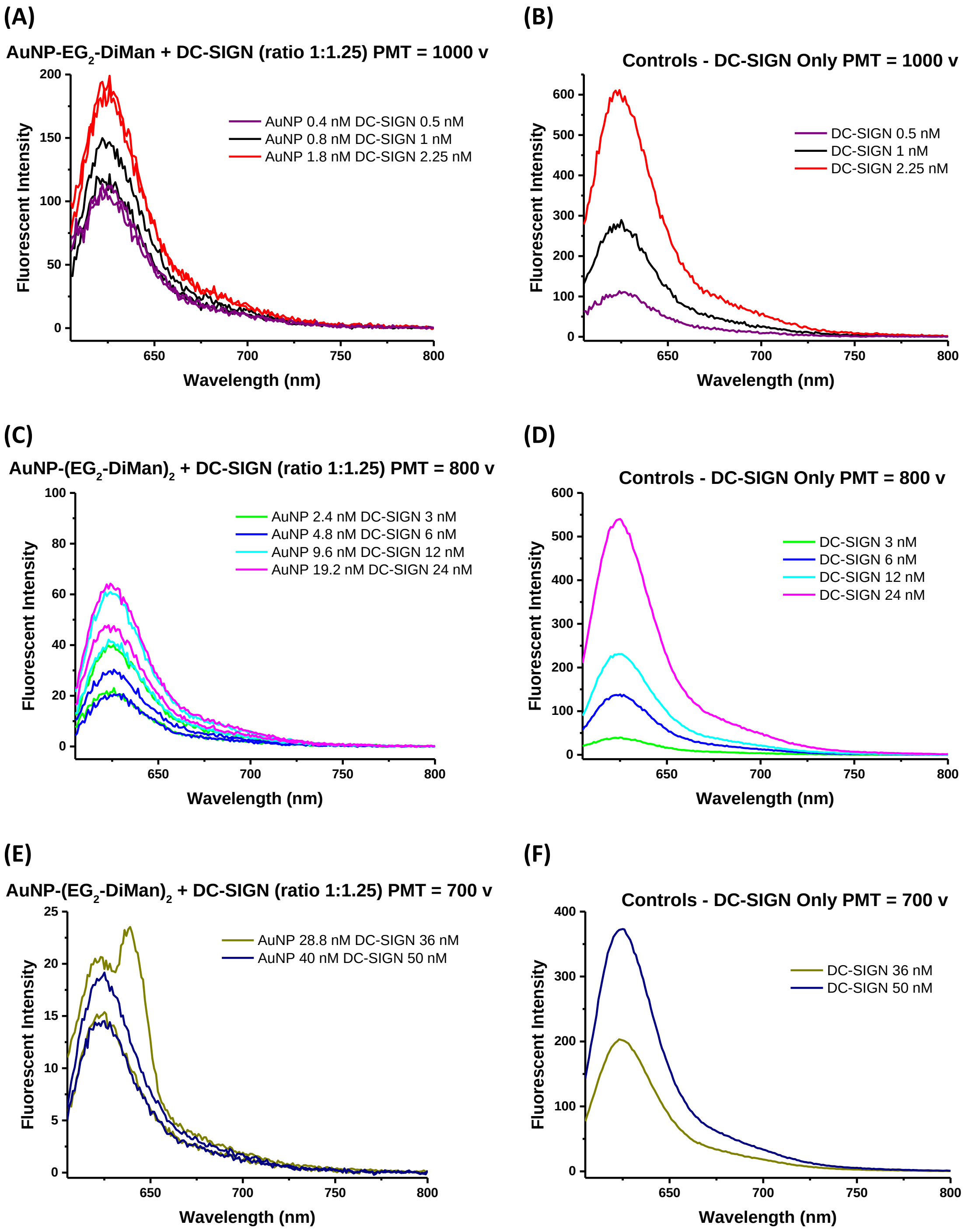

Figure A.6.4: Fluorescence Measurements between 605 – 800 nm for **(A)** AuNP-(EG$_2$-DiMan)$_2$ (0.4 – 1.8 nM) + labelled DC-SIGN (0.5 – 2.25 nM), **(C)** AuNP-(EG$_2$-DiMan)$_2$ (2.4 – 19.2 nM) + labelled DC-SIGN (3 – 24 nM) **(E)** AuNP-(EG$_2$-DiMan)$_2$ (28.8 – 40 nM) + labelled DC-SIGN (36 – 50 nM) and **(B)**, **(D)** and **(F)** Control samples where only labelled DC-SIGN was used at the same concentrations and the same machine settings.

AuNP-(EG-DiMan)$_3$:

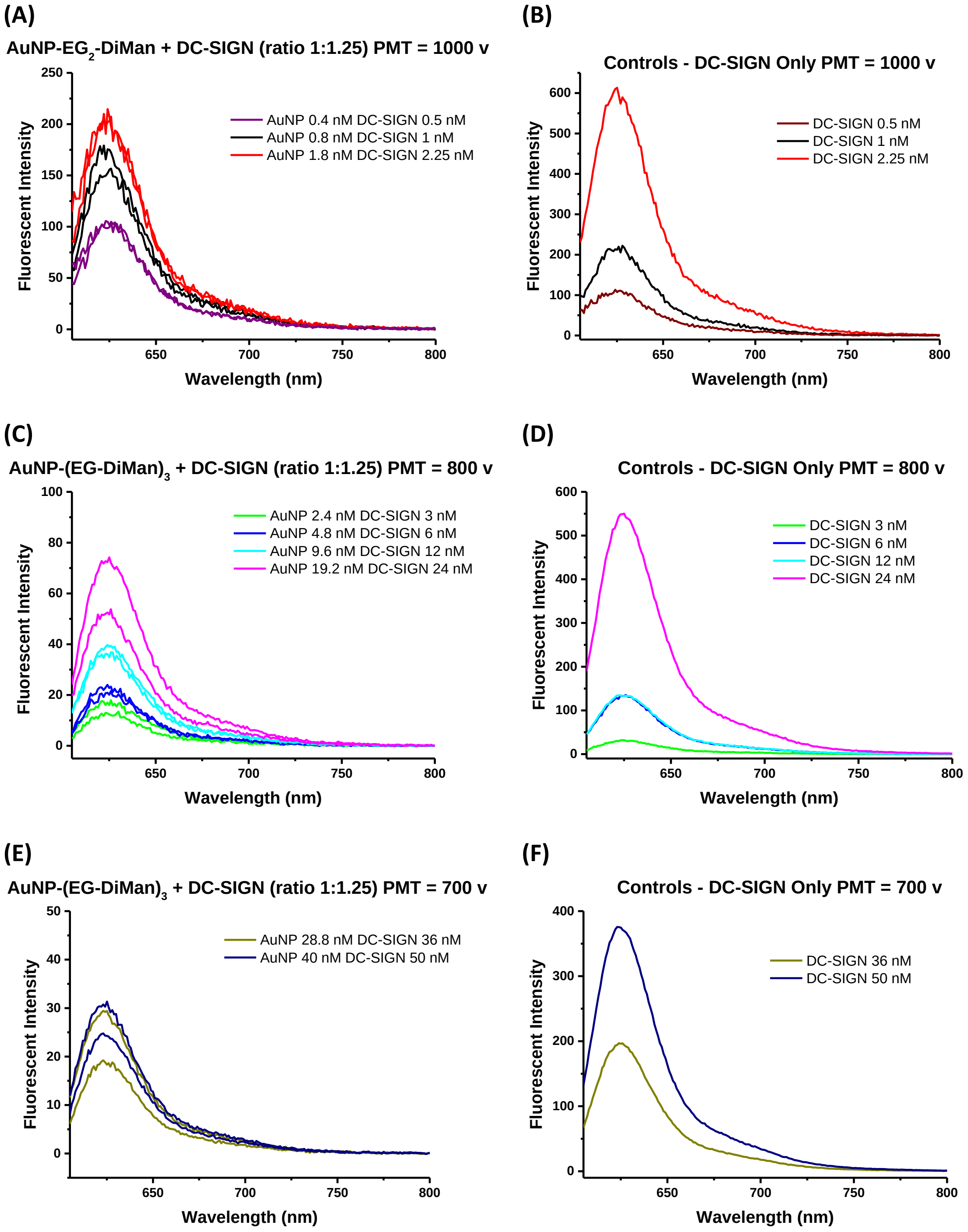

Figure A.6.5: Fluorescence Measurements between 605 – 800 nm for **(A)** AuNP-(EG-DiMan)$_3$ (0.4 – 1.8 nM) + labelled DC-SIGN (0.5 – 2.25 nM), **(C)** AuNP-(EG-DiMan)$_3$ (2.4 – 19.2 nM) + labelled DC-SIGN (3 – 24 nM) **(E)** AuNP-(EG-DiMan)$_3$ (28.8 – 40 nM) + labelled DC-SIGN (36 – 50 nM) and **(B)**, **(D)** and **(F)** Control samples where only labelled DC-SIGN was used at the same concentrations and the same machine settings.

AuNP-PEG$_{750}$-OMe:

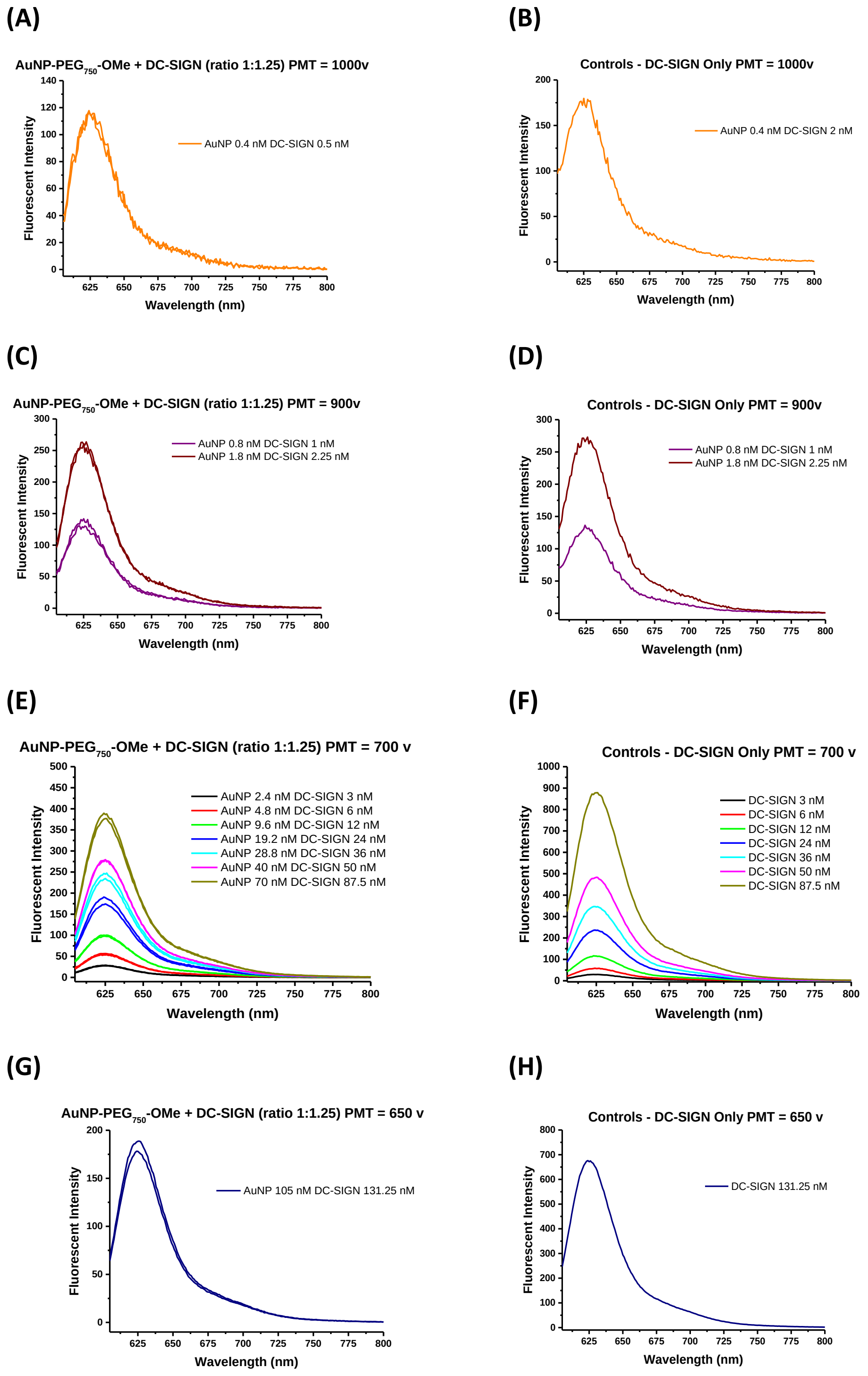

Figure A.6.6: Fluorescence Measurements for **(A)** AuNP-(PEG$_{750}$-OMe) (0.4 nM) + DC-SIGN (0.5 nM), **(C)** AuNP-(PEG$_{750}$-OMe) (0.8 – 1.8 nM) + DC-SIGN (1 – 2.25 nM), **(E)** AuNP-(PEG$_{750}$-OMe) (2.4 – 70 nM) + DC-SIGN (3 – 87.5 nM), **(G)** AuNP-(PEG$_{750}$-OMe) (105 nM) + DC-SIGN (131.25 nM) and **(B)**, **(D), (F)** and **(H)** Control DC-SIGN was used at the same concentrations and machine settings.

AuNP-(PEG_{750}-OMe)$_2$:

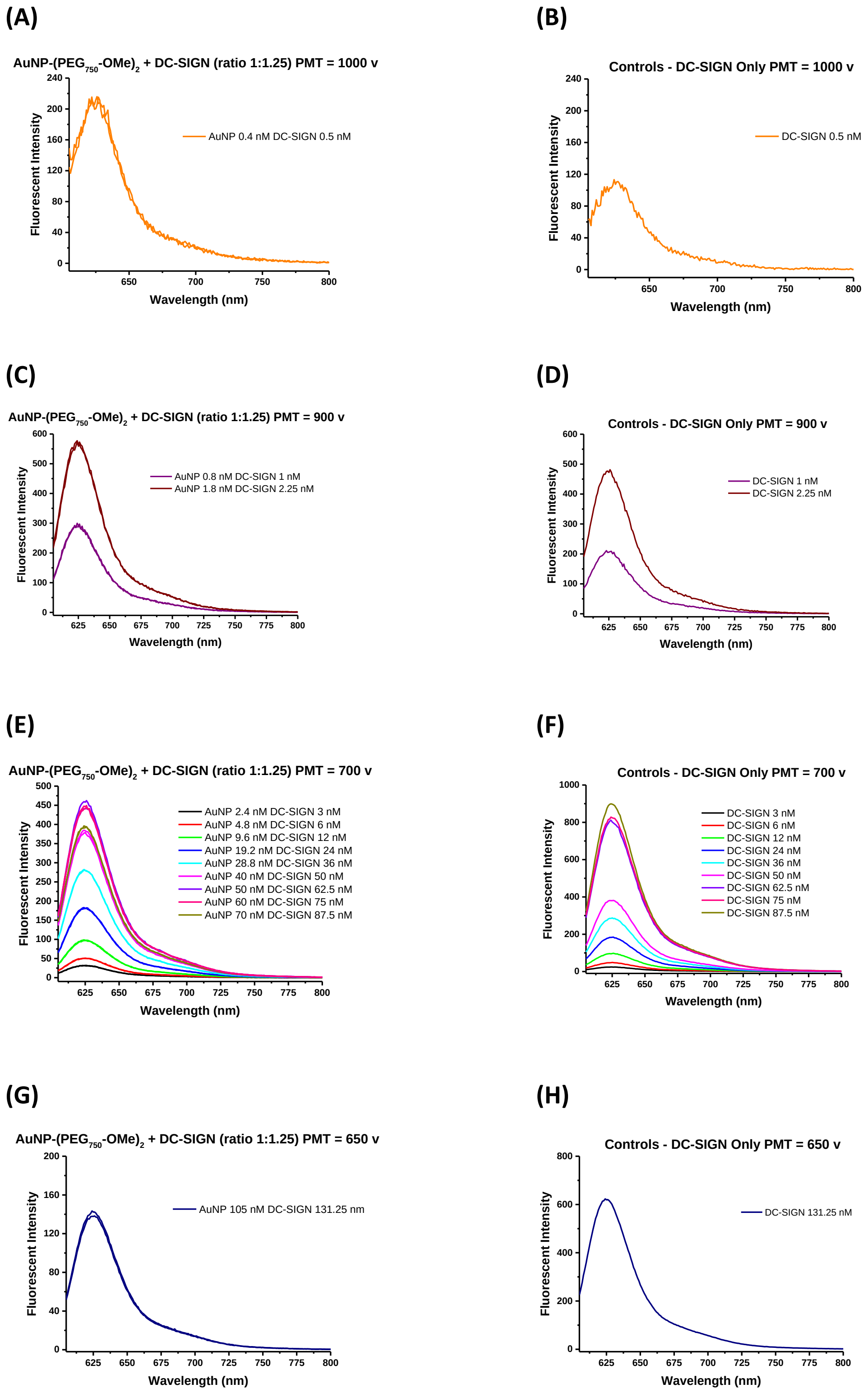

Figure A.6.7: Fluorescence Measurements for **(A)** AuNP-(PEG_{750}-OMe)$_2$ (0.4 nM) + DC-SIGN (0.5 nM), **(C)** AuNP-(PEG_{750}-OMe)$_2$ (0.8 – 1.8 nM) + DC-SIGN (1 – 2.25 nM), **(E)** AuNP-(PEG_{750}-OMe)$_2$ (2.4 – 70 nM) + DC-SIGN (3 – 87.5 nM), **(G)** AuNP-(PEG_{750}-OMe)$_2$ (105 nM) + DC-SIGN (131.25 nM) and **(B)**, **(D), (F)** and **(H)** Control DC-SIGN was used at the same concentrations and machine settings

AuNP-(PEG$_{750}$-OMe)$_3$:

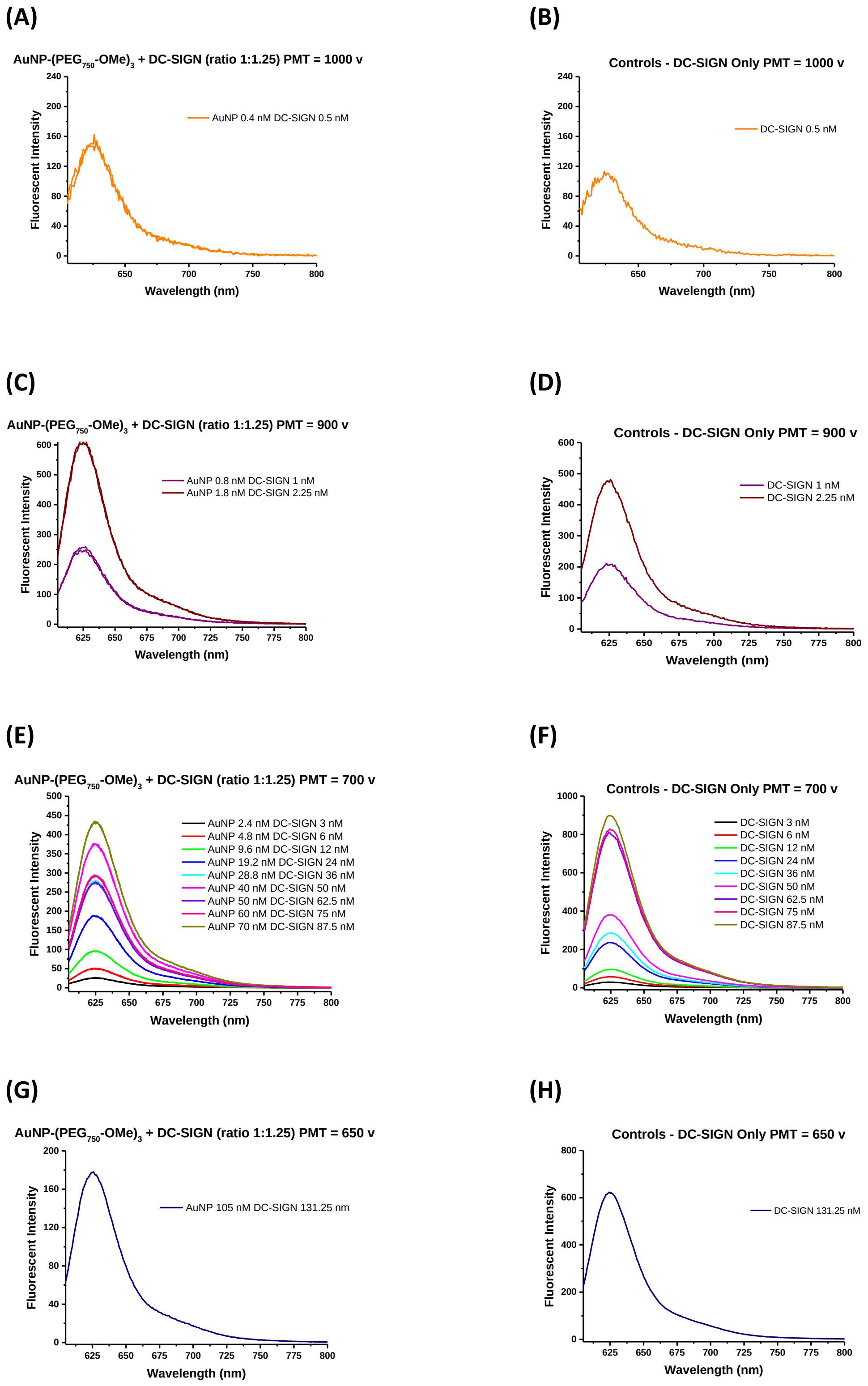

Figure A.6.8: Fluorescence Measurements for **(A)** AuNP-(PEG$_{750}$-OMe)$_3$ (0.4 nM) + DC-SIGN (0.5 nM), **(C)** AuNP-(PEG$_{750}$-OMe)$_3$ (0.8 – 1.8 nM) + DC-SIGN (1 – 2.25 nM), **(E)** AuNP-(PEG$_{750}$-OMe)$_3$ (2.4 – 70 nM) + DC-SIGN (3 – 87.5 nM), **(G)** AuNP-(PEG$_{750}$-OMe)$_3$ (105 nM) + DC-SIGN (131.25 nM) and **(B)**, **(D), (F)** and **(H)** Control DC-SIGN was used at the same concentrations and machine settings

A.6.2 DC-SIGNR

AuNP-(EG$_2$-Man)$_2$:

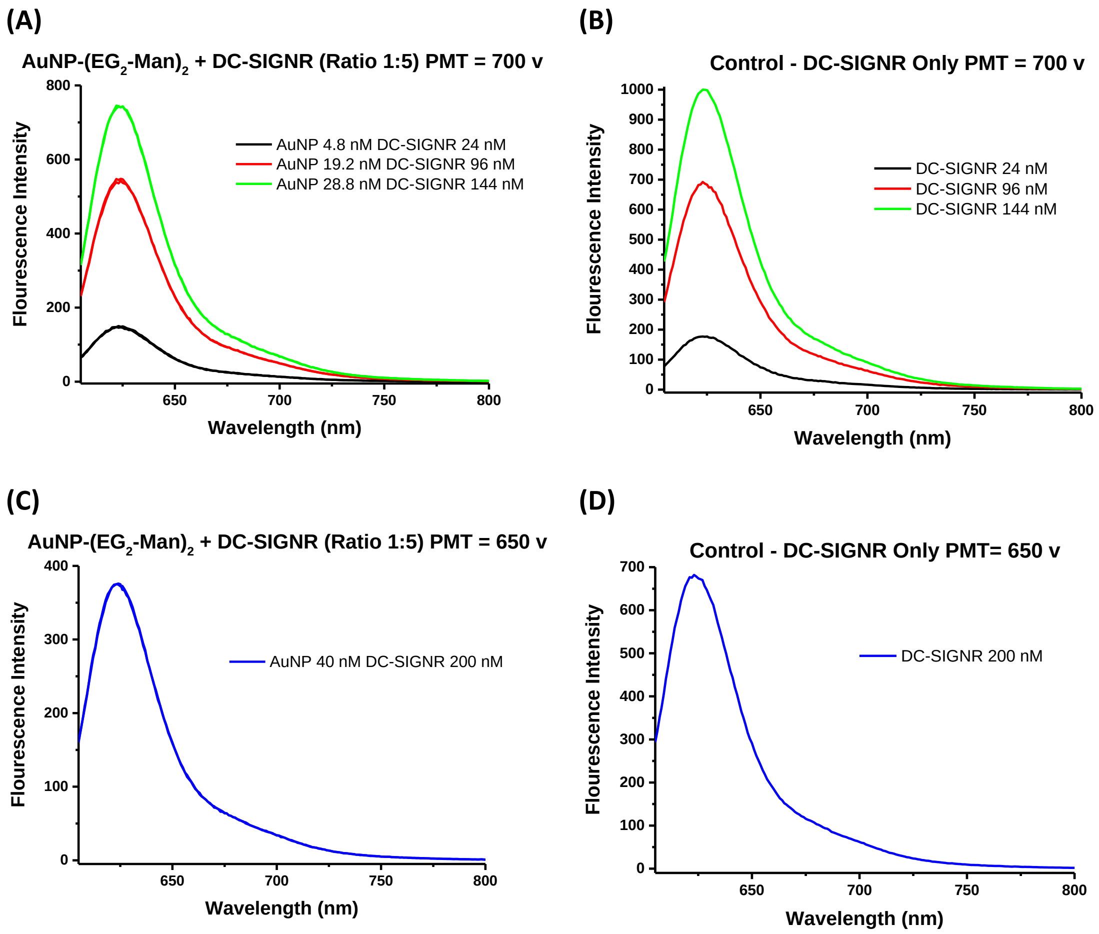

Figure A.6.9: Fluorescence Measurements between 605 – 800 nm for **(A)** AuNP-(EG$_2$-Man)$_2$ (4.8 – 28.8 nM) + labelled DC-SIGNR (24 – 144 nM), **(C)** AuNP-(EG$_2$-Man)$_2$ (40 nM) + labelled DC-SIGNR (200 nM) and **(B)** and **(D)** Control samples where only labelled DC-SIGN was used at the same concentrations and the same machine settings.

AuNP-(EG-Man)$_3$:

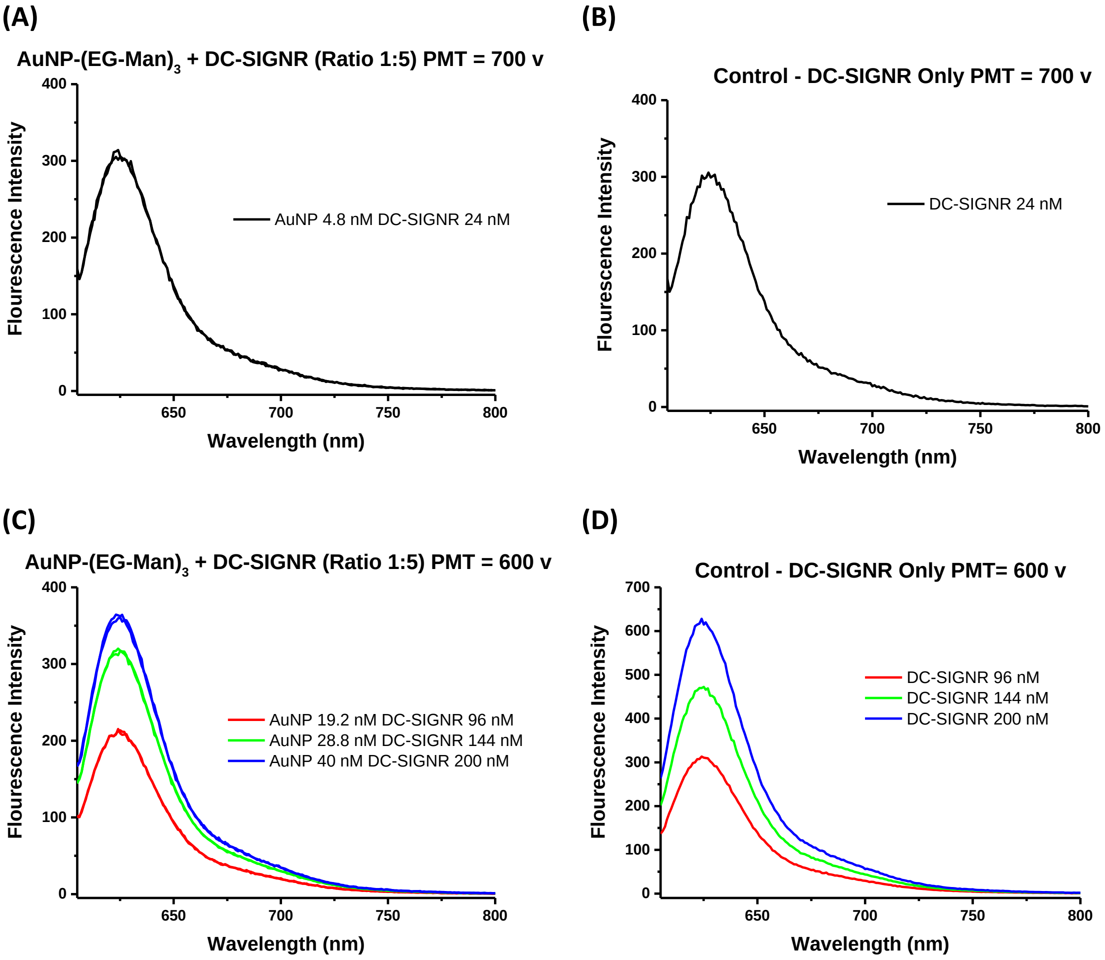

Figure A.6.10: Fluorescence Measurements between 605 – 800 nm for **(A)** AuNP-(EG-Man)$_3$ (4.8 nM) + labelled DC-SIGNR (24 nM), **(C)** AuNP-(EG-Man)$_3$ (19.2 – 40 nM) + labelled DC-SIGNR (96 – 200 nM) and **(B)** and **(D)** Control samples where only labelled DC-SIGN was used at the same concentrations and the same machine settings

AuNP-EG$_2$-DiMan:

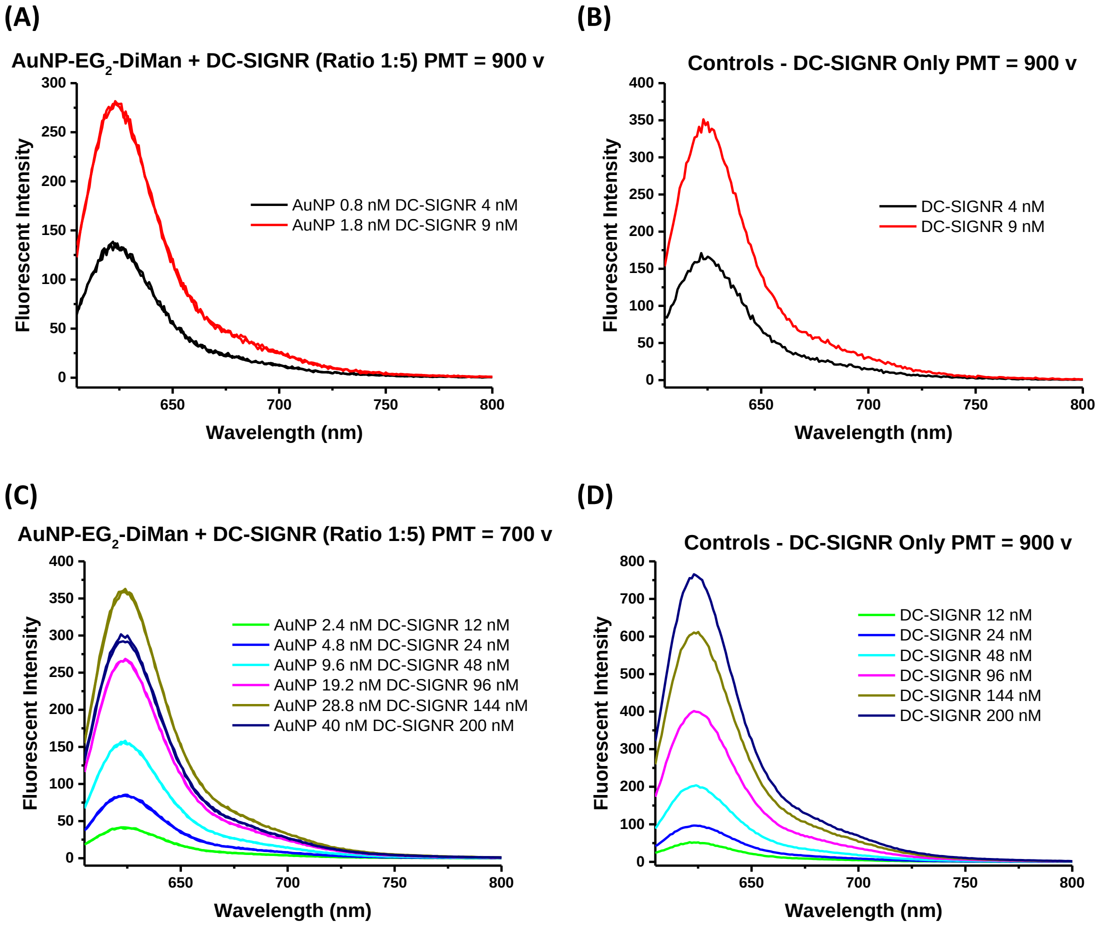

Figure A.6.11: Fluorescence Measurements between 605 – 800 nm for **(A)** AuNP-EG$_2$-DiMan (0.8 – 1.8 nM) + labelled DC-SIGNR (4 – 9 nM), **(C)** AuNP-EG$_2$-DiMan (2.4 – 40 nM) + labelled DC-SIGNR (12 – 200 nM) and **(B)** and **(D)** Control samples where only labelled DC-SIGN was used at the same concentrations and the same machine settings.

AuNP-(EG$_2$-DiMan)$_2$:

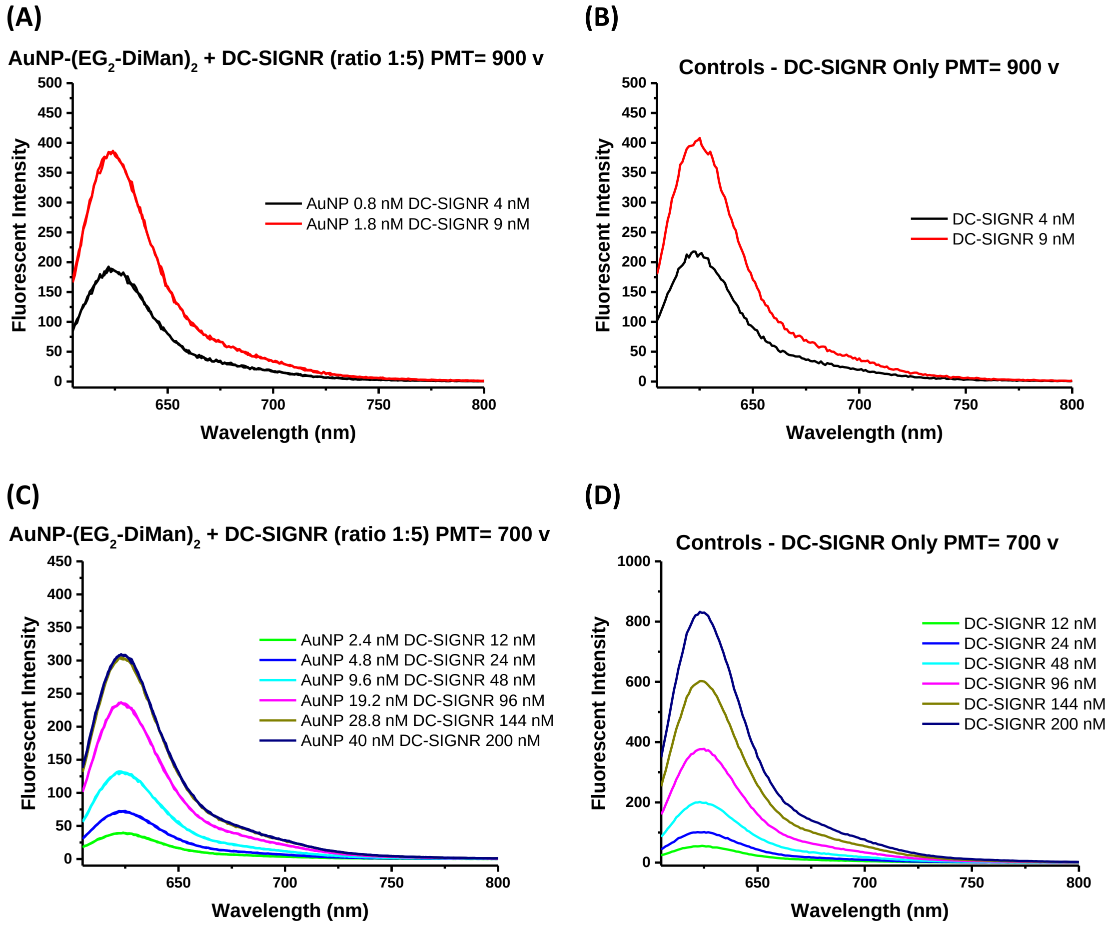

Figure A.6.12: Fluorescence Measurements between 605 – 800 nm for **(A)** AuNP-(EG$_2$-DiMan)$_2$ (0.8 – 1.8 nM) + labelled DC-SIGNR (4 – 9 nM), **(C)** AuNP-(EG$_2$-DiMan)$_2$ (2.4 – 40 nM) + labelled DC-SIGNR (12 – 200 nM) and **(B)** and **(D)** Control samples where only labelled DC-SIGNR was used at the same concentrations and the same machine settings.

AuNP-(EG-DiMan)$_3$:

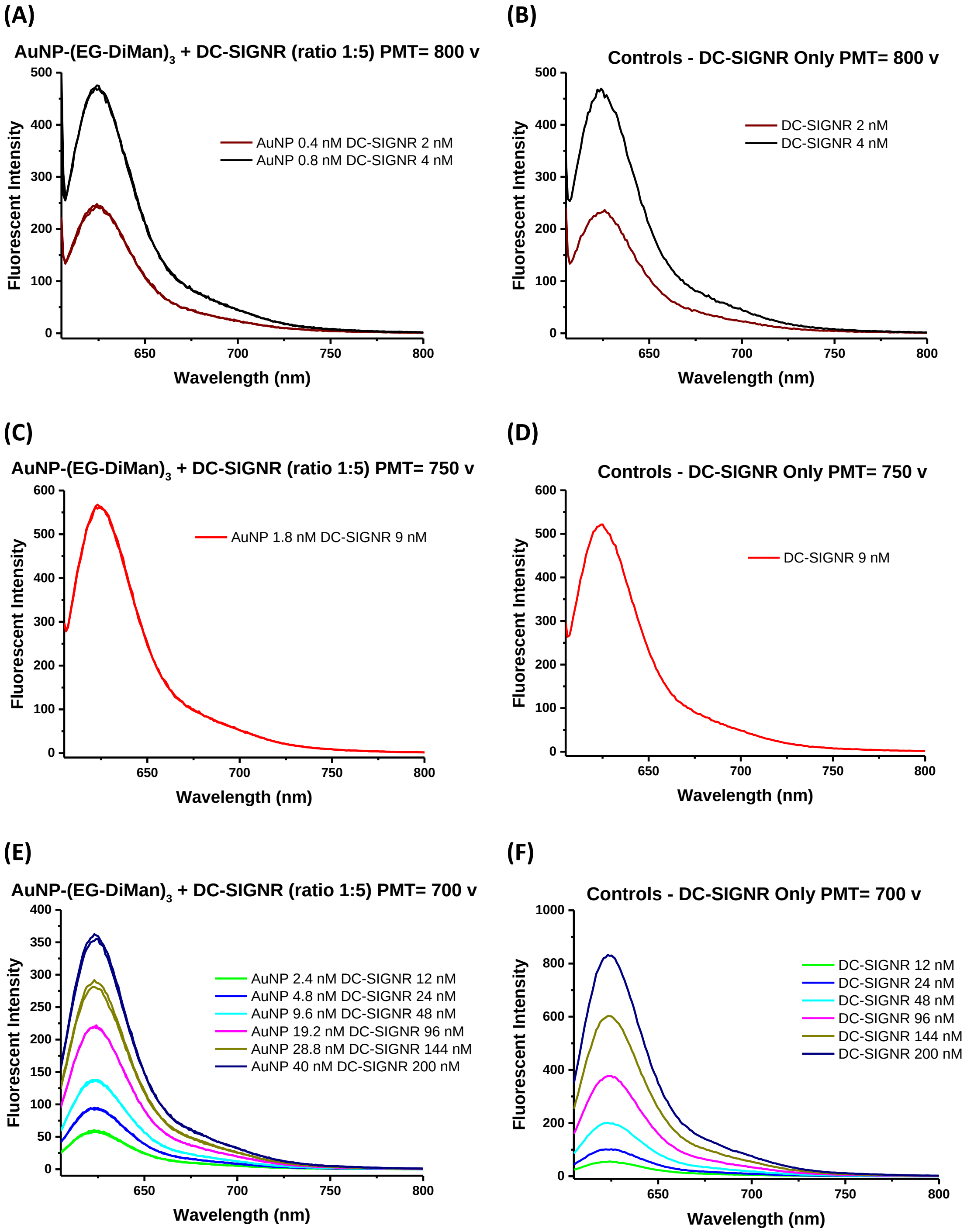

Figure A.6.13: Fluorescence Measurements between 605 – 800 nm for **(A)** AuNP-(EG-DiMan)$_3$ (0.4 – 0.8 nM) + labelled DC-SIGNR (2 – 4 nM), **(C)** AuNP-(EG-DiMan)$_3$ (1.8 nM) + labelled DC-SIGNR (9 nM), **(E)** AuNP-(EG-DiMan)$_3$ (2.4 – 40 nM) + labelled DC-SIGNR (12 – 200 nM) and **(B)**, **(D)** and **(F)** Control samples where only labelled DC-SIGN was used at the same concentrations and the same machine settings.

AuNP-PEG$_{750}$-OMe:

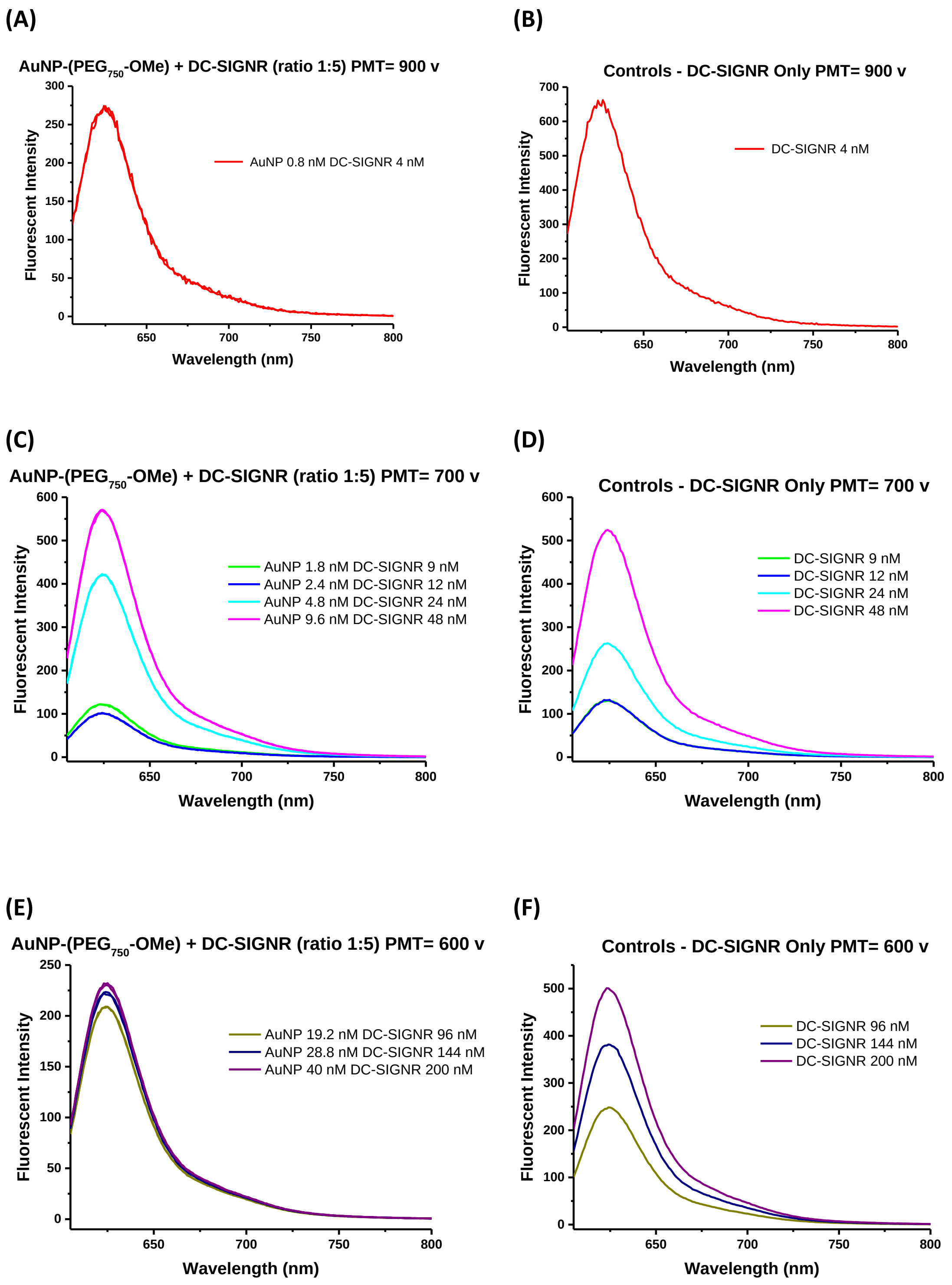

Figure A.6.14: Fluorescence Measurements between 605 – 800 nm for **(A)** AuNP-PEG$_{750}$-OMe (0.8 nM) + labelled DC-SIGNR (4 nM), **(C)** AuNP-PEG$_{750}$-OMe (1.8 – 9.6 nM) + labelled DC-SIGNR (9 – 48 nM), **(E)** AuNP-PEG$_{750}$-OMe (19.2 – 40 nM) + labelled DC-SIGNR (96 – 200 nM) and **(B), (D)** and **(F)** Control samples where only labelled DC-SIGN was used at the same concentrations and the same machine settings.

AuNP-(PEG$_{750}$-OMe)$_2$:

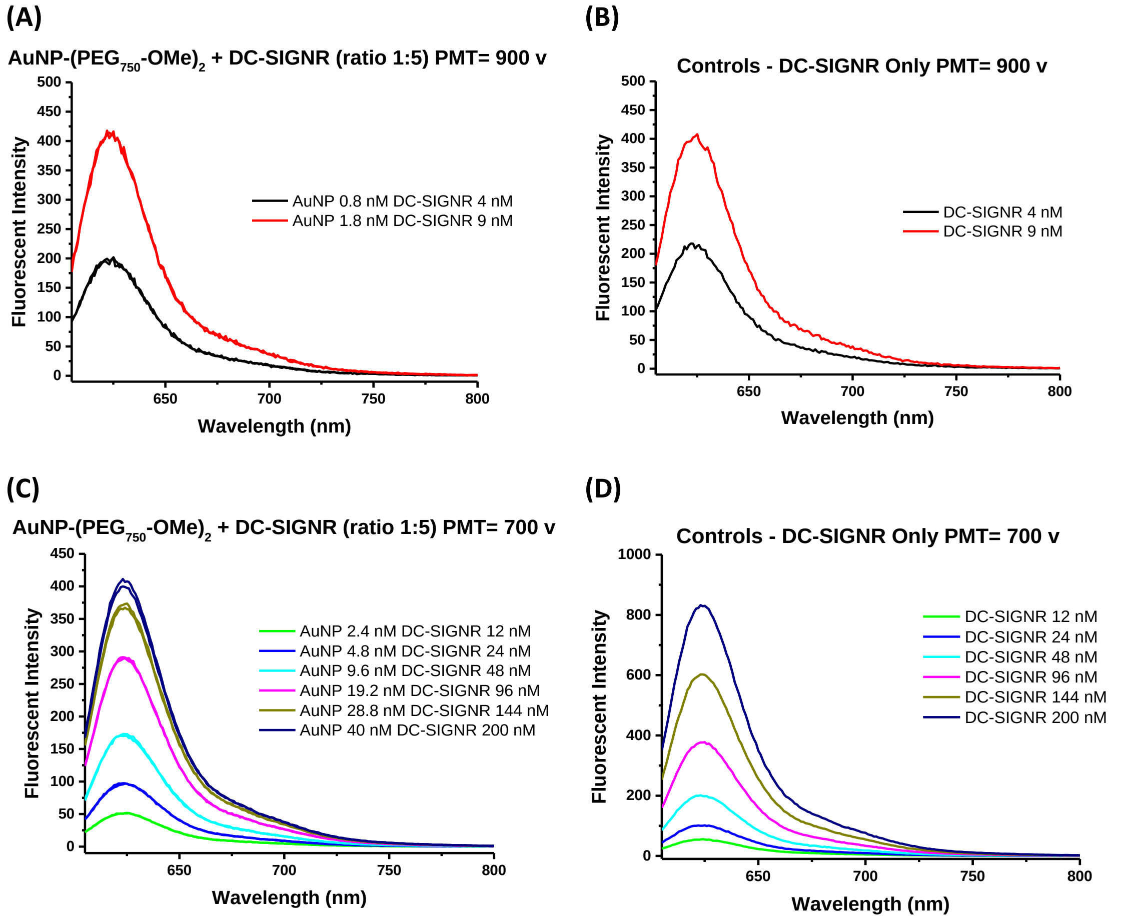

Figure A.6.15: Fluorescence Measurements between 605 – 800 nm for **(A)** AuNP-(PEG$_{750}$-OMe)$_2$ (0.8 – 1.8 nM) + labelled DC-SIGNR (4 – 9 nM), **(C)** AuNP-(PEG$_{750}$-OMe)$_2$ (2.4 – 40 nM) + labelled DC-SIGNR (12 – 200 nM) and **(B)** and **(D)** Control samples where only labelled DC-SIGN was used at the same concentrations and the same machine settings.

AuNP-(PEG$_{750}$-OMe)$_3$:

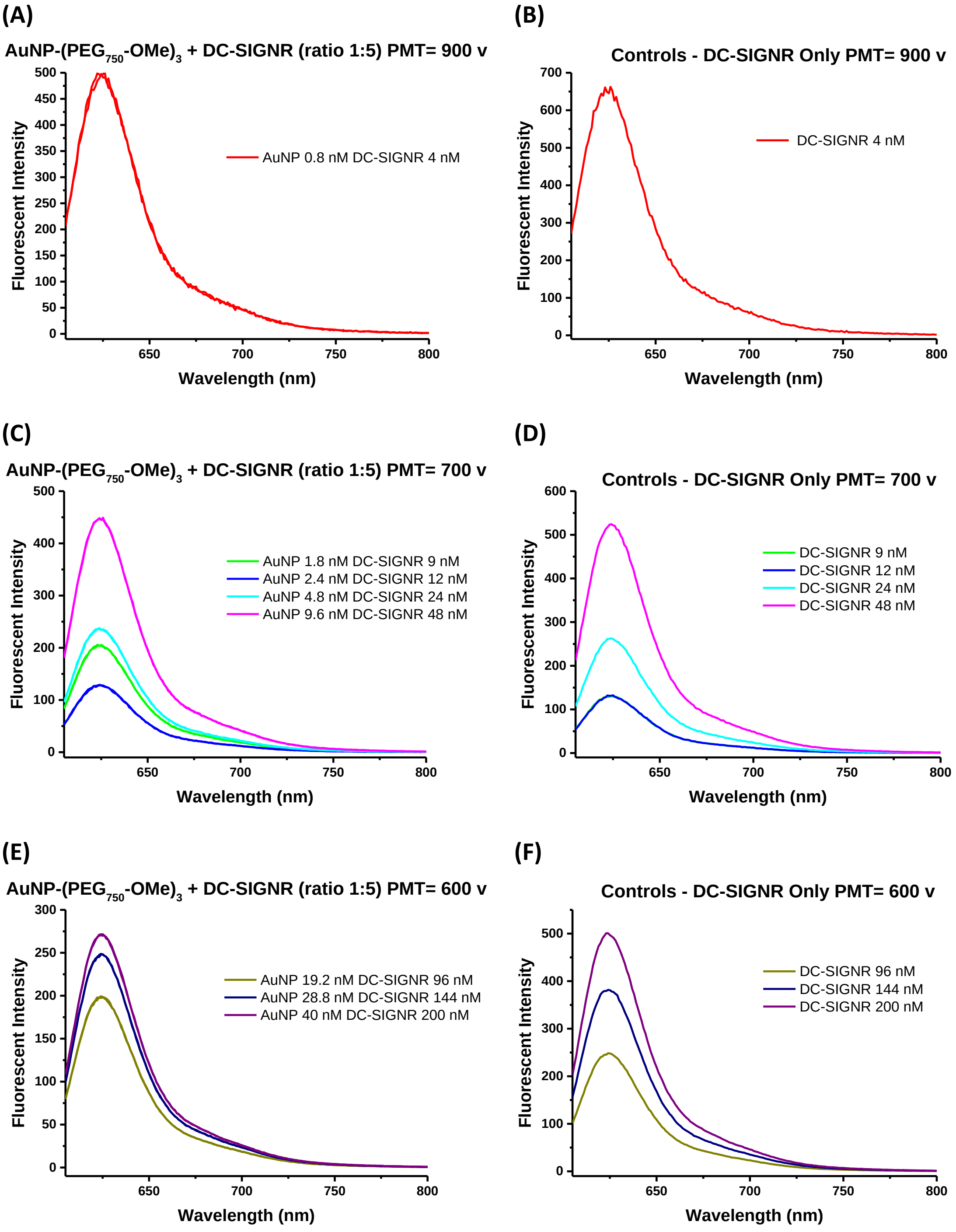

Figure A.6.16: Fluorescence Measurements between 605 – 800 nm for **(A)** AuNP-(PEG$_{750}$-OMe)$_3$ (0.8 nM) + labelled DC-SIGNR (4 nM), **(C)** AuNP-(PEG$_{750}$-OMe)$_3$ (1.8 – 9.6 nM) + labelled DC-SIGNR (9 – 48 nM), **(E)** AuNP-(PEG$_{750}$-OMe)$_3$ (19.2 – 40 nM) + labelled DC-SIGNR (96 – 200 nM) and **(B)**, **(D)** and **(E)** Control samples where only labelled DC-SIGN was used at the same concentrations and the same machine settings.

A.7 AuNP + DC-SIGN/R Hydrodynamic Sizes

A.7.1 DC-SIGN (1:15 AuNP: Protein Ratio)

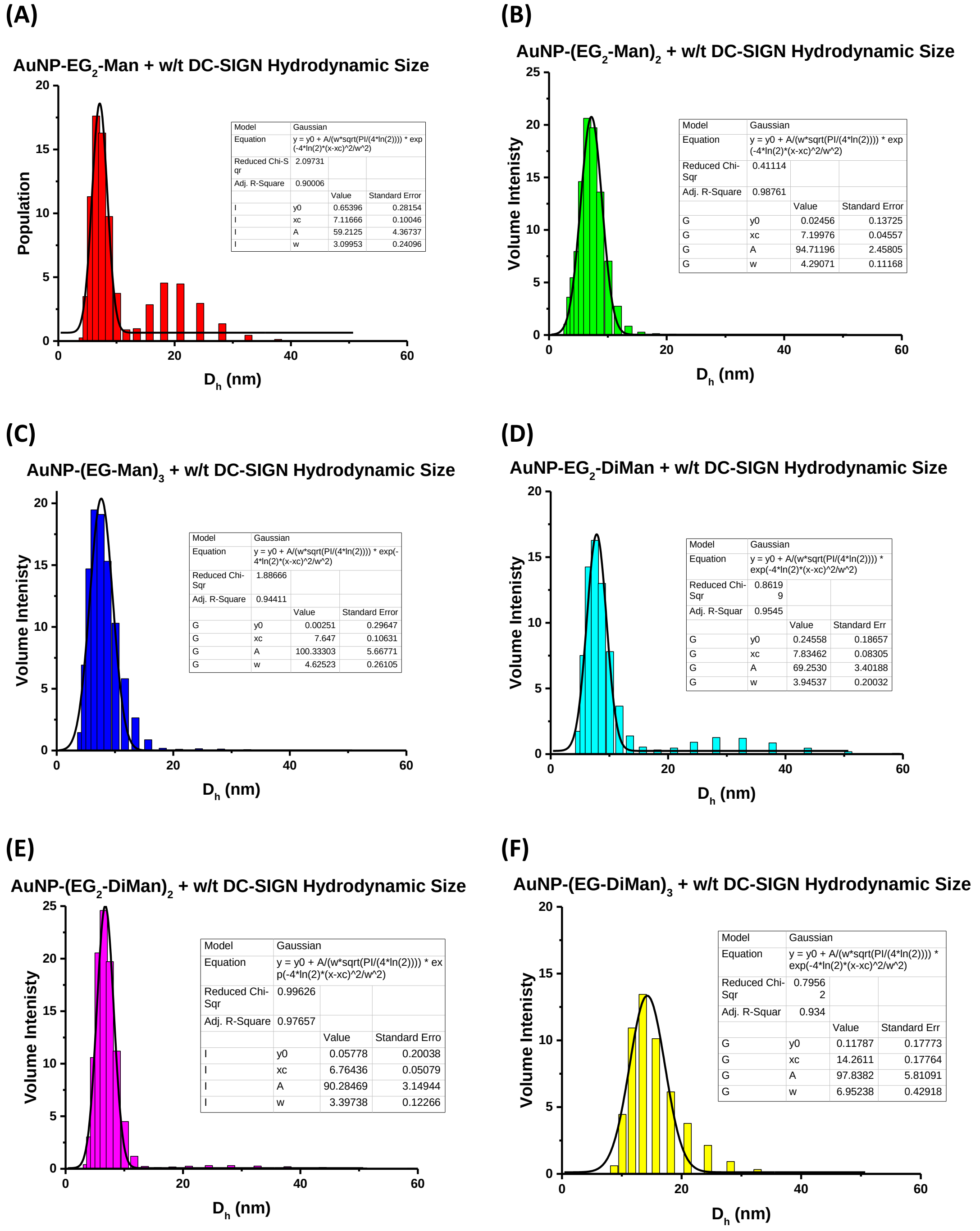

Figure A.7.1: Shows the resulting histograms of the range of hydrodynamic size for glycan AuNP- DC-SIGN interactions, using an AuNP: Proetin ratio of 1:15 **(A)** AuNP-EG_2-Man, **(B)** AuNP-(EG_2-Man)$_2$, **(C)** AuNP-(EG-Man)$_3$, **(D)** AuNP-EG_2-DiMan, **(E)** AuNP-(EG_2-DiMan)$_2$ and finally **(F)** AuNP-(EG-DiMan)$_3$.

A.7.2 DC-SIGN (1:3.75 AuNP: Protein Ratio)

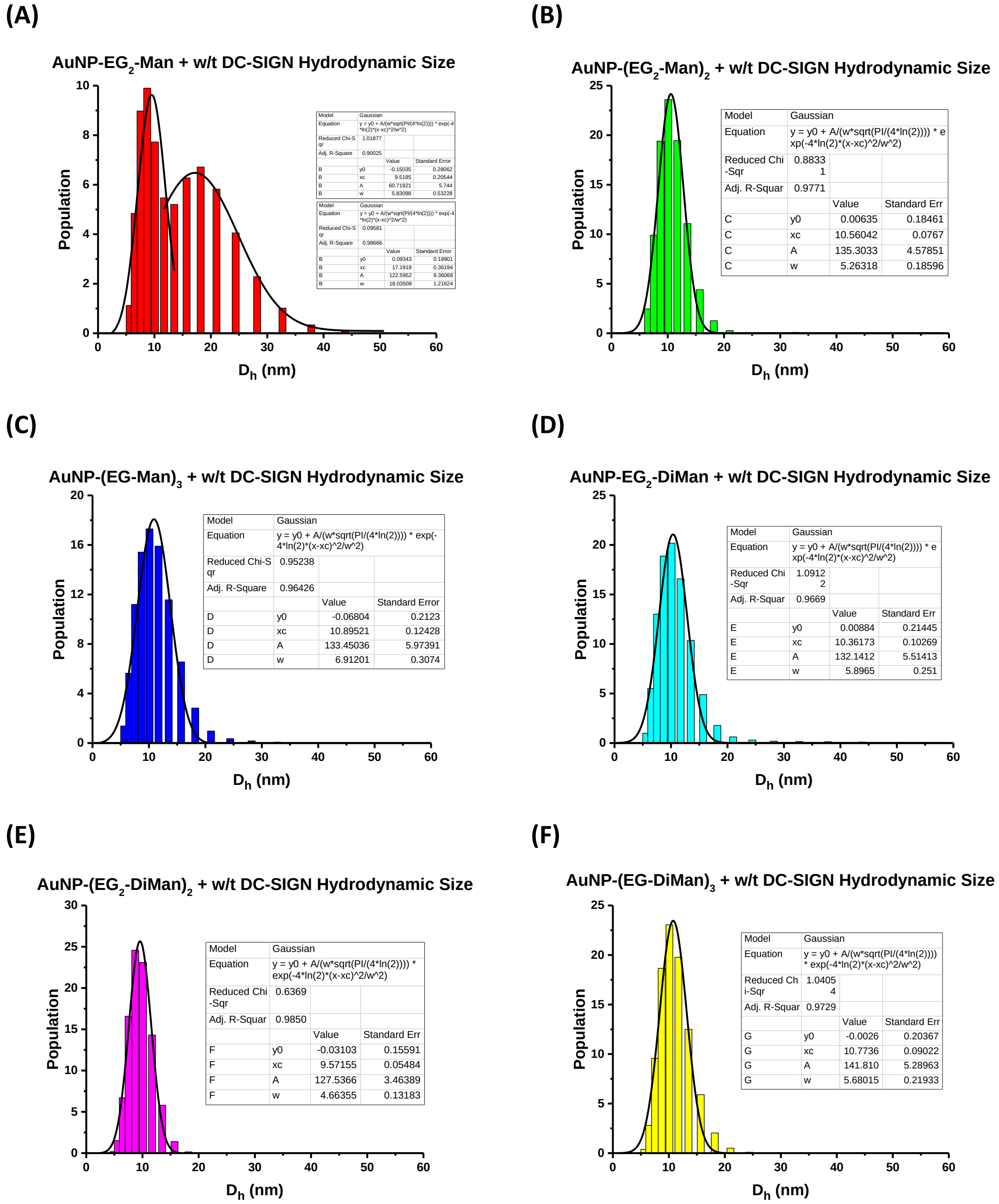

Model	Gaussian		
Equation	y = y0 + A/(w*sqrt(PI/(4*ln(2)))) * exp(-4*ln(2)*(x-xc)^2/w^2)		
Reduced Chi-Sqr	1.01877		
Adj. R-Square	0.90025		
		Value	Standard Error
B	y0	-0.15035	0.28062
B	xc	9.5185	0.20544
B	A	60.71921	5.744
B	w	5.83098	0.53228

Model	Gaussian		
Equation	y = y0 + A/(w*sqrt(PI/(4*ln(2)))) * exp(-4*ln(2)*(x-xc)^2/w^2)		
Reduced Chi-Sqr	0.09581		
Adj. R-Square	0.98666		
		Value	Standard Error
B	y0	0.09343	0.18901
B	xc	17.1919	0.36194
B	A	122.5952	9.36068
B	w	18.03508	1.21624

Model	Gaussian		
Equation	y = y0 + A/(w*sqrt(PI/(4*ln(2)))) * exp(-4*ln(2)*(x-xc)^2/w^2)		
Reduced Chi-Sqr	0.88331		
Adj. R-Squar	0.9771		
		Value	Standard Err
C	y0	0.00635	0.18461
C	xc	10.56042	0.0767
C	A	135.3033	4.57851
C	w	5.26318	0.18596

Model	Gaussian		
Equation	y = y0 + A/(w*sqrt(PI/(4*ln(2)))) * exp(-4*ln(2)*(x-xc)^2/w^2)		
Reduced Chi-Sqr	0.95238		
Adj. R-Square	0.96426		
		Value	Standard Error
D	y0	-0.06804	0.2123
D	xc	10.89521	0.12428
D	A	133.45036	5.97391
D	w	6.91201	0.3074

Model	Gaussian		
Equation	y = y0 + A/(w*sqrt(PI/(4*ln(2)))) * exp(-4*ln(2)*(x-xc)^2/w^2)		
Reduced Chi-Sqr	1.09122		
Adj. R-Squar	0.9669		
		Value	Standard Err
E	y0	0.00884	0.21445
E	xc	10.36173	0.10269
E	A	132.1412	5.51413
E	w	5.8965	0.251

Model	Gaussian		
Equation	y = y0 + A/(w*sqrt(PI/(4*ln(2)))) * exp(-4*ln(2)*(x-xc)^2/w^2)		
Reduced Chi-Sqr	0.6369		
Adj. R-Squar	0.9850		
		Value	Standard Err
F	y0	-0.03103	0.15591
F	xc	9.57155	0.05484
F	A	127.5366	3.46389
F	w	4.66355	0.13183

Model	Gaussian		
Equation	y = y0 + A/(w*sqrt(PI/(4*ln(2)))) * exp(-4*ln(2)*(x-xc)^2/w^2)		
Reduced Chi-Sqr	1.04054		
Adj. R-Squar	0.9729		
		Value	Standard Err
G	y0	-0.0026	0.20367
G	xc	10.7736	0.09022
G	A	141.810	5.28963
G	w	5.68015	0.21933

Figure A.7.2: Shows the resulting histograms of the range of hydrodynamic size for glycan AuNP- DC-SIGN interactions, using an AuNP: Proetin ratio of 1:3.75 **(A)** AuNP-EG$_2$-Man, **(B)** AuNP-(EG$_2$-Man)$_2$, **(C)** AuNP-(EG-Man)$_3$, **(D)** AuNP-EG$_2$-DiMan, **(E)** AuNP-(EG$_2$-DiMan)$_2$ and finally **(F)** AuNP-(EG-DiMan)$_3$

A.7.3 DC-SIGNR (1:15 AuNP: Protein Ratio)

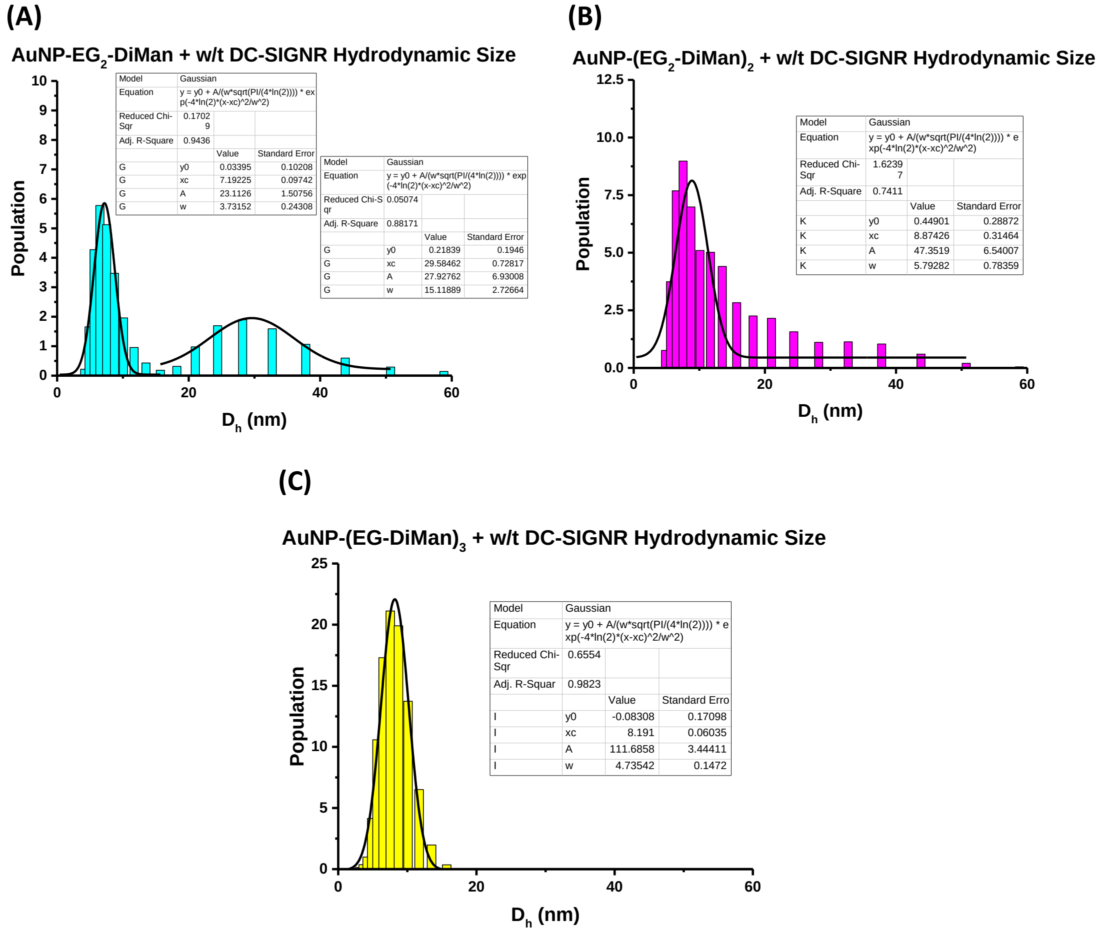

Model	Gaussian		
Equation	y = y0 + A/(w*sqrt(PI/(4*ln(2)))) * exp(-4*ln(2)*(x-xc)^2/w^2)		
Reduced Chi-Sqr	0.17029		
Adj. R-Square	0.9436		
		Value	Standard Error
G	y0	0.03395	0.10208
G	xc	7.19225	0.09742
G	A	23.1126	1.50756
G	w	3.73152	0.24308

Model	Gaussian		
Equation	y = y0 + A/(w*sqrt(PI/(4*ln(2)))) * exp(-4*ln(2)*(x-xc)^2/w^2)		
Reduced Chi-Sqr	0.05074		
Adj. R-Square	0.88171		
		Value	Standard Error
G	y0	0.21839	0.1946
G	xc	29.58462	0.72817
G	A	27.92762	6.93008
G	w	15.11889	2.72664

Model	Gaussian		
Equation	y = y0 + A/(w*sqrt(PI/(4*ln(2)))) * exp(-4*ln(2)*(x-xc)^2/w^2)		
Reduced Chi-Sqr	1.62397		
Adj. R-Square	0.7411		
		Value	Standard Error
K	y0	0.44901	0.28872
K	xc	8.87426	0.31464
K	A	47.3519	6.54007
K	w	5.79282	0.78359

Model	Gaussian		
Equation	y = y0 + A/(w*sqrt(PI/(4*ln(2)))) * exp(-4*ln(2)*(x-xc)^2/w^2)		
Reduced Chi-Sqr	0.6554		
Adj. R-Squar	0.9823		
		Value	Standard Erro
I	y0	-0.08308	0.17098
I	xc	8.191	0.06035
I	A	111.6858	3.44411
I	w	4.73542	0.1472

Figure A.7.3: Shows the resulting histograms of the range of hydrodynamic size for glycan AuNP- DC-SIGNR interactions, using a 1:15 AuNP: Protein ratio: **(A)** AuNP-EG$_2$-DiMan, **(B)** AuNP-(EG$_2$-DiMan)$_2$ and **(C)** AuNP-(EG-DiMan)$_3$.

A.7.4 DC-SIGNR (1:7.5 AuNP: Protein Ratio)

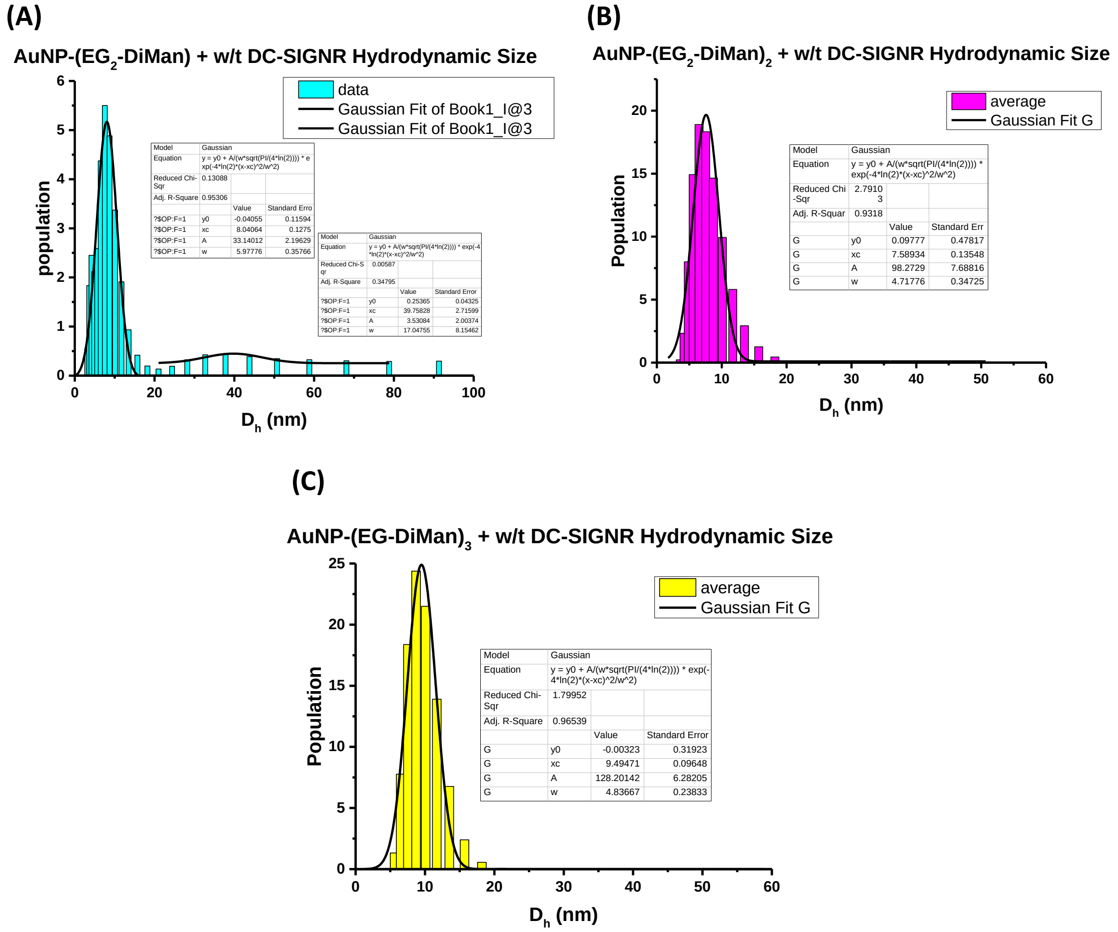

Model	Gaussian		
Equation	y = y0 + A/(w*sqrt(PI/(4*ln(2)))) * exp(-4*ln(2)*(x-xc)^2/w^2)		
Reduced Chi-Sqr	0.13088		
Adj. R-Square	0.95306		
		Value	Standard Erro
?$OP:F=1	y0	-0.04055	0.11594
?$OP:F=1	xc	8.04064	0.1275
?$OP:F=1	A	33.14012	2.19629
?$OP:F=1	w	5.97776	0.35766

Model	Gaussian		
Equation	y = y0 + A/(w*sqrt(PI/(4*ln(2)))) * exp(-4*ln(2)*(x-xc)^2/w^2)		
Reduced Chi-Sqr	0.00587		
Adj. R-Square	0.34795		
		Value	Standard Error
?$OP:F=1	y0	0.25365	0.04325
?$OP:F=1	xc	39.75828	2.71599
?$OP:F=1	A	3.53084	2.00374
?$OP:F=1	w	17.04755	8.15462

Model	Gaussian		
Equation	y = y0 + A/(w*sqrt(PI/(4*ln(2)))) * exp(-4*ln(2)*(x-xc)^2/w^2)		
Reduced Chi-Sqr	2.79103		
Adj. R-Squar	0.9318		
		Value	Standard Err
G	y0	0.09777	0.47817
G	xc	7.58934	0.13548
G	A	98.2729	7.68816
G	w	4.71776	0.34725

Model	Gaussian		
Equation	y = y0 + A/(w*sqrt(PI/(4*ln(2)))) * exp(-4*ln(2)*(x-xc)^2/w^2)		
Reduced Chi-Sqr	1.79952		
Adj. R-Square	0.96539		
		Value	Standard Error
G	y0	-0.00323	0.31923
G	xc	9.49471	0.09648
G	A	128.20142	6.28205
G	w	4.83667	0.23833

Figure A.7.4: Histograms of the range of hydrodynamic size for glycan AuNP- DC-SIGNR interactions, using a 1:7.5 AuNP: Protein ratio: **(A)** AuNP-EG$_2$-DiMan, **(B)** AuNP-(EG$_2$-DiMan)$_2$ and **(C)** AuNP-(EG-DiMan)$_3$.

A.8 Viral Inhibition Studies – Control Glycoproteins

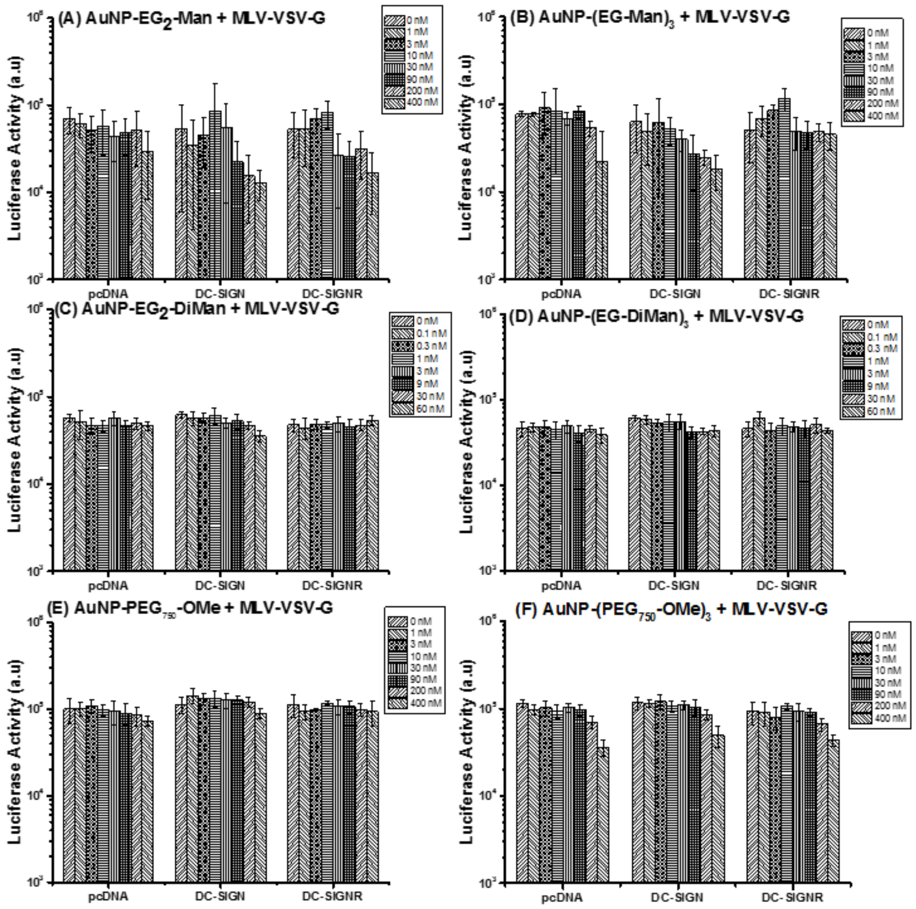

Figure A.8.1: Human embryonic kidney cells (293 T) were transfected with the identified plasmids and pre incubated with AuNP-EG$_2$-Man (**A**), AuNP-(EG-Man)$_3$ (**B**), AuNP-EG$_2$-DiMan (**C**), AuNP-(EG-DiMan)$_3$ (**D**), AuNP-PEG$_{750}$-OMe (**E**), AuNP-(PEG$_{750}$-OMe)$_3$ (**F**) and inoculated with Murine Leukemia Virus (MLV) particles modified to contain the control, vesicular stomatitis virus glycoprotein (VSV-G). The inhibitor concentrations were calculated after addition of particles. Luciferase activities in cell lysates were measured at 72 hrs post-transduction.

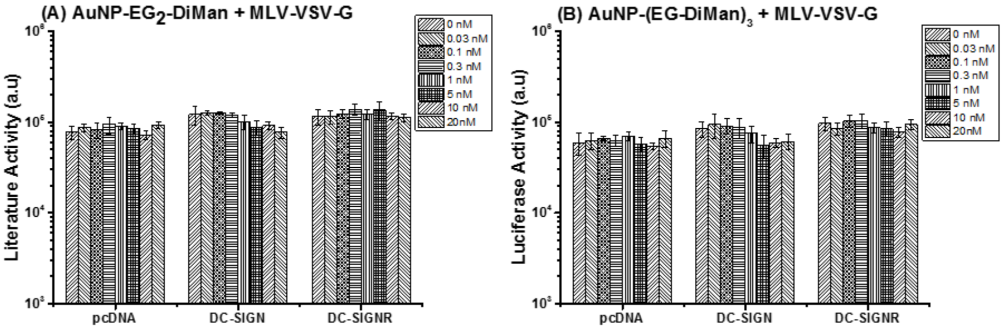

Figure A.8.2: Human embryonic kidney cells (293 T) were transfected with the identified plasmids and pre incubated with AuNP-EG$_2$-DiMan (**A**) and AuNP-(EG-DiMan)$_3$ (**B**) repeats at lower concentration and inoculated with Murine Leukemia Virus (MLV) particles modified to contain the control, vesicular stomatitis virus glycoprotein (VSV-G). The inhibitor concentrations were calculated after addition of particles. Luciferase activities in cell lysates were measured at 72 hrs post-transduction.

A.9 Viral Inhibition Studies – Initial DiMan + EBOV-GP

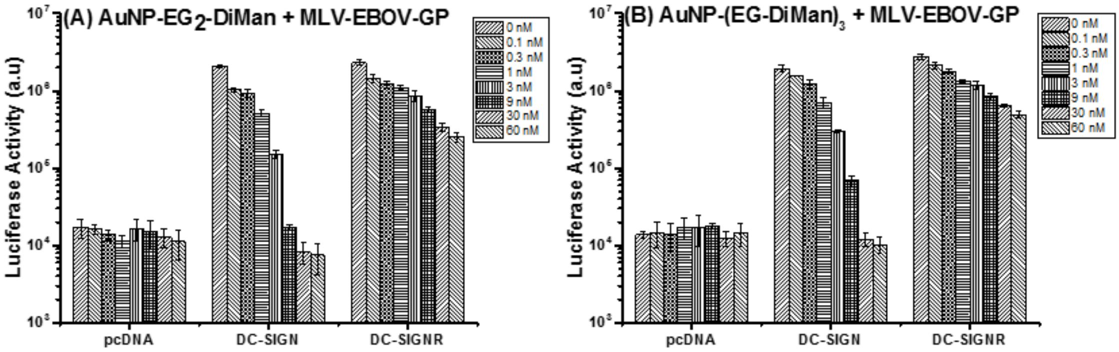

Figure A.9.1: Human embryonic kidney cells (293 T) were transfected with the identified plasmids and pre incubated with AuNP-EG$_2$-DiMan (**A**) and AuNP-(EG-DiMan)$_3$ (**B**) and inoculated with Murine Leukemia Virus (MLV) particles modified to contain the control, vesicular stomatitis virus glycoprotein (VSV-G). The inhibitor concentrations were calculated after addition of particles. Luciferase activities in cell lysates were measured at 72 hrs post-transduction.

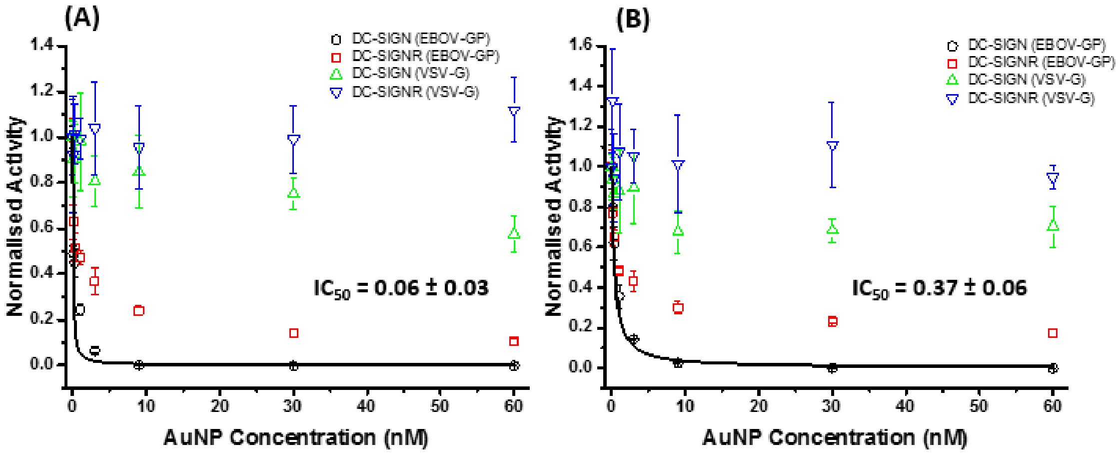

Figure A.9.2: Normalised luciferase activities of the DC-SIGN or DC-SIGNR expressing 293T cells measured as a function of the pre-treatment (**A**) AuNP-EG$_2$-DiMan and (**B**) AuNP-(EG-DiMan)$_3$ concentrations. The data shown in circles and squares correlate to the virus particles containing the EBOV-GP and the triangles to the control glycoprotein (VSV-G). Data was fitted using a comparable competitive binding model